FLORIDA INTERNATIONAL UNIVERSITY

Miami, Florida

EVALUATION OF CONCRETE PILE TO FOOTING OR CAP CONNECTIONS

A dissertation submitted in partial fulfillment of

the requirements for the degree of

DOCTOR OF PHILOSOPHY

in

CIVIL ENGINEERING

by

Isabella Rakestraw

2023

To: Dean John L. Volakis
College of Engineering and Computing

This dissertation, written by Isabella Rakestraw, and entitled Evaluation of Concrete Pile to Footing or Cap Connections, having been approved in respect to style and intellectual content, is referred to you for judgment.

We have read this dissertation and recommend that it be approved.

_____
Armin Mehrabi

_____
Seung Jae Lee

_____
Kingsley Lau

_____
Wallied Orabi

_____
David Garber, Major Professor

Date of Defense: June 27, 2023

The dissertation of Isabella Rakestraw is approved.

_____
Dean John L. Volakis
College of Engineering and Computing

_____
Andrés G. Gil

Vice President for Research and Economic Development
and Dean of the University Graduate School

Florida International University, 2023

DEDICATION

To my parents for giving me the opportunity to study abroad,

and to my husband for all the support throughout this journey.

ACKNOWLEDGMENTS

I would like to express my gratitude to my advisor Dr. David Garber for the opportunity to work on this project and for providing invaluable guidance throughout the years.

I would also like to thank the Florida Department of Transportation for providing the funding that made this project possible. Special thanks to Christina Freeman, and Olga Iatsko for their support and technical contributions to the project. Also, special gratitude to the team of engineers and staff at the Marcus H. Ansley Structure Research Center for their efforts on instrumentation, construction, and testing of the specimens throughout this research.

ABSTRACT OF THE DISSERTATION

EVALUATION OF CONCRETE PILE TO FOOTING OR CAP CONNECTIONS

by

Isabella Rakestraw

Florida International University, 2023

Miami, Florida

Professor David Garber, Major Professor

Foundations for many bridges consist of driven piles embedded in pile caps or footings whereby axial loads, lateral loads and moments are transferred from the bridge to underlying soil and/or bedrock. The connection between the pile and pile cap will affect the way forces are transferred through the bridge. The pile-to-cap connection is typically either assumed to be a pinned or a fixed connection. Current design recommendations for pinned and fixed connections vary in different states. Assuming a different level of fixity between pile and pile cap can lead to undesirable behavior of a structure. The disconnect between current design provisions and past research would suggest that many structures may have a different level of actual fixity between piles and pile caps than assumed.

The primary objective of this research is to better understand the connection between the pile and pile cap, to analyze the impact of the connection in the overall structure, and to provide a better guidance to engineers. These objectives were accomplished through three interdependent research efforts, which included a literature review of previous research; an analytical investigation and numerical modeling to explore possible experimental

variables; and an experimental testing to evaluate the level of fixity and impact of primary variables.

Experimental testing was completed involving ten prestressed concrete pile specimens embedded into cast-in-place pile caps. Two different square pile sizes were investigated, 18-inch and 30-inch, that were simply embedded into the pile cap to lengths between 0.25 and 1.5 times the diameter of the piles. The tests were conducted to determine the moment capacity of the connection at failure. In all cases, the capacity of the connection was higher than expected due to the confining stress provided by the pile cap, which tends to decrease the development length of the strands.

Recent research has shown that current design recommendations can be conservative under certain circumstances, e.g., a fixed connection can be achieved with a much shorted embedment length. A better design guidance of the connection between precast prestressed concrete piles and cast-in-place pile caps is needed to assure designs are completed correctly and conservatively.

TABLE OF CONTENTS

LIST OF TABLES

LIST OF FIGURES

FIGURE PAGE

1. INTRODUCTION

1.1. BACKGROUND

Foundations for many bridges consist of driven piles embedded in pile caps or footing whereby axial loads, lateral loads and moments are transferred from the bridge to underlying soil and/or bedrock. Piles can also be subjected to large lateral deflections in the event of an earthquake or vessel impact, which can result in high local curvature and moment demands at various locations along the pile lengths.

The connection between the pile and pile cap or footing will affect the way forces are transferred through the bridge. Bridge superstructure can transfer axial loads, lateral loads, and moments. This connection is typically either assumed to be a pinned connection, allowing for transfer of axial and lateral forces but no moments, permitting some rotation to eliminate excessive moment build-up, or a fixed connection, allowing transfer of axial and lateral forces and development of the full moment capacity of the pile. The assumed connection between the pile and pile cap or footing will impact the stresses in the rest of the structure.

Currently, 24 states specify a required pile embedment length into the cast-in-place (CIP) footing or pile cap. Three of these states (Florida [1], Minnesota [2], and Wisconsin [3]) specify a pile embedment length for pinned connections of 0.5 feet or 1.0 foot. Six of these states, [1], [3]- [4] specify a pile embedment length for fixed connection between 1.0 foot and 4.0 feet with two states [5], [4] calculating required pile embedment lengths based on the plastic moment capacity of the pile about the strong axis, concrete compressive strength, and width of the pile. The other states specify a required embedment length, but

do not clarify in their specification whether that embedment detail will lead to a pinned or fixed connection behavior.

Past research, [6]-[7] has shown that even short embedment lengths (0.5 times the pile diameter or less) can achieve significant moment capacity (up to 40 to 60 percent of the moment capacity). Past researches [6], [8], [9] have also found that the full moment capacity can be developed with embedment lengths much shorter than the 4-foot embedment required by some states.

Assuming a different level of fixity between pile and pile cap or footing can lead to undesirable behavior of a structure. The disconnect between current design provisions and past research would suggest that many structures may have a different level of actual fixity between piles and pile caps or footing than assumed.

Engineers currently use these assumptions to design the connection between pile and footing or pile cap, which influences the design of the rest of the structure. Recent research has shown these assumptions are unrealistic and can be unconservative under certain circumstances, e.g., a fixed connection can be achieved with a much shorter embedment length. A better understanding of the connection between prestressed concrete piles and CIP footings and pile caps is needed to assure designs are completed correctly and conservatively.

1.2. OBJECTIVES AND SCOPE OF RESEARCH

The primary objective of this research is to better understand the connection between the pile and pile cap or footing to provide better design guidance to engineers and allow for more informed design reviews. This primary objective will require the following objectives:

1. Determine the required pile embedment length and detail to achieve pinned connection
2. Determine the required pile embedment length and detail to achieve fixed connection
3. Estimate the level of partial fixity for embedment lengths between pinned and fully fixed connections

1.3. RESEARCH METHODOLOGY

These objectives will be accomplished through three interdependent research efforts, which include a (1) literature review and synthesis, (2) analytical investigation, and (3) experimental testing. The literature review will be used to review all previous research and resources from different DOTs and provide guidance for the analytical and experimental programs. The analytical program and numerical modeling will be used to initially explore the possible experimental variables and provide guidance for the experimental work. The experimental program will be used to experimentally evaluate the level of fixity and impact of primary variables. Results from the experimental work will also be used to validate and refine the numerical models. The numerical models can then be used to investigate the impact of secondary variables not tested experimentally, develop equations for predicting level of fixity, and seeing impact on sensitive structures.

2. LITERATURE REVIEW ON PILE TO CAP CONNECTIONS

The foundation for many bridges in Florida consists of driven piles embedded in pile caps or footings. Piles transfer axial loads and moments from the bridge into the soil and bedrock. Piles can also be subjected to large lateral deflections in the event of an earthquake, which can result in high local curvature and moment demands at various locations along the pile length. Similar demand on the connections can occur during a barge impact. The typical construction procedure for this type of foundation is shown in Figure 2.1 and involves the following steps:

1. Precast piles are driven to a sufficient depth based on end bearing and side friction capacities, shown in Figure 2.1 (a). The length that the pile needs to be driven may be different from pile to pile, which may even require pile splicing to achieve longer pile lengths.
2. After all the piles have been driven, the tops of the piles are cut off, so the piles all have the same length extending from the ground, shown in Figure 2.1 (b). This length is based on the connection detail between the precast piles and pile cap or footing, specifically the required embedment length.
3. Reinforcement is placed and formwork installed around the precast piles to construct the cast-in-place pile cap or footing, shown in Figure 2.1 (c). Some states require interface reinforcement between precast pile and pile cap or footing, which would be installed at this time.

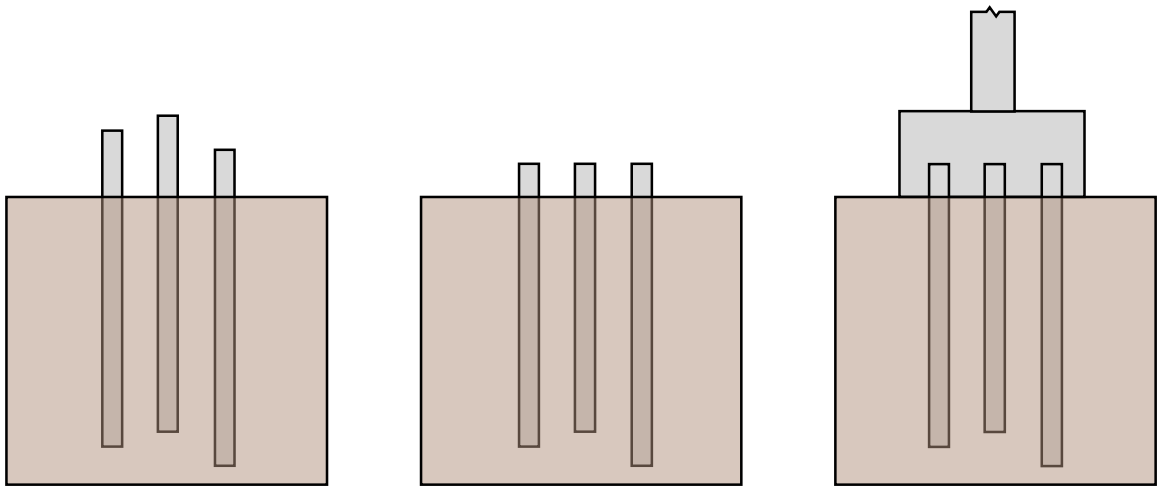

Figure 2.1:Typical construction procedure for piles with cast-in-place pile cap

The connection between the pile and pile cap or footing will affect the way forces are transferred through the bridge. Bridge superstructures can transfer axial loads, lateral loads, and moments, as shown in Figure 2.2 (a). This connection is typically either assumed to be a pinned connection, allowing for transfer of axial and lateral forces but no moments, or a fixed connection, allowing transfer of axial and lateral forces and development of the full moment capacity of the pile, as shown in Figure 2.2 (b) and (c) respectively. The assumed connection between the pile and pile cap or footing will impact the stresses in the rest of the structure.

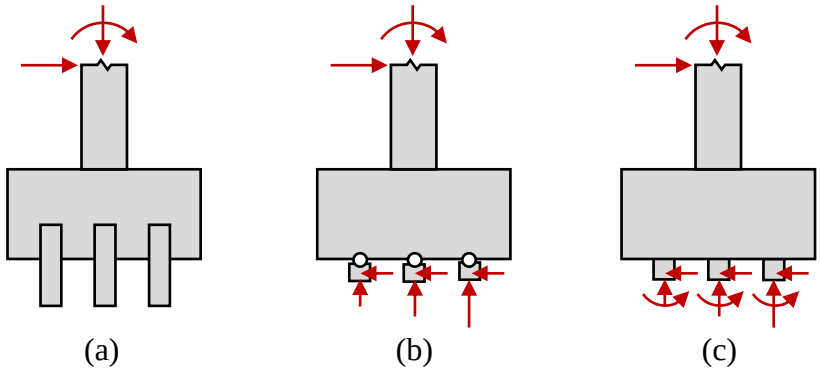

Figure 2.2: (a) Forces from the above structure assumed to be transferred to piles either through (b) pinned or (c) fixed connections

2.1. TYPES OF PRECAST PILE-TO-CAP CONNECTIONS

There are several different options for connecting precast piles to cast-in-place concrete pile caps or footings. These connections can be broken into four main categories, as shown in Figure 2.3:

1. ***Plain embedment***: This connection consists of the pile embedded directly into the pile cap with no reinforcement connecting the pile to pile cap. The surface of the pile can remain untreated or can also be intentionally roughened to different magnitudes.
2. ***Vertical or horizontal dowels***: Reinforcement can be extended from the pile into the pile cap. This reinforcement can be either vertical or horizontal and can be straight or hooked. Spiral reinforcement can also be provided around the dowels to improve their development behavior. These connections typically have shorter pile embedment lengths than plain embedment.

3. ***Pile development with spirals***: square or round spirals can be placed around the embedded pile to improve the pile development. The pile can either be untreated or have an intentionally roughened surface.
4. ***Exposed strands***: strands from the pile can be exposed and either broomed, as shown in Figure 2.3 (d) or extended straight into the cap and enclosed with spirals, similar to what is shown in Figure 2.3 (c). This type of connection typically has a shorter embedment length.

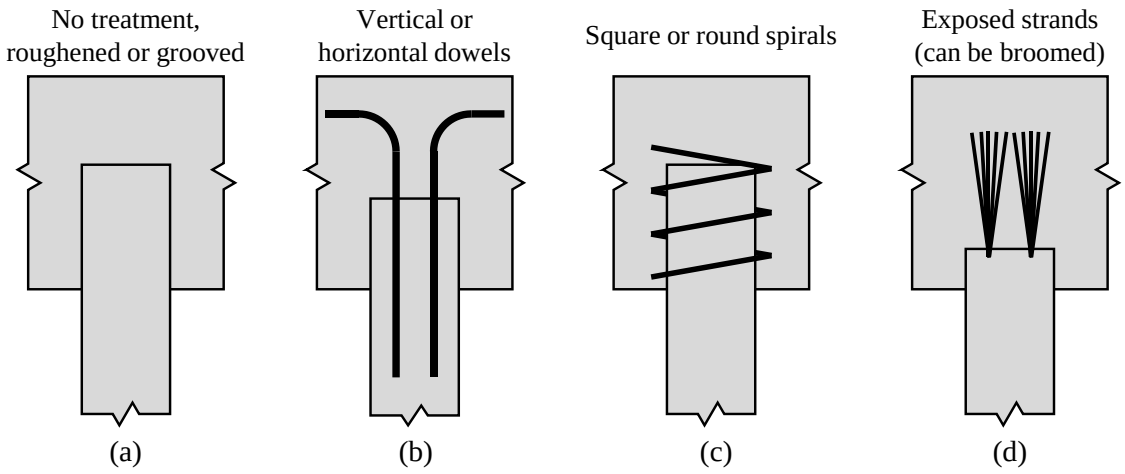

Figure 2.3: Types of pile embedment details (modified from [6] and [10])

2.2. PINNED CONNECTION BETWEEN PILE AND CAP

A pinned connection between pile and pile cap is typically required to have a positive connection between the pile and cap while still permitting some rotation to eliminate excessive moment build-up [10]. FDOT specifies a 12-inch embedment for pinned connections [1], which is based on a rule of thumb. Other states typically require pinned connections be achieved with embedment lengths between 6 and 12 inches [1].

2.2.1. Summary of Past Research

There is limited research on specifically developing a pinned connection between pile and pile cap. Rollins and Stenlund [8] experimentally investigated two connections with shallow embedments (0.5 to 1.0 times the pile diameter) with a reinforcement cage connection and two deeper embedments (1 to 2 time the pile diameter) with no reinforcement cage connection, shown in Figure 2.4. They found that the shallow embedments still developed at least 40 to 60 percent of the moment capacity of the pile.

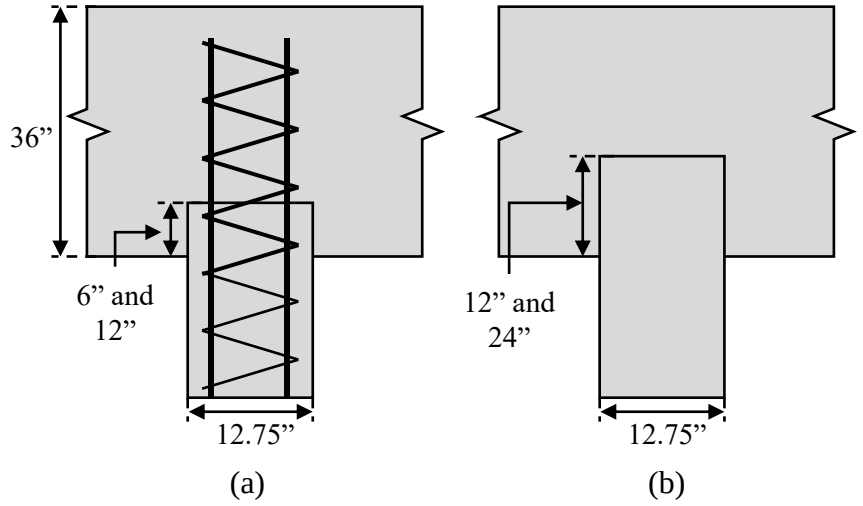

Figure 2.4: Embedment details for Rollins and Stenlund [8] specimens (a) with and (b) without interface steel

Xiao [11] tested three full-scale prestressed concrete pile-to-cap connections: two with constant axial load and cyclic lateral load and one with no lateral load and cyclic axial load. These connections were all shallow embedment lengths with dowel bars extending from the pile into the pile cap, shown in Figure 2.5 (a). Xiao found that a significant moment and rotation could be achieved with the shallow embedment and reinforcement. Xiao also found that there was no degradation in behavior caused by cycling the axial load.

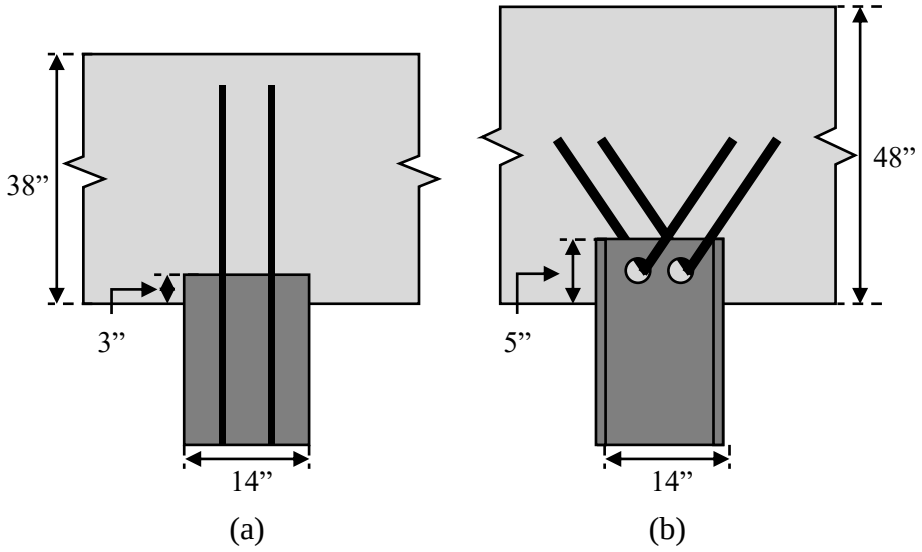

Figure 2.5: Embedment details for (a) Xiao [11] and (b) Harries et al. [6]

Xiao et al. [11] tested pile-to-cap connections for steel HP piles with shallow embedment lengths and diagonal dowel bars extending from the piles into the cap, shown in Figure 2.5 (b). This connection was expected to behave more like a hinge, only developing approximately 6 percent of the plastic moment capacity of the pile based on Shama et al.[7], but ended up developing between 25 and 66 percent of the plastic moment capacity of the pile.

2.3. FIXED CONNECTION BETWEEN PILE AND PILE CAP

The typical objective for the connection between the pile and pile cap is to provide a connection capable of developing the moment capacity of the pile [6]. An additional objective is to ensure the connection is rigid enough so that rotation of the pile within the cap does not significantly contribute to the overall drift of the assembly [6]. This fixed connection can be developed using any of the connection types shown above in Figure 2.3 by a combination of the below methods:

1. Providing sufficient embedment length,
2. Roughening the surface of the pile,
3. Providing spirals around the embedded portion of the pile, and
4. Using mechanical shear connectors or supplemental mild steel reinforcement. [10]

However, Joen and Park [12] found that embedding the pile into the pile cap was the easiest to construct and resulted in the least damage to the pile cap. Primarily because of its ease of construction, a plain pile embedment into pile cap is typically used to achieve a moment connection.

2.3.1. Required Behavior / Mechanism

Several different mechanisms can control the moment capacity, shown in Figure 2.6. Each of these failure mechanisms must be prevented to develop the moment capacity of the pile:

1. ***Slip of prestressing strands in embedded pile***: The available development of the strands must be sufficient to fully develop the prestressing force in the strands.
2. ***Slip between pile and pile cap***: The shear friction capacity at the cold joint between the precast pile and cast-in-place cap must be sufficient so that slip does not occur at the interface before the moment capacity of the pile is achieved.
3. ***Bearing failure between pile and pile cap***: If the compression strength in the pile cap is not sufficient, then there can be crushing of the concrete in the pile cap at the interface.

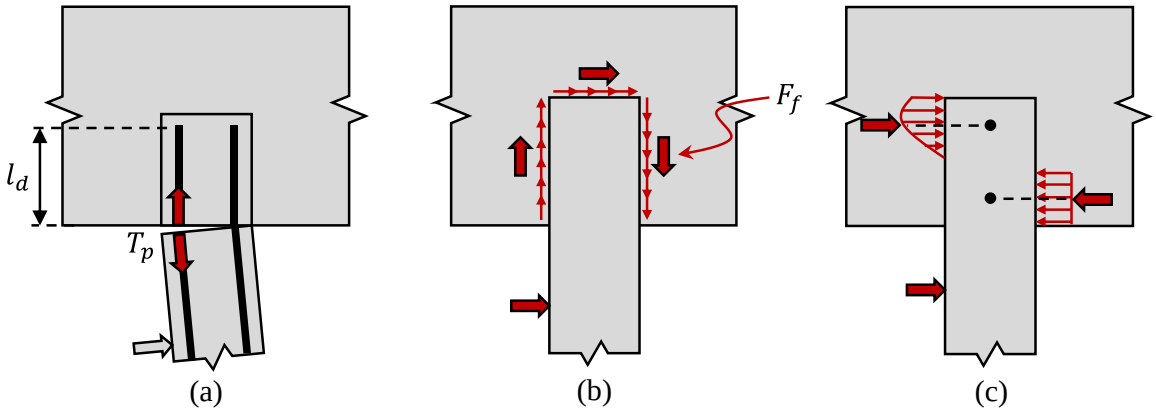

Figure 2.6: Failure of this connection can be controlled by (a) development length of the prestressing strand, (b) shear friction capacity between the pile and pile cap, and (c) bearing between the pile and cap

Each of these mechanisms will be discussed in more detail in the following sections. Note that the shear friction capacity, shown in Figure 2.6 (b), seems to become an influential factor in tension piles.

2.3.2. Summary of Past Research

Several different researchers have previously investigated this type of connection using different types of piles, different sizes of piles, and different loading configurations. A summary of the results from some of these studies is shown in Table 2.1. The current FDOT recommended embedment length to achieve the full moment capacity of prestressed concrete piles is 48 inches [1]. This is based on experimental testing conducted by Issa [13] on square 30-inch depth prestressed concrete piles with an internal pipe void. Issa [13] tested two pile-to-pile cap connections with the piles embedded the entire way through the 48-inch thick pile cap. They found that failure occurred in the pile just outside the connection, so the pile was able to develop its full theoretical bending strength. No axial

load was applied to the piles tested in this program. Note that the 48-inch embedment is equal to 1.6 times the pile diameter/depth in this case.

Since this testing was completed, there have been several additional studies from which researchers have concluded that the full moment capacity of the pile can be developed in embedment lengths less than 48 inches: ranging from an embedment length equal to the pile depth to two times the pile depth [6], [14], [15]. These tests were performed on different pile types, diameters, and depths and with either constant or variable axial loads.

Table 2.1: Recommended embedment lengths to develop full moment capacity of piles from previous research

Research	Year	Recommended Embedment Length to Develop Full Moment Capacity of Pile	Type of Pile	Pile Size	Notes
Castilla et al. [16]	1984	2 x pile depth or diameter	Steel HP 14x73 and 14x117	14”	Based on results from numerical modeling
Joen and Park [12]	1990	No recommendation made, testing of 2 x pile depth or diameter provided full moment capacity	Octagonal, prestressed concrete	15.7”	Embedded pile surface was roughened; constant axial load; also tested 2 other types of pile-to-cap connections and found embedded pile connection to be best
Shahawy and Issa [17]	1992	50”	Square, prestressed concrete	14”	Added external clamping force with jacks simulating shrinkage of cap; no axial load
Issa [13]	1999	48”	Square, prestressed concrete with internal pipe void	30”	Testing referenced in FDOT Structures Design Guidelines [18]; no axial load
Harries and Petrou [6]	2001	Width of pile; greater than 12 inches	Square, prestressed concrete	18”	Constant axial load
Rollins and Stenlund [14]	2010	Recommend embedment of 24” for their 12” diameter steel pipes (2 x pile depth or diameter)	Steel pipe	12”	Piles were driven to a depth of 40 feet into soil; no externally applied axial load
Larosche et al. [15]	2013	1.3 x pile depth or diameter	Square, prestressed concrete	18”	Variable axial load; cyclic loading

2.4. CURRENT DOTS RECOMMENDATIONS

2.4.1. Florida Recommendation for Pinned Connections

The FDOT Structures Design Guidelines [1] currently specifies a 1-foot embedment length for a pinned connection, as shown in Figure 2.7. The strand development length is specified to be in accordance with the sections on development length of prestressing strands (§5.11.4) in the AASHTO LRFD Bridge Design Specification [19], as shown in Figure 2.7.

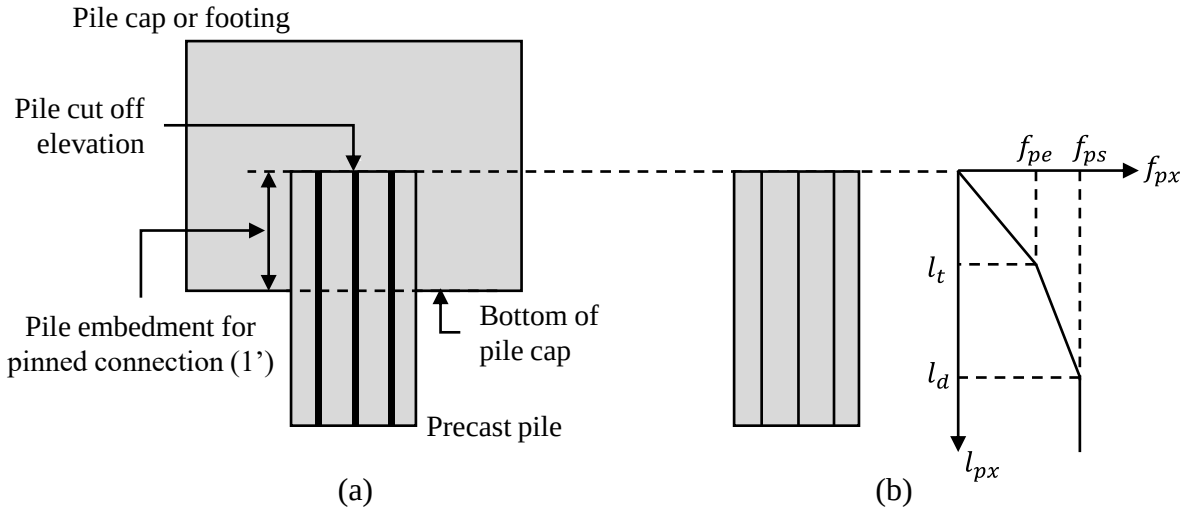

Figure 2.7: (a) FDOT pinned connection details and (b) strand development

The strand stress can be determined using either Equation 1-2.1 or Equation 1-2.2, depending on if the location of interest is within the transfer length or between the transfer and development lengths.

Within transfer length:

$$f_{px} = \frac{f_{pe} l_{px}}{60 d_b}$$

Equation 1-2.1
AASHTO LRFD
(5.11.4.2-2)

Between transfer length and development length:

$$f_{px} = f_{pe} + \left(\frac{l_{px} - 60d_b}{l_d - 60d_b}\right)(f_{ps} - f_{pe})$$

Equation 1-2.2
AASHTO LRFD
(5.11.4.2-3)

where:

f_{px} = design stress in pretensioned strand at nominal flexural strength at section of member under consideration (ksi)

l_{px} = distance from free end of pretensioned strand to section of member under consideration (in.)

d_b = nominal strand diameter (in.)

f_{ps} = average stress in prestressing steel at the time for which the nominal resistance of the member is required

f_{pe} = effective stress in the prestressing steel after losses (ksi)

l_d = development length of the strand required to develop f_{ps}, found using (5.11.4.2-1) (in.)

The strand stress development can be used to determine how the moment develops in the pile away from the hinge location.

2.4.2. Florida Recommendations for Fixed Connections

Currently, the prestressed concrete pile embedment length is based on a research conducted by Issa [13] and the FDOT Structures Research Center, which recommends an embedment length of 4 feet to develop the full bending capacity of the pile as shown in Figure 2.8. The pile must be solid for 8 feet from the end of the pile (i.e., for the 4-foot embedment length and for 4 feet below the bottom of the pile cap).

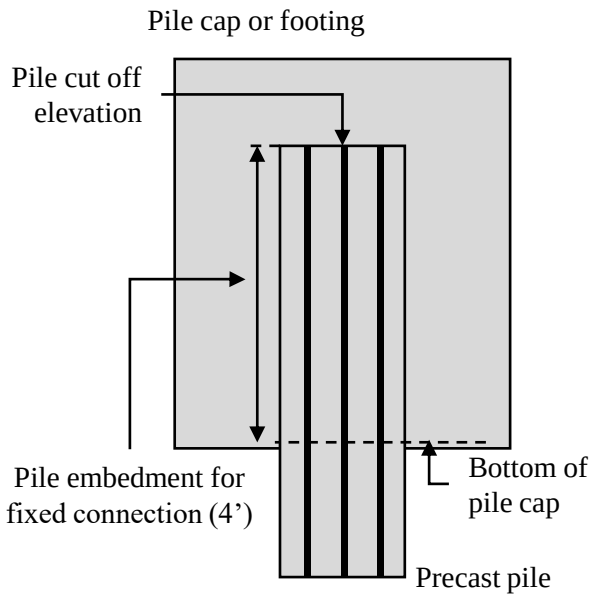

Figure 2.8. FDOT fixed connection details

2.4.3. Other DOTS Recommendations

A summary of the embedment requirements for other states is provided in Table 2.2. The embedment requirements are organized by recommendations for pinned connections and fixed connections. Several states specify a required embedment length, but do not state whether the required embedment length is for a fixed or pinned connection.

The only states that specify a pile embedment length for pinned connections are Florida (1 foot), Minnesota (1 foot) and Wisconsin (0.5 feet).

Table 2.2: Embedment Details from other DOTs

State	Embedment Length			Notes	Source
	Pinned	***Fixed***	***Not specified***		
Alaska	-	-	≥ 1' 6"	Only details for Steel H-piles and Steel pipe piles	[20]

State	Embedment Length			Notes	Source
	Pinned	***Fixed***	***Not specified***		
Colorado	-	Equation 2.3			[5]
Connecticut	-	-	≥ 1’		[21]
Delaware	-	-	≥ 1’	Dowel bars are used for connection with precast piles; minimum embedment is for Steel H-piles	[22]
Florida	1’	4’	-		[18]
Idaho	-	-	1’or 2’	Positive means of anchorage and 1’ embedment if uplift is present; 2’ for stubby abutments where superstructure is integral with pile cap; 1’ without anchorage for most other cases	[23]
Illinois	-	2’	-	Details for reinforcement between Steel H-piles and cap are provided to reduce embedment length	[24]
Illinois Tollway	-	-	1’		[25]
Indiana	-	-	1.5’	5’ pile embedment is required into the stem of a wall pier with a single row of piles	[26]
Iowa	-	-	2’	1.5’ for continuous concrete slab pile bent cap (not monolithic with slab) and 1’ when monolithic with slab	[27]
Kansas	-	-	1’	1’ embedment into a footing; 2’ to 3’ embedment into an abutment	[28]
Michigan	-	-	0.5’	1’ when a tremie seal is used	[29]

State	Embedment Length			Notes	Source
	Pinned	***Fixed***	***Not specified***		
Minnesota	1’	-	-	1’ for embedment into a footing; 2.33’ for embedment for a low parapet abutment footing	[2]
Montana	-	-	1.58’	Embedment may be reduced by extending reinforcement into the footing	[30]
Nevada	-	-	1’	Larger of 1’ and 1.0 x pile width; no roughening of pile is required	[31]
New Hampshire	-	1’	-	Typically extend 1.5’ into stub abutments, 2’ into integral abutments, and 1’ into pier or other footings; CIP piles with reinforcement extending have minimum embedment of 0.5’	[32]
New York	-	-	1’		[33]
Ohio	-	-	1’	Piles supporting capped pile piers should be embedded 1.5’; substructure units on a single row of piles should be embedded 2’	[34]
Oregon	-	Equation 2.3	-	1’ minimum embedment length if lateral load capacity is not needed	[4]
Pennsylvania	-	-	≥ 1’	1.5' for a single row of piles	[35]
Rhode Island	-	-	≥ 1’	Piles must be positively anchored into the footing	[36]
South Carolina	-	-	1 x pile width	No roughening of the pile is required; 1.25' minimum embedment for steel pipe pile connection	[37]
Vermont	-	-	≥ 1’		[38]

State	Embedment Length			Notes	Source
	Pinned	***Fixed***	***Not specified***		
West Virginia	-	-	≥ 1’		[39]
Wisconsin	0.5’	≥ 2’	-		[3]

Washington does not allow precast, prestressed piles for permanent bridge structures. They use cast-in-place concrete piles with a specified reinforcement embedment length from the pile into the pile cap of l_d when the footing/cap connection is not a plastic hinge and $1.25l_d$ when the connection is a plastic hinge zone.

Only a few states have requirements for fixed connections. Florida has the longest requirement (4 feet). Wisconsin and Illinois DOT both require 2-foot embedments for fixed connections. New Hampshire has the shortest required connection (1 foot for piles into piers or other footings) for transferring moment, shear, and axial loads. Colorado and Oregon use a variable embedment length calculated using Equation 2.3.

$$L = \sqrt{\frac{4M_{up}}{\phi f'_c b_f}} \qquad \text{Equation 2.3}$$

where:

L = Required pile embedment into cap (in)

ϕ = Strength reduction factor for concrete bearing

f'_c = 28-day compressive strength of concrete (ksi)

M_{up} = Plastic moment capacity of pile about strong axis (kip-in)

b_f = Pile flange width

2.5. RESISTING MECHANISMS

2.5.1. Strand Development for Fixed Connections

The available development length for the prestressing strand in the pile will affect the ability of the pile to develop its full moment capacity at the interface with the footing or cap. The available development length is the distance from the end of the strands in the embedded pile to the point when the pile exits the footing or cap, as shown in Figure 2.9 (a).

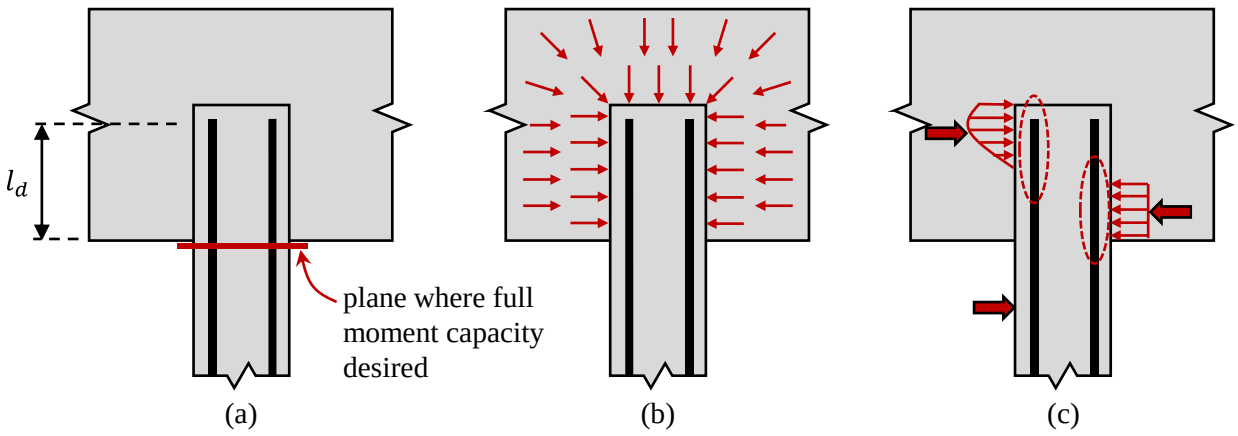

Figure 2.9: Strand development in embedded prestressed concrete pile: (a) Available development length and plane where full moment capacity is desired, (b) shrinkage of the footing

or cap will actively confine the embedded pile, and (c) bending of the pile will place compressive stresses on portions of the pile bearing against footing or cap

The strand must be able to develop its full stress at ultimate (f_{ps}) if the connection will allow the pile to develop its full moment capacity. The specified development length (l_d) for bonded strands in AASHTO LRFD [22] is shown in Equation 2.4. A version of this equation was first presented by Zia and Mostafa [40].

$$l_d \geq \kappa \left(f_{ps} - \frac{2}{3} f_{pe} \right) d_b$$

Equation 2.4
AASHTO LRFD
(5.9.4.3.2-1)

where:

d_b = nominal strand diameter

f_{ps} = average stress in prestressing steel at the time for which the nominal resistance of the member is required (ksi)

f_{pe} = effective stress in the prestressing steel after losses (ksi)

κ = 1.0 for piling (and other members) with a depth less than or equal to 24”

= 1.6 for pretensioned members with depth greater than 24”

For typical stresses, the required development length is greater than 68 inches for 0.5-inch diameter strands and 80 inches for 0.6-inch diameter strands. As shown in Table 2.1, many researchers have found that the full moment capacity of the pile can be developed with much shorter embedment lengths than would be required by AASHTO LRFD to fully develop the strands. This is because the actual required strand development length for the pile embedded in a footing or cap is significantly shorter than the development length calculated using AASHTO LRFD. There are two primary reasons for this, as illustrated in Figure 2.9 (b) and (c):

1. Shrinkage of the cast-in-place (CIP) footing or cap will create a clamping force around the embedded pile, which will decrease the required development length. [9], [17], [41]–[43]
2. Compressive stresses develop as a moment is placed on the pile and causes bearing stresses between the pile and footing or cap, which provides active confinement on the strands further decreasing the required development length. [42]

Several researchers [9], [17], [41]–[43] have measured the strains from shrinkage and observed the decreased required development length caused by these effects.

The shrinkage differential will only occur for CIP pile caps. The shrinkage in the CIP pile cap creates the clamping force around the precast pile, which already experienced creep and shrinkage effects. Clamping forces from shrinkage would not be expected for precast pile caps, where most shrinkage would occur prior to the cap being connected with the precast piles in the field. This behavioral difference would suggest that findings from this research project would not be applicable for precast pile caps.

Strand development failures would be expected in connections with shallower embedment lengths where slip does not occur between pile and cap.

2.5.2. Shear Friction Capacity of Interface

The shear friction capacity at the interface between the precast pile and cast-in-place footing or cap is another mechanism that can control the capacity of the connection. There are two scenarios in which the shear friction capacity controls the behavior. The first is by the moment that would result from the friction force components, as shown in Figure 2.6 (b). The second would be the friction between the pile and footing or cap required to resist

tension that may occur in the connection, as shown in Figure 2.10. Three of the four pile caps tested by Rollins and Stenlund [14] failed due to a pullout failure of the back pile, Figure 2.6 (b). Two of these had a reinforcement cage between the pile and pile cap with embedment lengths of 0.5 and 1.0 times the diameter of the steel pipe pile. The other was connection with pile embedment equal to 2 times the diameter of the steel pipe pile and no reinforcement cage between pile and pile cap. The pullout failure occurred because the back pile was in tension from the loading setup, as shown in Figure 2.10 .

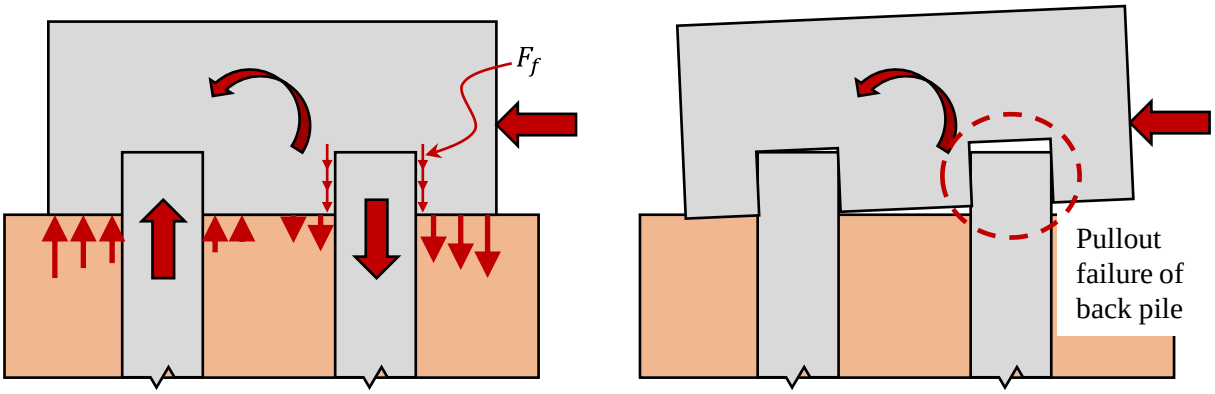

Figure 2.10: Test setup for pile-to-cap connection testing conducted by Rollins and Stenland

Castilla et al. [16] investigated three different coefficients of friction between the cap and exterior surfaces of the pile in a parametric analysis: 0.4, 0.7, and 1.4. They found that increasing the coefficient of friction did not have a significant impact on the shape of the displacement curve but did decrease the maximum displacement and maximum rotation of the pile.

Additionally, there is also ongoing research being conducted by the principal investigator investigating the shear friction capacity of interfaces without any reinforcement crossing the interface plane. Results from this research would be used to guide the shear friction component of this project.

This type of failure would be expected in connections with shallower embedment lengths with a smooth interface surface between pile and cap.

2.5.3. Bearing Capacity of Interface

A moment placed on the pile will also be resisted by the bearing forces between the pile and footing or cap, illustrated in Figure 2.11. Two proposed methods were developed to account for the bearing strength of the cap concrete at the interface between pile and cap: Mattock and Gaafar [44] and Marcakis and Mitchell [45]. Both models were developed for steel members embedded into concrete. They consider the capacity of the resultant load (horizontal in this case) acting on the connection to be dependent on the forces caused by bearing between the embedded member and the concrete, as shown in Figure 2.11.

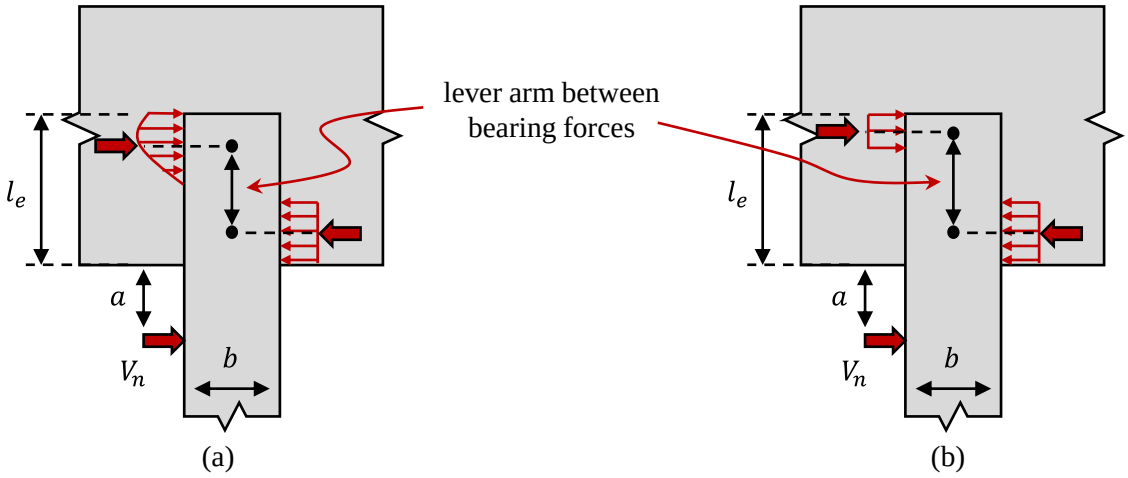

Figure 2.11: Capacity of resultant of horizontal load (V_n) dependent on bearing stress between embedded pile and cap, details for model proposed by (a) Mattock and Gaafar [44] and (b) Marcakis and Mitchell [45] are shown

The equations proposed by Mattock and Gaafar [ref] are shown in Equation 2.5 and Equation 2.6.

$$V_n = 54\sqrt{f'_c}\left(\frac{b'}{b}\right)^{0.66}\beta_1 b l_e\left(\frac{0.58 - 0.22\beta_1}{0.88 + {}^{a}/_{l_e}}\right) \quad \text{Equation 2.5}$$

$$M_{max} = V_n a + \frac{V_n}{108b\sqrt{f'_c}\left(\frac{b'}{b}\right)^{0.66}} \quad \text{Equation 2.6}$$

where:

a = distance from concentrated load to face of pile cap

b = width of pile or embedded section (i.e. bearing width of embedment)

b' = width of pile cap (for single pile) or pile spacing (for pile groups)

f'_c = 28-day compressive strength of concrete (psi)

l_e = embedment length of pile inside pile cap

β_1 = ratio of average concrete compressive strength to maximum stress

The equations proposed by Marcakis and Mitchell [ref] are shown in Equation 2.7 and Equation 2.8.

$$V_n = \frac{0.85 f'_c b l_e}{1 + 3.6\,{}^{e}/_{l_e}} \quad \text{Equation 2.7}$$

$$M_{max} = V_n a + \frac{{V_n}^2}{1.7 f'_c b} \quad \text{Equation 2.8}$$

where:

e = eccentricity of resultant of vertical loads from center of embedment

Other variables are the same as defined for Equation 2.5 and Equation 2.6.

Marcakis and Mitchell [45] found through their experimental testing that the effective width of the connection (b in Equation 2.7 and Equation 2.8) measured to the outside of the reinforcement surrounding the embedded element, limited to 2.5 times the embedded member width.

Harries and Petrou [6] recommended that the embedment length in the above equations be modified to account for the possible spalling of the soffit of the pile cap. This modification results in Equation 2.9 and Equation 2.10.

$$V_n = 54\sqrt{f'_c}\left(\frac{b'}{b}\right)^{0.66}\beta_1 b l_e\left(\frac{0.58 - 0.22\beta_1}{0.88 + {a}/{(l_e - c)}}\right) \qquad \text{Equation 2.9 (modified Equation 2.5)}$$

$$V_n = \frac{0.85 f'_c b(l_e - c)}{1 + 3.6\,{e}/{(l_e - c)}} \qquad \text{Equation 2.10 (modified Equation 2.7)}$$

where:

c = depth of concrete cover in pile cap face toward embedded pile

Both estimation procedures [44], [45] have been found to conservatively estimate the required plain embedment length of prestressed concrete piles into caps [6].

This type of failure would be expected in connections with larger embedment lengths where the concrete in the cap is weaker than the concrete in the prestressed pile.

2.6. TESTING DETAILS FROM PREVIOUS RESEARCH

2.6.1. Experimental Variables

There are several different variables that researches have previously studied. Some of these important variables that have been previously investigated are:

- Embedment length,
- Use of interface reinforcement and type,
- Pile shape and size,
- Dimensions of pile cap, and
- Reinforcement in pile cap.

There do not appear to be any researchers that have systematically investigated the effect of pile and pile cap concrete strength on the performance of the connection, though there have been different concrete strengths tested due to the variability of concrete.

2.6.1.1. Embedment Length and Interface Reinforcement

Embedment length has been one of the primary variables that has been previously investigated. The embedment length dictates the available development length for the prestressing strands and the available interface area for bearing and shear friction interactions between the pile and the cap. Previous research efforts that have investigated multiple embedment lengths are summarized in Table 2.3.

Table 2.3: Previous experimental research investigating multiple embedment lengths

Researcher	Pile Size	Embedment Lengths	Embedment lengths
ElBatanouny et al. [9]	18” square, prestressed concrete	18 in., 22 in., 26 in.	$1d_p$, $1.22d_p$, $1.44d_p$
Harries and Petrou [6]	18” square, prestressed concrete	18 in., 24in.	$1d_p$, $1.33d_p$
Joen and Park [12]	15.7” octagonal reinf. concrete	2 in.*, 31.5 in.	$0.127d_p$*, $2d_p$
Larosche et al. [15]	18” square, prestressed concrete	2 in.*, 22 in., 24in., 26 in.	$0.11d_p$*, $1.22d_p$, $1.33d_p$, $1.44d_p$

Researcher	Pile Size	Embedment Lengths	Embedment lengths
Rollins and Stenlund [14]	12” steel pipe pile	6 in.*, 12 in.*, 12 in., 24 in.	0.5d_p, 1d_p*, 1d_p, 2d_p
Shahawy and Issa [17]	14” square, prestressed concrete	32in, 42in, 48 in, 60 in	2.28d_p, 3d_p, 3.43d_p, 4.28d_p
Shama et al. [46]	9” circular timber pile	9 in., 14 in.	1d_p, 1.56d_p

*interface reinforcement was provided between pile and cap

The embedment details done by these researchers included plain embedment of the pile into the cap, shown in Figure 2.12 (a), and embedments with interface steel extending from the pile into the pile cap, shown in Figure 2.12 (b). The reinforcement extending from the pile into the cap either consisted of prestressing strands or reinforcement continuing out of the pile into the cap or dowel bars being grouted into the top of the pile and extended into the cap. This reinforcement was either extended straight into the cap or hooked to shorten the required length.

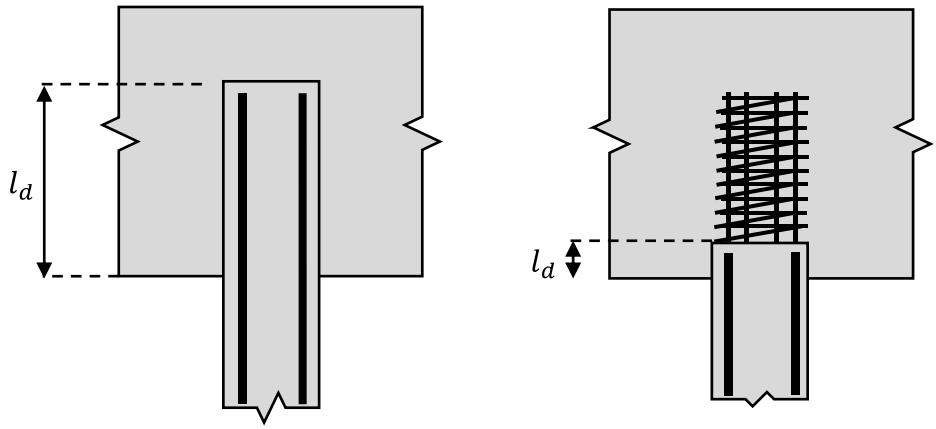

Figure 2.12: Types of connections

Harries and Petrou [6] studied two simple embedded connections of 18-inch prestressed concrete square piles without interface reinforcement under a constant axial load equal to

approximately $0.1f'_cA_g$. The two lengths they selected were based on the previous embedment length recommended by South Carolina Department of Transportation (24 inches) and the calculated embedment length required to develop the capacity of the pile (18 inches). They found that the pile with 24-inch embedment was able to develop a moment of 3,636 k-in., while the 18-inch embedment developed 3,144 k-in. The estimated capacity of the pile using RESPONSE2000 was 3,420 k-in. Based on these test results, they proposed a minimum embedment length equal to the width of the pile but not less than 12 inches with no special interface reinforcement required.

ElBatanouny et al. [9] studied three different embedment lengths (18, 22, and 26 inches) of 18-inch square prestressed piles and found that the deeper embedments had higher moment capacities. They also determined the prestressing strand stress at time of failure to see if any slipping of the strands occurred. A summary of their test results is shown in Table 2.4. They did not report the estimated full moment capacity of the piles, only the estimated capacity accounting for insufficient development length of the prestressing strands. The measurement capacities were significantly larger than the estimated capacities including the effect of insufficient development lengths.

Table 2.4: Summary of test results from ElBatanouny et al. [9]

Specimen ID	Embedment Length	Moment Capacity	Slipping Stress
BC-18-1	18”	2,350 k-in.	185 ksi
BC-18-2	18”	2,090 k-in.	160 ksi
BC-22-1	22”	2,950 k-in.	270 ksi
BC-26-1	26”	2,770 k-in.	270 ksi

Larosche et al. [15], Rollins and Stenlund [14], and Joen and Park [12] all investigated multiple different embedment lengths with much smaller embedment lengths (as small as 0.111 times the pile width or diameter) with interface reinforcement between the pile and pile cap. The goal of these smaller embedment lengths was to determine the amount of moment transferred between pile and cap in an assumed pinned connection. These researchers found that it is difficult to create a true pinned connection as the short embedment lengths were still able to develop significant moment transfer (up to 30 percent higher than the estimated pile capacity). Larosche et al. [15] also investigated the behavior of plastic hinges developing adjacent to this connection and concluded that increasing the pile embedment will lead to the improvement of the plastic hinge development and the associated moment capacity.

Shama [46] studied timber piles connected to concrete pile caps. One of the specimens had an embedment length equal to the pile diameter and the other 1.5 times the diameter. Specimens were found to have satisfactory performance when the embedment length equaled the diameter of the pile, although the specimen with the larger embedment length had a higher capacity.

Shahawy and Issa [17] also investigated several different embedment lengths. They tested four different embedment lengths (36, 42, 48, and 60 inches) for 14-inch prestressed concrete square piles. They did not embed these piles into actual pile caps but used a reaction frame to imitate the clamping force provided by the pile cap, as shown in Figure 2.13. They were attempting to isolate the relationship between the embedment length and the development of the prestressing strands.

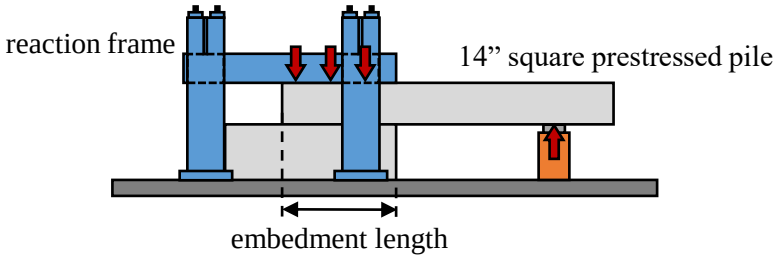

Figure 2.13: Test setup used by Shahawy and Issa [17]

Results from Shahawy and Issa [17] are summarized in Table 2.5 as the average measured and theoretical ultimate moments for all specimens with similar embedment lengths. There was no apparent strength gain as the embedment increased from 36 inches to 60 inches, although slip of prestressing strands was reported for more specimens with shorter embedment lengths. Although Shahawy and Issa [17] had the most systematic and complete evaluation of embedment length, the range of embedment lengths investigated was above the range of interest for 14-inch prestressed concrete square piles and there are questions as to whether the clamping provided by the reaction frame accurately represents the conditions of an actual pile-to-pile cap connection.

Table 2.5: Summary of test results from Shahawy and Issa [17]

Embedment Length (in.)	# of specimens	Avg. Measured ultimate moment (k-ft)	Avg. Theoretical ultimate moment (k-ft)	Avg. Measured/ Theoretical	# specimens where slip was reported
36	4	140.3	124.9	1.13	2
42	6	142.3	127.3	1.12	4
48	6	139.1	128.2	1.09	1
60	3	141.0	127.9	1.10	0

Embedment length for plain embedment details will be the primary variable of interest for the future experimental testing of this project.

2.6.1.2. Pile Details

No single researcher has previously isolated the effect of pile shape on the connection behavior. The pile sections that have been investigated by previous researchers are summarized in Table 2.6 and shown in Figure 2.14.

Table 2.6: Previously tested pile types

Pile Type	Dimensions	Researcher
Square prestressed concrete with internal pipe void	30”	Issa [13]
Square prestressed concrete	14”	Xiao [47], Shahawy and Issa [17]
	18”	ElBatanouny et al. [9], Harries and Petrou [6], Larosche et al. [15]
Octagonal prestressed concrete	15.7”	Joen and Park [12]
Steel HP	HP10x42	Shama et al. [7]
	HP14x89	Xiao et al. [11]
Steel pipe	8”	Stephens and McKittrick [48], Kappes et al. [49]
	12”	Rollins and Stenlund [14]
Circular timber	9”	Shama and Mander [46]

Square, prestressed concrete piles have been the most tested pile type with 18-inch being the most tested size. Most of the prestressed pile tests have investigated the embedment length required to develop the full capacity of prestressing strands and thus the full capacity of the pile. Most of tests using the steel pile types have investigated pile cap details by forcing failure of the specimens into the pile cap.

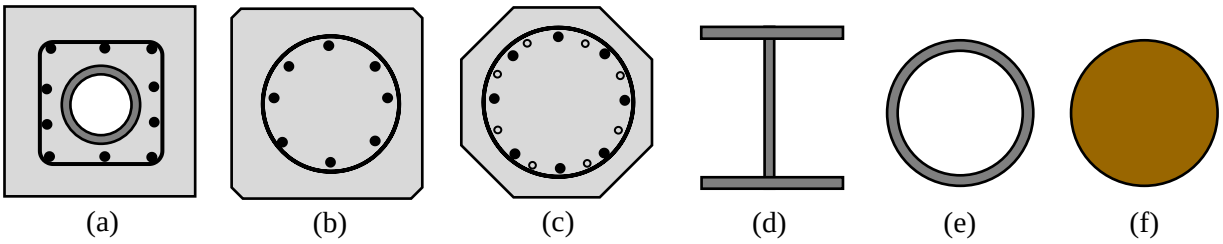

Figure 2.14: Previously investigated pile cross sections: (a) square prestressed concrete pipe pile, (b) square prestressed concrete pile, (c) octagonal prestressed concrete pile, (d) steel HP piles, (e) steel pipe pile, and (f) circular timber pile

The shape and type of pile will affect how the pile and pile cap interact. Unlike square piles, round or octagonal piles will develop bearing forces directed radially from the embedment which may result in greater deterioration of the pile cap and embedment region [6], as shown in Figure 2.15. These radially directed bearing stresses may result in tension developing in the pile cap and may result in failure in the pile cap rather than the pile.

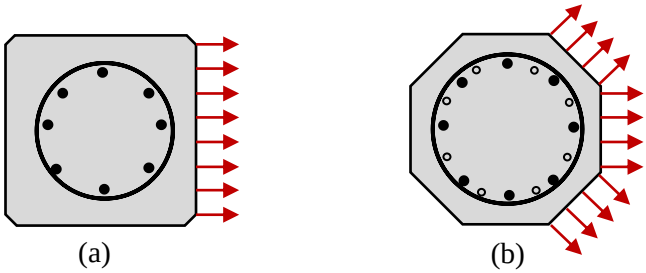

Figure 2.15: Direction of bearing stresses in (a) square and (b) octagonal piles

Pile shape will not be a primary variable investigated experimentally in this project. Several different sizes for square prestressed concrete piles will be investigated experimentally. Pile shape may be investigated through numerical modeling efforts.

The surface of the embedded piles were intentionally roughened for two pile specimens in Joen and Park [12]. The surface of these two piles were roughened to a magnitude of 0.12 inches using a pneumatic hammer before the pile caps were cast. This is the surface

roughness required for a Type B construction joint by the New Zealand Standard Specification for Concrete Construction, NZS 3109 [50].

2.6.1.3. Pile Cap Details

There have been several studies that have investigated the impact of pile cap dimensions and reinforcement detail on the pile-to-cap connection performance.

Larosche et al. [15] investigated several different pile cap details with 18-inch square prestressed concrete piles. Their control specimen had an 18-inch embedment (embedment equal to pile size) and pile cap dimensions and reinforcement detail in line with the practice used at the time in South Carolina, as shown in Figure 2.16.

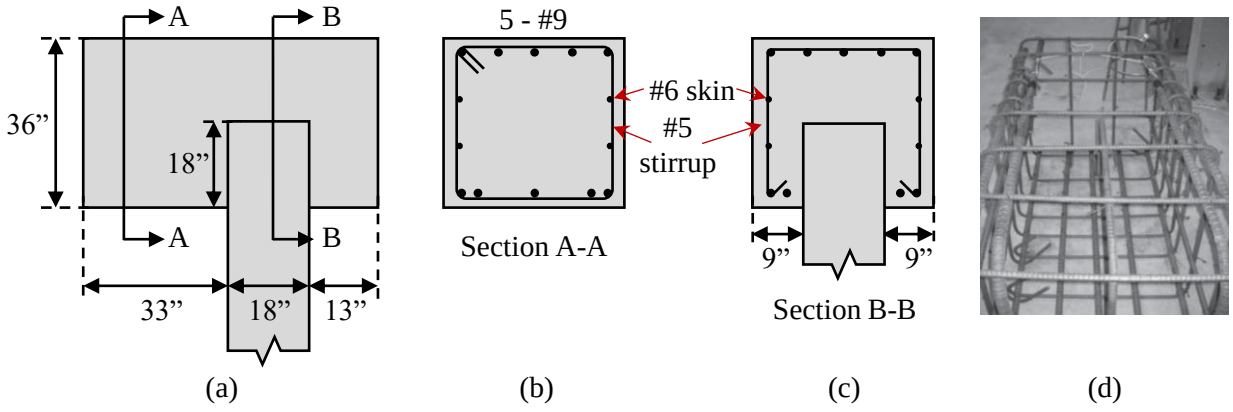

Figure 2.16: Control pile cap detail for Larosche et al. [15], (a) Elevation, (b) Section A-A, (c) Section B-B views and (d) picture of reinforcement cage for Specimen EB-18

Two modifications were made by Larosche et al. [15] to the pile cap design to improve the behavior of the connection. Additional reinforcement was provided in the cap of EB-26, shown in Figure 2.17 (a). Additional distance was provided between the edge of the pile and edge of the pile cap for EB-22, shown in Figure 2.17 (b).

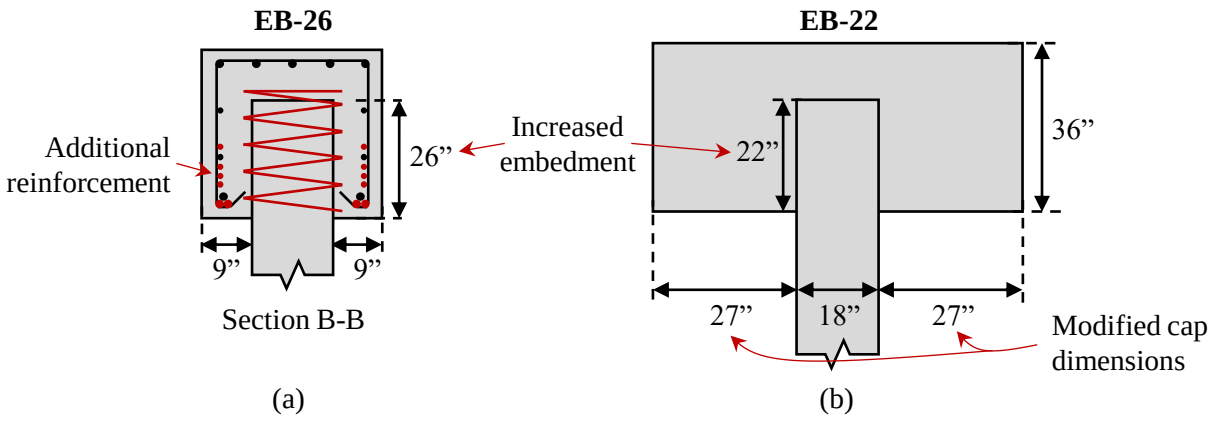

Figure 2.17: Modifications to pile cap design for Larosche et al. [15] for (a) EB-26 and (b) EB-22

A summary of some relevant details related to pile cap design and maximum failure moments for the moment connection tests from Larosche et al. [15] is provided in Table 2.7.

Table 2.7: Summary of moment capacity for moment connection specimens from Larosche et al. [15]

Specimen ID	Reinforcement Percent per Cap Volume	Minimum Edge Distance	Maximum Failure Moment
EB-18	1.62%	13”	1,416 k-in*
EB-26	2.71%	13”	2,744 k-in
EB-22	1.62%	27”	2,832 k-in

*failure occurred in pile cap

The two modified pile cap designs moved the failure from the pile cap into the pile. Both increasing the reinforcement ratio in the pile cap and increasing the minimum edge distance in the direction of bending increased the capacity of the pile-to-cap connection enough to move the failure into the pile.

Stephens and McKittrick [48] tested five different pile cap reinforcing schemes for 8” diameter steel pipe piles with a 9-inch embedment length. Cap reinforcement was the

primary variable. The control specimen had the recommended reinforcement plan in Montana at the time of testing. The four other details had a thinner pipe wall thickness and up to seven times the amount of reinforcement in the cap, as shown in Table 2.8. They found that increasing the amount of reinforcement in the cap increased the capacity in the connection and eventually caused failure in the steel pipe pile and not in the cap.

Table 2.8: Summary of test results from Stephens and McKittrick [48]

ID	Pipe wall thickness (in)	Longitudinal steel ratio (%)	Transverse steel ratio (%)	Concrete strength (ksi)	Maximum moment at failure (k-ft)
PC-1	0.32	0.41	0.09	4.83	82
PC-2	0.25	0.41	0.09	5.33	74
PC-3	0.25	1.09	0.24	3.15	76
PC-3a	0.25	2.11	0.65	3.95	102
PC-4	0.25	2.83	0.70	4.68	121*

*only specimen that failed due to plastic hinging in steel pipe pile

Kappes et al. [49] also investigated pile cap reinforcement for connections between 8-inch diameter concrete filled tube (CFT) piles and pile caps. One type of reinforcement that they investigated in more depth was the use of U-bars around the embedded pile, as shown in Figure 2.18.

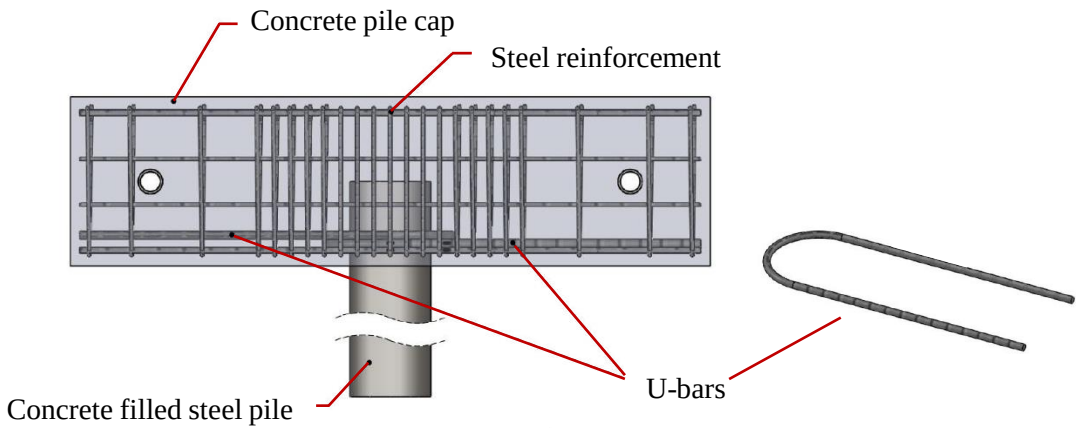

Figure 2.18: Cap reinforcement details from Kappes et al. [49] with single #7 U-bar in each direction

A summary of the test results from Kappes et al. [49] is shown in Table 2.9. The pile design for VT1 was made to be consistent with previous testing done by Stephens and McKittrick [48]. The design strength of the pile was increased to exceed the pile cap strength for the remainder of the specimens.

Table 2.9: Summary of test results from Kappes et al. [49]

Specimen ID	U-Bar Configuration	U-Bar Location	Pile Embedment Length	Concrete Strength	Failure Mechanism	Maximum Moment at Failure
VT1	Single #7 U-bar in each direction	Exterior only	9.0 in.	6.25 ksi	Plastic hinge in steel pipe pile	119.2 k-ft
VT2	Single #4 and #5 U-bar in each direction	Exterior only	11.75 in.	3.8 ksi	Fracture of concrete pile cap	173.8 k-ft
VT2.5	Single #7 U-bar in each direction	Exterior only	9.0 in.	6.25 ksi	Fracture of concrete pile cap	138.5 k-ft
VT3	Single #7 U-bar in each direction	Exterior only	10.375 in.	4.1 ksi	Fracture of concrete pile cap	151.7 k-ft
CT1	Single #4 and #5 U-bar in each direction	Exterior only	11.75 in.	4.2 ksi	Fracture of concrete pile cap	172.4 k-ft
CT2	Single #4 and #5 U-bar in each direction	Interior and Exterior	11.75 in.	4.2 ksi	Fracture of concrete pile cap	181.8 k-ft

The single #4 and #5 U-bar detail with 11.75-inch embedment, shown in Figure 2.19, was found to perform better than the single #7 U-bar detail. The single #4 and #5 U-bar detail with U-bars located both on the interior and exterior, shown in Figure 2.19 (b), was the best performing detail.

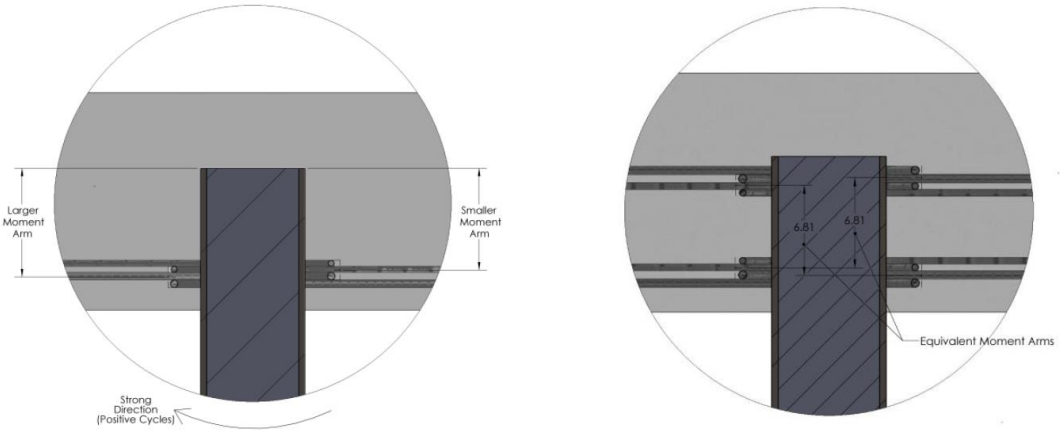

(a) (b)

Figure 2.19: Single #4 and #5 U-bar detail from Kappes et al. [49] for (a) CT1 exterior only and (b) CT2 exterior and interior

The reinforcement detail in the pile cap is currently not a primary detail for this project. The design of the pile cap will be decided on based on current Florida practice and integrating some of the research discussed in this section as appropriate.

2.6.1.4. Compressive Strength

As previously stated, there has been no previous research systematically investigating the effect of pile and pile cap concrete compressive strengths on the behavior of the connection. The range of compressive strengths that have been achieved in previous research in the pile and pile cap are summarized in Table 2.10.

Table 2.10. Previous experimental research investigating multiple concrete compressive strength

Researcher	Pile Concrete Strength Range (ksi)	Pile Cap Concrete Strength Range (ksi)
ElBatanouny et al. [9]	7.3 to 8.3	4.3 to 5.5
Harries and Petrou [6]	6.7	3.0 to 5.0
Issa [13]	10.1	9.0
Joen and Park [12]	6.3 to 7.3	3.6 to 4.8
Larosche et al. [15]	7.3 to 8.3	5.1 to 6.4
Shahawy and Issa [17]	5.6 to 7.8	n/a
Xiao [47]	8.6	5.9

A higher quality concrete is used for the precast piles than the cast-in-place pile cap, so the strength of the pile concrete has been greater than the pile cap concrete in all previous research.

2.6.2. Test Setups

Several different test setups have been used by past researchers to experimentally evaluate the connection between piles and pile caps, as shown in Figure 2.20. Three of the five test setups required fixture to a strong floor, Figure 2.20 (a) to (c). Two of the test setups are self-equilibrating, Figure 2.20 (d) and (e).

1. **Harries and Petrou** [6]: This test setup required load and support frames. The support frame was anchored to the strong floor and the pile cap to prevent displacement and rotation of the pile cap. Two load frames were required: one to apply a constant axial load to the system and one to apply the variable lateral load. Two hydraulic jacks were used at the location of the lateral load, one bearing

against the strong floor and one against the load frame, to apply lateral loads in both directions.

2. **Shahawy and Issa** [17]: This test setup relied on a single reaction beam connected to the strong floor with high-strength threaded rods to provide moment restraint for the pile cap. The lateral load was applied through a hydraulic jack bearing against the strong floor. No axial load was applied to the system.
3. **Xiao** [47]: This test setup was the only setup with a vertically oriented pile. The pile cap was anchored directly to the strong floor to provide moment restraint. Two load frames with two hydraulic jacks were used to provide a constant axial load and variable lateral load.
4. **Issa** [13]: This test setup was self-equilibrating. Two piles were cast into a single pile cap. A hydraulic jack was placed between the two piles and lateral load applied to failure. Both piles were tested at the same time under this setup. No axial load was applied.
5. **Larosche et al.** [15]: This test setup was self-equilibrating. A modified W-shape steel section was chemically anchored to the side of the pile cap. A diagonally oriented hydraulic jack extended between the W-shape connected to the pile cap and a pinned connection device to the end of the pile. Using this setup, a single jack was used to apply axial load, moment, and shear to the connection. A variable compressive and tensile axial load was applied during testing.

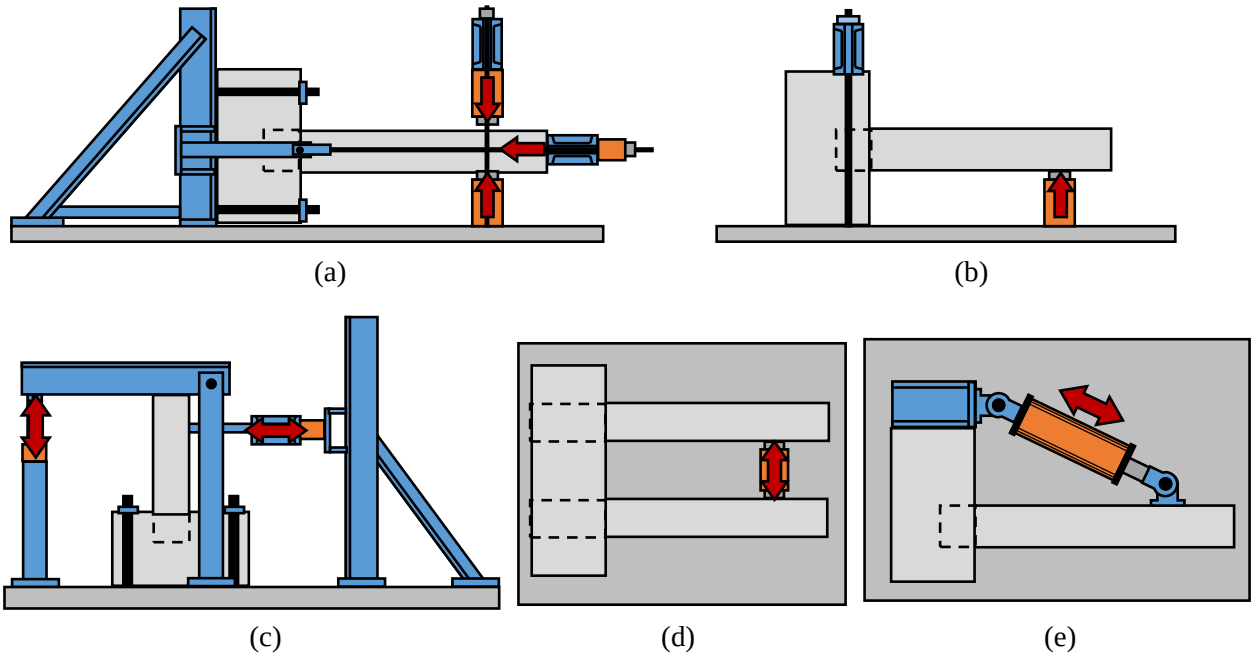

Figure 2.20: Test setups from previous research (a) Harries and Petrou [6] (elevation), (b) Shahawy and issa [17] (elevation), (c) Xiao [47] (elevation), (d) Issa [13] (plan), (e) Larosche et al. [15] (plan)

Several different types of tests have been previously conducted by researchers, as shown in Table 2.11. Most of previous testing has been conducted using a constant axial load and cyclic lateral load to failure.

Table 2.11: Types of tests previously conducted by researchers

Axial Load	Lateral Load	References
Constant	Cyclic to Failure	Harries and Petrou [6], Xiao [47], ElBatanouny et al. [9], Joen and Park [12]
None	Monotonic to Failure	Shahawy and Issa [17], Issa [13]
Cyclic to Failure	None	Xiao [47]
Variable	Variable	Larosche et al. [15]

2.6.3. Instrumentation Layouts

Previous researchers have used different types of gauges and instrumentation to measure displacement, curvature, strand slip, and strain in reinforcement, prestressing strands, and concrete. Some relevant details on the types of instrumentation used by these previous researchers are organized by goal of instrumentation in the following sections.

2.6.3.1. Displacement and Load Measurement

Displacement was typically measured at the point where the lateral load was applied typically using either linear or string potentiometers. The displacement measurement point was shifted in some studies due to limited access at the point of load application. Load was typically measured using load cells at the load application points. Load cells or pressure transducers were also used to verify the constant applied axial loads.

2.6.3.2. Curvature in Plastic Hinge Region

ElBatanouny et al. [9] and Larosche et al. [15] both used four linear variable differential transducers (LVDTs) fixed in series to two opposite faces of the pile in the plastic hinge region, as shown in Figure 2.21. These LVDTs are used to measure displacement, which can be then used to determine the strain on opposite faces. Assuming strains are linear across the section, these strains can be used to determine the curvature along the length of the hinge region.

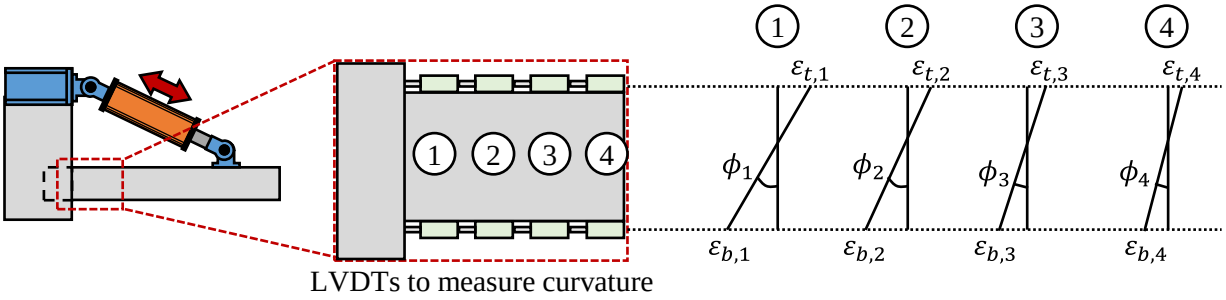

Figure 2.21: Procedure for measuring curvature in hinge region with LVDTs

Similar instrumentation was also used by Xiao [47] to measure the curvature in the pile near the connection.

2.6.3.3. Confining stresses

ElBatanouny et al. [9] used two vibrating wire strain gauges (VWGs) embedded in the end of one of their pile specimens (BC-22-1) to measure internal concrete strains in two directions perpendicular to the pile, as shown in Figure 2.22 (a). They used these measured strains in the pile to determine the confinement provided in both directions by the bearing stresses between the pile and pile cap.

Shahawy and Issa [17] used VWGs mounted in the pile cap oriented in the x, y, and xy directions, shown in Figure 2.23 (b), at four different heights along the length of the embedment. They used these gauges to measure the shrinkage strain in the pile cap along the length of the embedment. They assumed that this shrinkage strain in the pile cap applied clamping stresses to the embedded pile, which they assumed decreased the development length of the prestressing strands.

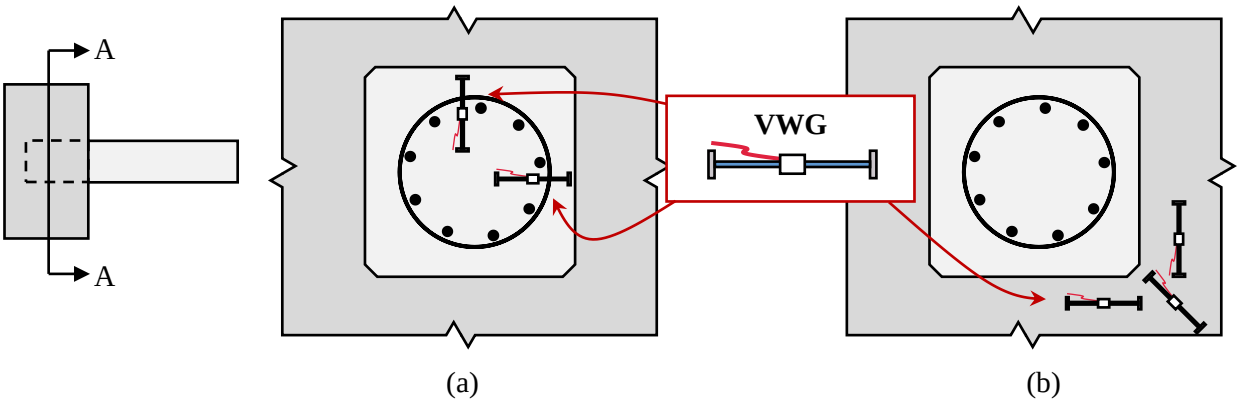

Figure 2.22: Location of VWGs at Section A-A for (a) ElBatanouny et al. [9] and (b) Shahawy and Issa [17]

2.6.3.4. Strand slip

Shahawy and Issa [17] used horizontal LVDTs at the free end of the pile (extending through the pile cap) to measure the slip of the prestressing strands during testing, as shown in Figure 2.23. Measurement of the strand slip using this technique was only possible because the pile extended through the entire pile cap (i.e. the pile embedment length was equal to the pile cap depth).

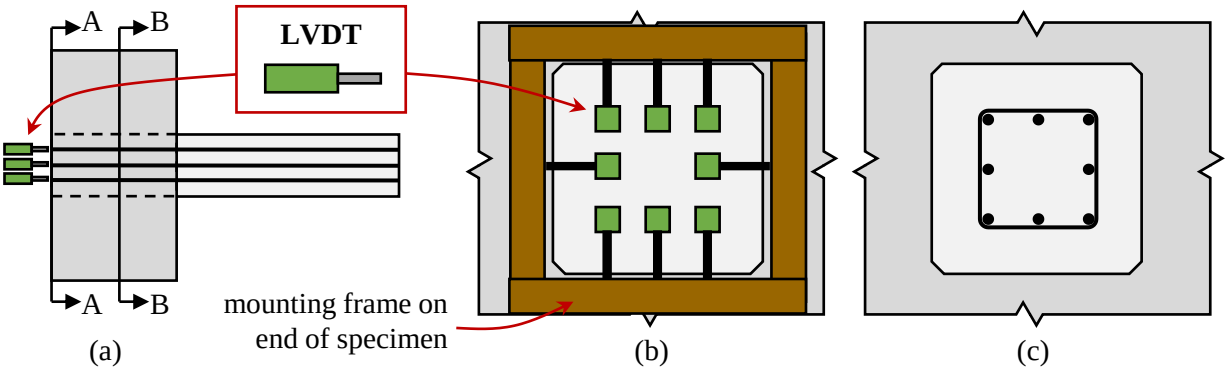

Figure 2.23: LVDTs used by Shahawy and Issa [17] to measure strand slip (a) elevation, (b) section A-A and (c) Section B-B

ElBatanouny et al. [9] stated that they used two LVDTs mounted on the top and bottom strands of each pile within the bent cap to measure strand slip. The pile embedment does not equal the pile cap depth though, so it is not clear how these gauges were installed.

2.6.3.5. Prestress Losses

Joen and Park [12] used demountable mechanical (Demec) strain gauges on the piles to measure the concrete strains immediately after transfer and periodically up until testing. These strains were used to determine the prestress losses due to creep and shrinkage. Internally-mounted, longitudinally-oriented VWGs could also be used to monitor prestress losses in the pile up to the time of testing.

2.6.3.6. Engagement of reinforcement

Joen and Park [12] used typical resistance strain gauges on spiral reinforcement in the pile and pile cap and also on some of the longitudinal non-prestressed steel in the piles. Xiao [47] also used resistance strain gauges mounted on some of the reinforcement in the pile cap, although the specific location of the instrumentation was not specified by the author. ElBatanouny et al. [9] used five strain gauges on some of the longitudinal reinforcement within the bent cap, although the specific location of gauges was not specified.

3. SENSITIVITY STRUCTURE ANAYSIS

A numerical analysis was performed using a non-linear finite element analysis software (FEA) MIDAS Civil to determine the impact of pile-to-cap fixity assumptions on the design and behavior of sensitive structures.

The sensitive structures analysis focused on the analysis of the following primary types of structures:

1. Simple spans with uneven span lengths with piles embedded in pier cap
2. PT segmental box girder bridge with fixed pier table subjected to lateral load
3. Straddle bent with pile cap subjected to temperature effects
4. PT segmental box girder bridge with fixed pier table and forced displacement at end of span

3.1. BRIDGE #1: SIMPLE-SPANS WITH UNEVEN SPAN LENGTHS

The stability of substructures can be dependent on the degree of pile fixity in the cap. One example of a substructure dependent on the pile fixity is the construction of tall pile bents using relatively small embedment lengths into the bent cap, shown in Figure 3.1 (a). The bearings for down-station and up-station girders are placed on the bent cap offset from the centerline of the pier, as shown in Figure 3.1 (b). A hinge assumption would result in an unstable linkage across the depth of the bent cap. This detail works because of the consideration of some degree of fixity between the pile and pile cap.

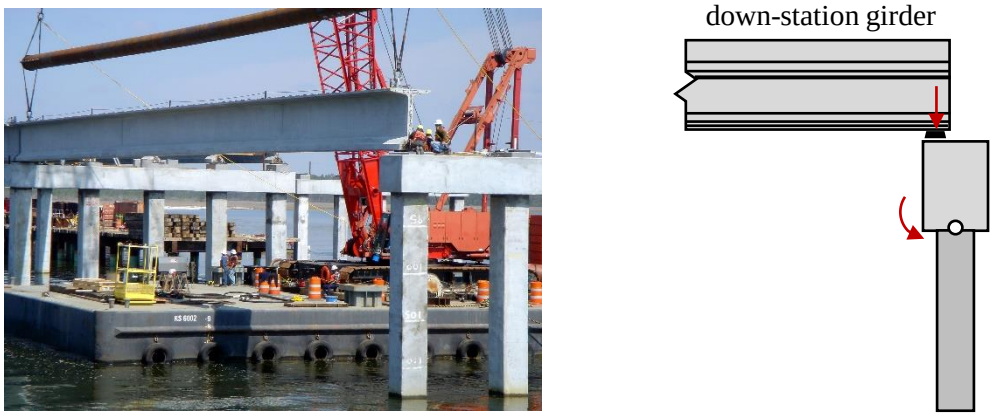

Figure 3.1: (a) Construction of a bridge with tall pile bents (courtesy of Corven Engineering) and (b) schematic of unstable bent with assumed pinned connection

The first structure considered was a simple-span bridge with piles directly embedded in the pier cap, similar to that shown in Figure 3.1. The analysis of this structure investigated the moment developed at the pile-to-cap connection at different construction stages. Analyzing at different construction stages allowed for investigating any in-service impact of the pile-to-cap connection fixity. The fixity of the connection was also varied using a rotational spring connection.

3.1.1. Base Structure

The base structure had five girder lines spaced at eight feet on center, as shown in Figure 3.2 and specified in Table 3.1. The number of girders was decided to equal to the number of piles, and girders were located directly over the piles. The bridge layout was based on sample drawings provided by FDOT, although the properties were not the same as the provided drawings.

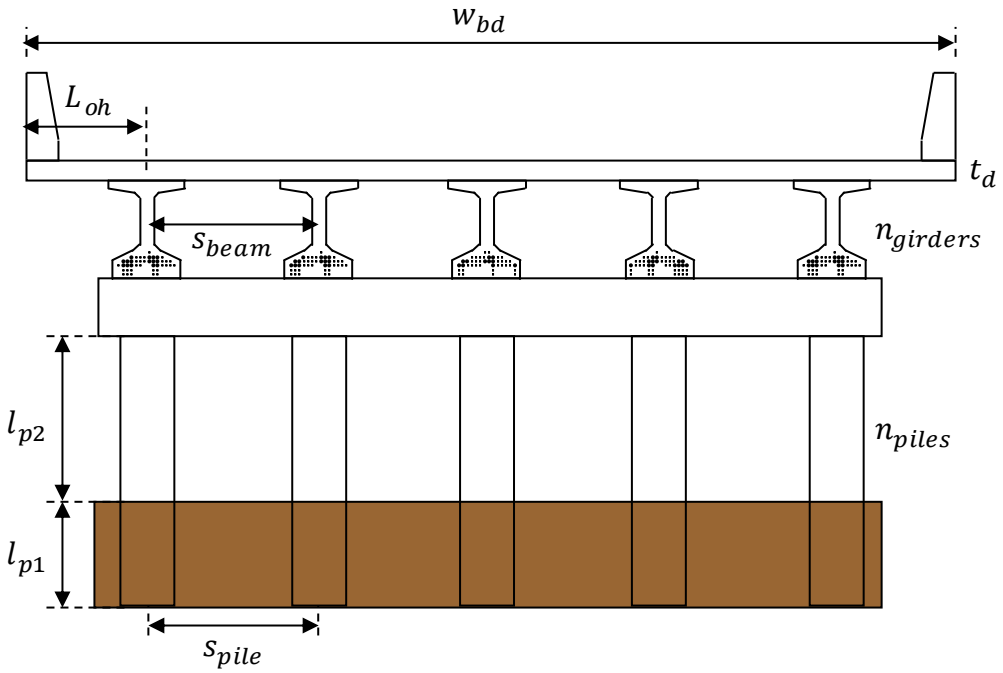

Figure 3.2: Section of interior bent for Bridge #1

The base structure was a three-span bridge with simply supported, non-continuous girders in each span. The middle span had a much longer span length than the first and third spans, as shown in Figure 3.3.

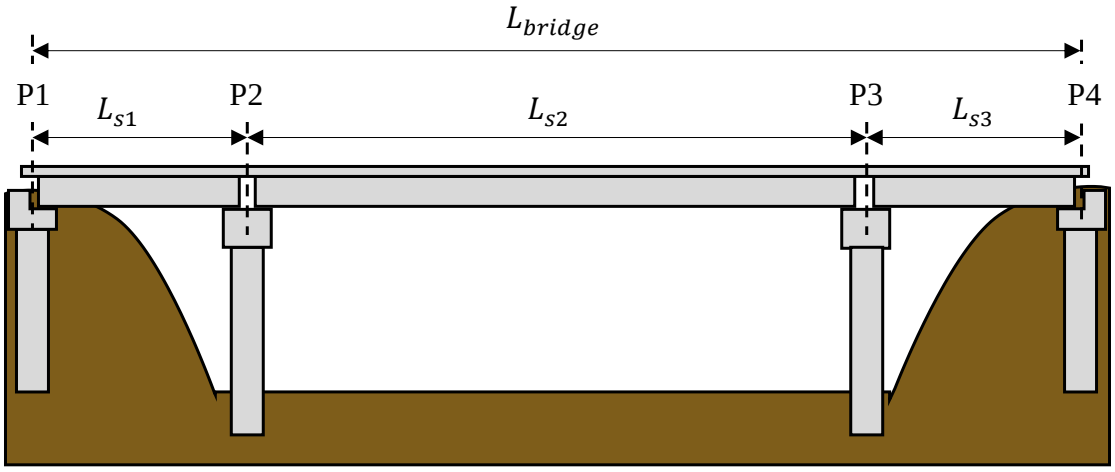

Figure 3.3: Elevation of Bridge #1

The values used in the base structure are summarized in Table 3.1. Note that several of the variables are interdependent, e.g., beam spacing and span length will control the beam cross section design. The parameters selected for this base structure were determined to represent the general behavior of this type of structure.

Table 3.1: Variable values for Bridge #1

Variable		Base Case
Pile spacing	s_{pile}	8’
Driven pile depth	l_{p1}	40’
Exposed pile length	l_{p2}	15’
Pile width	d_{pile}	18”
Number of piles at each pier	n_{piles}	5
Number of girders	$n_{girders}$	5
Beam spacing	s_{beam}	8’
Bridge width	w_{bd}	40’
Overhang length	L_{oh}	4’
Bridge length	L_{bridge}	176’
Shorter span length	L_{s1}, L_{s3}	40’
Longer span length	L_{s2}	100’
Beam cross section		FIB 45
Deck thickness	t_d	8”

3.1.2. Concrete Strength Properties

The concrete strength used in each structural element is summarized in Table 3.2.

Table 3.2: Concrete strength properties for Bridge#1

Component	Concrete Strength
Deck	Class IV
Piles	Class V (Special)
Pile Cap	Class IV
Girders	Class IV
Piers	Class IV

3.1.3. Cross Section Details for Members

3.1.3.1. Prestressed Beam Details

The 45-inch deep Florida I-Beam (FIB-45) was selected as the cross section for this base bridge, as it is the appropriate cross section for the longer 100-foot span length with 8-foot beam spacing, as shown in Figure 3.4. The general cross section geometry and properties for the FIB-45 are shown in Figure 3.5.

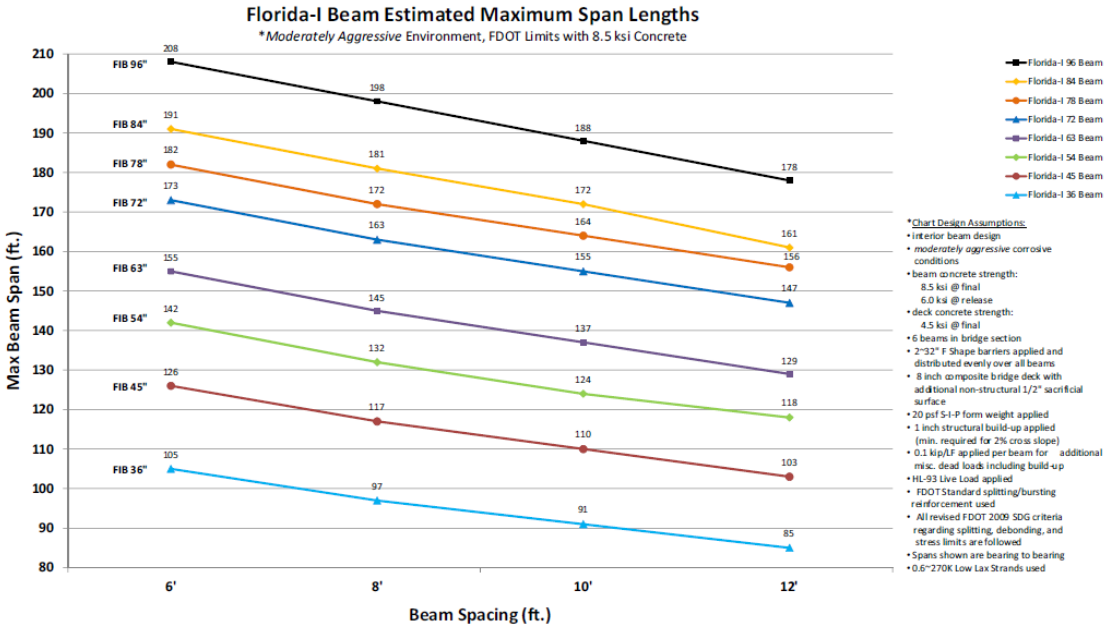

Figure 3.4: FDOT Design Aid for Florida-I beams [51]

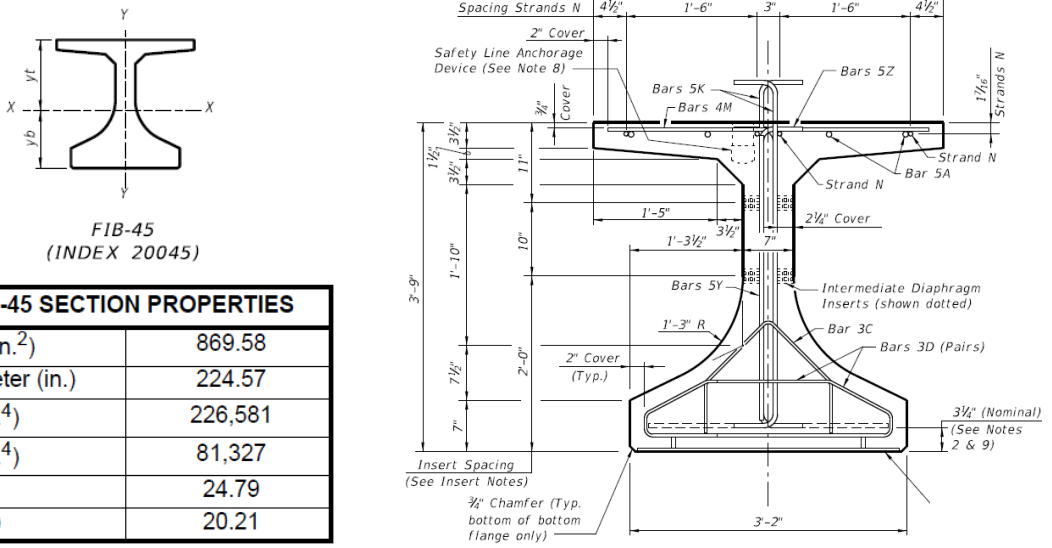

FIB-45 SECTION PROPERTIES	
Area (in.^{2})	869.58
Perimeter (in.)	224.57
Ixx (in.^{4})	226,581
Iyy (in.^{4})	81,327
yt (in.)	24.79
yb (in.)	20.21

Figure 3.5: General properties for FIB-45 [51]

The FDOT design software "Prestressed Beam" [52] was used to design the beams. Strand layouts determined for the longer and shorter span lengths are shown in Figure 3.6. The

section properties and strand location and strand properties are all inputs in the software being used for this study.

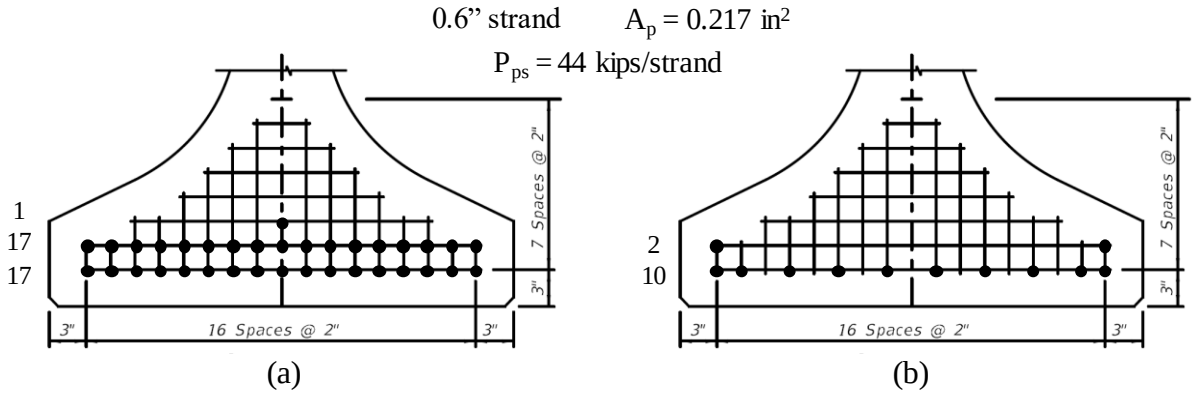

Figure 3.6: Strand layout for (a) 100-ft span and (b) 40-ft span

3.1.3.2. End and Interior Bents

The cross-section dimensions for the end and interior bents were based on the sample drawings provided by FDOT. No reinforcement details are required in the input for the analyses.

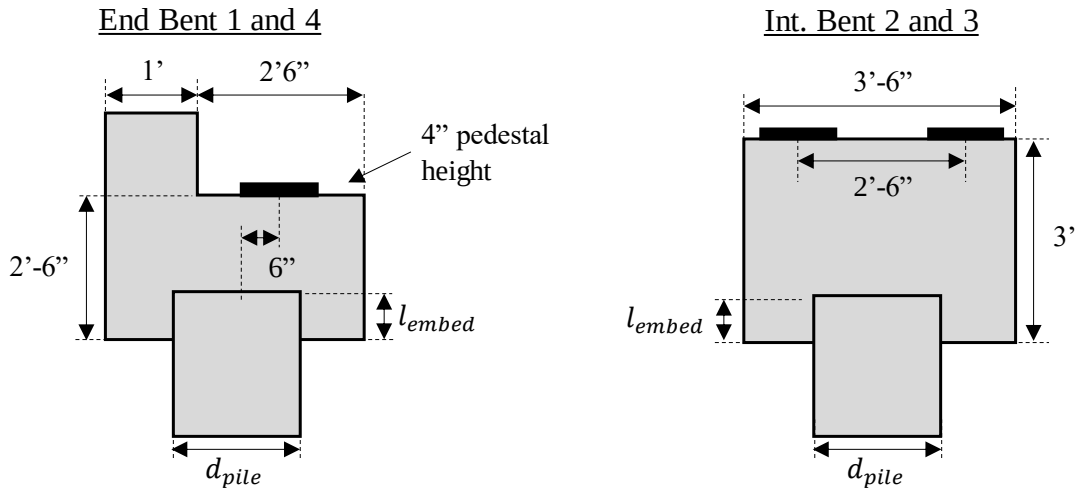

Figure 3.7: Typical cross section dimensions for pier caps

3.1.3.3. Piles

Pile designs were based on FDOT standard plans for prestressed concrete piles[53]. Square prestressed concrete piles with 18-inch width and height were used for Bridge #1; details for 18-inch piles are shown in Figure 3.8. The pile section and concrete properties are provided as inputs in the software used for this study. Details for the prestressing strands are not inputs in the analysis software.

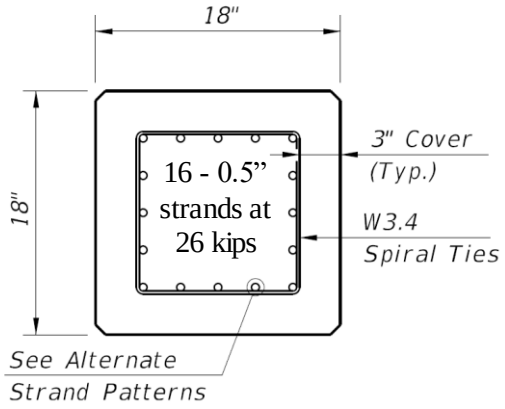

Figure 3.8: Details for 18-inch square prestressed concrete pile used in Bridge #1 [53]

3.1.4. Construction Procedure

This bridge was modeled using construction stages to investigate the impact of placement of each girder and the final stage. The construction procedure for girder placement included the stages shown in Figure 3.9. All the girders in a span were placed at the same time for these analyses. Effects of the weight of the deck during construction were analyzed in Construction Stages 4a through 4c. Results are presented for Construction Stages 1, 2, 4a, 4c, and 5 (completed structure).

1. Girders placed for Span 1

2. Girders placed for Span 2

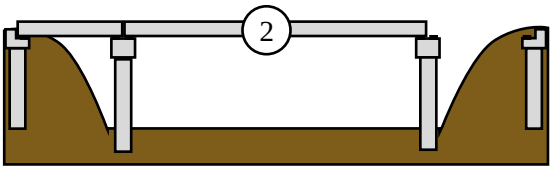

3. Girders placed for Span 3

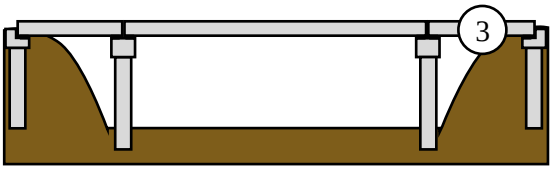

4. Deck cast by span

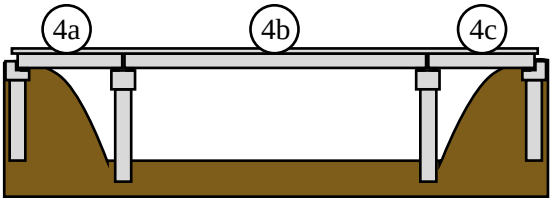

5. Completed structure under service loading

Figure 3.9: Assumed construction procedure for Bridge #1

The placement of the second span girders (Construction Stage 2) causes the maximum moment on the pile-to-cap connection of the right interior support. This construction procedure (i.e., with the Span 2 girders placed after the Span 1 girders) was selected as it resulted in the maximum moment in the connection.

The construction stages for Bridge #1 investigated through numerical modeling are shown in Figure 3.10. Construction Stage 3 and 4c were found to not control, so they were not modeled.

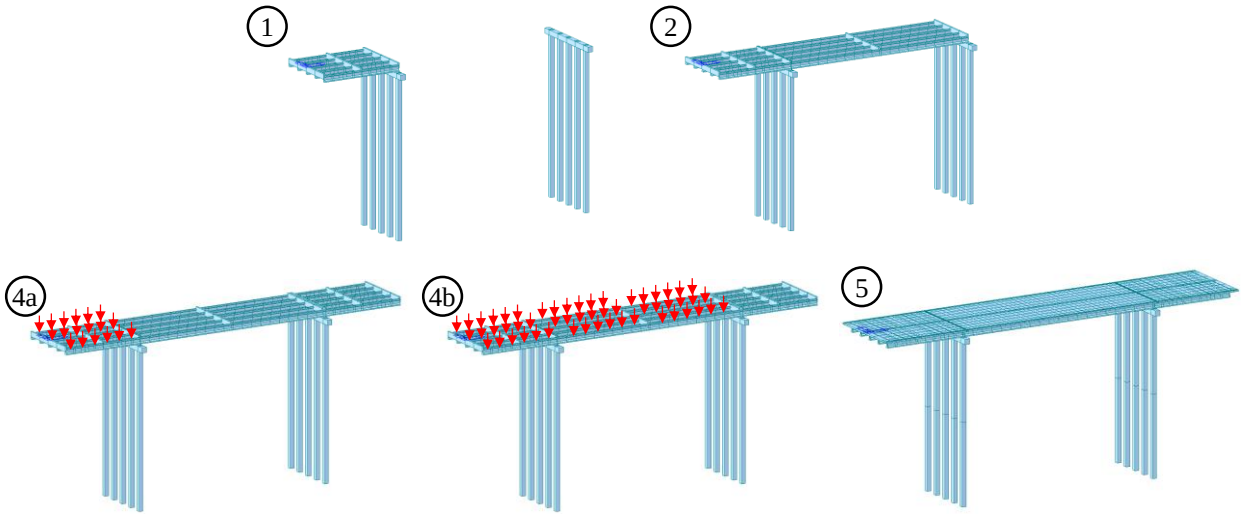

Figure 3.10: Sample model for Bridge #1 with construction stages analyzed

The weight of the deck during construction stage 4 was added using a distributed load with a magnitude of 0.8 k/ft. This distributed load was determined based on an 8-inch thick deck, 8-foot beam spacing, and normal weight concrete (150 pcf). The distributed load was applied to each girder individually in the model.

3.1.5. Fixed verses Pinned Connection

Several different connections can be assumed between the pile and pile cap, as shown in Figure 3.11. A fixed connection between pile and pile cap, Figure 3.11 (a), assumes full moment transfer between the pile and pile cap with a rotational stiffness equal to that of the pile. A pinned connection, Figure 3.11 (b), results in an unstable system as there is no moment restraint between pile and pile cap to resist the moment caused by the off-center loading from the adjacent span. A rotational spring, Figure 3.11 (c), can also be used at the connection between pile and pile cap to allow for moment transfer between the elements with a smaller rotational stiffness than the fixed connection.

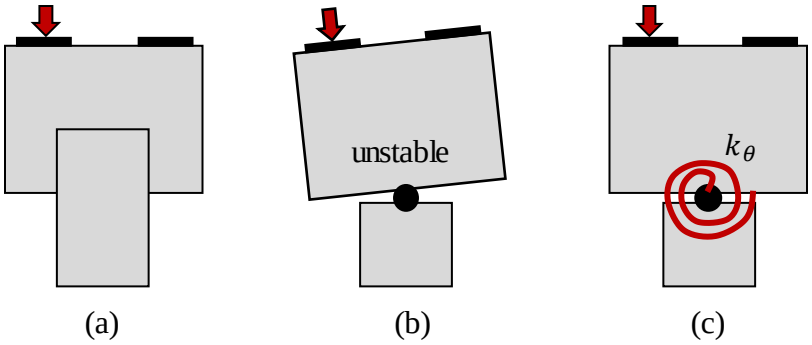

Figure 3.11: Possible assumed connections between pile and pile cap, (a) fixed, (b) pinned, and (c) pinned with rotational spring

The stiffness of the rotational spring was determined from numerical modeling results based on different embedment lengths. The rotational stiffness was determined by plotting the moment versus rotation assuming rigid body kinetic rotation about the connection between pile and pile cap, as shown in Figure 3.12. The rotational stiffness was then found based on the slope of the moment-rotation plot in the linear elastic region. The rotational stiffness was determined from one shallow embedment ($0.25d_{pile}$) and used as the connection input in the Midas model.

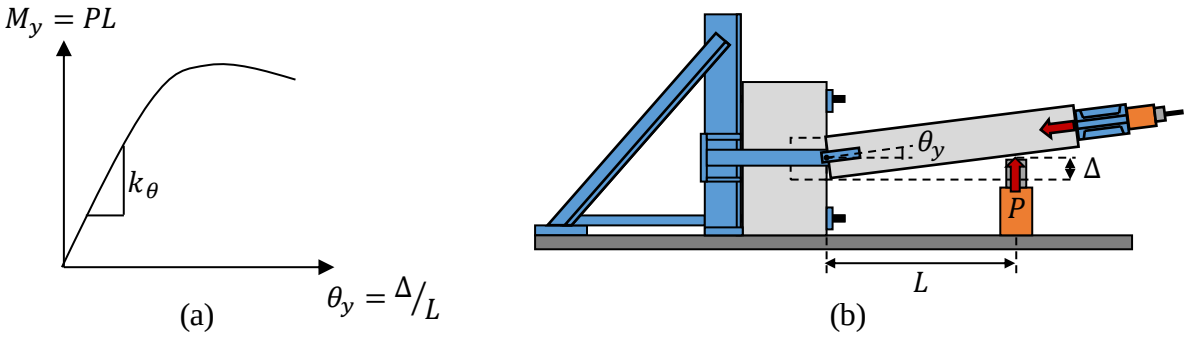

Figure 3.12: Stiffness of rotational spring determined from (a) M-θ from (b) numerical results assuming kinetic rotation about a hinge at the connection

The moment versus rotation plot for the 18-inch piles with $0.25d_b$ pile embedment is shown in Figure 3.13. The $0.25d_p$ embedment would not meet current FDOT specifications; it was

chosen to simulate a pinned connection. As shown the rotational stiffness was determined based on two points from the elastic response.

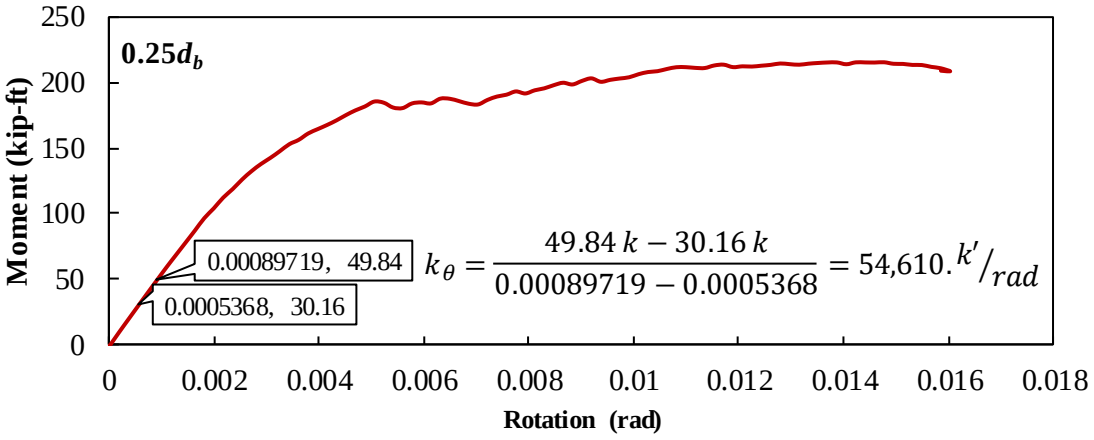

Figure 3.13: Moment versus rotation plot for 18-inch pile with 0.25d_b pile embedment from numerical analyses

3.1.6. Boundary Conditions and Modeling Assumptions

The piles, piers, beams, and deck were modeled as general beam elements. The pile caps were modeled as plate elements with a section thickness corresponding to the cap depth. The boundary conditions at the end of the beams were modeled as pinned connection. The piles were modeled assuming a pinned connection at the tip of the pile, Figure 3.14 (a), and point springs along the length of the embedded pile to model the soil-structure interaction, Figure 3.14 (b). FDOT Structure Design Guidelines [1] specifies that the modulus of subgrade reaction should be obtained from the geotechnical engineer. For purposes of this project, a modulus of subgrade reaction of 0.23 kips/in^3 in the K_x and K_y direction was selected, which corresponds to a dense soil [1].

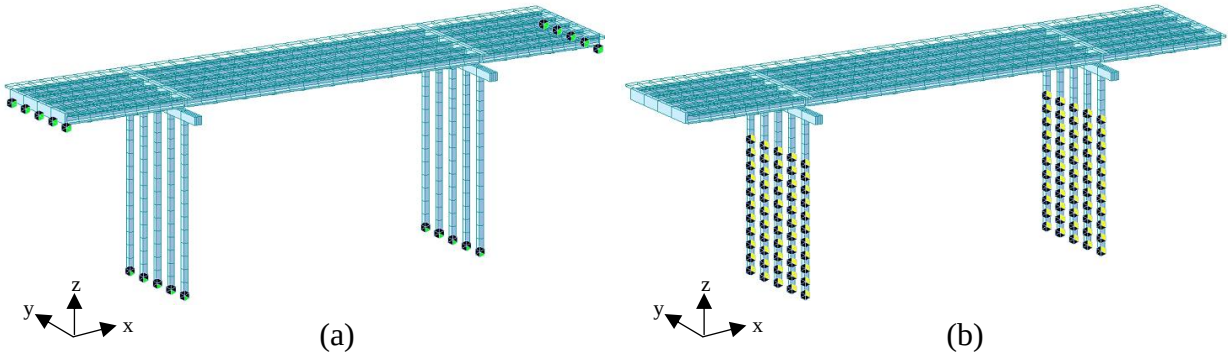

Figure 3.14: Boundary conditions for Bridge #1 (a) supports (b) soil-structure interaction

The beam element for the pile comes into a shared node with the pile cap. This creates a fixed connection unless a beam end release is applied to the node, in which case a pinned connection is realized. A beam end release with the corresponding rotational stiffness was used to simulate the pinned connection. Elastic links (simulating bearing pads) were used to connect the beam elements for beams to the pile caps at one point at the ends of the beams. The stiffness of bearing pads is manufacturer dependent; the elastic links in this model were specified to have a horizontal stiffness of 8.3 kips/inch and vertical stiffness of 7,686 kips/inch, common values for bearing pads with 7-inch thickness. In the last construction stage, the beams were modeled as composite sections with the deck. The full bridge (Construction Stage 5) was modeled two different ways: one with a continuous deck (SDCL) and one with a joint over the supports.

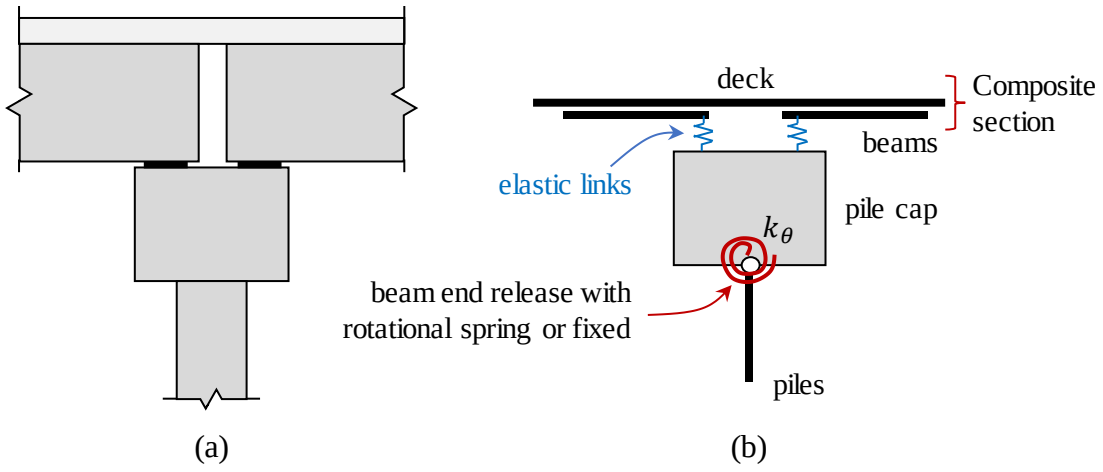

Figure 3.15: Bridge #1 modeling assumptions: (a) elements intersecting between spans at pile caps and (b) representation of elements and links between elements at this location

3.1.7. Summary of Results

A summary of all results from these analyses on Bridge #1 are presented in Section 7. A summary of some of the major findings are presented below.

The moment responses for the piles in Bridge #1 at Construction Stages 1 and 2 are shown in Figure 3.16 (a) and (b), respectively. The moment at the pile-to-cap interface was not influenced by the type of connection, as this moment is dictated by the eccentricity and magnitude of the loads provided from the two spans. The moment at the soil level was not influenced by the type of connection, all moments were minor in comparison to the pile and pile-to-cap connection capacities (about 10 percent of the full moment capacity of the 18-inch piles).

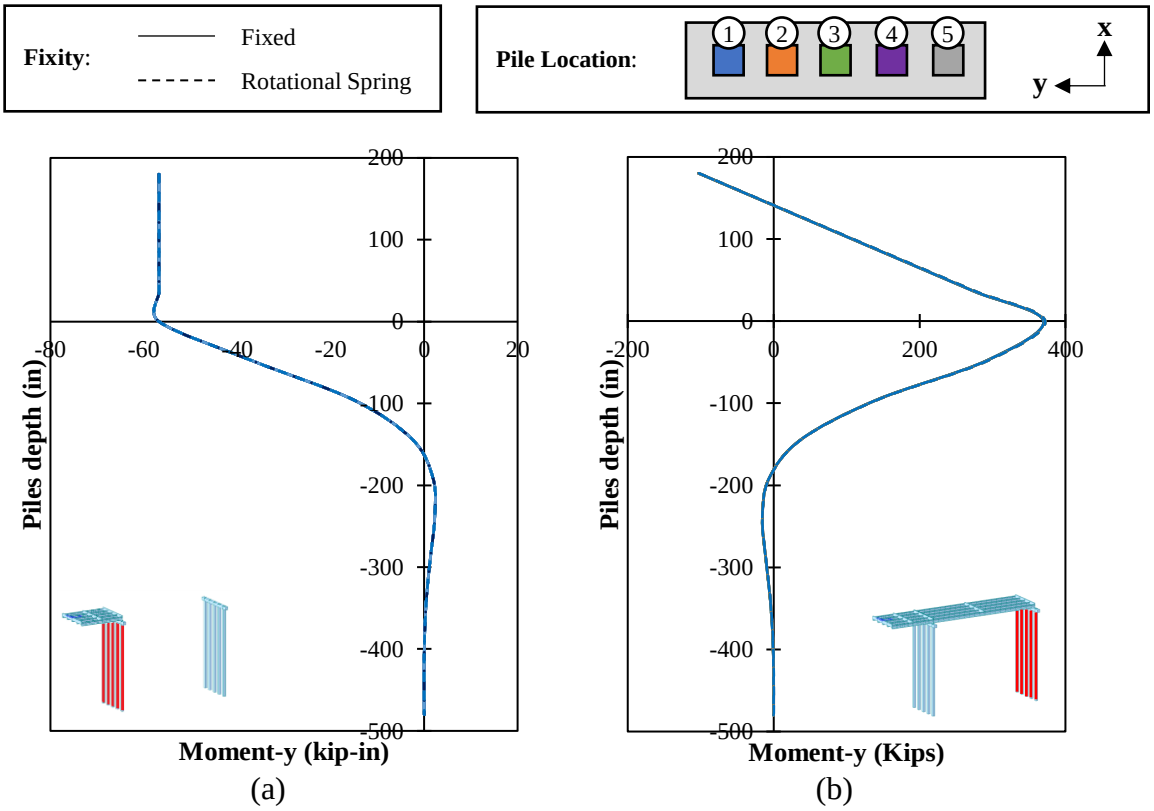

Figure 3.16: Moment response for select piles in Bridge #1 at (a) Construction Stage 1 and (b) Construction Stage 2

The moments in the beams for Construction Stage 1 and 2 were unaffected by the type of connection between the pile and cap, as shown in Figure 3.17.

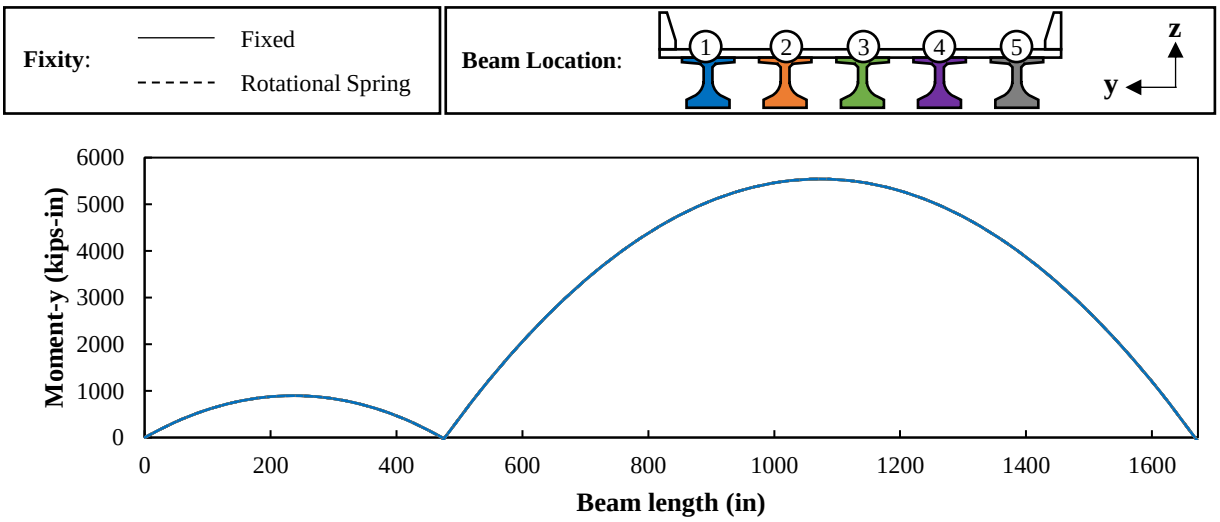

Figure 3.17: Moment response for beams in Bridge #1 at Construction Stage #2

The moment responses for the piles in Bridge #1 at Construction Stages 4a and 4b are shown in Figure 3.18, respectively.

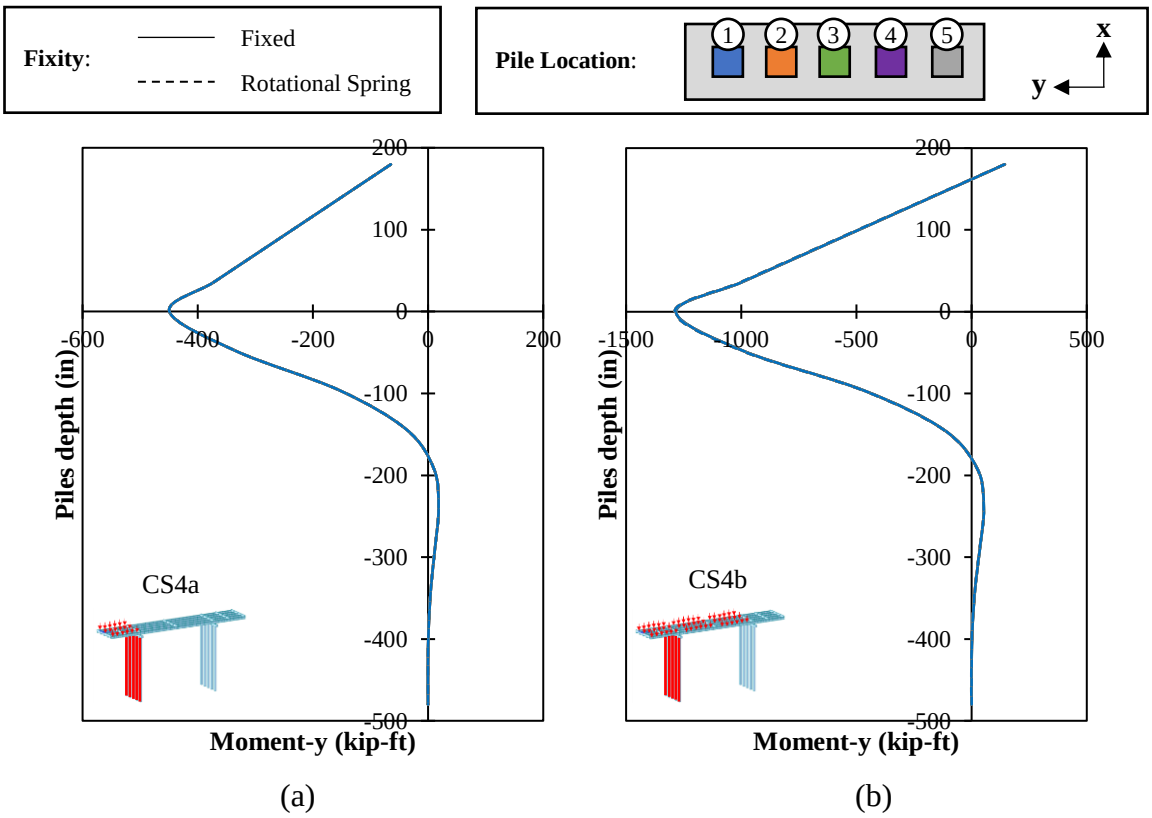

Figure 3.18: Moment response for select piles in Bridge #1 at (a) CS4a (b) CS4b

The moments in the beams for Construction Stage 4a and 4b were unaffected by the type of connection between the pile and cap, as shown in Figure 3.19.

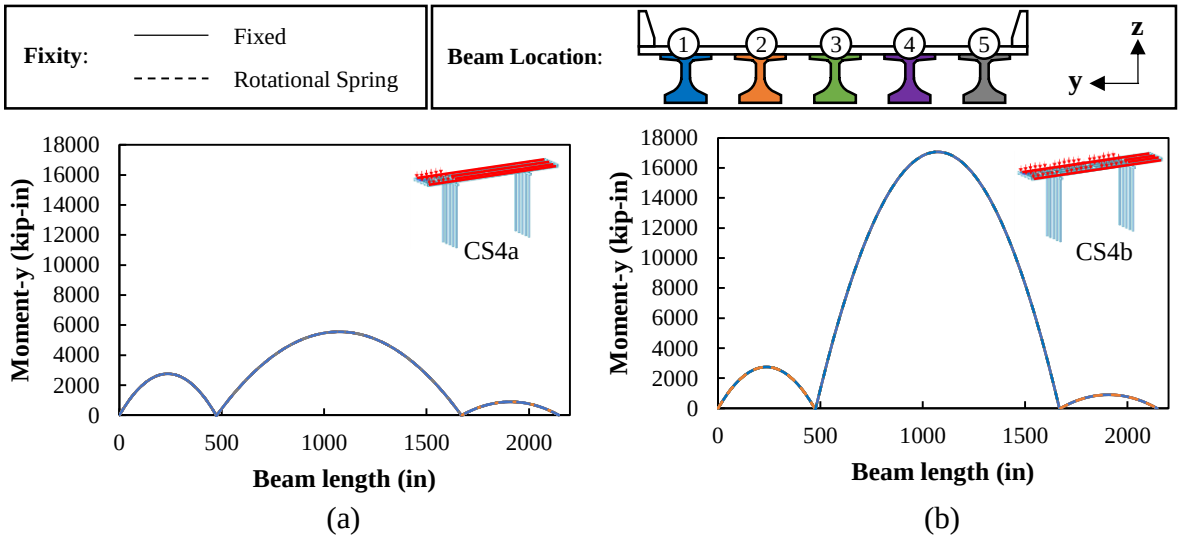

Figure 3.19: Moment response for beams in Bridge #1 at (a) CS4a (b) CS4b

The moment response in the composite beams with a continuous deck from live load and piles is shown in Figure 3.20 (a) and (b), respectively. There was no observed difference in the moment in the composite beams between the fixed and rotational spring connections, but there was a slight difference in the moments in the piles with the rotational springs resulting in slightly smaller moments at the pile-to-cap connection.

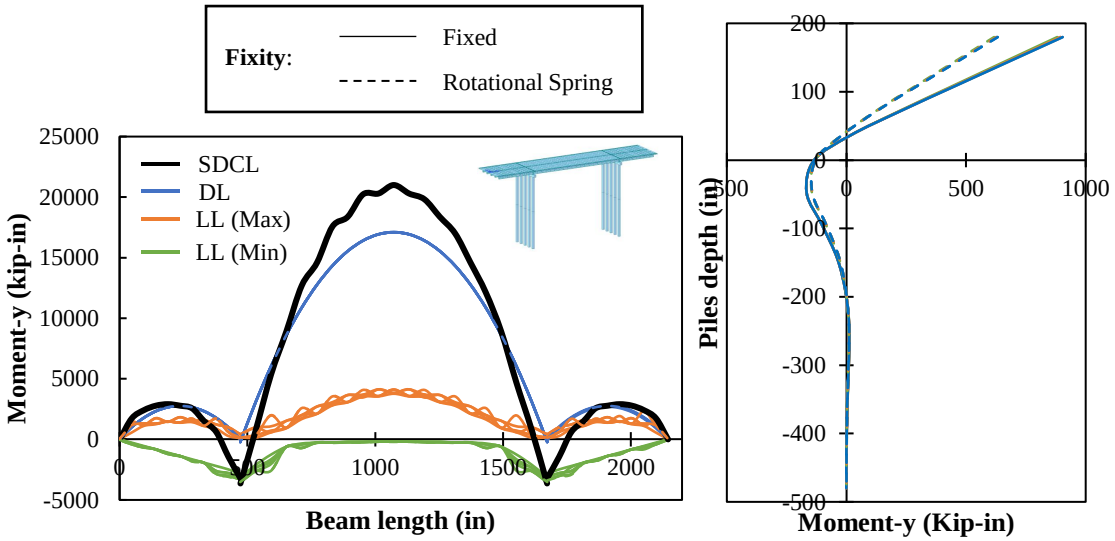

Figure 3.20: Moment response in (a) composite beam and (b) piles for Bridge #1 with continuous deck in service (Construction Stage 5)

The moment response in the composite beams with a non-continuous deck from live load and piles is shown in Figure 3.21 (a) and (b), respectively. There was again no observed difference in the moment in the composite beams between the fixed and rotational spring connections, but a slight difference in the pile moments. There was a slightly smaller moment at the pile-to-cap connection and a slightly larger moment at the ground level.

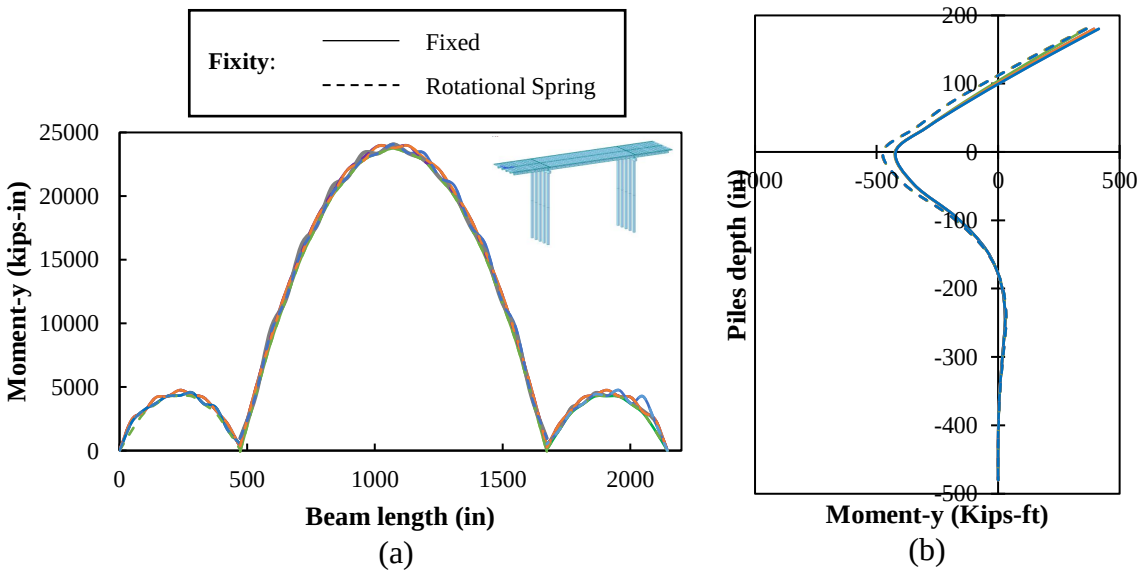

Figure 3.21: Moment response in (a) composite beam and (b) piles for Bridge #1 with non-continuous deck in service (Construction Stage 5)

The type of joint had no impact on the axial load in any of the piles for any of the construction stages.

3.2. BRIDGE #2: PT SEGMENTAL BOX GIRDER WITH FIXED PIER TABLE AND LATERAL LOAD ON SUBSTRUCTURE

Structures that are designed to resist large lateral loads (e.g., ship impact or seismic loads) are sensitive to the assumed fixity between the pile and pile cap or footing. Bridges in Florida that are located over navigable waters must be designed including consideration for possible vessel impact (e.g. from barges or ocean going ships) [54].

The second base structure analyzed was a segmental box girder with a fixed pier table with pile cap and pier, similar to the structure shown in Figure 3.22. This structure was used to analyze the effect of pile fixity on the structural response of vessel impacts.

(a) (b)

Figure 3.22: Wekiva River Bridge (a) fixed pier table and (b) bridge elevation [55]

3.2.1. Base Structure

The base structure was a one-cell segmental box girder fixed to a pier with a constant depth *D*, as shown in Figure 3.23, with three spans, as shown in Figure 3.24.

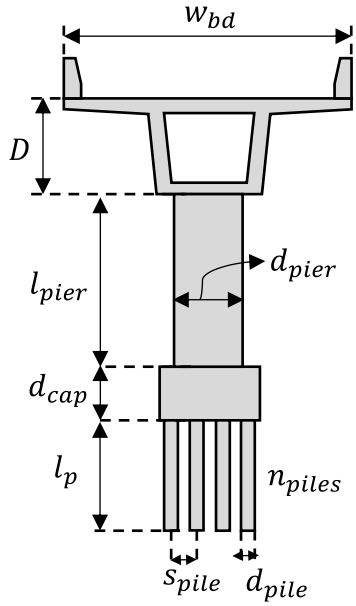

Figure 3.23: Typical section for Bridge #2

The primary variables selected for the analysis are summarized in Table 3.3. The cap width and length were based on the pile size and pile configuration.

Table 3.3: Variable values for Bridge #2

Variable		Base Case
Pile spacing	s_{pile}	$3.0d_p$
Pile length	l_p	40’/55’
Pier height	l_{pier}	65’/85’
Pile width	d_{pile}	24” and 30”
Pier width	d_{pier}	10’
Cap depth	d_{cap}	4’
Number of piles at each pier	n_{piles}	12
Bridge width	w_{bd}	35’
Bridge length	L_{bridge}	435’

The span length was determined based on whether the structure had three equal spans, Figure 3.24 (a), or was constructed using a balanced cantilever approach, Figure 3.24 (b). The bridge length was kept the same for both cases. For the equal span length configuration, all spans were 145 feet. The spans for the balanced cantilever were selected such that the outside span lengths were 0.6 times the main span length, giving span lengths of 118, 199, and 118 feet for the three spans.

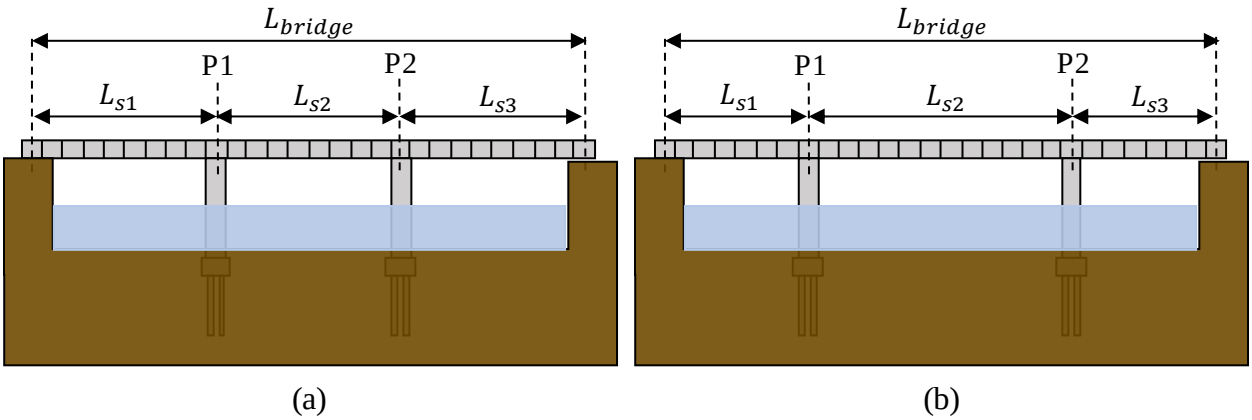

Figure 3.24: Elevation of Bridge #2 with (a) equal spans and (b) balanced cantilever configuration

The pile cap in this type of structure can either be located at the water line, which is most typical, or at the soil level under the water, both shown in Figure 3.25. The location of the lateral load will be at the water level, so it will be applied at mid-height of the pier for the soil-level pile cap and directly to the pile cap when the pile cap is at the water line. When the pile cap is at soil level, the entire pile (40 feet) will have soil-structure interaction and the pier will have a height of 85 feet. When the pile cap is at the water level, 40 feet of the pile is embedded in soil and 15 feet of the pile will not have soil-structure interaction, which is the distance from bottom of pile cap to soil. The piers in this case will extend 65 feet above the water line, which is typical for navigation clearance.

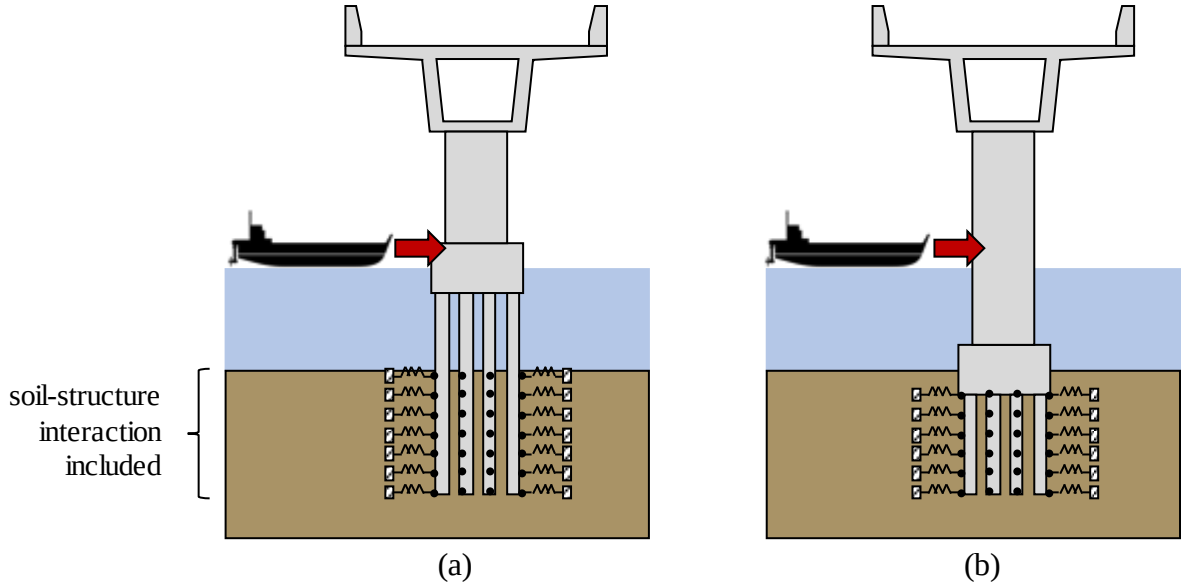

Figure 3.25: Pile cap location for Bridge #2 (a) at water line and (b) at soil level

3.2.2. Concrete Strength

The concrete strengths used in each structural element are summarized in Table 3.4.

Table 3.4: Concrete Strength Properties for Bridge#2

Component	Concrete Strength
Box girder	Class IV
Piles	Class V (Special)
Pile Cap	Class IV
Piers	Class IV

3.2.3. Cross Section Details for Members

3.2.3.1. Segmental Box Girder

The AASHTO-PCI-ASBI Standard box girder 2100-1 with a deck width of 34.5 feet (10,500 mm) was selected as the cross section for this bridge. The AASHTO general cross section is shown in Figure 3.26 and properties summarized in Table 3.5.

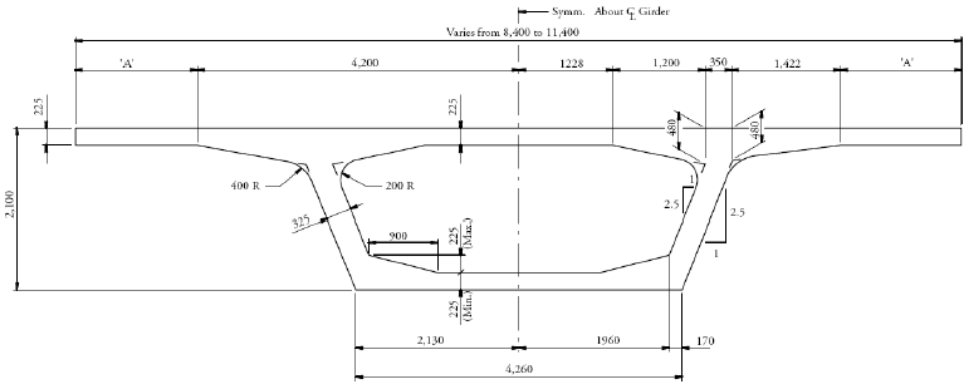

Figure 3.26: AASHTO-PCI ASBI Standard 2100-1 box beam [56]

Table 3.5: Section properties for AASHTO-PCI ASBE Standard 2100-1 box beam [56]

Deck Width (in.)	A (in.)	Area (in.^{2})	Wt. (k/ft.)	I_x (in.^{4})	y_t (in.)
414	41.3	8,353	8.86	7.621 x 10^9	29.1

3.2.3.2. Piles

Pile designs were based on FDOT standard plans for prestressed concrete piles [53]. Square prestressed concrete piles with 24-inch width and height were used for the initial pile configuration for Bridge #2; details for 24-inch piles are shown in Figure 3.27 (a). The pile size was later increased to 30-inch piles, Figure 3.27 (b), and pile configuration modified to reduce the demand on individual piles. The pile section and concrete properties are

provided as inputs in the software used for this task. Details for the prestressing strands are not inputs in the analysis software.

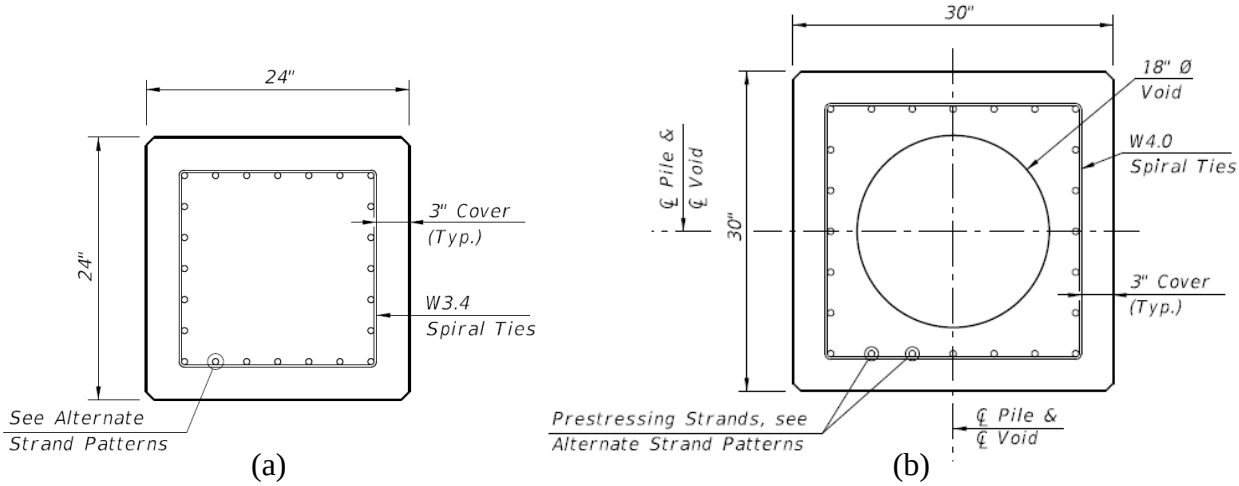

Figure 3.27: Details for (a) 24-inch and (b) 30-inch square prestressed concrete piles used in Bridge #2 [53]

3.2.3.3. Pile Cap

Details for the base pile cap configuration are shown in Figure 3.28. The preliminary pile cap investigated had a pile grid of 3 by 4 piles, which was thought to be typical for the bridge configuration and lateral load applied. Additional pile grids were investigated as described below to decrease the demand on individual piles. The spacing of the piles was based on a minimum center-to-center spacing of $3d_b$ [1].

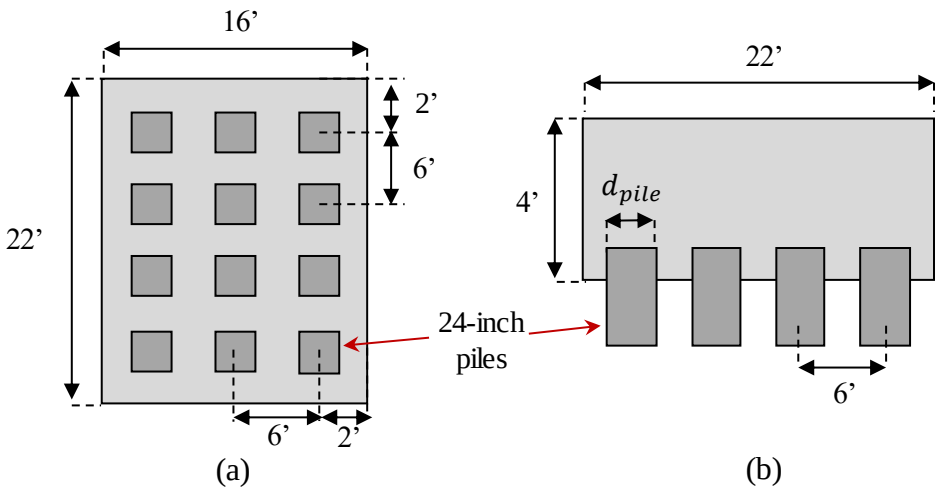

Figure 3.28: Pile cap details (a) Plan view (b) Cross section

3.2.3.4. Piers

Square concrete columns with 10ft width and height were used for Bridge #2. The cross section of the pier is shown in Figure 3.29.

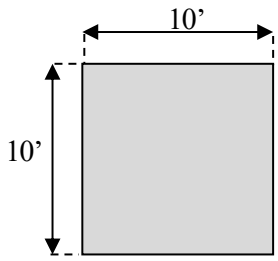

Figure 3.29: Pier cross section

3.2.4. Loading

FDOT Structures Design Guidelines [1] specifies that the design of all bridges over navigable waters must include consideration of vessel impact. To analyze the bridge response under extreme events, a lateral force representing the vessel collision was applied. A 2,000-kip lateral force was applied to Pier 1 to represent the vessel impact on the bridge.

The analysis was performed under the load combination “Extreme Event II” as shown in Equation 3.1.

$$1.00\,DC + 0.50LL + 1.00CV \qquad \text{Equation 3.1}$$

3.2.5. Boundary Conditions and Modeling Assumptions

The models for Bridge #2 are shown in Figure 3.30 for all equal spans and the balanced cantilever configuration. The global x-y-z coordinate system is shown; this coordinate system is referenced in many of the results figures to help with orientation.

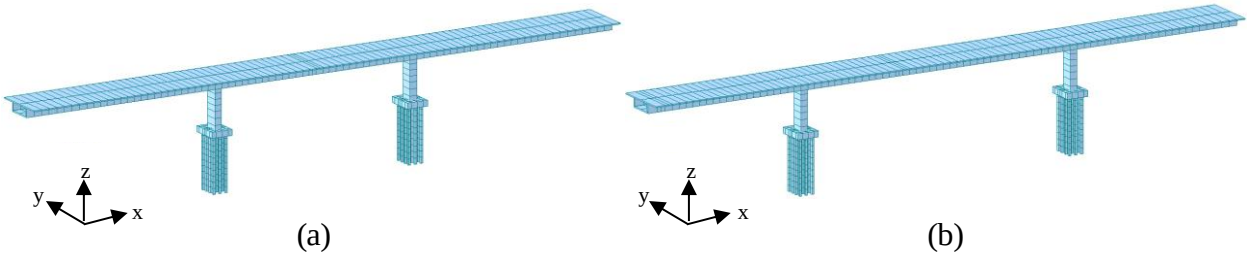

Figure 3.30: Bridge #2 with (a) all equal spans and (b) balanced cantilever configuration

The piles, piers, and box beams were all modeled as general beam elements. The pile caps were modeled as plate elements with a section thickness corresponding to the cap depth. An elastic link was provided between the top of the pier and the box segment on top of the pier, like those described for Bridge #1. The structure was modeled as a three-span continuous structure. Like Bridge #1, the piles were modeled assuming a pinned connection at the bottom tip of the pile and point springs along the length of the embedded pile, simulating soil-structure interaction. A beam end release was defined between pile and pile cap to simulate a pinned connection; otherwise, the connection behaves as fully fixed. A rotational spring was not used for pinned connections between pile and cap (like

in Bridge #1) in these models as all models were stable with fully pinned connections. Modeling these extremes also enveloped all possible results between a pinned and fixed connection.

When the pile cap was located at the water level, the lateral load was applied to the pile cap and soil structure interaction (i.e., point springs) in the pile was initiated at 15 feet below the pile cap, as shown in Figure 3.31 (a). The soil structure interaction was included along the entire length of the pile for the case of the pile cap at soil level, as shown in Figure 3.31 (b).

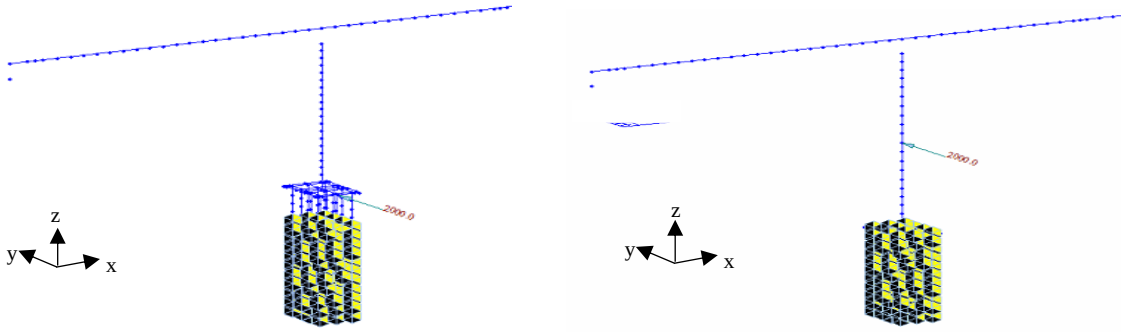

(a) (b)

Figure 3.31: Boundary conditions for half of structure (showing Pier 1) with (a) pile cap at water level and (b) pile cap at soil level

3.2.6. Summary of Results

A summary of some of the major findings are presented below. Note that similar results were observed for equal span length and balanced cantilever analyses.

The axial load in the piles of the pier with the lateral load are shown in Figure 3.32. In the waterline pile cap, an axial tension force (maximum of 285 kips tension) was observed for

some of the piles with pinned pile-to-cap connections while almost no axial tension (maximum of 40 kips tension) was observed in the piles with fixed pile-to-cap connections. Larger axial compression was also observed in the piles with pinned pile-to-cap connections (maximum of 574 kips compression compared to a maximum of 285 kips for piles with fixed pile-to-cap connections).

In the soil-level pile cap, axial tension was present in some piles with pinned (maximum of 325 kips tension) and fixed (maximum of 388 kips tension) pile-to-cap connections, a difference of about 16%. There was also a smaller difference between the maximum axial compression in piles with pinned (600 kips compression) and fixed (664 kips compression) pile-to-cap connections, a difference of about 10%.

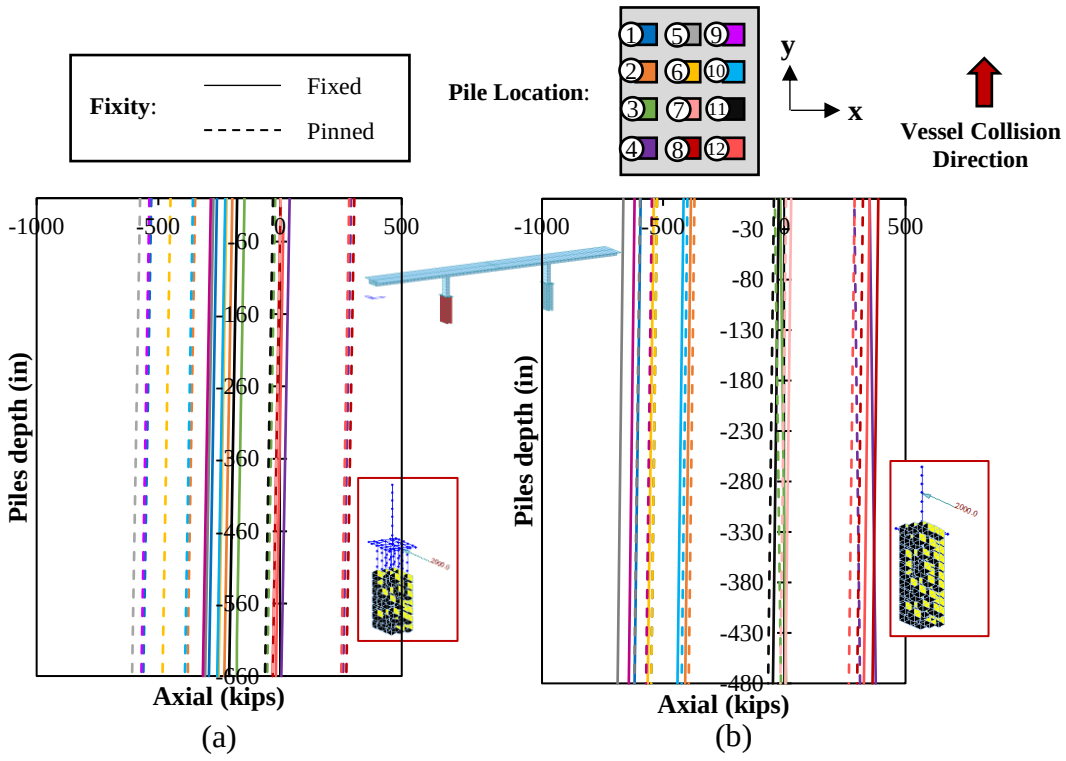

Figure 3.32: Axial load response for Bridge #2 with all equal spans for select piles supporting the loaded pier for (a) pile cap at water level and (b) pile cap at soil level

The moment demand in the piles of the pier with the lateral load (caused by the lateral load) are shown in Figure 3.33. A pinned connection resulted in a slightly higher maximum moment (1,774 kip-ft) in the pile compared to the fixed connection (1,713 kip-ft) for water-level pile cap location (3% increase). For soil-level pile cap, a fixed connection resulted in a higher maximum moment (420 kip-ft) compared to a pinned connection (251 kip-ft) which corresponds to a 40% difference. The location of the maximum moment also changes based on connection fixity, between the embedded portion of the pile for pinned connection to the connection between pile and cap for the fixed connection.

The pinned connection produced the maximum axial tension and compression forces in the piles for the water-level pile cap, while the fixed connection had larger axial tension and compression forces in the piles for the soil-line pile cap. The lateral force produced much higher moments in general for the water-line pile caps compared to the soil-level pile caps; an 85% increase for pinned connections and 75% increase for fixed connections.

The analysis results showed that the ultimate capacity of the 24-inch piles (681 kip-ft) was not sufficient for the water-level pile cap. Several other pile grids were investigated to decrease the demand on the piles.

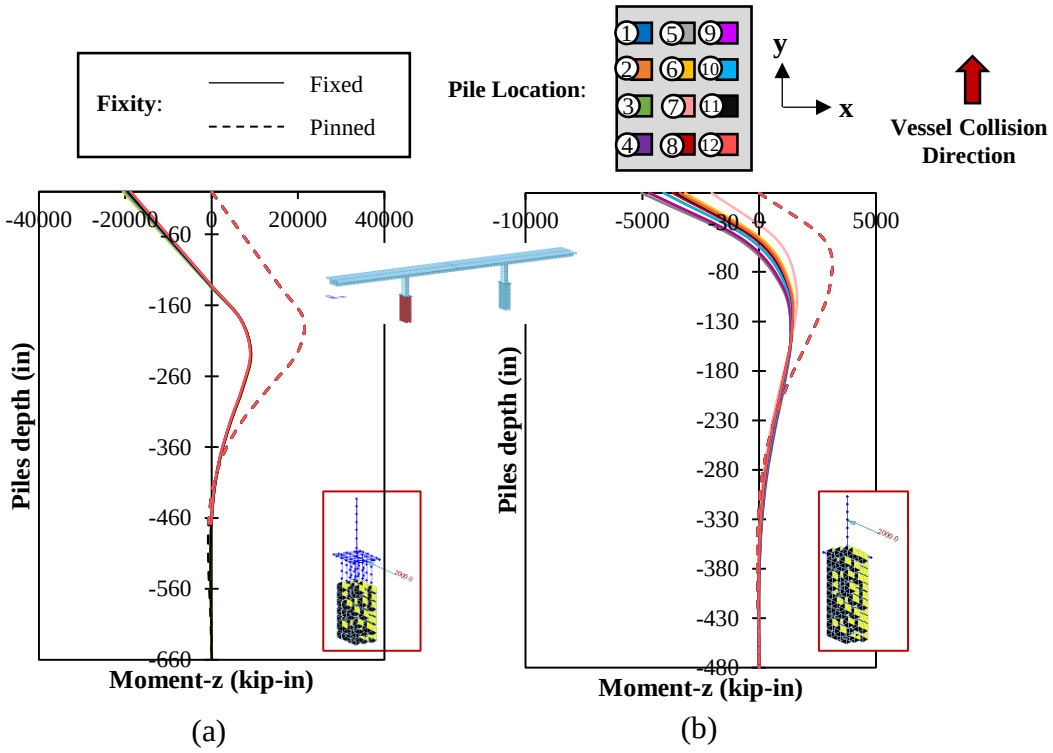

Figure 3.33: Moment (z direction) response for Bridge #2 with all equal spans for select piles supporting the loaded pier for (a) pile cap at water level and (b) pile cap at soil level

The next pile grid and pile size that was investigated was a 4 by 5 pile grid of 30-inch piles, as shown in Figure 3.34. The pile spacing was still $3d_{pile}$ and pile cap geometry was $11d_{pile}$ by $14d_{pile}$.

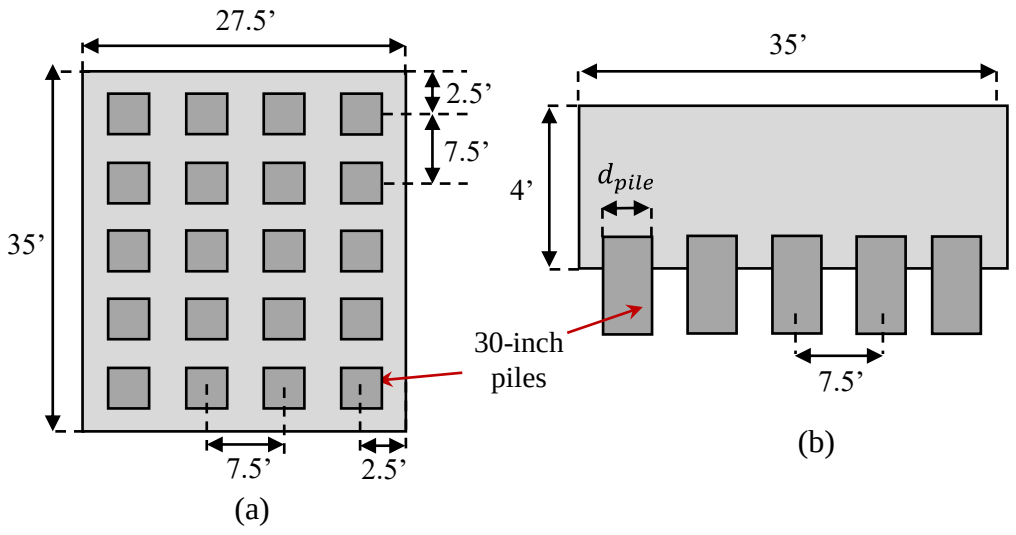

Figure 3.34: Pile cap details for 4x5 grid of 30-inch piles (a) plan view (b) cross section

The axial load in the piles of the pier with the lateral load are shown in Figure 3.35. Increasing the number of piles and pile size significantly decreased the overall demand on the individual piles and changed the way pile-to-cap fixity affected the pile response, compared to the 4 by 3 grid of 24-inch piles. For the water-level pile cap, the maximum tension was observed in the piles with fixed pile-to-cap connections (maximum of 137 kips tension compared to a maximum of 19 kips tension for pinned pile-to-cap connections). The maximum compression was still in the piles with pinned pile-to-cap connections (329 kips compression compared to 261 kips for fixed pile-to-cap connections).

For the soil-level pile cap, there was a smaller difference in the maximum axial tension between pile-to-cap fixities (142 kips tension for fixed and 104 kips tension for pinned) and no difference in the maximum axial compression (507 kips compression for pinned and 507 kips compression for fixed).

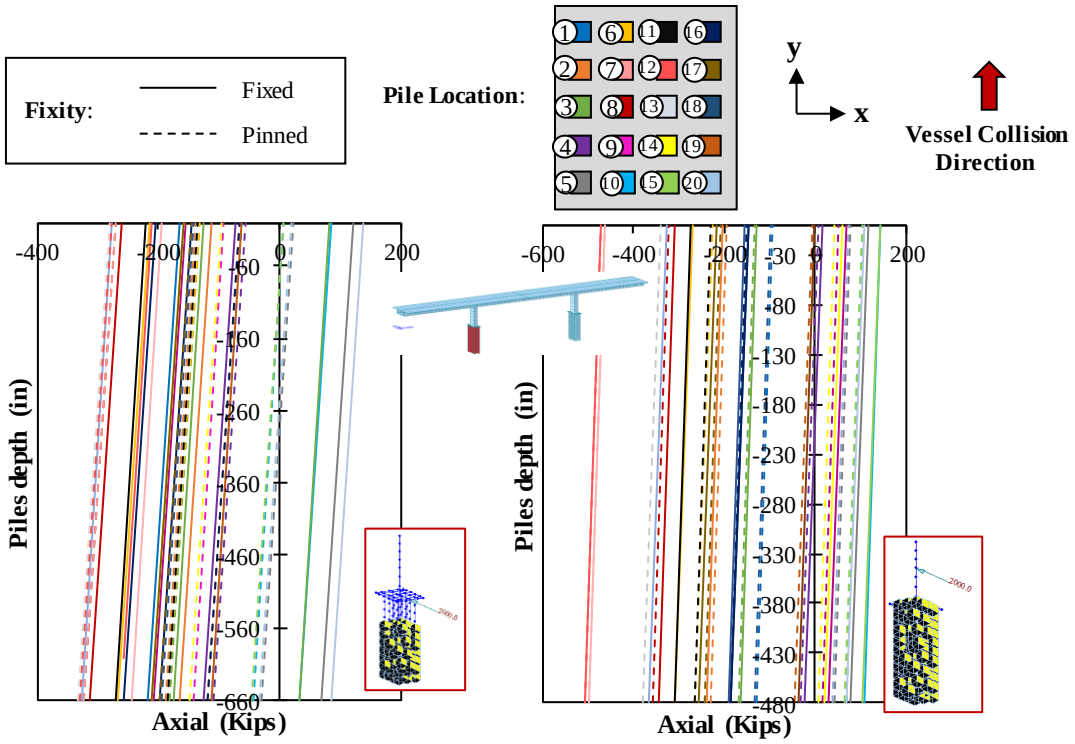

Figure 3.35: Axial load response for Bridge #2 4x5 grid with all equal spans for select piles supporting the loaded pier for (a) pile cap at water level and (b) pile cap at soil level

The moment caused by the lateral load in the piles of the pier with lateral load are shown in Figure 3.36. In the water-level pile cap, there was little difference in the maximum moment for fixed and pinned connection (1,466 kip-ft for fixed compared to 1,403 kip-ft for pinned). For soil-level pile cap, a fixed connection resulted in a higher maximum moment (392 kip-ft) compared to a pinned connection (187 kip-ft) which corresponds to a 52% increase.

The moment demand was less for the soil-level pile cap than the water-level pile cap for both pinned and fixed pile-to-cap connections.

The moments obtained for the new pile cap configuration with 30-inch piles are smaller compared to the moments with twelve 24-inch piles, but still greater than the ultimate capacity of the 30-inch piles (1,098 kip-ft).

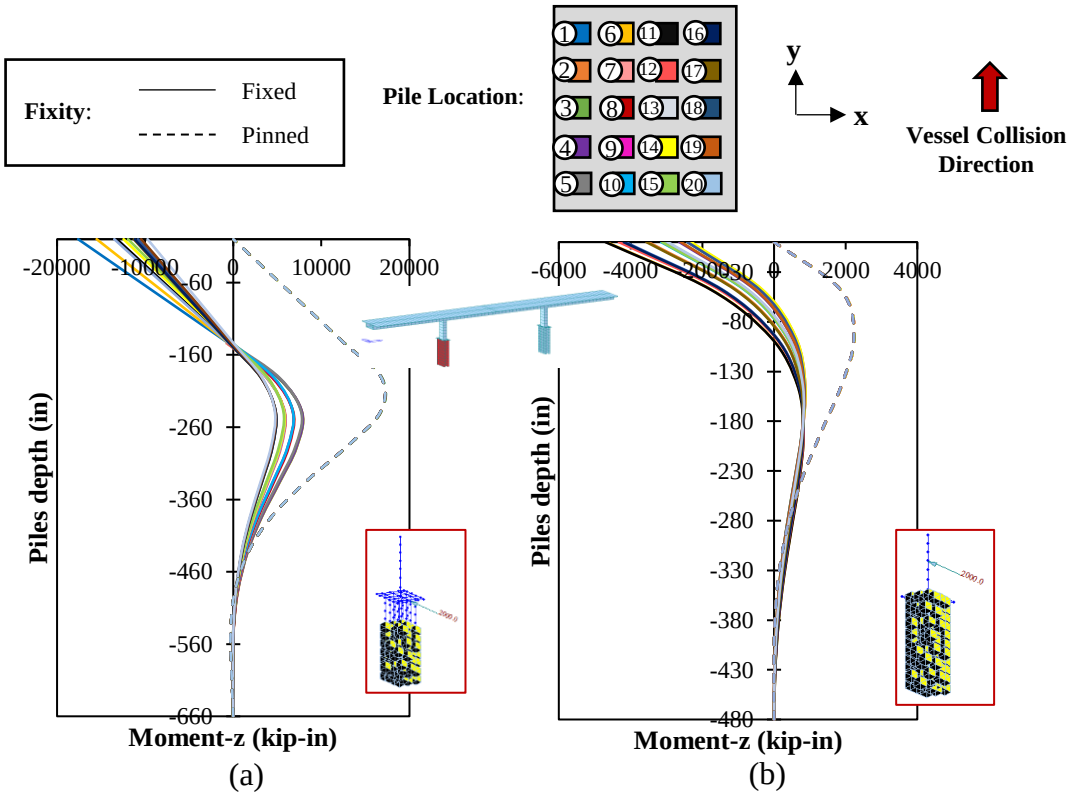

Figure 3.36: Moment (y direction) response for Bridge #2 4x5 grid with all equal spans for select piles supporting the loaded pier for (a) pile cap at water level and (b) pile cap at soil level

The next pile grid and pile size that was investigated was a 5 by 5 pile grid of 30-inch piles, as shown in Figure 3.37. The pile spacing was still $3d_{pile}$ and pile cap geometry was $14d_{pile}$ by $14d_{pile}$.

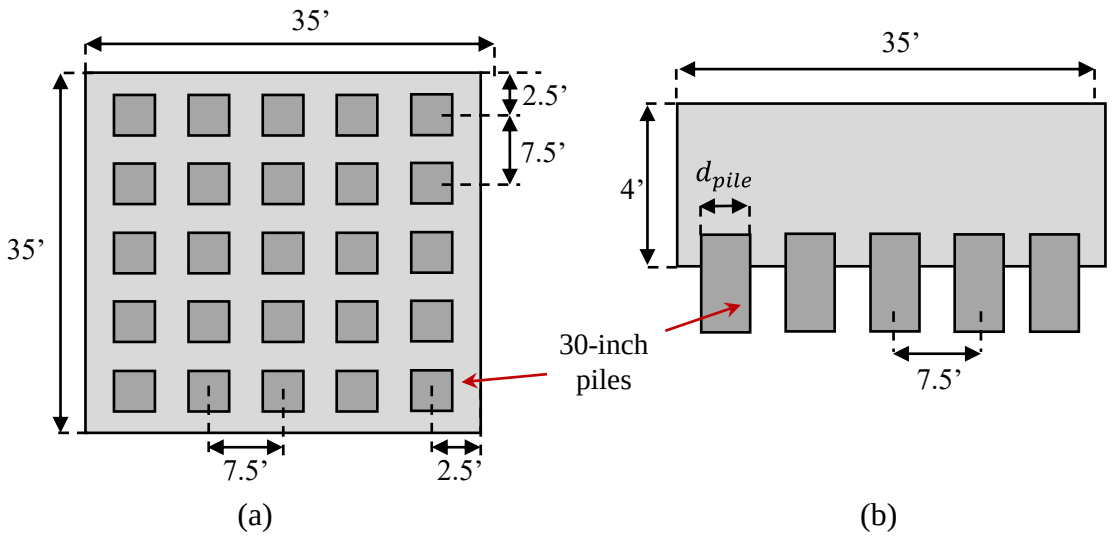

Figure 3.37: Pile cap details for 5x5 grid (a) Plan view (b) Cross section

The axial load and moment in the piles of the pier with lateral load are shown in Figure 3.38 and Figure 3.39, respectively. The maximum axial compression, axial tension, and maximum moment (absolute value) are summarized in Table 3.6. Adding the five additional piles to the pile configuration further decreased the demand on the individual piles. Also, in general, there was less of a difference in the pile behavior between pinned and fixed pile-to-cap connection (similar maximum axial compression for both, axial tension for soil level, and maximum moment for water-level pile caps). Fixed pile-to-cap connections resulted in higher axial tension with water-level pile caps (64% increase) and higher maximum moment with soil-level pile caps (71% increase).

Table 3.6: Summary axial load and moment (z direction) for pile cap at water level and pile cap at soil level

Pile Cap Location	**Water Level**		**Soil Level**	
Pile-to-Cap Connection	*Pinned*	*Fixed*	*Pinned*	*Fixed*
Maximum Axial Compression (kips)	325	306	493	492

Pile Cap Location	Water Level		Soil Level	
Maximum Axial Tension (kips)	22	79	103	127
Maximum Moment (M_z) (kip-ft)	996	919	140	476

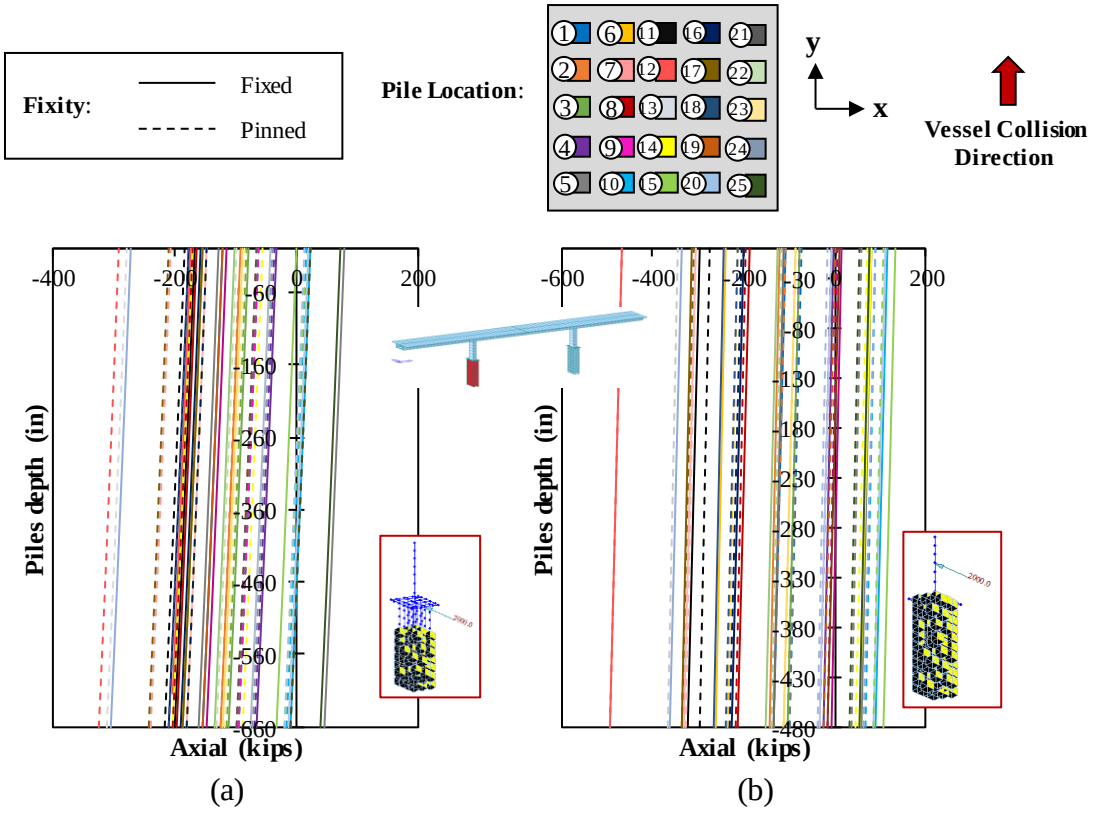

Figure 3.38: Axial load response for Bridge #2 5x5 grid with all equal spans for select piles supporting the loaded pier for (a) pile cap at water level and (b) pile cap at soil level

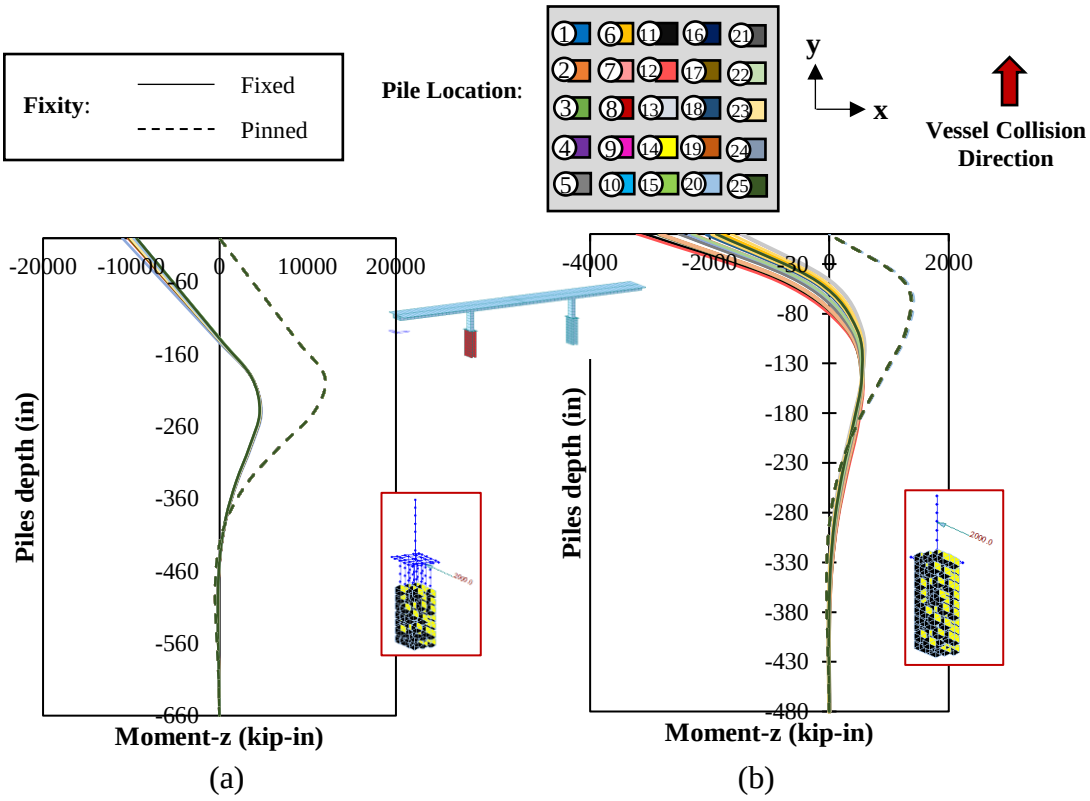

Figure 3.39: Moment (z direction) response for Bridge #2 5x5 grid with all equal spans for select piles supporting the loaded pier for (a) pile cap at water level and (b) pile cap at soil level

The moments obtained for the grid with twenty-five, 30-inch piles are smaller compared to the moments with twenty 30-inch piles. As previously mentioned, the ultimate capacity of the 30-inch pile is 1,098 kip-ft, which satisfy the demand for all the piles in the soil-level and water-level pile cap, as shown in Figure 3.40.

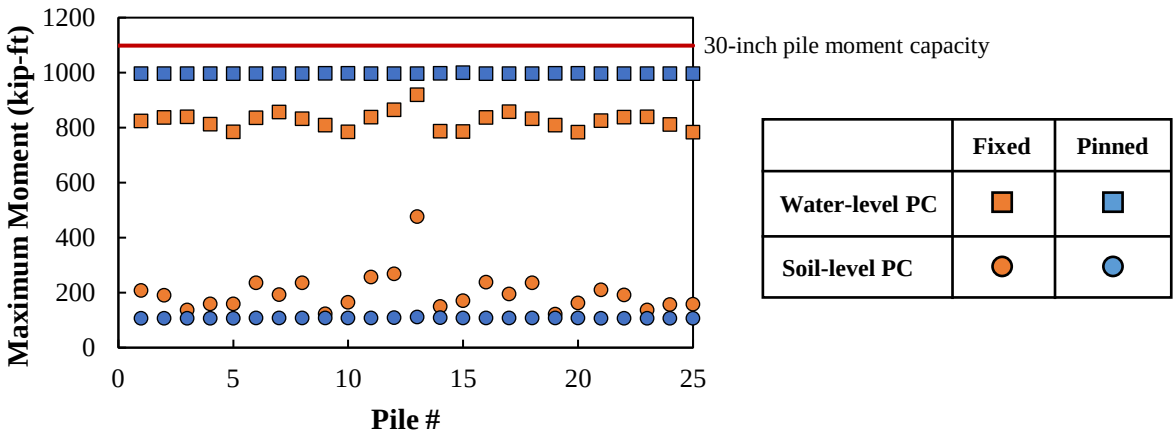

Figure 3.40: Maximum moment for piles supporting the loaded pier for pile cap at water and soil level

After different iterations, the final geometry of the segmental box girder bridge that satisfies the moment demands, consists of twenty-five 30-inch piles in each pile cap, as shown in Figure 3.41. The results obtained showed that higher moments were obtained with the water-level pile cap, but the structure was more sensitive to the connection (pinned or fixed) for the soil-level pile cap.

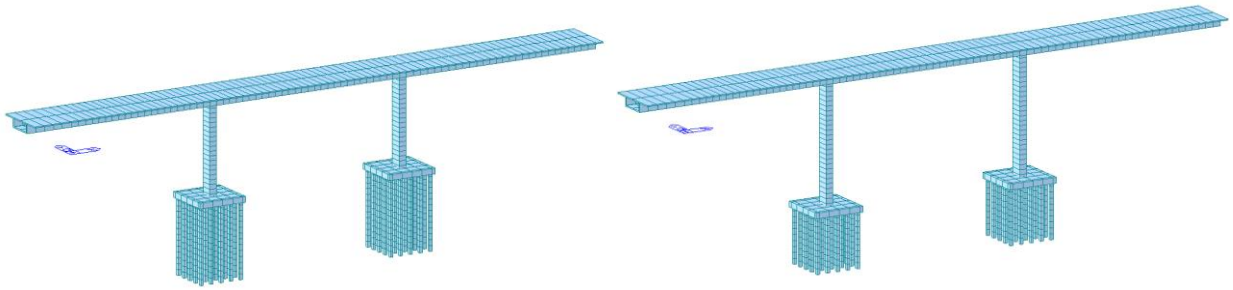

(a) (b)

Figure 3.41: Final geometry for Bridge#2 (a) water-level pile cap (b) soil-level pile cap

The axial load in the piers was unaffected by the type of connection between pile cap and the location of pile cap and applied lateral load.

The moment in the piers was unaffected by the pile-to-cap connection for the soil-level pile cap as shown in Figure 3.42. On the contrary, the pier where the lateral load is applied, is highly affected by the type of connection in the water-level pile cap.

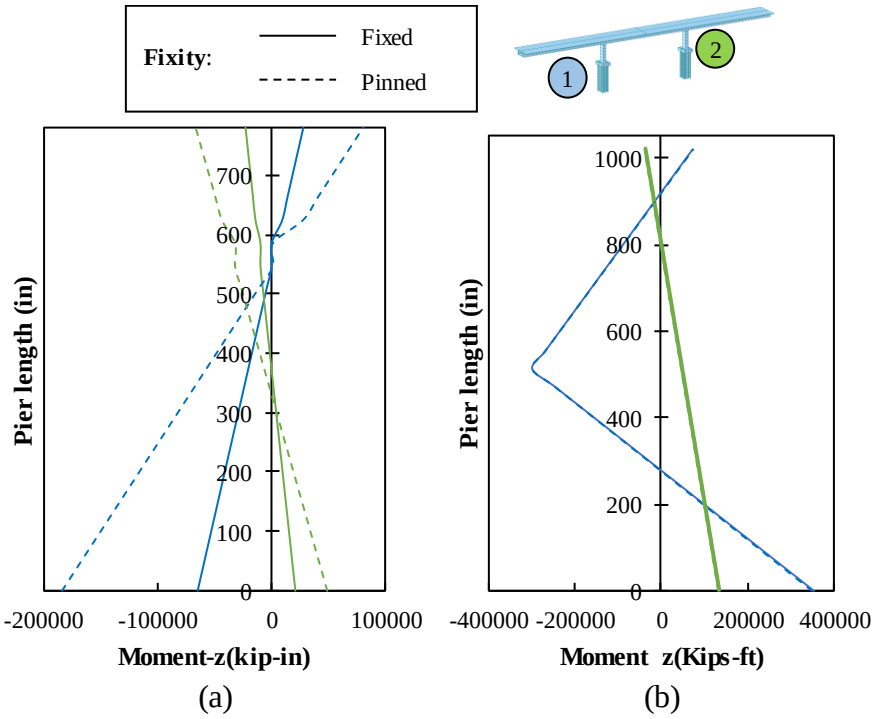

Figure 3.42: Moment (z direction) response for Bridge #2 with all equal spans for laterally loaded piers for (a) pile cap at water level and (b) pile cap at soil level

The response of the box beam was unaffected by whether a fixed or pinned connection in the soil-level pile cap. On the water-level pile cap case a higher shear response and moment in the z direction was obtained for the pinned connection, as shown in Figure 3.43.

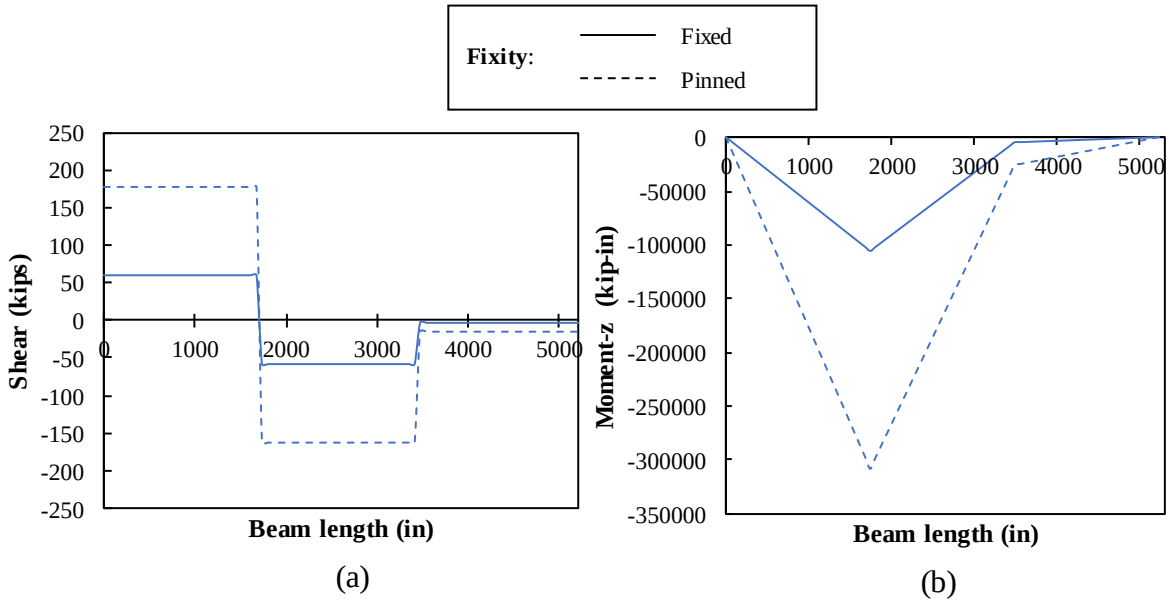

Figure 3.43: (a) Shear (y direction) and (b) moment response for Bridge #2 with all equal spans and water-level pile caps along length of beam

3.3. BRIDGE #3: STRADDLE BENT

The assumed fixity between pile and cap can also impact the design of bridges where the stiffness of the substructure can impact the behavior of the superstructure. These bridges include segmental box girder bridges with fixed pier tables, and straddle bents, although it is not necessarily a feature of structures with integral superstructures. Foundation stiffness for short piers was closely considered to capture the change in forces for time-dependent creep and shrinkage, support settlement, transit breaking loads, etc.

The third base structure to be evaluated was a straddle bent, similar to the one shown in Figure 3.44, considering temperature effects and approximate loading from the superstructure.

Figure 3.44: Straddle bent (courtesy of Corven Engineering)

3.3.1. Base Structure

The details for the straddle bent are shown in Figure 3.45 and Table 3.7.

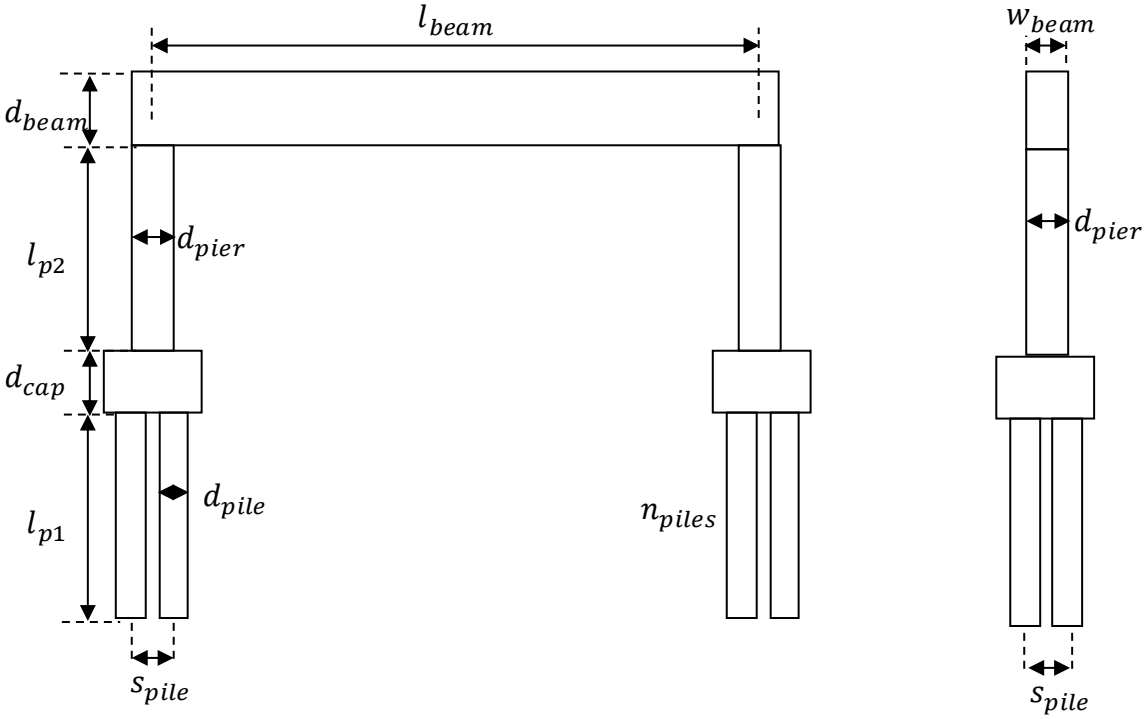

Figure 3.45: Details for Bridge #3

Table 3.7: Variable values for Bridge #3

Variable		Base Case
Pile spacing	s_{pile}	5’
Driven pile depth	l_{p1}	40’

Variable		Base Case
Pier height	l_{p2}	20’
Pile width	d_{pile}	18”
Pier width	d_{pier}	5’
Number of piles at each pile cap	n_{piles}	4
Beam length	l_{beam}	40’
Beam depth	d_{beam}	6’
Beam width	w_{beam}	5’
Cap depth	d_{cap}	5’

3.3.2. Cross Section Details for Members

3.3.2.1. Pile Cap

Details for the pile cap are shown in Figure 3.46. The preliminary pile cap investigated has a pile grid of 2 by 2 piles, which is typical for this bridge configuration. The spacing of the piles is based on a minimum center-to-center spacing of $3d_b$ [1].

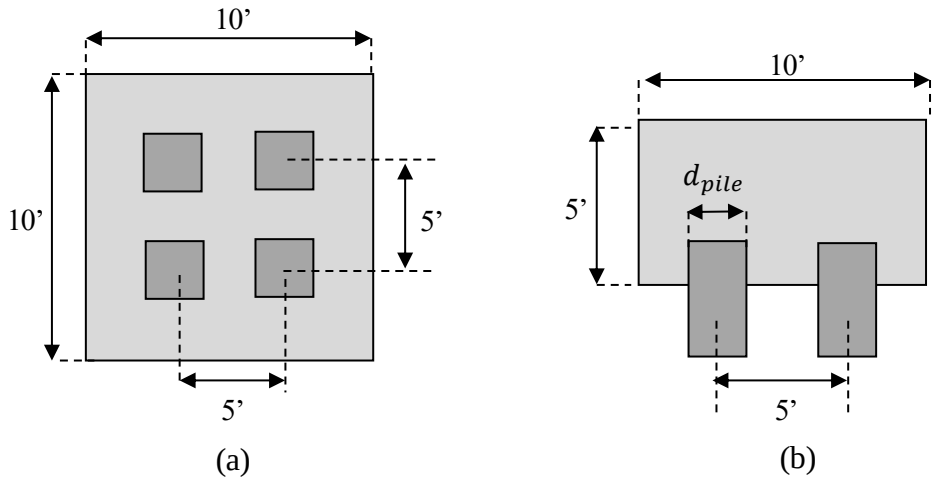

Figure 3.46: Pile cap details (a) Plan view (b) Cross section

3.3.2.2. Pile

Pile designs were based on FDOT standard plans for prestressed concrete piles [53]. Square prestressed concrete piles with 18-inch width and height were used for Bridge #3; details for 18-inch piles are shown in Figure 3.47. The pile section and concrete properties are provided as inputs in the software used for this task. Details for the prestressing strands are not inputs in the analysis software.

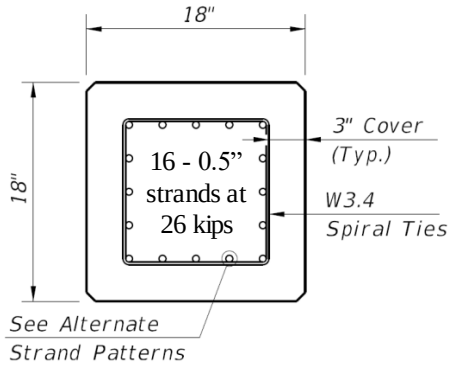

Figure 3.47: Details for 18-inch square prestressed concrete pile used in Bridge #3 [53]

3.3.2.3. Straddle Bent

Details for the straddle beam are shown in Figure 3.48. The section investigated consists of six 6-inch ducts with twelve 0.6-inch strands in each duct. The strand pattern was based on a Midas tutorial: Straddle Beam Design using Midas Civil [57].

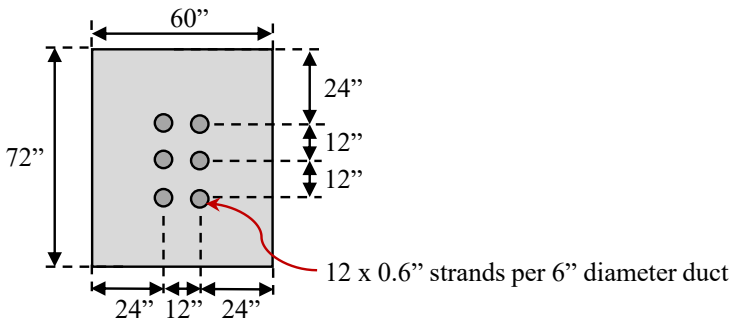

Figure 3.48: Straddle beam cross section

3.3.3. Loading

Two loading-related variables were investigated for Bridge #3: temperature effects and superstructure loading. A uniform temperature profile and temperature gradient were both investigated on Bridge #3. Temperature effects are considered a force effect due to superimposed deformation [1]. The temperature range selected for the uniform temperature range was based on Table 2.7.1-1 in the FDOT Structures Design Guidelines [1]; for concrete only structures, temperature varies from 35°F to 105°F.

The temperature gradient for concrete superstructures was determined based on AASHTO LRFD [22]. Florida is in Solar Radiation Zone 3, which has a T_1 = 41°F and T_2 = 11°F. These values were used as input in the computer software. SDG [1] specifies that the effects of temperature gradient need only be taken into account for continuous concrete superstructures. A temperature gradient was investigated for this substructure element to mimic the influence of post-tensioning that is common in these bent caps.

The effect of applying a vertical load from the superstructure was also investigated. The maximum vertical load applied from the superstructure was determined from the axial load in the piers from the Bridge #2 model (considering only dead and live loads); this force

was found to be 1,200 kips (factored). A point load was applied at mid-span of the bent cap for some of the load cases to see the effect of the vertical load with uniform temperature and temperature gradient effects.

The post-tensioning described above was applied to all the different load cases. Long-term effects were included in the analysis by considering long-term material properties for creep and shrinkage and concrete compressive strength.

The creep coefficient and shrinkage strain were automatically calculated by Midas using the AASHTO LRFD Bridge Design Specification [22], considering the volume to surface ratio and the compressive strength of concrete at age of 28 days. Two long term properties were created, one for the concrete strength of 5.5 ksi and for 6.0 ksi. Results for the creep coefficient and shrinkage strain for 5.5 ksi are shown in Figure 3.49.

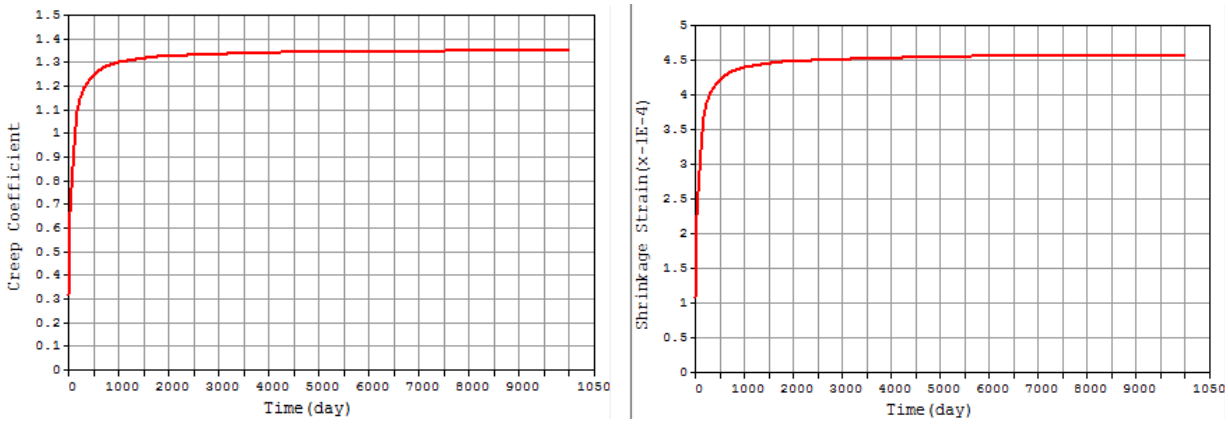

(a) (b)

Figure 3.49: Long-term properties (a) creep coefficient for 5.5 ksi (b) shrinkage strain for 5.5 ksi

A time dependent material property was defined for the compressive strength of the concrete to reflect the variation of the modulus of elasticity with time. Midas calculates the development of concrete compressive strength and stiffness using equations found ACI

209R-08 [58] considering the concrete strength at 28 days and the concrete strength factors (A and B). Typical values for the concrete strength factors were used (A = 4 and B = 0.85).

Four different load cases were applied to Bridge #3:

1. Uniform temperature, no vertical load, PT
2. Uniform temperature, vertical load, PT
3. Temperature gradient, no vertical load, PT
4. Temperature gradient, vertical load, PT

A schematic of these different load cases is shown in Figure 3.50.

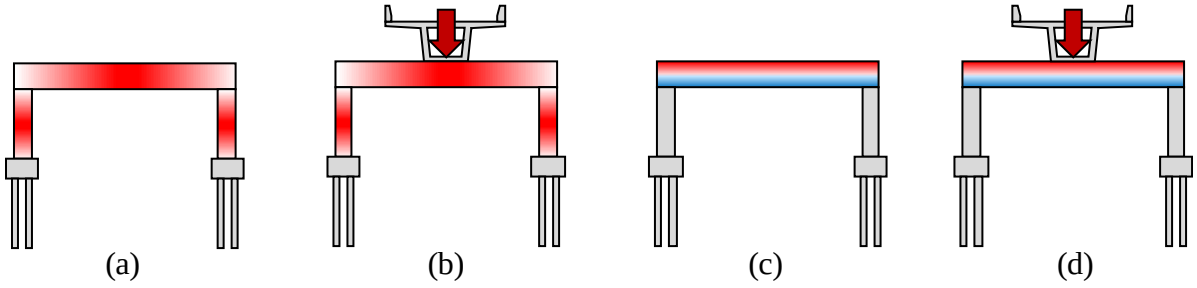

Figure 3.50: Four load cases investigated for Bridge #3: (a) uniform temperature, no vertical load; (b) uniform temperature with vertical load; (c) temperature gradient, no vertical load; and (d) temperature gradient with vertical load

3.3.4. Boundary Conditions and Modeling Assumptions

The base model for Bridge #3 is shown in Figure 3.51. The piles, columns, and bent cap were all modeled as general beam elements. The pile caps were modeled as plate elements with a section thickness corresponding to the cap depth. An elastic link with infinite stiffness was provided between the columns and bent cap to provide a moment connection between these elements. Like Bridges #1 and #2, the piles were modeled assuming a pinned connection at the tip of the pile and point springs along the length of the embedded pile,

simulating soil-structure interaction. Like Bridge #2, a beam release was defined between pile and pile cap to simulate a pinned connection; otherwise, the connection behaves as fully fixed.

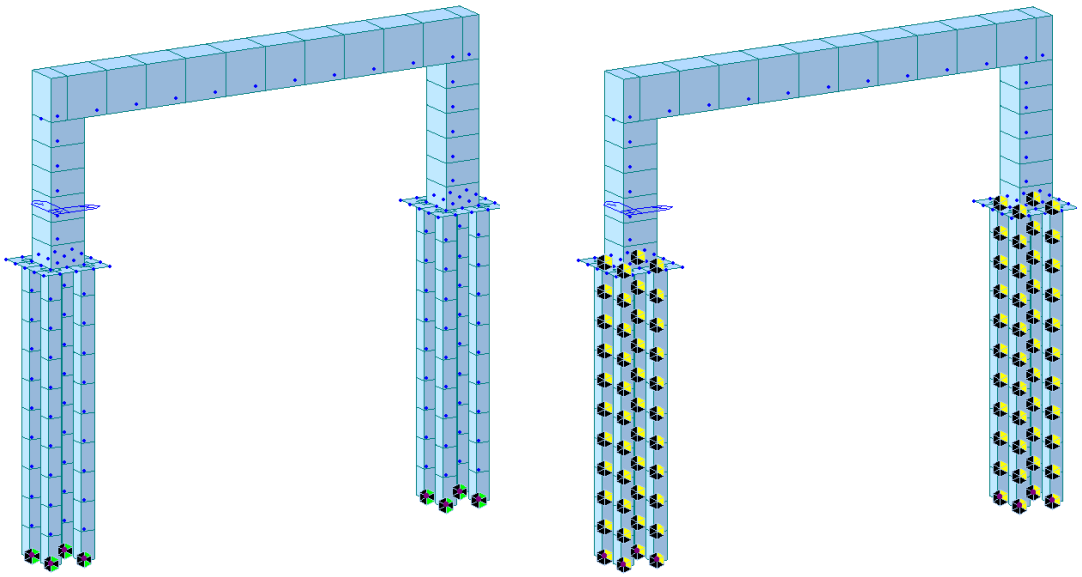

(a) (b)

Figure 3.51: Boundary conditions for bridge #3. (a) supports (b) soil-structure interaction

Element temperature was modeled in MIDAS by defining the initial and final temperature of the element. The two models analyzed with uniform temperature changes are shown in Figure 3.52 (a) without vertical load and (b) with vertical load.

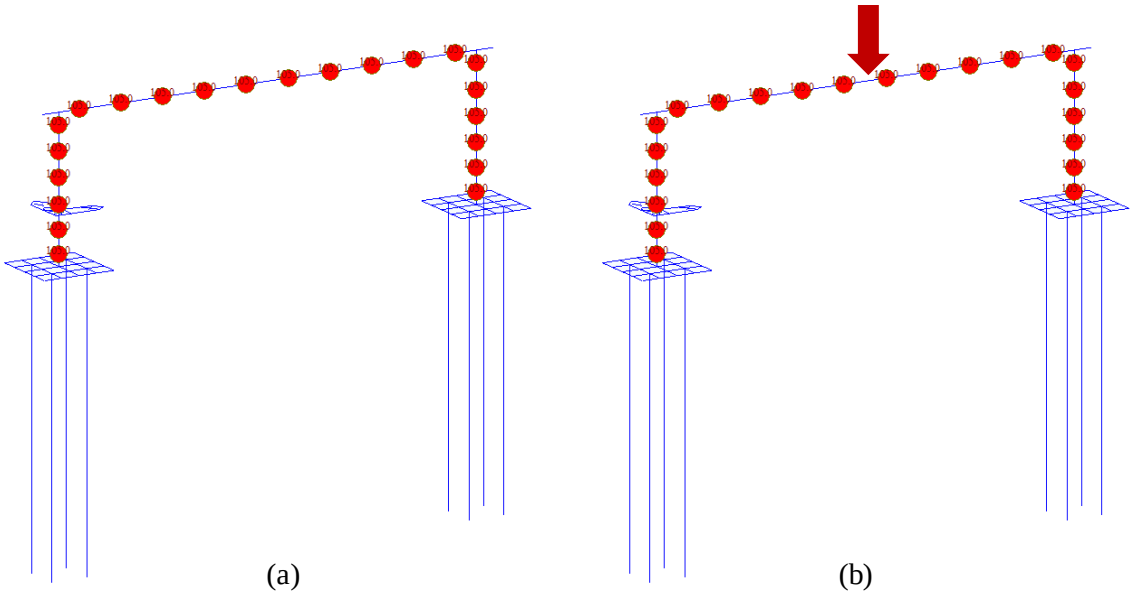

Figure 3.52. Bridge #3 model with uniform element temperature (a) without vertical load (b) with vertical load

As mentioned, a temperature gradient of T_1 - T_2 = -30°F was also applied to the structure.

The two models with gradient are shown in Figure 3.53.

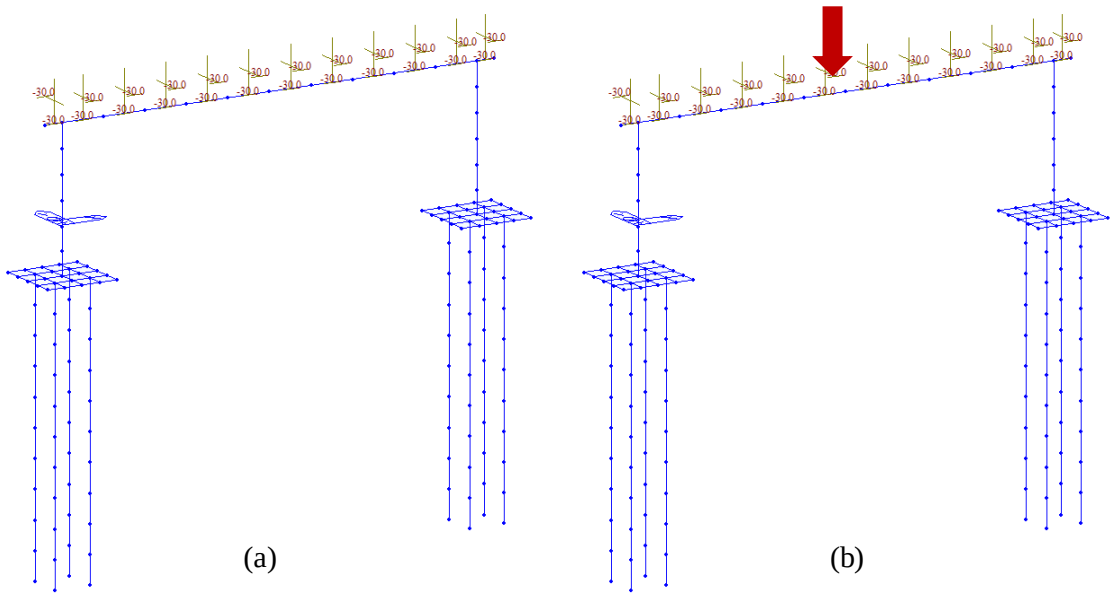

Figure 3.53: Bridge #3 with temperature gradient (a) without vertical load (b) with vertical load

Post-tensioning was included in the straddle bent, as shown in Figure 3.54. All strands were stressed to 202 ksi. The effects of the post-tensioning were included in all analyses.

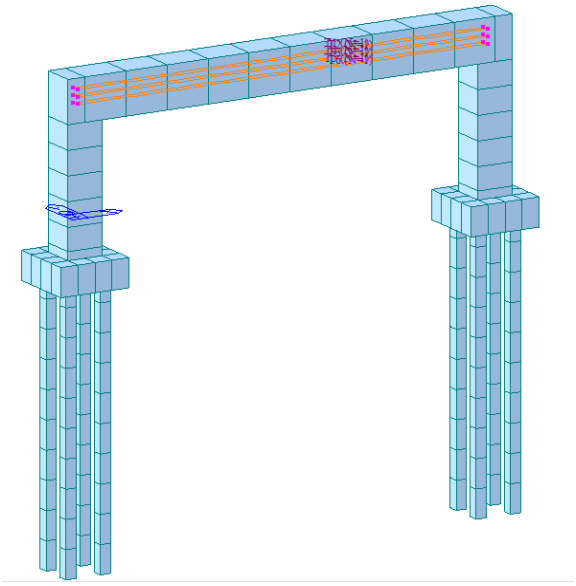

Figure 3.54: Post-tensioned loading for Bridge#3

3.3.5. Summary of Results

The axial load in the piles remained in compression in all four load cases for pinned and fixed connections between pile and pile cap. The axial load was not significantly affected for the cases without vertical applied load as shown in Figure 3.55 (a). The most significant difference was seen for the load cases with vertical applied load shown in Figure 3.55 (b), where the fixed connection resulted in an increased axial compression of about 10%.

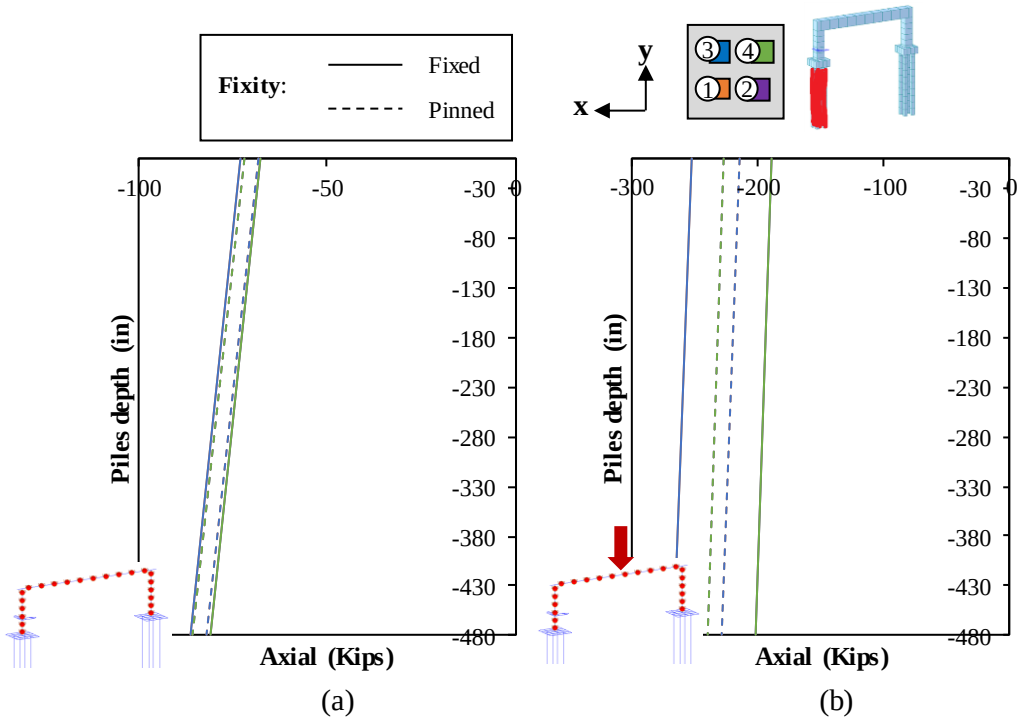

Figure 3.55: Axial load response for Bridge #3 piles with (a) uniform temperature only and (b) uniform temperature with vertical applied load

The maximum moment in the piles was found to be larger for bridges with a fixed pile-to-cap connection in all load cases. The maximum moment was between 35% and 60% larger with a fixed pile-to-cap connection compared to a pinned connection. An example of the difference between fixed and pinned connection is shown in Figure 3.56.

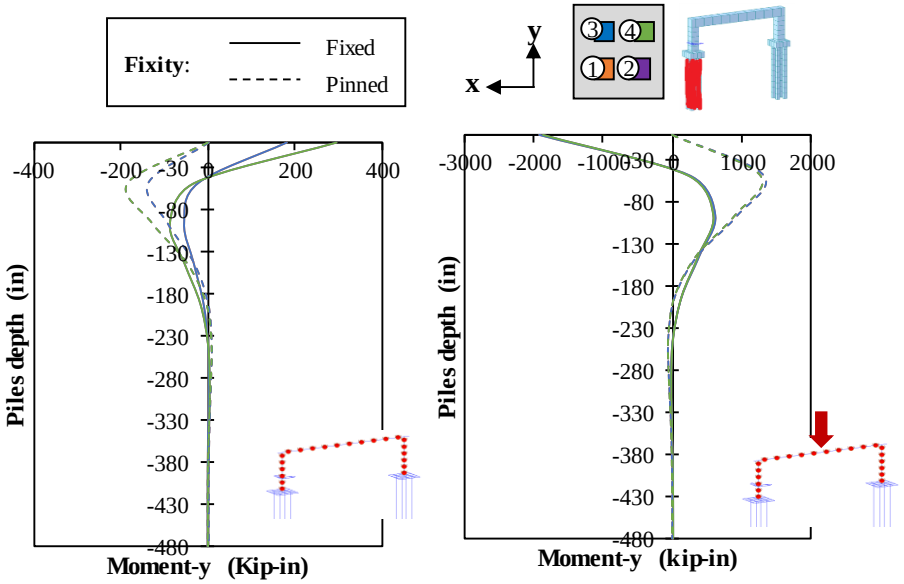

Figure 3.56: Moment response for Bridge #3 piles with (a) uniform temperature only and (b) uniform temperature with vertical applied load

Little to no difference in column or bent cap behavior was observed between bridges with fixed and pinned pile-to-cap connections for all four load cases. A sample response for the axial load and moment response in the piers is shown in Figure 3.57.

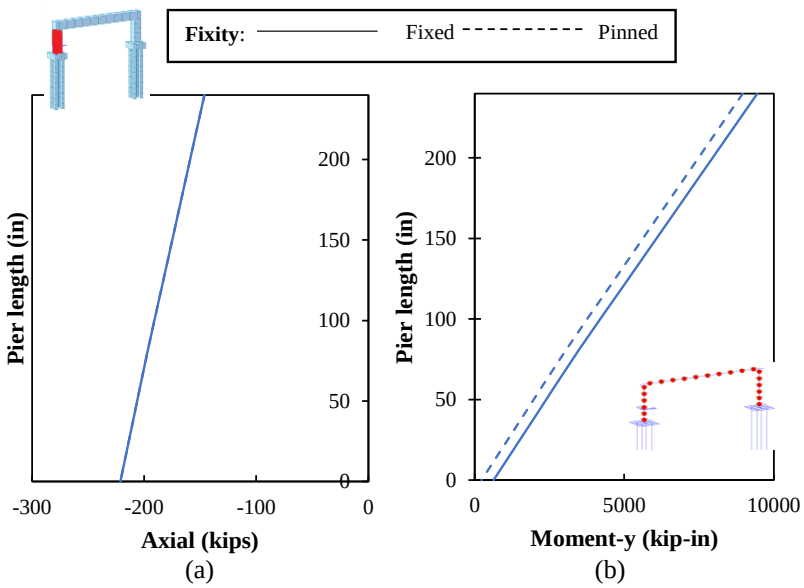

Figure 3.57: (a) Axial load and (b) moment response for Bridge #3 columns with uniform temperature only

3.4. BRIDGE #4: PT SEGMENTAL BOX GIRDER WITH FIXED PIER TABLE

The last structure that was analyzed was a segmental box girder bridge with fixed pier tables, similar to Bridge #2, except with an applied displacement in the middle of the span to simulate erection tolerances at the closure pour between the cantilevered spans. The difference in elevation at this point is typically taken care of by using steel strong back system with jacks to force the tips of the two cantilevered spans to align. The closure pour is then cast, the continuity tendons stressed along the top and bottom of the section, and then the strong back released, which locks in the stresses in the structure. These locked in stresses need to be considered in the superstructure and substructure designs and the assumed fixity of the pile-to-cap connection will affect how these stresses are handled.

3.4.1. Base Structure

The same base structure as Bridge #2 was used with a balanced cantilever configuration and pile caps at soil level, as shown in Figure 3.58. Variables and parameters used in this model are presented in Table 3.3 and previous sections.

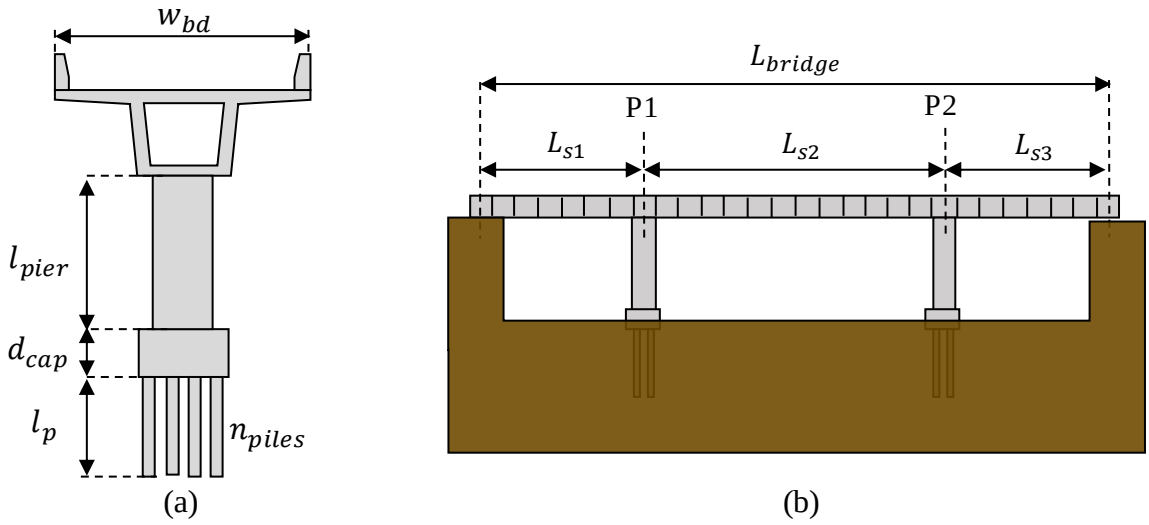

Figure 3.58: (a) Typical section for Bridge #4 and (b) elevation of balanced cantilever configuration

3.4.2. Elevation and Detail

FDOT Structures Design Guideline [1] requirements for cantilever bridges with fixed pier tables specify an erection tolerance of *L*/1000 (where *L* is the cantilever length from the center of the pier to the cantilever tip), as shown in Figure 3.59. For a main span of 199 feet (corresponding to the main span length of the balanced cantilever configuration), the cantilever length is 99.5 feet, and the corresponding tolerance is 1.19 inches.

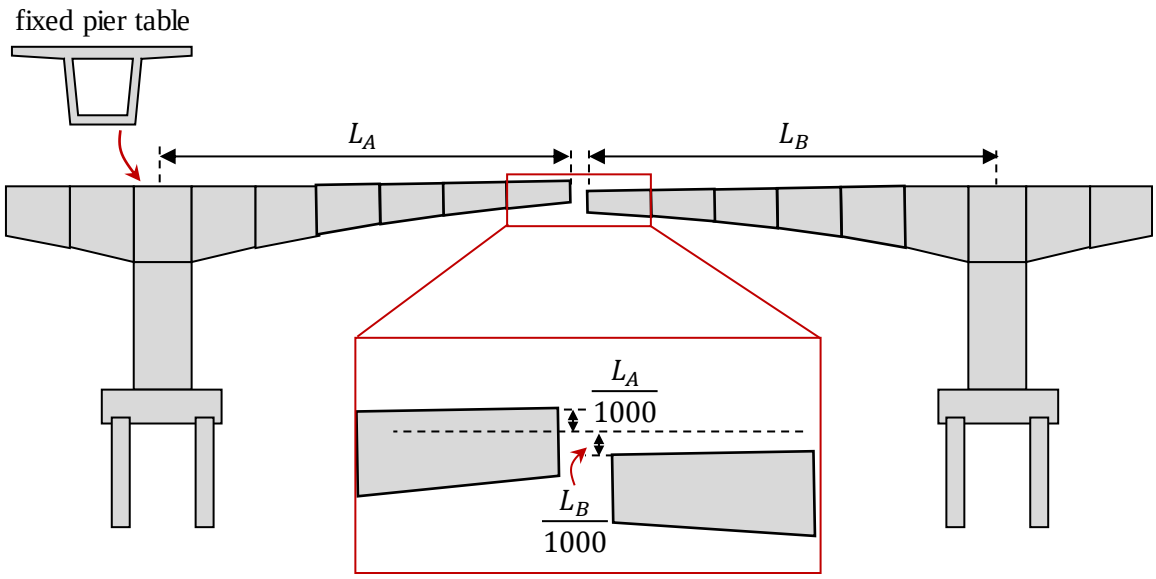

Figure 3.59: Post-tensioned segmental box girder bridge with fixed pier table

Half of the structure will be modeled with this applied displacement of 1.19 inches at the location where the forced displacement would be locked in, as shown in Figure 3.60.

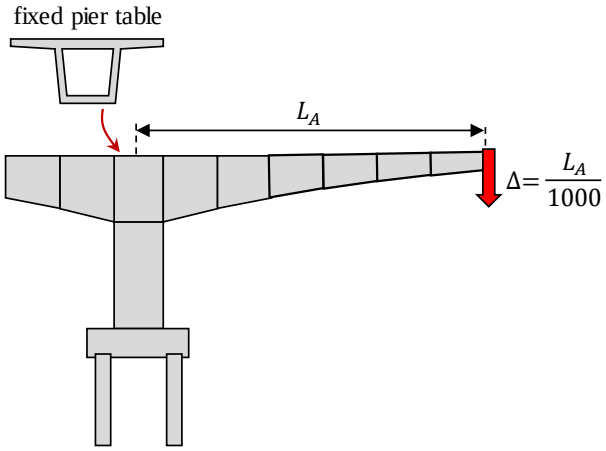

Figure 3.60: Imposed deflection at cut in half-bridge model

3.4.3. Pile Layout

Three different pile orientations were investigated for Bridge #4:

- 3x4 grid of 18-inch piles

- 2x4 grid of 24-inch piles
- 2x3 grid of 30-inch piles

The investigated pile layouts are also shown in Figure 3.61.

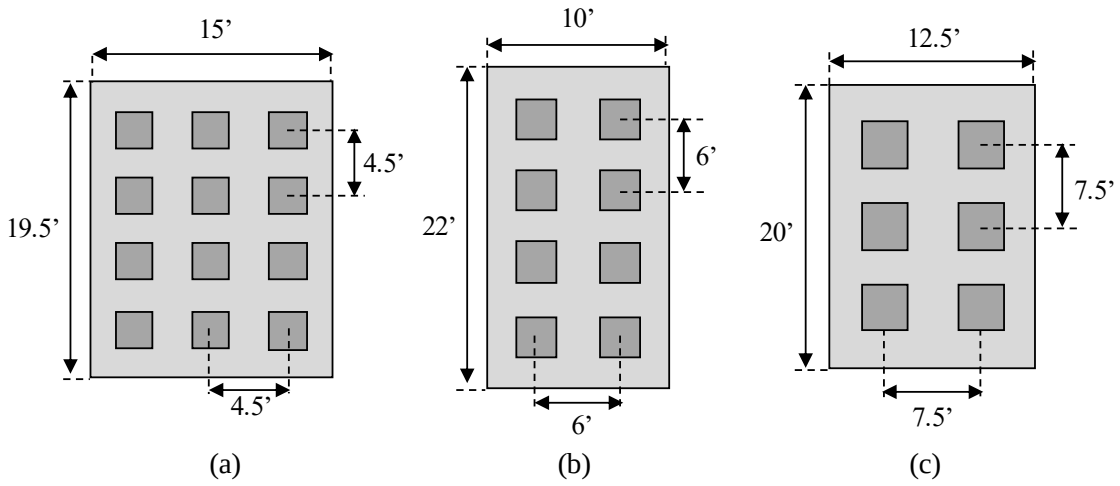

Figure 3.61: Pile layouts used for Bridge #4 with (a) 3x4 grid of 18-inch piles, (b) 2x4 grid of 24-inch piles and (c) 2x3 grid of 30-inch piles

3.4.4. Boundary Conditions and Modeling Assumptions

The base model for Bridge #4 with the three different pile layouts is shown in Figure 3.62.

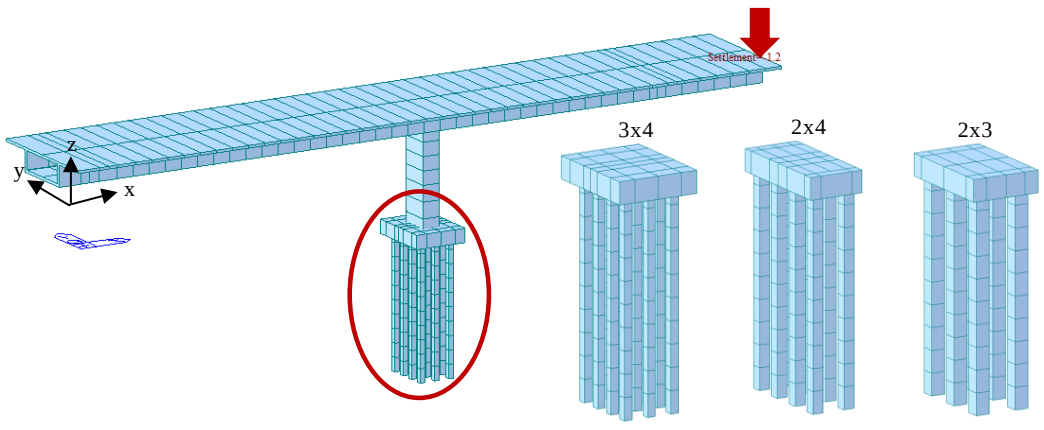

Figure 3.62: Bridge #4 modeling

The piles, piers, and box beams were all modeled as general beam elements. The pile caps were modeled as plate elements with a section thickness corresponding to the cap depth. An elastic link was provided between the top of the pier and the box segment on top of the pier with infinite stiffness. The structure was modeled such that the beam was continuous over the interior pier. The piles were modeled assuming a pinned connection at the tip of the pile and point springs along the length of the embedded pile, simulating soil-structure interaction. A beam release was defined between pile and pile cap to simulate a pinned connection; otherwise, the connection behaves as fully fixed. The applied soil-structure interaction and applied settlement of 1.19 inches are shown in Figure 3.63.

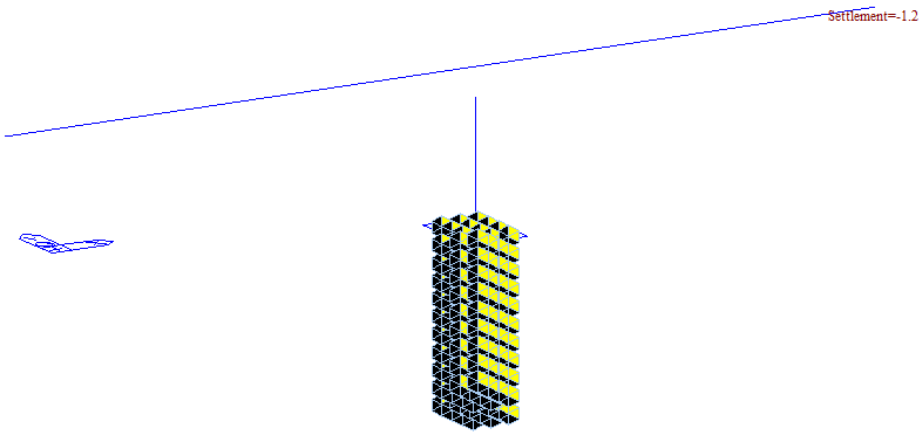

Figure 3.63: Boundary conditions for bridge 4

3.4.5. Summary of Results

A summary of the major findings is presented below.

There was not a significant difference in axial load in the piles between bridges with fixed and pinned pile-to-cap connections, as shown in Figure 3.64.

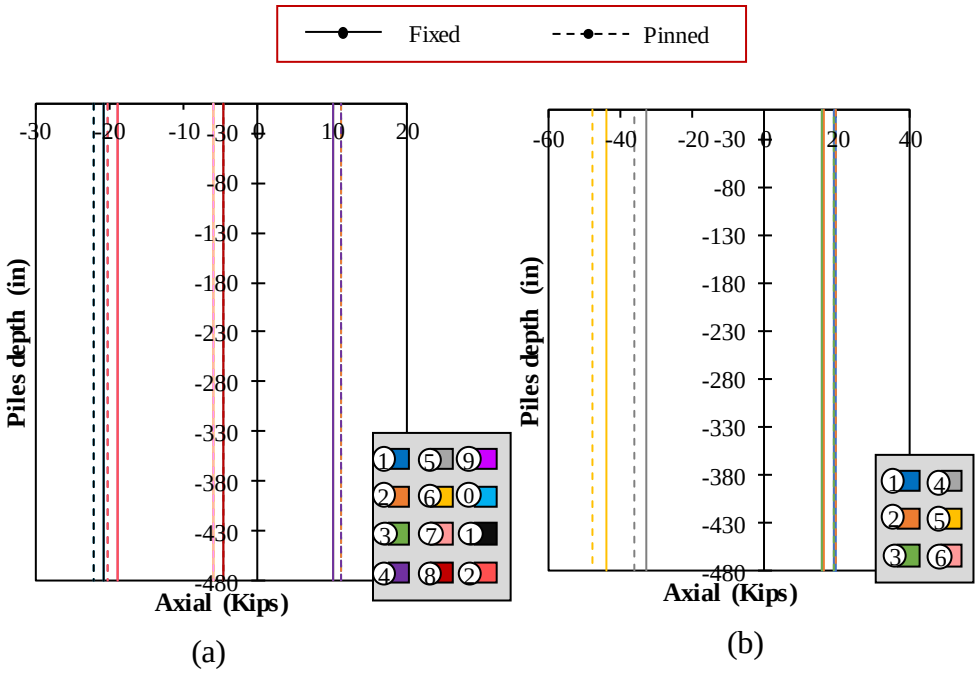

Figure 3.64: Axial load response for select piles in Bridge #4 with (a) 3x4 grid of 18-inch piles and (b) 2x3 grid of 30-inch piles

The observed moment in the piles for the 3x4 and 2x3 pile configurations is shown in Figure 3.65. No moment was experienced in piles for bridges with pinned pile-to-cap connections. Only minor moment was seen in the piles for bridges with fixed pile-to-cap connections. The moment per pile does increase as the number of piles decreases and pile size increases.

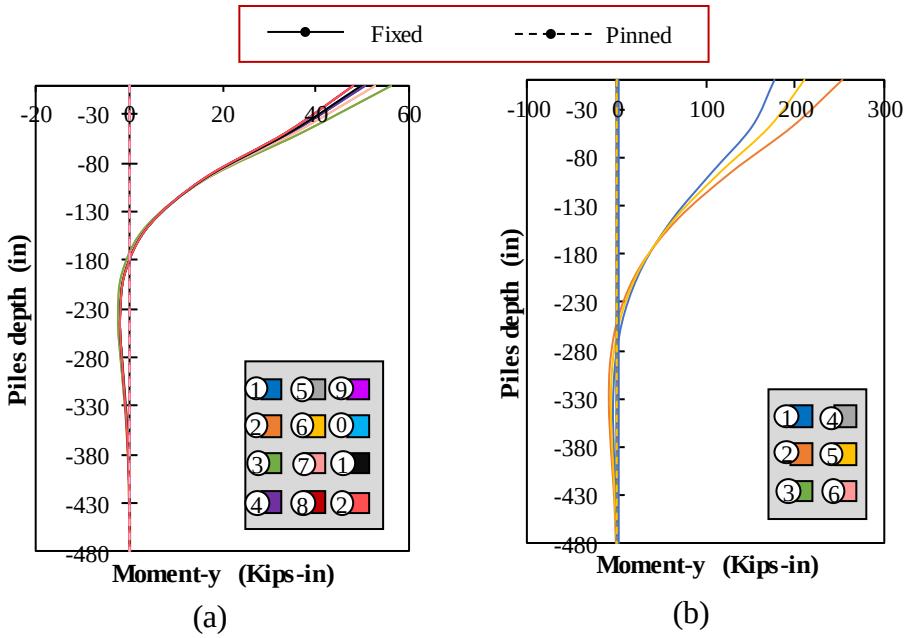

Figure 3.65: Moment response for select piles in Bridge #4 with (a) 3x4 grid of 18-inch piles and (b) 2x3 grid of 30-inch piles

There was little to no difference in the behavior of the beam or pier based on whether a pinned or fixed pile-to-cap connection was used. An example of the similar behavior is shown in Figure 3.66 for the axial load and moment response of the pier.

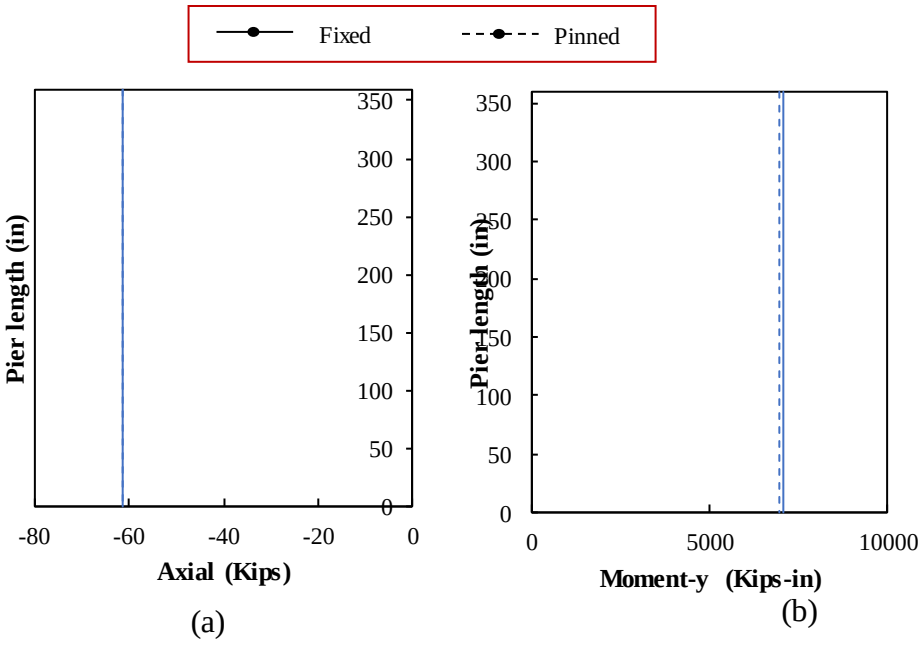

Figure 3.66: (a) Axial load and (b) moment response for pier in Bridge #4

4. PRELIMARY NUMERICAL STUDY

A preliminary numerical analysis was performed using a non-linear finite element analysis software ATENA to investigate the variables impacting the behavior of the connection and the required embedment lengths for fixed and pinned connections. Results for this preliminary study helped determined the primary and secondary variables tested in the experimental program.

4.1. BOUNDARY CONDITIONS AND MODELING ASSUMPTIONS FOR PILE-TO-CAP CONNECTION MODELS

ATENA is a FEA software specifically designed for reinforced concrete structures. It was used to study the failure mechanisms of over 100 different specimens with different connection details. The program has detailed bond-slip models that will be capable of capturing the slip of the prestressing strands, detailed interface material models, detailed concrete material models, and detailed crack patterns.

The prestressed pile and cast in place pile cap will be modeled considering its construction process. First, the strands in the pile are going to be prestressed to the desired stress; after this, the pile cap will be cast and an axial load will be applied to the pile; finally, a lateral load will be applied to the pile and reactions in this point will be record.

ATENA provides the possibility of modeling the construction process of different structures. Three different intervals, with the steps described above, were created, and analyzed. Details of the construction process and intervals are in subsequent sections.

4.1.1. Model Geometry

The geometry was first drawn in AutoCAD 3D. Typical models consisted of six 3D volume components (pile cap, pile, and plates) and 1D lines representing the reinforcing steel, see Figure 4.1 (a). After defining the geometry in AutoCAD 3D, each section was imported into ATENA, as shown in Figure 4.1 (b).

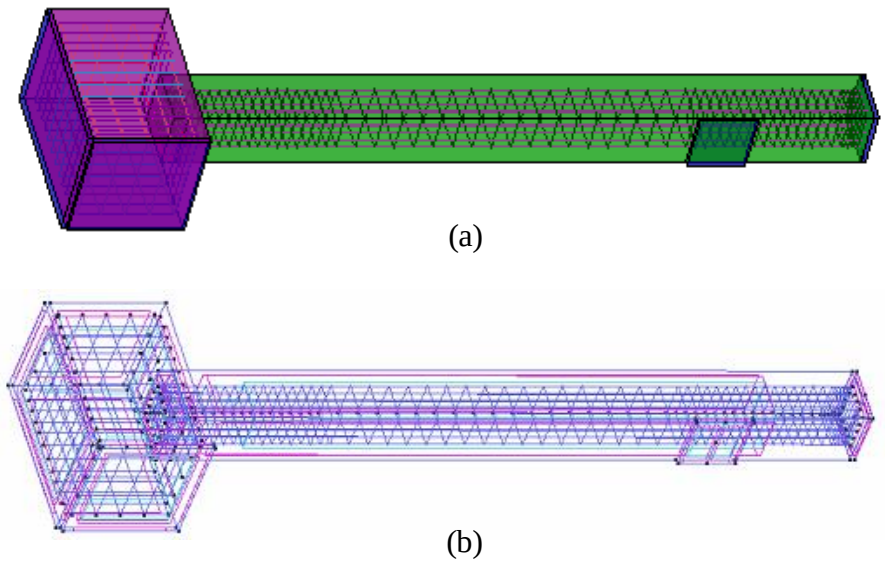

Figure 4.1: Example of (a) AutoCAD model (b) ATENA model used for pile-to-cap connection models

Interfaces were defined between volume elements with different materials that shared common surfaces. As an example, a fixed contact (Master-Slave) connection was defined between the concrete pile and an elastic plate where load was applied and between the pile cap and two elastic plates where boundary conditions were applied, as shown in Figure 4.2.

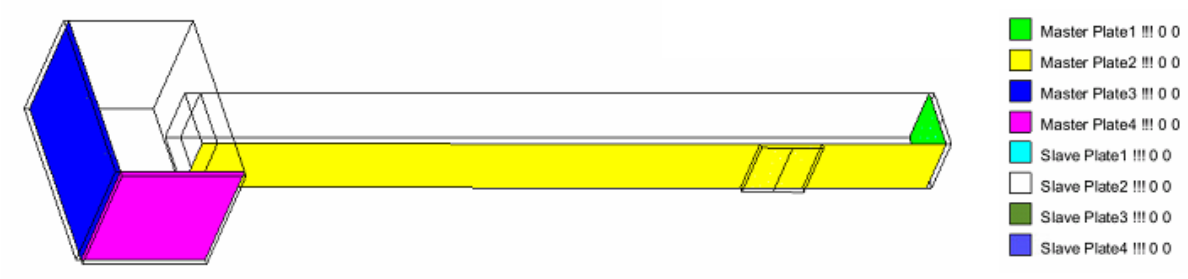

Figure 4.2: Sample of Master-Slave conditions used at interfaces between volume elements

The reinforcement scheme used in the typical pile-to-pile cap connection specimens is shown in Figure 4.3. Prestressing strands were either 0.5-inch or 0.6-inch diameter strands. Conventional reinforcement (#5, #6, #9, and W3.4 wire) was used in the piles and pile caps.

Figure 4.3: Reinforcement layout for typical pile-to-pile cap connection specimens

4.1.2. Material Assumptions

Three different materials were used for the analysis: (1) a solid concrete material for the pile and pile cap, (2) an elastic solid material for the plates, and (3) 1D reinforcement for the reinforcing bars and prestressing strands.

The SOLID Concrete material was used for the pile and pile cap. Concrete models were created for all the investigated concrete strengths, parameters for three example concrete types are shown in Table 4.1. Two of the concrete models shown were used for modeling the pile cap during testing (Concrete6000 and Concrete5500). The third concrete model

shown was used to model the pile cap during the prestressing of the pile, so that the pile cap did not restrain the pile during the prestressing process (Concrete Soft).

Table 4.1: Sample material parameters of concrete

Material Parameter	Concrete6000	Concrete5500	Concrete Soft
Young's modulus [ksi]	4415.2	4227.2	1.45
Poisson's ratio	0.2	0.2	0.2
Compressive strength [ksi]	-6.0	-5.5	-6.5

The material used for the steel plates was generated using the Solid Elastic option with the properties shown in Table 4.2. Similar to the concrete, a soft elastic material with no stiffness was used for the steel plates during the prestressing of the piles.

Table 4.2: Material parameters of steel plates

Material Parameter	Steel Plate	Steel Plate Soft
Young's modulus [ksi]	29000	1.45
Poisson's ratio	0.3	0.3

The reinforcing steel in the pile cap (#5, #6, and #9 bars) and the W3.4 wires confining the strands in the piles were all modeled as 1D reinforcement with a yield strength (f_1) of 60 ksi, yield strain (ε_1) of 0.00207, an ultimate strength (f_2) of 90 ksi and a strain at ultimate strength (ε_2) of 0.025 with a stress-strain relationship similar to that shown in Figure 4.4 (a).

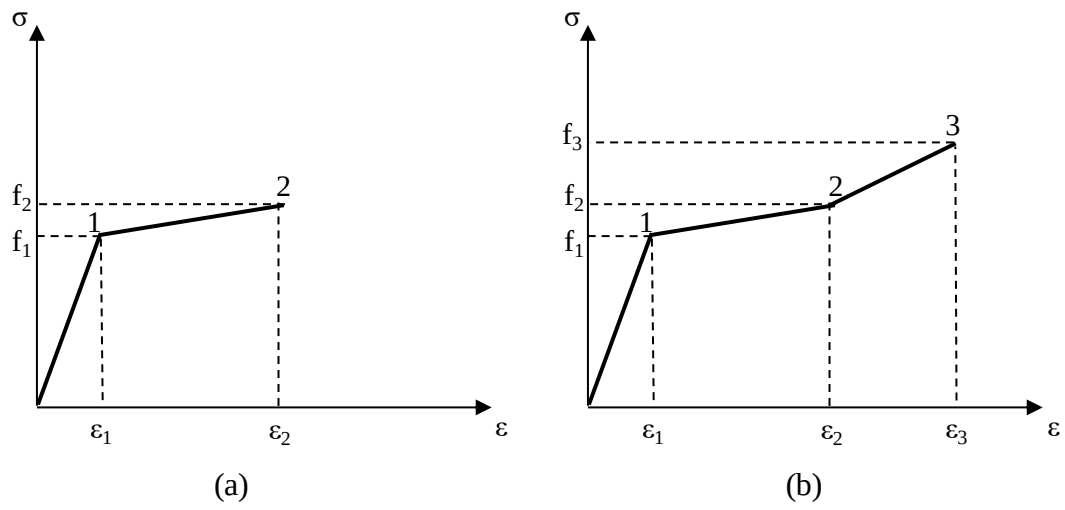

Figure 4.4: Stress-strain curve (a) Reinforcement (b) tendons

The prestressing strands were also created using the 1D reinforcement option, but with a tendon type option. The stress-strain relationship used for the prestressing strands is shown in Figure 4.4 (b). The critical values used for this curve are the following: yield strength (f_1) of 204 ksi, yield strain (ε_1) of 0.007, second critical stress (f_2) of 243 ksi, second critical strain (ε_2) of 0.011, ultimate strength (f_3) of 270 ksi and strain at ultimate strength (ε_3) of 0.043. These values were roughly based on the Ramberg-Osgood stress-strain relationship. A prestrain was applied to the prestressing strands in 10 load steps to model the initial stress in the strands.

4.1.3. Test Set Up/Boundary Conditions

The pile-to-pile cap connection was tested as a cantilever beam in the horizontal position fixed to a strong floor, as shown in Figure 4.5. An axial load was applied and kept constant throughout the model. A lateral load was applied and increased until failure occurred in the specimens; the deflection at the location of the lateral load was measured using a point monitor.

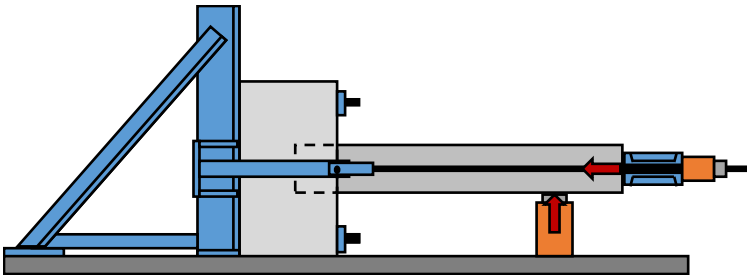

Figure 4.5: Test configuration used for modeling connection specimens

Two plates were used to create a fixed condition for the pile cap, as shown in Figure 4.6 (a). A plate with a constraint in the z direction was placed on the back of the pile cap (opposite the pile); a plate with x and y constraints was placed on the bottom of the pile (on a face adjacent to the face with the pile), both shown in Figure 4.6 (b). These boundary conditions created a moment restrain in the pile cap similar to what would be expected in the laboratory, with the bottom of the pile cap resting on the strong floor and the back fixed to a reaction frame like in Figure 4.5.

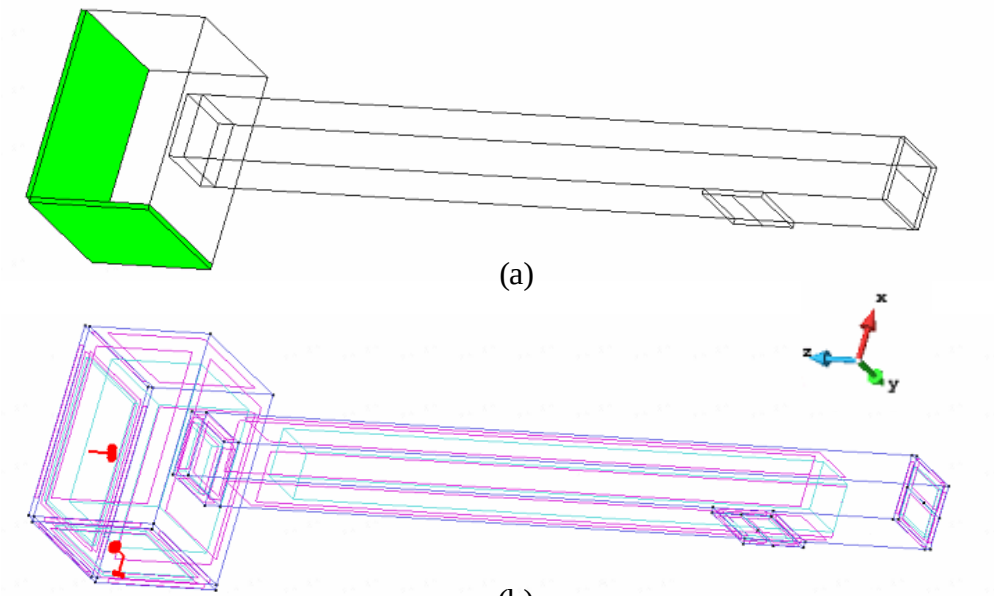

Figure 4.6: Boundary conditions (a) Plates (b) Restrictions

4.1.4. Load Protocol

A construction process was required to properly apply the prestressing and axial load in the piles before the lateral load was applied to fail the specimens. Three different loading stages were used, which are similar to how the specimens would be loaded in the laboratory and in the field.

1. *Load Stage #1*: prestrain applied to the prestressing strands
2. *Load Stage #2*: axial load applied to the piles
3. *Load Stage #3*: lateral load applied to piles until failure of system

4.1.4.1. Load Stage #1

The purpose of Load Stage #1 was to prestress the strands in the piles. The pile concrete strength was defined with typical stiffness. The pile cap concrete was specified with a stiffness close to zero, so the pile cap did not restrain the pile during prestressing, as shown in Figure 4.7. The total desired prestrain was applied to the piles in 10 steps.

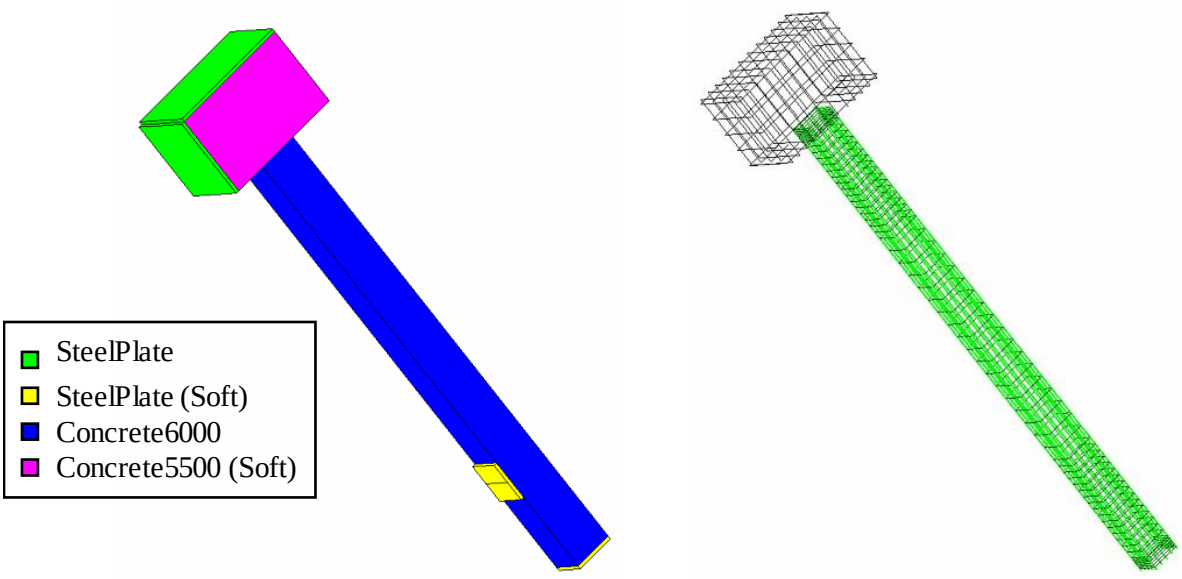

(a) (b)

Figure 4.7: Load Stage #1 (a) defined materials and (b) applied prestrain of -0.007 per step in prestressing strands

The prestrain was locked in and kept constant at the end of this load stage.

4.1.4.2. Load Stage #2

The purpose of Load Stage #2 was to apply the axial load to the pile in the complete system. The "soft" materials were redefined with the material properties desired for the final test, as shown in Table 4.3.

Table 4.3: New material definitions for Load Stage #2

Old Material	New Material
Concrete5500 (Soft)	Concrete5500
SteelPlate (Soft)	SteelPlate

An axial load was applied to the end of the pile, as shown in Figure 4.8 (a) in 10 separate steps. The axial load was then kept constant on the pile at the end of this load stage.

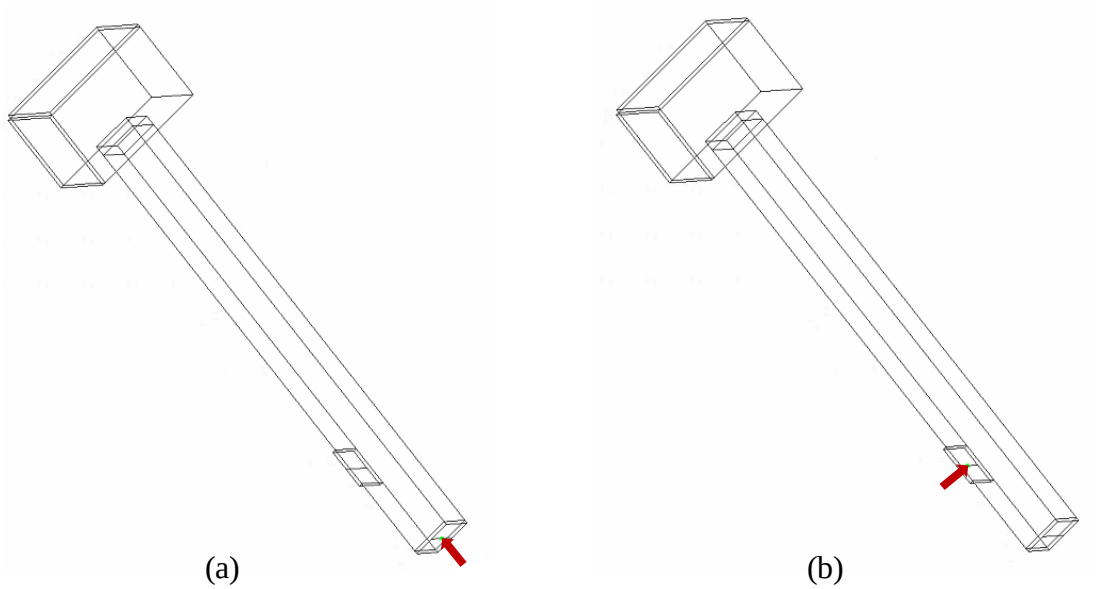

(a) (b)

Figure 4.8: (a) Axial load applied during Load Stage #2 and (b) lateral load applied during Load Stage #3

4.1.4.3. Load Stage #3

The purpose of Load Stage #3 was to determine the moment capacity of the pile-to-cap connection by applying a lateral load until failure of the pile or connection. The prestrain in the pile prestressing strands and axial load in the pile were both kept constant during this load stage. Lateral load was applied, as shown in Figure 4.8 (b), by applying an additional small displacement for 90 steps. The maximum observed load was recorded as the failure load. The load significantly decreased after the failure load in all cases.

4.1.5. Finite Element Mesh

The finite element mesh quality has an important influence on the quality of the analysis results and speed [60], [61]. Meshing was selected such that all volumes would have at least four elements per thickness (e.g., 4.5-inch mesh for 18-inch piles). Linear elements were used for the 1D reinforcement and tetrahedra elements for all 3D volumes, as shown

in Figure 4.9. This mesh size was selected to allow for all the desired models to be run in a reasonable time. This mesh was also previously shown to produce reasonable results when compared to previous experimental results.

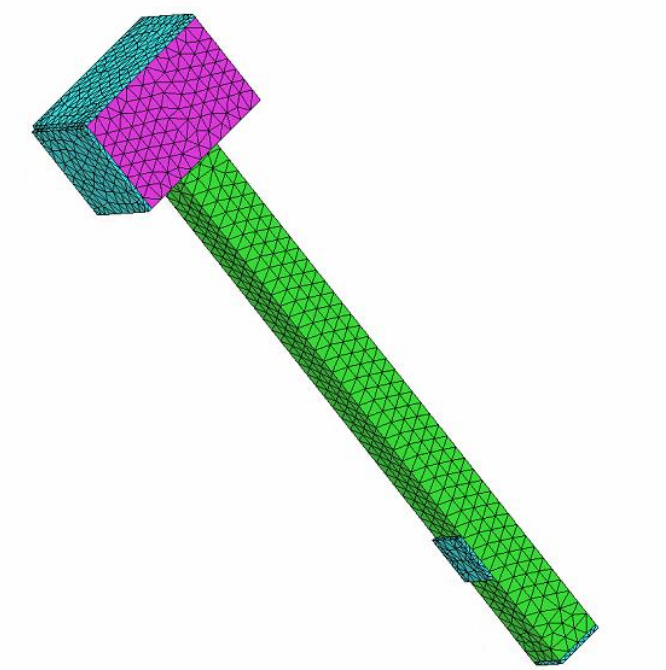

Figure 4.9: Sample mesh for pile-to-cap connection analyses

4.2. NUMERICAL RESULTS FOR PILE-TO-CAP CONNECTION MODELS

4.2.1. Pile Capacity

The capacities of the piles with two different strand configurations were determined using RESPONSE 2000. The moment-curvature responses are shown in Figure 4.10 and maximum moment capacities shown in Table 4.4. There is minimal difference in the moment-curvature behavior of piles with different strand patterns.

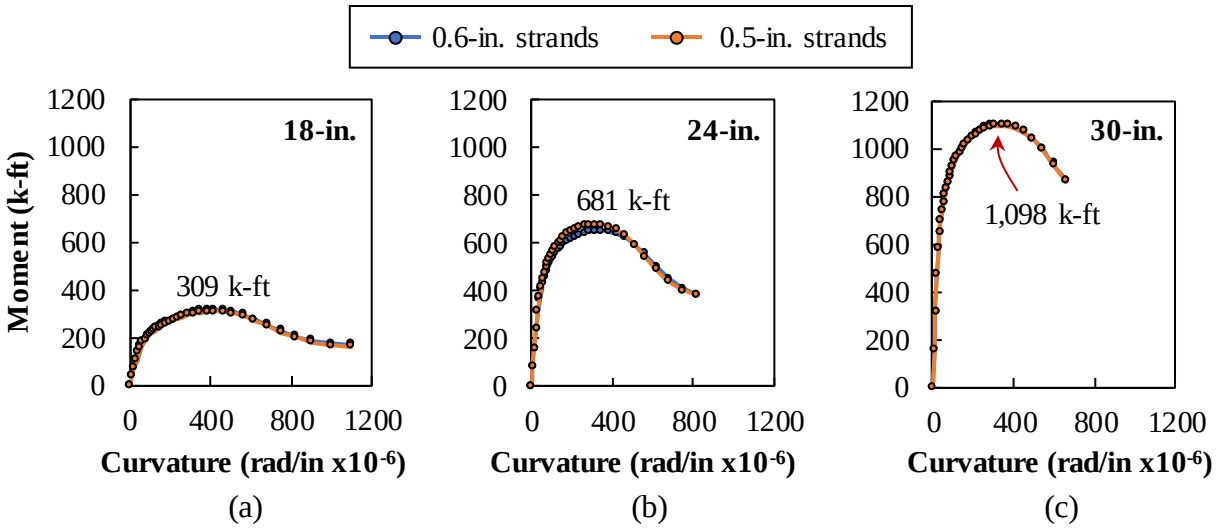

Figure 4.10: Moment-curvature response for (a) 18-inch, (b) 24-inch, and (c) 30-inch piles (highlighted capacities for piles with 0.5-inch strands)

Table 4.4: Maximum moment capacities for piles

Pile Size:	***18-inch***	***24-inch***	***30-inch***
M_n (0.5-inch strands):	308.9 k-ft.	681.4 k-ft.	1,098 k-ft.
M_n (0.6-inch strands):	315.7 k-ft.	653.7 k-ft.	1,102 k-ft.

The axial load versus moment response for all pile sizes is shown in Figure 4.11.

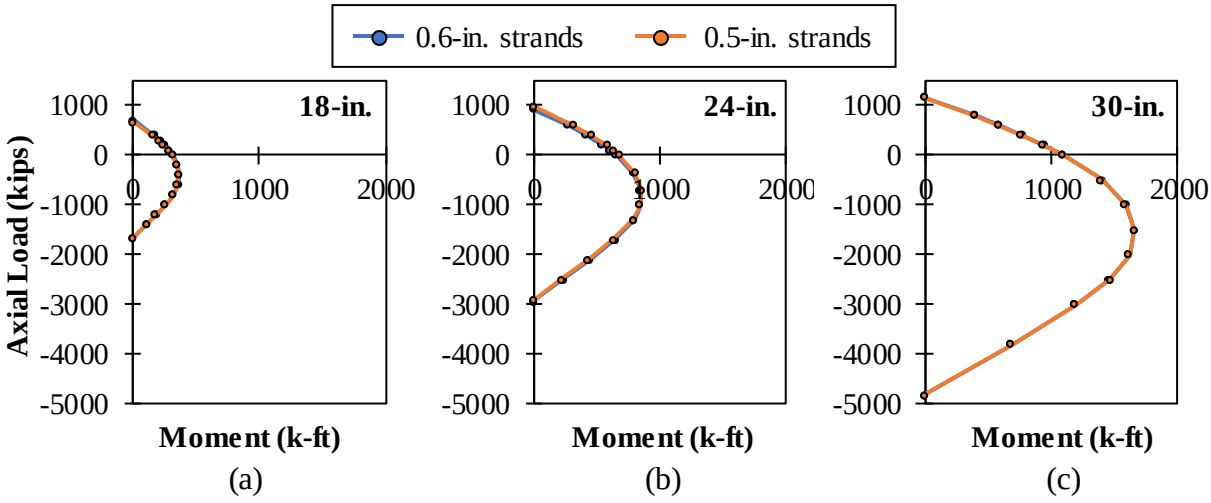

Figure 4.11: Moment-axial load response for (a) 18-inch, (b) 24-inch, and (c) 30-inch piles

4.2.2. Effect of Embedment Length

The first primary variable investigated through the pile-to-cap connection modeling was the effect of embedment length. Specimens with six to eight different embedment lengths were investigated for each pile diameter where there was no interface reinforcement between the pile and cap. Five to seven different embedment lengths were investigated for each pile diameter where there was interface reinforcement between the pile and cap. The $1.5d_b$ pile embedment specimens were not possible because there was not sufficient room available in the pile cap for the interface reinforcement. Sample moment versus deflection curves for the 18-inch piles with different embedment lengths are shown in Figure 4.12.

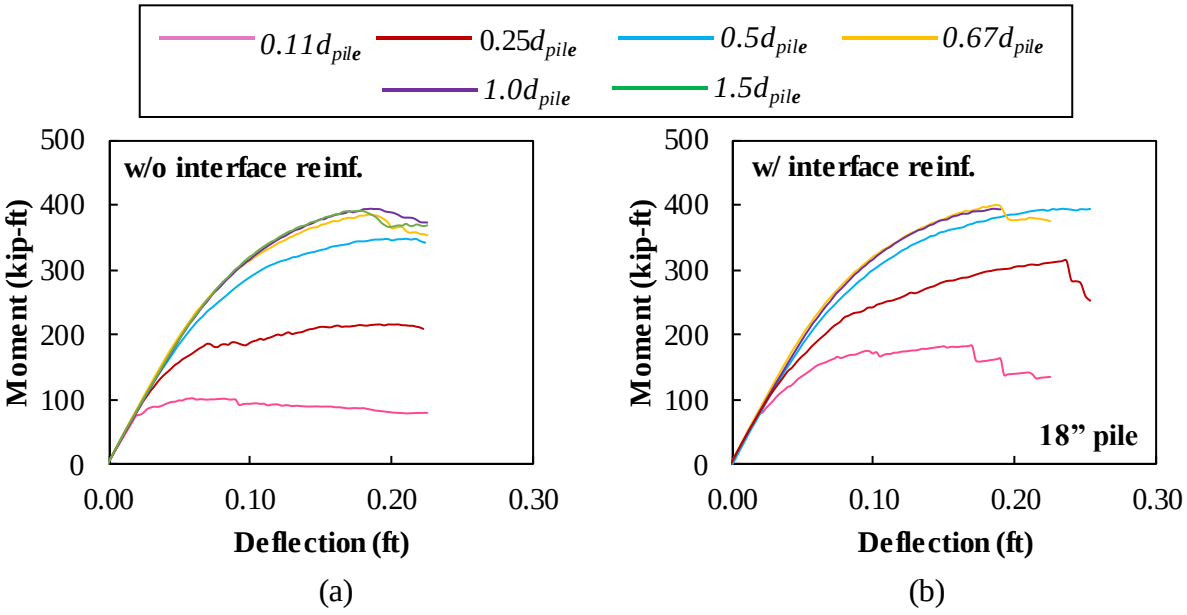

Figure 4.12: Sample moment versus deflection responses for 18-inch piles (a) without and (b) with interface reinforcement with varying embedment length

The maximum moment was determined from the moment-deflection plots and plotted versus the embedment length in Figure 4.13. The maximum moment determined from RESPONSE2000 is also shown in this plot.

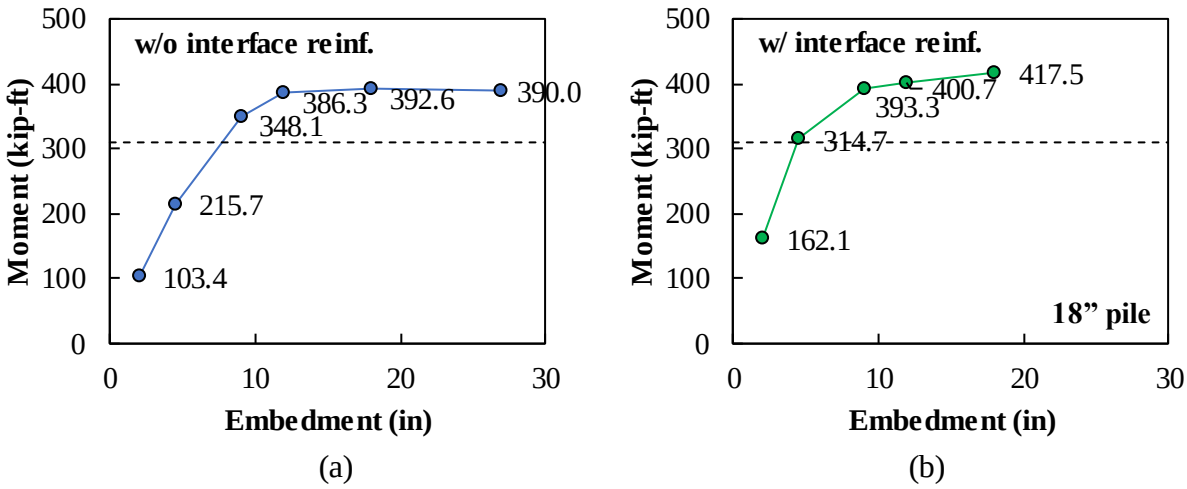

Figure 4.13: Sample moment versus embedment length responses for 18-inch piles (a) without and (b) with interface reinforcement

Cracking patterns were obtained for the models to determine the mode of failure controlling the failure of the specimens. Two of the primary failure mechanisms are shown in Figure 4.14. Shallow pile embedments resulted in failure of the cap, as shown in Figure 4.14 (a). Deeper embedments resulted in failure of the pile, as shown in Figure 4.14 (b).

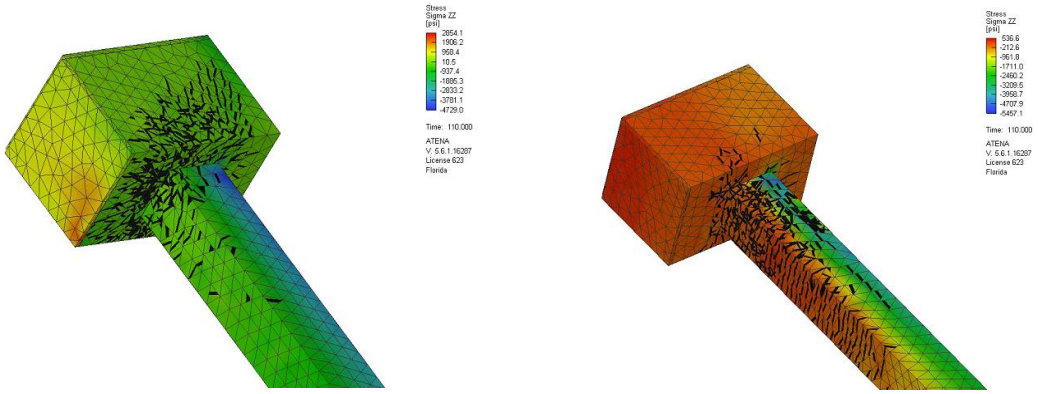

Figure 4.14: Sample crack patterns for 18-inch piles without interface reinforcement with (a) $0.25d_b$ and (b) $1.5d_b$ embedment lengths

The moment response for the 18-inch, 24-inch and 30-inch piles was normalized based on the estimated pile capacity from the layered-section analysis (RESPONSE 2000). The normalized moment versus embedment length (normalized by the pile size) is shown in Figure 4.15 for specimens without interface reinforcement, Figure 4.16 for specimens with interface reinforcement.

The embedment length required to reach the capacity of the pile estimated using layer-section analysis and the embedment length required for transition of failure mechanism from connection to pile are highlighted in Figure 4.15 and Figure 4.16. The embedment length required to reach the moment capacity of the pile and transition failure from connection into pile are relatively consistent between the different embedment lengths when no interface reinforcement is present.

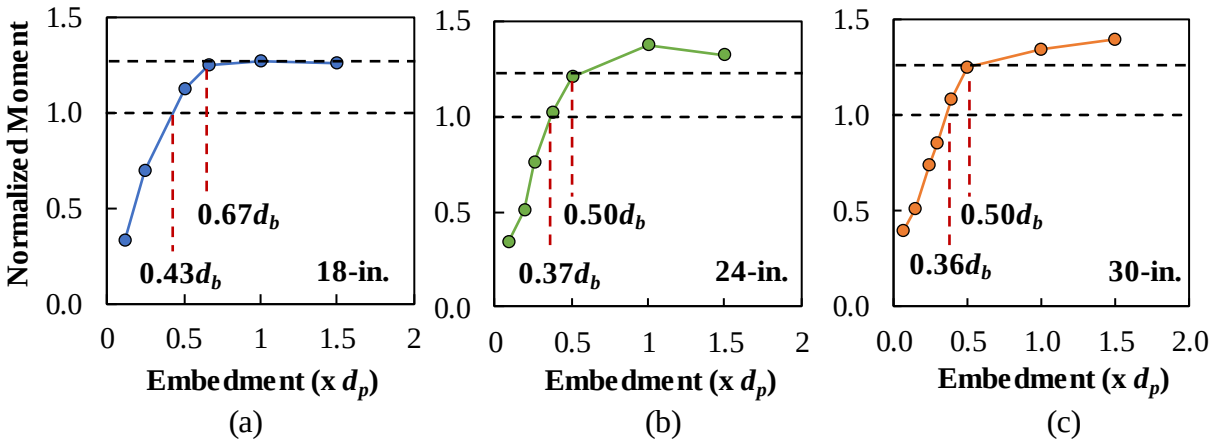

Figure 4.15: Normalized moment versus embedment length for (a) 18-inch, (b) 24-inch, and (c) 30-inch piles without interface reinforcement

The presence of the interface reinforcement slightly decreases the required embedment to develop the moment capacity of the pile but has minimal effect on the embedment length required to transition failure from the connection to the pile.

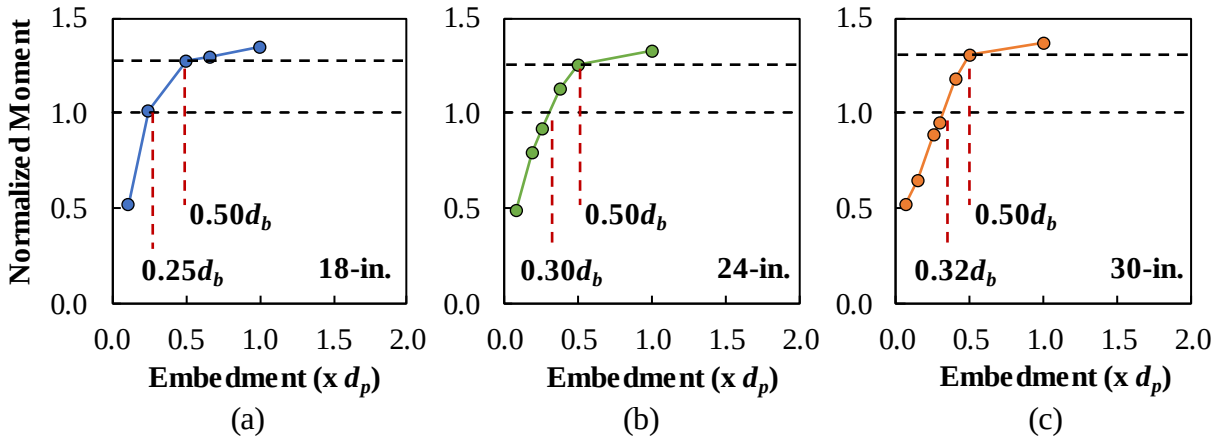

Figure 4.16: Normalized moment versus embedment length for (a) 18-inch, (b) 24-inch, and (c) 30-inch piles with interface reinforcement

The interface reinforcement has more of an effect on the behavior of the 18-inch piles compared to the 24 and 30-inch piles. This is because the location of the interface reinforcement has a larger relative lever arm compared to the location of the prestressing strands, as shown in Figure 4.17.

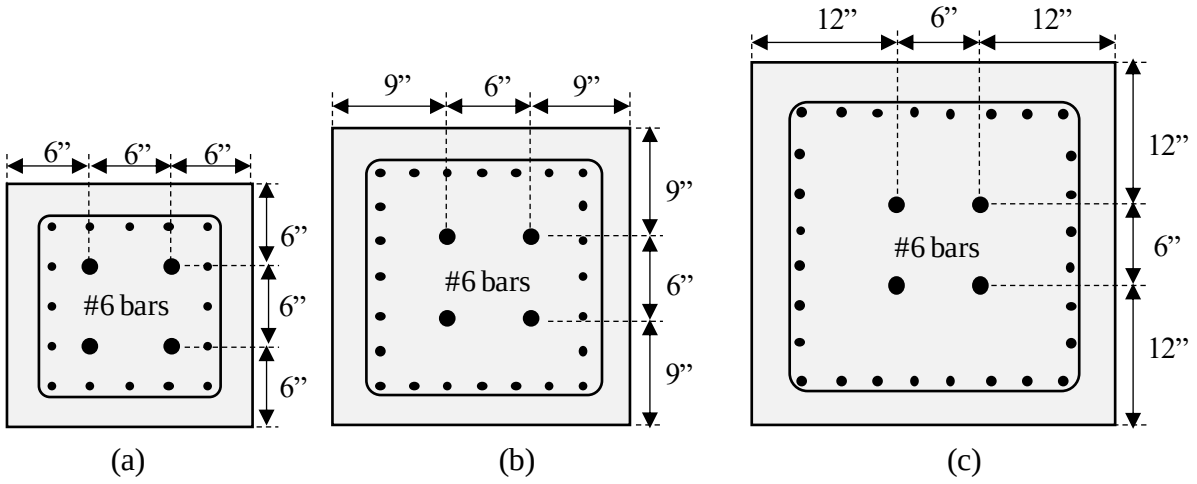

Figure 4.17: Location of interface steel layout in (a) 18-inch, (b) 24-inch, and (c) 30-inch square prestressed piles

The response of the system with all three pile sizes with and without interface reinforcement are shown in Figure 4.18. There appears to be a linear relationship between

embedment length and connection capacity until the capacity of the pile begins to control. The following two equations can be used to reasonably approximate the relationship between embedment and connection capacity without considering any other variables other than embedment length.

Without interface reinforcement: $\left({M_c}/{M_{pile}}\right) = 2.0\left({L_e}/{d_p}\right) + 0.2 \leq 1.0$ Equation 4.1

With interface reinforcement: $\left({M_c}/{M_{pile}}\right) = 1.8\left({L_e}/{d_p}\right) + 0.4 \leq 1.0$ Equation 4.2

Equation 4.1 and Equation 4.2 are included with the normalized moment versus embedment length plots in Figure 4.18. There is reasonable agreement between the numerical results and the estimates from the embedment length equations.

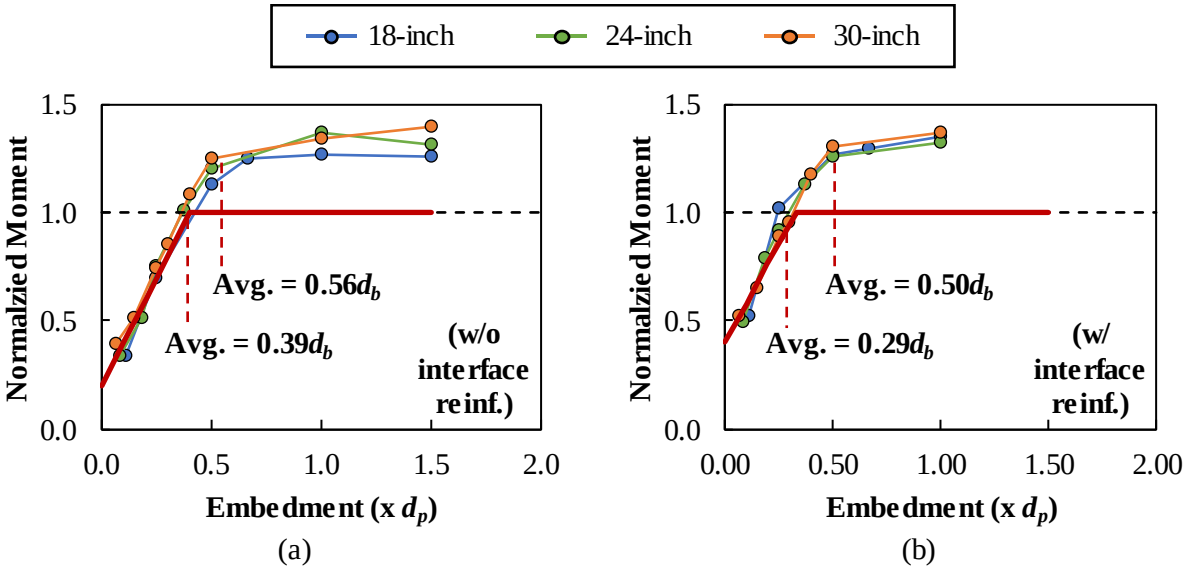

Figure 4.18: Normalized moment versus embedment length for pile-to-cap connections (a) without and (b) with interface reinforcement

Embedment length clearly influences the behavior of the connections. Embedment length should be one of the primary variables investigated during the experimental testing program. The numerical results from these preliminary models suggests that even shallow

pile embedments produce moment. Interface steel should be investigated for the shallower pile embedment lengths with an alternate detail to try and develop a pinned response. One idea for a pinned connection is shown in Figure 4.19.

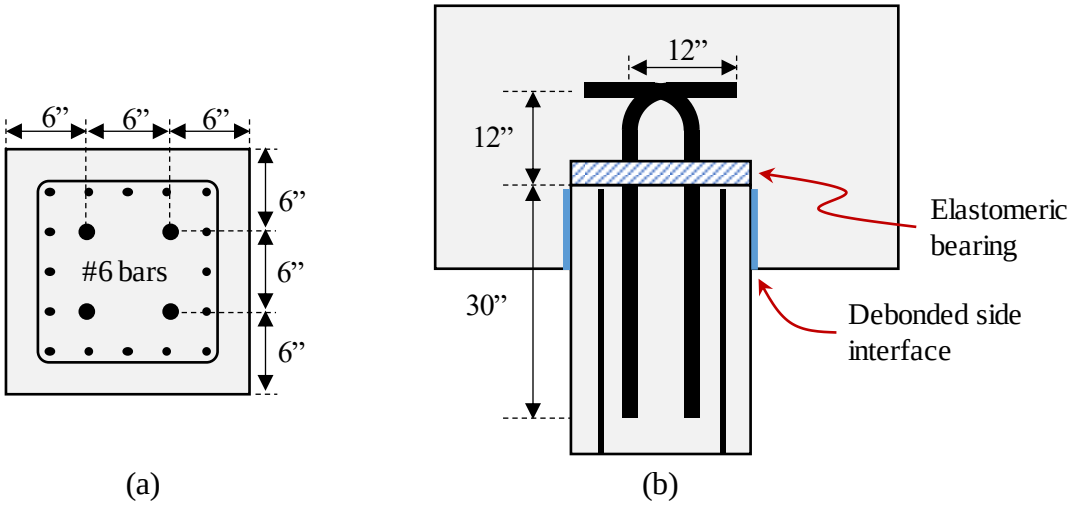

Figure 4.19: Idea for pinned connection between pile and pile cap (a) cross section and (b) elevation

4.2.3. Effect of Axial Load

The next variable investigated was the applied axial load to the pile. The effect of axial load on the behavior of the pile-to-cap connection was investigated for one shallow and one deep embedment, shown in Figure 4.20. This practice was repeated for all the secondary variables to investigate the effect of a variable on the connection when the connection controlled the failure and when the flexural strength of the pile controlled the failure. The axial load generally had two effects on the behavior of the system:

1. Axial compression would improve the performance of the connection, as shown in Figure 4.20 (a). The axial load was found to have the largest impact on the 30-inch diameter piles, where going from an axial compression load of $0.1A_g f'_c$ to $0.2A_g f'_c$

increased the capacity of the system by about 33%. The 18-inch and 24-inch pile systems saw a smaller increase in capacity of about 10%.

2. Axial compression generally increased the capacity of the pile itself, as shown in Figure 4.20 (b). The 30-inch pile saw an increase in capacity of about 4% when going from an axial compression load of $0.1A_g f'_c$ to $0.2A_g f'_c$.

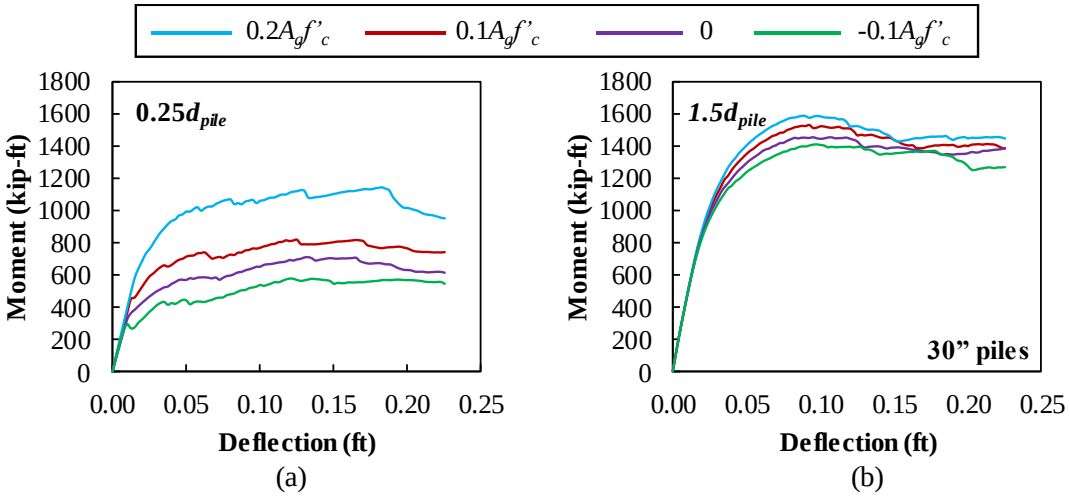

Figure 4.20: Sample moment versus deflection responses for 30-inch piles with (a) shallow ($0.25d_b$) and (b) deep ($1.5d_b$) embedments with varying axial load

An additional series of models were analyzed to evaluate the effect of interface reinforcement on the behavior of the system under various axial loads. The moment-deflection responses for 30-inch piles with and without interface reinforcement subjected to various constant axial loads are shown in Figure 4.21. The presence of interface reinforcement increased the capacity of the connection and decreased the impact of axial load on the behavior of the connection.

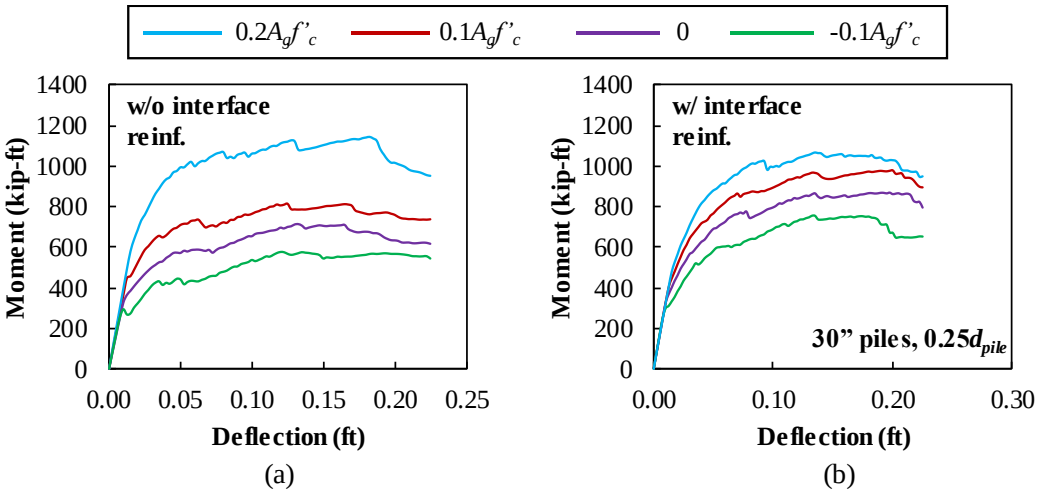

Figure 4.21: Sample moment versus deflection responses for 30-inch piles (a) without and (b) with interface reinforcement with varying axial load

4.2.4. Effect of Pile Concrete Strength

The moment versus deflection responses for systems with 30-inch piles and different pile concrete strengths are shown in Figure 4.22. The pile concrete strength did not significantly impact the behavior of the system when the failure of the system occurred at the connection, see Figure 4.22 (a). This is due to the failure of the connection occurring due to a failure in the cap. Increasing the strength of concrete in the pile did tend to increase the capacity of systems with larger pile embedments; this is because the strength of these systems was controlled by the pile capacity.

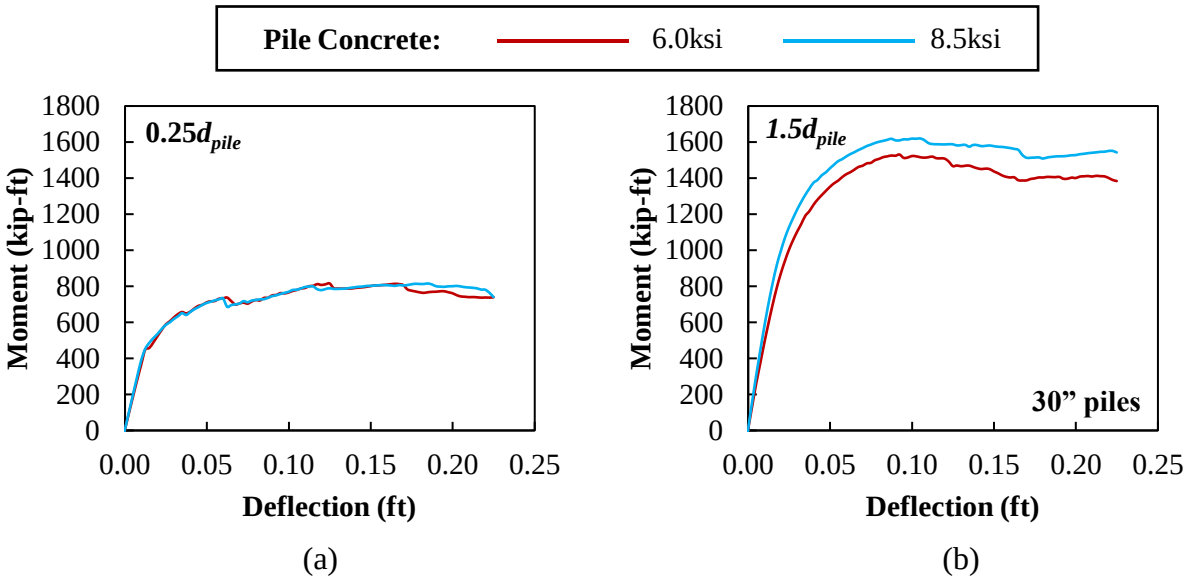

Figure 4.22: Sample moment versus deflection responses for 30-inch piles with (a) shallow ($0.25d_b$) and (b) deep ($1.5d_b$) embedments with varying pile concrete strength

4.2.5. Effect of Pile-Cap Concrete Strength

The influence of the pile-cap concrete strength on the behavior of the system was investigated with $0.1A_g f'_c$ (axial compression) and $-0.1A_g f'_c$ (axial tension), shown in Figure 4.23 and Figure 4.24, respectively. In both cases, the concrete strength only affected the strength of the system when the connection failed before the pile, as in Figure 4.23 (a) and Figure 4.24 (a). Because increasing the pile-cap concrete strength increased the strength of the system, the system is likely controlled by the crushing of the pile-cap concrete next to the embedded pile. The strength of the system was unaffected by an increase in pile cap concrete strength when failure occurred in the pile.

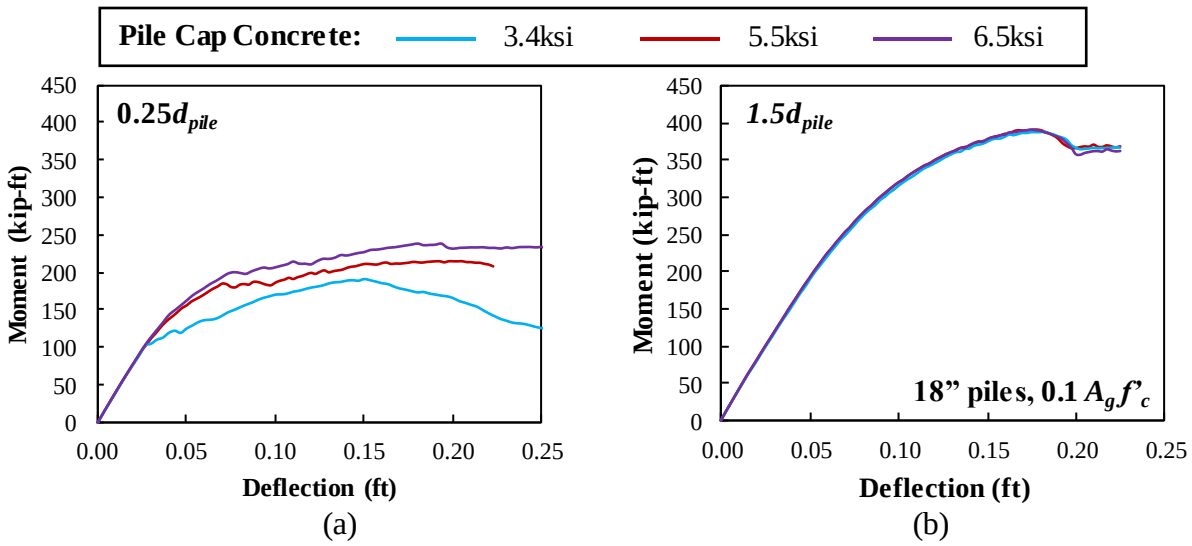

Figure 4.23: Sample moment versus deflection responses for 18-inch piles with (a) shallow ($0.25d_b$) and (b) deep ($1.5d_b$) embedments with axial compression and varying pile cap concrete strength

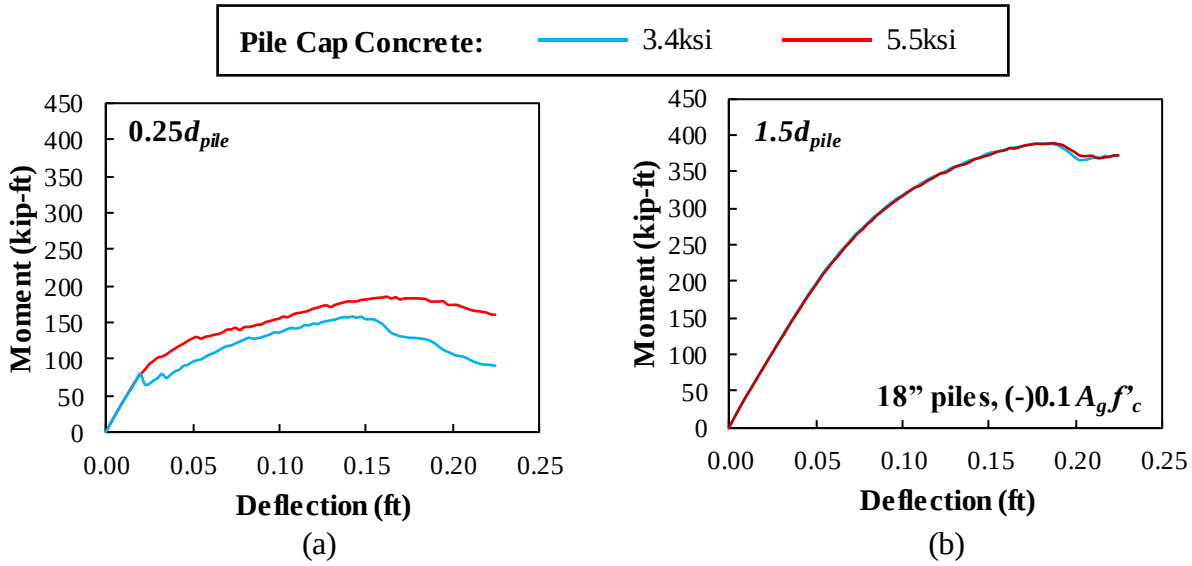

Figure 4.24: Sample moment versus deflection responses for 18-inch piles with (a) shallow ($0.25d_b$) and (b) deep ($1.5d_b$) embedments with axial tension and varying pile cap concrete strength

4.2.6. Effect of Pile Cap Size

Five difference pile cap sizes were investigated, shown Figure 4.25.

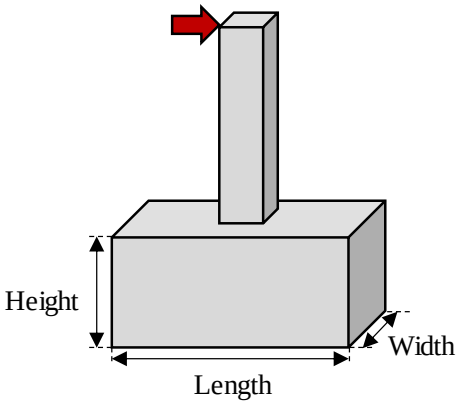

Pile Cap Sizes

(Width x Length x Height)

PC1 - $2.0d_{pile}$ x $3.0d_{pile}$ x $2.0d_{pile}$

PC1* - $1.78d_{pile}$ x $3.0d_{pile}$ x $2.0d_{pile}$

PC2 - $2.5d_{pile}$ x $3.5d_{pile}$ x $2.5d_{pile}$

PC3 - $3.0d_{pile}$ x $4.0d_{pile}$ x $3.0d_{pile}$

PC4 - $2.0d_{pile}$ x $2.0d_{pile}$ x $2.0d_{pile}$

Figure 4.25: Investigated pile cap sizes for analytical program

The size of the pile cap generally did not affect the behavior of the connection. Sample moment versus deflection responses for the systems with 30-inch piles are shown in Figure 4.26 for shallow and deep pile embedments. The capacity of the system with the shallow embedment was only affected by the pile cap size with a $2d_p$ length, Figure 4.26 (a). The pile cap size has no influence on the system performance when failure was controlled by the pile, Figure 4.26 (b).

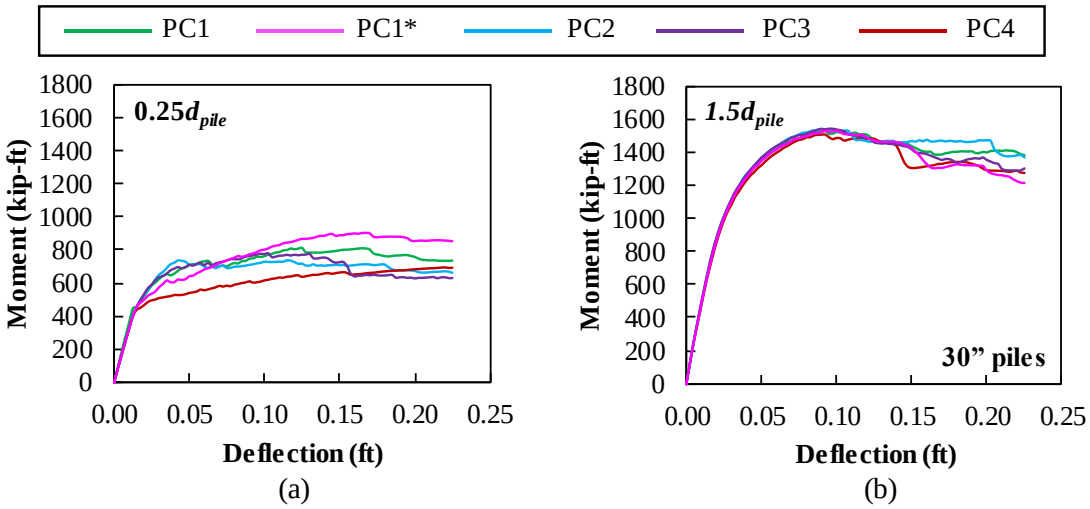

Figure 4.26: Sample moment versus deflection responses for 30-inch piles with (a) shallow ($0.25d_b$) and (b) deep ($1.5d_b$) embedments with different pile cap sizes

4.2.7. Effect of Reinforcement around Pile

Confinement reinforcement around the pile did not have a significant effect on the performance of the system regardless of embedment length, as shown in Figure 4.27. This would suggest that the cap (without the additional confinement reinforcement) already had enough reinforcement close enough to the embedded pile to sufficiently confine the concrete bearing against the pile.

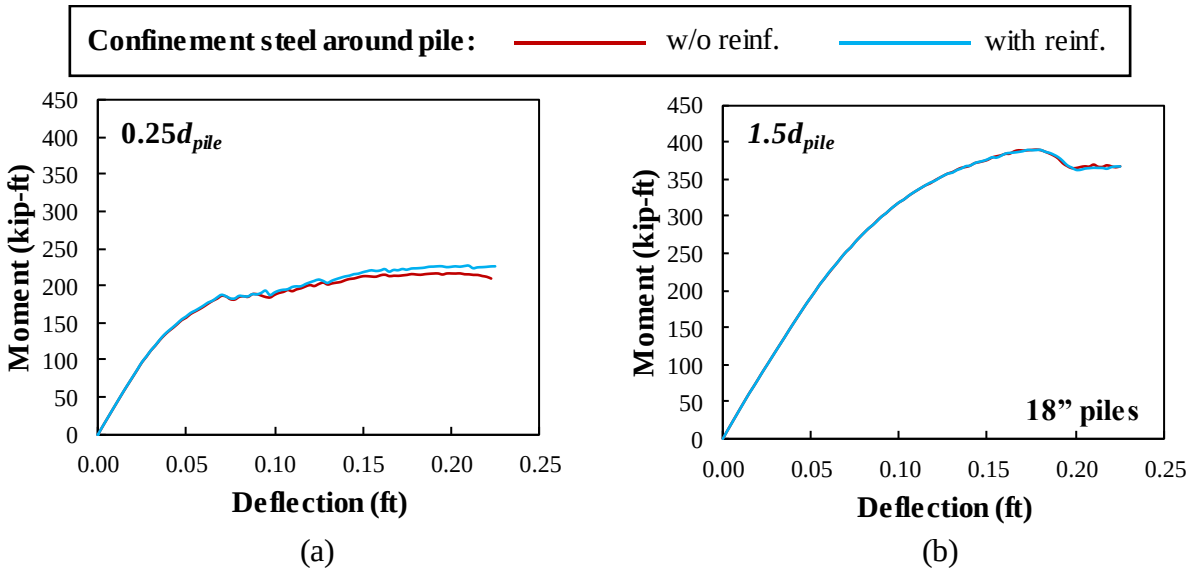

Figure 4.27: Sample moment versus deflection responses for 18-inch piles with (a) shallow ($0.25d_b$) and (b) deep ($1.5d_b$) embedments with and without confinement reinforcement around embedded pile

4.2.8. Effect of Strand Pattern

The effect of the strand pattern on the behavior of the system is shown in Figure 4.28.

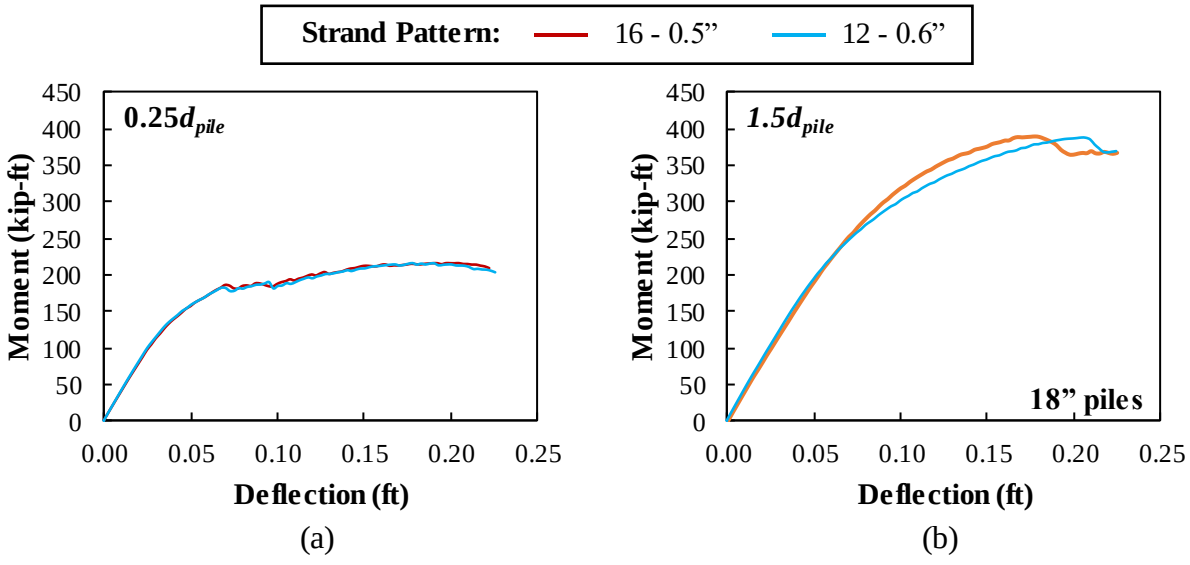

Figure 4.28: Sample moment versus deflection responses for 18-inch piles with (a) shallow ($0.25d_b$) and (b) deep ($1.5d_b$) embedments with different strand patterns

The strand type and pattern had minimal effect on the behavior of the system. A monitor was placed in all the strands for the 24-inch specimens to measure the maximum stress in the strand along the length. As shown in Figure 4.29, the strands were not able to fully develop in shorter embedment lengths. The length required to develop the strand is significantly shorter than the required development length from AASHTO LRFD [19]. This may be due to the large compression stresses adjacent to the strands caused by the compression block in the pile bearing against the pile cap as bending of the pile takes place. This should be further investigated during the experimental testing program to see if the development lengths are truly this short. Experimental results from 0.5-inch diameter strands should indicate how 0.6-inch strands will behave (and vice-versa), so strand diameter is not thought to be a variable that should be investigated in the experimental program.

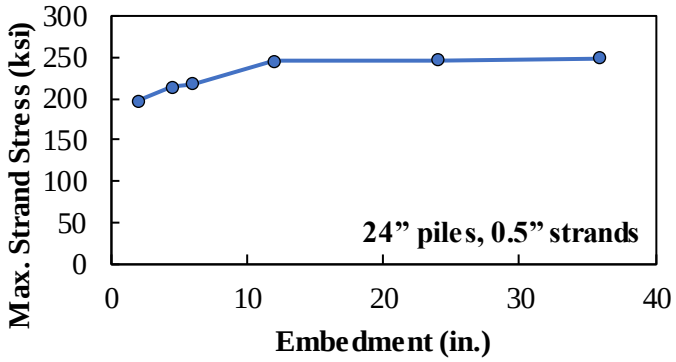

Figure 4.29: Maximum stress in prestressing strands in 24-inch piles with different embedment lengths

4.2.9. Summary of Results

One of the primary goals of the preliminary computational analyses of the pile-to-cap connection was to determine the variables that should be investigated in the experimental program. The following conclusions can be made from these analyses related:

1. Embedment length appears to be linearly related to the moment capacity of the connection until the capacity of the pile is reached. The embedment length should be the primary variable investigated in the experimental program. The development of the prestressing strands likely controls the failure of shallower embedment lengths, so instrumentation should be designed in the experimental program to investigate development length and factors that affect development length.
2. Shallow pile embedments still develop significant moment, so it is not likely that a shallow embedment alone can provide an adequate pin connection. Interface reinforcement between the pile and pile cap caused shorter embedment lengths to develop higher moments than those without interface reinforcement. An alternate detail, like Figure 4.19, should be investigated during the experimental program to explore to what extent a pinned connection can be achieved.
3. There appears to be a similar ratio between the normalized moment and normalized embedment length for 18-inch, 24-inch, and 30-inch piles. It may only be necessary to test two different pile sizes (rather than the three initially proposed).
4. Additional axial compression improves the performance of the connection and increases the moment capacity in the pile. Specimens with no axial load may be

useful (in addition to the originally proposed specimens with $0.1A_g f'_c$ axial compression) to get more conservative values for shallow embedments.

5. Pile concrete strength did not impact the performance of the shallow embedments in the models.
6. Pile-cap concrete strength did affect the performance of the connection, as it appears that concrete crushing in the pile cap adjacent to the embedded pile controlled failure. This could also be an additional variable investigated in the experimental program if one less pile size is selected.
7. The size of the pile cap did not seem to have a significant effect on the performance of the connection. Confinement reinforcement around the pile also did not have a significant effect. Both observations are likely a result of there being enough reinforcement in the cap to confine the embedded pile and prevent splitting of the cap before concrete crushes next to the pile. A reinforcement detail that closely resembles current practice should be selected, but these should likely not be variables further investigated in the experimental program.
8. There was little observed difference between the connection performance for piles with 0.5-inch and 0.6-inch diameter prestressing strands. There was a significantly shorter development length observed from the numerical analysis results. Strand stress should be monitored near the location of the edge of the pile in the experimental program, but only one size of strand should be selected.

5. EXPERIMENTAL PROGRAM

The selection of the specimens to be tested were based on results from previous computational analyses. The primary variables that were selected for the initial specimens are pile size and embedment length. Axial load, interface reinforcement, and pile cap concrete strength were selected as secondary variables.

5.1. TEST MATRIX

The primary goal of the preliminary numerical analysis was to determine the variables that should be investigated in the experimental program. These preliminary analyses suggested that variables such embedment length, pile size, interface reinforcement, and axial load had more impact on the connection performance than pile concrete strength, size of the pile cap, and strand pattern. These results were used to develop the experimental test matrix. The experimental matrix is shown in Table 5.1.

Table 5.1: Proposed experimental matrix

Specimen No.	Pile Size	Embedment Length		Interface Reinforcement	Axial Load	Pile Cap f'_c
1	18”	$0.33d_{pile}$	6.0”	w/o interface reinforcement	$0A_g f'_c$	Class IV
2	18”	$0.33d_{pile}$	6.0”	w/o interface reinforcement	$0.1A_g f'_c$	Class IV
3	18”	$0.33d_{pile}$	6.0”	w/interface reinforcement	$0A_g f'_c$	Class IV
4	18”	$0.5d_{pile}$	9.0”	w/o interface reinforcement	$0A_g f'_c$	Class IV
5	18”	$0.5d_{pile}$	9.0”	w/o interface reinforcement	$0.1A_g f'_c$	Class IV
6	18”	$0.67d_{pile}$	12.0”	w/o interface reinforcement	$0A_g f'_c$	Class IV
7	18”	$1.0d_{pile}$	18.0”	w/o interface reinforcement	$0A_g f'_c$	Class IV
8	18”	$1.5d_{pile}$	27.0”	w/o interface reinforcement	$0A_g f'_c$	Class IV
9	30”	$0.4d_{pile}$	12.0”	w/o interface reinforcement	$0A_g f'_c$	Class IV

Specimen No.	Pile Size	Embedment Length		Interface Reinforcement	Axial Load	Pile Cap f'$_c$
10	30”	1.0d_{pile}	30.0”	w/o interface reinforcement	0$A_g f'_c$	Class IV

5.1.1. Primary Variables

5.1.1.1. Pile Size

The ratio between normalized moment and normalized embedment length for 18-inch, 24-inch and 30-inch appears to be similar (from the numerical study results). Therefore, only two different pile sizes (18-inch and 30-inch) were tested, as shown in Figure 5.1. The interface reinforcement is shown in Figure 5.1, but this was only included in one specimen.

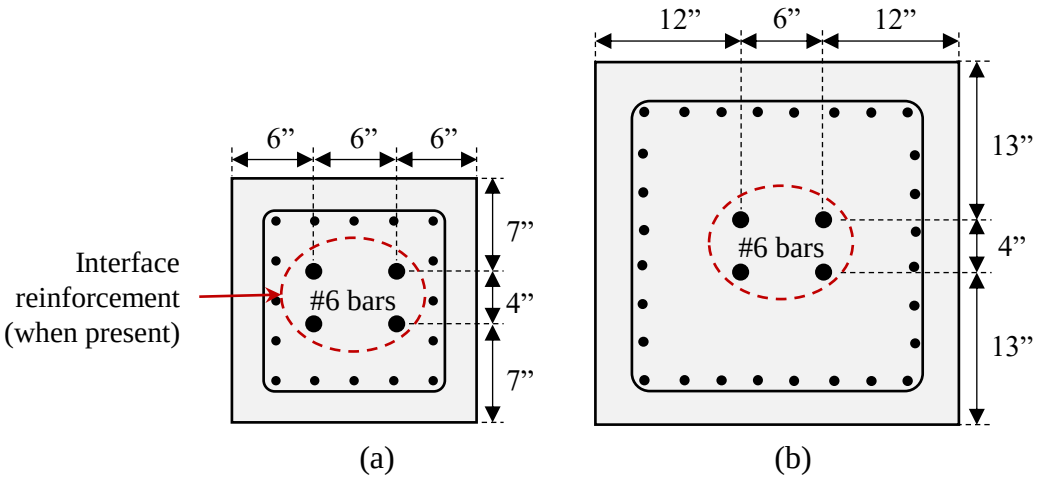

Figure 5.1: Details for (a) 18-inch and (b) 30-inch pile sizes

5.1.1.2. Embedment Length

The embedment length had the largest impact on the strength and behavior of the pile-to-cap connection in the numerical study. There appeared to be a linear relationship between the embedment length and the moment capacity of the connection. The full moment capacity of the pile was achieved at approximately 1.0d_{pile}, which is consistent with what was found in previous experimental testing. Four different embedment lengths were tested

between partial and full moment connections and one longer embedment length ($1.5d_{pile}$) to ensure that a test is conducted where the full moment capacity can be developed.

5.1.2. Secondary Variables

5.1.2.1. Axial Load

From the numerical analysis results, axial load was found to improve the performance of the connection and increase the capacity of the pile itself. Two of the shallow embedment lengths (6" and 9") were tested with an axial load of $0.1A_g f'_c$, which is a typical axial compression range, to better understand how axial load improves the connection performance.

5.1.2.2. Interface Reinforcement

An interface reinforcement detail based on Larosche et al. [15] was implemented for one of the specimen in the experimental program, as shown in Figure 5.1 and Figure 5.2. The presence of interface reinforcement was found in the numerical analyses to slightly decrease the embedment length required to develop the full moment capacity of the pile and increase the rotation capacity of the connection. The interface reinforcement had more of an effect on the behavior of the 18-inch piles compared to the 24 and 30-inch pile.

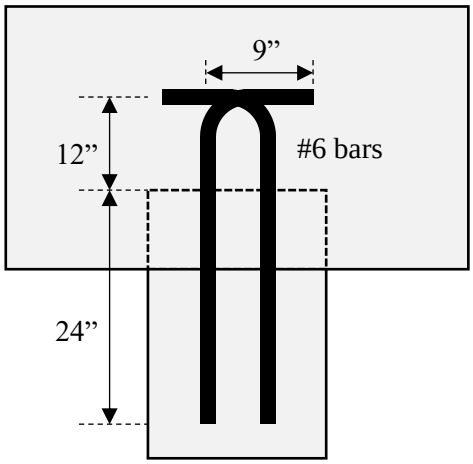

Figure 5.2: Details of proposed interface reinforcement for testing

5.2. SPECIMEN DESCRIPTION

5.2.1. Pile Details

The pile details are based on the FDOT Standard Plans [53], as shown in Figure 5.3. All piles had a length of 18 feet. The load point will be kept consistent, so the distance from the load point to the end of the pile will vary with different pile embedment lengths. Detailed pile drawings are provided in APPENDIX.

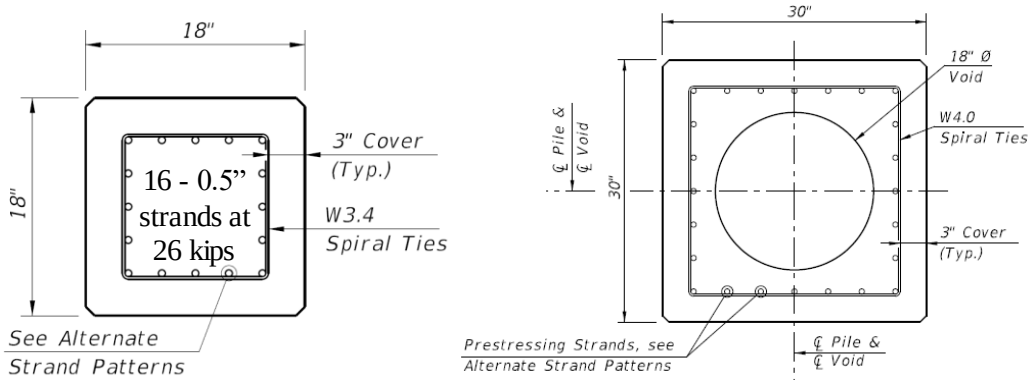

(a) (b)

Figure 5.3: Typical details for (a) 18-inch and (b) 30-inch piles

5.2.2. Pile Cap Details

The pile cap reinforcement scheme was selected considering previous research and select projects and following the FDOT Structures Detailing Manual [1]

5.2.2.1. Pile Cap Dimensions

The basic dimensions for the pile caps used in the experimental program are shown in Figure 5.4. Detailed drawings of the test specimens are provided in APPENDIX.

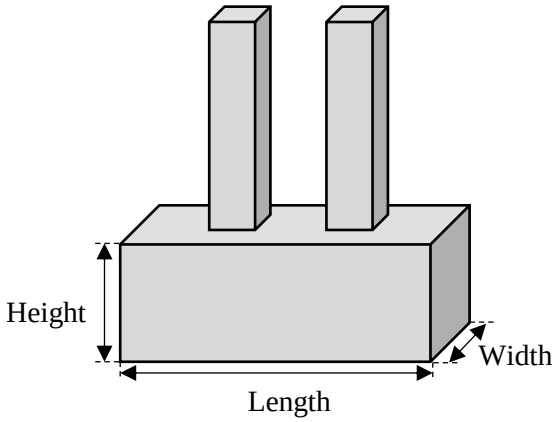

Pile Cap Sizes

(Width x Length x Height)

($3.0d_p$ x $5.0d_p$ x $2.0d_p$*)

PC1 (18" piles) – 4.5' x 7.5' x 3.0'

PC2 (30" piles) – 7.5' x 12.5' x 4.0'

*PC2 only has a $1.8d_p$ height due to weight limitations

Figure 5.4: Pile cap dimensions for 18-inch and 30-inch piles

The length of the pile caps was selected considering center-to-center pile spacing and edge distance requirements, as shown in Figure 5.5. FDOT Structures Detailing Manual [1] (§ 3.5.4) specifies that center-to-center pile spacing should not be less than $3.0d_{pile,}$ and AASHTO LRFD [19] (§10.7.1.2) specifies the minimum edge distance as 9-inch. In common practice, the edge distance varies with pile size; it is typical practice to use a minimum edge distance of $0.5d_{pile}$, which is equal to the 9-inch minimum requirement for 18-inch piles and is 15 inches for 30-inch piles. The width of the pile caps was selected to have a $1.5d_{pile}$ distance between the center of the pile and edge of the pile cap, which is

equal to half of the minimum center-to-center pile spacing. The height of the pile caps was selected to be 2.0d_{pile} for the 18-inch specimens. For the 30-inch pile cap the height was fixed to 54-inch because of weight limits of the specimen.

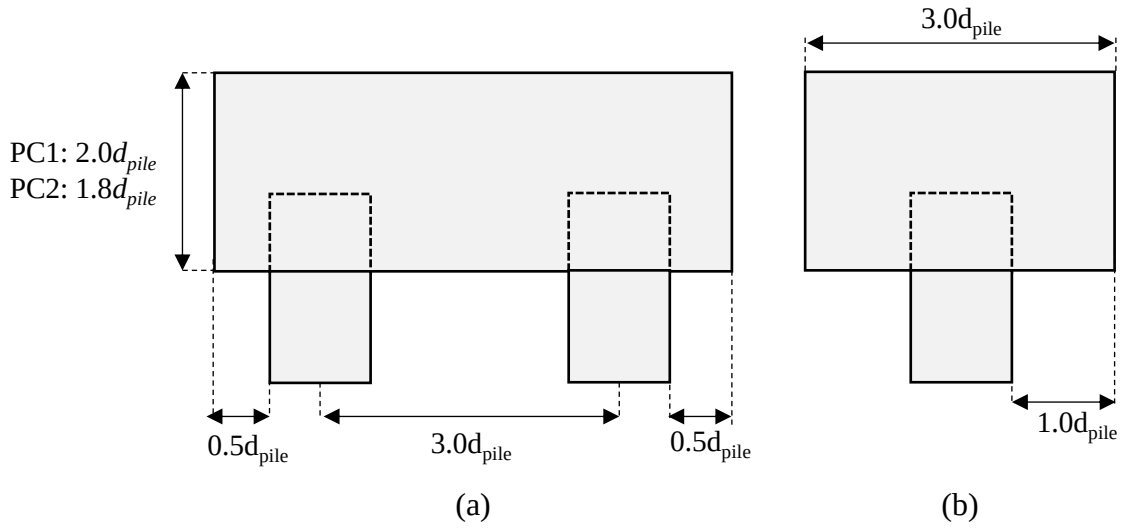

Figure 5.5: General pile cap dimension details (a) plan and (b) elevation views

5.2.2.2. Reinforcement Specifications

- Minimum Spacing of Bars

For cast-in-place (CIP) concrete, AASHTO LRFD [19] (§5.10.3.1.1) specifies that the distance between parallel bars in a layer should not be less than the largest of the following:

- 1.5 times the nominal diameter of the bars
- 1.5 times the maximum size of the coarse aggregate
- 1.5 inches

The minimum spacing of bars was checked for all reinforcement, but specifically for the longitudinal reinforcement in the top and bottom of the pile cap.

- Maximum Spacing of Bars

FDOT Structures Detailing Manual [1] §4.3.1 specified maximum bar spacing according to AASHTO LRFD [19] §5.10.6. The area of reinforcement per foot on each face and in each direction should satisfy the following equation:

$$A_s \geq \frac{1.30bh}{2(b+h)f_y} \qquad \text{AASHTO LRFD 2017 (5.10.6-1)}$$

$$0.11 \leq A_s \leq 0.60 \qquad (5.10.6\text{-}2)$$

where:

A_s = area of reinforcement in each direction and each face (in^2/ft)

b = least width of component section (in)

h = least thickness of component section (in)

f_y = specified minimum yield strength of reinforcement ≤ 75 ksi

The spacing of the reinforcement shall not exceed 12 inches for walls and footings greater than 18 inches thick.

The required reinforcement for the 18-inch and 30-inch pile cap specimens are summarized in Table 5.2.

Table 5.2: Minimum required reinforcement on each face of pile cap

d_{pile} (in)	b (in)	h (in)	f_y (ksi)	$A_{s,req}$ (in^2/ft)
18	54	36	60	0.234
30	90	54	60	0.366

The skin reinforcement in the pile caps was designed to meet these minimum area and maximum spacing requirements.

- Minimum Concrete Cover

The requirements for concrete cover are listed in the FDOT Structures Design Guidelines [1] §1.4.2. For external surfaces cast against earth and surfaces in contact with water the recommended cover is 4 inches; and for exterior formed surfaces, columns, and tops of footing not in contact with water is 3 inches, for slightly and moderately aggressive environments. A sample detail for a pile cap is shown in Figure 5.6.

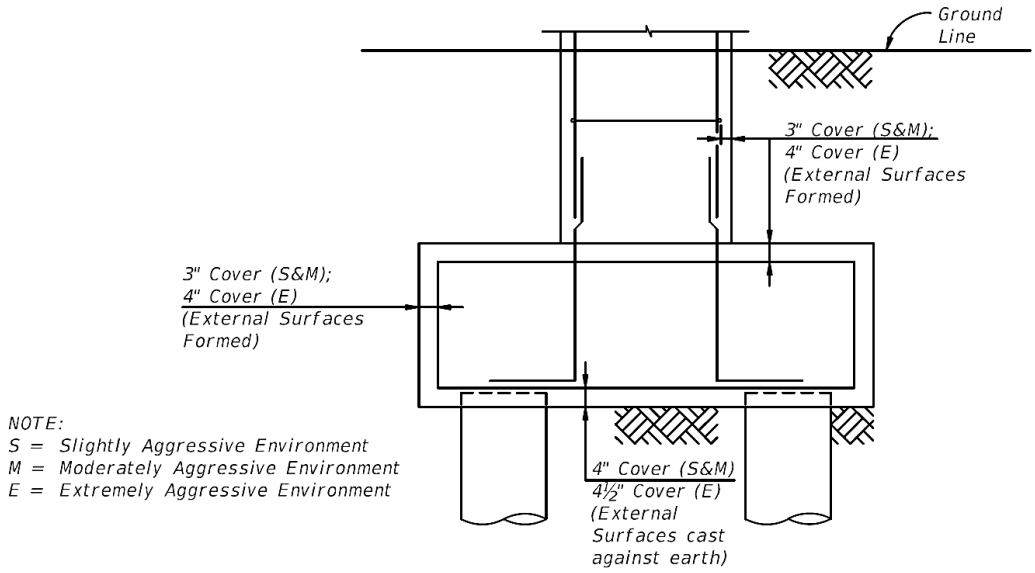

Figure 5.6: Sample cover requirements from FDOT Structures Design Guidelines [1]

A slightly aggressive (S) or moderately aggressive (M) exposure condition was assumed for the developed details.

- Maximum Reinforcing Steel Bar Sizes

FDOT Structures Detailing Manual [1] §4.3.11 specifies a maximum reinforcing steel bar size of #11 bars for footings. The maximum bar size used in the pile caps is #9 bars for the longitudinal steel.

5.2.2.3. Basis for Pile Cap Reinforcement Scheme

The reinforcement scheme used for the pile caps was based primarily on two research projects (Larosche et al. [15] and Issa [13]) and contract plans obtained for two constructed bridges (from the ABC Project Database [62]). An initial pile cap reinforcement scheme was developed and then refined based on discussions with FDOT and Corven Engineering, Inc.

Larosche et al. [15] investigated several different pile cap details with 18-inch square prestressed concrete piles. Their control specimen had an 18-inch embedment (embedment equal to pile size) and pile cap dimensions and reinforcement detail in line with the practice used at the time in South Carolina, as shown in Figure 5.7. Reinforcement included five No. 9 in the top spaced evenly across the width of the cap and four No. 9 placed in the bottom. Shear reinforcement consisted of No.5 bars spaced at 6-inch. And four No.6 bars as skin reinforcement, spaced evenly between top and bottom.

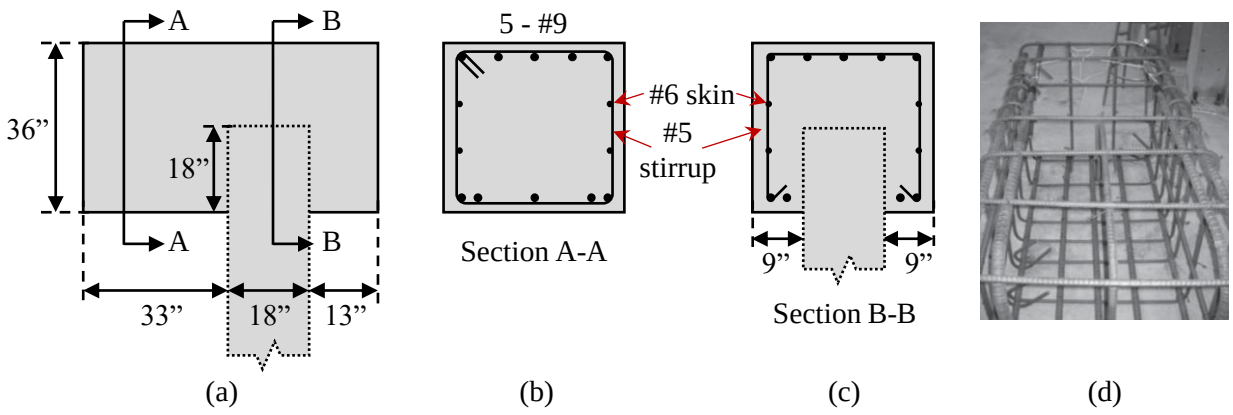

Figure 5.7: Typical pile cap reinforcement from Larosche et al. [15]

Issa [13] tested two 30-inch square prestressed piles with 48-inch embedment into a single pile cap. A schematic of the reinforcement scheme for this testing is shown in Figure 5.8 and a photograph of the reinforcement shown in Figure 5.9. A significant amount of reinforcement was provided in this cap.

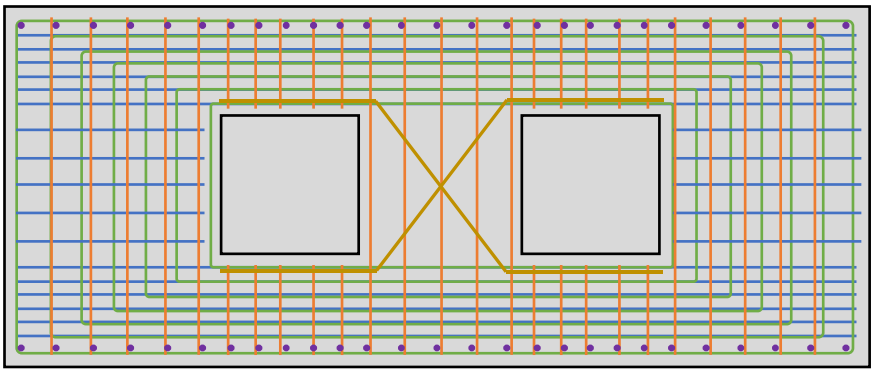

(a)

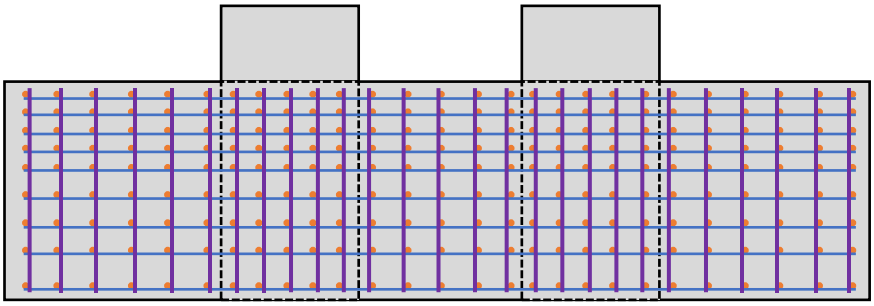

(b)

Figure 5.8: Schematic of pile cap reinforcement scheme used by Issa [13] (a) plan and (b) elevation views

Figure 5.9: Photograph of pile cap reinforcement used by Issa [13]

Two sample contract plans were obtained from the ABC Project Database [62]; these are shown in Figure 5.10.

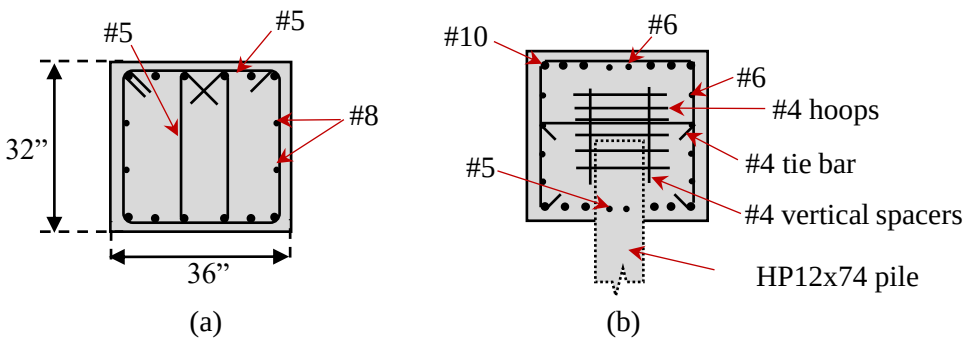

Figure 5.10: Sample pile cap reinforcement from (a) UPRR Bridge 126.31 (b) Burnt River Bridge projects

These sample reinforcement schemes were used as a starting point for the proposed pile cap reinforcement. The reinforcement scheme was further refined through discussion with FDOT engineers and amongst the project team.

5.2.2.4. Types of Pile Cap Reinforcement

The specimens with 18-inch and 30-inch piles had similar reinforcement schemes, except the amount of steel increases for the 30-inch pile cap. There are six different types of reinforcement that were considered for the pile cap reinforcement, as shown in Figure 5.11 and Figure 5.12. The longitudinal reinforcement, #9 bars spaced at 6.0 inches in Figure 5.11 (a), resists the flexural stresses that develop in the pile cap from bending of the piles. The vertical skin reinforcement, #5 bars at 5.5 inches in Figure 5.11 (b), and horizontal skin reinforcement, #6 bars at 6.0 inches in Figure 5.11 (b), help to limit cracking of the pile cap and are consistent with what has been used in previous research and the sample contract plans. This reinforcement is typical for this type of pile cap.

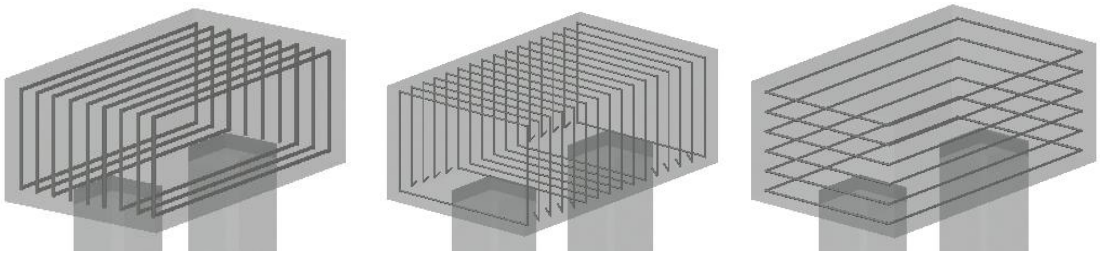

(a) (b) (c)

Figure 5.11: Pile cap reinforcement (a) primary tension, (b) vertical skin, and (c) horizontal skin reinforcement

The additional reinforcement that is not typical for this type of pile cap are shown in Figure 5.12. The interior horizontal reinforcement, Figure 5.12 (a), was used by Issa [13] and in the Burnt River Bridge project [62] and may help prevent splitting of the pile cap; this reinforcement is not typically provided. The interior vertical reinforcement, Figure 5.12 (b), is used when additional shear strength is needed. These members are typically designed to not require shear reinforcement for strength though, so this vertical reinforcement is typically not required. The confinement reinforcement around the pocket, Figure 5.12 (c), can be provided to help confine the pile, which is thought to decrease the development length of the prestressing strand in the pile. This confinement reinforcement is not typically provided though. The reinforcement shown in Figure 5.12 was not selected for the test specimens as it is not typical in pile caps.

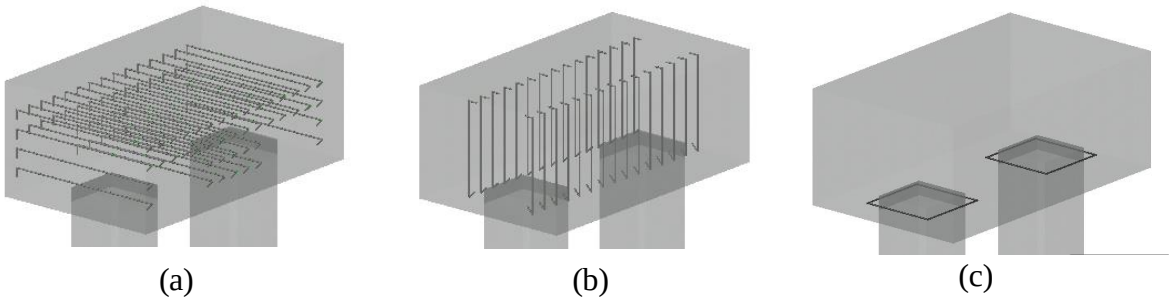

Figure 5.12: Interior pile cap reinforcement (a) horizontal, (b) vertical, and (c) embedded pile confinement reinforcement

5.2.2.5. Nominal Flexural Strength of Pile Cap

Loading of the piles in the proposed test setup will result in a large moment developing in the pile cap between the piles. The flexural strength of the pile cap must be greater than the demand with a sufficient factor of safety to prevent failure of the pile cap in flexure. The longitudinal reinforcement (#9 bars) will resist the tension developed by this moment. The moment demand on the pile caps when the piles are pushed together is shown in Figure 5.13.

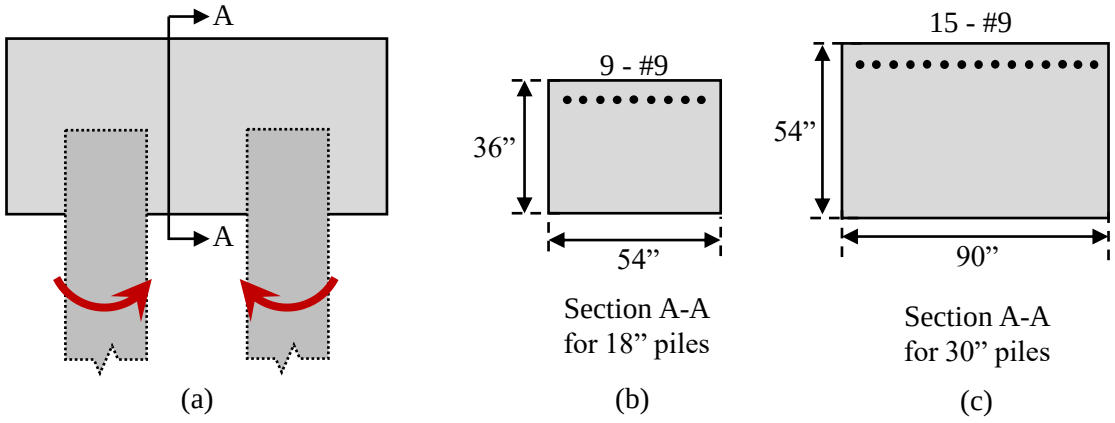

Figure 5.13: (a) Moment demand on pile cap for piles being pushed together, (b) cross section with 18-inch pile and (c) cross section with 30-inch pile

The moment demand will be opposite if the piles are pushed apart, as shown in Figure 5.14. There is less tensile reinforcement that will be available in this scenario because there is not longitudinal reinforcement extending the length of the pile cap at the location of the embedded piles.

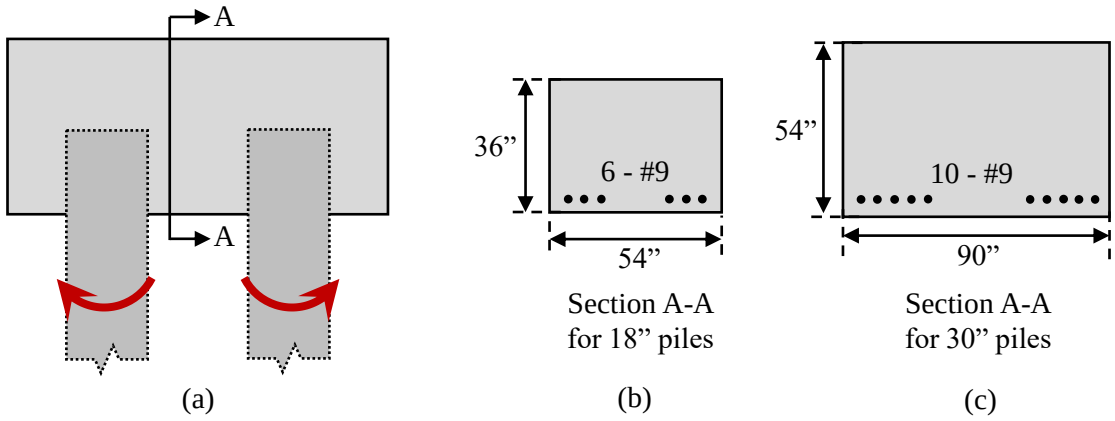

Figure 5.14: (a) Moment demand on pile cap for piles being pushed apart, (b) cross section with 18-inch pile and (c) cross section with 30-inch pile

The nominal moment can be found using rectangular stress block assumptions and equilibrium, shown in Equation 5.1 and Equation 5.2.

Nominal Moment: $$M_n = A_s f_y \left(d - \frac{\beta_1 c}{2}\right)$$ Equation 5.1

Stress block: $$c = \frac{A_s f_y}{0.85 f'_c \beta_1 b}$$ Equation 5.2

The nominal flexural strength for the pile caps compared to the moment demand in each case are summarized in Table 5.3, where PC18-1 is 18-inch pile with piles being pushed together and PC 18-2 is the 18-inch pile with piles being pushed apart for testing.

Table 5.3: Pile cap flexural capacity between piles

	PC18-1	**PC18-2**	**PC30-1**	**PC30-2**
h (in)	36	36	54	54
d (in)	32	32	50	50
b (in)	54	54	90	90
A_s (in^2)	9.0	6.0	15.0	10.0
f_y (ksi)	60	60	60	60
f'_c (ksi)	6.0	6.0	6.0	6.0
β_1	0.75	0.75	0.75	0.75
c (in)	2.61	1.74	2.61	1.74
ε_s	0.0337	0.0521	0.0544	0.0831
M_n (k-in)	16,751	11,285	44,118	29,608
M_u (k-in)	3,708	3,708	13,176	13,176
M_n/M_u	4.52	3.04	3.35	2.25

The pile cap had sufficient flexural capacity between the piles in all cases as long as all the longitudinal reinforcement is engaged.

5.2.2.6. Engagement of Longitudinal Reinforcement

One question that arose during the development of the pile cap reinforcement scheme is what longitudinal reinforcement will be engaged when there is a small distance provided between the edge of the pile and edge of the pile cap, as shown in Figure 5.15. Some designers select the distance between the pile and edge of the pile cap based on the size of the longitudinal reinforcement and bend diameter of this reinforcement. Common practice is to ensure that the standard hook dimension ends before the edge of the pile, as shown in Figure 5.15 (a). There is no specification on this, but this can lead to a larger edge distance than the minimum 9 inches allowed by AASHTO LRFD.

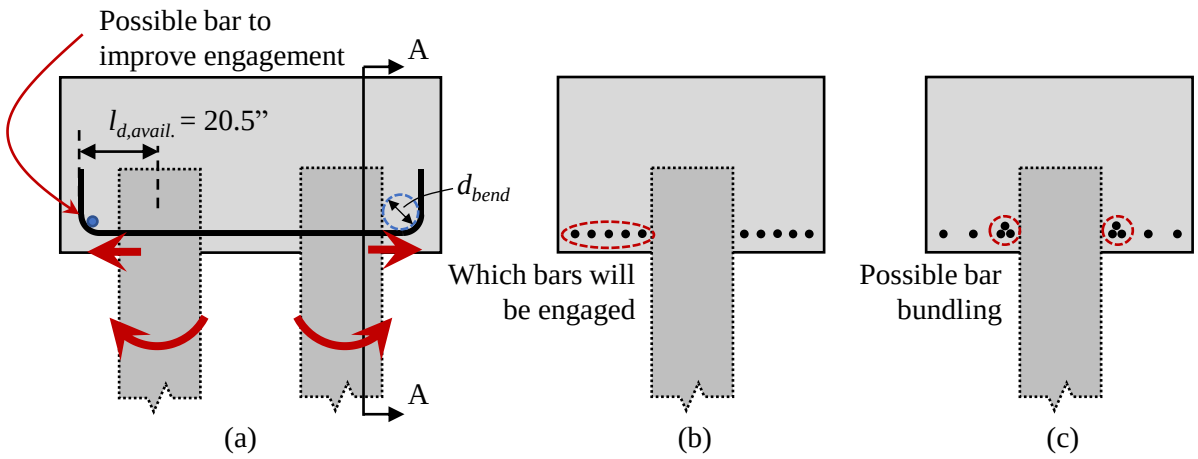

Figure 5.15: (a) Engagement of longitudinal reinforcement around pile, (b) cross section of typical longitudinal reinforcement, and (c) cross section with possible bar bundling if reinforcement engagement does control

The development length of the longitudinal reinforcement (#9 bars) was found using AASHTO LRFD [19] §5.10.8.2.4.a

Development length:	$l_{dh} = l_{hb}\left(\frac{\lambda_{rc}\lambda_{cw}\lambda_{er}}{\lambda}\right)$	Equation 5.3
Not epoxy coated, normal -weight concrete:	$\lambda_{rc} = \lambda_{cw=}\lambda_{er} = \lambda = 1.0$	
Basic development length:	$l_{hb} = \frac{38d_b}{60.0}\left(\frac{f_y}{\sqrt{f'_c}}\right)$	Equation 5.4
Development length:	$l_{dh} = l_{hb} = \frac{38(1.128")}{60.0}\left(\frac{60ksi}{\sqrt{5.5ksi}}\right) = 18.3"$	

The available development is the distance from the back of the hook to the point where the full moment demand is required, which is assumed to be at the mid-depth of the embedded pile, as shown in Figure 5.15. The required development length (18.3 in.) is less than the available development length (20.5 in.), so the yield stress can be developed in this reinforcement.

The pile cap reinforcement is proposed to have typical distributed bars with strain gauges to measure which bars are engaged during testing.

An additional bar will be provided inside the bend on one side of the pile cap, as shown in Figure 5.15 (a), to see how this improves the engagement of reinforcement and if it improves the behavior of the connection.

5.3. TEST SETUP

Three different test setups were considered for testing of these specimens, as shown in Figure 5.16. Each of the test frames was evaluated based on the impact of support conditions on the connection behavior (using numerical analyses) and available steel beams in FDOT's Structures Research Center (SRC).

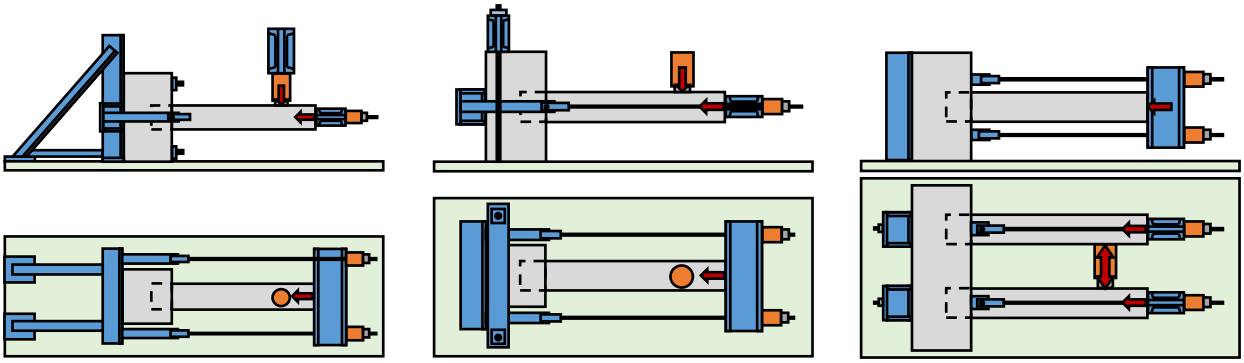

Figure 5.16: Investigated options for test setup, (a) rear support, (b) top support, and (c) self-reacting frames

The selected test setup was a self-reacting frame system with two piles, as shown in Figure 5.17. The self-reacting frame was decided to have the least impact on the connection behavior and the simplest setup in the lab.

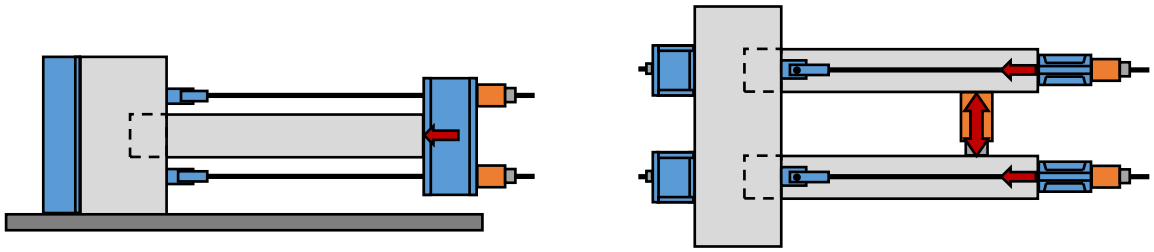

(a) (b)

Figure 5.17: Schematic of proposed test setup (a) elevation and (b) plan view

Loading the piles from the outside (pushing pile ends together) and from the inside (pushing pile ends apart) were also both evaluated using numerical modeling. One of the primary objectives of the testing was to evaluate the connection based on the minimum possible edge distance. Loading the piles from the inside was found to lead to higher stresses at the edges of the pile caps than loading from the outside. A sample of the numerical results is provided in Figure 5.18 for a shallow embedment of $0.25d_p$ where the pile reached a moment of 253.5 kip-ft, which is approximately 82% of their moment capacity.

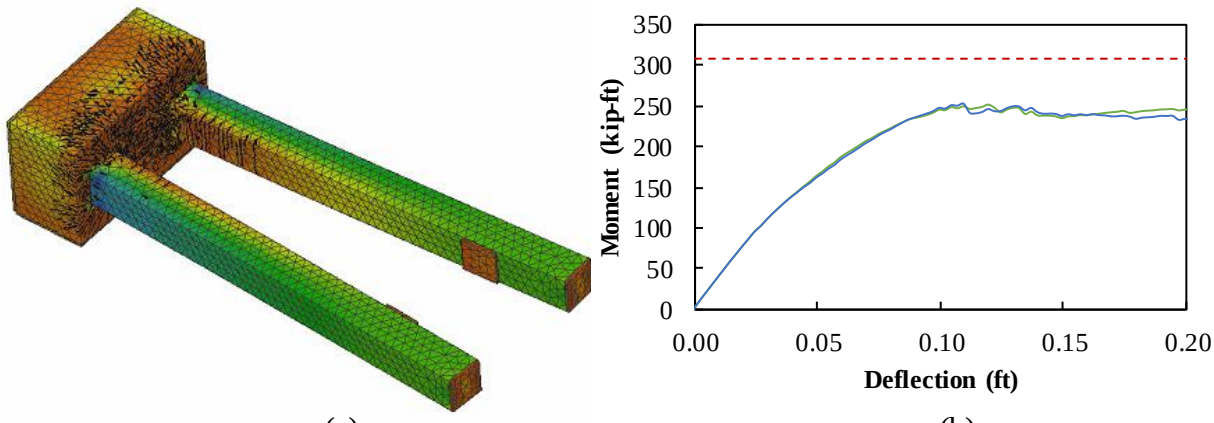

(a) (b)

Figure 5.18: Numerical analyses for test set up

5.3.1. Spreader Beams

The test setup did not require any spreader beams when no axial load is applied. The only connection was four threaded rods extending through the specimens and attaching the specimen to the strong floor, as shown in Figure 5.19 (a). These were not required for the boundary condition but were used to stabilize the specimens during testing.

This test set up required four spreader beams when an axial load was applied. Two at the end of the piles and two restraining the back of the pile cap, as shown in Figure 5.19(b).

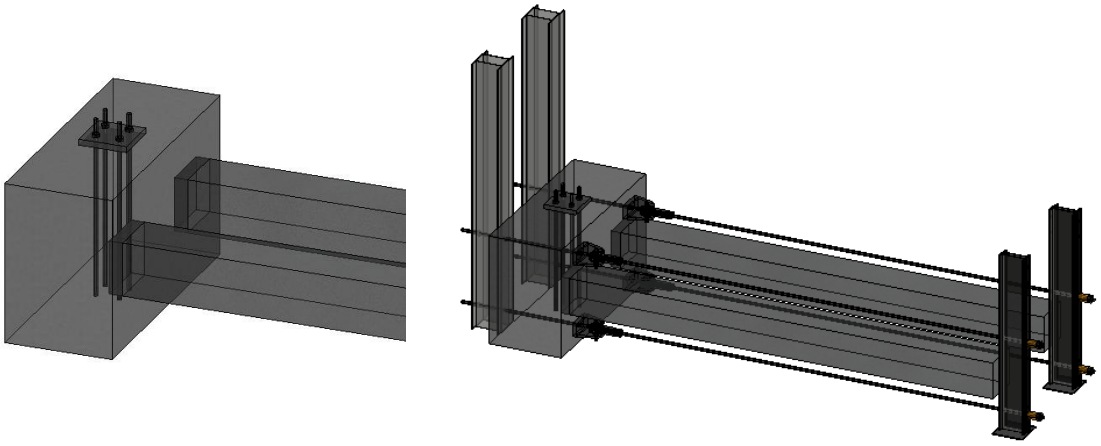

(a) (b)

Figure 5.19: (a) Tie down point to strong floor and (b) setup for axial load application

5.3.2. Threaded Rods

Three different threaded rod lengths were required for axial load application and securing the specimens to the strong floor, as shown in Figure 5.20. The threaded rods have the following naming convention:

- Rod 1: correspond to the rods extending through the pile cap and attaching the specimen to the strong floor

- Rod 2: correspond to the rods attached to the spreader beams at the back of the cap, extending through the pile cap, and attached to the pin connection
- Rod 3: corresponds to the rods connected to the pin connection, extending the length of the pile, and attached to the spreader beams at the end of the piles.

Rods 2 and 3 transferred the tension applied by the hydraulic jack to the back of the pile cap to apply the constant axial load to the piles.

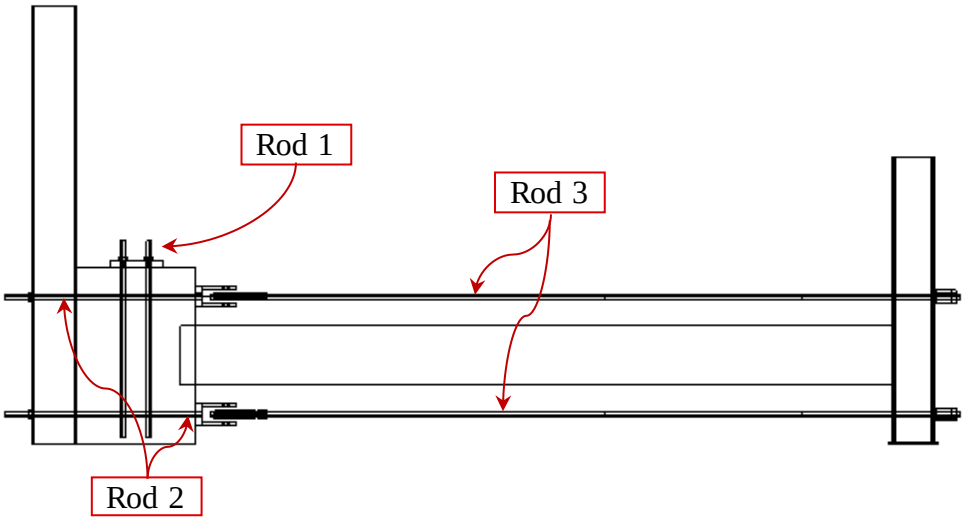

Figure 5.20: Threaded rods configuration

5.4. EXPERIMENTAL PROCEDURE

5.4.1. Without Axial Load

No spreader beams were required for the specimens tested without axial load, and only the threaded rods attaching the pile cap to the strong floor were needed. The experimental procedure consisted of the application of the lateral load using a hydraulic jack pushing the piles apart until failure, as shown in Figure 5.21 (a).

Preliminary numerical models for shallow embedment showed a maximum displacement of 1.2 inch and a failure load of 19.6 kips for the 18-inch piles. For 30-inch piles with shallow embedment preliminary results showed a maximum displacement of 0.5 inch and a failure load of 61.5 kips. For deeper embedment lengths ($1.5d_{pile}$), the failure load for 18-inch and 30-inch piles increase approximately to 32 kips and 118 kips, respectively.

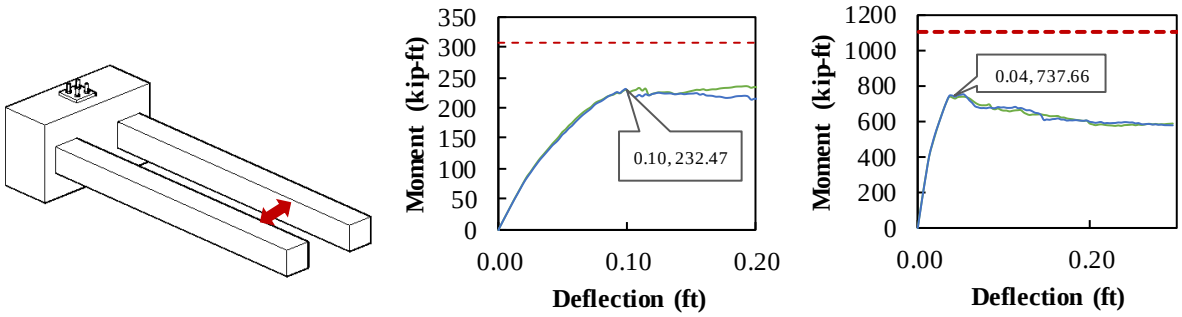

(a) (b) (c)

Figure 5.21: (a) Experimental procedure without axial load (b) numerical modeling results for shallow embedment for 18-inch piles (c) numerical modeling results for shallow embedment for 30-inch piles

The piles were loaded incrementally until failure. The loading protocol for strength testing consisted of 5 loading steps, shown in Table 4. The specimens were visually inspected for cracks and photographs were taken between each of the loading stages. The first cracking load from visual observation was documented along with the location of first cracking.

Table 4: Loading protocol for specimens without axial load

Specimen Description			Loading Protocol					
Specimen	**Pile Size**	**Failure Load**	**Load Rate**	**Step 1**	**Step 2**	**Step 3**	**Step 4**	**Step 5**
1	18”	25 kips	0.03 k/s	3 k	6 k	9 k	15 k (60% est. capacity)	Load to failure
3	18”	30 kips	0.03 k/s	4 k	8 k	12 k	18 k (60% est. capacity)	Load to failure
4	18”	30 kips	0.03 k/s	4 k	8 k	12 k	18 k (60% est. capacity)	Load to failure
6	18”	31 kips	0.03 k/s	4 k	8 k	12 k	18 k (60% est. capacity)	Load to failure
7	18”	32 kips	0.03 k/s	4 k	8 k	12 k	18 k (60% est. capacity)	Load to failure
8	18”	35 kips	0.03 k/s	5 k	10 k	15 k	21 k (60% est. capacity)	Load to failure
9	30”	60 kips	0.1 k/s	9 k	18 k	27 k	36 k (60% est. capacity)	Load to failure
10	30”	115 kips	0.1 k/s	17 k	34 k	51 k	69 k (60% est. capacity)	Load to failure

5.4.2. With Axial Load

Spreaders beams at the back of the pile cap and at the end of the piles were needed for the application of the axial load. The experimental procedure consisted of two primary steps, as shown in Figure 5.22. First, the axial load was applied through two center-hole hydraulic jacks to the threaded rods, which transferred the tension to the pile cap. Two center hole hydraulic jacks with 60-ton capacity were used to tension the threaded rods (e.g., Enerpac Tall Blue) and put the piles in axial compression.

Once the desired axial load was reached it was left constant during the rest of the experimental procedure. Finally, a lateral load was applied using hydraulic jacks pushing the piles apart until failure of the specimens occurred.

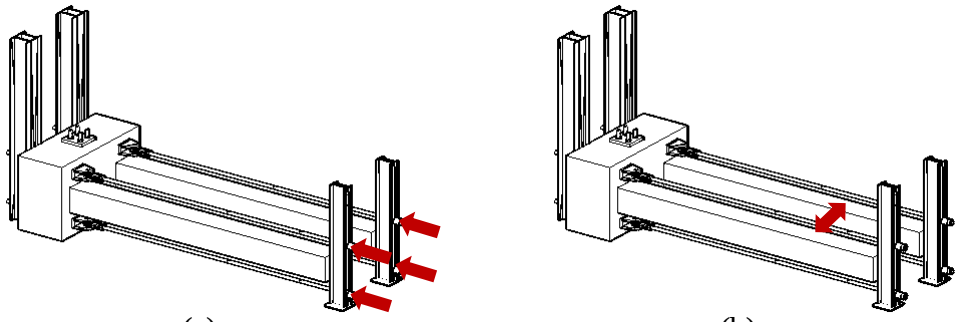

(a) (b)

Figure 5.22: Experimental procedure with axial load (a) application of axial load (b) application of lateral load

The piles were loaded incrementally until failure. The loading protocol for strength testing consisted of 5 loading steps, shown in Table 5. The specimens were visually inspected for cracks and photographs were taken between each of the loading stages. The first cracking load from visual observation as be documented along with the location of first cracking.

Table 5: Loading protocol for specimens with axial load

Specimen Description			**Loading Protocol**					
Specimen	**Pile Size**	**Failure Load**	**Load Rate**	**Step 1**	**Step 2**	**Step 3**	**Step 4**	**Step 5**
2	18”	25 kips	0.03 k/s	3 k	6 k	9 k	15 k (60% est. capacity)	Load to failure
5	18”	30 kips	0.03 k/s	4 k	8 k	12 k	18 k (60% est. capacity)	Load to failure

5.5. INSTRUMENTATION PLAN

A general overview of the instrumentation is provided in this section.

5.5.1. Deflection Gauges

Load cells were located next to the hydraulic jack to measure the load that was being applied to the piles. Fourteen laser displacement transducers (LDTs) were placed across the length of the piles and cap, to measure deflection. Additionally, two LDTs were place on top of the piles to measure out-of-plane displacement. Figure 5.23 shows details of these gauges.

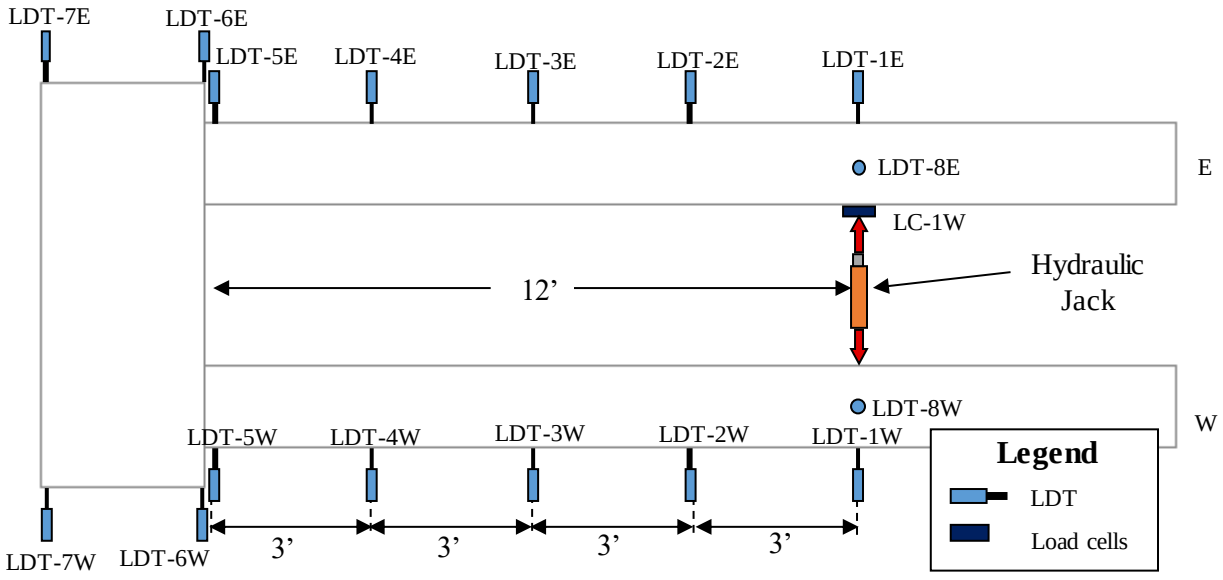

Figure 5.23: Deflection gauges(LVDT) and load cells (top view)

The length of the plastic hinge zone is 2.5 feet which was estimated based on visual observations of damage in the numerical models, as shown in Figure 5.24. To measure curvature in the plastic hinge region of the piles, sixteen (16) crack displacement transducers were placed along both sides of the piles, as shown in Figure 5.25 These CDTs measured the curvature and rotation of the pile in the plastic hinge zone.

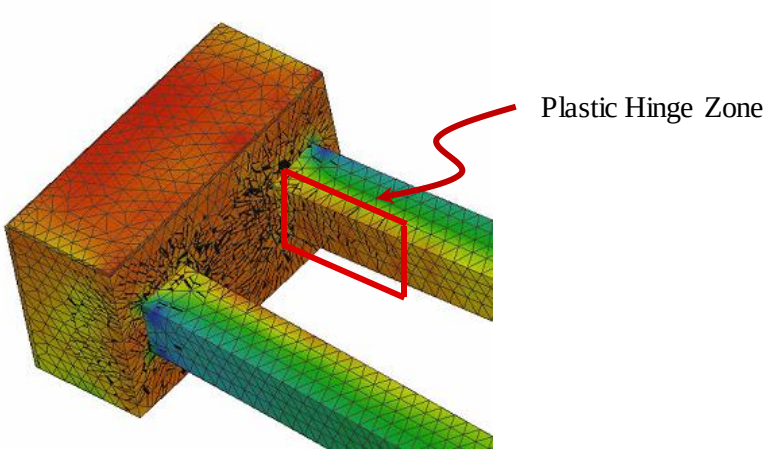

Figure 5.24: Plastic hinge zone observation assumptions

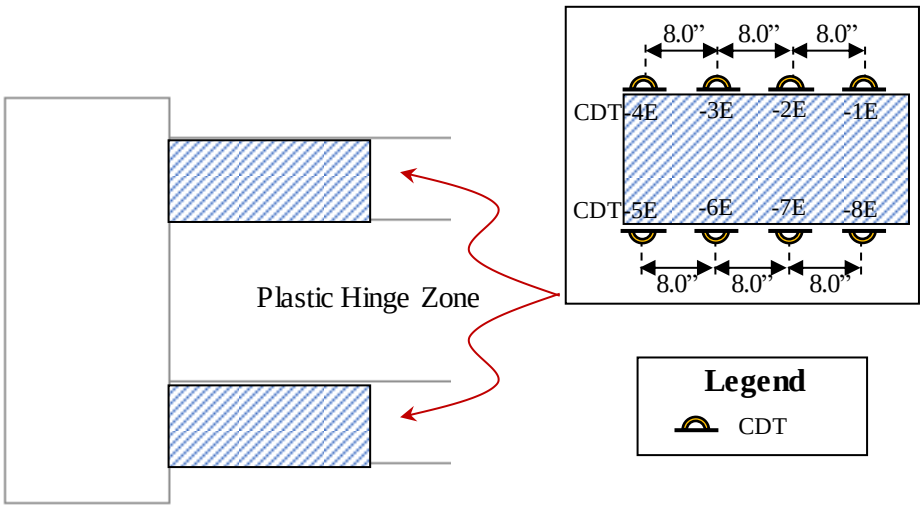

Figure 5.25: CDT in the plastic hinge zone

5.5.2. Surface Gauges

Preliminary numerical analyses were performed using a shallow and deep pile embedments, as shown in Figure 5.26. Cracking patterns were obtained for the models to determine the mode of failure controlling the specimens. Shallow embedments resulted in

failure of the cap, as shown in Figure 5.26 (a). Deeper embedments resulted in failure of the piles, as shown in Figure 5.26 (b).

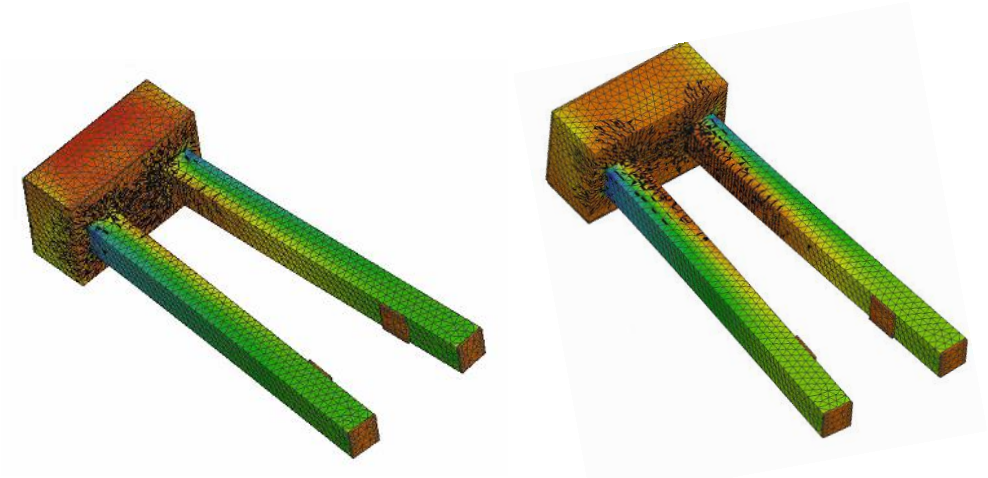

(a) (b)

Figure 5.26: ATENA modeling for specimens (a) shallow embedment (b) deep embedment

These cracking patterns were used to determine the location of the concrete surface gauges. For a shallow and deep embedment, the pile cap is showing failure in the front face between the piles and in the edges. Cracking is also happening in the lateral faces of the cap. A total of 25 concrete surface gauges (CSGs) were used, 19 located on the front view of the pile cap, and three on each lateral face, as shown in Figure 5.27. CSGs perpendicular to the load application measured the splitting stresses that develop in the pile cap. CSGs parallel to load application measured the compressive stress developing from the pile bearing on the pile cap (on the outside) and the tensile stresses developing from flexure on the pile cap (between the piles).

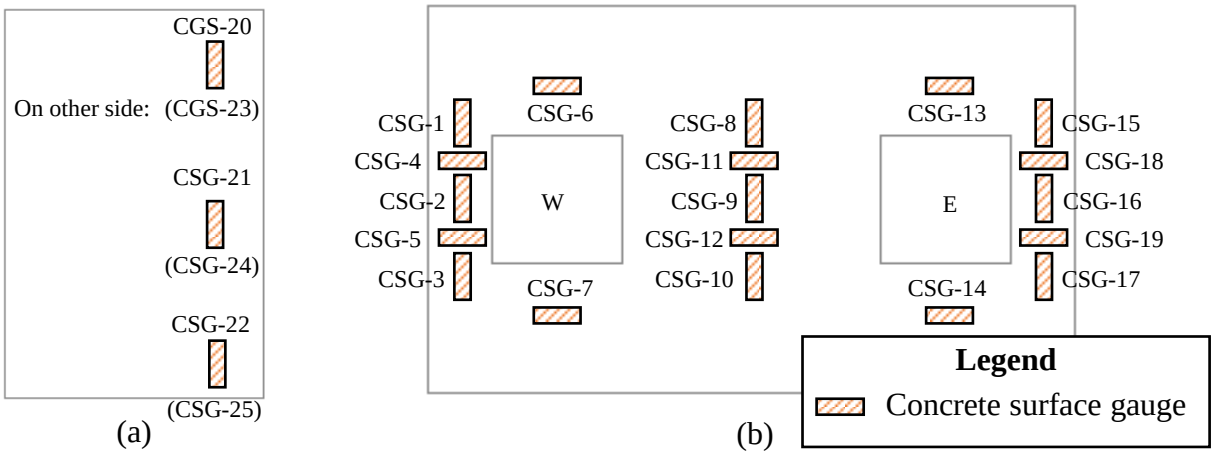

Figure 5.27: Concrete Surface Gauges (a) Side view (b) front view

5.5.3. Rebar Gauges

The stress in the rebars in the numerical analyzes are shown in Figure 5.28. The longitudinal reinforcement resisting the flexural stresses in the pile caps was heavily engaged, as shown in Figure 5.28 (c). The transverse reinforcement on the face of the pile cap where the piles extend from are also engaged, as shown in Figure 5.28 (a) and (b).

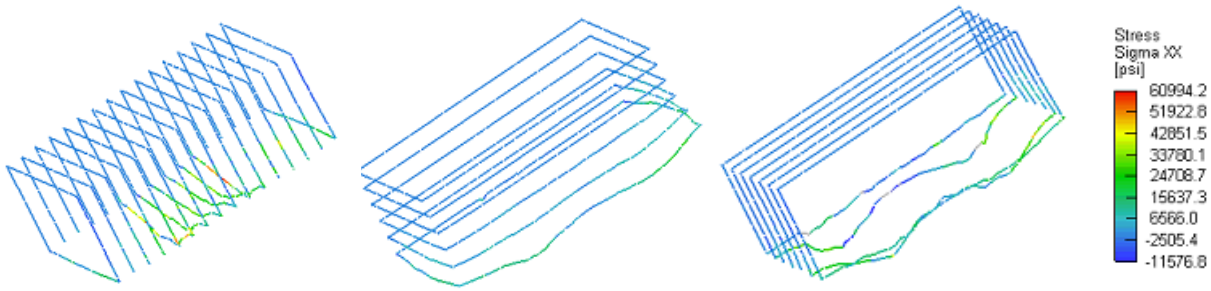

Figure 5.28: Stress in Rebars (a) N6 bars (b) N5 bars (c) N9 bars

Rebar strain gauges (RSGs) were used to measure the strain in the reinforcement with the highest observed stresses from the numerical analyses. The RSG layout is shown in Figure 5.29 with a total of 36 RSGs per specimen.

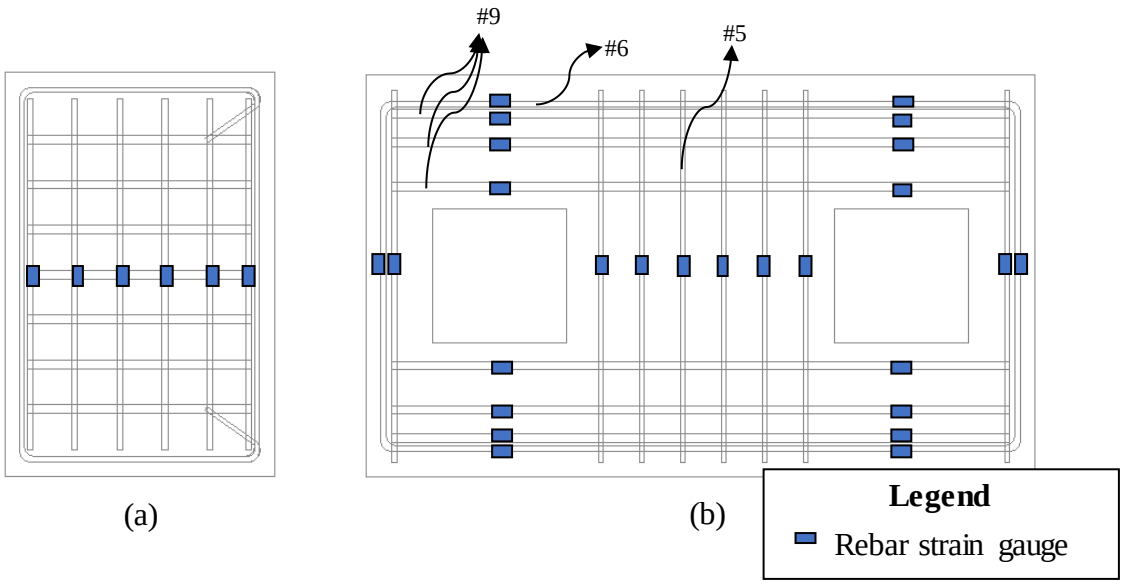

Figure 5.29: Rebar strain gauges (a) side view (b) front view

5.5.4. Vibrating Wire Strain Gauges (VWSG)

Vibrating wire strain gauges (VWSGs) were used to measure the confining stresses in the pile caps around the embedded piles, as shown in Figure 5.30. Two VWSGs were also placed in the precast piles to measure the prestress losses and shrinkage strains that occur in the piles before being cast in the pile caps.

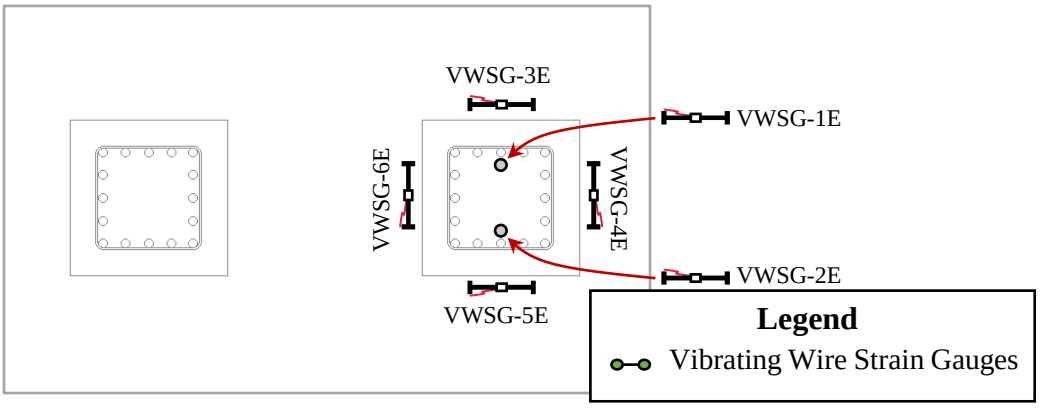

Figure 5.30: Vibrating Wire Strain Gauges

5.5.5. Fiber Optic Sensors

Fiber optic sensors were used to measure the behavior of the embedded portion of the pile and the rotation in the plastic hinge zone to determine the exact point at which fixity occurs in the embedded portion of the pile. The fiber optic sensors were attached to a #3 GFRP bar for internal embedment, as shown in Figure 5.31. The fiber optic gauges extended 72 inches from the end of the pile for all specimens (18-inch and 30-inch piles of all embedment lengths).

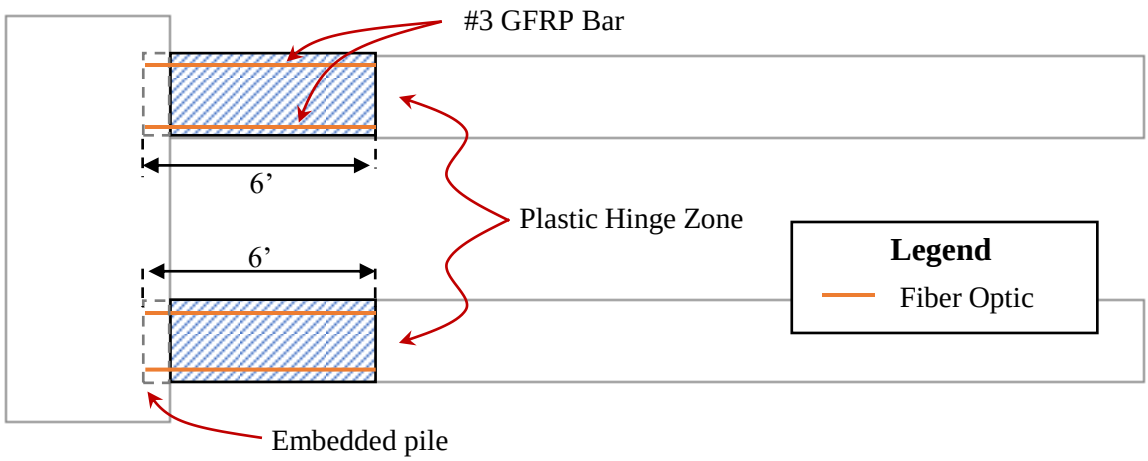

Figure 5.31: Proposed location for the fiber optic sensors

5.6. SPECIMEN CONSTRUCTION

The 18-inch specimens (18-inch piles and caps with embedded piles) and 30-inch piles were constructed by CDS Manufacturing in Tallahassee, FL. A total of 20 piles and eight pile caps were cast at CDS Manufacturing. The 30-inch pile caps for Specimen 9 and Specimen 10 were constructed by Florida Department of Transportation at the SRC with concrete delivered from Smyrna Ready Mix (SRM). A summary of casting and testing

dates is provided in Table 5.6. Construction drawings for all piles and pile cap specimens are provided in Appendix.

Table 5.6: Summary of casting and testing dates

Specimen	Pile Cast Date (West)	Pile Cast Date (East)	Cap Cast Date	Test Date	West Pile Age (days)	East Pile Age (days)	Cap Age (days)
SP-01	4/21/2021	4/21/2021	8/25/2021	4/18/22	362	362	236
SP-02	4/13/2021	4/13/2021	8/19/2021	8/4/22	478	478	350
SP-03	4/13/2021	4/13/2021	8/26/2021	4/22/22	374	374	239
SP-04	4/21/2021	4/13/2021	8/27/2021	5/9/22	383	391	255
SP-05	4/21/2021	4/21/2021	8/30/2021	8/1/22	467	467	336
SP-06	4/13/2021	4/21/2021	9/1/2021	5/12/22	394	386	253
SP-07	4/13/2021	4/21/2021	10/12/2021	5/31/22	413	405	231
SP-08	4/13/2021	4/21/2021	10/14/2021	6/3/22	416	408	232
SP-09	1/7/2021	1/7/2021	12/20/2022	1/19/23	742	742	30
SP-10	1/7/2021	1/7/2021	3/13/2023	4/3/23	816	816	21

5.6.1. 18-inch Specimens

A total of sixteen (16) 18-inch piles and eight pile caps were constructed at CDS Manufacturing between April 2021 and October 2021. The construction process is shown in Figure 5.32.

(a) (b)

Figure 5.32: 18-inch specimen construction (a) pile casting (b) pile cap casting

The piles were cast with a Class VI FDOT mixture [1] with a specified concrete compressive strength of 8.5 ksi. CDS Manufacturing uses a Class VI FDOT mixture for all members cast at their facility. The 18-inch piles had a strand configuration of (12) ½-in. special strands stressed at 34 kips. The first casting phase for the piles started 4/13/2021 with detensioning on 4/14/2021. The second phase started 4/20/2021 with detensioning on 4/21/2021. A summary of the piles casting dates and instrumentation are shown in Table 5.7. No vibrating wire strain gages were installed in pile P9 through P16. A different labeling system was used by CDS Manufacturing and FDOT, as shown in Table 5.7.

Table 5.7: Summary of 18-inch piles

Pile FDOT label	Pile CDS label	Casting Date	Fiber Optic Sensors	Vibrating Strain Gages
P1	FIU-18-001	4/13/2021	FOS 01 FOS 09	VWSG-P1-1E VWSG-P1-2E VWSG-P1-3E
P2	FIU-18-002	4/13/2021	FOS 02 FOS 10	VWSG-P2-1E VWSG-P2-2E VWSG-P2-3E
P3	FIU-18-003	4/13/2021	FOS 03 FOS 11	VWSG-P3-1E VWSG-P3-2E VWSG-P3-3E

Pile FDOT label	Pile CDS label	Casting Date	Fiber Optic Sensors	Vibrating Strain Gages
P4	FIU-18-004	4/13/2021	FOS 04 FOS 12	VWSG-P4-1E VWSG-P4-2E VWSG-P4-3E
P5	FIU-18-010	4/21/2021	FOS 17 FOS 25	VWSG-P5-1E VWSG-P5-2E VWSG-P5-3E
P6	FIU-18-012	4/21/2021	FOS 18 FOS 26	VWSG-P6-1E VWSG-P6-2E VWSG-P6-3E
P7	FIU-18-014	4/21/2021	FOS 19 FOS 27	VWSG-P7-1E VWSG-P7-2E VWSG-P7-3E
P8	FIU-18-016	4/21/2021	FOS 20 FOS 28	VWSG-P8-1E VWSG-P8-2E VWSG-P8-3E
P9	FIU-18-008	4/13/2021	FOS 05 FOS 13	-
P10	FIU-18-007	4/13/2021	FOS 06 FOS 14	-
P11	FIU-18-006	4/13/2021	FOS 07 FOS 15	-
P12	FIU-18-005	4/13/2021	FOS 08 FOS 16	-
P13	FIU-18-009	4/21/2021	FOS 21 FOS 29	-
P14	FIU-18-011	4/21/2021	FOS 22 FOS 30	-
P15	FIU-18-013	4/21/2021	FOS 23 FOS 31	-
P16	FIU-18-015	4/21/2021	FOS 24 FOS 32	-

The 18-inch pile caps were constructed between 8/2/2021 and 10/14/2021. A summary of casting dates and description of each specimen is shown in Table 5.8.

Table 5.8: Summary of 18-inch specimens

Specimen	Casting Date	Target Embedment	East Pile	West Pile
SP-01	8/25/2021	$0.33d_{pile}$ (6”)	FIU-18-016	FIU-18-008
SP-02	8/19/2021	$0.33d_{pile}$ (6”)	FIU-18-002	FIU-18-001

Specimen	Casting Date	Target Embedment	East Pile	West Pile
SP-03	8/26/2021	$0.33d_{pile}$ (6”)	FIU-18-010	FIU-18-009
SP-04	8/27/2021	$0.5d_{pile}$ (9”)	FIU-18-013	FIU-18-011
SP-05	8/30/2021	$0.5d_{pile}$ (9”)	FIU-18-014	FIU-18-015
SP-06	9/1/2021	$0.67d_{pile}$ (12”)	FIU-18-012	FIU-18-006
SP-07	10/12/2021	$1.0d_{pile}$ (18”)	FIU-18-004	FIU-18-005
SP-08	10/14/2021	$1.5d_{pile}$ (27”)	FIU-18-003	FIU-18-007

5.6.2. 30-inch Specimens

A total of four 30-inch piles were cast at CDS Manufacturing and two pile caps at FDOT SRC. The construction process for the 30-inch specimens is shown in Figure 5.33.

(a) (b)

Figure 5.33: Construction of the 30-inch specimens (a) pile casting at CDS, (b) pile cap casting at FDOT SRC

The piles were cast with a Class VI FDOT mixture [1] with a specified concrete compressive strength of 8.5 ksi. The 30-inch piles had a strand configuration of (24) ½-in. special strands stressed to 34 kips. The casting date for the 30-inch piles was 1/7/2021 with detensioning of strands on 1/8/2021. A summary of the casting date and instrumentation is shown in Table 5.9.

Table 5.9: Summary of 30-inch piles

Pile FDOT label	Pile CDS label	Casting Date	Fiber Optic Sensors	Vibrating Strain Gages
P1	FIU-30-1	1/7/2021	FOS-P1-1E FOS-P1-1W	VWSG-P1-1E VWSG-P1-2E VWSG-P1-3E
P1	FIU-30-2	1/7/2021	FOS-P1-2E FOS-P1-2W	-
P2	FIU-30-3	1/7/2021	FOS-P2-1E FOS-P2-1W	VWSG-P2-1E VWSG-P2-2E VWSG-P2-3E
P2	FIU-30-4	1/7/2021	FOS-P2-2E FOS-P2-2W	-

The 30-inch pile caps were constructed at FDOT Research lab. A summary of the casting dates and description of each specimen is shown in Table 5.10.

Table 5.10: Summary of 30-inch specimens

Specimen	Casting Date	Target Embedment	East Pile	West Pile
SP-09	12/20/2022	0.33 d_{pile} (12”)	FIU-30-1	FIU-30-2
SP-10	3/13/2022	1.0 d_{pile} (30”)	FIU-30-3	FIU-30-4

Due to the large pile cap dimensions (7.5-ft. by 4.0-ft. by 12.5-ft.), the 30-inch pile caps were cast with a mass concrete mix. The mass concrete mix was developed in discussion with FDOT State Materials Office (SMO). A mass concrete mix is used when the element being constructed will likely exceed the maximum allowable temperature or temperature differential (between the center of mass and the surface of the element) during curing [1]. Too large of a temperature differential can lead to cracking of the concrete due to differential volume change (relative thermal expansion). According the FDOT Structures Design Guidelines [1] §1.4.4, the concrete element should be considered mass concrete if:

- The “least dimension” is more than 3 ft. and

- The volume-to-surface area (V/S) is greater than 1 ft.

The least dimension (LD) and volume-to-surface area (V/S) for the pile caps for the 30-inch piles are shown below.

Least dimension: $$LD = 4.0 \text{ ft} > 3.0 \text{ ft}$$

V/S $$\frac{V}{S} = \frac{375 \text{ ft}^3}{347.5 \text{ ft}^2} = 1.079 \text{ ft} > 1.0 \text{ft}$$

The concrete mix recommended for the 30-inch pile caps by the mass concrete specialist at SRM in consultation with the FDOT SMO was a Class IV concrete mix design with 30% to 50% replacement of Portland Cement with Class F fly ash and total CM of 700 lb/yd^3 or less. Suplerplastizers were added to the concrete mix to make it self-consolidating (SCC). Upon arrival of the concrete the Standard Slump Flow Test (ASTM C1611) was performed, as shown in Figure 5.34. The target slump flow for the SCC mix was between 23-30 inches.

(a) (b)

Figure 5.34: Standard slump flow test for SP-10 (a) inverted mold, (b) slump of 25 inches

A summary of the results is shown in Table 5.11.

Table 5.11: Standard slump flow test results for 30-inch pile cap self-consolidating concrete mix

Specimen	Batch	d1 (in)	d2 (in)	Slump flow (in)
SP-09	1	25	25	25
	2	15	15	15
SP-10	1	19	19	19
	2	25	24	24.5

FDOT Standard Specification for Road and Bridge Construction [63], Section 346-4.2, specifies that the concrete core temperature for any mass concrete element does not exceed the maximum allowable temperature of 180 °F and that the differential temperatures between the element core and surface do not exceed the maximum allowable temperature differential of 35 °F.

Temperature recordings were taking at the top, north side, west side, and core of the pile cap. For SP-09 readings were taken every minute the first day, and then every 30 minutes in the second and third day. For SP-10 readings were taken every 30 minutes for 7 days. Temperature readings for Specimen 9 and Specimen 10 are shown in Figure 5.35.

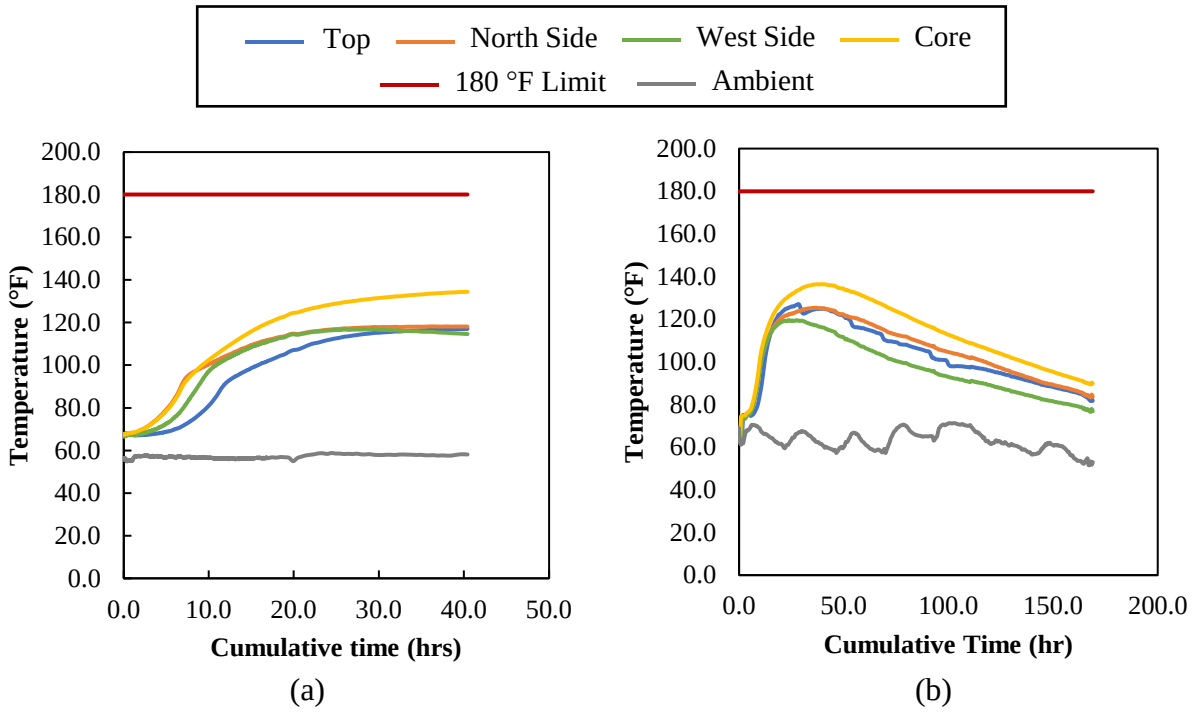

Figure 5.35: Temperature readings (a) SP-09, (b) SP-10

Temperature gradients were calculated by finding the temperature difference at the top, north and west sides of the pile cap with the core temperature. Temperature gradients for Specimen 9 and Specimen 10 are shown in Figure 5.36

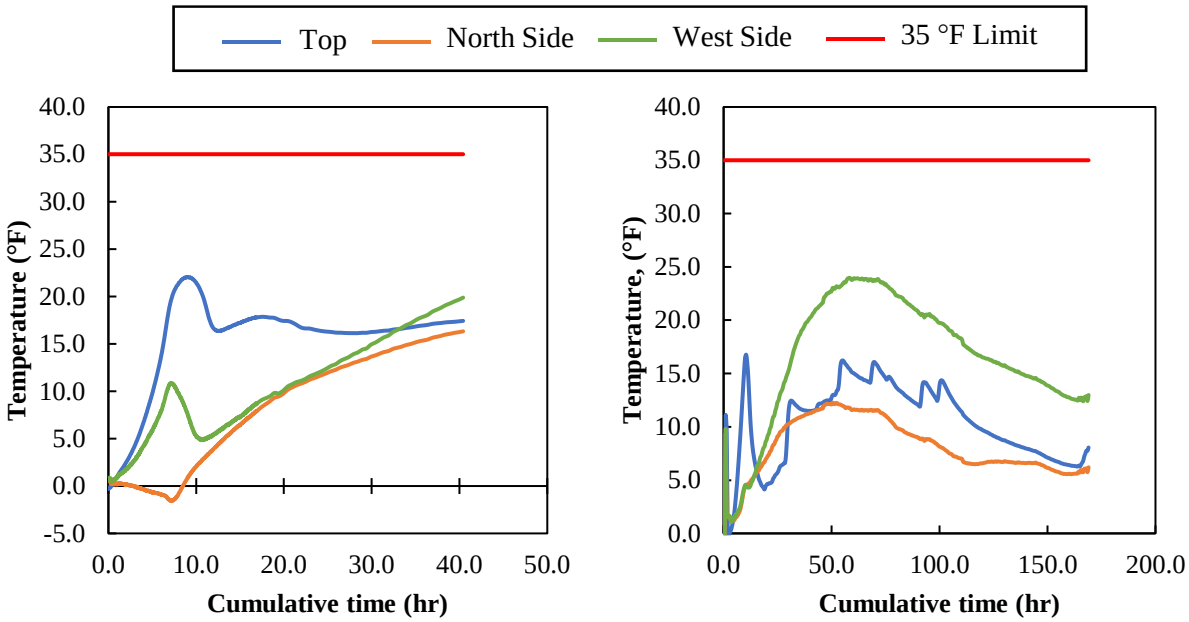

(a) (b)

Figure 5.36: Temperature gradient (a) SP-09, (b) SP- 10

After monitoring the temperature, the formwork was removed. No temperature or shrinkage cracks were observed on Specimen 9. Cracks developed on Specimen 10 at mid-height . Specimens 9 and 10 are shown in Figure 5.37.

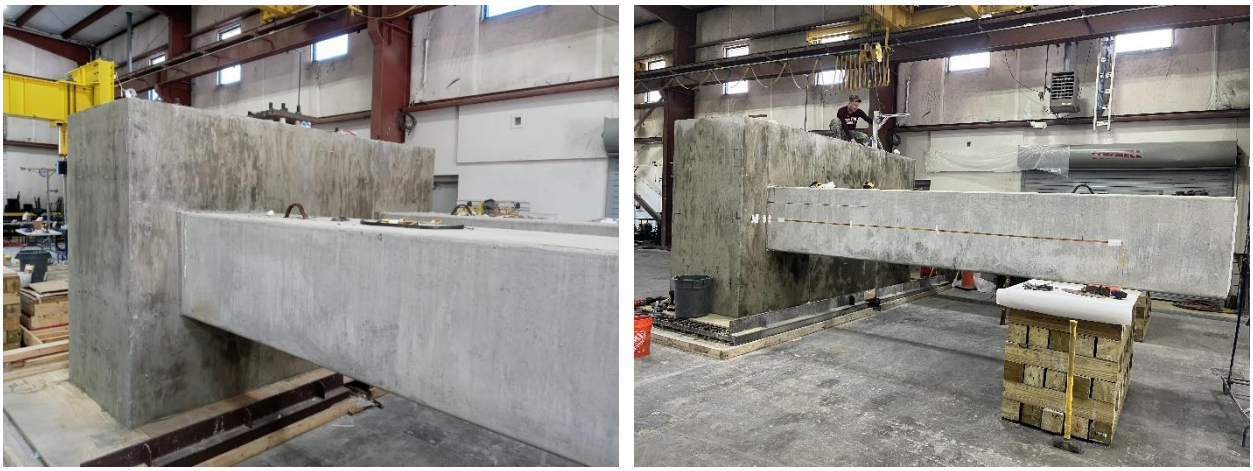

(a) (b)

Figure 5.37: Finished 30-inch specimens (a) SP-09, (b) SP- 10

5.7. TEST SETUP AND PROTOCOL

5.7.1. Without Axial Load Application

A self-reacting frame system was used for specimens without axial load application, as shown in Figure 5.38. This frame was determined to be the simplest setup to be used in SRC and have the least impact on the pile-to-cap connection behavior. Four threaded rods were extended through the pile caps and attached to the strong floor to provide additional stability to the specimen during testing. Specimen 10 was not fixed to the strong floor to simplify demolition. Wood supports were constructed and located at ends of the piles with Teflon installed between the pile and support to minimize friction between elements.

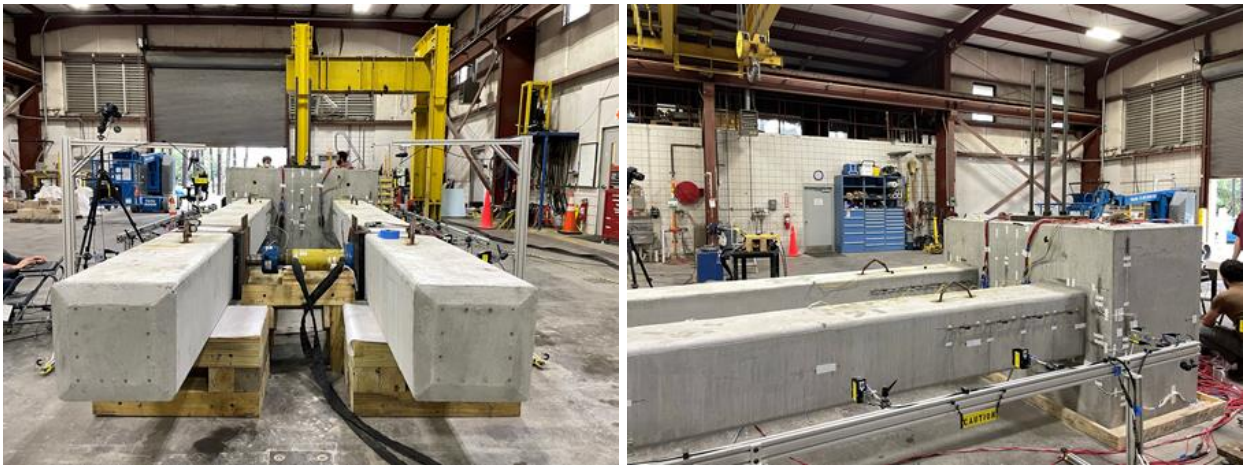

Figure 5.38: Test setup for specimens without axial load application

The piles were loaded from the inside using a hydraulic jack located between 6 ft. and 12 ft. from the pile-to-cap interface. The piles were loaded incrementally until failure. The loading protocol for strength testing consisted of different loading steps, which were pre-

determined based on numerical modeling results. The specimens were visually inspected for cracks and photographs were taken between each of the loading stages.

5.7.2. Axial Load Application

A self-reacting frame with spreader beams was used for specimens with axial load application, as shown in Figure 5.39. A total of four spreader beams were installed, two at the end of the piles and two restraining the back of the pile cap. Threaded rods extended from the spreader beam bearing against the back of the pile cap to steel hinges and clevises located at the face of the cap. Additional threaded rods extended from the clevis to the spreader beam on the end of the piles. These rods were used to transfer the tension applied to the piles by the hydraulic jack to the back of the pile cap. The hinge and clevis located at the face of the cap and base of the pile allowed for rotation of the pile during testing.

Figure 5.39: Test setup for specimens with axial load application

A total of 193.8 kips was applied to each pile, which corresponded to $0.052A_g f'_{c,pile}$ (using the measured concrete strength). The applied axial load was less than the $0.1A_g f'_{c,pile}$ initially planned due to a higher measured concrete strength (11.5 ksi) than the design value

(6.5 ksi). The axial load application apparatus (e.g., rods, hinge, spreader beams) were designed for the axial load of 194 kips.

The elongation of the threaded rod was estimated using Equation 5.4, to provide a validation to the pressure being read during the tensioning of the threaded rods.

Elongation: $$\Delta_{rod} = \frac{FL}{AE}$$ Equation 5.4

where:

F = applied force

L = length of the threaded rod

A = area of the threaded rod

E = modulus of elasticity

During tensioning, measures of the actual elongation were recorded in the four threaded rods (top and bottom of the east pile, and top and bottom of the west pile). A summary of the estimated and actual elongation for Specimen 2 and Specimen 5 are in Table 5.12.

Table 5.12: Estimated and actual elongation for SP-02 and SP-05

Specimen	**Estimated elongation (in)**	**Actual Elongation**			
		Top East (in)	**Bottom East (in)**	**Top West (in)**	**Bottom West (in)**
SP-02	0.411	0.879	0.699	0.709	0.787
SP-05	0.407	--	--	0.470	0.506

The process to apply the axial load included the following steps:

- Blocks and jacks were positioned on the pile, as shown in Figure 5.40 (a).

- Pressure was applied manually to each rod in steps. Stops were set at 400 psi, 2,000 psi, 4,000 psi and 7,600 psi, which corresponds to 5%, 25%, 50%, 100% required for settlement support. Elongations reading was taken at each step and nuts were tightening.
- Blocks and jacks were removed after reaching 7,600 psi.

This process was followed to tension the west and east pile.

(a) (b)

Figure 5.40: Axial load application (a) tensioning of west pile (b) tensioning east pile

A similar process was followed for de-tensioning of the piles after testing.

5.8. PILES CAPACITY

5.8.1. Capacity of 18-inch Piles

Two 18-inch piles were cut from Specimen 2 after failure of the interface and tested for flexure in the FDOT SRC. The test setup consisted of a simply supported beam with two point loads, as shown in Figure 5.41.

(a) (b)

Figure 5.41: Flexure test pile setup

Both piles were cast on 4/13/2021 and had an age of 525 days on the day of testing (9/20/2022). The measured concrete strength on the day of testing was 11.45 ksi for both piles. A summary of the measured failure load, displacement at failure load, and moment capacity calculated from the measured failure load is shown in Table 5.13.

Table 5.13: Summary of results flexure test

Pile	Failure Load (kips)	Displacement at Failure Load (in)	Moment Capacity (k-ft)
P1	105.4	2.16	329.5
P2	106.4	2.06	332.5

Displacements were recorded along the length of the piles through 10 laser displacement transducers (LDTs). Load versus displacement and moment versus displacement curves at midspan for both piles are shown in Figure 5.42. The maximum load reached by Pile 1 was 105.4 kips, which corresponds to a moment capacity of 329.5 kip-ft. Pile 2 reached a maximum load of 106.4 kips, with a moment capacity of 332.5 kip-ft.

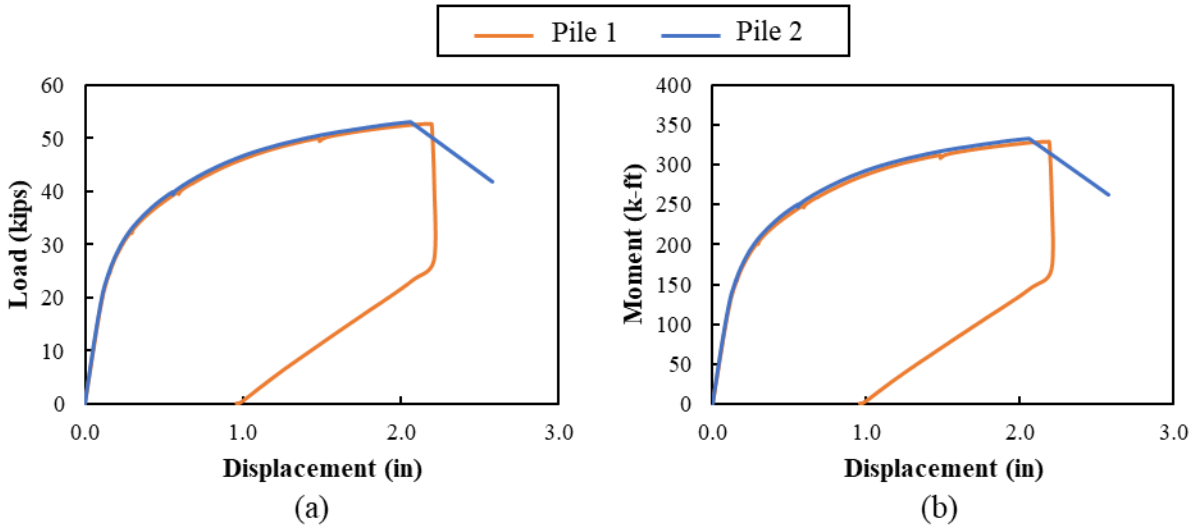

Figure 5.42: (a) Load versus displacement and (b) moment versus displacement curves for Pile 1 and Pile 2

Fiber optic sensors (FOS) were located at the west side of the pile to measure strains at two depths, which allows for curvature to be calculated. One FOS was located 4 in. from the top face of the pile and one FOS 6 in. from the bottom face of the pile. The average strain in the constant moment region was used; a strain of 10,000με was used when the sensor exceeded this strain at a location. The strain profile at midspan for both piles is shown in Figure 5.43, assuming a linear strain profile between the two measured strains. The measurements by the FOS in the bottom of Pile 2 were not consistent with the observed behavior and expected readings in the sensor at loads above 70 kips. There may have been an issue with failure of the epoxy for the sensor at higher loads for this sensor in Pile 2.

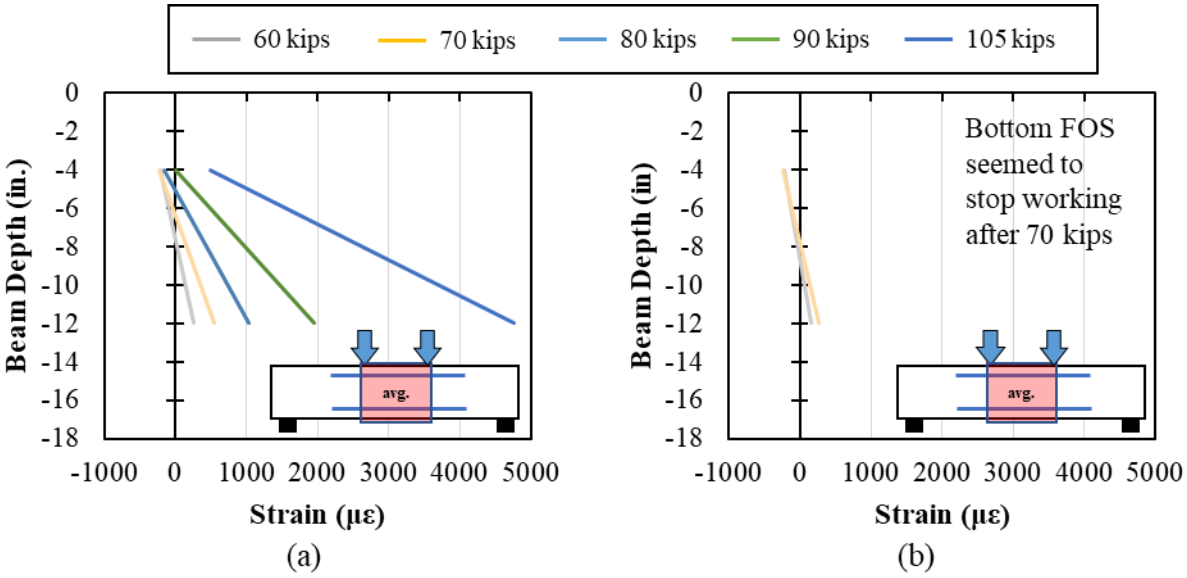

Figure 5.43: Average measured strain profile in constant moment region for (a) Pile 1 and (b) Pile 2

The curvature was determined from the measured strains in the FOS and the distance between the sensors. The moment-curvature response for both piles is shown in Figure 5.44. The moment capacity of the 18-inch determined using RESPONSE2000 was 325 k-ft. There was good agreement between the measured response for Pile 1 and the estimated response using RESPONSE2000.

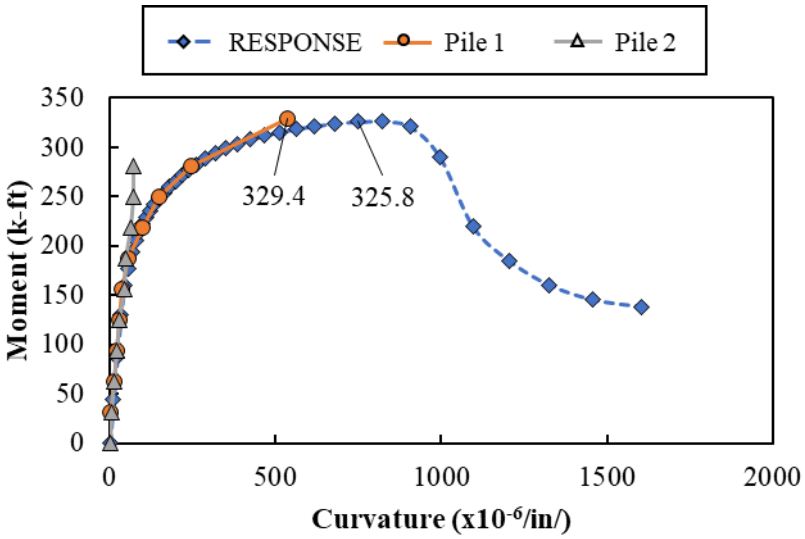

Figure 5.44: Measured and estimated moment versus curvature response for Pile 1 and Pile 2

5.8.2. Capacity of 30-inch Piles

The capacity of the 30-inch piles could not be tested experimentally because of limited time, the demolition required for the pile caps, and the length of the pile not being sufficient for a flexure test. There was good agreement between the measured results and estimated behavior from RESPONSE2000, so RESPONSE2000 was used to determine the baseline pile capacity for the 30-inch piles. The capacity of the 30-inch piles was found using the concrete strength on test day to be 1,188 k-ft with the moment versus curvature response shown in Figure 5.45.

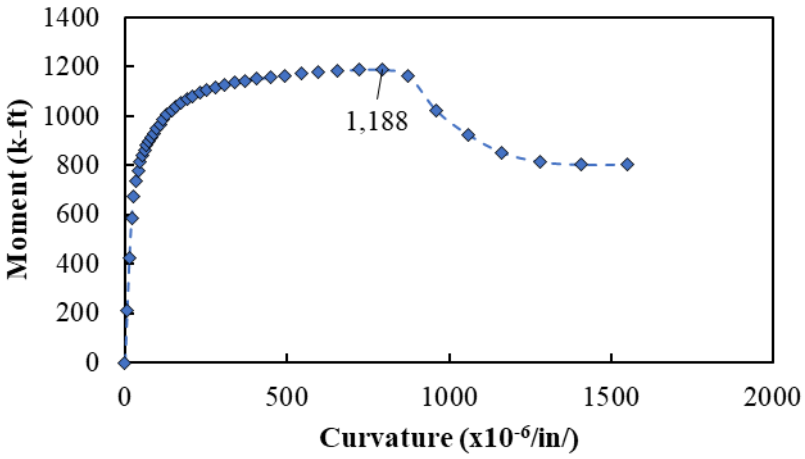

Figure 5.45: Estimated moment versus curvature for 30-inch piles using RESPONSE2000

5.9. SUMMARY OF RESULTS

Results of the experimental testing are summarized in this section. The results for each individual test, including graphs for all gages, are provided in Appendix.

5.9.1. Specimen Detail Summary

A total of 10 specimens were tested at the FDOT Structures Research Center (SRC). The primary experimental variable was the embedment length, which varied from 0.33 to 1.5 times the diameter of the pile (d_p). Two of the 18-inch specimens (SP-02 and SP-05) had an applied axial load, and one 18-inch specimen had interface reinforcement between the pile and the pile cap (SP-03). A summary of the experimental program is provided in Table 5.14.

Table 5.14: Experimental matrix for full-scale experimental test program

Specimen	Pile Size (in)	A_g (in^2)	Embedment (in)	Embedment (d_p)	Axial Load (approx.)	Interface Reinforcement
SP-01	18	324	6	$0.33d_p$	--	--
SP-02	18	324	6	$0.33d_p$	$0.1A_gf'_c$	--
SP-03	18	324	6	$0.33d_p$	--	(4) - #6 bars
SP-04	18	324	9	$0.50d_p$	--	--
SP-05	18	324	9	$0.50d_p$	$0.1A_gf'_c$	--
SP-06	18	324	12	$0.67d_p$	--	--
SP-07	18	324	18	$1.00d_p$	--	--
SP-08	18	324	27	$1.50d_p$	--	--
SP-09	30	900	12	$0.40d_p$	--	--
SP-10	30	900	30	$1.00d_p$	--	--

The applied axial load was less than the $0.1A_gf'_{c,pile}$ initially planned due to a higher concrete strength (11.5 ksi) than the design value (6.5 ksi). A total of 193.8 kips was applied to each pile, which corresponded to $0.052A_gf'_{c,pile}$. The axial load application apparatus (e.g., rods, hinge, spreader beams) were designed for the axial load of 194 kips. A summary of the applied axial load is provided in Table 5.15.

Table 5.15: Axial load applied to piles in each specimen

Specimen	Initial Axial Load	Applied Axial Load (kips)	Axial Load / $A_g*f'_{c,pile}$
SP-01	--	0.0	0.000
SP-02	$0.1A_gf'_c$	193.8	0.052
SP-03	--	0.0	0.000
SP-04	--	0.0	0.000
SP-05	$0.1A_gf'_c$	194.0	0.050
SP-06	--	0.0	0.000
SP-07	--	0.0	0.000
SP-08	--	0.0	0.000
SP-09	--	0.0	0.000
SP-10	--	0.0	0.000

5.9.2. Material Properties

Cylinders (4-in. diameter with 8-in length) were cast with the same batch of concrete during casting of the piles and pile caps. These were used to determine the compressive strength at the time of testing. The measured compressive strength for the for piles and pile caps the day of testing are provided in Table 5.16.

Table 5.16: Measured compressive strength on test day for concrete in piles and pile caps

Specimen	$f'_{c,pile,west}$ (ksi)	$f'_{c,pile,east}$ (ksi)	$f'_{c,cap}$ (ksi)
SP-01	11.90	11.90	12.48
SP-02	11.45	11.45	12.36
SP-03	11.58	11.58	12.70
SP-04	11.90	11.58	11.93
SP-05	12.02	12.02	13.26
SP-06	11.58	11.90	11.40

SP-07	11.58	11.90	10.32
SP-08	11.58	11.90	12.57
SP-09	13.13	13.13	9.37
SP-10	13.82	13.82	8.95

5.9.3. Transfer Length

5.9.3.1. Method for Determining Transfer Length

Transfer lengths were determined based on the 95% Average Maximum Strain (AMS) method developed by Russell and Burns [64] and used by Al-Kaimakchi and Rambo-Roddenberry [65]. In this method, the transfer length is determined to be the point where the strain curve intersects 95% of the average maximum strain, as shown in Figure 5.46.

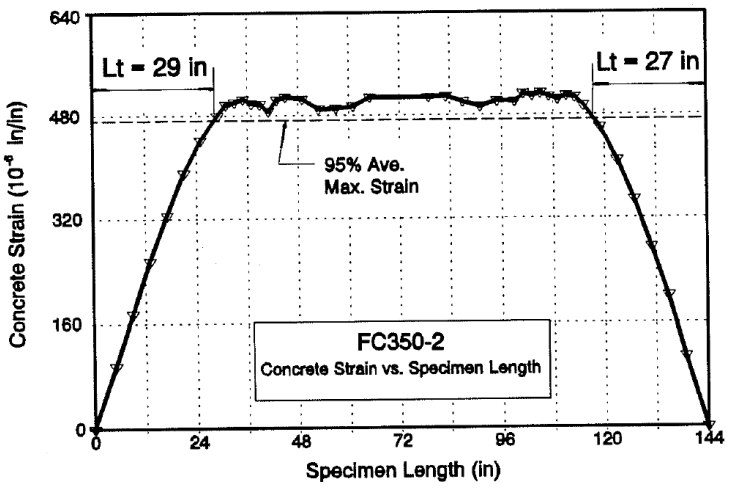

Figure 5.46: 95% Average Maximum Strain (AMS) method for determining transfer length from Russell and Burns [64]

The strains were measured using fiber optic sensors (FOS) for 10 to 15 minutes after detensioning of the last prestressing strands, which was about 25 minutes after the start of detensioning. The final readings at approximately 25 minutes were used. Strain

measurements were taken every 0.25 inches starting at 1.0 inch from the end of the pile. Each pile had two FOS. Only one FOS was monitored during the detensioning process for the 18-inch piles. Both FOS sensors were monitored in each pile for the 30-inch piles.

The data was post-processed by first removing any extraneous readings, highlighted in a sample of the data processing for Pile 1 in Figure 5.47 (a). The data was then zeroed based on the first reasonable reading, highlighted in Figure 5.47 (b). The data was then smoothed using the same procedure as Russell and Burns and used by Al-Kaimakchi and Rambo-Roddenberry, as shown in Equation 5.5.

$$\varepsilon_i = \frac{\varepsilon_{i-1} + \varepsilon_i + \varepsilon_{i+1}}{3} \qquad \text{Equation 5.5}$$

The smoothed data in the sample for Pile 1 is shown in Figure 5.47 (c). The average maximum strain (AMS) was determined based on a range of stresses from when there was a noticeable change in slope in the strain diagram and the end of the FOS, shown in Figure 5.47 (c). The transfer length was then determined by finding the point when the measured strain reached 95% of the AMS, shown in Figure 5.47 (d).

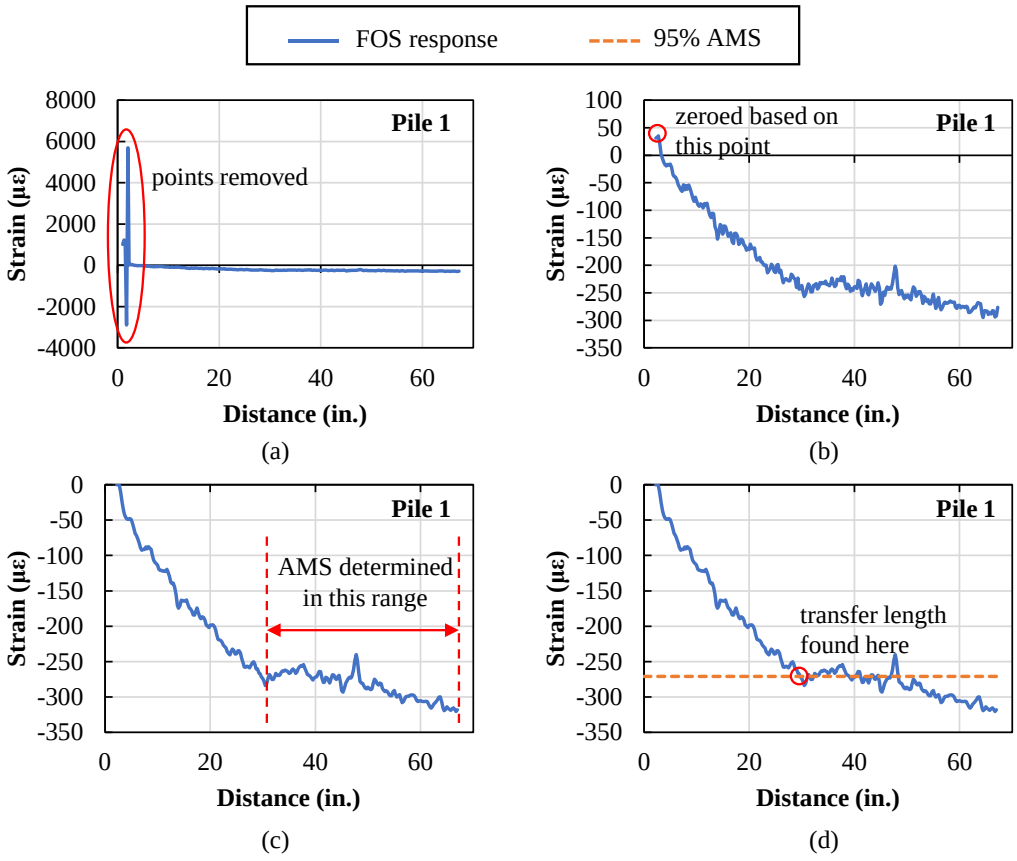

Figure 5.47: Sample of data processing steps taken, (a) removing extraneous points, (b) zeroing based on first relevant point, (c) smoothing data and determining AMS, and (d) determining transfer length

5.9.3.2. Measured Transfer Lengths

A summary of the measured transfer lengths for 18-inch piles and 30-inch piles are shown in Table 5.17. The strand pattern in each pile was assumed to be symmetrical about both axes, so it was assumed that only axial strains would occur at release. For this reason, data was only recorded for one fiber optic sensor per pile for the 18-inch specimens. Both FOS in the 30-inch piles were monitored during release.

Table 5.17: Measured transfer lengths for 18-inch and 30-inch piles

`	Pile	Fiber Optic Sensors	Measured Transfer Length
SP-01	FIU-18-016	*FOS 20* FOS 28	22.0”
	FIU-18-008	*FOS 05* FOS 13	30.0”
SP-02	FIU-18-002	*FOS 02* FOS 10	23.0”
	FIU-18-001	*FOS 01* FOS 09	27.0”
SP-03	FIU-18-010	*FOS 17* FOS 25	27.0”
	FIU-18-009	*FOS 21* FOS 29	32.0”
SP-04	FIU-18-013	*FOS 23* FOS 31	22.0”
	FIU-18-011	*FOS 22* FOS 30	24.0”
SP-05	FIU-18-014	*FOS 19* FOS 27	22.0”
	FIU-18-015	*FOS 24* FOS 32	23.0”
SP-06	FIU-18-012	*FOS 18* FOS 26	28.0”
	FIU-18-006	*FOS 07* FOS 15	n/a
SP-07	FIU-18-004	*FOS 04* FOS 12	25.0”
	FIU-18-005	*FOS 08* FOS 16	30.0”
SP-08	FIU-18-003	*FOS 03* FOS 11	28.0”
	FIU-18-007	*FOS 06* FOS 14	25.0”
SP-09	FIU-30-001	FOS-P1-1E FOS-P1-1W	16.0” 13.0”
	FIU-30-002	FOS-P1-2E FOS-P1-2W	n/a 14.0”
SP-10	FIU-30-003	FOS-P2-1E FOS-P2-1W	17.0” 13.0”
	FIU-30-004	FOS-P2-2E FOS-P2-2W	15.0” 14.0”

The average measured transfer length for was 26 inches for the 18-inch piles and 14.6 inches for the 30-inch piles. The estimated transfer length for both piles is 31.2 inches based on AASHTO LRFD BDS [23].

5.9.4. Prestress Losses

5.9.4.1. Prestress Loss Estimates

Prestress losses estimates were found using AASHTO LRFD Bridge Design Specification (§5.9.3) [23].

In pretensioned members:
AASHTO 5.9.3.1-1

$$\Delta f_{pT} = \Delta f_{pES} + \Delta f_{pLT} \qquad \text{Equation 5.6}$$

where:

Δf_{pT} = total loss (ksi)

Δf_{pES} = sum of all losses or gain due to elastic shortening or extension at the time of application of prestress and or external loads (ksi)

Δf_{pLT} = losses due to long-term shrinkage and creep of concrete, and relaxation of the steel (ksi)

Loss due to elastic shortening in pretensioned members was estimated using Equation 5.7.

AASHTO LRFD
(C5.9.3.2.3a-1)

$$\Delta f_{pES} = \frac{A_{ps} f_{pbt}\left(I_g + {e_m}^2 A_g\right) - e_m M_g A_g}{A_{ps}\left(I_g + {e_m}^2 A_g\right) + \frac{A_g I_g E_{ci}}{E_p}} \qquad \text{Equation 5.7}$$

The long-term prestress loss, Δf_{pLT}, due to creep of concrete, shrinkage of concrete, and relaxation of steel should be found using the approximate estimate equation, shown in Equation 5.8.

AASHTO 5.9.3.3-1

$$\Delta f_{pLT} = 10.0 \frac{f_{pi} A_{ps}}{A_g} \gamma_h \gamma_{st} + 12.0 \gamma_h \gamma_{st} + \Delta f_{pR}$$

Equation 5.8

In which:

AASHTO 5.9.3.3-2

$$\gamma_h = 1.7 - 0.01H$$

Equation 5.9

AASHTO 5.9.3.3-3

$$\gamma_{st} = \frac{5}{(1 + f'_{ci})}$$

Equation 5.10

where:

f_{pi} = prestressing steel immediately prior to transfer (ksi)

H = average annual ambient relative humidity (percent)

y_h = correction factor for relative humidity of the ambient air

y_{st} = correction factor for specified concrete strength at time of prestress transfer to the concrete member

f_{pR} = an estimate of relaxation loss taken as 2.4 ksi for low relaxation strand and in accordance with the manufacturers recommendations for other types of strands (ksi)

Estimated losses for the piles are shown in Table 5.18.

Table 5.18: Estimated prestress losses and effective stress in strands for 18-inch and 30-inch piles

Pile Size	Elastic Shortening Loss (ksi)	Long-Term Prestress Loss (ksi)	Total Prestress Losses (ksi)	Effective Stress after all Losses (ksi)
18-inch	7.4	18.8	26.2	177.4
30-inch	5.4	16.4	21.8	181.8

5.9.4.2. Measured Losses and Effective Stress in Strands

Elastic shortening and long-term losses were found using two vibrating wire strain gages (VWSG) located in the piles in the longitudinal direction. The standard temperature correction was applied to the data to account for different coefficients of thermal expansion between concrete and the steel wire located in the VWSG, shown in Equation 5.11.

$$\varepsilon_{\Delta} = (R_1 - R_0)B + (T_1 - T_0)(C_1 - C_2) \qquad \text{Equation 5.11}$$

where:

ε_{Δ} = measured change in strain

R_0 = initial reading

R_1 = current reading

B = batch gage factor (input in VWSG reader or DAQ)

T_0 = initial temperature

T_1 = current temperature

C_1 = coefficient of expansion of steel: 12.2 με/°C

C_2 = coefficient of expansion of concrete: assumed to be 10 με/°C

A summary of the measured losses is shown in Table 5.19. No readings were taken for SP-04, SP-05, and SP-10. SP-04 did not have any VWSG installed in the piles, due to one of the instrumented piles being installed in the wrong cap. The VWSGs installed in SP-05 and SP-10 did not appear to be working correctly and returned unreliable data. Strain measurements for the elastic shortening losses were taken before and after pile detensioning. The elastic shortening loss was recorded as the average readings of the two vibrating wire gages. The average prestress losses due to elastic shortening was 7.2 ksi for

the 18-inch piles and 5.9 for the 30-inch piles, which were within 2.2% and 8.6% of the estimated elastic shortening losses, respectively.

Long-term losses were measured by taking the difference in strain readings taken after release and immediately before testing. The average long-term loss measured for the 18-inch piles was 16.2 ksi (within 13.9% of estimated loss) and 9.8 ksi for the 30-inch piles (40.1% less than estimate).

Table 5.19: Measured elastic shortening and long-term losses using VWSG

	Strain Readings			Elastic Shortening			Long Term		
SP	**Before Release (με)**	**After Release (με)**	**Before Testing (με)**	**Strain Change (με)**	**ES Losses (ksi)**	**Δf_{pES} (ksi)**	**Strain Change (με)**	**LT Losses (ksi)**	**Δf_{pLT} (ksi)**
SP-1	0	-352.1	-900.1	352.1	10.04	9.66	547.9	15.62	15.34
	0	-325.5	-854.3	325.5	9.28		528.8	15.07	
SP-2	0	-352.5	-1153.4	352.5	10.05	10.00	800.9	22.83	22.83
	0	-349.4	--	349.4	9.96		--	--	
SP-3	0	-316.7	-835.4	316.7	9.03	9.02	518.8	14.78	15.57
	0	-316.1	-889.8	316.1	9.01		573.8	16.35	
SP-6	0	-323.1	-822.1	323.1	9.21	9.28	499.0	14.22	14.36
	0	-328.0	-836.9	328.0	9.35		508.9	14.50	
SP-7	0	-358.6	-793.7	358.6	10.22	9.81	435.1	12.40	12.84
	0	-330.0	-795.7	330.0	9.40		465.8	13.27	
SP-8	0	-366.6	-944.8	366.6	10.45	10.08	578.2	16.48	16.17
	0	-340.5	-897.2	340.5	9.70		556.8	15.87	
SP-9	--	--	--	--	--	5.88	--	--	9.85
	0	-206.3	-552.0	206.3	5.88		345.7	9.85	
SP-10	0	-210.1	--	210.1	5.99	5.99	--	--	--
	--	--	--	--	--		--	--	

The measured total losses and effective stress in strands are summarized in Table 5.20.

Table 5.20: Summary of measured total losses and effective stress in strands

Specimen	f_{pT} (ksi)	f_{pe} (ksi)
SP-01	25.0	178.6
SP-02	32.8	170.8
SP-03	24.6	179.0
SP-06	23.6	180.0
SP-07	22.6	180.9
SP-08	26.3	177.3
SP-09	15.7	187.9

5.9.5. Ultimate Strength Testing Results

Ultimate strength testing was performed at the FDOT SRC. The application of the lateral load was initially located at 12 ft. from the pile-to-cap interface. The lever arm, shown in Figure 5.48, was reduced for future tests due to not having sufficient stroke in the hydraulic jack for the 12-ft. lever arm.

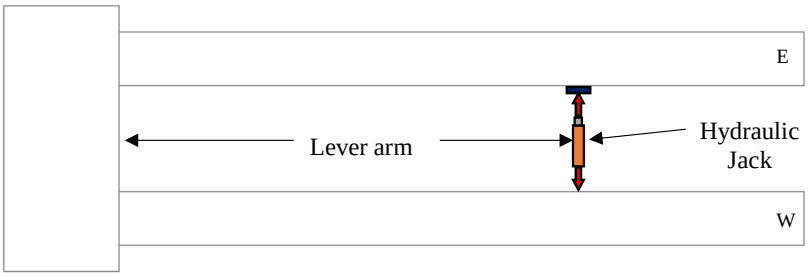

Figure 5.48: Location of applied lateral load.

The test date and lever arm used for testing for each specimen are shown in Table 5.21. The 18-inch pile specimens without axial load were tested first, followed by the 18-inch pile specimens with axial load, and finally the 30-inch pile specimens.

Table 5.21: Test date and lever arm

Specimen	Testing day	Lever arm (ft)	Reason for Stopping Test
SP-01	4/18/2022	12	Ran out of stroke on jack, load was maintaining
SP-02	8/4/2022	6	Ran out of stroke on jack, load was maintaining
SP-03	4/22/2022	9	Load dropping at end of test, ran out of stroke on jack
SP-04	5/9/2022	9	Ran out of stroke on jack, load was maintaining
SP-05	8/1/2022	6	Ran out of stroke on jack, load was maintaining
SP-06	5/12/2022	9	Ran out of stroke on jack, load was maintaining
SP-07	5/31/2022	6	Ran out of stroke on jack, load was maintaining
SP-08	6/3/2022	6	Ran out of stroke on jack, load was maintaining
SP-09	12/20/2022	9	Dropping in capacity, damage to pile
SP-10	4/3/2023	9	Damage to cap

A summary of the ultimate strength testing results is presented in Table 5.22. These results are analyzed in more detail in the following sections.

Table 5.22: Summary of ultimate strength testing

Specimen	Pile Size	Cracking Load (kips)	Failure Load (kips)	Failure Mechanism	Failed Pile	Moment developed (k-ft)	Percentage of capacity of pile
SP-01	18”	6	9.5	Strand Development	West	114.1	34.5%
SP-02	18”	10	40.8	Strand Development	West	244.6	73.9%
SP-03	18”	8	21.2	Strand Development	West	190.8	57.6%
SP-04	18”	9.5	13.6	Strand Development	West	122.8	37.1%
SP-05	18”	20	41.0	Strand Development	West	246.2	74.4%
SP-06	18”	10	17.7	Strand Development	East	159.4	48.2%
SP-07	18”	20	33.6	Strand Development	West	201.4	60.8%
SP-08	18”	30	44.6	Strand Development	West	267.6	80.8%

Specimen	Pile Size	Cracking Load (kips)	Failure Load (kips)	Failure Mechanism	Failed Pile	Moment developed (k-ft)	Percentage of capacity of pile
SP-09	30”	32	63.8	Strand Development	West	574.6	48.3%
SP-10	30”	90	96.4	Punching Shear	West	868.1	73.0%

5.10. ANALYSIS OF RESULTS

5.10.1. Observed Failure Mechanism

All specimens experienced a ductile failure mechanism, where there was significant deflection after the maximum load was reached, as shown in Figure 5.49. All 18-inch pile specimens held close to the ultimate capacity while additional deflection was observed. The 30-inch pile specimens experienced a drop in capacity immediately after the ultimate load was reached.

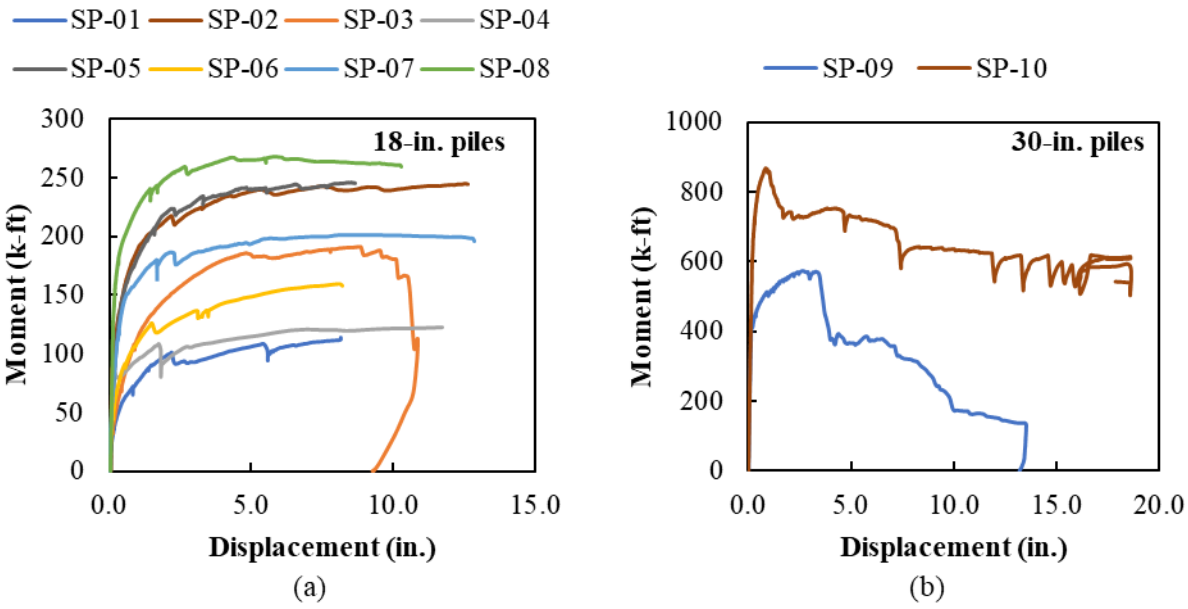

Figure 5.49: Moment versus displacement curves for (a) 18-inch and (b) 30-inch pile specimens

Based on the literature review, three different mechanisms were expected to control the moment capacity of the connection: (1) slip of prestressing strands in embedded pile, (2) slip between pile and pile cap, and (3) bearing failure between pile and pile cap, shown in Figure 5.50.

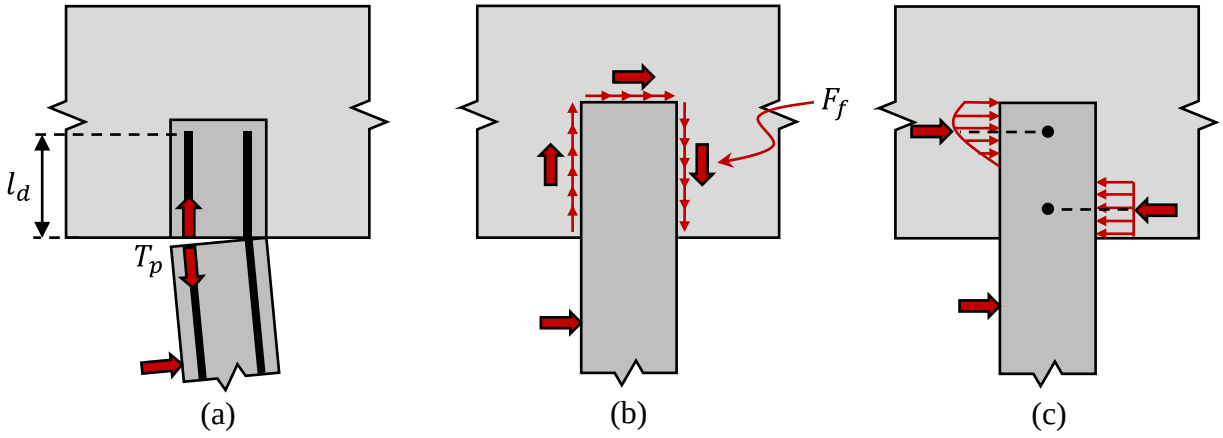

Figure 5.50: Expected failure mechanisms of the pile-to-cap connection (a) development length of prestressing strand, (b) shear friction capacity between the pile and pile cap, and (c) bearing between the pile and cap.

A strand development failure was observed in the 18-inch specimens and the shallower 30-inch embedment. A punching shear failure was observed in the deeper embedment of the 30-inch specimens.

5.10.1.1. Strand Development Failure

A strand development failure is defined as the inability of the pile to develop its full moment capacity at the pile-to-cap interface due to insufficient available development length for the prestressing strand to develop its full stress at ultimate (f_{ps}). For pile-to-cap connections, the available development length corresponds to the pile embedment length. This type of failure is a ductile failure where the section will maintain some capacity as the strand slips. It is typically assumed that the strand slip will be accompanied by a drop in

capacity when the slip initiates, but this is not always the case. This type of failure would result in a large crack at the location where the strands begin to slip.

This type of failure was observed in all the 18-inch specimens with a crack in the pile at the pile-to-cap interface, as shown in Figure 5.51 (a). The moment versus deflection curves, shown in Figure 5.49, all are what would be expected for a strand development failure with the specimens holding load as the strand slip is occurring. In the case of SP-03, which included interface reinforcement between the pile and pile cap, the strand development failure was observed at the end of the interface reinforcement in the pile, as shown in Figure 5.51 (b).

(a) (b)

Figure 5.51: Photographs after failure for (a) SP-04 and (b) SP-03 with observed strand development failure

A strand development failure was also observed in SP-09, as shown in Figure 5.52. Failure occurred in two stages: development of a crack in the pile at the pile-to-cap interface followed by a second larger crack developing in the pile about 3 inches inside the pile cap. After testing was completed, the spalled concrete in the pile cap around the west pile was

removed to inspect the damage inside the embedded pile, as shown in Figure 5.52 (b). A second pile crack was found inside the cap. The strands were in good condition but slipping of the strand was visually observed.

(a) (b)

Figure 5.52: SP-09 strand development failure (a) SP-09 failure, (b) after removing spalled concrete in the cap

After cracking in the pile occurred, the pile started to slip out of the cap as the second larger crack in the pile grew, as shown in Figure 5.53 (a). Diagonal cracking was observed in the cap extending from the corners of the pile, as shown in Figure 5.53 (b). This cracking is commonly observed with punching shear failures.

(a) (b)

Figure 5.53: SP-09 failure (a) pile slipping out of pile cap (b) damage in pile cap

5.10.1.2. Punching Shear Failure in the Pile Cap

A punching shear failure of the edge of the pile cap adjacent to the embedded pile was observed in SP-10. There were no significant cracks in the pile at the pile-to-cap interface, as shown in Figure 5.54 (a). Wide shear cracks in the shape of a punching shear cone were observed at the west side of the pile cap, as shown in Figure 5.54 (b). The east side of the embedded pile pulled away from the pile cap as it punched out the west side of the cap. The cracks initiated at the corners of the pile, with an inclination angle of approximately 45 degrees, and then propagated towards the top of the pile cap, as shown in Figure 5.54 (b).

(a) (b)

Figure 5.54: SP-10 failure (a) pile slipping out of pile cap, (b) punching shear failure

The N5 bars located toward the west side of the pile cap (strains measured by RSG-01 and RSG-02) began to be engaged at around 96 kips as the side of the cap punched out, as shown in Figure 5.55. The maximum measured strain in RSG-01 was 1,408 με when the load was removed.

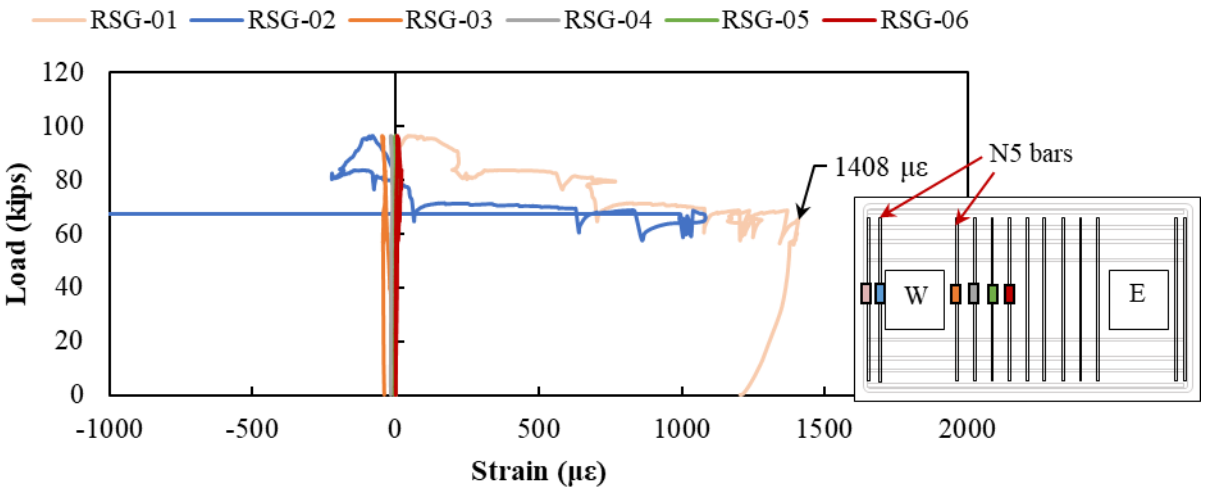

Figure 5.55: SP-10 rebar strain data for N5 bars

Minor punching shear cracking was also observed in 18-inch pile specimens with pile embedment lengths of 12 inches and greater; two examples are shown in Figure 5.56 (a) and (b). Punching shear cracks were also observed in the 30-inch pile specimen with 12-inch pile embedment, shown in Figure 5.56 (c).

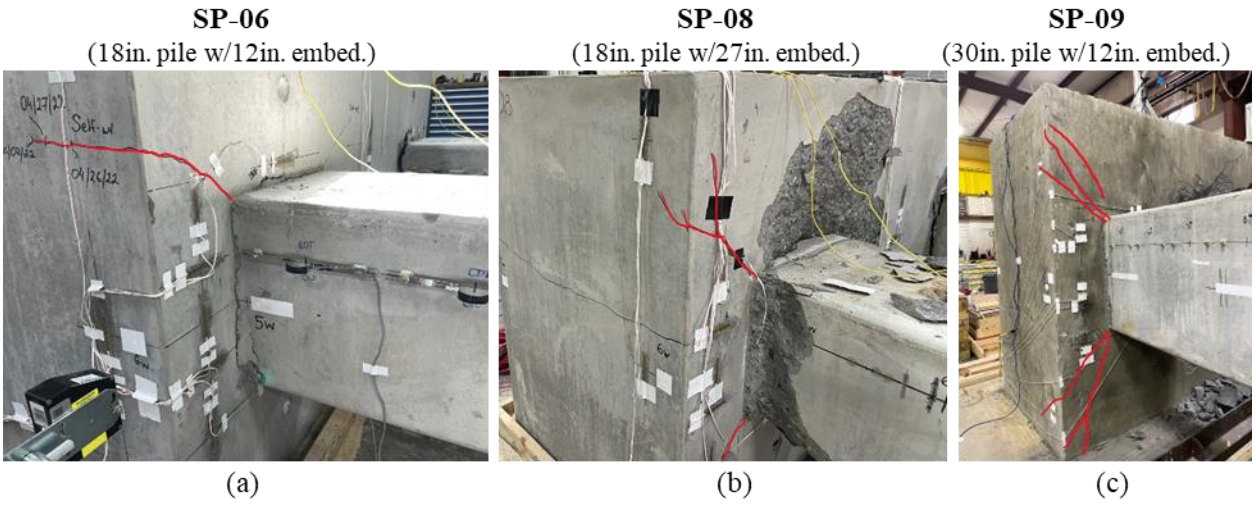

Figure 5.56: Punching shear cracking observed in (a) SP-06, (b) SP-08, and (c) SP-09

The measured rebar strain in the reinforcement in these pile caps (SP-06, SP-08, and SP-09) between the embedded pile and edge of the pile cap was significantly less than the measured strains in SP-10, see Figure 5.57 and Figure 5.58.

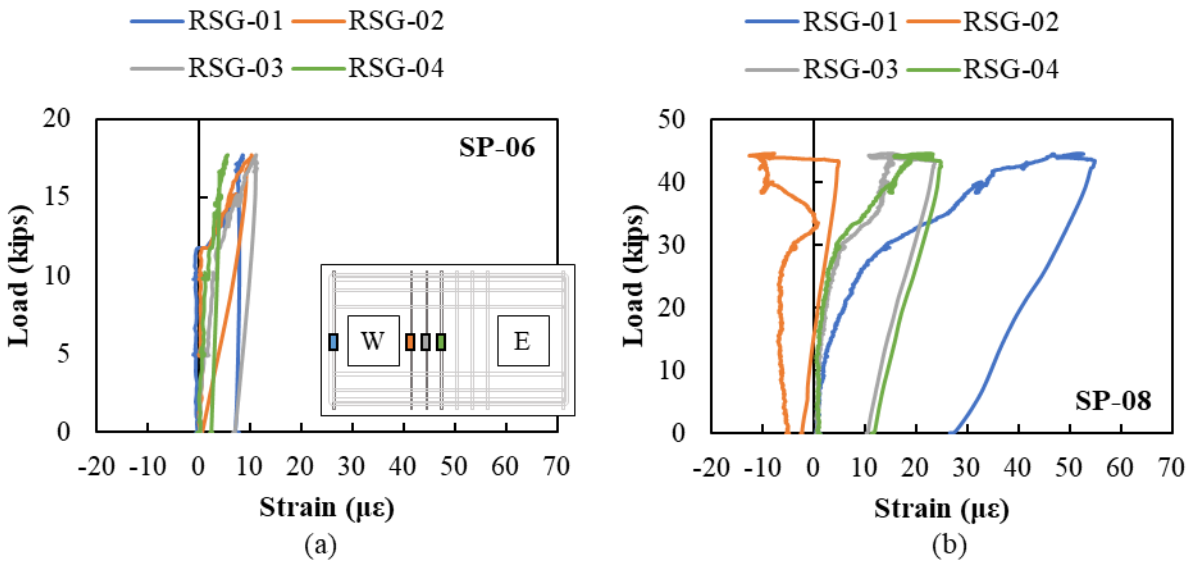

Figure 5.57: Load versus rebar strain for pile cap reinforcement around the west embedded pile for (a) SP-06 and SP-08

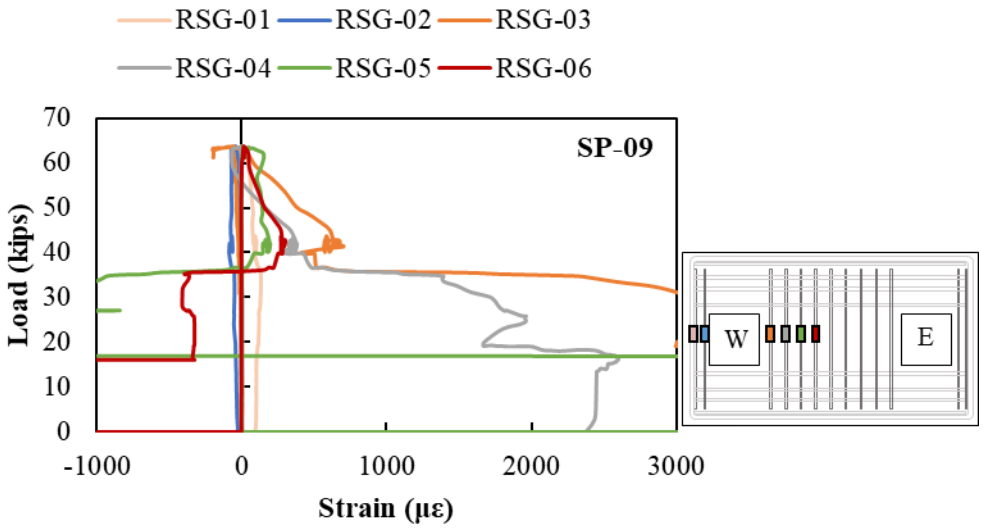

Figure 5.58: Load versus rebar strain for pile cap reinforcement around the west embedded pile for SP-09

5.10.1.3. Rigid Body Rotation

A hinge typically developed in the pile at the large crack near the pile-to-cap interface with rigid-body rotation of the pile occurring after the strands began to slip. The hinge was accompanied by a large crack on the tension face of the pile and spalling of the concrete on the compression face, highlighted in Figure 5.59.

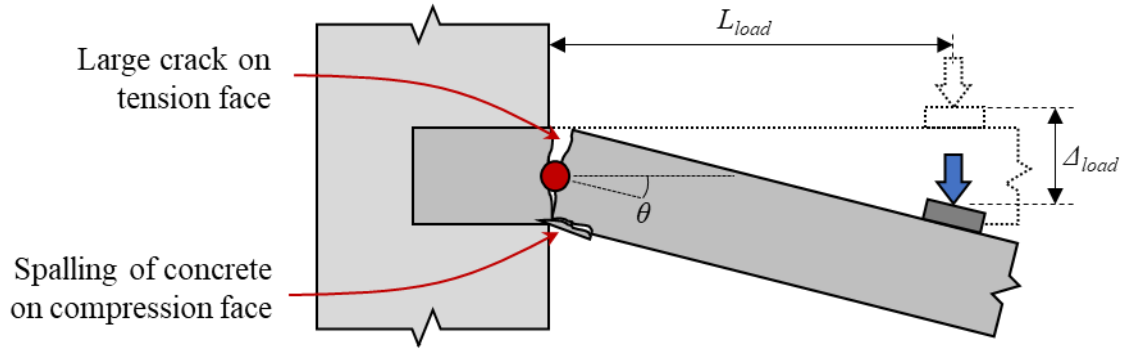

Figure 5.59: Assumed rigid body rotation of pile during testing with typical damage at failure highlighted

Photographs of some of the large cracks on the tension face are shown above in Figure 5.51 through Figure 5.53. Photographs of examples of spalling of the concrete on the compression face of the pile are shown in Figure 5.60.

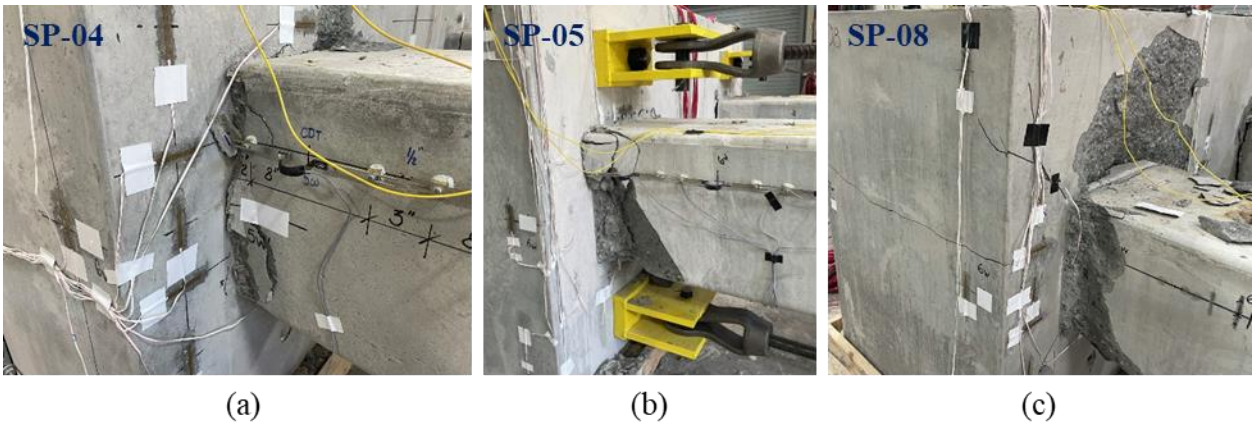

Figure 5.60: Examples of spalling of concrete on compression face of pile for (a) SP-04, (b) SP-05, and SP-08 during failure

The rigid body rotation of the pile was verified through observation of the laser displacement transducers (LDTs) along the length of the pile. The displacement versus distance from cap plots for SP-01 and SP-4 are shown in Figure 5.61.

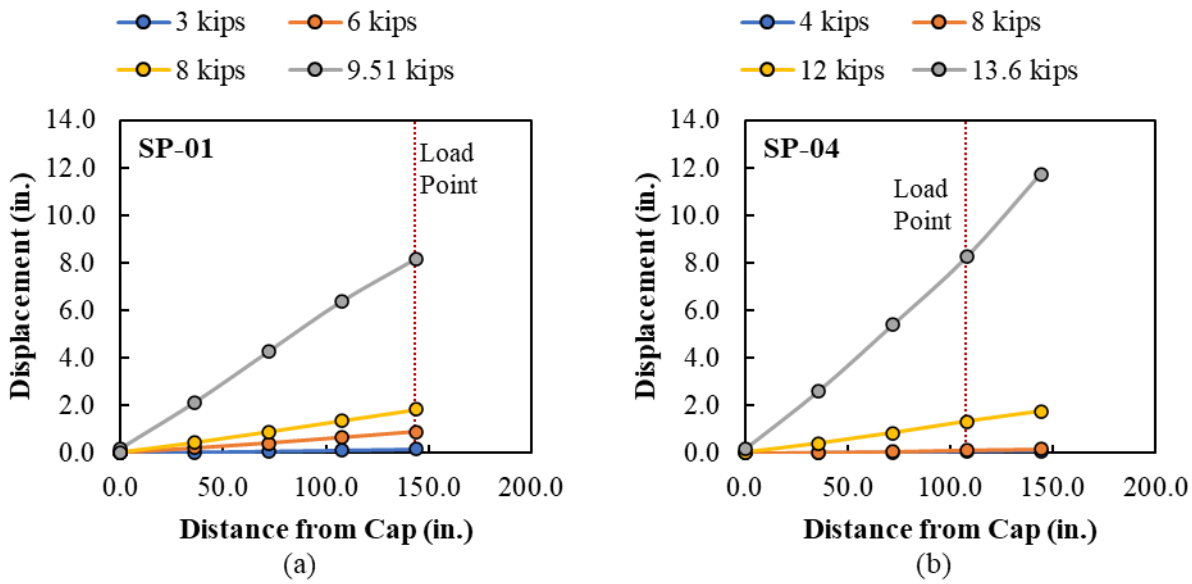

Figure 5.61: Sample displacement versus distance from cap for (a) SP-01 and (b) SP-04

The rotation capacity and moment versus rotation diagrams can be determined using this assumption, as shown in Figure 5.59 and Equation 5.12.

$$\theta = \tan^{-1}\frac{\Delta_{load}}{L_{load}}$$ Equation 5.12

A summary of all the moment versus rotation curves for the specimens is shown in Figure 5.62.

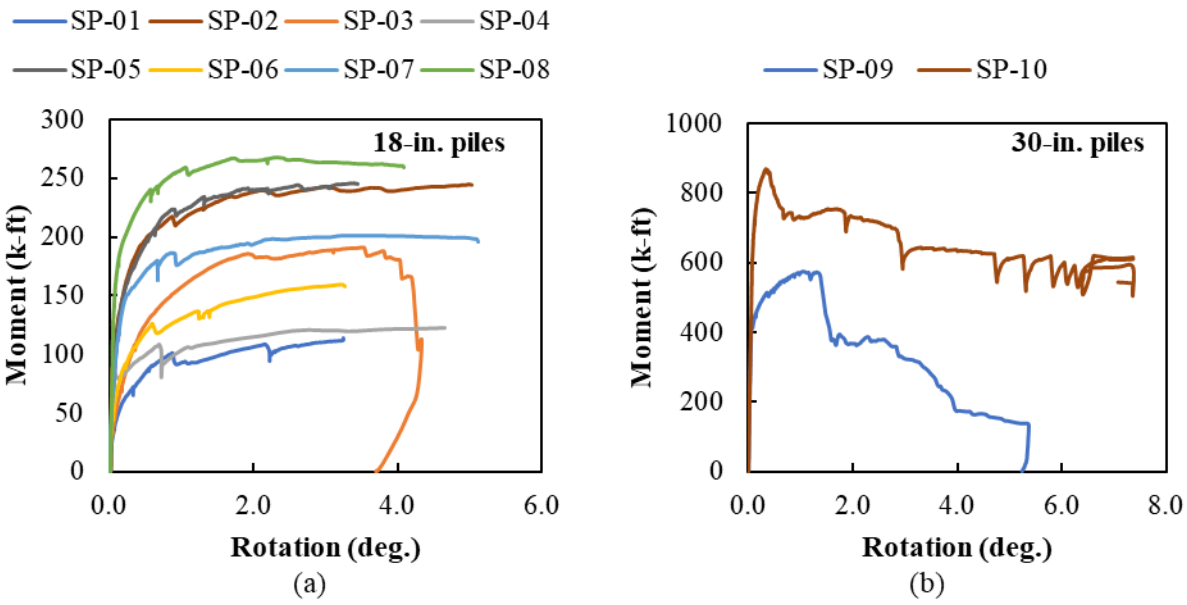

Figure 5.62: Moment versus rotation responses for (a) 18-inch and (b) 30-inch pile specimens

5.10.2. Moment Capacity and Pile Embedment Length

The primary variable studied in the experimental program was the embedment length. For the 18-inch and 30-inch specimens, embedment lengths between 0.33 and 1.5 times the diameter of the piles were tested. A summary of the moment developed and the percentage of the pile capacity for specimens without axial load or interface reinforcement is shown in Table 5.23. The observed failure mechanism for each specimen is also included in Table 5.23. All specimens except SP-10 failed due to slipping of the prestressing strands (strand

development). SP-10 failed due to a punching shear type failure of the edge of the pile cap adjacent to the embedded pile.

With respect to capacity, the 18-inch pile specimens with $0.33d_p$ (6-inch) and $0.5d_p$ (9-inch) embedments (SP-01 and SP-04) still developed 34% and 37% of the pile capacity, respectively.

The two specimens (SP-06 and SP-09) with the current FDOT-specified embedment length for pinned connections (12-inches) each developed 48% of their respective pile capacity. These specimens had two different pile sizes (SP-06 had 18-inch piles and SP-09 had 30-inch piles), so the capacity did not correspond to the relationship between pile size and pile embedment. Both specimens had the same strand type (0.5-inch special strands), which suggests that the capacity of the connection is more dependent on the available development length of the strand.

The 18-inch pile specimens with the deepest pile embedments (SP-08 with 27-inch embedment) developed 81% of the pile capacity while the 30-inch pile specimen with 30-inch embedment (SP-10) developed only 73% of the pile capacity. The smaller capacity developed by SP-10 was likely due to punching shear of the edge of the pile cap occurring before the slipping of the strands occurred. Different failure modes were also observed between these two specimens, SP-08 with a strand development failure and SP-10 with a punching shear failure. The different concrete strengths between the pile and the pile cap in SP-10, as shown in Table 5.16 reflected a field condition between the precast piles and the cast in place pile caps, which likely contributed to the punching shear failure.

Table 5.23: Summary of failure moments and failure mechanisms for specimens with different embedment lengths

Specimen	Pile Size	Embedment	Failure Moment (k-ft)	Percentage of Pile Capacity	Failure Mechanism
SP-01	18”	6” ($0.33d_p$)	114.1	34%	Strand Development
SP-04	18”	9” ($0.50d_p$)	122.8	37%	Strand Development
SP-06	18”	12” ($0.67d_p$)	159.4	48%	Strand Development
SP-07	18”	18” ($1.00d_p$)	201.4	61%	Strand Development
SP-08	18”	27” ($1.50d_p$)	267.6	81%	Strand Development
SP-09	30”	12” ($0.40d_p$)	574.5	48%	Strand Development
SP-10	30”	30” ($1.00d_p$)	868.1	73%	Punching Shear

The moment versus displacement curves for the five different pile embedment lengths for the 18-inch pile specimens are shown in Figure 5.63 (a). The ultimate moment capacity of the connection is plotted versus the pile embedment length in Figure 5.63 (b). There is a linear relationship between the pile embedment length and the ultimate moment capacity. The predicted embedment length to reach the full moment capacity of the 18-inch pile is 35.3 inches, which is less than the current FDOT specified embedment length of 48 inches for a fixed connection.

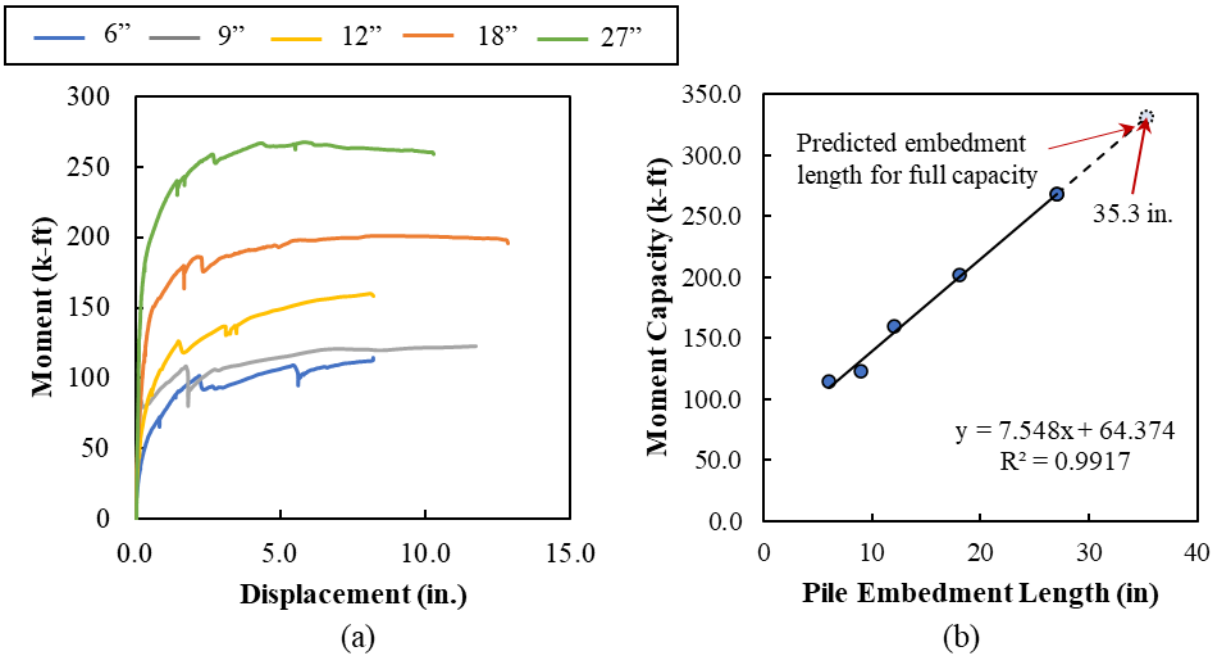

Figure 5.63: Results for the 18-inch specimens (a) moment-displacement curve, (b) relationship between embedment length and moment capacity

The moment versus curvature responses are provided for three of the specimens with different embedment lengths in Figure 5.64. These responses were determined using the fiber optic sensors (FOS) embedded in the specimens by assuming a linear strain profile between the FOS on the east and west sides of the pile that failed during testing. Maximum measured strains around interface were used to calculate curvature. The FOS sensors debonded from the GFRP at a measured strain of approximately 10,000 με. All 18-inch pile specimens failed due to a strand development failure, which led to a large crack developing near the interface. The FOS stopped reading correct strains at the large crack at strains greater than about 10,000 με. This affected ability to find a moment versus curvature response for the other specimens.

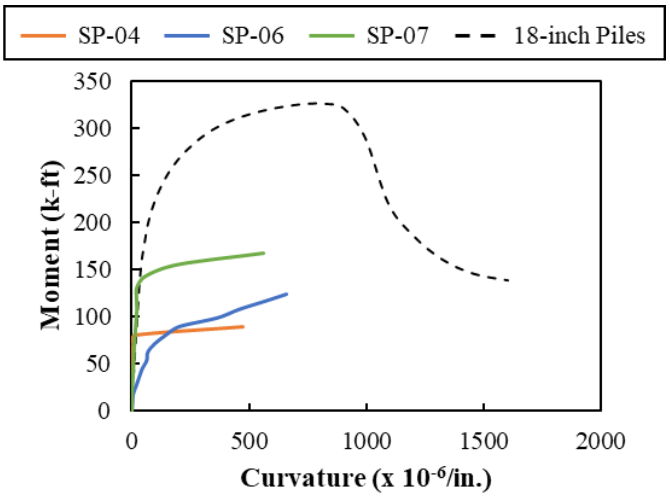

Figure 5.64: Moment versus curvature response for 18-inch specimens

All specimens that failed due to strand development had one large crack develop at the base of the pile at or near the pile-to-cap interface. Only two of the 18-inch specimens (without interface reinforcement or axial load) had additional flexural cracks develop along the length of the pile, shown in Figure 5.65.

(a) (b)

Figure 5.65: Flexural cracks in piles after testing for (a) SP-07 and (b) SP-08

A brief comparison of some strains measured by RSGs and CSGs for the shallowest 18-inch pile embedment (6 inches for SP-01) and the deepest (27 inches for SP-08) is provided

in Figure 5.66 through Figure 5.70. The scale in these figures is different between SP-01 and SP-08 since there were different failure loads and typically significantly different measured strains.

Although both SP-01 and SP-08 failed due to strand development, more cracking and larger concrete strains were observed in the pile cap in SP-08 compared to SP-01. The load versus concrete strain in the face of the pile cap with the embedded pile toward the edge of the cap is shown in Figure 5.66. Strains in the exterior edge of the pile reached 885 με tension in SP-08 near failure compared with less than 40 με tension in SP-01.

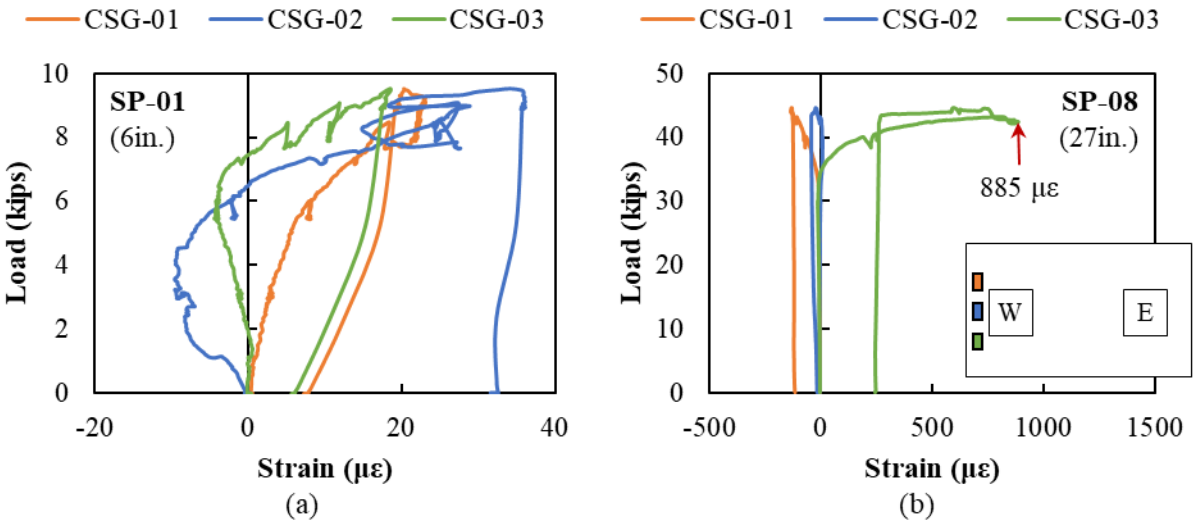

Figure 5.66: Load versus concrete strain on the edge of the pile cap for (a) SP-01 and (b) SP-08 (axes have different scales)

Larger concrete strains were also measured on the side face of the pile caps in SP-08 compared with SP-01, as shown in Figure 5.67. Tensile strains developed at mid-width of the pile cap with compression strains developing toward the edges of the pile cap. Concrete strains in SP-08 reached -320 με compression and 90 με tension compared with less than -5 με compression and less than 20 με tension for SP-01.

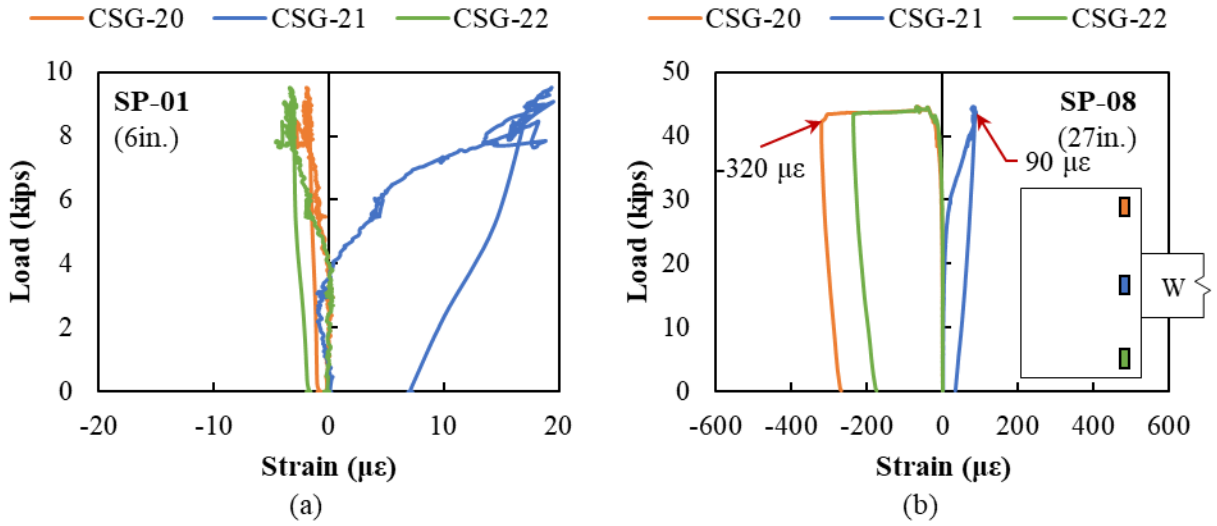

Figure 5.67: Load versus concrete strain on the side face of the pile cap for (a) SP-01 and (b) SP-08 (axes have different scales)

The reinforcement parallel to the edge of the cap was not heavily engaged in either SP-01 or SP-08 with strains less than 60 με for each, as shown in Figure 5.68.

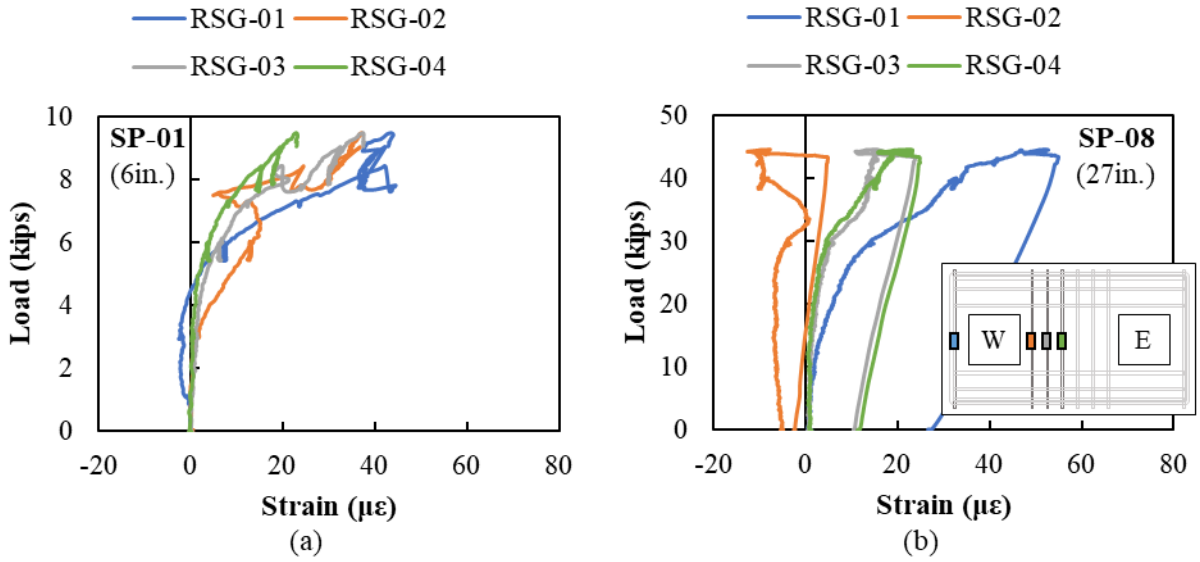

Figure 5.68: Load versus rebar strain for pile cap reinforcement around the embedded piles for (a) SP-01 and (b) SP-08

There were larger measured strains in the longitudinal reinforcement extending along the length of the pile caps in SP-08 than SP-01, as shown in Figure 5.69. Longitudinal rebar strains in SP-01 were less than around 50 με, while strains in SP-08 reached 491 με.

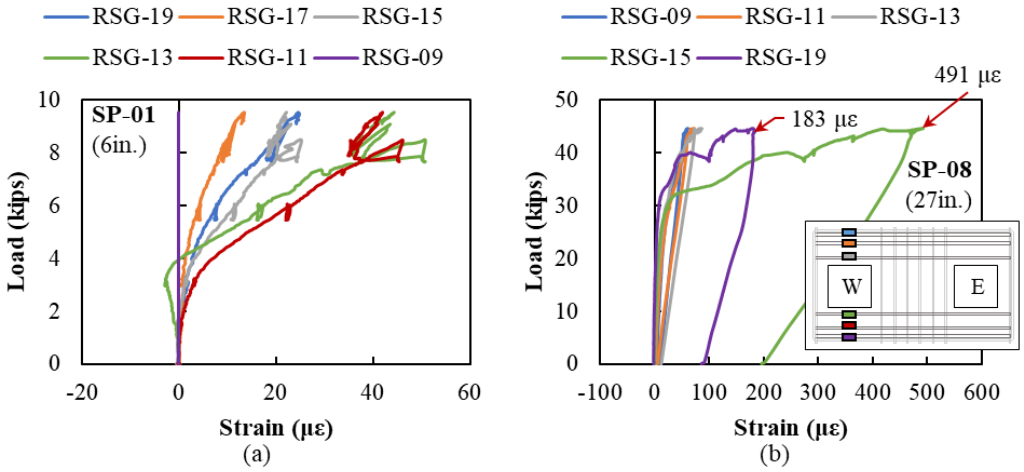

Figure 5.69: Load versus rebar strain for pile cap reinforcement around the embedded piles for (a) SP-01 and (b) SP-08

The load versus rebar strain for the reinforcement spaced across the west face of the pile cap for SP-01 and SP-08 are shown in Figure 5.70. The rebar strains are generally higher for SP-08 than SP-01.

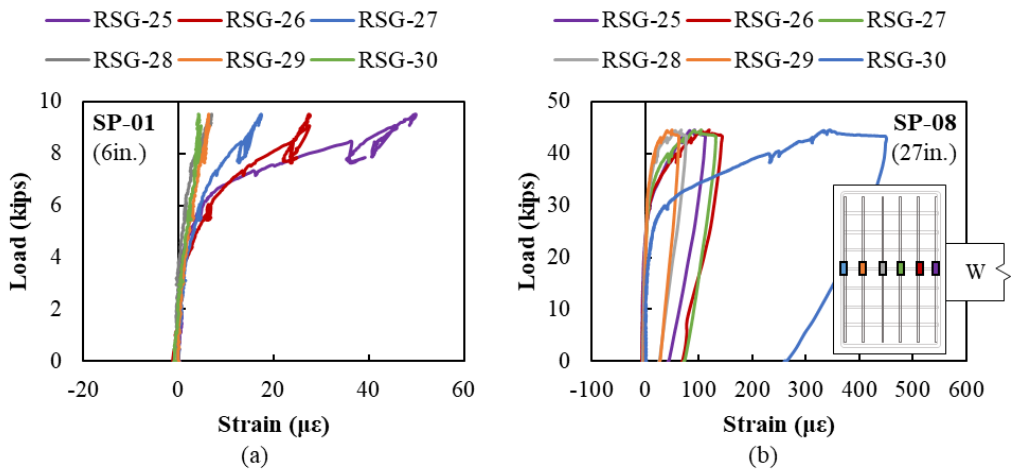

Figure 5.70: Load versus rebar strain for reinforcement along the west face of the pile cap for (a) SP-01 and (b) SP-08

The largest measured strain in SP-08 were measured toward the face of the pile cap opposite the pile embedment, as shown in Figure 5.71. It is unclear why the strain in RSG-30 was the largest in this specimen. Strains were generally the largest in reinforcement closest to the pile cap face with the embedded piles, as was the case for SP-01 in Figure 5.70 (a).

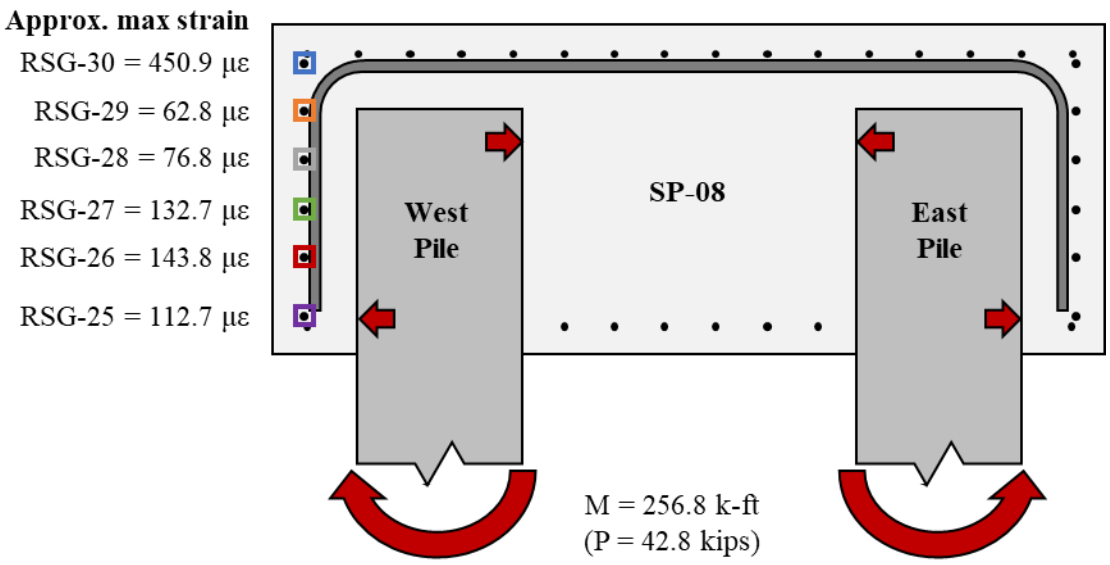

Figure 5.71: Maximum strains in reinforcement in west face of the pile cap for SP-08

5.10.2.1. Development Length and Confining Stress

The observed failure mechanism for nine of the test specimens was strand development. Different estimation procedures for development length and to account for the confinement provided by the shrinkage of the cap concrete are discussed in this section.

- Estimated Development Length

Estimated transfer and development lengths were found using AASHTO LRFD Bridge Design Specification (BDS) §5.9.4.3.2 [23]. The transfer and development lengths are found using Equation 5.14 and Equation 5.13, respectively.

Required transfer length: AASHTO LRFD §5.9.4.3.1	$l_t = 60 d_b$	Equation 5.13
Required development length: AASHTO LRFD (5.9.4.3.2-1)	$l_d \geq \kappa \left(f_{ps} - \frac{2}{3} f_{pe} \right) d_b$	Equation 5.14

where:

d_p = nominal strand diameter (in)

f_{ps} = average stress in prestressing steel at the time for which the nominal resistance of the member is required (ksi)

f_{pe} = effective stress in the prestressing steel after losses (ksi)

κ = 1.0 for pretensioned panels, piling, and other pretensioned members with a depth of less than or equal to 24.0 in

κ = 1.6 for pretensioned members with a depth greater than 24.0 in

The stress in the prestressing steel at nominal moment (f_{ps}) is found from AASHTO LRFD BDS §5.6.3.1.

AASHTO LRFD (5.6.3.1.1-1)

$$f_{ps} = f_{pu}\left(1 - k\frac{c}{d_p}\right)$$ Equation 5.15

AASHTO LRFD (5.6.3.1.1-2)

$$k = 2\left(1.04 - \frac{f_{py}}{f_{pu}}\right)$$ Equation 5.16

AASHTO LRFD (5.6.3.1.1-4)

$$c = \frac{A_{ps}f_{pu} + A_s f_s - A'_s f'_s}{\alpha_1 f'_c \beta_1 b + kA_{ps}\frac{f_{pu}}{d_p}}$$ Equation 5.17

where:

A_{ps} = area of prestressing steel (in^2)

f_{pu} = specified tensile strength of prestressing steel (ksi)

f_{py} = yield strength of prestressing steel (ksi)

A_s = area of nonprestressed tension reinforcement (in^2)

A'_s = area of compression reinforcement (in^2)

f_s = stress in the nonprestressed tension reinforcement at nominal flexural resistance (ksi)

f'_s = stress in nonprestressed compression reinforcement at nominal flexural resistance (ksi)

b = width of the compression face of the member (in)

d_p = distance from extreme compression fiber to the centroid of the prestressing force (in)

c = distance from the extreme compression fiber to the neustral axis (in)

α_1 = stress block factor

β_1 = stress block factor

The rectangular stress distribution factors (β_1 and α_1) can be found in AASHTO LRFD BDS §5.6.2.2.

For $f'_c \leq 10$ ksi: $$\alpha_1 = 0.85$$ Equation 5.18

For $f'_c > 10$ ksi: $$\alpha_1 = 0.85 - 0.02\left(f'_c - 10\ ksi\right) \geq 0.75$$ Equation 5.19

The other stress block factor is also based on the compressive strength of concrete.

For $f'_c \leq 4$ ksi: $$\beta_1 = 0.85$$ Equation 5.20

For $f'_c > 4$ ksi: $$\beta_1 = 0.85 - 0.05\left(f'_c - 4\ ksi\right) \geq 0.65$$ Equation 5.21

The losses found in §5.9.4 were used to find the effective stress in the prestressing (f_{pe}). Some of the significant values in the transfer length and development length calculations are summarized in Table 5.24 for the 0.5-in. special strands in the 18-inch and 30-inch piles.

Table 5.24: Estimated transfer and development length for 18-inch and 30-inch piles using AASHTO LRFD BDS

Pile	***d_b (in)***	**f_{pe} (ksi)**	**Transfer length, l_t (in)**	***c* (in)**	**f_{ps} (ksi)**	**κ**	**Development length, l_d (in)**

18-inch	0.52	177.4	31.2	2.30	256.9	1.0	72.1
30-inch	0.52	181.8	31.2	2.56	261.8	1.6	117.0

The average transfer length measured using the fiber optic sensors for the 18-inch and 30-inch piles was 25.86 and 14.57 inches, respectively.

A bilinear relationship is assumed in AASHTO LRFD BDS for determining the stress in the strands when the available development length is less than the required development length. The stress in the prestressing strand varies linearly from 0 ksi at the point where bonding starts to the effective stress after losses, f_{pe}, at the end of the transfer length, l_t. Between the end of the transfer length and the development length, l_d, the strand stress is assumed to increas linearly, reaching the stress at nominal resistance, f_{ps}, at the development length. The idealized relationship between steel stress and distance from the free end of strand aper AASHTO LRFD BDS is shown in Figure 5.72.

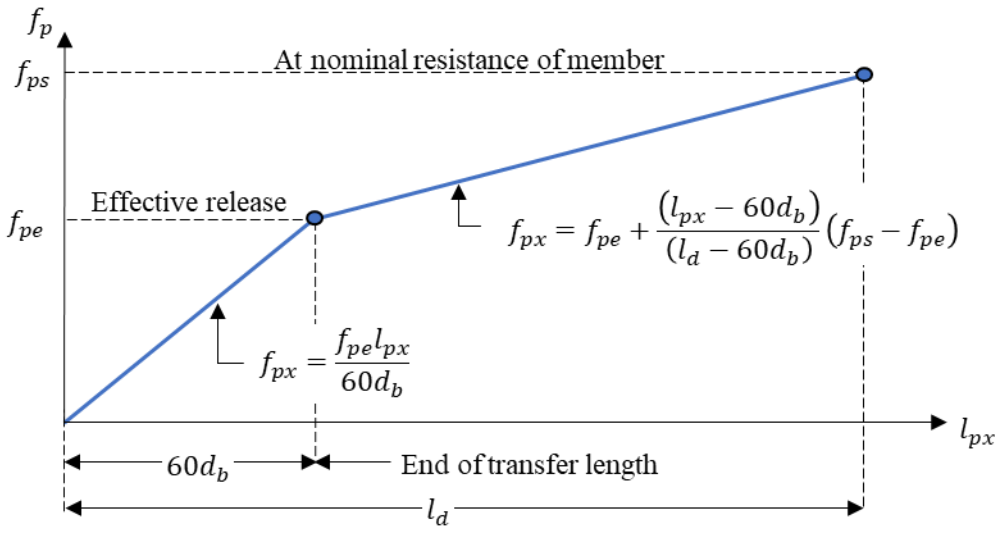

Figure 5.72: Idealized relationship between strand stress and distance from free end of strand [23]

The stress versus available development length plots found using AASHTO LRFD BDS for the 18-inch and 30-inch piles are shown in Figure 5.73.

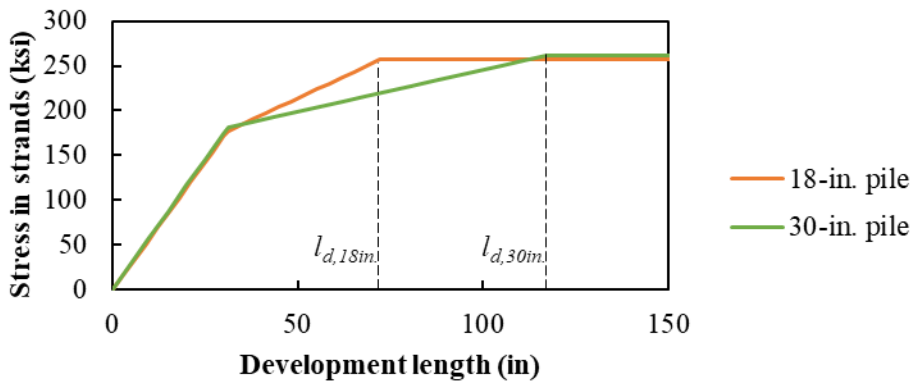

Figure 5.73: Estimated strand stress versus development length for 18-inch and 30-inch piles found using AASHTO LRFD BDS equations

- Background on Transfer and Development Length Equations

In 1973, AASHTO adopted the transfer and development length equation from the ACI Building Code, which was proposed by Mattock and members of ACI Committee 423 [67], [68]. The development length equation in ACI 318-19 [69], shown in Equation 5.22, divides the development length into two parts: transfer length and flexural bond length. Mattock [68] developed this equation based on results of a study conducted by Hanson and Kaar [70], where tests were conducted on specimens not subject to confining stresses.

Required development length:
ACI 318-19 (25.4.8.1)

$$l_d = \left(\frac{f_{se}}{3000}\right) d_b + \left(\frac{f_{ps} - f_{se}}{1000}\right) d_b \qquad \text{Equation 5.22}$$

where:

f_{se} = effective prestress in the prestressing steel (ksi)

f_{ps} = stress in the prestressing steel at the nominal strength of the member (ksi)

The average transfer bond stress, $\bar{u}_t$=400 psi, was stated in the study by Hanson and Kaar [70] and adopted by Mattock [68]. For the average flexural bond stress, Mattock [68] constructed a straight-line relationship by subtracting the estimated transfer length from

the embedment length of the strand. The increase in strand stress due to flexure was determined to be the difference between the strand stress at the load causing slip and the effective stress due to prestressing. An average flexural bond stress of $\bar{u}_{fb}$=140 psi was used. The expressions created for transfer length and flexural bond length by Mattock are shown in Equation 5.23 and Equation 5.24, respectively.

Transfer length (Mattock) $$L_t = \frac{A_{ps} f_{se}}{\sum o\, \bar{u}_t} = \frac{f_{se}}{7.36\bar{u}_t} d_b = \frac{f_{se}}{3000} d_b$$ Equation 5.23

Flexural bond length (Mattock) $$L_{fb} = \frac{f_{ps} - f_{se}}{7.36\bar{u}_{fb}} d_b = \frac{f_{ps} - f_{se}}{1000} d_b$$ Equation 5.24

Where:

$\sum o$ = perimeter of the strand (in) = 4/3πd_b

A_{ps} = cross-sectional area of the strand (in2) = 0.725 $\pi d_b^2/4$.

Based on a study conducted by Johnston and Zia [71] questioning the development length of prestressing strands, the Federal Highway Administration [72] later added the application of 1.6 multiplier for pretensioned members with a depth greater than 24.0 inches.

The calibration of the ACI 318-19 and AASHTO LRFD BDS development length equations did not include specimens with confining stresses on the strands during testing, which would likely help to reduce the required development length of the strands.

- Effect of Cap Confinement on Transfer and Development Length

As summarized in the literature review, many researchers have found that the full moment capacity of the piles can be developed with much shorter embedment lengths than required

by AASHTO LRFD BDS to fully develop the strands. This suggests that the actual required strand development length for the pile embedded in a footing or cap is significantly shorter than the development length calculated using AASHTO LRFD BDS. It has been proposed by previous researchers [67] that the primary reason for this is the shrinkage of the cast-in-place footing or cap creating a clamping force around the embedded pile and decreasing the required development length. This compressive stress affects both the average transfer bond stress and the average flexural bond stress, which will decrease the development length required for the full capacity of the prestressing strand.

Three different mechanisms are typically assumed to contribute to the transfer bond stress: adhesion, friction, and mechanical interlock. Friction, which has the most significant effect, results from the slipping of the strand along the transfer length. For the development of frictional bond stresses, radial compressive stresses are required. Hoyer's Effect and confining stress contributes to this radial compressive stress, affecting the frictional bond stress directly. The confined transfer bond stress can be found by adding the average bond stress and the average confining stress multiply by the friction coefficient between steel and concrete, as shown in Equation 5.25.

Confined transfer bond stress: $$\bar{u}_{tc} = 400 + \mu\sigma_{cav}$$ Equation 5.25

where:

σ_{cav} = average confining stress (psi)

μ = coefficient of friction between steel and concrete

For the confined flexural bond stress, it was assumed that the confining stress will only affect the friction stress. The cracks that form in the flexural bond stress zone will decrease

the friction forces that result from the confining stress. A ratio of $(\bar{u}_t/\bar{u}_{fb})$ = 2.86 has been used by previous researchers [67] to decrease the effect of the confining stress, as shown in Equation 5.26.

Confined flexural bond stress: $$\bar{u}_{fbc} = 140 + \frac{\mu\sigma_{cav}}{2.86}$$ Equation 5.26

where:

σ_{cav} = average confining stress (psi)

μ = coefficient of friction between steel and concrete

ElBatanouny and Ziehl [67] assume that confining stress is dependent on several variables, including pile stiffness, pile cap stiffness, dimensions of the pile/pile cap system, time between casting of pile and casting of pile cap, and time between casting of the pile cap and loading of specimen. They developed an equation for the estimation of the confining stress for purposes of design. The equation uses Lames equations for the calculation of stresses in thick-walled cylinders. The confining stress can be calculated using Equation 5.27.

Confining stress [67]: $$\sigma_c = \frac{(D_o)\left(\varepsilon_{sh} - \frac{(d_o)(\sigma_c)}{E_p}\right)(1 - v_p)}{\left(\frac{d_o}{E_{BC}}\right)\left(\frac{D_o^2 + d_o^2}{D_o^2 - d_o^2} + v_{BC}\right) + \frac{d_o}{E_p}(1 - v_p)}$$ Equation 5.27

Shrinkage strain by ACI 209R-92 $$\varepsilon_{sh} = \frac{t}{35 + t}(\varepsilon_{sh})_u$$ Equation 5.28

where:

σ_c = confining stress (psi)

d_o = smallest dimension of pile (in)

D_o = smallest dimension of pile cap

ε_{sh} = shrinkage strain (in/in)

E_p = young's modulus of pile (psi)

ν_p = poisson's ratio of the pile (0.2 for concrete)

E_{BC} = young's modulus of pile cap (psi)

V_{BC} = poisson's ratio of the pile cap (0.2 for concrete)

t = time between casting of the bent cap and loading of the specimen (days)

$(\varepsilon_{sh})_u$ ultimate shrinkage strain ($780x10^{-6}$ in/in)

This procedure was used to find the estimated confining stresses for each of the specimens, as shown in Table 5.25.

Table 5.25: Estimated confining stress found using ElBatanouny and Ziehl [67]

SP	D_o (in)	d_o (in)	E_p (psi)	E_{BC} (psi)	t (days)	ε_{sh} (in/in)	σ_c (psi)
SP-01	36	18	6,218,954	6,368,371	236	0.00068	2468.8
SP-02	36	18	6,099,600	6,337,558	350	0.00071	2547.0
SP-03	36	18	6,133,880	6,422,958	239	0.00068	2467.9
SP-04	36	18	6,218,954	6,225,256	255	0.00069	2462.5
SP-05	36	18	6,250,491	6,564,529	336	0.00071	2615.0
SP-06	36	18	6,133,880	6,085,758	253	0.00069	2414.9
SP-07	36	18	6,133,880	5,790,249	231	0.00068	2323.3
SP-08	36	18	6,133,880	6,390,533	232	0.00068	2451.9
SP-09	48	30	6,532,276	5,516,098	30	0.00036	834.2
SP-10	48	30	6,701,350	5,393,539	21	0.00030	676.6

ElBatanouny and Ziehl [67] and other researchers have developed equations to calculate the development length of the strands considering these confining stresses or clamping forces provided by the pile cap. ElBatanouny and Ziehl [67] modified the ACI development length equation (Equation 5.22) by replacing the values of $\bar{u}_t$ and $\bar{u}_{fb}$, with $\bar{u}_{tc}$ and $\bar{u}_{fb}$, respectively, in Equation 5.23 and Equation 5.24. This will increase the values of the average bond stress and average flexural bond stress which will lead to a decrease in the development length, as shown in Equation 5.29.

ElBatanouny [67]: $$L_{dc} = \frac{f_{se}}{5000} * d_b + \frac{f_{ps} - f_{se}}{1800} * d_b$$ Equation 5.29

where,

L_{dc} = confined development length (in)

f_{se} = effective stress of prestressing strand (psi)

f_{ps} = nominal strength of prestressing strand (psi)

d_b = nominal diameter of prestressing strand (in)

The transfer and development length for the 18- and 30-inch piles were found using Equation 5.29. Results are shown in Table 5.26.

Table 5.26: Estimated development length for 18-inch and 30-inch piles using ElBatanouny and Ziehl [67]

Pile Size	d_b ***(in)***	f_{pe} **(ksi)**	f_{ps} **(ksi)**	**Development length,** l_d **(in)**
18-inch	0.52	177.4	256.9	41.4
30-inch	0.52	181.8	261.8	42.0

This estimated development length is much less than the estimated development length found using AASHTO LRFD BDS, 72.1 in. for 18-inch piles and 117.0 in. for 30-inch piles.

An additional proposal from FDOT to AASHTO T-10 in 1993, summarized in Buckner [73], had a similar form to the recommendation from ElBatanouny and Ziehl [67], shown in Equation 5.30.

FDOT 1993 [73]:

$$L_d = \frac{\left[\frac{f_{pe} d_b}{3} + \left(f_{ps} - f_{pe}\right)\right]}{k_b \mu_{ave}} \qquad \text{Equation 5.30}$$

where:

k_b = dimensionless constant; 8 for piles embedded in concrete footing or pier cap, 4 for slabs and slender members, and 2 if the computed development length to member depth ratio is less than or equal to 3

μ_{ave} = average bond stress for development length, 0.25 ksi

The transfer length would be implied to be Equation 5.31.

Implied from FDOT 1993 [73]:

$$L_t = \frac{f_{pe} d_b}{3 k_b \mu_{ave}} \qquad \text{Equation 5.31}$$

Buckner [73] comments that Equation 5.30 results in about the same development length as the 1993 AASHTO equation for slender member, results in development lengths doubling for deep members, and results in half the development length for embedded piles.

Table 5.27: Estimated transfer and development length for 18-inch and 30-inch piles using FDOT 1993 from Buckner [73]

Pile Size	d_b (in)	f_{pe} (ksi)	f_{ps} (ksi)	Transfer length, l_d (in)	Development length, l_d (in)
18-inch	0.52	177.4	256.9	15.4	55.1
30-inch	0.52	181.8	261.8	15.8	55.8

- Measured Confining Stresses

The average confining stress was calculated for each specimen using the readings from the vibrating wire gages in the pile cap after casting and before testing. The measured strains were multiplied by the estimated modulus of elasticity of the cap concrete to find the confining stresses; this is like what was done by previous researchers [17]. Results for several specimens are shown in Table 5.28. Accurate readings were not obtained for the other specimens.

Table 5.28: Observed confining stress from VWSG in pile caps

Specimen	Age of Cap (days)	VWG-4 (με)	VWG-6 (με)	Average Strain (με)	E_{PC} (ksi)	σ_c (ksi)
SP-01	240	-72.8	-131.8	-102.3	6,368	-0.652
SP-03	240	-1.9	-72.6	-37.2	6,423	-0.239
SP-06	260	-39.4	-66.6	-53.0	6,086	-0.323
SP-10	20.8	-95.0	-78.5	-86.8	5,394	-0.468

The average measured confining stress for the pile caps with 18-inch embedded piles was 0.404 ksi and 0.468 ksi for the pile cap with 30-inch embedded pile. This is much higher than the estimated confining stresses found using Equation 5.27.

- Measured versus Estimated Strand Stress at Failure

The strand stress at failure was determined from the experimental results using RESPONSE2000. The maximum strand stress (f_{pu}) was modified in the material properties

until the calculated maximum moment was equal to the measured maximum moment. The strand stress was calculated for different pile embedment lengths based on AASHTO LRFD using the equations shown in Figure 5.72. The strand stress was also found using the equation proposed by ElBatanouny and Ziehl [67] for transfer length, Equation 5.32, and development length, Equation 5.29.

Transfer length using ElBatanouny and Ziehl [67]	$L_{dc} = \frac{f_{se}}{5000} * d_b$	Equation 5.32

The same bilinear relationship can be used to find the strand stress based on the available development length, shown in Figure 5.74.

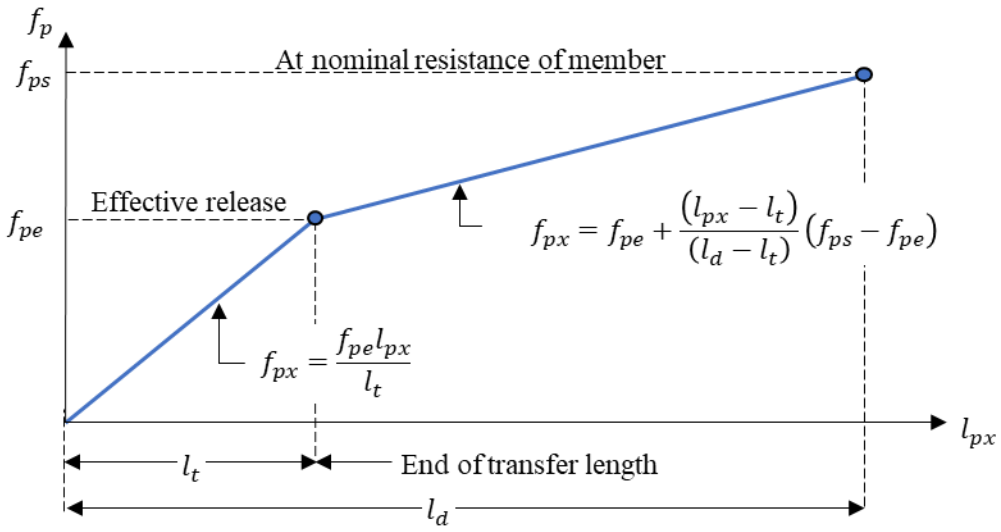

Figure 5.74: Bilinear relationship used for strand stress for ElBatanouny and Ziehl [67]

The calculated strand stress for each embedment length was used to find the corresponding maximum moment using RESPONSE2000. The slipping stress and maximum moments from the experimental testing, AASHTO LRFD BDS, and ElBatanouny and Ziehl [67] are summarized in Table 5.29. The ratio of the measured to estimated moment is provided for AASHTO LRFD BDS and ElBatanouny and Ziehl [67] along with the average, standard

deviation, and coefficient of variation. A measured-to-estimated strength ratio greater than 1.0 signifies a conservative estimate. The estimated value for SP-10 is not included in the statistical analysis, since SP-10 failed due to punching shear of the edge of the pile cap, which is not captured by the development length calculations. The maximum moment developed by SP-10 would have been higher if a punching shear failure hadn't occurred before the slipping of the strands. Both procedures conservatively estimated the strength of the specimens, on average, with the estimation procedure of ElBatanouny and Ziehl [67] resulting in the more accurate estimation.

Table 5.29:Maximum moment and slipping stress (experimental, AASHTO LRFD BDS, ElBatanouny and Ziehl)

Spec.	Experimental		AASHTO LRFD			Elbatanouny and Ziehl		
	Slipping stress (ksi) [1]	*Max. moment (k-ft)*	*Slipping stress (ksi)*	*Max. moment (k-ft)* [2]	*Meas./ Est.*	*Slipping stress (ksi)*	*Max. moment (k-ft)* [2]	*Meas./ Est.*
SP-01	81.0	114.1	35.2	50.5	2.26	57.7	82.4	1.38
SP-02	86.0	244.6	35.2	182.5	1.34	57.7	210.4	1.16
SP-03	80.0	190.8	35.2	140.7	1.36	57.7	163.0	1.17
SP-04	87.0	122.8	52.8	75.0	1.64	86.5	121.9	1.01
SP-05	88.0	246.2	52.8	204.8	1.20	86.5	244.9	1.01
SP-06	115.0	159.4	70.4	99.2	1.61	115.4	160.7	0.99
SP-07	148.0	201.4	105.6	146.9	1.37	173.1	232.9	0.86
SP-08	204.0	267.6	158.4	214.0	1.25	207.0	272.1	0.98
SP-09	121.0	574.6	71.7	344.3	1.67	115.4	542.6	1.06
SP-10 [3]	188.0	868.1	179.2	832.6	1.04 [3]	220.2	1015.1	0.86 [3]
				Average =	1.52		**Average =**	1.07
				St. Dev. =	0.31		**St. Dev. =**	0.14
				Co. of Var. =	0.20		**Co. of Var. =**	0.13

[1] Experimental slipping stress was determined using maximum moment developed by specimen into RESPONSE.

[2] Maximum moment was determined using value of slipping stress into RESPONSE.

[3] Failure of SP-10 was due to punching shear of the edge of the pile cap, so these values were not included in statistical analysis of the estimation procedures.

The stress in the pile strands versus available development length measured through the experimental testing is plotted with the strand stress estimation equations from AASHTO LRFD BDS and ElBatanouny and Ziehl [67] in Figure 5.75. The measured results generally align well with the estimated strand stress found using ElBatanouny and Ziehl [67].

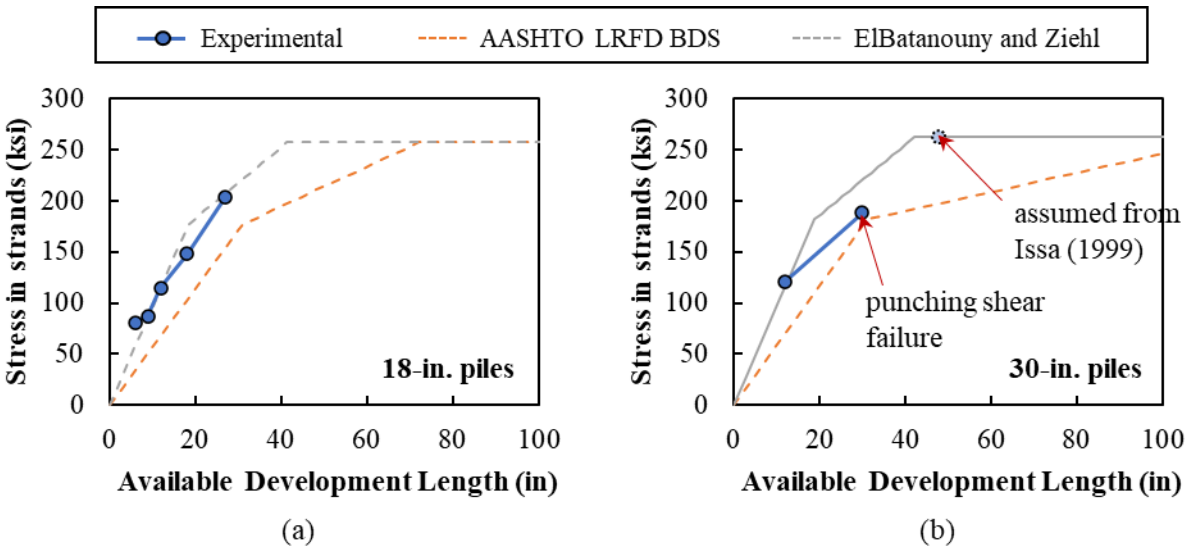

Figure 5.75: Stress in strand versus available development length plots for (a) 18-inch and (b) 30-inch pile specimens

The initial recommendation based on the experimental testing is to determine the required embedment length using the ElBatanouny and Ziehl [67] equations, where the punching shear capacity does not control the capacity of the connection.

5.10.2.2. Punching Shear Failure of Pile Cap Edge

One of the specimens (SP-10) failed due to a failure of the edge of the pile cap prior to a strand development or flexural failure of the pile. The cracking pattern and failure

mechanism observed for SP-10 was similar to a punching (two-way) shear failure for an edge column, as shown in Figure 5.54. The "column" for this punching shear failure can be assumed to be the compression force applied from the side bearing forces of the embedded pile, as shown in Figure 5.76.

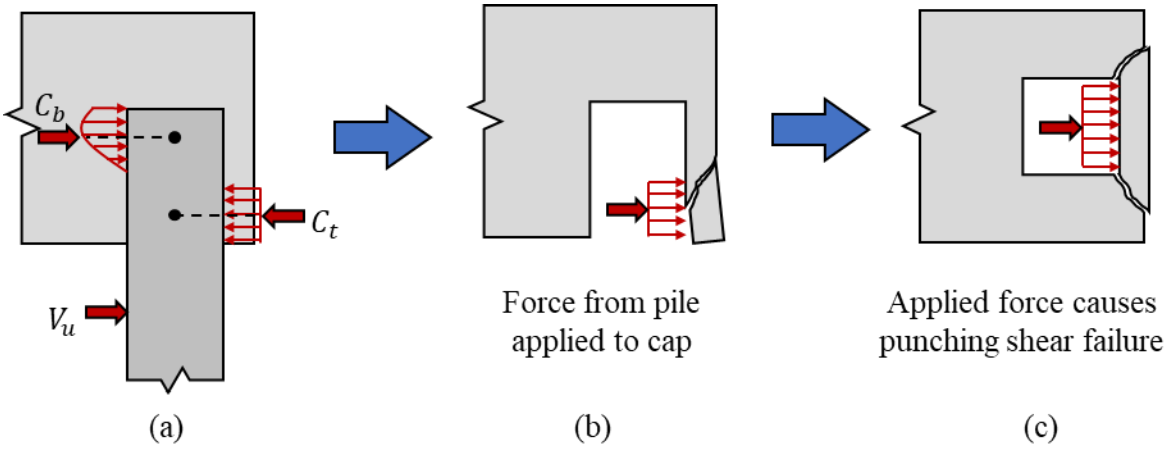

Figure 5.76:Punching shear failure in pile-to-cap connections

- Estimated Punching Shear Demand

Mattock and Gaafar [74] assumed a parabolic distribution of bearing stresses for C_b and a uniform stress distribution for C_f of $0.85f'_c$. The bearing stresses are distributed over the width of the embedded pile, b. The equation proposed by Mattock and Gaafar:

Mattock and Gaafar: $$V_u = 54\sqrt{f'_c}\left(\frac{b'}{b}\right)^{0.66}\beta_1 b L_e\left[\frac{0.58-0.22\beta_1}{0.88+\frac{a}{L_e-c}}\right]$$ Equation 5.33

where:

a = shear span of the pile (distance from pile cap to assumed point of zero moment) (in)

β_1 = concrete stress block factor defined in ACI 319-99

b' = width of the element into which the pile is embedded

b = width of the embedded pile

Mattock and Gaafar [74] propose simplified equations for design, shown in Equation 5.34 and Equation 5.35. They found that the maximum moment in the embedded element (steel sections for their research) occurred in the embedded portion of the element.

Mattock and Gaafar, simplified equations:

$$V_n = \frac{21\sqrt{b'/b}\sqrt{f'_c}bL_e}{\left(0.88 + a/L_e\right)} \qquad \text{Equation 5.34}$$

Max. moment (inside connection):

$$M_{max} = V_n\left(a + L_e/7\right) \qquad \text{Equation 5.35}$$

The strain and stress distribution proposed by Mattock and Gaafar [74] is shown in Figure 5.77. They suggested the shear span be increased by the concrete cover, c, to account for possible spalling of the soffit of the pile cap. The value of b' is intended to account for the spreading of the compressive stresses away from the embedment.

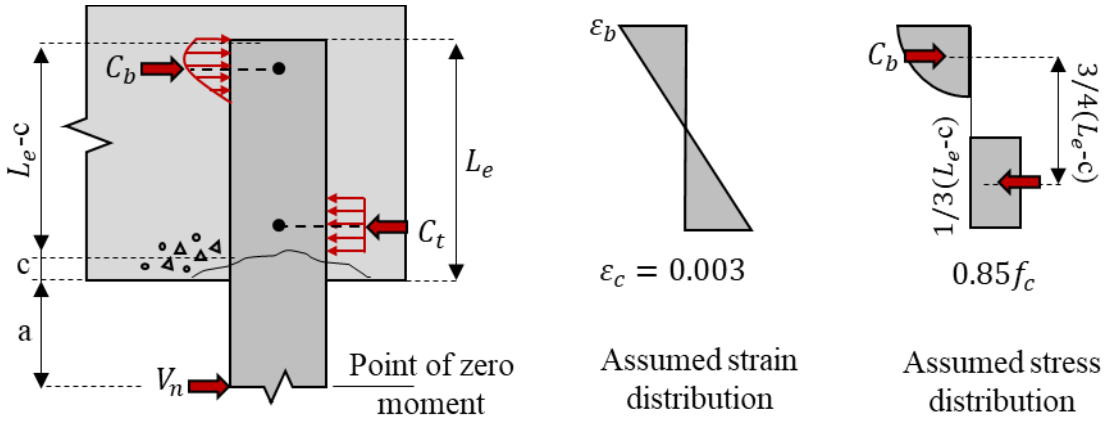

Figure 5.77: Bearing stresses proposed by Mattock and Gaafar [74]

The top "column" force to use for the punching shear check can be found using this strain and stress distribution as shown in Equation 5.36, assuming *c* of 0 in. since no spalling was observed in SP-10.

Mattock and Gaafar: $$C_t = 0.85f'_c\left(\frac{1}{3}\right)L_e b$$ Equation 5.36

This equation can be slightly modified to include the α_1 factor from AASHTO LRFD BDS (§5.6.2.2) to give Equation 5.37.

Mattock and Gaafar modified by AASHTO LRFD BDS: $$C_t = \alpha_1 f'_c\left(\frac{1}{3}\right)L_e b$$ Equation 5.37

The α_1 could be found using the concrete strength for the pile cap. The punching shear demand forces using this procedure are summarized in Table 5.30.

Table 5.30: Punching shear force found using Equation 5.37

Specimen	L_e (in.)	b (in.)	f'_c (ksi)	α_1	C_t (kips)
SP-01	6.0	18.0	12.48	0.80	359.7
SP-02	6.0	18.0	12.36	0.80	357.3
SP-03	6.0	18.0	12.70	0.80	363.9
SP-04	9.0	18.0	11.93	0.81	522.7
SP-05	9.0	18.0	13.26	0.78	562.0
SP-06	12.0	18.0	11.40	0.82	674.7
SP-07	18.0	18.0	10.32	0.84	940.2
SP-08	27.0	18.0	12.57	0.80	1626.2
SP-09	12.0	30.0	9.37	0.85	955.2
SP-10	30.0	30.0	8.95	0.85	2283.2

One issue with this approach is that it assumes that the concrete next to the embedded pile crushes, which may not occur depending on the capacity of the embedded pile. An alternate approach would be to use a modified compression block like that discussed in Collins and

Mitchell [75] and used by Belarbi et al. [76] that considers the stress block shape when the extreme compression fiber does not crush, shown in Equation 5.38 through Equation 5.40.

Belarbi et al. [76]: $$\beta_1 = \frac{4 - \frac{\varepsilon_{cc}}{\varepsilon'_c}}{6 - 2\left(\frac{\varepsilon_{cc}}{\varepsilon'_c}\right)}\left(1.1 - \frac{f'_c}{50}\right) \geq 0.65$$ Equation 5.38

Belarbi et al. [76]: $$\alpha_1 = \left(\frac{1}{\beta_1}\right)\left(\frac{\varepsilon_{cc}}{\varepsilon'_c} - \frac{1}{3}\left(\frac{\varepsilon_{cc}}{\varepsilon'_c}\right)^2\right)\left(1 - \frac{f'_c}{60}\right)$$ Equation 5.39

Belarbi et al. [76]: $$\varepsilon'_c = \left(1.6 + \frac{f'_c}{11}\right) * 10^{-3}$$ Equation 5.40

where:

ε_{cc} = compressive concrete strain at the flexural compressive face (face of the embedment for this connection

The assumed strain distribution and stress block with these assumptions is shown in Figure 5.78.

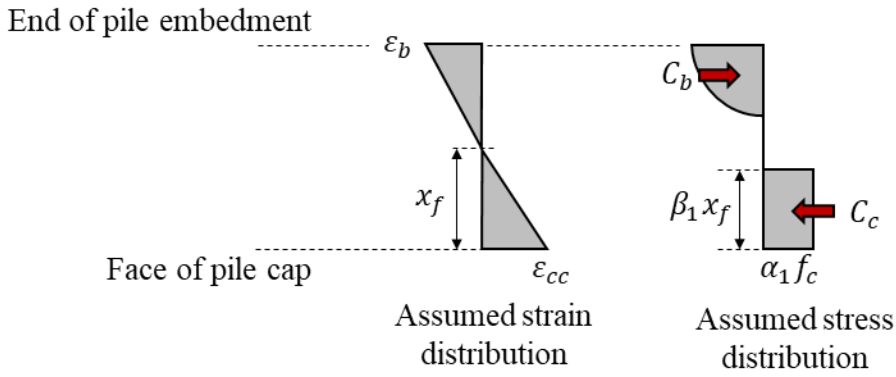

Figure 5.78: Assumed strain distribution and stress block for pile embedment

The assumed compression block force is shown in Equation 5.41. The compression block depth can be assumed to be the same depth as was proposed by Mattock and Gaafar [74], shown in Figure 5.77 and Equation 5.42.

Assumed Compression Block Force: $C_t = (\alpha_1 f_c)(\beta_1 x_f)b$ Equation 5.41

Assumed Compression Block Depth: $\beta_1 x_f = {}^{L_e}/_{3}$ Equation 5.42

The maximum compressive strains on the face of the pile cap were measured during testing. The maximum measured strain was used to find the compression block using the equation above. Examples of the plots used to determine the top fiber strains are shown in Figure 5.79.

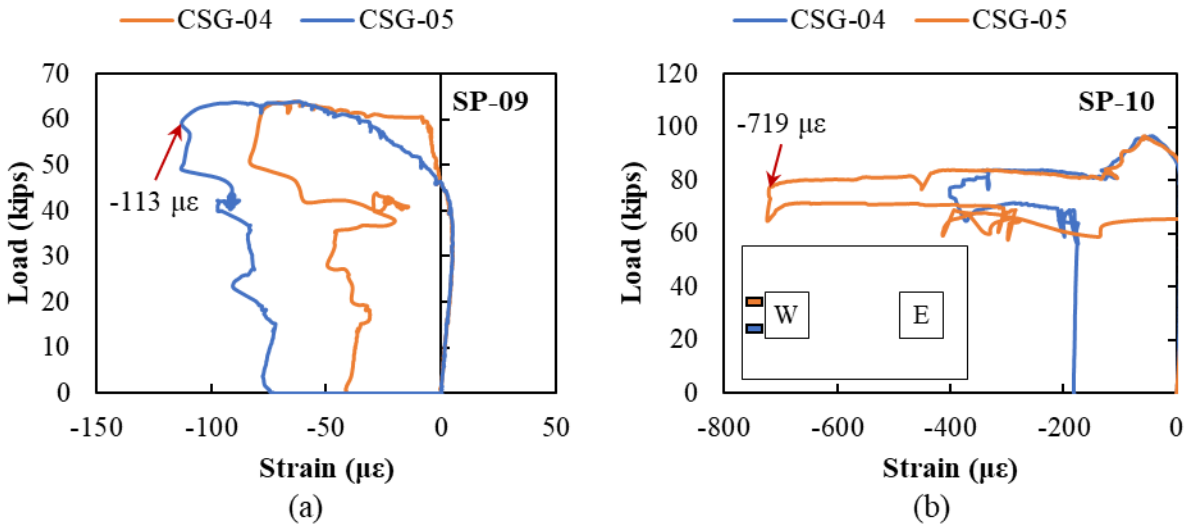

Figure 5.79: Measured compression strains on outside edge of pile caps for (a) SP-09 and (b) SP-10

The maximum measured strains for each specimen and the compression block force found using Equation 5.41 and Equation 5.42 are summarized in Table 5.31.

Table 5.31: Measured compression strains in pile cap face and associated compression block force for punching shear demand estimation

Specimen	f'_c (ksi)	ε_{cc} (με)	β_1	α_1	$\beta_1 x_f$ (in)	C_t (kips)
SP-01	12.48	80	0.65	0.008	2.00	3.6
SP-02	12.36	78	0.65	0.008	2.00	3.5
SP-03	12.70	140	0.65	0.014	2.00	6.3

Specimen	f'_c (ksi)	ε_{cc} (με)	β_1	α_1	$\beta_1 x_f$ (in)	C_t (kips)
SP-04	11.93	15	0.65	0.002	3.00	1.0
SP-05	13.26	20	0.65	0.002	3.00	1.4
SP-06	11.40	63	0.65	0.007	4.00	5.5
SP-07	10.32	128	0.65	0.014	6.00	16.0
SP-08	12.57	53	0.65	0.005	9.00	10.8
SP-09	9.37	113	0.65	0.013	4.00	15.1
SP-10	8.95	719	0.65	0.080	10.00	214.6

The C_t force found in Table 5.31 is the assumed punching shear demand, shown in Equation 5.43.

Punching Shear Demand: $$V_u = C_t = (\alpha_1 f_c)\left({}^{L_e}/_{3}\right) b$$ Equation 5.43

- Estimated Punching Shear Capacity

The punching shear capacity is typically found based on the critical shear perimeter, b_0, as shown in Figure 5.80 (a). The critical shear perimeter is based on the effective shear depth, d_v, or the distance between the compression face and centroid of the tension reinforcement. For a column located along the edge of the slab, the critical shear perimeter would be found as shown in Figure 5.80 (b). The punching shear capacity of the edge of the pile cap is assumed to have a critical shear perimeter as shown in Figure 5.80 (c) based on the width of the embedded pile, the edge distance, and the height of the compression block from Mattock and Gaafar [74] shown in Figure 5.77.

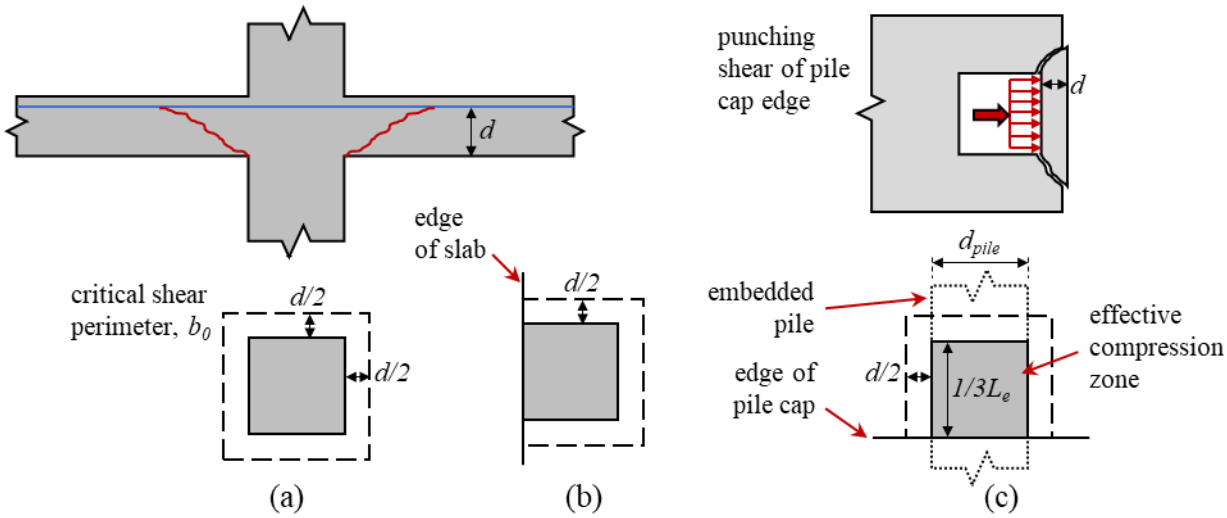

Figure 5.80: Typically assumed punching shear cracking and critical shear perimeter for (a) interior column and (b) edge column and (c) typical punch shear theory extended to embedded pile and pile cap edge

According to AASHTO LRFD BDS §5.7.2.8, the effective shear depth, d_v, is taken as the distance, measured perpendicular to the neutral axis, between the resultants of the tensile and compressive forces due to flexure; it need not be taken to be less than the greater of $0.9d_e$ and $0.72h$. This can conservatively be taken as $0.72h$ to be independent of the reinforcement provided in the edge of the pile cap, where h is equal to the edge distance.

With these assumptions, the critical shear perimeter can be found using Equation 5.44.

Assumed critical shear perimeter:

$$b_0 = \frac{3}{2}(0.72h) + d_{pile} + \frac{2}{3}L_e \qquad \text{Equation 5.44}$$

The estimated punching shear strength, of two-way action, for footings was calculated following AASHTO LRFD BDS §5.12.8.6 [23]. For two-way action for sections with transverse reinforcement, the nominal shear resistance is found using Equation 5.45 through Equation 5.47.

AASHTO 5.12.8.6.3-2 $$V_n = V_c + V_s \leq 0.192\lambda\sqrt{f'_c}b_o d_v$$ Equation 5.45

In which:

AASHTO 5.12.8.6.3-3 $$V_c = 0.0632\lambda\sqrt{f'_c}b_o d_v$$ Equation 5.46

AASHTO 5.12.8.6.3-4 $$V_s = \frac{A_v f_y d_v}{s}$$ Equation 5.47

where:

b_o = perimeter of the critical section for shear (in)

d_v = effective shear depth (in)

λ = concrete density modification factor

The amount of reinforcement to include in the punching shear resistance provided by the steel, Equation 5.47, is determined based on the transverse reinforcement provided in a slab. The reinforcement provided in the 30-inch pile cap is shown in Figure 5.81. The transverse reinforcement for the punching shear cone is the #9 bars labeled Bar 2A and shown in Figure 5.81 (b).

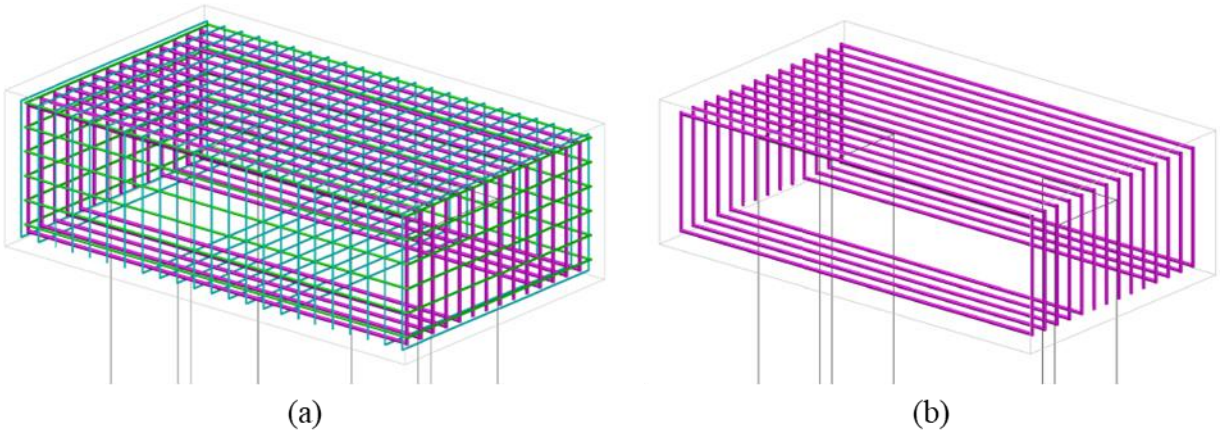

Figure 5.81: Reinforcement in 30-inch pile caps, (a) all reinforcement and (b) Bar 2A (#9 bars) rebar provided

It is assumed that there are two (2) #9 bars on each side of the 18-inch pile and three (3) #9 bars on each side of the 30-inch pile that engage the punching shear crack. These bars are assumed to be the transverse reinforcement provided in the punching shear cone with a width equal to the pile width plus two times the edge thickness, as shown in Figure 5.82.

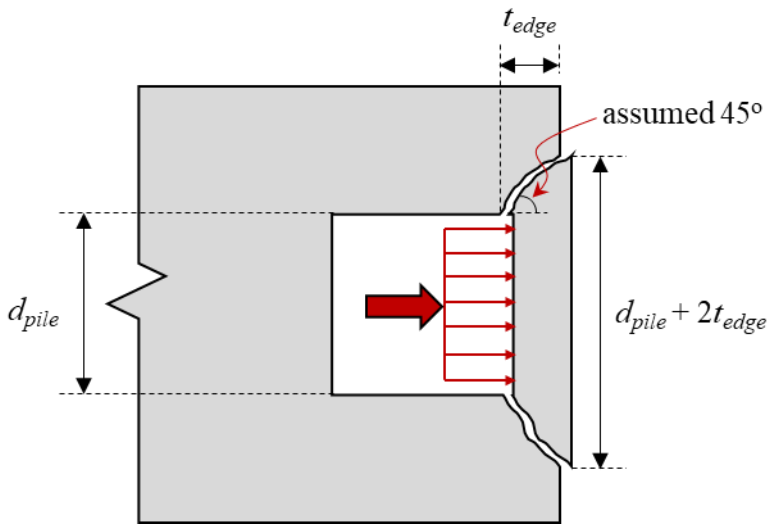

Figure 5.82: Assumed 45-degree spread for punching shear failure

The punching shear capacity can be found using Equation 5.45 through Equation 5.47. The concrete component and upper limit for the punching shear capacity for all experimental specimens are summarized in Table 5.32.

Table 5.32: Concrete component of punching shear capacity for edge of pile cap

Specimen	f'_c (ksi)	λ	t_{edge} (in)	d_v (in)	b_0 (in)	V_c (kips)	$V_{n,upper}$ (kips)
SP-01	12.5	1.0	9.0	6.48	31.72	45.90	139.4
SP-02	12.4	1.0	9.0	6.48	31.72	45.67	138.8
SP-03	12.7	1.0	9.0	6.48	31.72	46.29	140.6
SP-04	11.9	1.0	9.0	6.48	33.72	47.69	144.9
SP-05	13.3	1.0	9.0	6.48	33.72	50.29	152.8
SP-06	11.4	1.0	9.0	6.48	35.72	49.39	150.0
SP-07	10.3	1.0	9.0	6.48	39.72	52.25	158.7
SP-08	12.6	1.0	9.0	6.48	45.72	66.38	201.7
SP-09	9.4	1.0	15.0	10.80	54.20	113.21	343.9
SP-10	9.0	1.0	15.0	10.80	66.20	135.21	410.8

The steel component of punching shear resistance, nominal capacity, and demand are summarized in Table 5.33.

Table 5.33: Steel component and nominal punching shear capacity for edge of pile cap

Specimen	A_v (in^2)	A_v/s (in)	f_y (ksi)	V_s (kips)	V_n (kips)	V_u (kips)
SP-01	4.00	0.11	60.0	43.2	89.1	3.6
SP-02	4.00	0.11	60.0	43.2	88.9	3.5
SP-03	4.00	0.11	60.0	43.2	89.5	6.3
SP-04	4.00	0.11	60.0	43.2	90.9	1.0
SP-05	4.00	0.11	60.0	43.2	93.5	1.4
SP-06	4.00	0.11	60.0	43.2	92.6	5.5
SP-07	4.00	0.11	60.0	43.2	95.5	16.0
SP-08	4.00	0.11	60.0	43.2	109.6	10.8

Specimen	A_v (in^2)	A_v/s (in)	f_y (ksi)	V_s (kips)	V_n (kips)	V_u (kips)
SP-09	6.00	0.10	60.0	64.8	178.0	15.1
SP-10	6.00	0.10	60.0	64.8	200.0	214.6

The only specimen where the punching shear demand exceeded the capacity is SP-10, which is consistent with the observations from experimental testing.

- Limitations with Approach

The measured top fiber concrete strain was used in the procedure described in § to determine the punching shear demand. The demand values found assuming that the concrete crushes and top fiber strain is 0.003 are shown in Table 5.30. It would seemingly be excessive to design based on these values.

5.10.2.3. Effect of Axial Load

Two of the specimens had applied axial load with embedment lengths of 6 inches (SP-02) and 9 inches (SP-05). The total axial load applied for each specimen was 194 kips per pile. The procedure for applying the axial load to the piles is presented in §5.7.

Failure of SP-02 and SP-05 was caused by strand development failure. Failure of SP-02 is shown in Figure 5.83; the failure of SP-02 was like that of SP-05. Damage occurred in the compression zone of the embedded piles with axial force as the hinge developed in the base of the pile near the pile cap, as shown in Figure 5.83 (b).

(a) (b)

Figure 5.83: Photographs after failure of SP-02.

The moment versus displacement responses for the specimens with axial load (SP-02 and SP-05) and the similar specimens without axial load (SP-01 and SP-04) are shown in Figure 5.84. SP-02 which had the same embedment length as SP-01 developed a moment of 244.6 k-ft, which corresponds to 74% of the 18-inch pile capacity. SP-05, with the same embedment length as SP-04 developed 246.2 k-ft, around 74% of the 18-inch pile capacity. The application of the $0.05f'_cA_g$ axial load led to an increased average connection capacity of 107%.

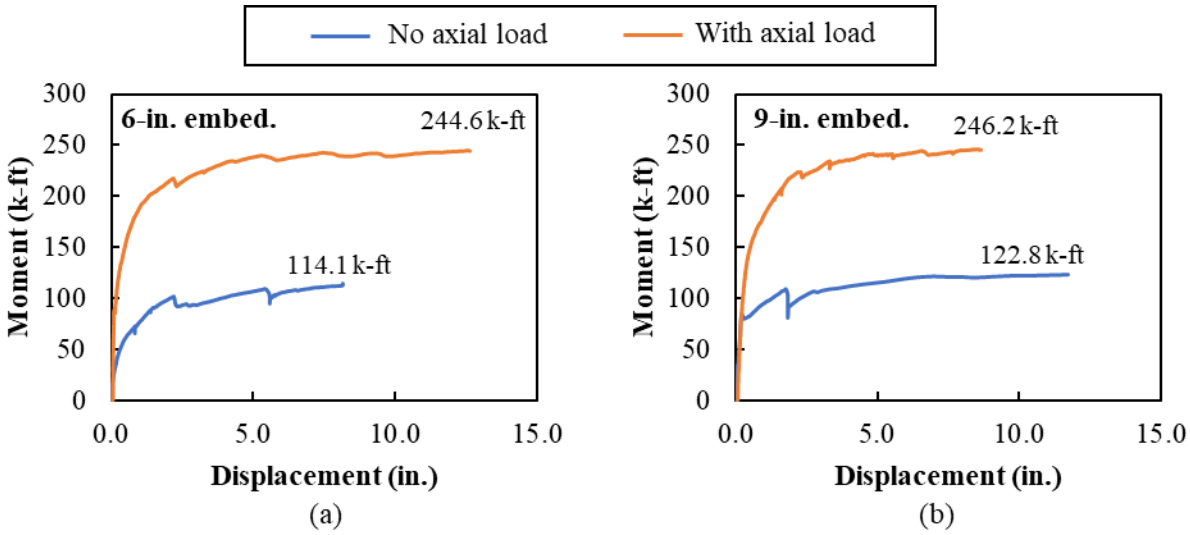

Figure 5.84: Moment-displacement for specimens with axial load (a) 6-inch embedment length, (b) 9-inch embedment length

The moment-curvature plots for 18-inch and 30-inch piles with varying levels of axial force assuming the full development of the strands were found using RESPONSE2000, as shown in Figure 5.85. These curves were found using the measured compressive strength and the strand configuration used in the constructed piles. The axial load levels shown correspond to $0A_g f'_{c,pile}$, $0.05A_g f'_{c,pile}$, and $0.10A_g f'_{c,pile}$, with the $0.05A_g f'_{c,pile}$ for the 18-inch pile being equal to the actual axial load applied.

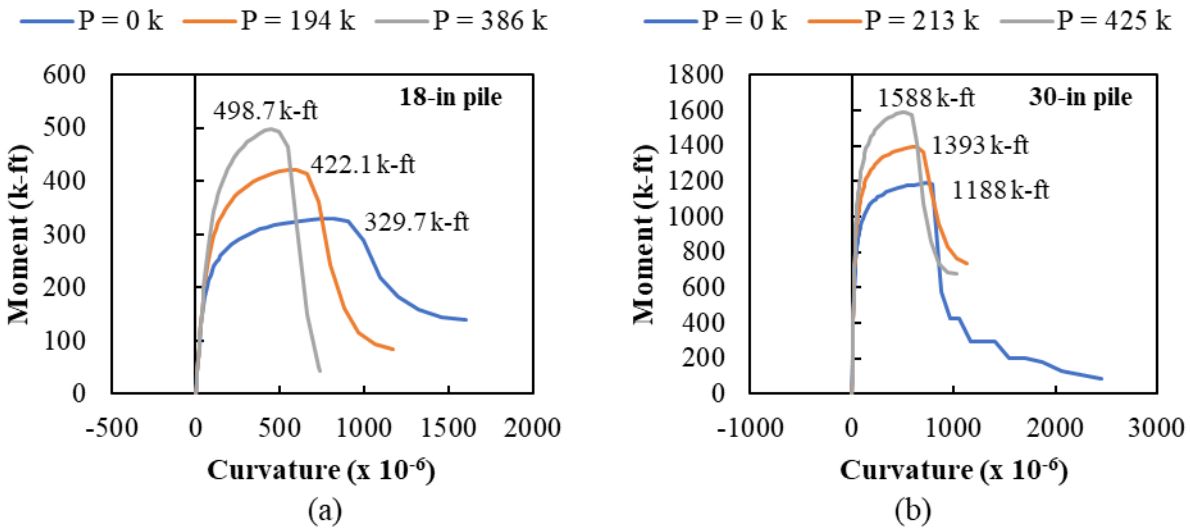

Figure 5.85: Moment versus curvature plots for (a) 18-inch and (b) 30-inch piles with different levels of applied axial load

The maximum moment and slipping stress for these specimens is summarized in Table 5.34. From RESPONSE2000 assuming fully developed strands, the increase in capacity from 0 kips to 194 kips of axial load for the 18-inch pile was 329.7 kip-ft to 422.1 kip-ft (28% increase). This is less than the average 107% increase in capacity of the connection observed through the experimental testing. The application of axial force had a much larger impact on the strength of the piles when the strands were not fully developed. The slipping stress found from the experimental results was not influenced significantly by the application of the axial force (an average 4% increase). The estimated slipping stresses using AASHTO LRFD BDS [23] and ElBatanouny and Ziehl [67] is not affected by an applied axial force.

Table 5.34:Maximum moment and slipping stress (experimental, AASHTO LRFD BDS, ElBatanouny and Ziehl)

Spec.	Experimental		AASHTO LRFD			Elbatanouny and Ziehl		
	Slipping stress (ksi) [1]	*Max. moment (k-ft)*	*Slipping stress (ksi)*	*Max. moment (k-ft)* [2]	*Meas./ Est.*	*Slipping stress (ksi)*	*Max. moment (k-ft)* [2]	*Meas./ Est.*
SP-01	81.0	114.1	35.2	50.5	2.26	57.7	82.4	1.38
SP-02	86.0	244.6	35.2	182.5	1.34	57.7	210.4	1.16
SP-04	87.0	122.8	52.8	75.0	1.64	86.5	121.9	1.01
SP-05	88.0	246.2	52.8	204.8	1.20	86.5	244.9	1.01

[1] Experimental slipping stress was determined using maximum moment developed by specimen into RESPONSE.

[2] Maximum moment was determined using value of slipping stress into RESPONSE.

Larger transverse tensile strains were measured in the pile cap for the members with axial force, likely a result of there being a larger moment capacity of the connection. An example of the larger observed concrete strains is shown in Figure 5.86.

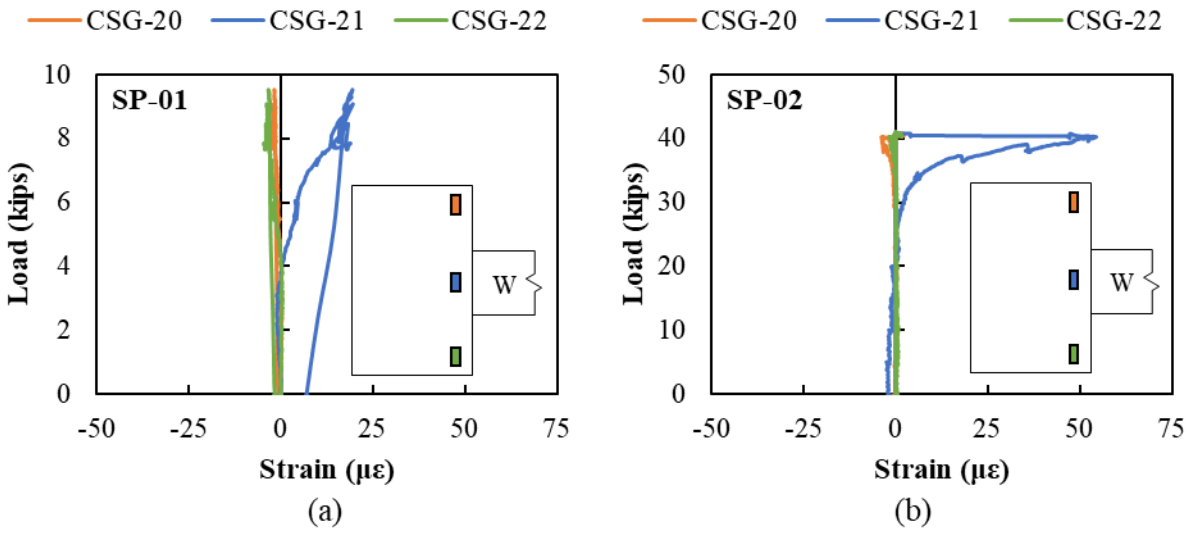

Figure 5.86: Measured concrete strains on the west side face of the pile cap in (a) SP-01 and (b) SP-02 with 6-inch pile embedment lengths

Larger strains were also measured in the reinforcement in the pile cap for the specimens with axial force, also likely a result of the higher moment capacity of the connection with axial force. An example of the measured rebar strains for specimens with and without axial force and 6-inch pile embedment is shown in Figure 5.87.

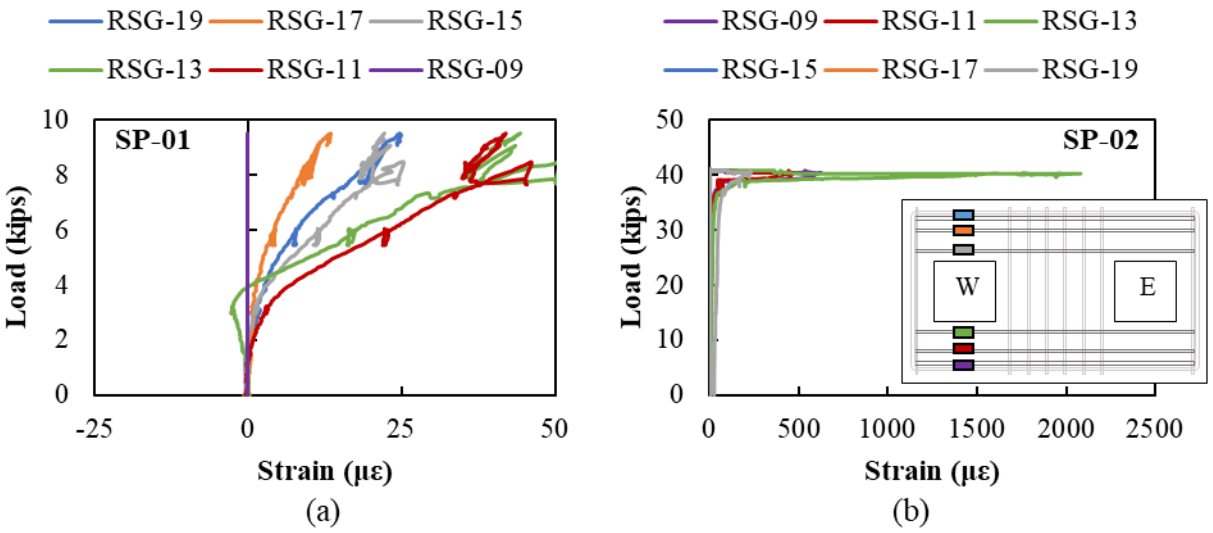

Figure 5.87: Measure pile cap longitudinal reinforcement strain for (a) SP-01 and (b) SP-02 with 6-inch pile embedment lengths

In general, a small axial compression force greatly increased the capacity of the connection; an average 107% increase in capacity of the connection was observed when $0.05A_g f'_{c,pile}$ axial compression was applied to the pile and connection.

5.10.3. Effect of Interface Reinforcement

Interface reinforcement was provided in one specimen (SP-03) with the same 6-inch embedment as SP-01 without interface reinforcement. The details for the interface reinforcement, based on Larosche et al. [77], are shown in Figure 5.88. Four #6 bars were embedded 24 inches in the ends of the piles during pile casting. The bars extended 12 inches into the pile cap with 9-inch hooks on the ends.

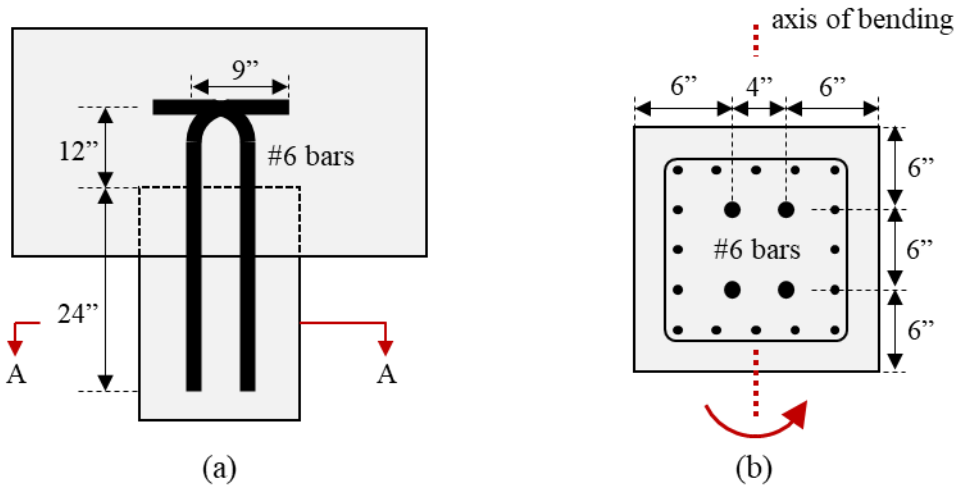

Figure 5.88: Details of interface reinforcement for SP-03, (a) elevation and (b) Section A-A

Photographs from failure of SP-03 are shown in Figure 5.89. Two cracks developed in SP-03 during failure: one at the pile-to-cap connection and a second at the location where the interface reinforcement ended (24 inches from the end of the pile and 18 inches from the pile cap face). A strand development failure was defined for SP-02. Significant cracking of the pile cap was also observed in this specimen and spalling of concrete around the embedded piles.

(a) (b)

Figure 5.89: Photographs of the failure of SP-03

The two large cracks during failure were also observed in the fiber optic sensors, shown in Figure 5.90 with the location of the two increases in strain coinciding with the location of the pile cap face and end of the interface reinforcement.

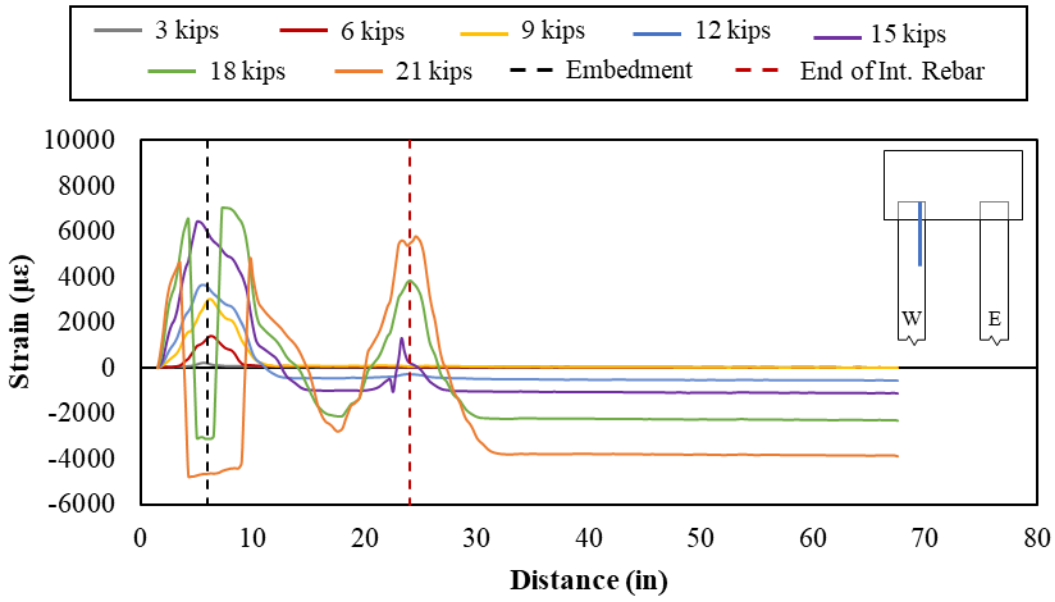

Figure 5.90: Strains along the east side of the west pile measured by FOS for SP-03

The available development length would be the distance between the end of the pile and the failure crack. Since there were two large cracks that developed during failure, the available development length could have been 6 inches (to the pile-to-cap interface) or 24 inches (to the end of the interface reinforcement). The estimated slipping stresses using ElBatanouny and Ziehl [67] for each of the assumed available development lengths and the corresponding moment capacity found from RESPONSE are summarized in Table 5.35. The analysis of the section at the interface (with 6-inch development length) included the interface reinforcement. The analysis of the section at the end of the interface reinforcement (with 24-inch development length) did not include the interface reinforcement. Using an available development length of 6-inches and including the interface reinforcement resulted in a lower estimated moment capacity and one that was closer to the actual measured moment capacity of the connection. For design of connections with interface reinforcement, it is recommended to use the minimum of these two capacities to estimate the strength of the connection.

Table 5.35: Maximum moment and slipping stress (experimental and ElBatanouny and Ziehl)

Spec.	**Assumed $l_{d,avail.}$ (in)**	**Experimental**		**Elbatanouny and Ziehl**		
		Slipping stress (ksi) [1]	*Max. moment (k-ft)*	*Slipping stress (ksi)*	*Max. moment (k-ft)* [2]	*Meas./ Est.*
SP-01	6.0	81.0	114.1	57.7	82.4	1.38
SP-03a	6.0	80.0	190.8	57.7	163.0	1.17
SP-03b[3]	24.0			196.6	260.2	0.73

[1] Experimental slipping stress was determined using maximum moment developed by specimen into RESPONSE.

[2] Maximum moment was determined using value of slipping stress into RESPONSE.

[3] Analysis of this point did not include the interface reinforcement because the section being analyzed is right at the end of the reinforcement

The moment versus displacement response for SP-01 (without interface reinforcement) and SP-03 (with interface reinforcement) is shown in Figure 5.91. The specimen with the interface reinforcement (SP-03) developed a moment capacity 67% higher than the similar specimen without interface reinforcement (SP-01), both with 6-inch pile embedment lengths. The capacity of SP-01 corresponded to 34% of the 18-inch pile capacity SP-03 with 58% of the 18-inch pile capacity. The test for SP-01 needed to be stopped due to running out of stroke in the hydraulic jack. It is not clear from testing that the presence of the interface reinforcement affected the rotational capacity of the connection.

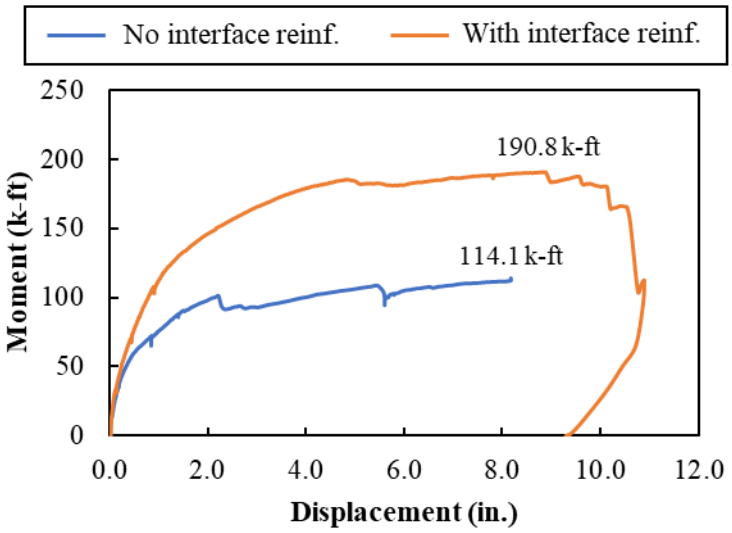

Figure 5.91: Moment versus displacement curves for 18-inch pile with 6-inch embedment with and without interface reinforcement

The reinforcement in the pile cap was significantly more engaged for SP-03 compared to SP-01, as shown in Figure 5.92 through Figure 5.94. The transverse reinforcement in SP-03 toward the center of the pile cap was more engaged than any other specimen and had

larger strains than reinforcement toward the outside face of the pile cap, see Figure 5.92 (b).

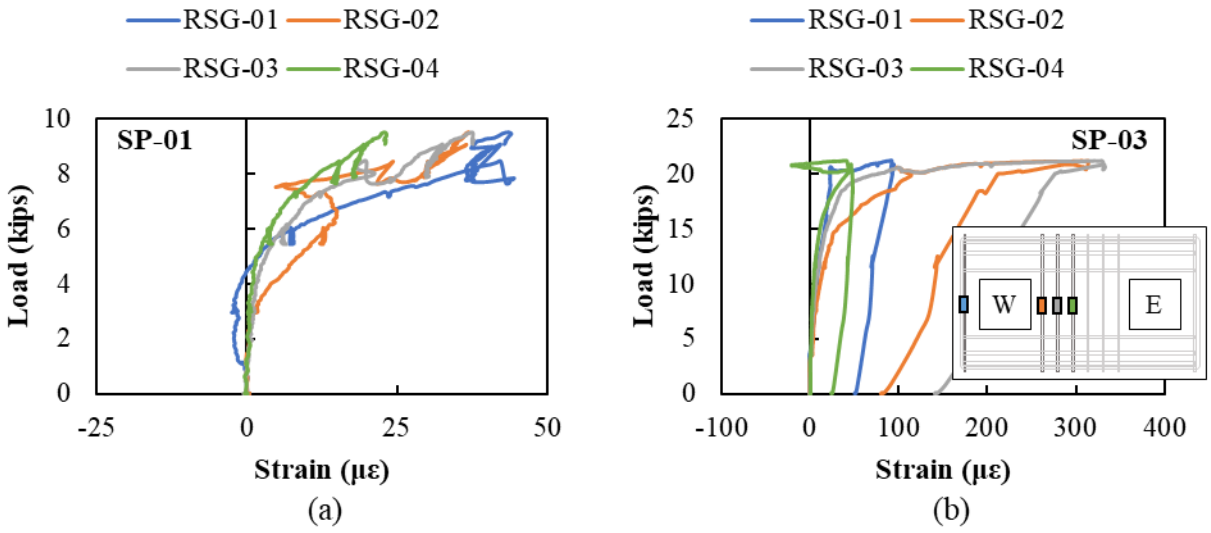

Figure 5.92: Load versus rebar strain for transverse pile cap reinforcement in the connection face for (a) SP-01 and (b) SP-03

The longitudinal reinforcement in the pile cap was also more engaged in SP-03 than SP-01, see Figure 5.93. The strains in SP-03 were highest in the longitudinal reinforcement immediately adjacent to the embedded pile.

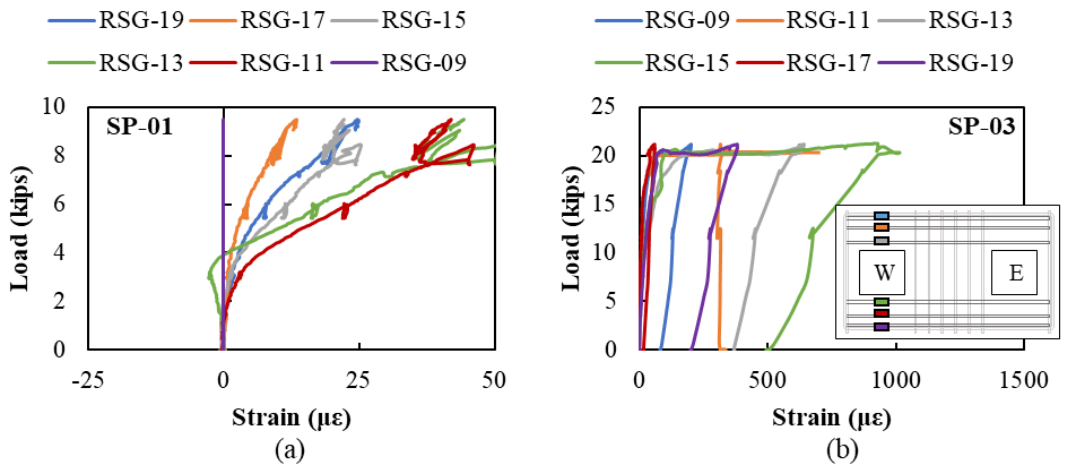

Figure 5.93: Load versus rebar strain for longitudinal pile cap reinforcement in the connection face for (a) SP-01 and (b) SP-03

The pile cap reinforcement along the west side face was also more engaged in SP-03 than SP-01, see Figure 5.94. The reinforcement strains are greater toward the face of the pile cap with the embedded pile.

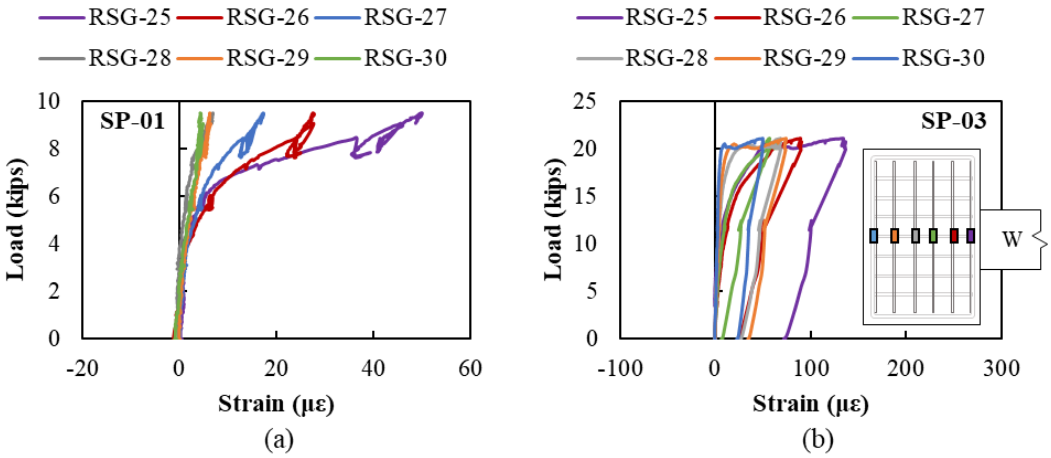

Figure 5.94: Load versus rebar strain for transverse pile cap reinforcement in the west side face for (a) SP-01 and (b) SP-03

The curvature found using the crack displacement transducers (CDT) was generally minimal. This was a result of the failure crack in the specimens typically occurring at the interface, which was outside of the CDT closest to the interface. The measured moment-

curvature response with CDTs for most specimens resembled the response shown for SP-01 in Figure 5.95 (a). A large crack occurred in SP-03 during failure within the range of a CDT, as shown in Figure 5.89. This led to a larger curvature being measured during testing, as shown in Figure 5.95 (a).

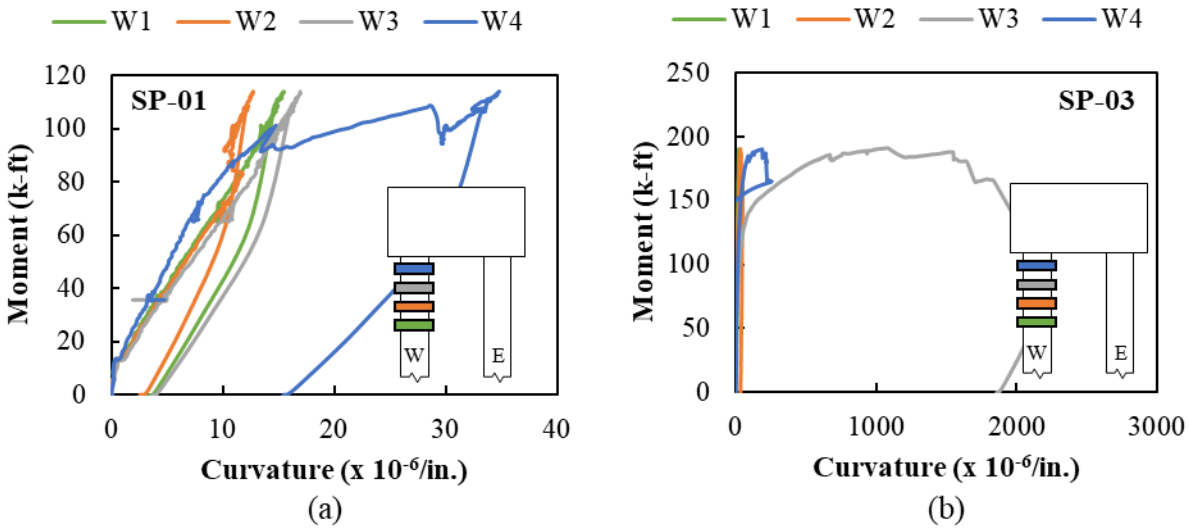

Figure 5.95: Moment versus curvature measured using the crack displacement transducers for (a) SP-01 and (b) SP-03

5.10.4. Effect of Pile Size

Two pile sizes were tested in the experimental program: 18-inch and 30-inch. Six of the specimens that can be used to compare the effect of pile size are summarized in Table 5.36. The piles with a similar embedment length had developed a similar percentage of the pile capacity, compare 12-inch embedment length for 18-inch and 30-inch piles (SP-06 and SP-09). The effect of the embedment length as a proportion of pile size did not seem to have a similar effect for 18-inch and 30-inch pile embedment specimens. This supports the idea that the capacity of the connection is dependent on the available development length and not necessarily the pile size.

Table 5.36: Effect of pile size summary of results

Specimen	Pile Size	Embedment Length	Pile Capacity (k-ft)	Max Moment Developed (k-ft)	% Of Pile Capacity	Failure Mechanism
SP-01	18”	6” ($0.33d_p$)	331.0	114.1	34%	Strand Development
SP-06	18”	12” ($0.67d_p$)	331.0	159.4	48%	Strand Development
SP-07	18”	18” ($1.00d_p$)	331.0	201.4	61%	Strand Development
SP-08	18”	27” ($1.50d_p$)	331.0	267.6	81%	Strand Development
SP-09	30”	12” ($0.40d_p$)	1188.5	574.6	48%	Strand Development
SP-10	30”	30” ($1.00d_p$)	1188.5	868.1	73%	Punching Shear

6. NUMERICAL STUDY

A numerical analysis was performed to validate the previous computational analysis with the experimental work and a preliminary study was developed to expand the computational study by investigating other variables that couldn't be tested in the experimental program.

6.1. VALIDATION OF THE PILE-TO-CAP MODEL

A non-linear finite element analysis software specifically designed for reinforced concrete structures, ATENA, was used to validate the specimens in the experimental matrix presented in Table 6.1. The program has detailed bond-slip models that are capable of capturing the slip of the prestressing strands, detailed interface material models, detailed concrete material models, and detailed crack patterns.

Table 6.1: Experimental matrix

Specimen No.	Pile Size	Embedment Length		Interface Reinforcement	Axial Load
1	18"	$0.33d_{pile}$	6.0"	w/o interface reinforcement	$0A_g f'_c$
2	18"	$0.33d_{pile}$	6.0"	w/o interface reinforcement	$0.1A_g f'_c$
3	18"	$0.33d_{pile}$	6.0"	w/interface reinforcement	$0A_g f'_c$
4	18"	$0.5d_{pile}$	9.0"	w/o interface reinforcement	$0A_g f'_c$
5	18"	$0.5d_{pile}$	9.0"	w/o interface reinforcement	$0.1A_g f'_c$
6	18"	$0.67d_{pile}$	12.0"	w/o interface reinforcement	$0A_g f'_c$
7	18"	$1.0d_{pile}$	18.0"	w/o interface reinforcement	$0A_g f'_c$
8	18"	$1.5d_{pile}$	27.0"	w/o interface reinforcement	$0A_g f'_c$
9	30"	$0.4d_{pile}$	12.0"	w/o interface reinforcement	$0A_g f'_c$
10	30"	$1.0d_{pile}$	30.0"	w/o interface reinforcement	$0A_g f'_c$

6.1.1. Boundary Conditions and Modeling Assumptions

6.1.1.1. Model Geometry

The geometry of the models was updated from the preliminary numerical study, based on the final test set up for the experimental program where a self-reacting frame with two piles embedded in one pile cap was used.

The geometry was first drawn in AutoCAD 3D. Typical models consisted of five 3D volume components (pile cap, two piles, and two plates) and 1D lines representing the rebar in the pile cap, and strands and wires in the pile, as shown in Figure 6.1 (a). After defining the geometry in AutoCAD 3D, each section was imported into ATENA, as shown in Figure 6.1(b).

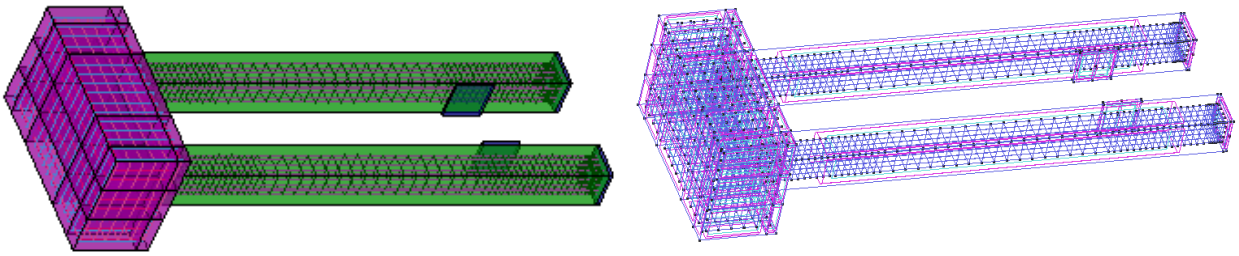

(a) (b)

Figure 6.1:Numerical models geometry (a) AutoCAD drawing (b) ATENA model

Interfaces were defined between volume elements with different materials that shared common surfaces. As an example, a fixed contact (Master-Slave) connection was defined between the concrete pile and elastic plate where load was applied.

The reinforcement scheme used in the typical pile-to-cap connection specimens is shown in Figure 6.2. The prestressing strands were ½" special strands with a diameter of 0.52

inches. Conventional reinforcement (#5, #6, #9 and W3.4 wire) was used in the piles and pile caps.

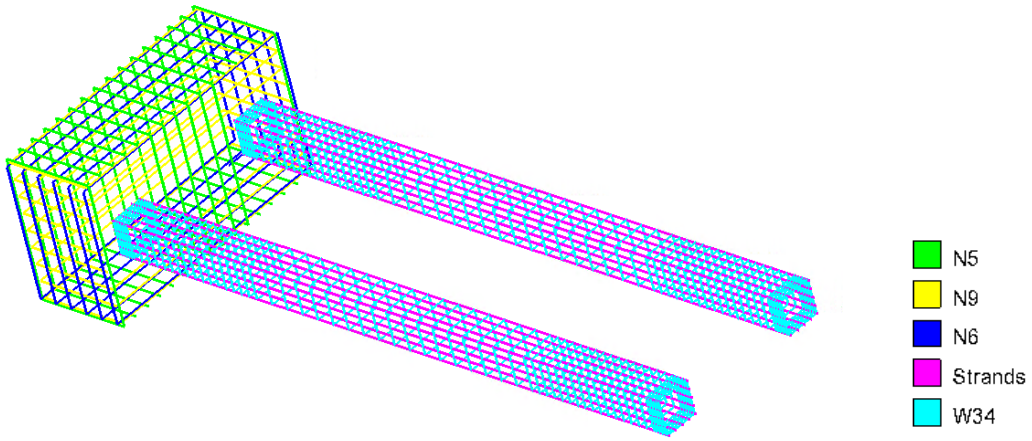

Figure 6.2: Reinforcement scheme in piles and pile cap

6.1.1.2. Material Assumptions

Three different materials were used for the analysis: (1) a solid concrete material for the pile and pile cap, (2) an elastic solid material for the plates, and (3) 1D reinforcement for the reinforcing bars and prestressing strands.

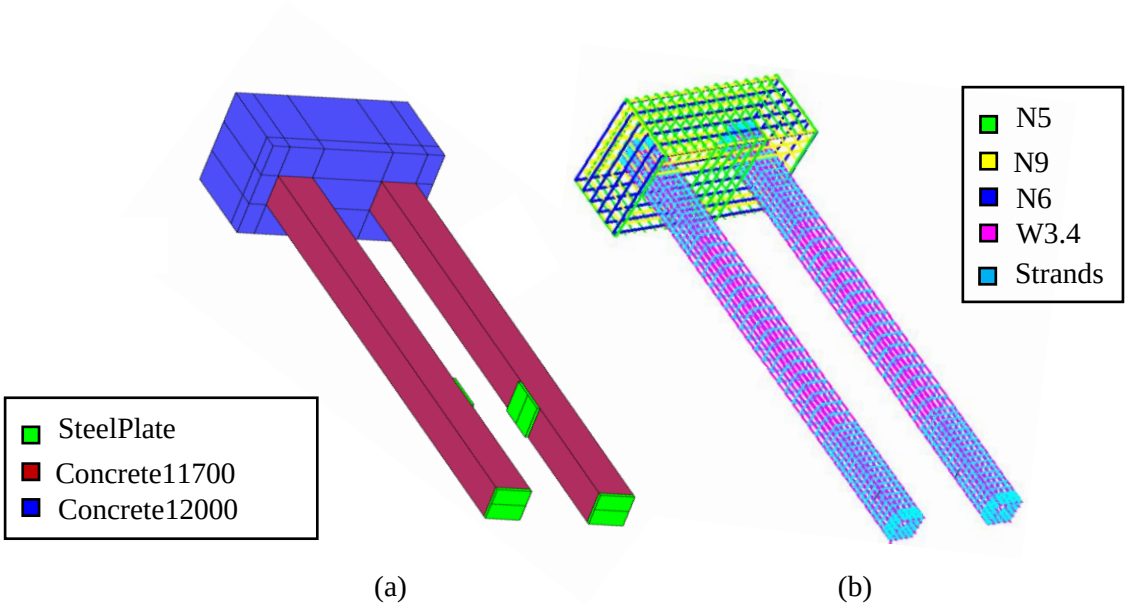

Figure 6.3: Material properties (a) solid materials (b) 1D reinforcement

A solid concrete material was defined for the piles and the pile cap. Concrete models were created based on the average concrete strengths at the time of testing for each element, parameters are shown in Table 6.2. Concrete 11,700 (which corresponds to a concrete strength of 11.7 ksi) was used in the piles and concrete 12,000 in the cap. The third concrete model shown was used to model the pile cap during the prestressing of the pile, so that the pile cap did not restrain the pile during the prestressing process (Concrete12000Soft).

Table 6.2: Material parameters of concrete

Material Parameter	**Concrete11700**	**Concrete12000**	**Concrete12000Soft**
Young's modulus (ksi)	6165.5	6244	1.45
Poisson's ratio	0.2	0.2	0.2
Tensile strength (ksi)	0.811	0.821	0.821
Compressive strength (ksi)	-11.7	-12.0	-12.0

The material used for the steel plates was generated using the Solid Elastic option with the properties shown in Table 6.3. Similar to the concrete, a soft elastic material with no stiffness was used for the steel plates during the prestressing of the piles.

Table 6.3: Material parameters of steel plates

Material Parameter	Steel Plate	Steel Plate Soft
Young's modulus [ksi]	29000	1.45
Poisson's ratio	0.3	0.3

The reinforcing steel in the pile cap (#5, #6, and #9 bars) and the W3.4 wires confining the strands in the piles were all modeled as 1D reinforcement with a yield strength (f_1) of 60 ksi, yield strain (ε_1) of 0.00207, an ultimate strength (f_2) of 90 ksi and a strain at ultimate strength (ε_2) of 0.025 with a stress-strain relationship similar to that shown in Figure 6.4 (a).

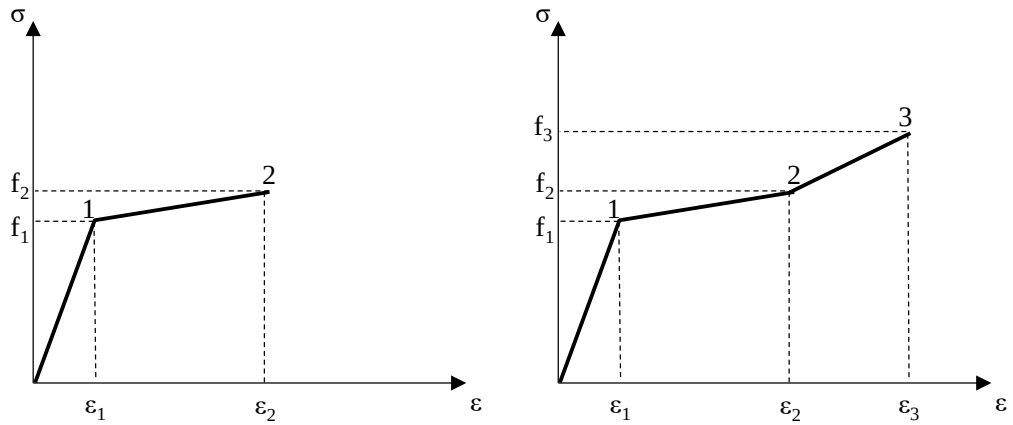

Figure 6.4: stress-strain relationship (a) reinforcing steel (b) strands

The prestressing strands were also created using the 1D reinforcement option, but with a tendon type option. The stress-strain relationship used for the prestressing strands is shown

in Figure 6.4 (b). The critical values used for this curve are the following: yield strength (f_1) of 204 ksi, yield strain (ε_1) of 0.007, second critical stress (f_2) of 243 ksi, second critical strain (ε_2) of 0.011, ultimate strength (f_3) of 270 ksi and strain at ultimate strength (ε_3) of 0.043. These values were roughly based on the Ramberg-Osgood stress-strain relationship.

The stress in the strands was applied as an Initial Strain Function. The strain was calculated considering the actual jacking force of 34 kips, the area of the strands, 0.167 in^2, and the experimental long term losses. A summary of the strains used with each pile size is shown in Table 6.4

Table 6.4: Strain in strands after losses

Pile Size	Initial stress in strands (ksi)	Total losses (ksi)	Stress in strands after losses (ksi)	Strain in strands
18-inch	203.6	25.76	177.84	0.00613
30-inch	203.6	15.7	187.9	0.00647

6.1.1.3. Bond-Slip Relationship of Strands

The bond-slip relationship of strands had an important influence on the pile-to-cap connection system. The bond-slip relationship is usually neglected and a perfect connection between the prestressed strands and the concrete is assumed in most nonlinear numerical analysis. For some cases, this approach is appropriate, but in the pile-to-cap connection system the effect of the bond slip could not be neglected. Numerical results obtained with a perfect bond in the strands for SP-01 are shown in Figure 6.5. A perfect bond-slip relationship of the strands developed a stiffer behavior in comparison with the experimental results.

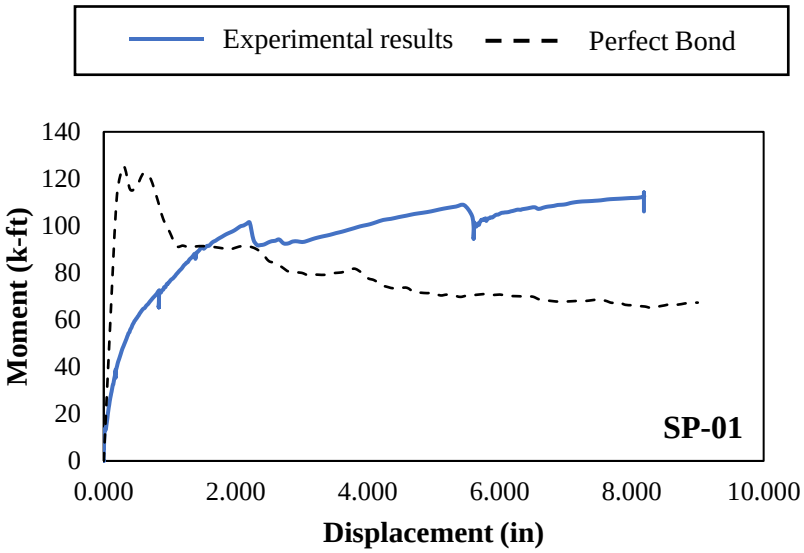

Figure 6.5: Moment-displacement curves for SP-01

A Reinforcement Bar with Bond was selected to model the prestressed strands, and CEB-FIB 1990 Model Code as the bond stress function. The bond-slip law is shown in Figure 6.6. This relationship defines the bond strength (cohesion) τ_b depending on the value of current slip between reinforcement and surrounding concrete. The laws are generated based on the concrete compressive strength, reinforcement diameter and reinforcement type.

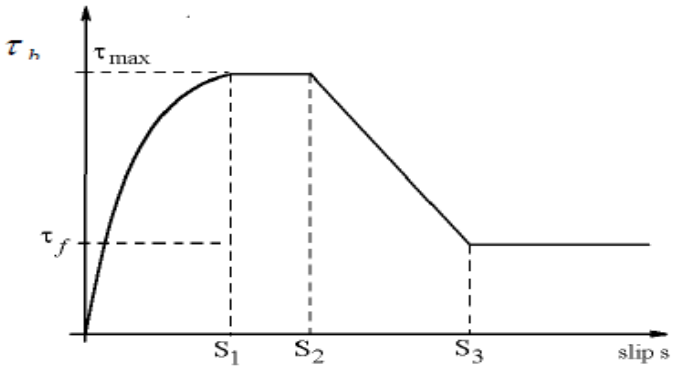

Figure 6.6: Bond-slip law by CEB-FIP model code 1990

The CEB-FIB Model Code consists of four different branches:

- an ascending curvilinear part, characterized by micro cracking and local crushing,
- a constant plateau to express crushing and shearing off of the concrete between the ribs, which occurs only in case of confined concrete,
- a descending branch which refers to a reduction in bond stress as concrete sheared off between the ribs,
- and a constant tail part indicating the frictional bond resistance.

The maximum bond strength and the frictional bond strength can be found using Equation 6.1 to Equation 6.4.

$$\tau_b = \tau_{max}\left(\frac{s}{s_1}\right)^{\alpha}, 0 \le s \le s_1 \quad \text{Equation 6.1}$$

$$\tau_b = \tau_{max}, s_1 < s \le s_2 \quad \text{Equation 6.2}$$

$$\tau_b = \tau_{max} - \left(\tau_{max} - \tau_f\right)\left(\frac{s - s_2}{s_3 - s_2}\right), s_2 < s \le s_3 \quad \text{Equation 6.3}$$

$$\tau_b = \tau_f, s_3 < s \quad \text{Equation 6.4}$$

The current CEB-FIB model automatically generated by ATENA is based on a stress-slip relationship for ribbed bars. Different studies have proposed stress-slip relationships for 7-wire strands. A modification of the CEB-FIB model is presented in this numerical analysis based on previous pull-out test and validation with the experimental work.

Two different bond models were created and validated for the specimens with deep and shallow embedment using Equation 6.1 to Equation 6.4. Parameters of the bond-slip

relationship are shown in Table 6.5. Specimens with an embedment length less than the pile diameter (SP-01 to SP-06) were considered shallow embedment, and specimens with an embedment length greater than the pile diameter (SP-07, SP-08), were considered deep embedment.

Table 6.5: Parameters for bond-slip relationship of strands for shallow and deep embedment models

Parameter	**Shallow embedment (Bond Model 1)**	**Deep embedment (Bond Model 2)**
S_1 (unit length)	4	4
S_2 (unit length)	5	5
S_3(unit length)	7	8
α	0.2	0.3
τ_{max} (ksi)	1.522	1.232
τ_f (ksi)	1.232	0.986

Bond-slip relationship models are shown in Figure 6.7.

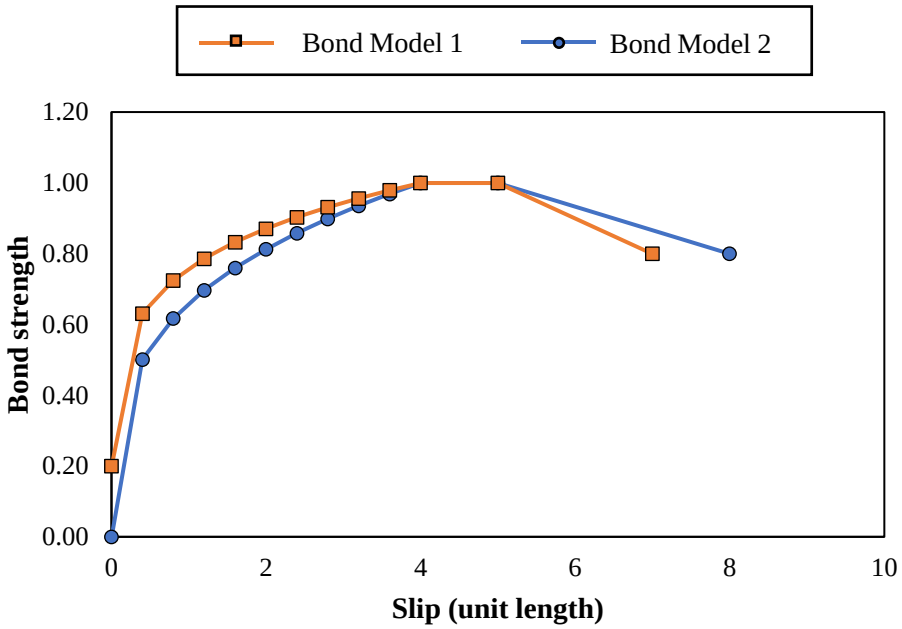

Figure 6.7: Bond-slip relationship of strands

6.1.1.4. Boundary Conditions

The experimental test setup was a self-reacting frame system with two piles, as shown in Figure 6.8. This frame was determined to be the simplest setup to be used and have the least impact on the pile-to-cap connection behavior. The piles were loaded from the inside located between 6 ft and 12 ft from the pile-to-cap interface.

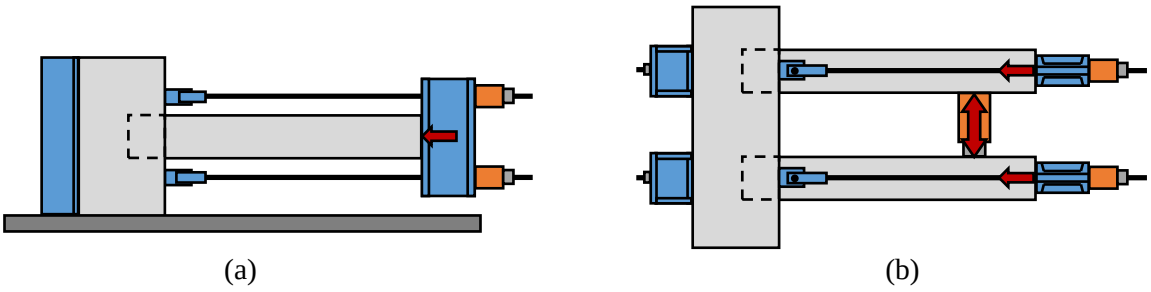

Figure 6.8: Test configuration used for modeling connection specimens

To create a fixed condition for the cap a constraint in the z direction was placed on the back of the pile cap (opposite to the pile); and a constraint in the x direction on the bottom of

the pile cap, as shown in Figure 6.9. These boundary conditions created a moment restrain in the pile cap similar to what was expected in the laboratory, with the bottom of the cap resting on the strong floor and the back fixed to a reaction frame.

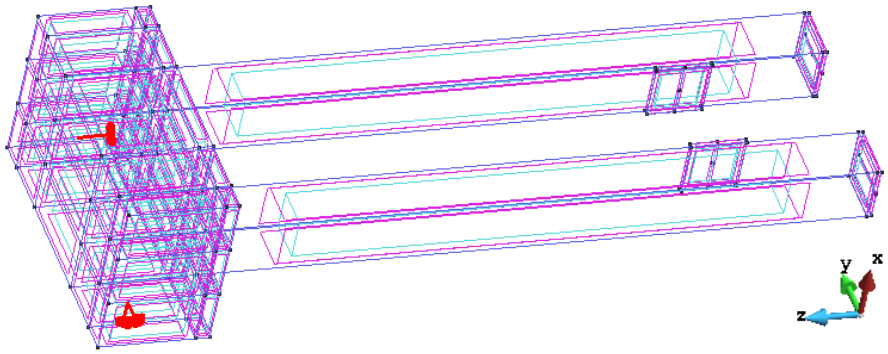

Figure 6.9: Boundary conditions

Boundary conditions are important parameter when defining the structure of the model, which showed to have a great impact in the stiffness of the model.

6.1.1.5. Load Protocol

A construction process was required to properly apply the prestressing and axial load in the piles before the lateral load was applied to fail the specimens. Three different loading stages were used, as shown in Figure 6.10, which are similar to how the specimens were loaded in the laboratory.

- *Load Stage #1*: prestrain applied to the prestressing strands
- *Load Stage #2*: axial load applied to the piles (if required)
- *Load Stage #3*: lateral load applied to piles until failure of system

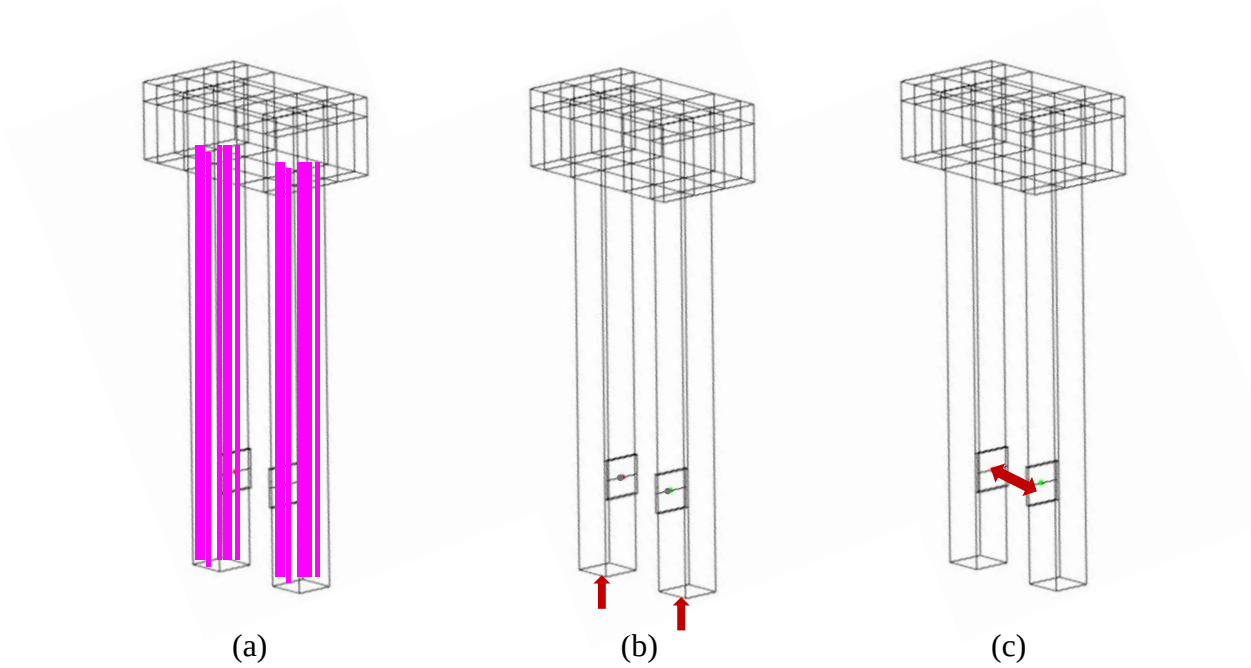

Figure 6.10: Load protocol (a) load stage #1 (b) load stage #2 (c) load stage #3

- *Load Stage #1*

The purpose of Load Stage #1 was to prestress the strands in the piles. The pile concrete strength was defined with typical stiffness. The pile cap concrete was specified with a stiffness close to zero, so the pile cap did not restrain the pile during prestressing. The total desired prestrain was applied to the piles in 10 steps. The pre-strain was locked in and kept constant at the end of this load stage.

- *Load Stage #2*

The purpose of Load Stage #2 was to apply the axial load to the pile in the complete system, if required. The "soft" materials were redefined with the material properties desired for the final test, as shown in Table 6.6. The axial load was applied to the end of the pile in 10

separate steps. The axial load was then kept constant on the pile at the end of this load stage.

Table 6.6: New material definitions for Load Stage #2

Old Material	New Material
Concrete12000 (Soft)	Concrete12000
SteelPlate (Soft)	SteelPlate

- *Load Stage #3*

The purpose of Load Stage #3 was to determine the moment capacity of the pile-to-cap connection by applying a lateral load until failure of the pile or connection. The prestrain in the pile prestressing strands and axial load in the pile were both kept constant during this load stage. Lateral load was applied, as shown in Figure 6.10 (c), by applying an additional small displacement for 90 steps. The maximum observed load was recorded as the failure load.

6.1.1.6. Finite Element Mesh

The finite element mesh had an important influence on the quality of the analysis results and speed of the numerical modeling. Linear elements were used for the 1D Reinforcement elements (strands and rebar in the pile cap).

Two variables were considered when creating a mesh for the 3D volumes (piles and pile cap): type and number of elements. The default mesh generated by ATENA is an unstructured mesh with hexahedra elements, as shown in Figure 6.11 (a). This mesh showed results 68% higher than the experimental results. A structure mesh was defined using tetrahedra elements, as shown in Figure 6.11 (b)

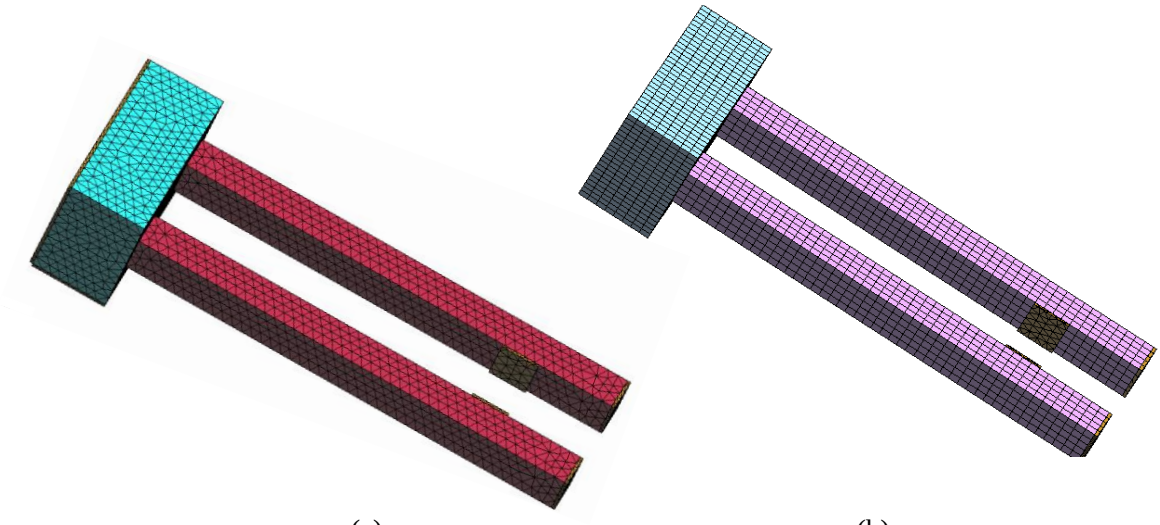

(a) (b)

Figure 6.11: Finite element mesh for pile-to-cap model (a) tetrahedra elements (b) hexahedra elements

Different mesh sizes were considered, as shown in Figure 6.12. The final mesh size was selected considering the time it took to process the numerical model and the percentage of error with the experimental results. For the 18-inch specimens a mesh size of 3 inches was selected, and for the 30-inch specimens a 5 inch mesh.

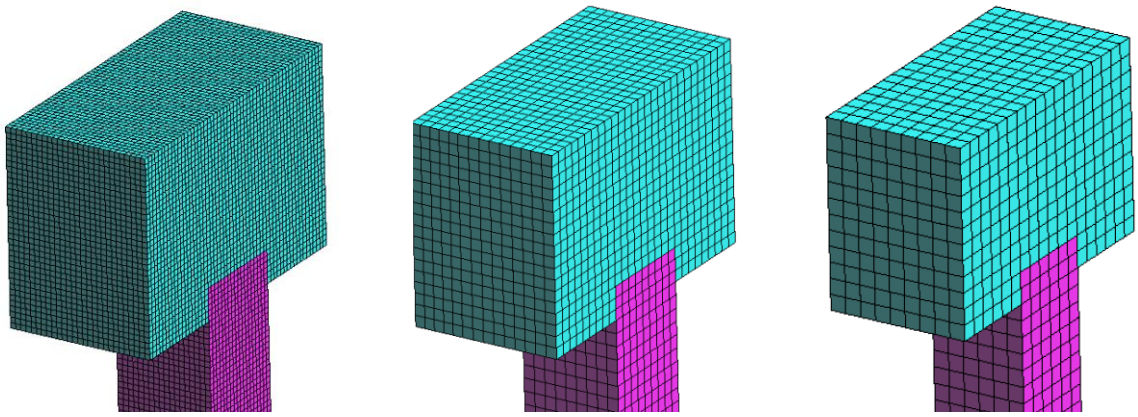

1 inch mesh
249,377 elements
(a)

2 inches mesh
37,965 elements
(b)

3 inches mesh
17,247 elements
(c)

Figure 6.12: Size of finite element mesh for the 18-inch pile-to-cap model (a) 1 inch (b) 2 inches (c) 3 inches

6.1.2. Numerical Results for Experimental Matrix

6.1.2.1. Moment-displacement

The first step to validate the pile-to-cap numerical models was to obtain the moment-displacement curves in ATENA and compared them with the results obtained in the experimental program. Different bond-slip relationship of strands, and mesh types were evaluated during this step. Final boundary conditions and modeling assumptions were previously described.

A summary of the numerical and experimental results for the 18-inch specimens without axial load or interface reinforcement is shown in Table 6.7. The maximum moment reached by the numerical model was recorded and compared to the experimental results. The average measured-to-estimate moment capacity ratio is 1.023, with standard deviation of 0.104, and coefficient of variation of 0.102.

Table 6.7:Summary of results for experimental and numerical study

Spec.	**Experimental**		**Numerical**		
	Failure Load (kips)	*Max. moment (k-ft)*	*Failure Load (kips)*	*Max. moment (k-ft)*	*Meas./ Est.*
SP-01	9.5	114.1	7.76	93.15	1.225
SP-04	13.6	122.8	14.40	126.23	0.973
SP-06	17.7	159.4	17.56	158.03	1.009
SP-07	33.6	201.4	36.23	217.75	0.933
SP-08	44.6	267.6	47.01	274.43	0.975
				Average =	1.023
				St. Dev. =	0.104
				Co. of Var. =	0.102

Numerical and experimental moment-displacement response for the 18-inch specimens without axial load or interface reinforcement are shown in Figure 6.13. The bond-slip model used in the strands showed a good relationship with the experimental program, with the specimens holding the load as the strand slip is occurring.

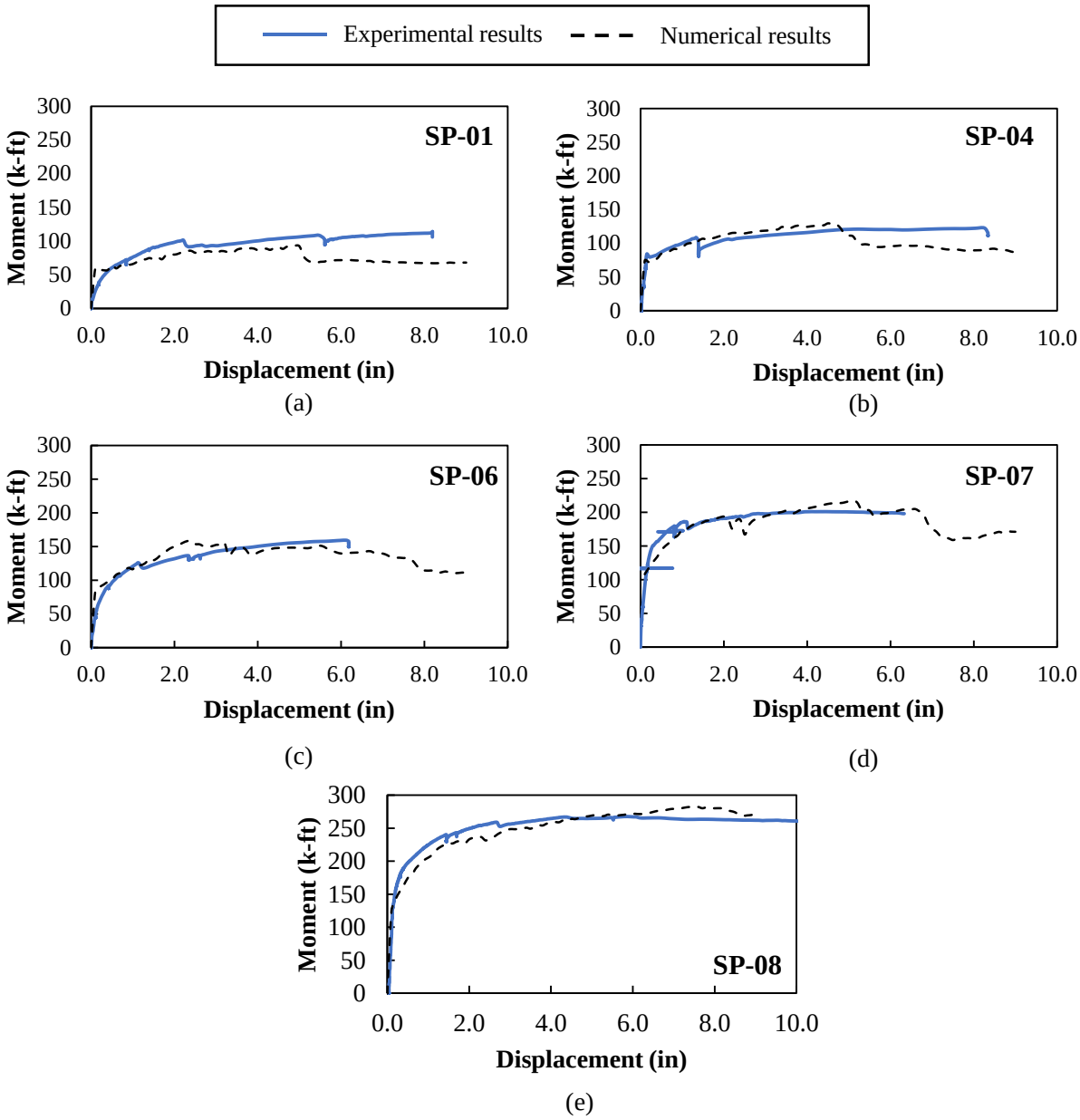

Figure 6.13: Moment-displacement response of pile-to-cap models for the 18-inch specimens

6.1.2.2. Crack pattern and Failure Mode

A realistic visualization of the crack pattern during different stages of the nonlinear analyses was obtained for the 18-inch specimens. In the experimental program a strand development failure was observed in all the 18-inch specimens with a large crack at the

base of the pile or near the pile-to-cap interface. A similar pattern was obtained in the numerical analyses.

In SP-01 strand development cracks developed in the tension zone of the piles at the maximum applied load, as shown in Figure 6.14 (a). In the numerical model this same pattern was observed, as shown in Figure 6.14 (b).

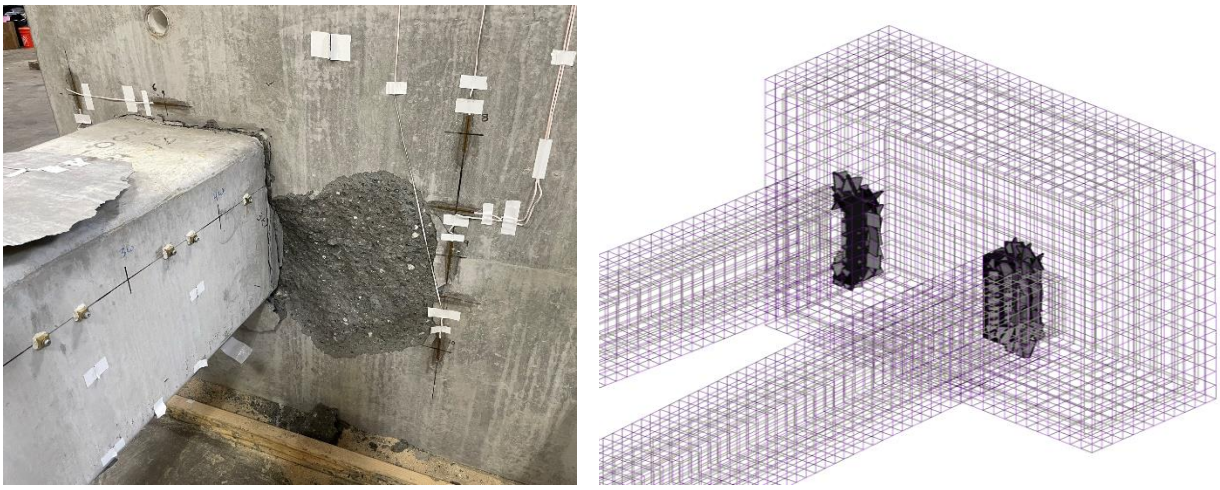

(a) (b)

Figure 6.14: Cracking pattern in SP-01 (a) experimental (b) numerical results

SP-07 and SP-08 with deeper embedment lengths, developed additional flexural cracks along the length of the pile. The crack pattern in the experimental program for SP-08 is shown in Figure 6.15 (a). The numerical analyses captured these cracks, right at the pile-to-cap interface and two in the piles, as shown in Figure 6.15 (b).

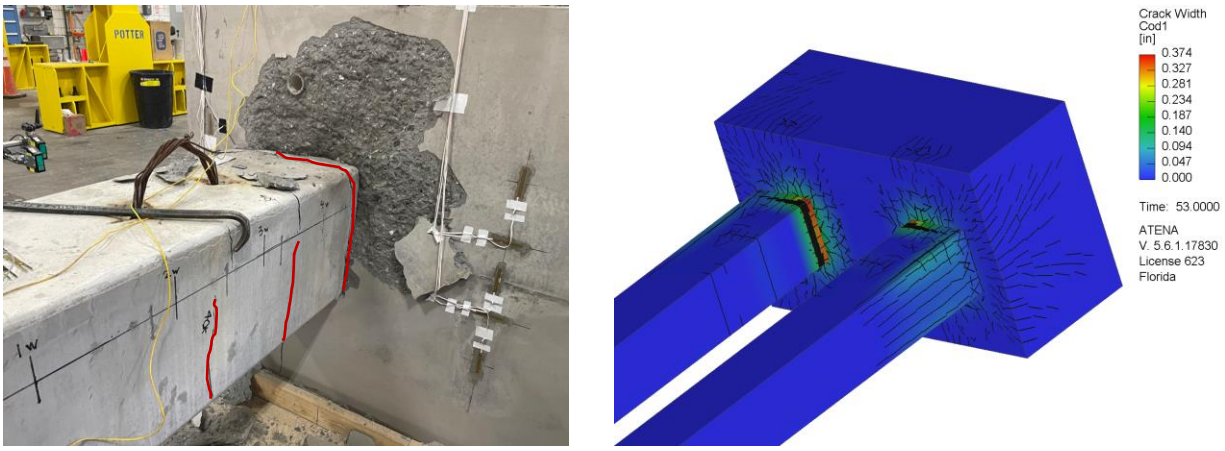

(a) (b)

Figure 6.15: crack pattern in SP-8 (a) experimental (b) numerical

The nonlinear FE analyses showed strong agreements of the overall moment deflection curves and failure modes of the pile-to-cap specimens, validating the experimental results.

6.2. EXPANDED NUMERICAL STUDY

The primary goal of the preliminary computational analyses of the pile-to-cap connection, was to determine the variables that should be investigated in the experimental program. The primary findings in this study concluded that the embedment length was linearly related to the moment capacity of the connection until de capacity of the pile was reached. This variable was the primary variable investigated in the experimental program. Other variables that were considered were the axial load, the interface reinforcement, and the pile size. Variables such as the pile cap concrete strength, and strand diameter, showed an impact in the performance of the connection but was not tested during the experimental program. A preliminary study was created in order to study variables that were not tested experimentally.

6.2.1. Embedment Length

For the 18-inch specimens, embedment lengths between 0.33 and 1.5 times the diameter of the piles were experimentally tested. The specimen with the deeper embedment length, SP-08 with 27-inch embedment, developed a moment of 81% the capacity of the pile.

As described in previous section, the estimated transfer and development length were found using AASHTO LRFD [23] and ElBatanouny and Ziehl [15] . A summary of the require transfer and development length for the 18-inch specimens is presented in Table 6.8. A pile embedment length of 41.4 inches for the 18-inch piles would be required for full moment capacity using ElBatanouny and Ziehl [15] and 72.1 inches using AASHTO LRFD BDS.

Table 6.8: Estimated development and transfer length for 18-inch piles

Specimen Description		**AASHTO LRFD BDS**		**ElBatanouny and Ziehl** [15]	
Pile Size	**Strand diameter (in)**	**Transfer length, l_t (in)**	**Development length, l_d (in)**	**Transfer length, l_t (in)**	**Development length, l_d (in)**
18-inch	0.52	31.2	72.1	18.4	41.4

Two numerical models with two new embedment lengths for the 18-inch specimens were created and analyzed in the numerical study. EMB-36 with an embedment length of 36-inch, and EMB-42 with an embedment length of 42-inch as recommended by ElBatanouny and Ziehl [15]

Numerical results for specimens with embedment lengths between 0.33 and 2.5 times the diameter of the pile is shown in Figure 6.16. The numerical results generally align well with the experimental results. EMB-36 developed a moment capacity of 291.44 k-ft, and EMB-42 developed a moment of 302.92 k-ft. A bilinear relationship was observed between moment developed and available embedment length. The full moment capacity of the 18-

inch pile was not obtained with an embedment length of 42 inches, which developed 92% of the capacity of the pile.

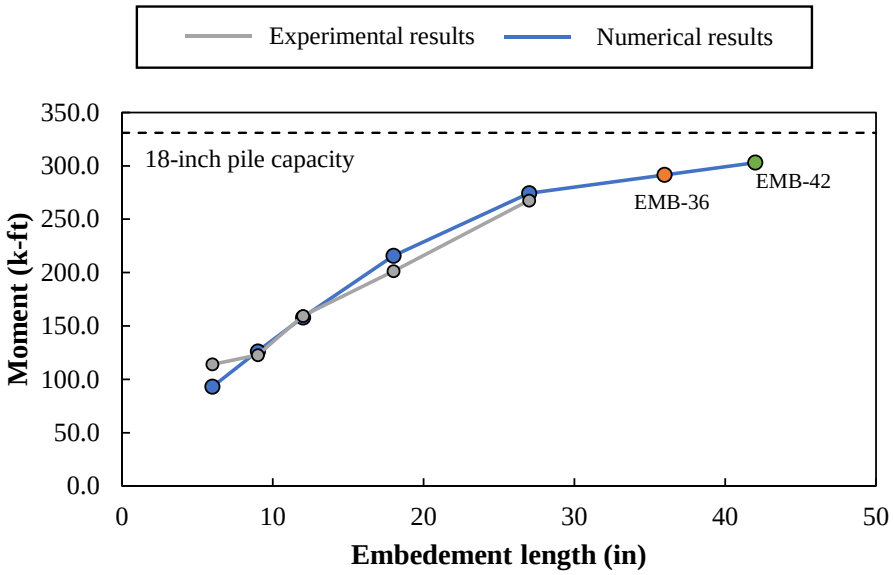

Figure 6.16: Numerical results for different embedment lengths for the 18-inch specimens

The calculated strand stress for each embedment length found using AASHTO and ElBatanouny [15] was used to find the corresponding maximum moment using RESPONSE2000, as shown in Figure 6.17. Both procedures conservatively estimated the strength of the specimens, on average, with the estimation procedure of ElBatanouny and Ziehl [15]resulting in the more accurate estimation.

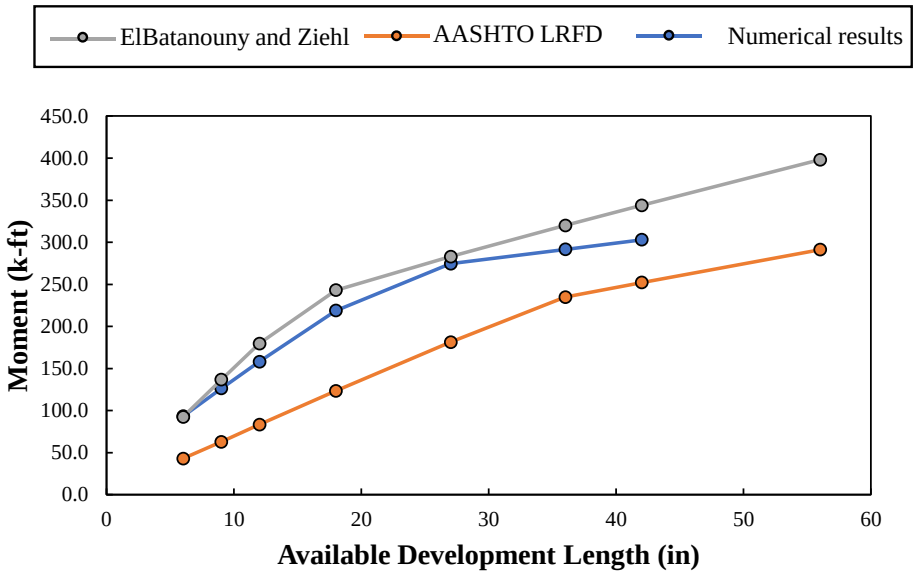

Figure 6.17: Moment versus available development length for 18-inch specimens

6.2.2. Strand Diameter

The second variable studied in the numerical program was the strand diameter. A typical strand diameter of 0.6-inch was selected. The strand pattern for 18-inch piles with 0.6-inch strands is similar as the pattern for 0.5-inch strands, as shown in Figure 6.18.

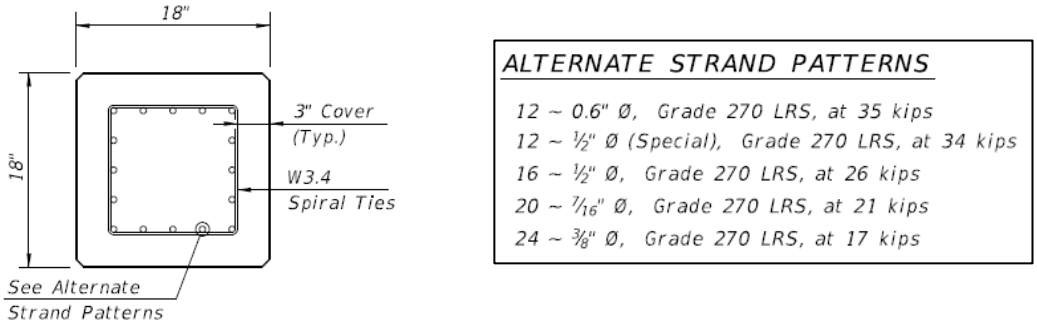

(a) (b)

Figure 6.18: FDOT Standard Plans (a) 18-inch pile cross section (b) alternate strand patterns

The capacity of the 18-inch piles with a strand pattern of 12-0.6-inch strands was determined using RESPONSE2000. The capacity was found to be 402.2 k-ft with the moment versus curvature response shown in Figure 6.19.

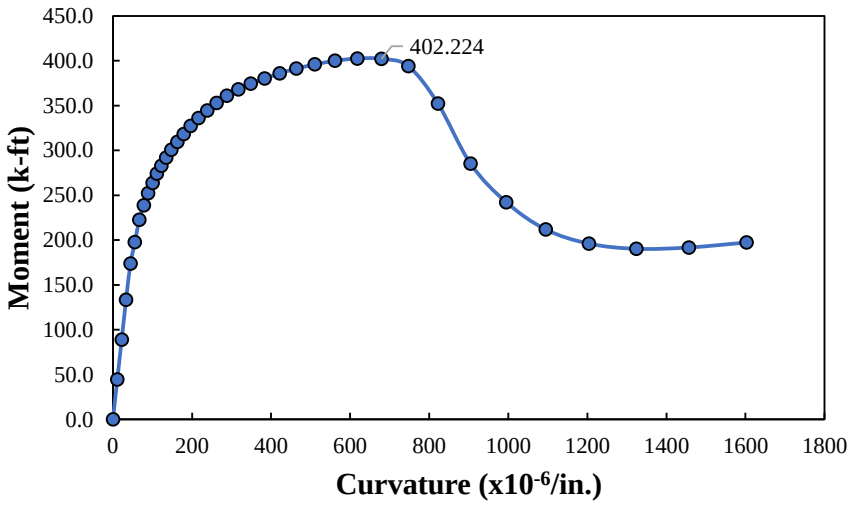

Figure 6.19: Estimated moment versus curvature for 18-inch piles with 0.6-inch strands using RESPONSE2000

The transfer and development length proposed by ElBatanouny and Ziehl [15] and specified by AASHTO LRFD BDS for 0.6-inch strands for 18-inch piles is shown in Table 6.9. A pile embedment length of 55.7 inches for the 18-inch piles with 0.6-inch strands would be required for full moment capacity using ElBatanouny and Ziehl, [15] and 98.02 inches using AASHTO LRFD. Increasing the diameter of the strands, increased the embedment length required to develop the full moment capacity of the pile.

Table 6.9: Estimated development and transfer length for 18-inch piles with 0.6-inch strands

Specimen Description		**AASHTO LRFD BDS**		**ElBatanouny and Ziehl** [15]	
Pile Size	**Strand diameter (in)**	**Transfer length, l_t (in)**	**Development length, l_d (in)**	**Transfer length, l_t (in)**	**Development length, l_d (in)**
18-inch	0.6	36.0	98.02	16.2	55.7

The slipping strand stress was found using AASHTO LRFD BDS and ElBatanouny and Ziehl [15] and used to find the corresponding maximum moment with RESPOSE2000.

The slipping stress and maximum moments for the 18-inch piles with 0.6-inch strand pattern are summarized in Table 6.10.

Table 6.10: Maximum moment and slipping stress for 0.6" strands

Emb	AASHTO LRFD BDS		ElBatanouny and Ziehl	
	Slipping stress (ksi)	**Maximum Moment (ksi)**	**Slipping stress (ksi)**	**Maximum Moment (ksi)**
6	22.5	42.8	50.0	92.4
9	33.7	62.8	75.0	136.7
12	44.9	83.3	100.0	179.5
18	67.4	123.3	140.2	243.1
27	101.0	181.2	167.2	282.9
36	134.7	234.7	194.2	320.0
42	146.2	252.1	212.2	343.8
56	172.9	291.1	254.2	398

The stress in the pile strands versus available development length found using equations from AASHTO LRFD BDS and ElBatanouny and Ziehl [15] are plotted in Figure 6.20. The estimated development length found using ElBatanouny and Ziehl [15] proposed equations are much less than the estimated development length found using AASHTO LRFD BDS, for the 0.6-inch strands.

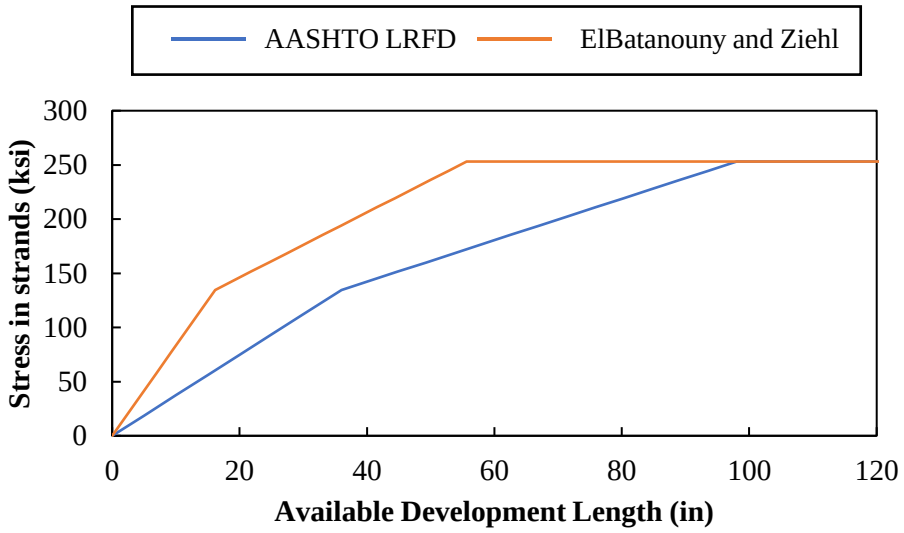

Figure 6.20: Stress in strand versus available development length plots for 0.6-inch strand pattern

A comparison between the stress in strands with different strand patterns (0.5-inch special and 0.6-inch) is shown in Figure 6.21. Increasing the diameter of the prestressing strands, increased the required pile embedment length to develop the full moment capacity of the pile.

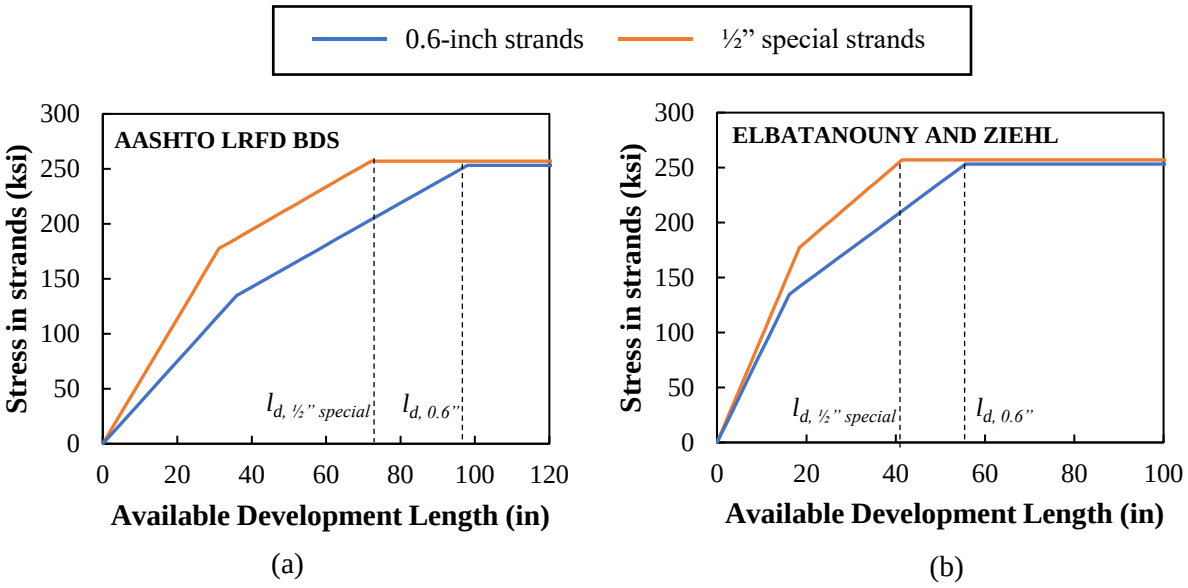

Figure 6.21: Stress in strand versus available development length plots using (a) AASHTO LRFD BDS, (b) ElBatanouny and Ziehl [15]

6.2.3. Pile Cap Concrete Strength

In the experimental testing, a punching shear of the edge of the pile cap was observed in SP-10. This specimen had a lower strength concrete in the cap than in the pile, which lead to a decreased punching shear capacity. These concrete strengths are more representative of field conditions where the piles would likely be made with higher strength concrete than the pile caps.

Two numerical models were created with a lower pile cap concrete strength of 5.5 ksi. PC-01 with a shallow embedment length of 6 inches, and SP-02 with a deeper embedment length of 27 inches. Moment-displacement curves are shown in Figure 6.22. In both cases, a lower pile cap concrete strength decreased the capacity of the connection.

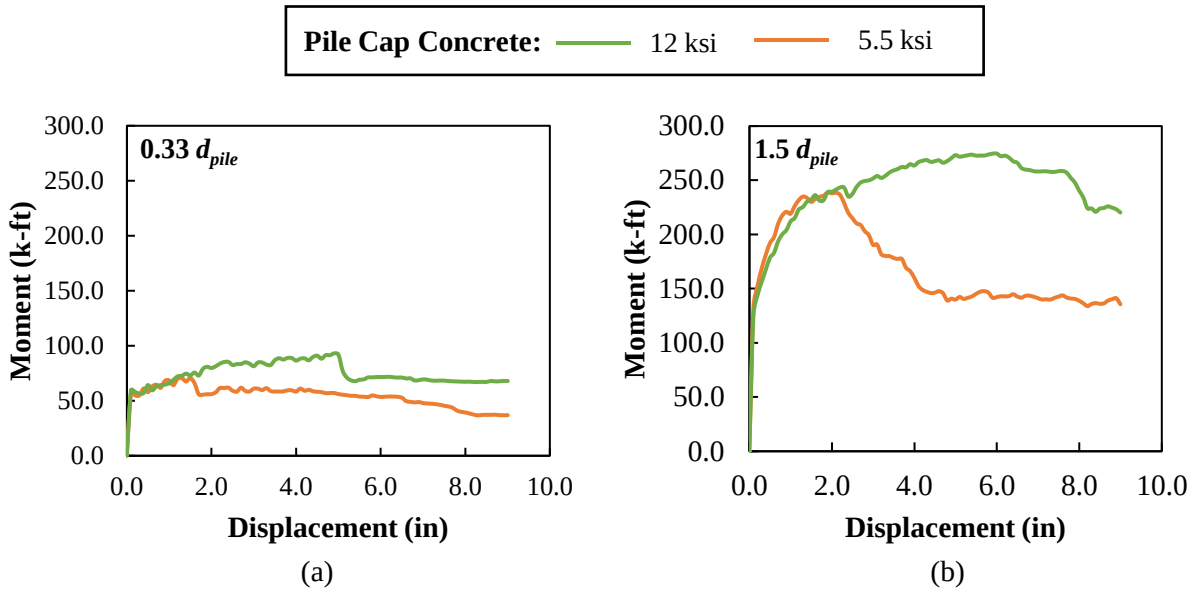

Figure 6.22: Moment versus displacement curves for (a) shallow embedment (b) deep embedment with different pile cap concrete strength

The failure mechanism observed in PC-02 corresponded to a punching shear failure. Cracks in the shape of a punching shear cone were observed in the pile cap, as shown in Figure 6.23.

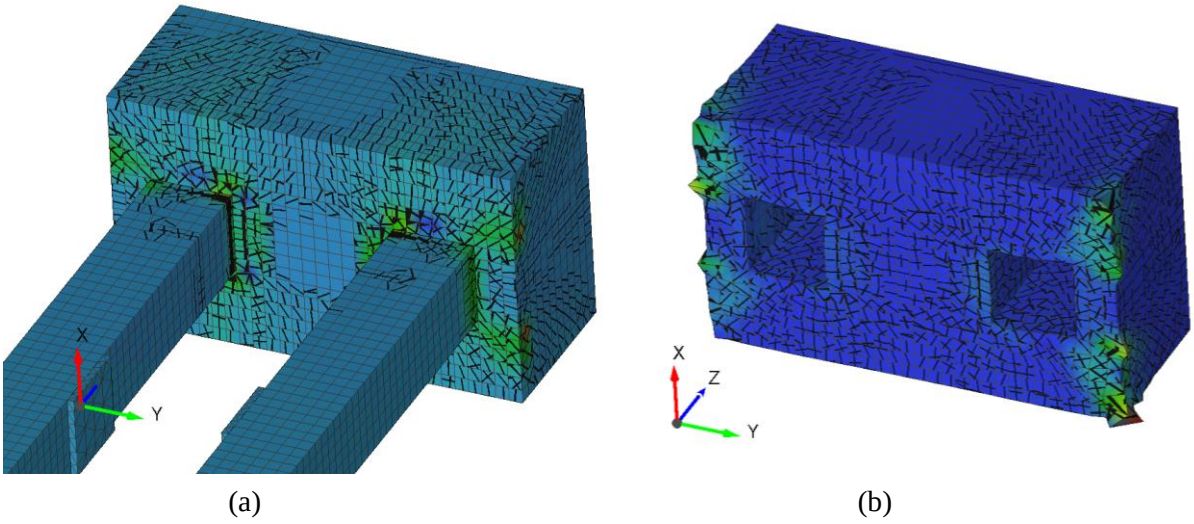

Figure 6.23: PC-02 failure mechanism (a) crack pattern in the pile-to-cap model (b) deformed pile cap

7. SUMMARY AND CONCLUSIONS

A summary of the observations and conclusions from the experimental testing and numerical study are as follows.

- The average measured transfer length for was 26 inches for the 18-inch piles and 14.6 inches for the 30-inch piles. The estimated transfer length for both piles is 31.2 inches based on AASHTO LRFD BDS [23].
- The average prestress losses due to elastic shortening was 7.2 ksi for the 18-inch piles and 5.9 for the 30-inch piles, which were within 2.2% and 8.6% of the estimated elastic shortening losses, respectively.
- The average long-term loss measured for the 18-inch piles was 16.2 ksi (within 13.9% of estimated loss) and 9.8 ksi for the 30-inch piles (40.1% less than estimate).
- Nine of the ten specimens failed due to slipping of the prestressing strand (strand development failure). These specimens had a large failure crack at the location where the strands began to slip, which was near the pile-to-cap interface for specimens without interface reinforcement. The 18-inch specimens all held a load around the maximum capacity of the connection as the strands were slipping and pile rotating. The 30-inch pile cap with strand slipping saw a drop in strength when the strands began to slip.
- Using the transfer and development length equations proposed by ElBatanouny and Ziehl [67] to estimate the moment capacity of the specimens that failed due to strand development led to an average measured-to-estimated ratio of 1.07, standard

deviation of 0.14, and coefficient of variation of 0.13. Using AASHTO LRFD BDS [22] led to an average measured-to-estimated ratio of 1.52, standard deviation of 0.31, and coefficient of variation of 0.20

- A pile embedment of 72.1 inches for 18-inch piles and 117.0 inches for the 30-inch piles would be required for full moment capacity using AASHTO LRFD BDS [22]. A pile embedment of 41.4 inches for 18-inch piles and 42.0 inches for the 30-inch piles would be required for full moment capacity using ElBatanouny and Ziehl [67].
- The failure of SP-10 resembled a punching shear failure where the side of the pile punched through the side face of the pile cap. The demand could be estimated using a compression block developed from Mattock and Gaafar [74] and Belarbi et al. [76] and the measured compressive strain in the face of the pile cap. The capacity could be estimated using standard punching shear equations from AASHTO LRFD BDS §5.12.8.6 [23].
- A small axial compression force greatly increased the capacity of the connection; an average 107% increase in capacity of the connection was observed when $0.05A_g f'_{c,pile}$ axial compression was applied to the pile and connection.
- The specimen with the interface reinforcement (SP-03) developed a moment capacity 67% higher than the similar specimen without interface reinforcement (SP-01), both with 6-inch pile embedment lengths.
- Because the tests needed to be stopped due to running out of stroke of the hydraulic jack, it is not clear if the presence of interface reinforcement affected the rotational capacity of the connection.

- The capacity of the specimen with interface reinforcement (SP-03) was controlled by the available development length at the pile-to-cap interface section (6 inches from the pile end) rather than the section at the end of the interface reinforcement (24 inches from the pile end). For design of connections with interface reinforcement, it is recommended to use the minimum of these two capacities to estimate the strength of the connection.
- The capacity of the connection did not appear to be dependent on the pile embedment length as a function of the pile size. The behavior of the connection appeared to be more dependent on the available strand development length provided by the pile embedment length.
- A factor of 0.6 is proposed as an addition to the current AASHTO LRFD BDS development length equation. This factor considers the confining stresses developed around the embedded pile, decreasing the required development length to reach full capacity of the piles in the pile-to-cap connection.
- Implementing an additional N6 bar around the embedded portion of the pile increased the moment developed by the pile-to-cap connection and prevented punching shear failure.

8. FUTURE RESEARCH

The limitations of this research point toward topics to be addressed in the future. The following are a few areas of future research:

- Effect of pile sizes. Only two specimens with different embedment lengths were tested experimentally for the 30-inch pile specimens.
- Effect of strand diameter and strand pattern. The scope of this research focused on 12 – ½" special strands (7 wire strands).
- Approach to estimate the punching shear demand of the pile cap or footing.

REFERENCES

[1] Florida Department of Transportation (FDOT), “Structures Design Guidelines - FDOT Structures Manual - Volume 1,” Jan. 2023.

[2] Minnesota Department of Transportation, “LRFD Bridge Design - 10 - Foundations,” Jun. 2007.

[3] Wisconsin Department of Transportation, “WisDOT Bridge Manual - Chapter 11 - Foundation Support,” Jan. 2019.

[4] Oregon Department of Transportation, “Bridge Design Manual,” May 2018.

[5] Colorado Department of Transportation, “CDOT Bridge Design Manual,” Jan. 2018.

[6] K. Harries and M. Petrou, “Behavior of Precast, Prestressed Concrete Pile to Cast-in-Place Pile Cap Connections,” *PCI J.*, vol. 46, no. 4, 2001.

[7] A. A. Shama, J. B. Mander, and A. J. Aref, “Seismic Performance and Retrofit of Steel Pile to Concrete Cap Connections,” *ACI Struct. J.*, vol. 99, no. 1, pp. 51–61, 2002.

[8] K. M. Rollins and T. E. Stenlund, “Laterally Loaded Pile Connections,” vol. UT-10.16, Aug. 2010.

[9] M. K. ElBatanouny, P. Ziehl, A. Larosche, T. Mays, and J. Calcedo, “Bent-Cap Confining Stress Effect on Slip of Prestressing Strands,” *ACI Struct. J.*, vol. 109, no. 4, pp. 487–496.

[10] C. D. White, R. W. Castrodale, and M. C. Nigels, “Prestressed Concrete Piles (Chapter 20 of the Bridge Design Manual),” Precast/Prestressed Concrete Institute (PCI), BM-20-04, 2004.

[11] Y. Xiao, H. Wu, T. T. Yaprak, G. R. Martin, and J. B. Mander, “Experimental studies on seismic behavior of steel pile-to-pile-cap connections,” *J. Bridge Eng.*, vol. 11, no. 2, pp. 151–159, 2006.

[12] P. H. Joen and R. Park, “Simulated Seismic Load Tests on Prestressed Concrete Piles and Pile-Pile Cap Connections,” *PCI J.*, vol. 35, no. 6, pp. 42–61, Dec. 1990.

[13] M. Issa, “Testing of Pile-to-Pile Cap Moment Connection for 30" Prestressed Concrete Pipe-Pile,” Florida Department of Transportation (FDOT), 98–9, 1999.

[14] K. M. Rollins and T. E. Stenlund, “Laterally Loaded Pile Cap Connections,” UT-10.16, Aug. 2010.

[15] A. Larosche, P. Ziehl, M. ElBatanouny, and J. Caicedo, “Plain Pile Embedment for Exterior Bent Cap Connections in Seismic Regions,” *J. Bridge Eng.*, vol. 19, no. 4, pp. 1–12, 2014.

[16] F. Castilla, P. Martin, and J. Link, “Fixity of Members Embedded in Concrete,” 1984.

[17] M. Shahawy and M. Issa, “Effect of Pile Embedment on the Development Length of Prestressing Strands,” *PCI J.*, vol. 37, no. 6, pp. 44–59, 1992.

[18] Florida Department of Transportation (FDOT), “Stuctures Design Guidelines - FDOT Structures Manual - Volume 1,” 2018.

[19] American Association of State Highway and Transportation Officials (AASHTO), “AASHTO LRFD Bridge Design Specification, Customary U.S. Units, 8th Edition,” Washington, D. C., Sep. 2017.

[20] Alaska Department of Transportation and Public Facilities, “Alaska Bridges and Structures Manual,” 2017.

[21] State of Connecticut Department of Transportation, “Bridge Design Manual,” Edition (Revised /11 2003.

[22] Delaware Department of Transportation, “Bridge Design Manual,” 2017.

[23] Idaho Transportation Department, “Load Resistance Factor Design (LRFD) Bridge Manual; Section 10.7.1.2,” 2008.

[24] Illinois Department of Transportation, “Bridge Manual,” 2012.

[25] Illinois Tollway, “Structures Design Manual,” Mar. 2018.

[26] Indiana Department of Transportation, “2013 Design Manual - Chapter 408 - Foundation,” Aug. 2018.

[27] Iowa Department of Transportation, “LRFD Bridge Design Manual,” Jan. 2019.

[28] Kansas Department of Transportation, “Bridge Construction Manual - 5.3 - Driven Piles,” May 2013.

[29] Michigan Department of Transportation, “Michigan Design Manual - Bridge Design - Chapter 7 - Design Criteria,” 2018.

[30] Montana Department of Transportation, “Montana Structures Manual - Chapter 20 - Foundations,” Aug. 2002.

[31] Nevada Department of Transportation, “Structures Manual - Chapter 17 - Foundations,” Sep. 2008.

[32] New Hampshire Department of Transportation, “Bridge Design Manual - Chapter 6 - Substructure,” Jan. 2015.

[33] New York State Department of Transportation, “Bridge Manual,” 2017.

[34] Ohio Department of Transportation, “Bridge Design Manual - Section 303.3.3 - Footing on Piles,” Jan. 2004.

[35] Pennsylvania Department of Transportation, “Design Manual - Part 4 - Structures - Procedures - Design - Plans Presentation,” Apr. 2015.

[36] State of Rhode Island Department of Transportation, “Rhode Island LRFD Bridge Design Manual,” 2007.

[37] South Carolina Department of Transportation, “SCDOT Bridge Design Manual,” Jun. 2006.

[38] Vermont Agency of Transportation, “VTrans Structures Design Manual,” 2010.

[39] West Virginia Department of Transportation, “Bridge Design Manual,” Mar. 2016.

[40] P. Zia and T. Mostafa, “Development Length of Prestressing Strands,” *PCI J.*, vol. 22, no. 5, pp. 54–65, Oct. 1977.

[41] M. K. ElBatanouny and P. Ziehl, “Determining Slipping Stress of Prestressing Strands in Confined Sections,” *ACI Struct. J.*, vol. 106, no. 6, pp. 767–776, Dec. 2012.

[42] M. Shahawy, M. Issa, and M. Polodna, “Development Length of Prestressed Concrete Piles,” Florida Department of Transportation (FDOT), SSR-01-90, 1990.

[43] M. F. Stocker and M. A. Sozen, “Investigation of Prestressed Reinforced Concrete for Highway Bridges - Part VI: Bond Characteristics,” 1969.

[44] A. Mattock and G. H. Gaafar, “Strength of Embedded Steel Sections as Brackets,” *ACI Struct. J.*, vol. 79, no. 2, pp. 83–93, 1982.

[45] K. Marcakis and D. Mitchell, “Precast Concrete Connections With Embedded Steel Members,” *PCI J.*, vol. 25, no. 4, pp. 88–116, Aug. 1980.

[46] A. A. Shama and J. B. Mander, “Behavior of Timber Pile-to-Cap Connections under Cyclic Lateral Loading,” *J. Bridge Eng.*, vol. 130, no. 8, pp. 1252–1262, Aug. 2004.

[47] Y. Xiao, “Experimental Studies on Precast Prestressed Concrete Pile to CIP Concrete Pile-Cap Connections,” *PCI J.*, vol. 48, no. 6, pp. 82–91, Dec. 2003.

[48] J. E. Stephens and L. R. McKittrick, “Performance of Steel Pipe Pile-to-Conctete Bent Cap Connections Subject to Seismic or High Transverse Loading: Phase II,” Montana State University - Bozeman, FHWA/MT-05-001/8144, Mar. 2005.

[49] L. Kappes, M. Berry, and J. E. Stephens, “Performance of Steel Pipe Pile-to-Concrete Cap Connections Subject to Seismic or High Transverse loading: Phase III Confirmation of Connection Performance,” FHWA/MT-13-001/8203, Jan. 2013.

[50] Standards Associaton of New Zealand, “New Zealand Standard Specification for Concrete Construction, NZS 3109,” Wellington, New Zealand, 1980.

[51] Florida Department of Transportation (FDOT), “Index 20010 Series Prestressed Florida-I Beams,” Tallahassee, 2012.

[52] Florida Department of Transportation (FDOT), “Prestressed Beam v5.2.” Nov. 07, 2018. [Online]. Available: https://www.fdot.gov/structures/proglib.shtm

[53] Florida Department of Transportation (FDOT), “Prestressed Concrete Piles - Standard Plans,” 455, 2019.

[54] Florida Department of Transportation (FDOT), “Stuctures Design Guidelines - FDOT Structures Manual,” 2017.

[55] Florida Department of Transportation (FDOT), “Final Design of Wekiva River Bridges,” Feb. 2014.

[56] Precast/Prestressed Concrete Institute (PCI), “Bridge Design Manual, 3rd Edition, Second Release, August 2014,” 2014.

[57] A. Ahmed, “Straddle Bent Design Using MIDAS CIVIL.” MIDAS TUTORIALS, Dec. 06, 2018.

[58] American Concrete Institute (ACI) Committee 209, “Guide for Modeling and Calculating Shrinkage and Creep in Hardened Concrete (ACI 209.2R-08),” American Concrete Institute (ACI), Farmington Hill, MI, Reapproved 2008.

[59] Florida Department of Transportation (FDOT), “FDOT Stuctures Design Guidelines - Structures Manual - Volume I,” 2019.

[60] V. Cervenka, J. Cervenka, Z. Janda, and D. Pryl, “ATENA Program Documentation - User’s Manual for ATENA-GiD Interface,” 2017.

[61] V. Cervenka, L. Jendele, and J. Cervenka, “ATENA Program Documentation - Part 1 - Theory,” 2018.

[62] D. Garber and M. L. Ralls, “ABC Project Database,” 2016. http://utcdb.fiu.edu/ (accessed May 24, 2016).

[63] Florida Department of Transportation (FDOT), “Standard Specification for Road and Bridge Construction, FY 2023-24,” 2023.

[64] B. W. Russell and N. H. Burns, “Design Guidelines for Transfer, Development and Debonding of Large Diameter Seven Wire Strands in Pretensioned Concrete Girders,” The University of Texas at Austin, Austin, TX, 1993.

[65] A. Al-Kaimakchi and M. Rambo-Roddenberry, “Measured transfer length of 15.2-mm (0.6-in.) duplex high-strength stainless steel strands in pretensioned girders,” *Eng. Struct.*, vol. 237, 2021, doi: https://doi.org/10.1016/j.engstruct.2021.112178.

[66] American Association of State Highway and Transportation Officials (AASHTO), “AASHTO LRFD Bridge Design Specification, Customary U.S. Units, 9th Edition,” Washington, D. C., 2020.

[67] M. ElBatanouny and P. Ziehl, “Determining Slipping Stress of Prestressing Strands in Confined Sections,” *Aci Struct. J.*, vol. 109, pp. 767–776, Nov. 2012.

[68] A. H. Mattock, “Proposed Redraft of Section 2611 - Bond of the Proposed Revision of Building Code Requirements for Reinforced Concrete (ACI 318-56),” *ACI 323 Corresp.*, 1962.

[69] American Concrete Institute (ACI) Committee 318, “Building Code Requirements for Structural Concrete (ACI 318-19) and Commentary,” Farmington Hills, MI, 2019.

[70] Norman W. Hanson and Paul H. Kaar, “Flexural Bond Tests of Pretensioned Prestressed Beams,” *ACI J. Proc.*, vol. 55, no. 1, Jan. 1959, doi: 10.14359/11389.

[71] T. E. Cousins, D. W. Johnston, and P. Zia, “Transfer and Development Length of Epoxy Coated and Uncoated Prestressing Strand,” *Pci J.*, vol. 35, pp. 92–103, 1990.

[72] Federal Highway Administration (FHWA), “A New Development Length Equation for Pretensioned Strands in Bridge Beams and Piles,” FHWA, U.S. Department of Transportation, Washington, DC, FHWA-RD-98-116, 1998.

[73] C. D. Buckner, “A Review of Strand Development Length for Pretensioned Concrete Members,” *PCI J.*, vol. 40, no. 2, pp. 84–105, Apr. 1995.

[74] A. H. Mattock and G. Gaafar, “Strength of Embedded Steel Sections as Brackets,” 1982.

[75] M. P. Collins and D. Mitchell, *Prestressed Concrete Structures*. Englewood Cliffs, New Jersey: Prentice-Hall, Inc., 1991.

[76] A. Belarbi *et al.*, *NCHRP Research Report 907: Design of Concrete Bridge Beams Prestressed with CFRP Systems*. Washington, DC: National Cooperative Highway Research Program (NCHRP), 2019.

[77] A. Larosche, P. Ziehl, and M. ElBatanouny, “Plain Pile Embedment for Exterior Bent Cap Connections in Seismic Regions,” *J Bridge Eng*, vol. 19, no. 4, pp. 1–12, 2014.

9. APPENDIX

A. CONSTRUCTION DRAWINGS

A.1. CONSTRUCTION PLANS FOR 18-INCH PILES

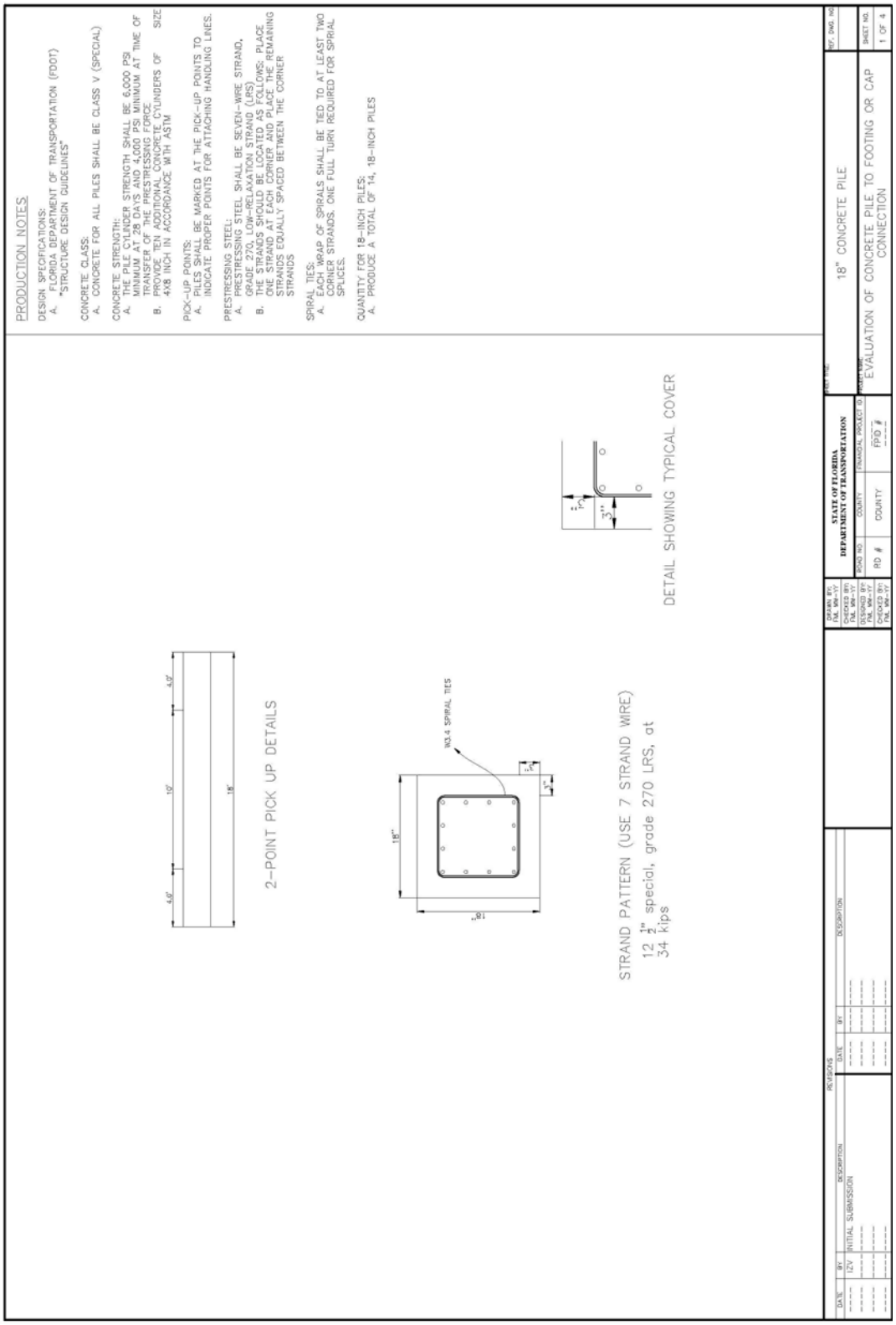

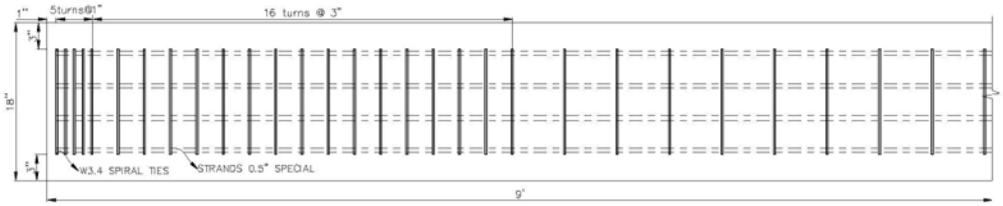

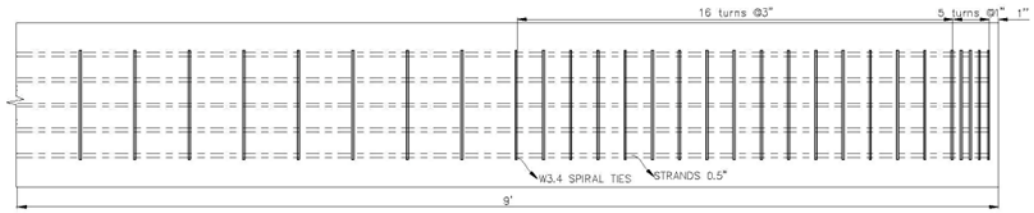

REVISIONS					
DATE	BY	DESCRIPTION	DATE	BY	DESCRIPTION
---	IZV	INITIAL SUBMISSION	---	---	---

DRAWN BY: FML MM-YY
CHECKED BY: FML MM-YY
DESIGNED BY: FML MM-YY
CHECKED BY: FML MM-YY

STATE OF FLORIDA
DEPARTMENT OF TRANSPORTATION

ROAD NO.	COUNTY	FINANCIAL PROJECT ID
RD #	COUNTY	FPID #

SHEET TITLE: 18" CONCRETE PILE

PROJECT NAME: EVALUATION OF CONCRETE PILE TO FOOTING OR CAP CONNECTION

REF. DWG. NO.:

SHEET NO.: 2 OF 4

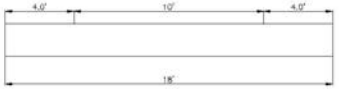

2–POINT PICK UP DETAILS

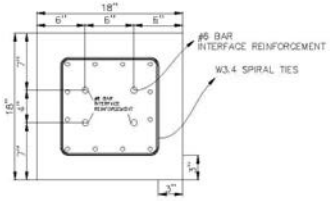

STRAND PATTERN (USE 7 STRAND WIRE)
12 $\frac{1}{2}$" special , grade 270 LRS, at
34 kips

INTERFACE REINFORCEMENT DETAIL

DETAIL SHOWING TYPICAL COVER

PRODUCTION NOTES

DESIGN SPECIFICATIONS:
A. FLORIDA DEPARTMENT OF TRANSPORTATION (FDOT) "STRUCTURE DESIGN GUIDELINES"

CONCRETE CLASS:
A. CONCRETE FOR ALL PILES SHALL BE CLASS V (SPECIAL)

CONCRETE STRENGTH:
A. THE PILE CYLINDER STRENGTH SHALL BE 6,000 PSI MINIMUM AT 28 DAYS AND 4,000 PSI MINIMUM AT TIME OF TRANSFER OF THE PRESTRESSING FORCE
B. PROVIDE TEN ADDITIONAL CONCRETE CYLINDERS OF SIZE 4X8 INCH IN ACCORDANCE WITH ASTM

PICK–UP POINTS:
A. PILES SHALL BE MARKED AT THE PICK–UP POINTS TO INDICATE PROPER POINTS FOR ATTACHING HANDLING LINES.

PRESTRESSING STEEL:
A. PRESTRESSING STEEL SHALL BE SEVEN–WIRE STRAND, GRADE 270, LOW–RELAXATION STRAND (LRS)
B. THE STRANDS SHOULD BE LOCATED AS FOLLOWS: PLACE ONE STRAND AT EACH CORNER AND PLACE THE REMAINING STRANDS EQUALLY SPACED BETWEEN THE CORNER STRANDS

SPIRAL TIES:
A. EACH WRAP OF SPIRALS SHALL BE TIED TO AT LEAST TWO CORNER STRANDS. ONE FULL TURN REQUIRED FOR SPRIAL SPLICES.

INTERFACE REINFORCEMENT:
A. ALL REINFORCING STEEL SHALL BE ASTM A615 DEFORMED BARS WITH YIELD STRENGTH Fy=60KSI
B. HOOK BARS CAN BE BENT AFTER CASTING

QUANTITY FOR 18–INCH PILES WITH INTERFACE:
A. PRODUCE A TOTAL OF 2, 18–INCH PILES WITH INTERFACE REINFORCEMENT

REVISIONS					
DATE	BY	DESCRIPTION	DATE	BY	DESCRIPTION
-----	IZV	INITIAL SUBMISSION	-----	-----	-----
-----	-----	-----	-----	-----	-----
-----	-----	-----	-----	-----	-----
-----	-----	-----	-----	-----	-----

DRAWN BY: FML, MM–YY
CHECKED BY: FML, MM–YY
DESIGNED BY: FML, MM–YY
CHECKED BY: FML, MM–YY

STATE OF FLORIDA
DEPARTMENT OF TRANSPORTATION

ROAD NO.	COUNTY	FINANCIAL PROJECT ID
RD #	COUNTY	FPID #

SHEET TITLE: 18" CONCRETE PILE WITH INTERFACE REINFORCEMENT
PROJECT NAME: EVALUATION OF CONCRETE PILE TO FOOTING OR CAP CONNECTION
REF. DWG. NO.
SHEET NO. 3 OF 4

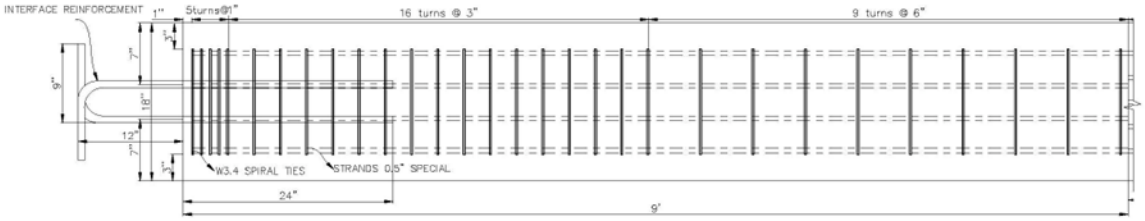

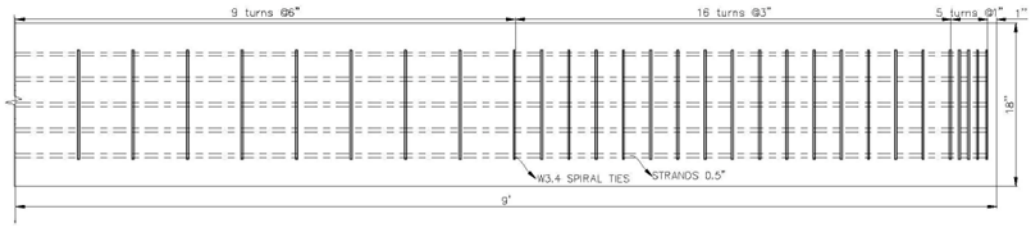

REVISIONS					
DATE	BY	DESCRIPTION	DATE	BY	DESCRIPTION
____	IZV	INITIAL SUBMISSION	____	____	____
____	____	____	____	____	____
____	____	____	____	____	____
____	____	____	____	____	____

DRAWN BY: FML MM-YY
CHECKED BY: FML MM-YY
DESIGNED BY: FML MM-YY
CHECKED BY: FML MM-YY

STATE OF FLORIDA
DEPARTMENT OF TRANSPORTATION

ROAD NO.	COUNTY	FINANCIAL PROJECT ID
RD #	COUNTY	FPID #

SHEET TITLE: 18" CONCRETE PILE WITH INTERFACE REINFORCEMENT

PROJECT NAME: EVALUATION OF CONCRETE PILE TO FOOTING OR CAP CONNECTION

REF. DWG. NO.

SHEET NO. 4 OF 4

A.2. CONSTRUCTION PLANS FOR 18-INCH CAP SPECIMENS

Embedment length varies per specimen

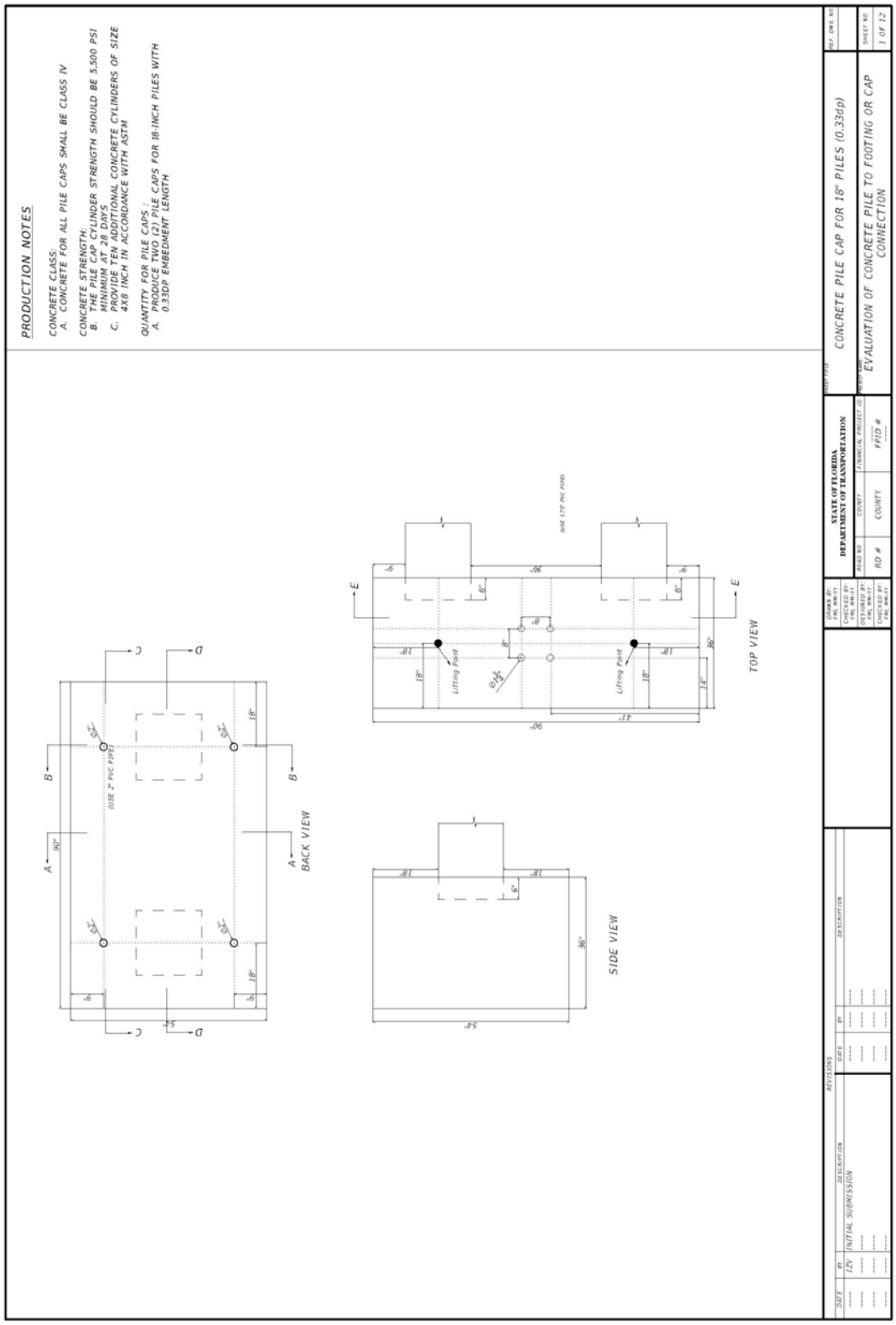

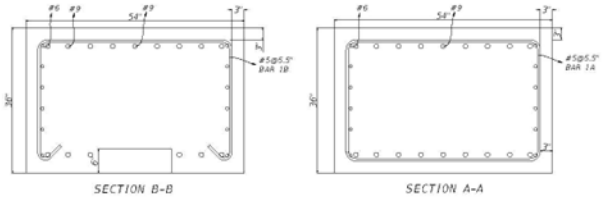

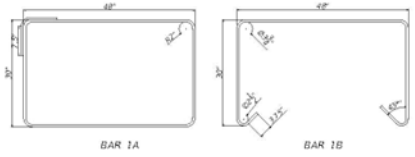

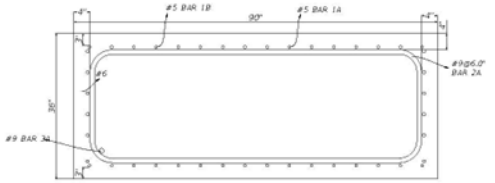

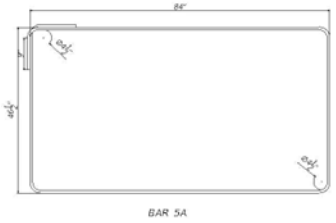

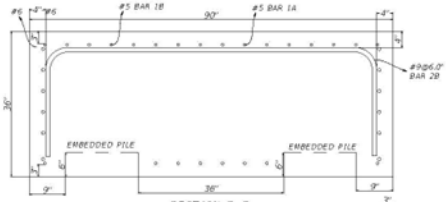

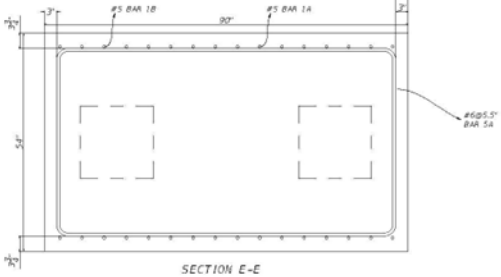

REBAR SCHEDULE (PILE CAP)

ITEM	SIZE	QTY	LENGTH	REMARKS
1A	#5	8	14'-5"	SEE DETAILS
1B	#5	8	9'-8"	SEE DETAILS
2A	#9	6	20'-10"	SEE DETAILS
2B	#9	3	11'-8"	SEE DETAILS
5A	#6	6	23'-4"	SEE DETAILS
3A	#9	1	5'-10"	SEE DETAILS

REVISIONS

DATE	BY	DESCRIPTION	DATE	BY	DESCRIPTION
-----	IZV	INITIAL SUBMISSION	-----	-----	-----
-----	-----	-----	-----	-----	-----
-----	-----	-----	-----	-----	-----

DRAWN BY: ENG. NM-YY
CHECKED BY: ENG. NM-YY
DESIGNED BY: ENG. NM-YY
CHECKED BY: ENG. NM-YY

STATE OF FLORIDA
DEPARTMENT OF TRANSPORTATION

ROAD NO.	COUNTY	FINANCIAL PROJECT ID
RD #	COUNTY	FPID #

STRUCTURE TYPE: CONCRETE PILE CAP FOR 18" PILES (0.33dp)

INDEX TITLE: EVALUATION OF CONCRETE PILE TO FOOTING OR CAP CONNECTION

REF. DWG. NO.

SHEET NO.
2 OF 12

A.3. CONSTRUCTION PLANS FOR 30-INCH PILES

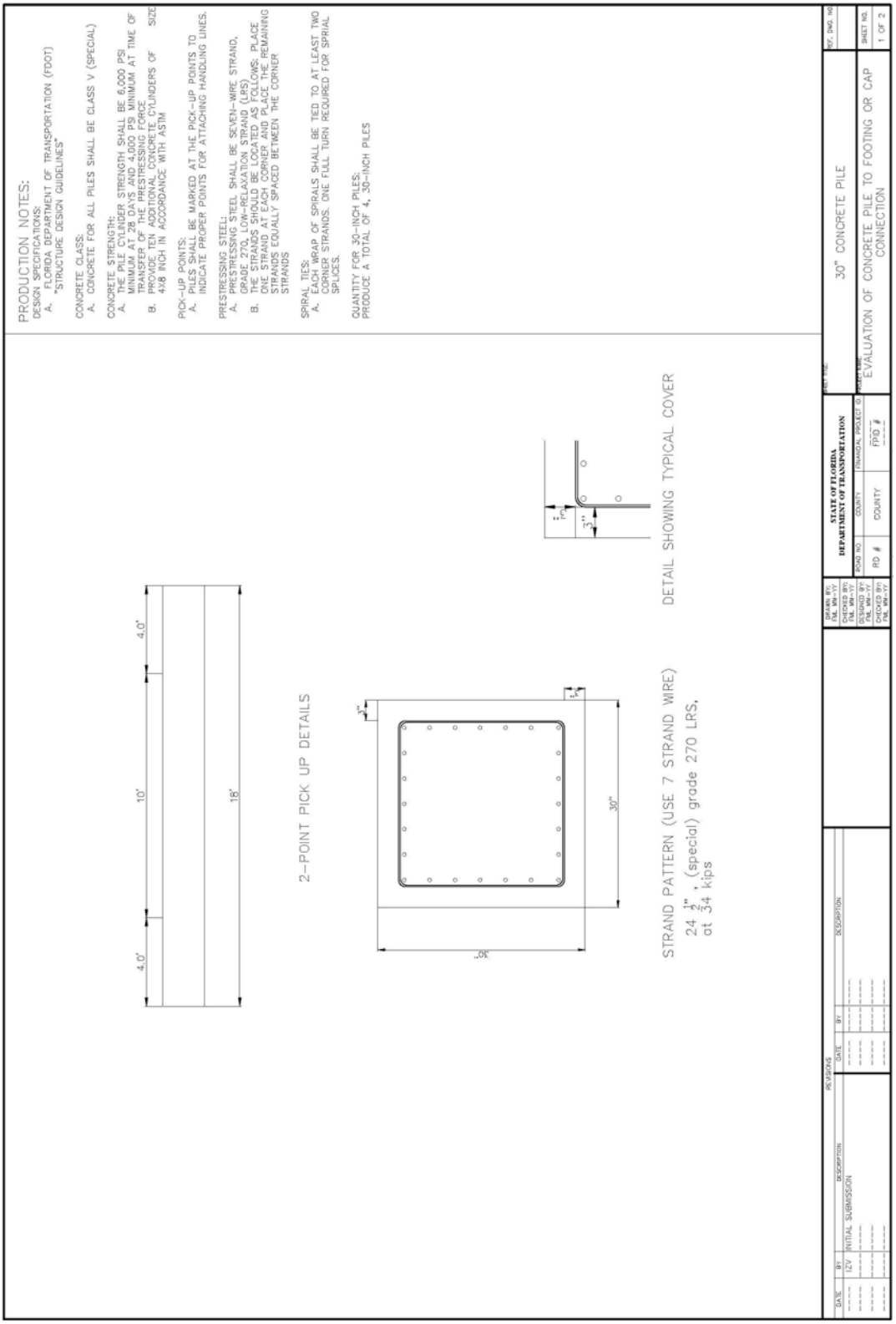

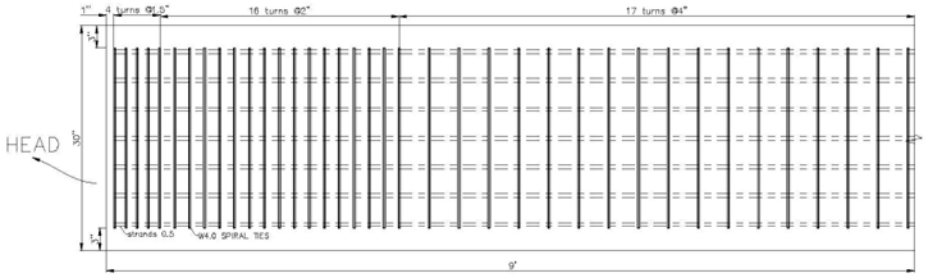

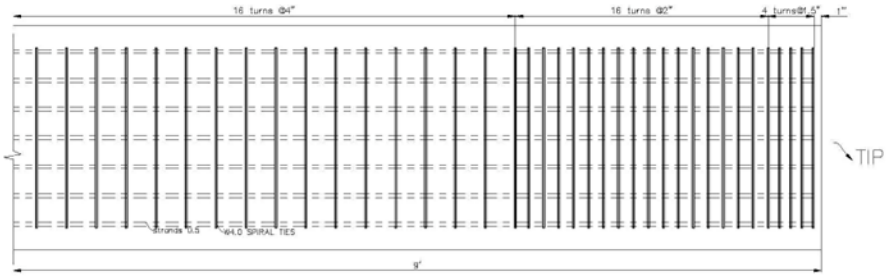

REVISIONS					
DATE	BY	DESCRIPTION	DATE	BY	DESCRIPTION
____	IZV	INITIAL SUBMISSION	____	____	____
____	____	____	____	____	____
____	____	____	____	____	____
____	____	____	____	____	____

DRAWN BY: FML MM-YY
CHECKED BY: FML MM-YY
DESIGNED BY: FML MM-YY
CHECKED BY: FML MM-YY

STATE OF FLORIDA
DEPARTMENT OF TRANSPORTATION

ROAD NO.	COUNTY	FINANCIAL PROJECT ID
RD #	COUNTY	FPID #

SHEET TITLE: 30" CONCRETE PILE

PROJECT NAME: EVALUATION OF CONCRETE PILE TO FOOTING OR CAP CONNECTION

REF. DWG. NO.

SHEET NO. 2 OF 2

A.4. CONSTRUCTION PLANS FOR 30-INCH PILE AND PILE CAP SPECIMENS

Embedment length varies per specimen

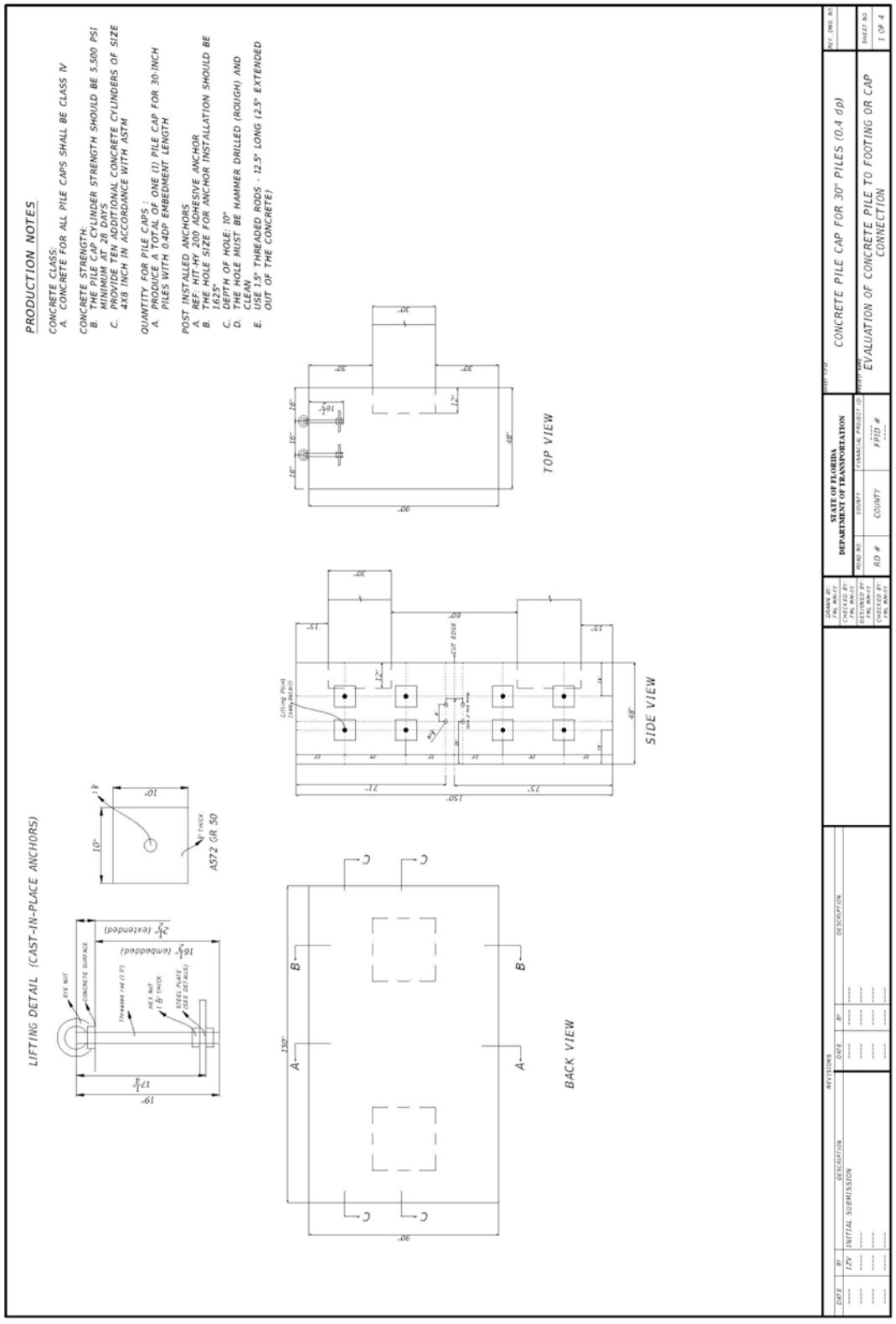

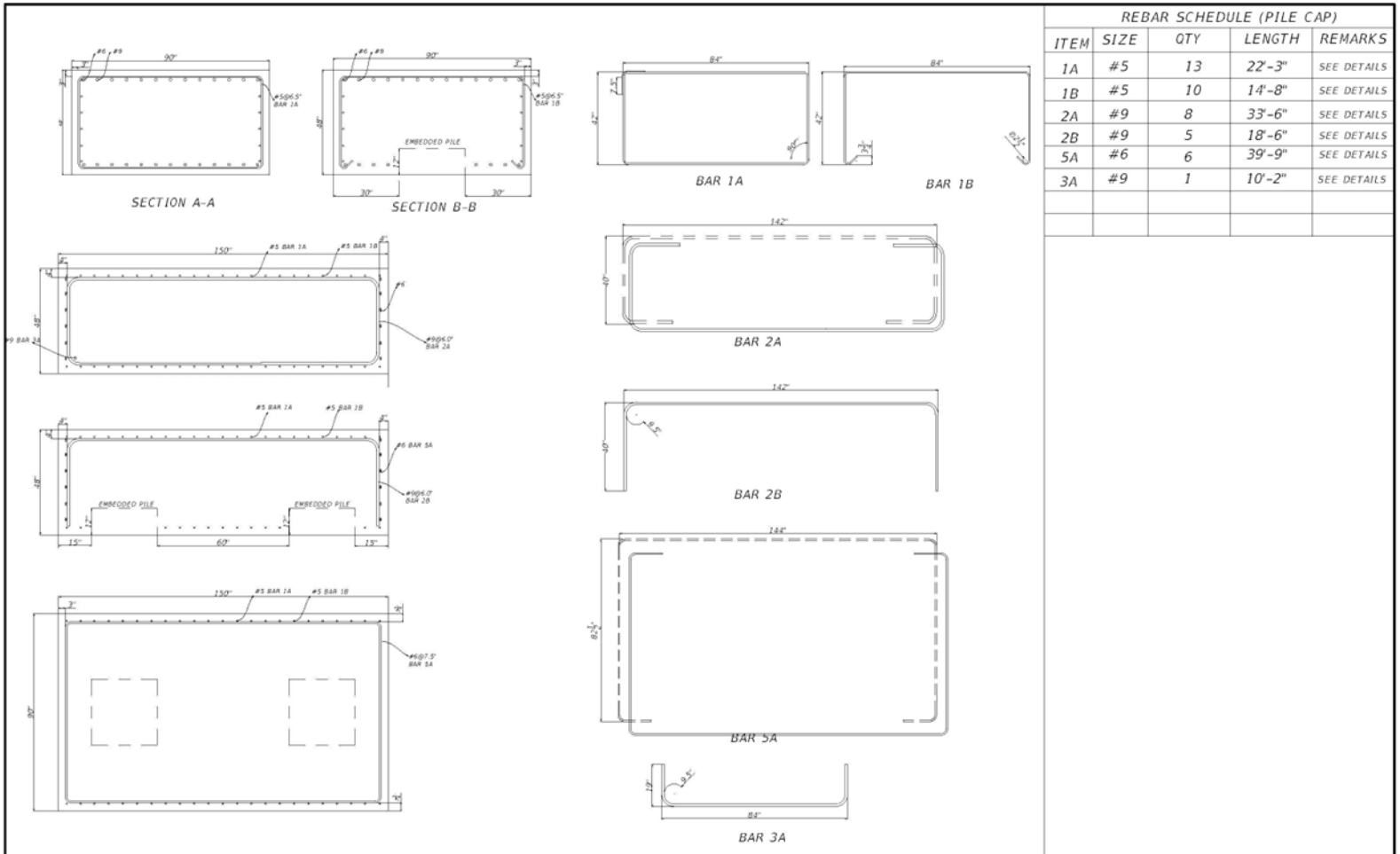

REBAR SCHEDULE (PILE CAP)

ITEM	SIZE	QTY	LENGTH	REMARKS
1A	#5	13	22'-3"	SEE DETAILS
1B	#5	10	14'-8"	SEE DETAILS
2A	#9	8	33'-6"	SEE DETAILS
2B	#9	5	18'-6"	SEE DETAILS
5A	#6	6	39'-9"	SEE DETAILS
3A	#9	1	10'-2"	SEE DETAILS

REVISIONS

DATE	BY	DESCRIPTION	DATE	BY	DESCRIPTION
-----	IZV	INITIAL SUBMISSION	-----	-----	-----
-----	-----	-----	-----	-----	-----
-----	-----	-----	-----	-----	-----
-----	-----	-----	-----	-----	-----

DRAWN BY: FML MM-YY
CHECKED BY: FML MM-YY
DESIGNED BY: FML MM-YY
CHECKED BY: FML MM-YY

STATE OF FLORIDA
DEPARTMENT OF TRANSPORTATION

ROAD NO.	COUNTY	FINANCIAL PROJECT ID
RD #	COUNTY	FPID #

SHEET TITLE: CONCRETE PILE CAP FOR 30" PILES (0.4 dp)

SHEET NAME: EVALUATION OF CONCRETE PILE TO FOOTING OR CAP CONNECTION

REF. DWG. NO.

SHEET NO.: 2 OF 4

B. TEST SETUP DRAWINGS

The test setup drawings and axial load applications procedure are provided in this appendix.

B.1. 18-INCH PILE FLEXURE TEST SETUP DRAWINGS

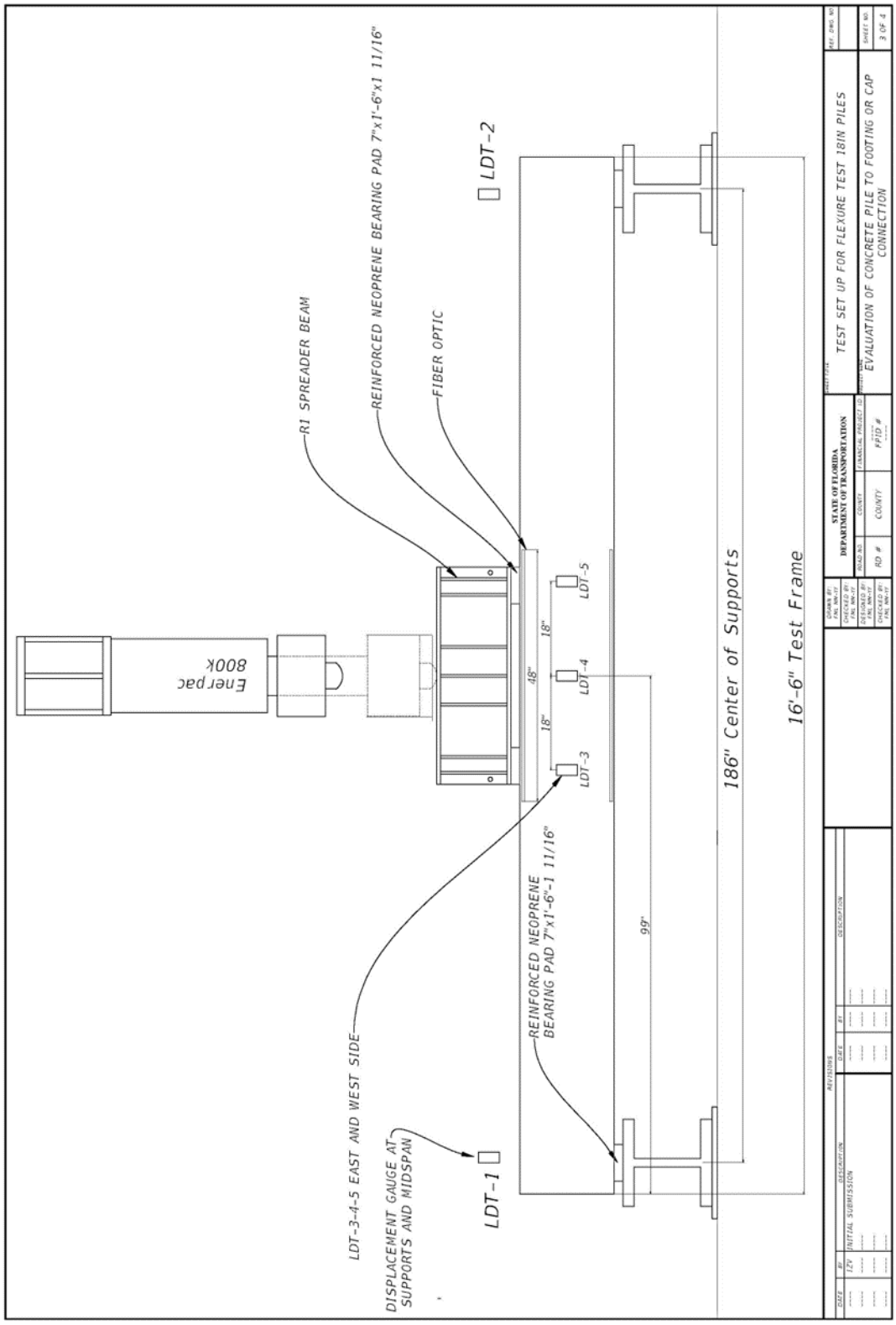

B.2. PILE-TO-CAP CONNECTION TEST SETUP DRAWINGS

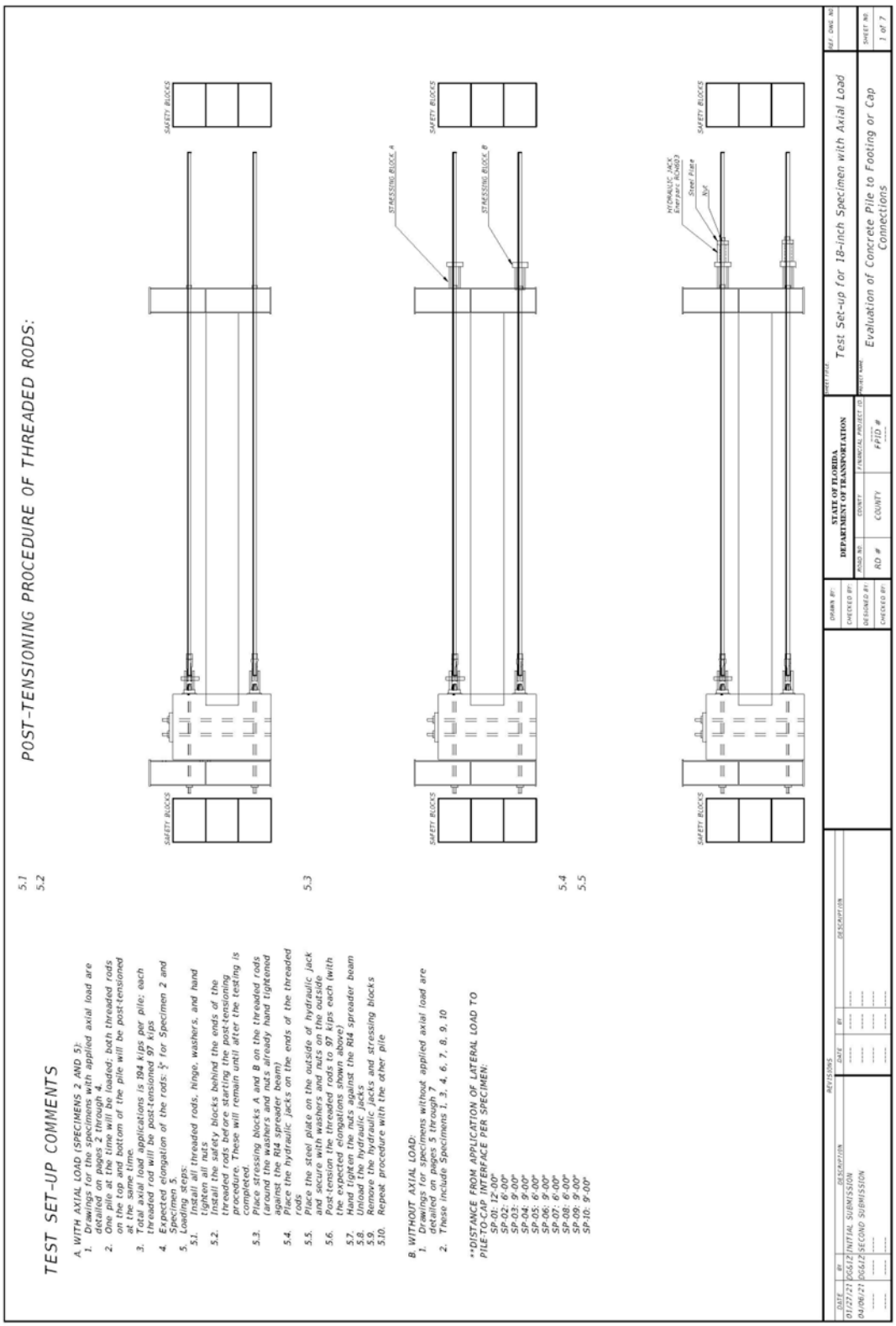

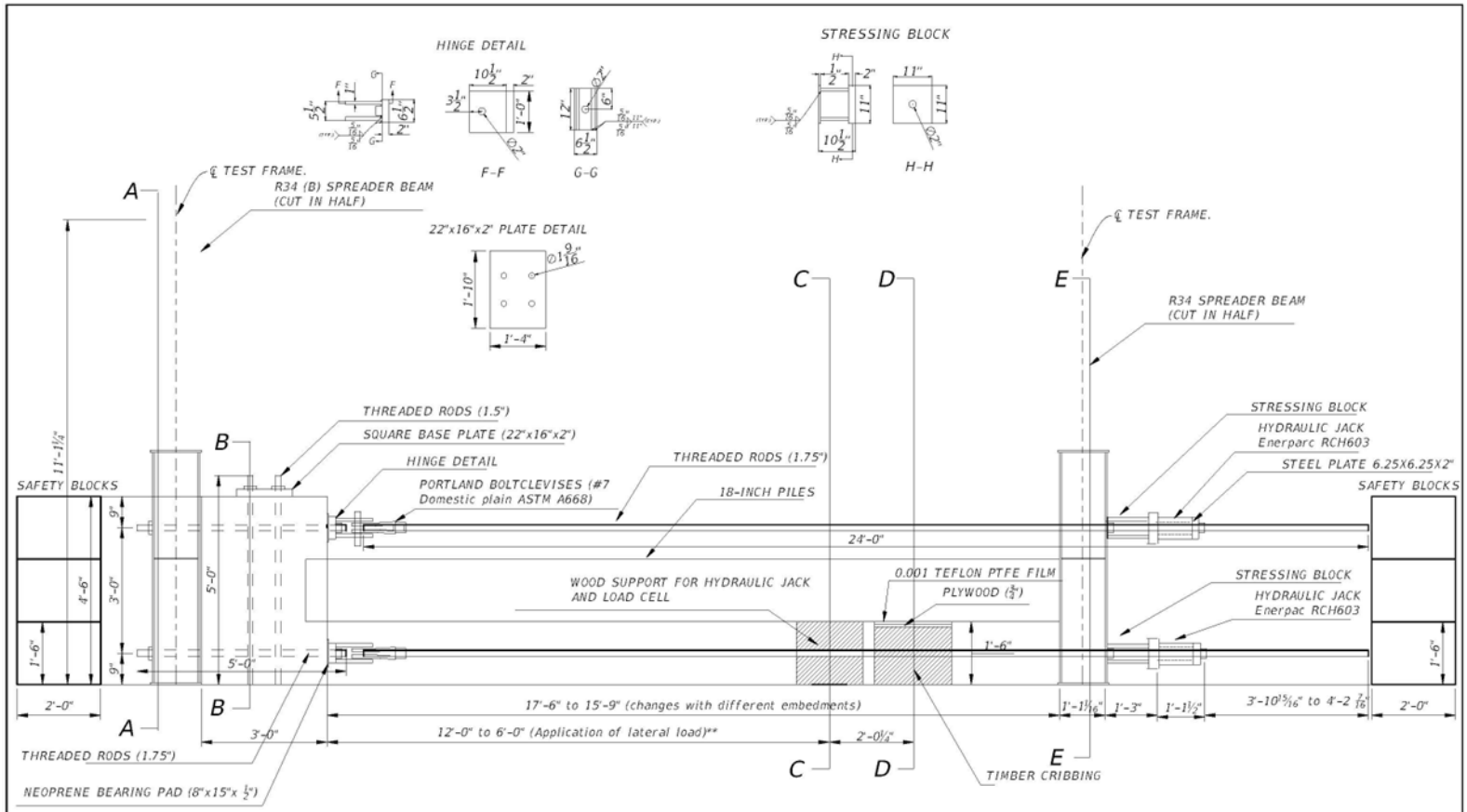

REVISIONS					
DATE	BY	DESCRIPTION	DATE	BY	DESCRIPTION
01/27/21	DG&IZ	INITIAL SUBMISSION	----	----	----
04/06/21	DG&IZ	SECOND SUBMISSION	----	----	----
----	----	----	----	----	----
----	----	----	----	----	----

DRAWN BY:
CHECKED BY:
DESIGNED BY:
CHECKED BY:

STATE OF FLORIDA
DEPARTMENT OF TRANSPORTATION

ROAD NO.	COUNTY	FINANCIAL PROJECT ID
RD #	COUNTY	FPID #

SHEET TITLE: Test Set-up for 18-inch Specimen with Axial Load

PROJECT NAME: Evaluation of Concrete Pile to Footing or Cap Connections

REF. DWG. NO.

SHEET NO. 2 of 7

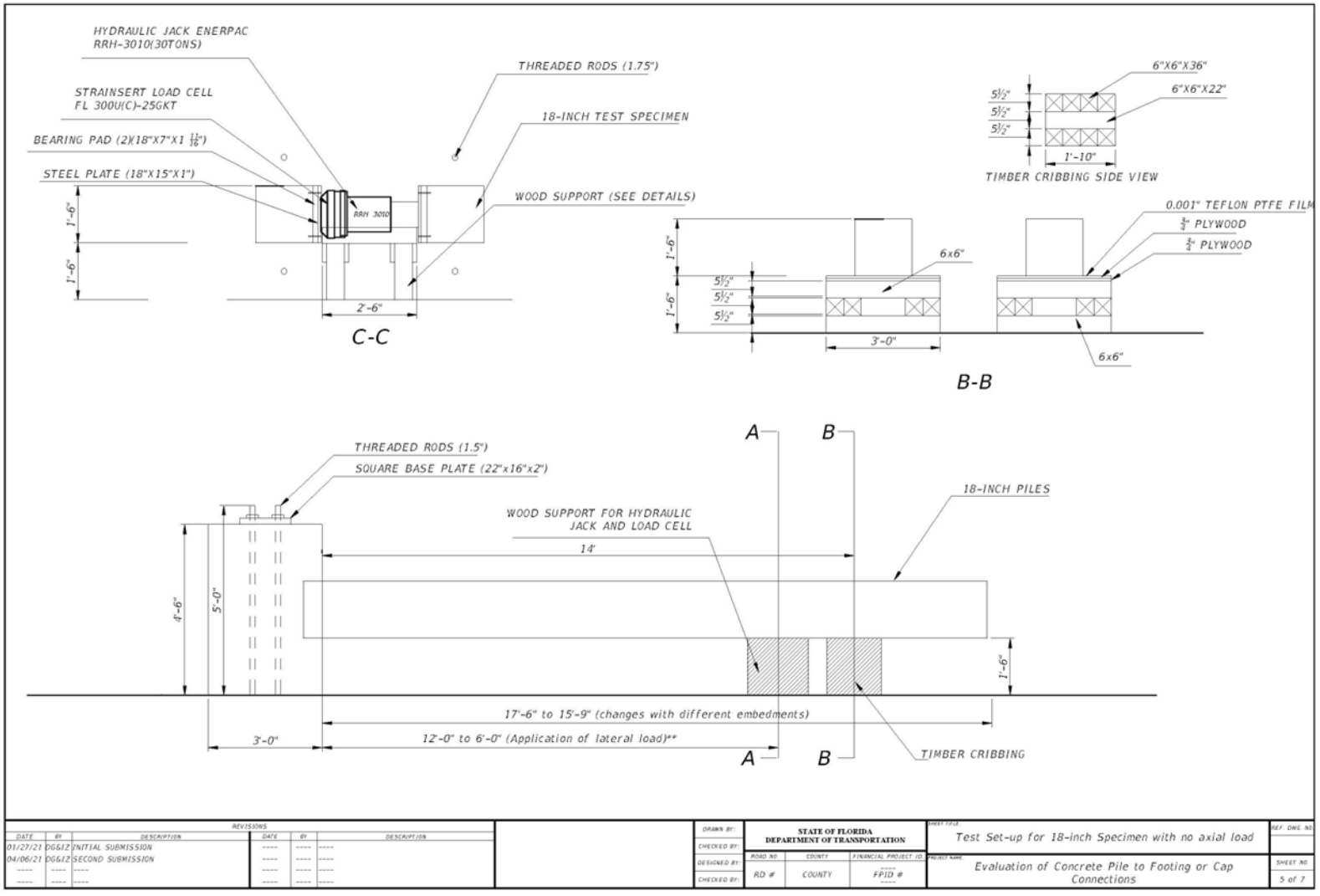

REVISIONS					
DATE	BY	DESCRIPTION	DATE	BY	DESCRIPTION
01/27/21	DG&JZ	INITIAL SUBMISSION	----	----	----
04/06/21	DG&JZ	SECOND SUBMISSION	----	----	----
----	----	----	----	----	----
----	----	----	----	----	----

DRAWN BY:
CHECKED BY:
DESIGNED BY:
CHECKED BY:

STATE OF FLORIDA
DEPARTMENT OF TRANSPORTATION

ROAD NO.	COUNTY	FINANCIAL PROJECT ID
RD.#	COUNTY	---- FPID # ----

SHEET TITLE: Test Set-up for 18-inch Specimen with no axial load

PROJECT NAME: Evaluation of Concrete Pile to Footing or Cap Connections

REF. DWG. NO.

SHEET NO. 5 of 7

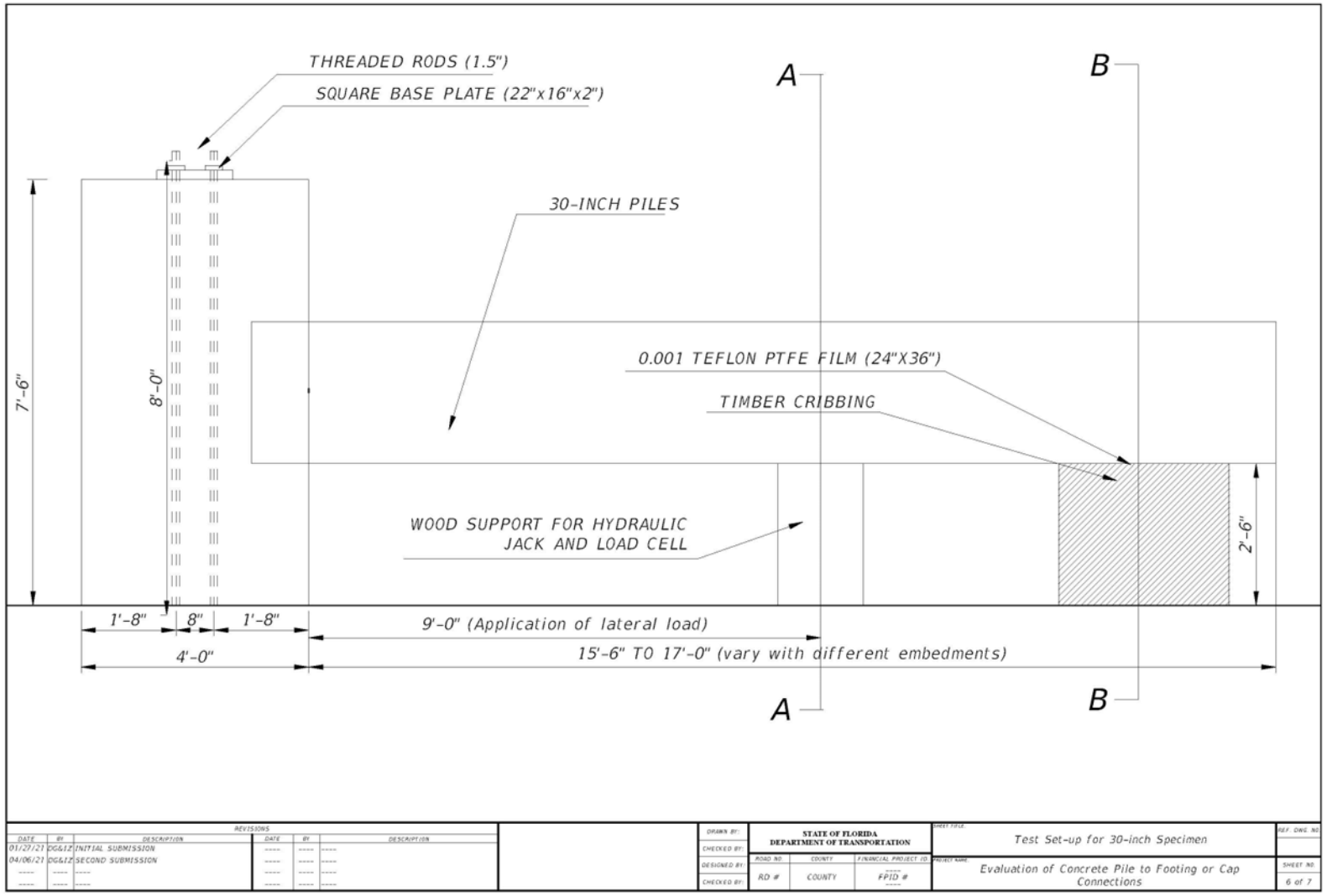

REVISIONS					
DATE	BY	DESCRIPTION	DATE	BY	DESCRIPTION
01/27/21	DG&IZ	INITIAL SUBMISSION	----	----	----
04/06/21	DG&IZ	SECOND SUBMISSION	----	----	----
----	----	----	----	----	----
----	----	----	----	----	----

DRAWN BY:
CHECKED BY:
DESIGNED BY:
CHECKED BY:

STATE OF FLORIDA
DEPARTMENT OF TRANSPORTATION

ROAD NO.	COUNTY	FINANCIAL PROJECT ID
RD #	COUNTY	FPID #

SHEET TITLE: Test Set-up for 30-inch Specimen

PROJECT NAME: Evaluation of Concrete Pile to Footing or Cap Connections

REF. DWG. NO.

SHEET NO. 6 of 7

C. PILE CAPACITY

Results of the experimental testing of 18-inch piles are shown in this section. Two piles were cut from Specimen 2 and tested for flexure to measure the actual capacity of the 18-inch piles. The test set up consisted of a simple supported beam with two-point loads.

C.1. PILE 1

Results of Pile 1 are summarized in Table C.1

Table C.1: P1 Summary of results

Pile 1	
Failure load (kips)	105.446
Maximum displacement at midspan (in)	2.17
Ultimate Moment Developed (k-ft)	329.52

Pile 1 and 2 had similar failure mechanism, crushing of the concrete at the top of the pile, as shown in Figure C.1. Symmetrical cracking behavior was observed on both sides of the pile

(a) (b)

Figure C.1: P1 18-inch pile (a) test set up (b) failure mechanism

C.1.1. Laser Displacement Transducers (LDT)

Displacements were recorded along the length of the piles through 10 laser displacement transducers (LDTs), as shown in Figure C.2.

Figure C.2: Location of laser displacements and test set up

The load-displacement curves are shown in Figure C.3. The maximum load reached by Pile 1 was 105.446 kips, which corresponds to a moment of 329.52 kip-ft. The behavior of the beam was symmetrical, with a vertical maximum displacement of 2.17 inches at midspan.

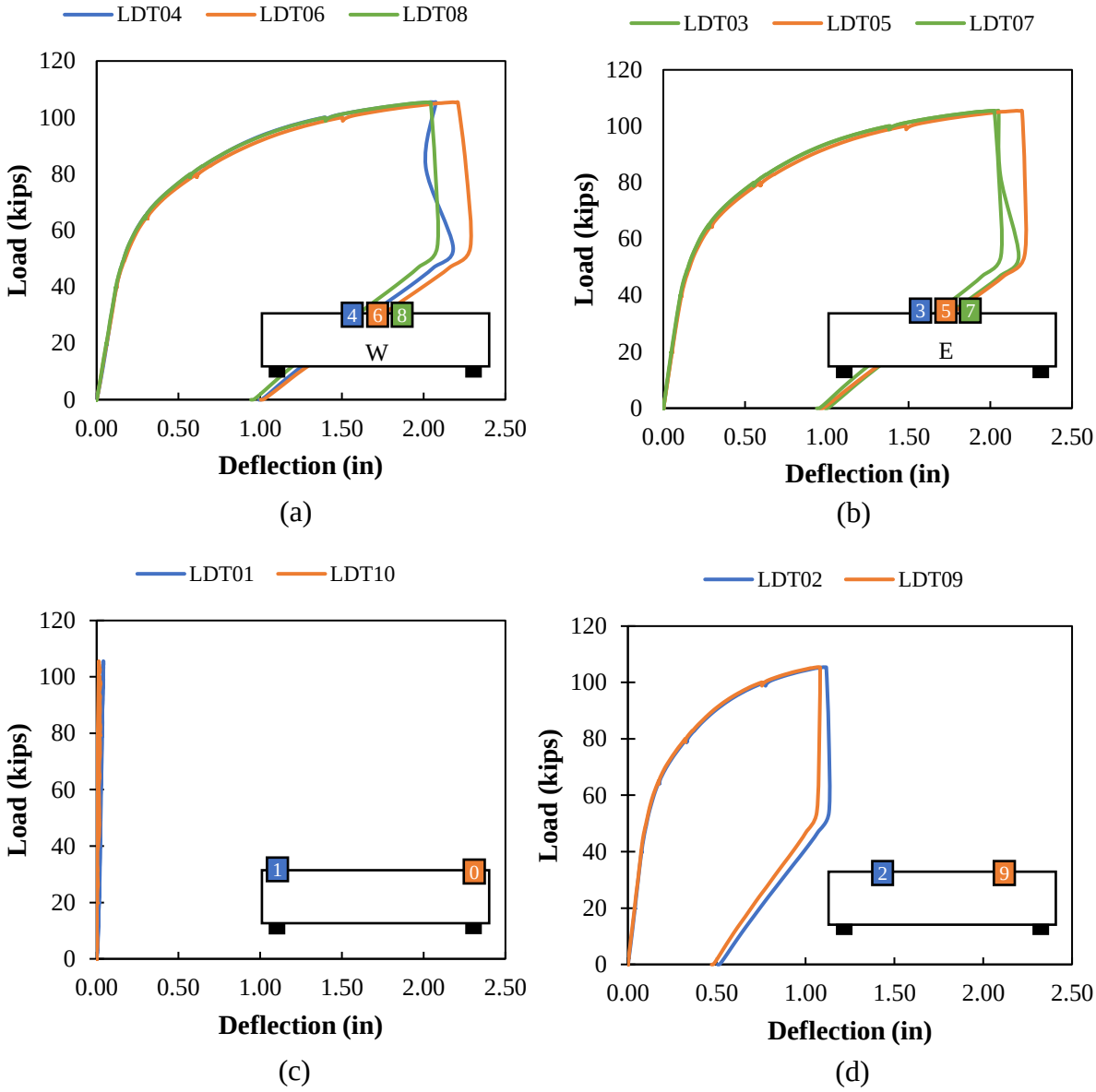

Figure C.3: P1 load displacement curves

C.1.2. Concrete Strain Gauges

Strain in the concrete was recorded in the east side of the piles using concrete strain gauges (CSGs) at different depths. Results are shown in Figure C.4.

The strains in SG-01to SG-03 measured compressive strains until approximately 95 kips, at which point tensile strains began to develop. SG-01 and SG-02 measured max tensile strains of 1900 με and 820 με, respectively, at load failure. SG-03 measure compressive strains less than 500.

SG-04 to SG-12, located at mid-depth and below, measured tensile strains less than 357 με.

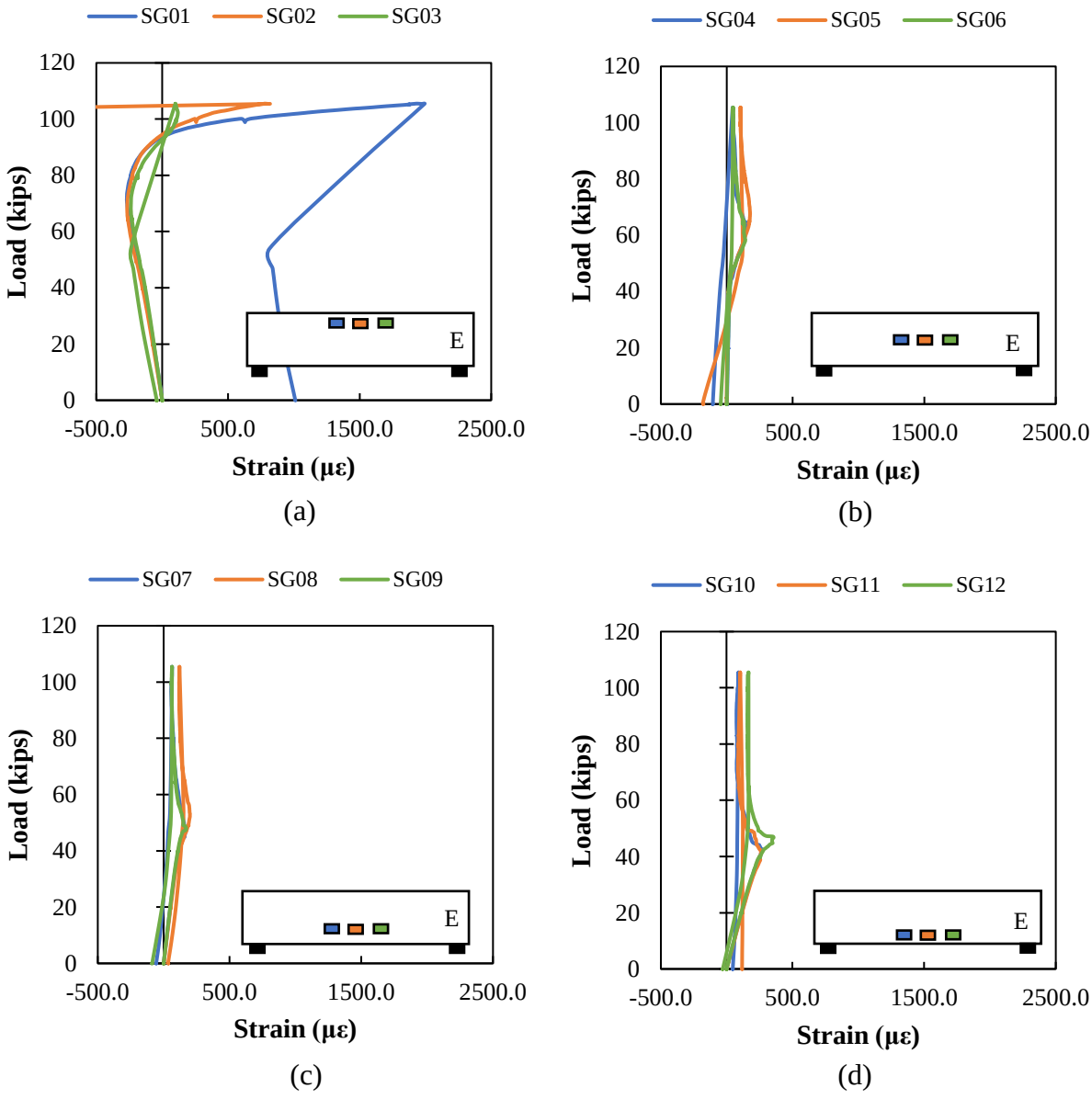

Figure C.4: P1 concrete strain data

C.1.3. Fiber Optic Sensors

Fiber optic sensos (FOS) were located at the west side of the pile to measure strains and enable curvature to be calculated. The top fiber was located at 4” from the top of the beam, and the bottom fiber at 6” from the bottom of the beam.

Strains along the length of the FOS at different loads are shown in Figure C.5. Compression strains developed at the top fiber of the pile until around 70 kips, at which point compressive strains started to decrease and tensile strains started to develop. This similar behavior can be observed in the concrete strain gauges SG-01 to SG-03. On the bottom fiber tension strains developed as the pile approached the failure load.

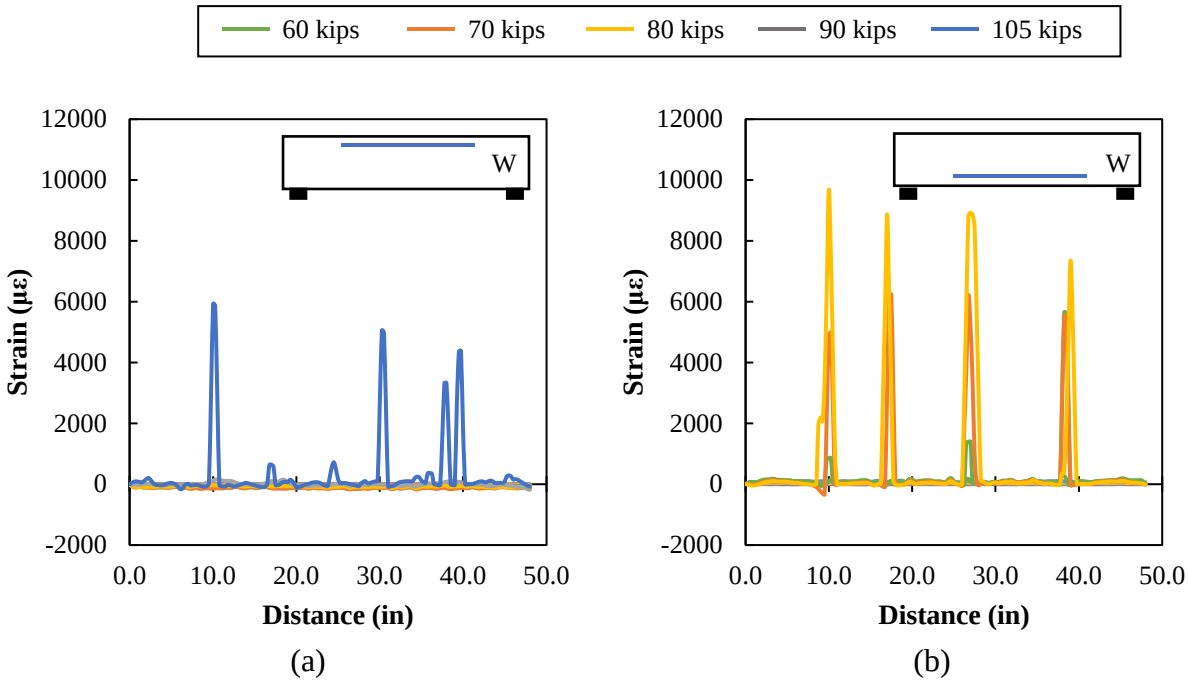

Figure C.5: P1 fiber optic data (a) top fiber (b) bottom fiber

The strain profile at midspan is shown in Figure C.6. Tensile strains were measured at the bottom fiber at about 9000 με at failure.

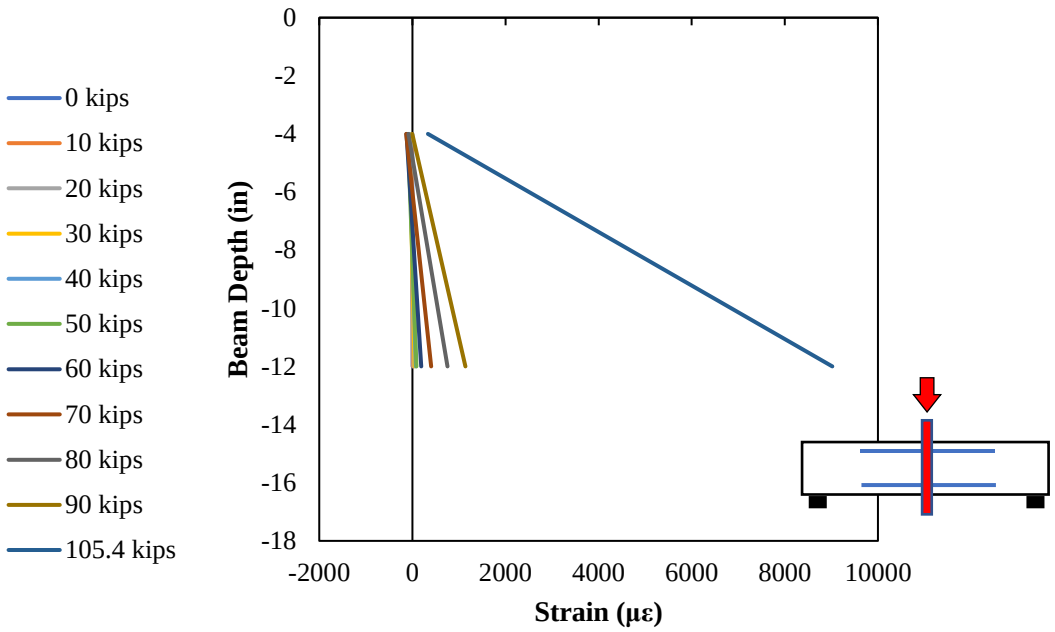

Figure C.6: P1 strain profile at midspan

The curvature was determined from the measured strains in the FOS and the distance between the sensors. The calculated moment-curvature response is shown in Figure C.7

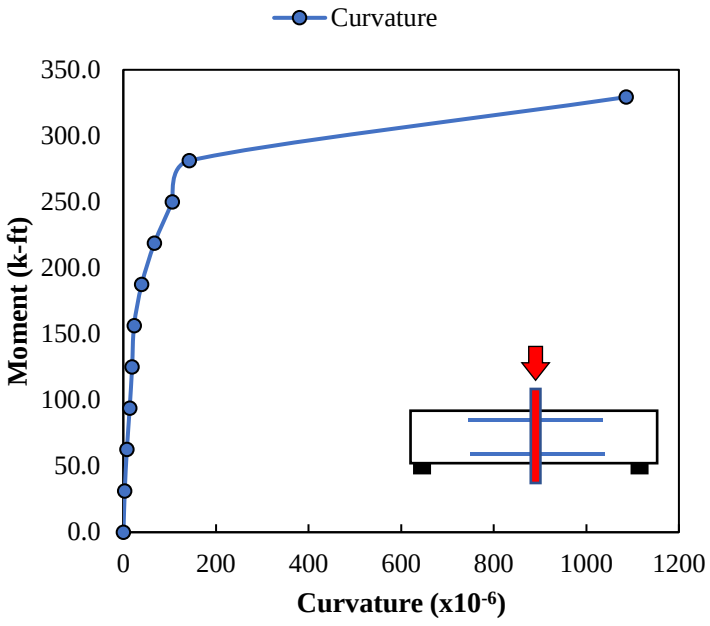

Figure C.7: P1 moment-curvature profile at midspan

C.2. PILE 2

Results of Pile 2 are summarized in Table C.2

Table C.2: Pile 2 Summary of results

Pile 2	
Failure load (kips)	106.414
Maximum displacement at midspan (in)	2.12
Ultimate Moment Developed (k-ft)	332.5

Pile 1 and 2 had similar failure mechanism, crushing of the concrete at the top of the pile, as shown in Figure C.8. Symmetrical cracking behavior was observed on both sides of the pile.

(a) (b)

Figure C.8: P2 (a) test set up (b) failure mechanism

C.2.1. Laser Displacement Transducers (LDT)

The load-displacement curves are shown in Figure C.9

The maximum load reached by Pile 1 was 106.414 kips, which corresponds to a moment of 332.5 kip-ft. The behavior of the beam was symmetrical, with a vertical maximum displacement of 2.12 inches at midspan.

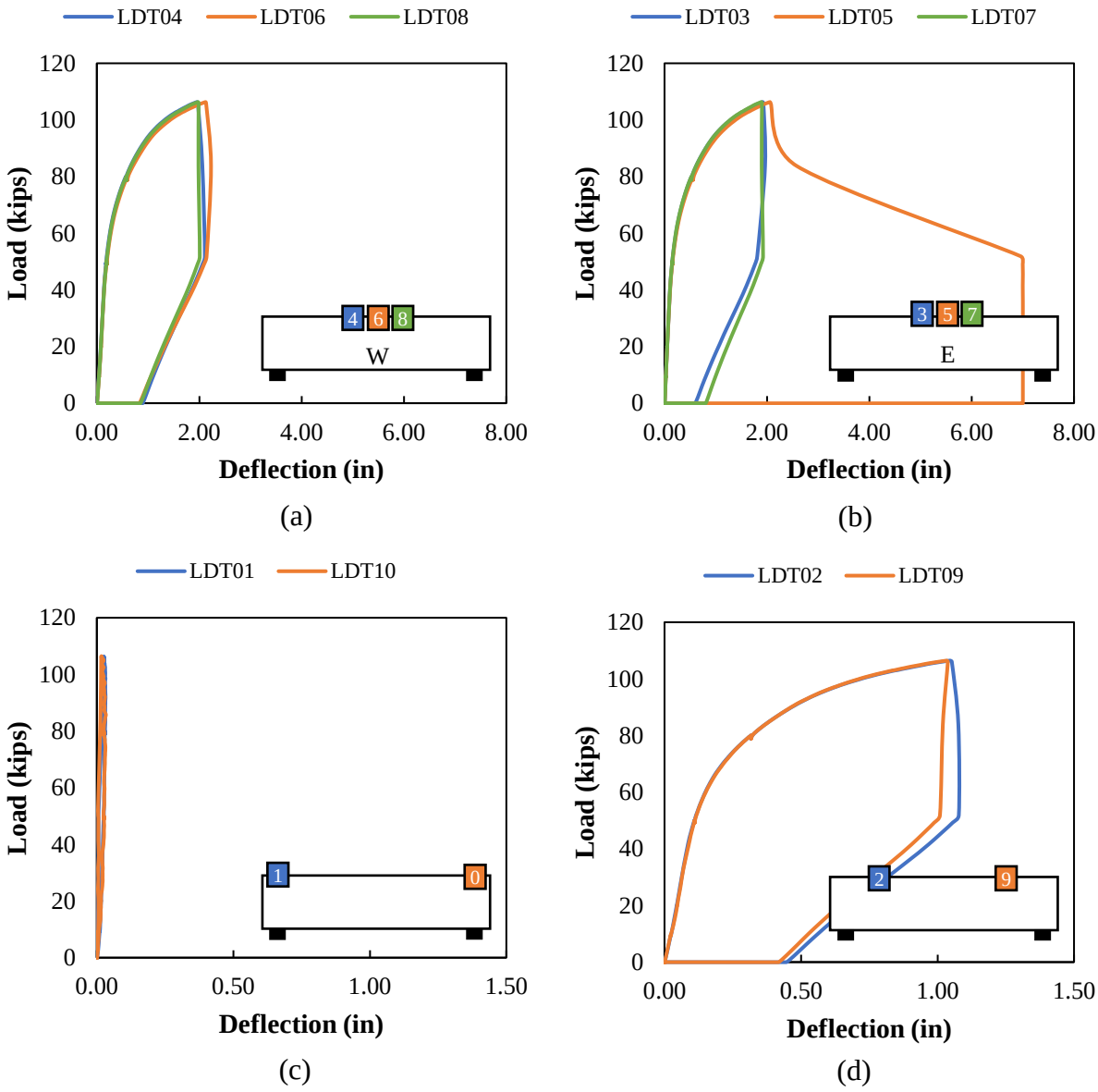

Figure C.9: P2 load deflection curves

C.2.2. Concrete Strain Gauges

Strain in the concrete was recorded in the east side of the piles using concrete strain gauges (CSGs) at different depths. Results are shown in Figure C.10.

The strains in SG-01 to SG-03 started with compressive strains until approximately 70 kips, at which point compressive strains started decreasing until around 105 kips were the pile failed. SG-04 and SG-05 measured tensile strains less than 170 με. SG-05 developed small increases of tensile strains until around 42 kips at which point tensile strains quickly began to be measured which correspond to a crack formed at this location. This same behavior can be seen in SG-09 and SG-12 where the crack opened.

SG-07, SG-08, SG-10 and SG-11, measure tensile strains less than 300 με.

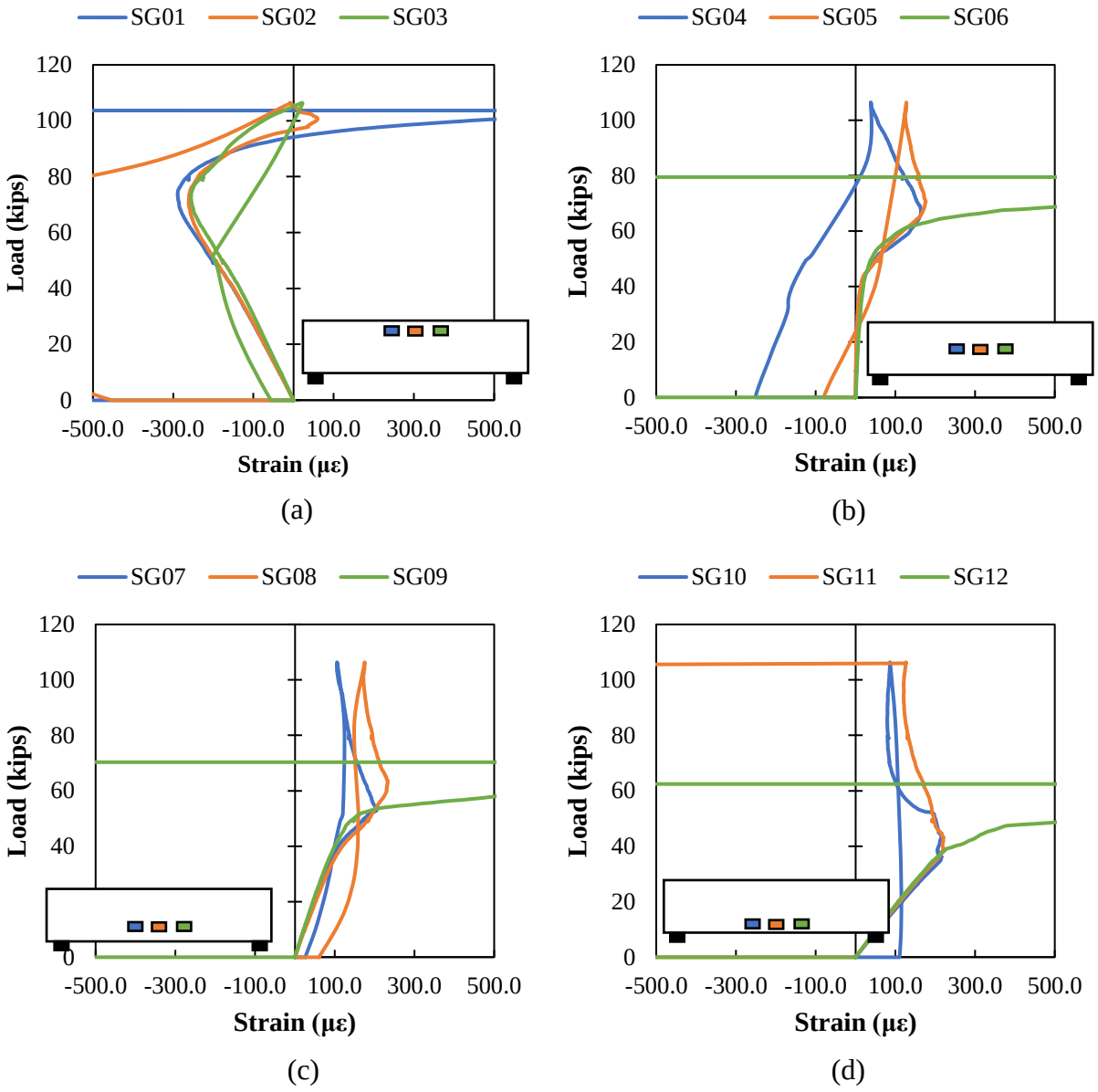

Figure C.10: P2 concrete strain data

C.2.3. Fiber Optic Sensors

Strains along the length of the FOS at different loads are shown in Figure C.11. Maximum compressive strains developed at the top fiber of the pile at 70 kip, compressive strains started to decrease until load failure, where maximum tensile strains developed in the top fiber. On the bottom fiber tension strains developed as the pile approached the failure load.

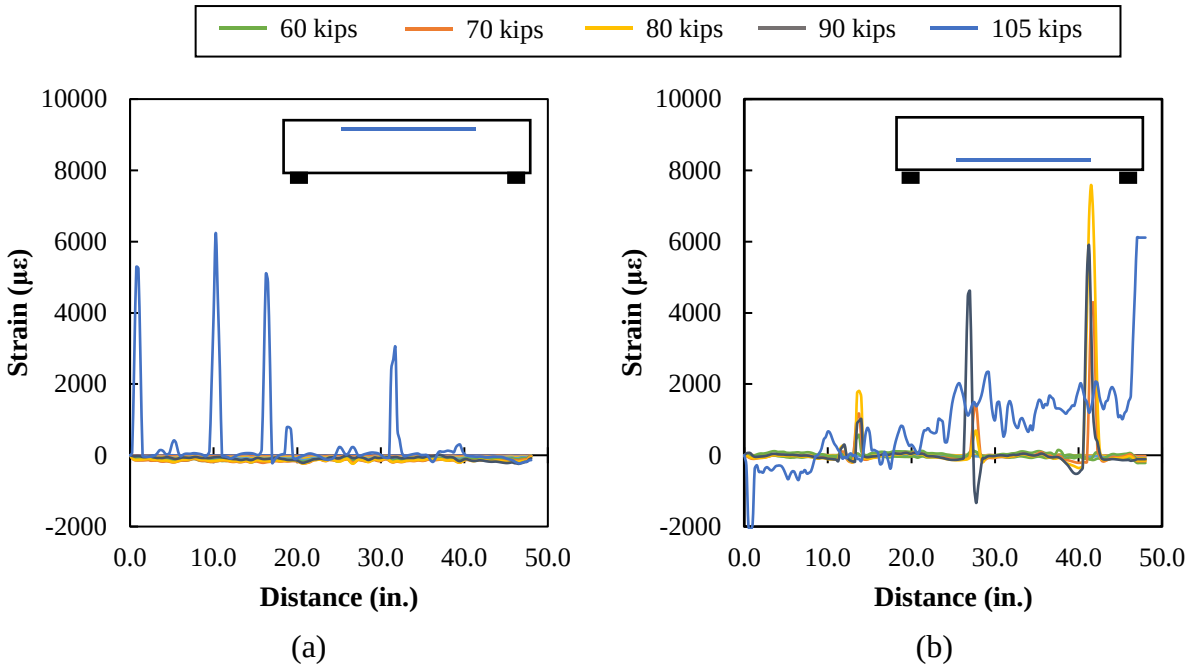

Figure C.11: P2 fiber optic data (a) top fiber (b) bottom fiber

The strain profile at midspan is shown in Figure C.12. Tensile strains were measured in the bottom fiber of the pile and compressive strains at the top. At failure compressive strains at about 8000 με developed in the bottom fiber.

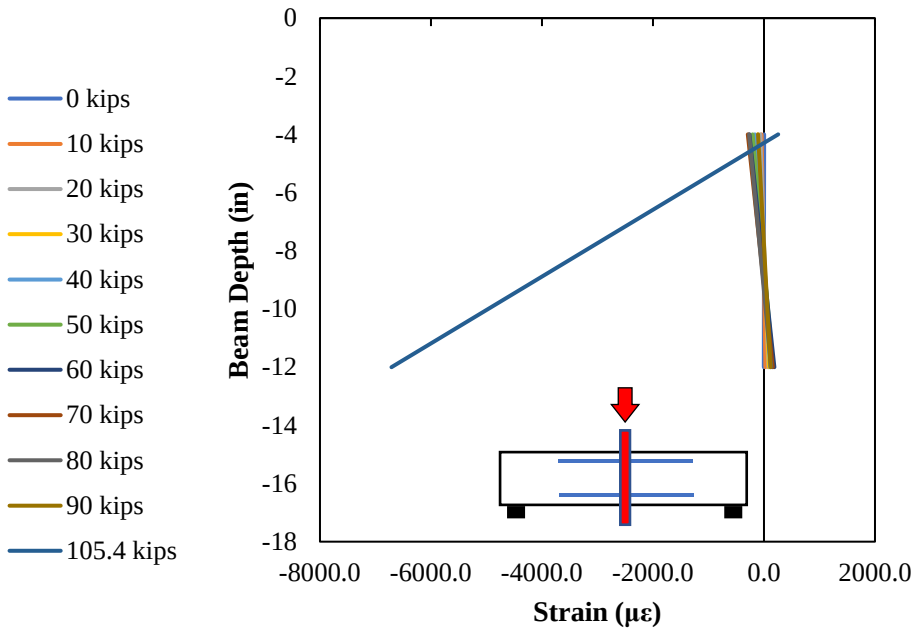

Figure C.12: P2 Strain profile at midspan

The curvature was determined from the measured strains in the FOS and the distance between the sensors. The calculated moment-curvature response is shown in Figure C.13

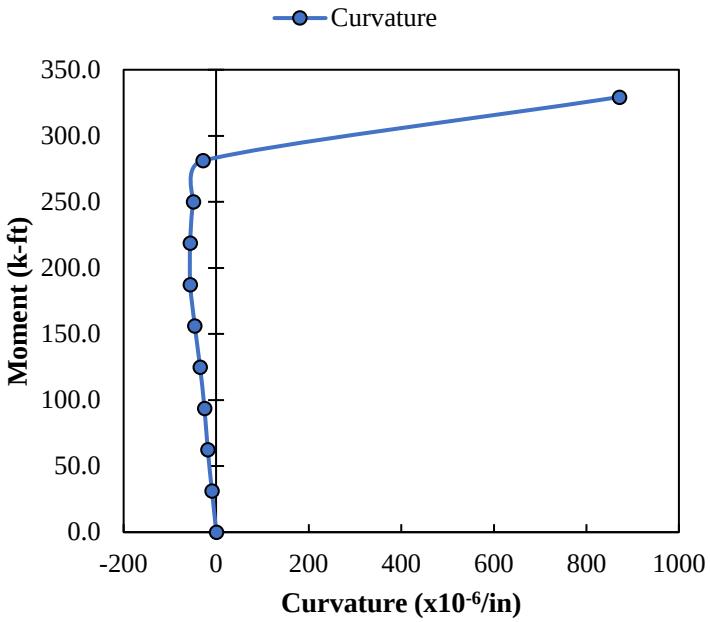

Figure C.13: P2 Moment-curvature at midspan

D. PILE-TO-CAP CONNECTION EXPERIMENTAL RESULTS

The results of the experimental testing are summarized in this section.

D.1. SP-01

D.1.1. Observations and Summary of Results

Results of Specimen 1 are summarized in Table D.1.

Table D.1: SP-01 Summary of results

Specimen 1	
Pile Embedment	6.0 in. ($0.33d_{pile}$)
Interface Reinforcement	none
Axial Load	0 kips ($0A_g f'_{c,pile}$)
Failure load (kips)	9.5
Distance from Load to Cap (ft.)	12.0
Failure Mechanism	Cap Crushing / Strand Development
Pile Failed	West
Maximum Displacement (in)	8.187
Ultimate Moment Developed (k-ft)	114.1
Percentage of capacity of pile	36.8 %

Specimen 1 had an embedment length of 6-inch, which was the shallowest embedment of all specimens in the experimental study; no axial load was applied to the piles, and no interface reinforcement was present between the pile and cap.

Failure of this specimen occurred in the west pile. The observed failure was likely caused by the crushing of the concrete around the pile. A large spalled concrete region was observed next to the pile, shown in Figure D.1, that was not observed in other specimens. A large crack was also

observed in the pile at the interface plane at the face of the cap, which would also suggest that there was also a strand development failure.

Figure D.1: SP-01 Failure mechanism (a) pile crushing (b) pile-to-cap interface

D.1.2. Laser displacement transducers (LDT)

Displacements were recorded along the length of both piles through five laser displacement transducers (LDTs), as shown in Figure D.2. The application of the lateral load in the piles for Specimen 1 was at 12 ft from the pile-to-cap interface, which was the same location as LDT-5.

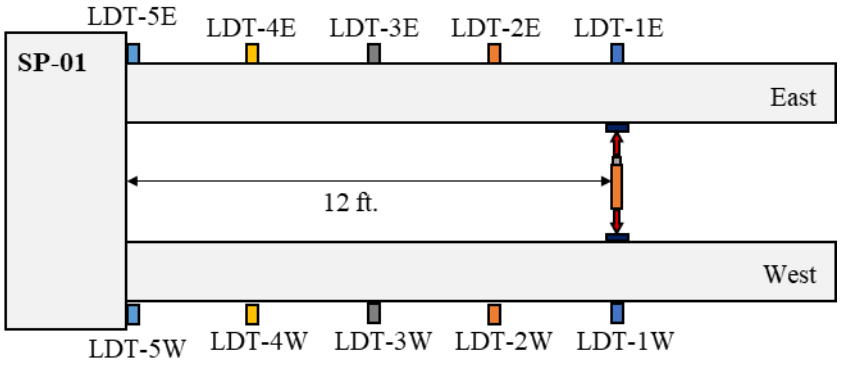

Figure D.2: Location of laser displacement transducers (LDT) and applied load for SP-01

The load-displacement curves of the west and east piles are shown in Figure D.3 (a) and (b), respectively. The maximum load reached by Specimen 1 was 9.51 kips, which corresponds to 36.8% the capacity of the 18-inch piles. The horizontal displacement in the west pile was 8.187-inch and in east pile 0.875-inch. The load-displacement curve was nearly horizontal at the time the hydraulic jack ran out of stroke and the load removed.

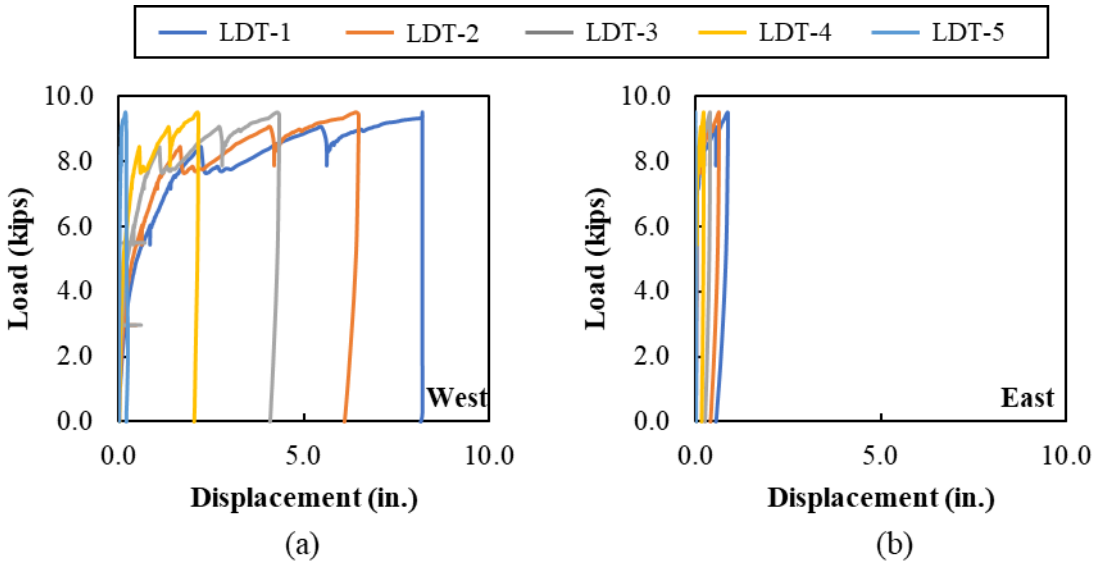

Figure D.3. SP-01 load-displacement curve (a) west pile (b) east pile

D.1.3. Concrete Strain Gauges

Strain in the concrete was recorded around the piles and in the middle of the pile cap using concrete strain gauges (CSGs). Vertical CSGs on the outside edge of the cap measured splitting stresses that developed in the pile cap, shown in Figure D.4 (a). Horizontal CSGs on the outside of the cap measured compressive stresses developing from the pile bearing on the pile cap, shown in Figure D.4 (b). Horizontal CSGs on the pile cap face above and below the embedded pile measured tension developing as the embedded pile was loaded, shown in Figure D.4 (c).

The strains in CSG-01 to CSG-07 were all less than the typical cracking strain for concrete (typically around 130 με). CSG-01, CSG-02, and CSG-03, which were perpendicular to load application had small tensile strain. CSG-04 and CSG-05, parallel to load application, which are located outside the piles, measured compression strains.

CSG-06, located above the embedded west pile, measured tensile strains less than 70 με at the maximum applied load. CSG-07, located below the embedded west pile, started with tensile strains until approximately 4 kips and 76 με, at which point tensile strains quickly decreased and compression strains began to be measured. This corresponded to cracking and spalling of concrete at this location, as shown in Figure D.4 (d).

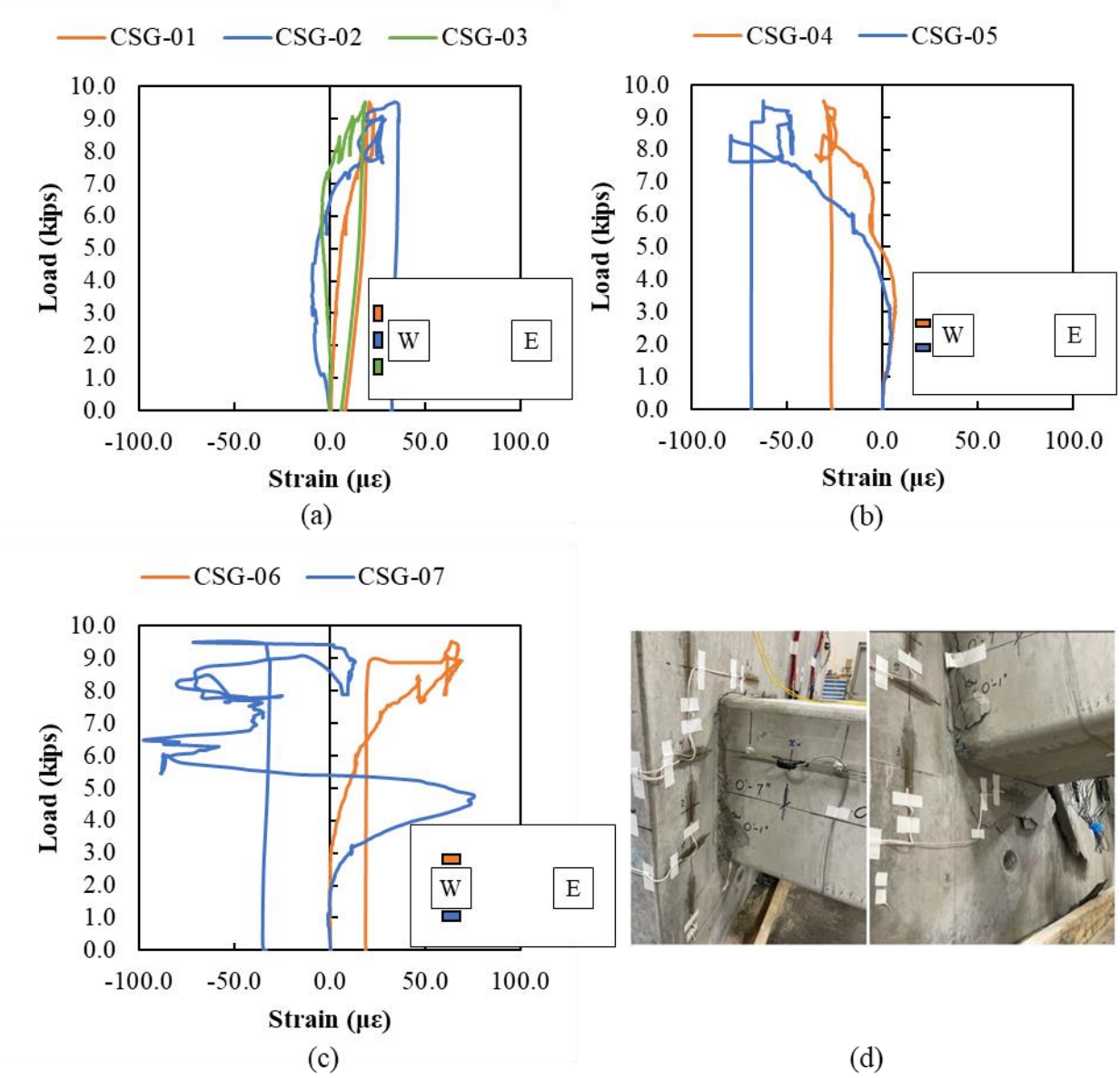

Figure D.4: SP-01 concrete strain data for CSG-01 to CSG-07

Vertical and horizontal concrete strains in the middle of the pile cap between the piles are shown in Figure D.5. Measured strains were minor in both directions until spalling of the concrete beside the west pile occurred between 8 and 8.5 kips. At this point, the tensile strain in CSG-09 and compression strain in CSG-12 increased rapidly.

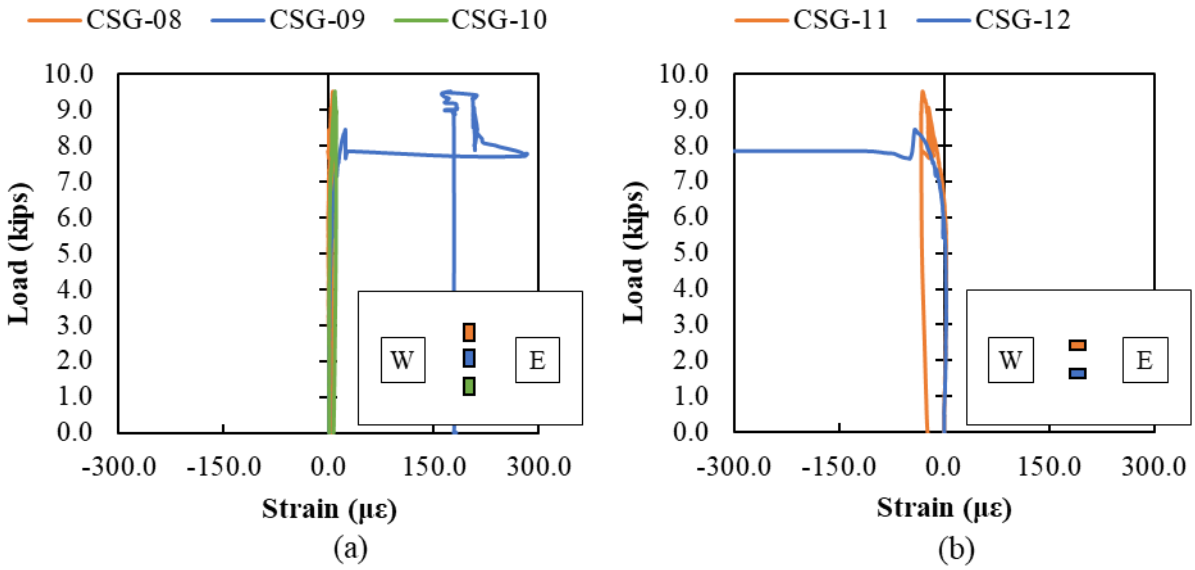

Figure D.5: SP-01 concrete strain data for CSG-08 to CSG-12

Concrete strains around the east pile are shown in Figure D.6. The response of these CSGs was generally like the CSGs around the west pile, shown in Figure D.4.

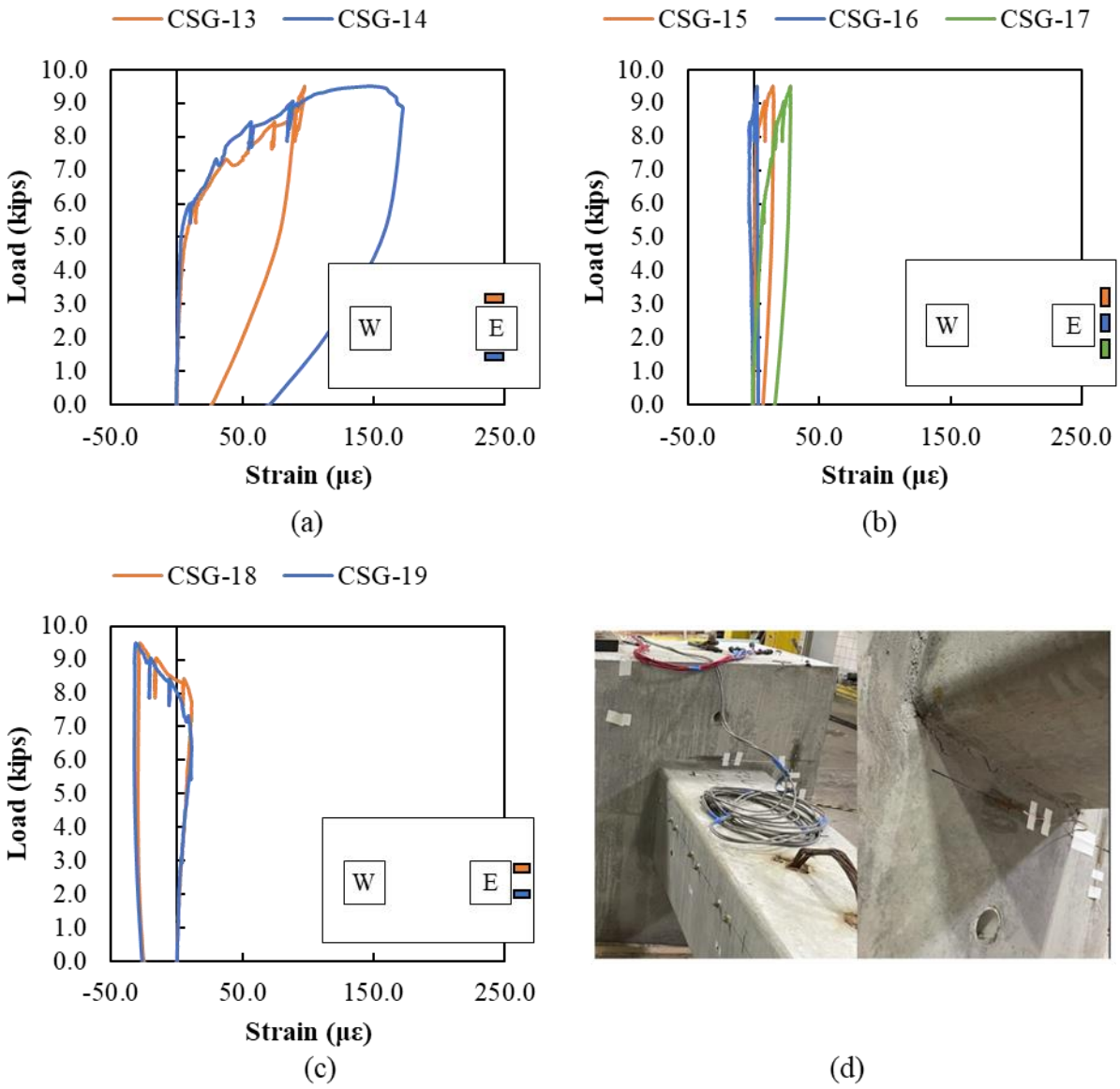

Figure D.6: SP-01 concrete strain data for CSG-13 to CSG-19

Concrete strains on the west and east faces of the pile cap are shown in Figure D.7. Measured strains on the west and east faces of the pile cap were less than 50 με at maximum applied loads.

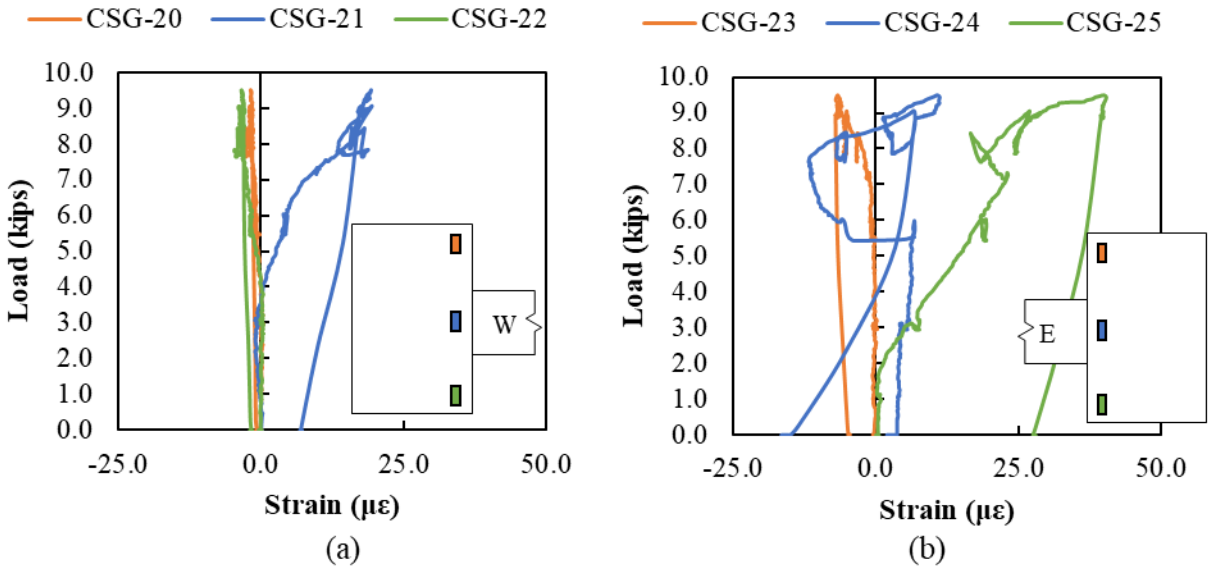

Figure D.7: SP-01 concrete strain data for CSG-20 to CSG-25 (a) west side (b) east side

D.1.4. Rebar Strain Gauges

Rebar strains in the N5 bars are shown in Figure D.8. The rebar strain gauges (RSGs) were located on the leg of the N5 ties toward the face of the pile cap with the embedded piles. Strains less than 50 με were measured in the bars with similar strains on the bars toward the exterior faces and between the embedded piles.

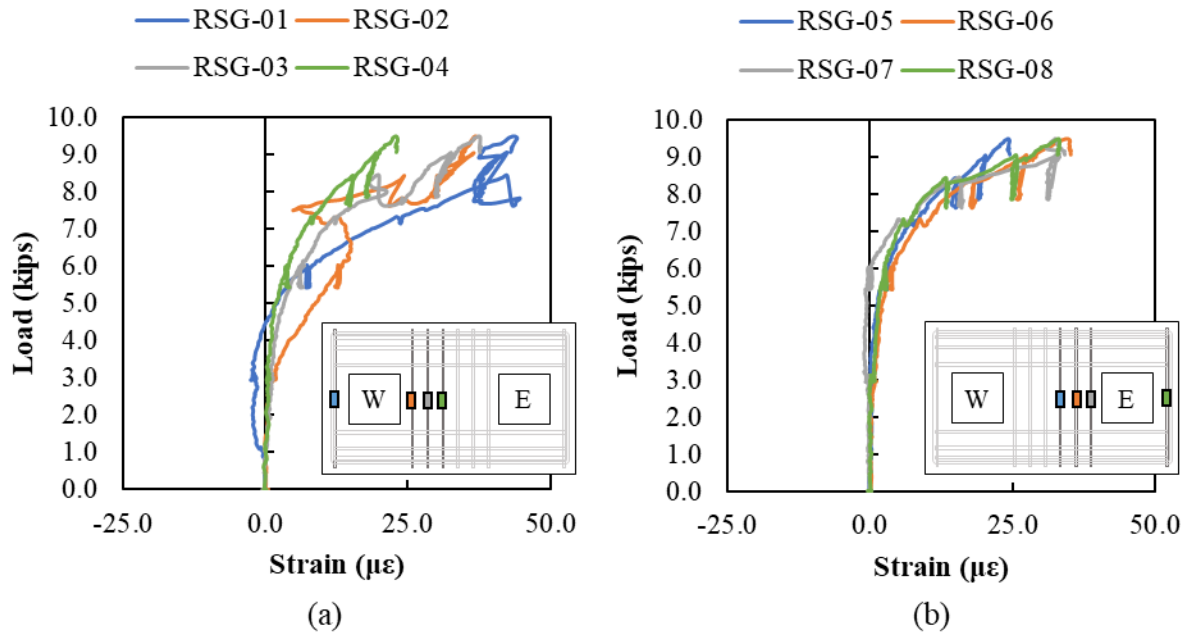

Figure D.8: SP-01 rebar strain data for N5 bars

Rebar strains in the N9 bars are shown in Figure D.9. RSGs were located on the leg of the N9 ties toward the face of the pile cap with the embedded piles. Maximum measured strains remained less than 50 με tension for all RSGs above and below the embedded piles. There was no apparent correlation between distance from embedded pile and rebar engagement.

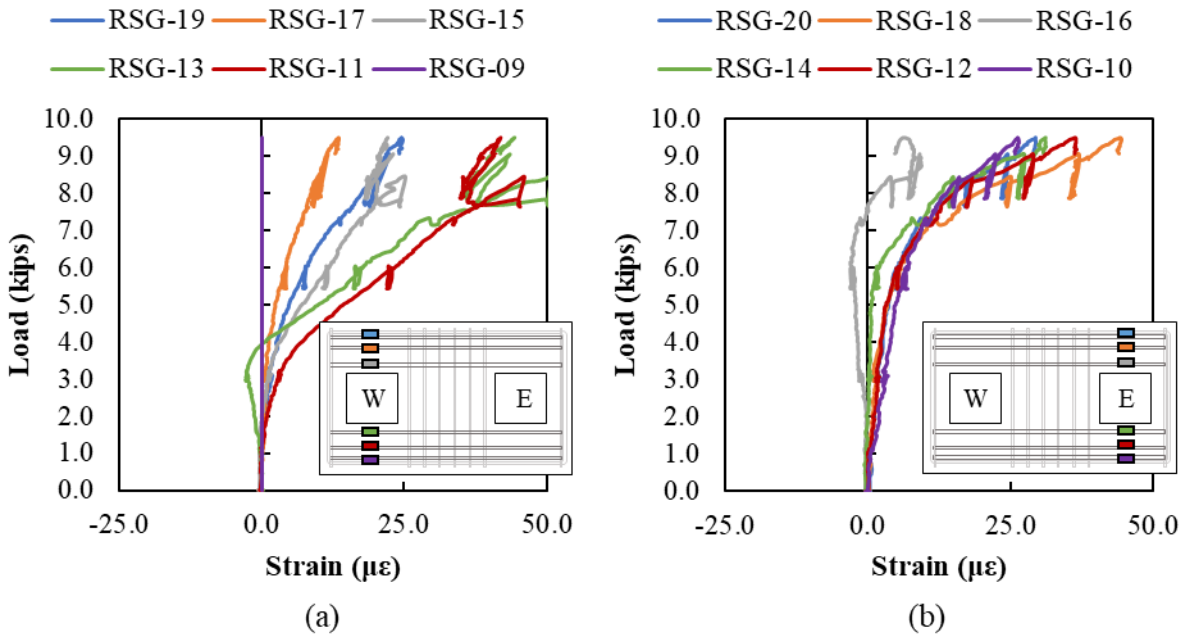

Figure D.9: SP-01 rebar strain data for N9 bars

Rebar strains in the N6 bars are shown in Figure D.10. RSGs were placed on the N6 bar close to the face of the pile cap with the embedded piles. Measured strains remained less than 50 με with the highest measured strains in RSG-25 located on the outside of the west pile.

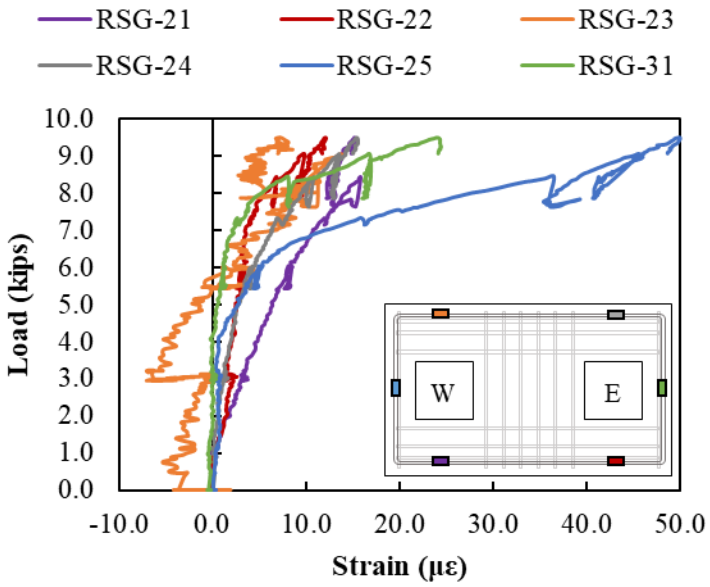

Figure D.10: SP-01 rebar strain data for N6 bars

Rebar strains in N6 bars on the side of the pile cap are shown in Figure D.11. Higher strains were measured on the west side of the pile cap, which correlates to the west pile embedment failing. Measured strains increased as bars were closer to the face of the pile cap with the embedded pile with the highest measured strains of around 50 με in RSG-25 toward the west face of the pile cap.

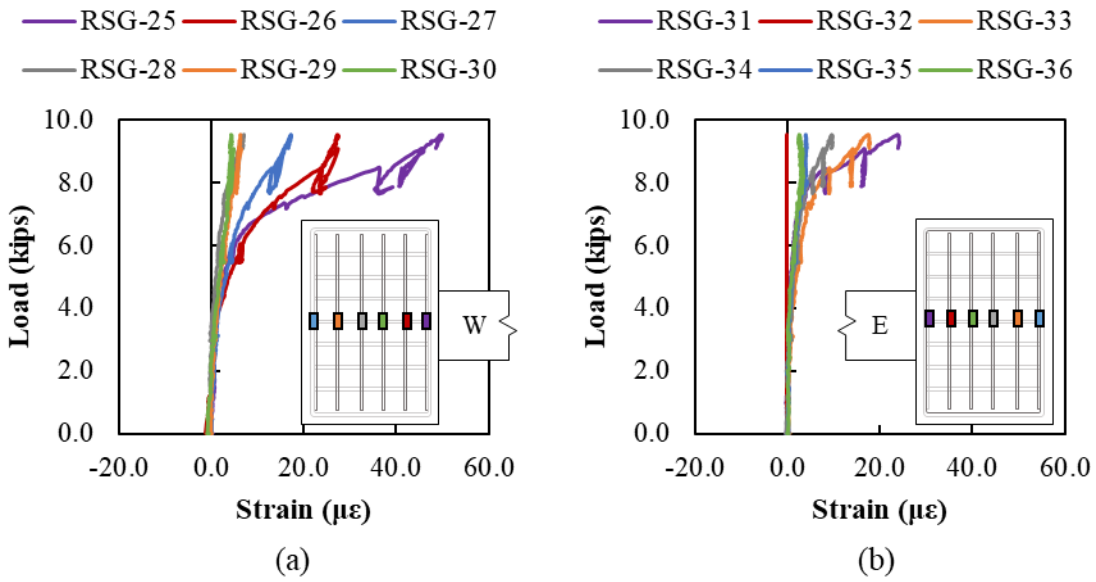

Figure D.11: SP-01 rebar strain data for N6 bars (a) west side (b) east side

D.1.5. Crack Displacement Transducers

Displacements were recorded in the plastic hinge zone of both piles using crack displacement transducers (CDTs); results are shown in Figure D.12 and Figure D.13. The closest CDTs to the face of the pile cap were 8 inches from the cap face, so the CDTs did not capture the crack at the interface of the cap and pile. Largest compression strains were measured in the CDT closest to the pile cap CDT-04E and CDT-05W. There was no correlation between strains on the tension face and distance from the pile cap.

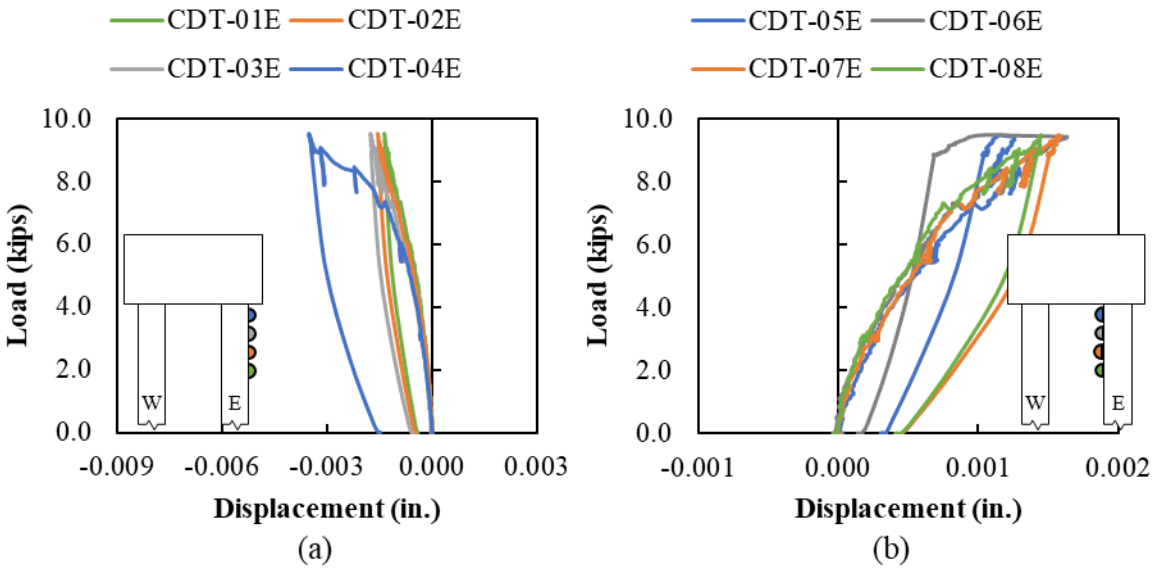

Figure D.12: SP-01 crack displacement data for the east pile

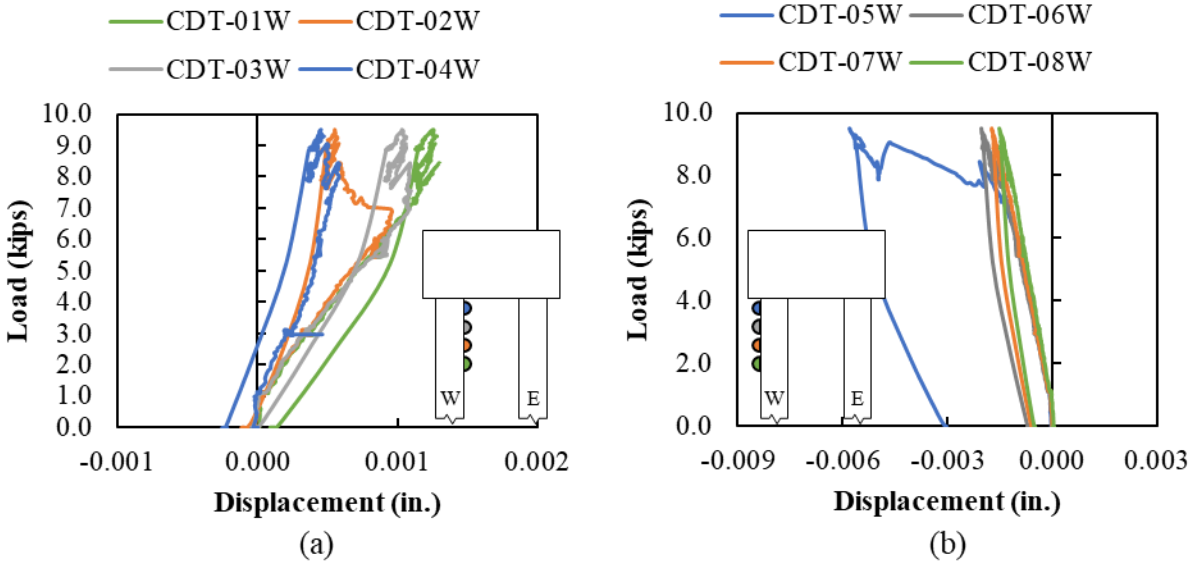

Figure D.13: SP-01 crack displacement data for the west pile

Moment-curvature was found using the measurements from the CDTs and distance between the tension and compression faces (18 inches for the 18-inch piles). The moment-curvature response found using the CDTs for the west and east piles are shown in Figure D.14. Higher curvature was measured in the west pile in the gauges closest to the pile-to-cap connection, but both piles are showing similar behavior.

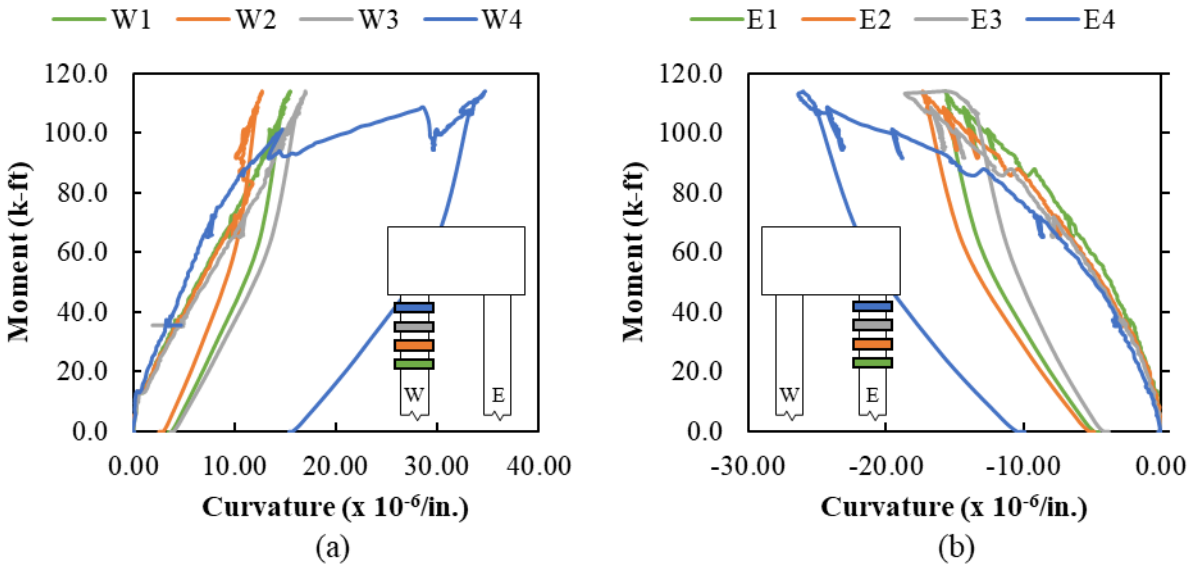

Figure D.14: SP-01 moment-curvature with crack displacement data (a) west pile (b) east pile

D.1.6. Vibrating Wire Gauges (Pile)

Vibrating wire gauge (VWG) data was recorded at different stages of the specimen life. The initial data was used to calculate the elastic shortening losses, and total losses of each specimen.

Initial stress in strands:

Jacking stress:
$$f_{pj} = \frac{F}{A} = \frac{34\ kips}{0.167\ in^2} = 203.6\ ksi$$

Readings from the longitudinal VWGs were recorded and used to find the stress in the strands after release (assuming E_p = 28,500 ksi):

Table D.2: SP-01 Elastic shortening losses calculation

VWG	**Before release** (με)	**After release** (με)	**Strain Change** (με)	**ES Losses** (ksi)
VWSG-P8-1E	0	-352.138	352.1	10.04
VWSG-P8-2E	0	-325.537	325.5	9.28
			Δf_{pES} =	9.66

Therefore, the average stress in strands after elastic shortening losses:

Stress after elastic shortening losses: $$f_{pi} - \Delta f_{pES} = 203.6\ ksi - 9.66\ ksi = 193.94\ ksi$$

Readings from the longitudinal vibrating gages were recorded and used to find the stress in the strands before testing (assuming E_p = 28,500 ksi):

Table D.3: SP-01 Total losses calculation

VWG	After release (με)	Before testing (με)	Strain change (με)	LT Losses (ksi)
VWSG-P8-1E	-352.138	-900.1	547.9	15.62
VWSG-P8-2E	-325.537	-854.3	528.8	15.07
			Δf_{pLT} =	15.34

The average stress in strands after all losses:

Stress after all losses immediately before testing: $$f_{pi} - \Delta f_{pES} - \Delta f_{pLT} = 203.6\ ksi - 9.66\ ksi - 15.34\ ksi = 178.6\ ksi$$

D.1.7. Vibrating Wire Gauges (Cap)

Vibrating wire gauge data was also recorded in the pile cap around the embedded east pile. Readings at different times are shown in Table D.4. Temperature can affect the strain gauges readings; therefore, a temperature correction was applied to the actual readings, taking as reference the before cap casting readings.

Table D.4: SP-01 Vibrating wire gauge data in pile cap

VWG	Before cap casting (με)	Before testing (με)	After Testing (με)
VWSG-4E	0	-72.788	-62.649
VWSG-5E	0	-82.677	-70.155
VWSG-6E	0	-131.847	-123.946
VWSG-7E	0	-128.075	-101.105

D.1.8. Fiber Optic Sensors

Fiber optic sensors (FOS) were located at the plastic hinge zone to measure strains and enable curvature to be calculated. Data was only measured in FOS in the east pile (FOS-20 and FOS-28) for Specimen 1. FOS in the west pile were not functional during the test, likely damaged during construction.

Strains along the length of the FOS at different loads are shown in Figure D.15. Tension strains developed at the interior face of the pile with maximum strains at the plane of the pile cap face, shown in Figure D.15 (a). Compression strains less than about 2,000 με were measured on the

exterior face of the east pile with maximum strains at the plane of the pile cap face, shown in Figure D.15 (b). Small tensile strains developed on the exterior face of the pile as the load approached the failure load.

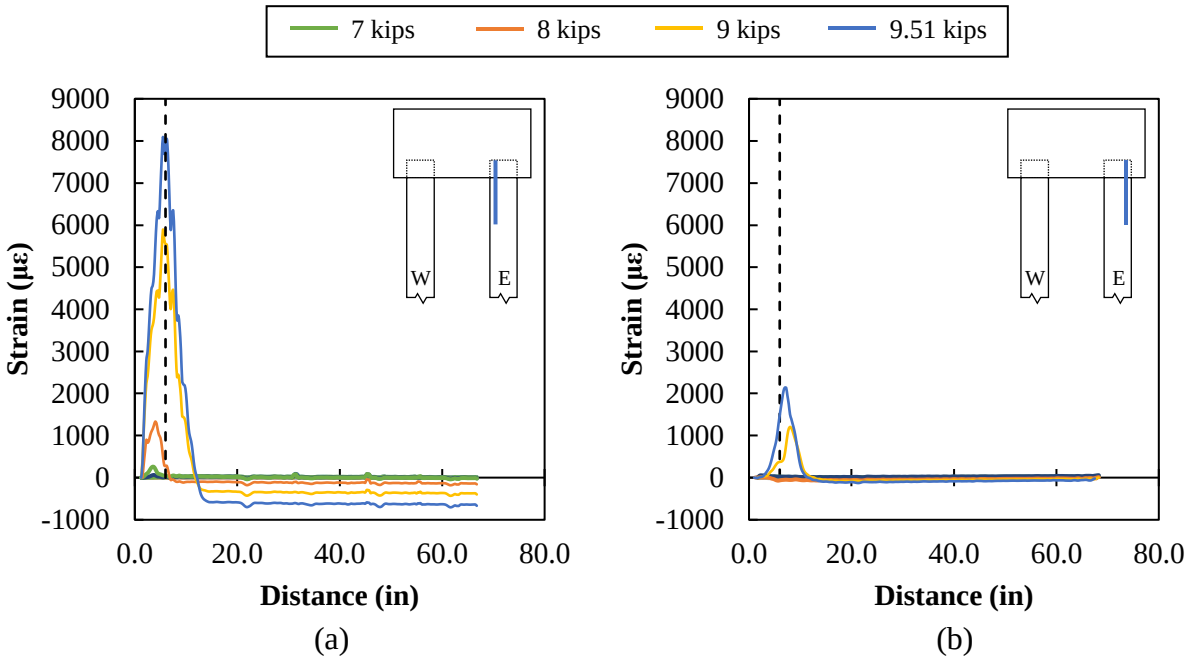

Figure D.15: SP-01 fiber optic data for east pile (a) FOS-20 (b) FOS-28

The vertical dotted line in Figure D.15 (a) and (b) represents the embedment length of the specimen (6 inches), which was the critical plane where failure occurred. The strain profile at this critical plane is shown in Figure D.16. Tensile strains were measured toward the bottom face at about 8,000 με at failure.

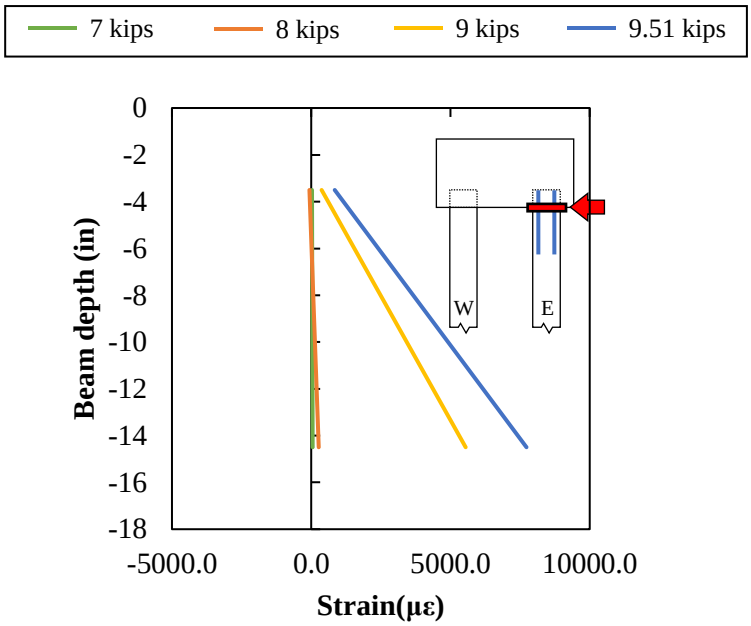

Figure D.16: SP-01 strain profile at critical section (6in) in the east pile

The curvature was determined from the measured strains in the FOS and the distance between the sensors. Strains in the FOS at different loads and the calculated moment-curvature response are shown in Figure D.17.

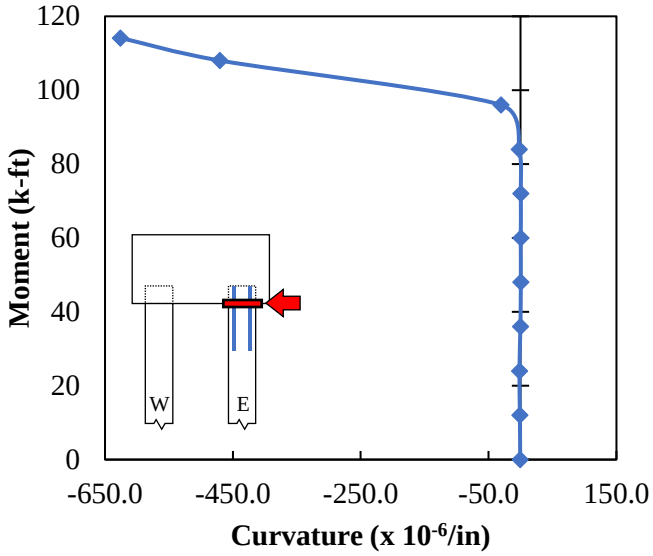

Figure D.17: SP-01 fiber optic data for east pile (a) strain and (b) moment-curvature profile at critical section (6in)

D.2. SP-02

D.2.1. Observations and Summary of Results

Results of Specimen 2 are summarized in Table D.1.

Table D.5: SP-02 Summary of results

Specimen 2	
Pile Embedment	6.0 in. ($0.33d_{pile}$)
Interface Reinforcement	none
Axial Load	193.8 kips ($0.052A_g f'_{c,pile}$)
Failure load (kips)	40.8
Distance from Load to Cap (ft.)	6.0
Failure Mechanism	Pile / Cap Crushing
Failed Pile	West
Maximum Displacement (in)	12.685
Ultimate Moment Developed (k-ft)	244.6
Percentage of capacity of pile	78.9 %

Specimen 2 had the same embedment length (6 inches) as Specimen 1, but with axial load application. Photographs of the failure of Specimen 2 are shown in Figure D.18. Spalling of the concrete in the pile cap occurred on the inside face of both piles, shown in Figure D.18 (a). Crushing of the concrete in the pile was evident on the outside of the west pile at failure, shown in Figure D.18 (b). No cracking in the pile-to-cap interface was observed.

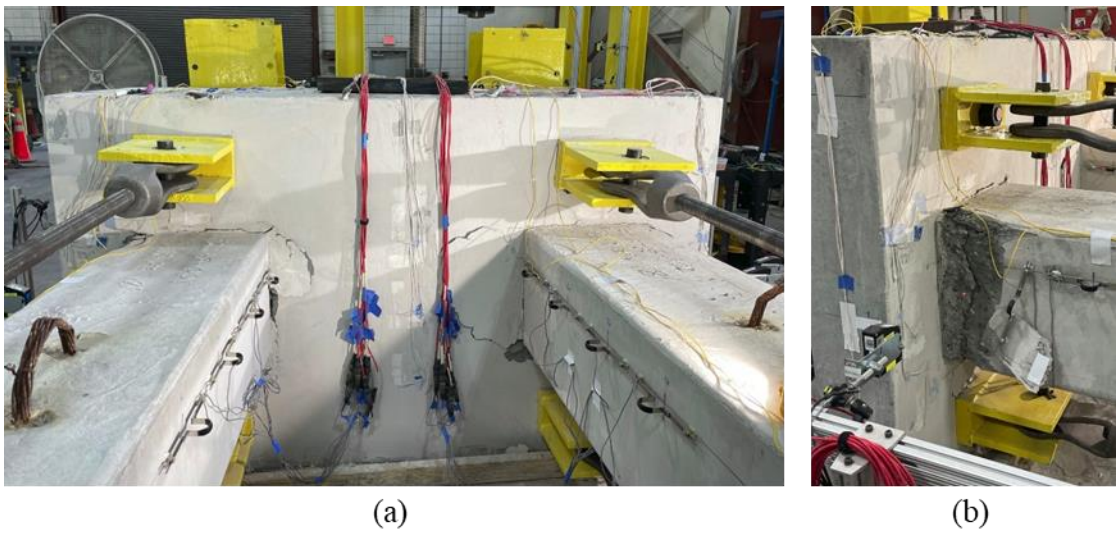

Figure D.18: SP-02 failure mechanism (a) pile cap crushing (b) spalling of concrete on west pile

D.2.2. Axial Load Application

As previously mentioned, Specimen 2 has applied axial load on both piles. A total of 193.8 kips was applied to each pile, which was $0.052A_g f'_{c,pile}$. The applied axial load was less than the $0.1A_g f'_{c,pile}$ initially planned due to a higher concrete strength (11.5 ksi) than the design value (6.5 ksi). The axial load application apparatus (e.g., rods, hinge, spreader beams) were designed for the axial load of 194 kips.

The process to apply the axial load included the following steps:

- The estimated elongation expected to reach 97 kips per rod was calculated.

$$\Delta_{rod} = \frac{(97\ kips)(295.5\ in)}{(2.4\ in^2)(29{,}000\ ksi)} = 0.411$$

- Blocks and jacks were positioned on the west pile, as shown in Figure D.19 (a).
- Pressure was applied manually to each rod in steps. Stops were set at 400 psi, 2000 psi, and 7600 psi. At each stop elongations readings were taken, and nuts were tightening.
- Blocks and jacks were removed from west pile.

This process was repeated for the east pile.

(a) (b)

Figure D.19: Axial load application (a) tensioning of west pile (b) tensioning east pile

A similar process was followed for detensioning of the piles after testing.

D.2.3. Laser displacement transducers (LDT)

Displacements were recorded along the length of both piles through five laser displacement transducers (LDTs), as shown in Figure D.20. The application of the lateral load in the piles for Specimen 2 was 6 ft from the pile-to-cap interface, which was the same location as LDT-3.

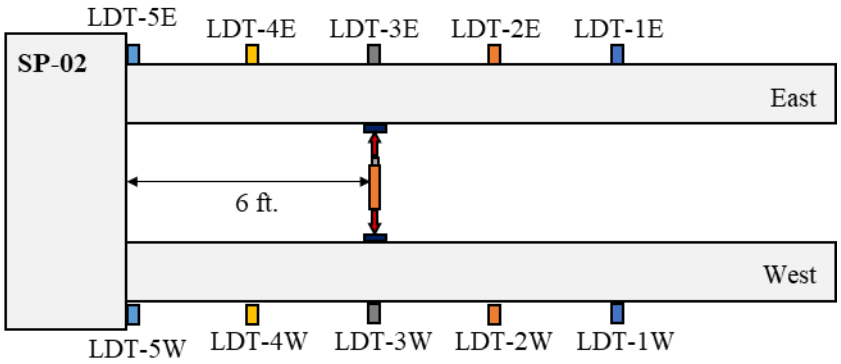

Figure D.20: Location of laser displacement transducers (LDT) and applied load for SP-02

The load-displacement curves of the west and east piles are shown in Figure D.21 (a) and (b), respectively. Maximum displacement in the west pile was 12.685-in, with maximum load of 40.8 kips. Specimen 2 reached 79.8% of the moment capacity of the 18-inch pile, which corresponds to 42% increased from Specimen 1, with same embedment length, but no axial load applied. The load-displacement curve was nearly horizontal at the time the hydraulic jack ran out of stroke and the load removed.

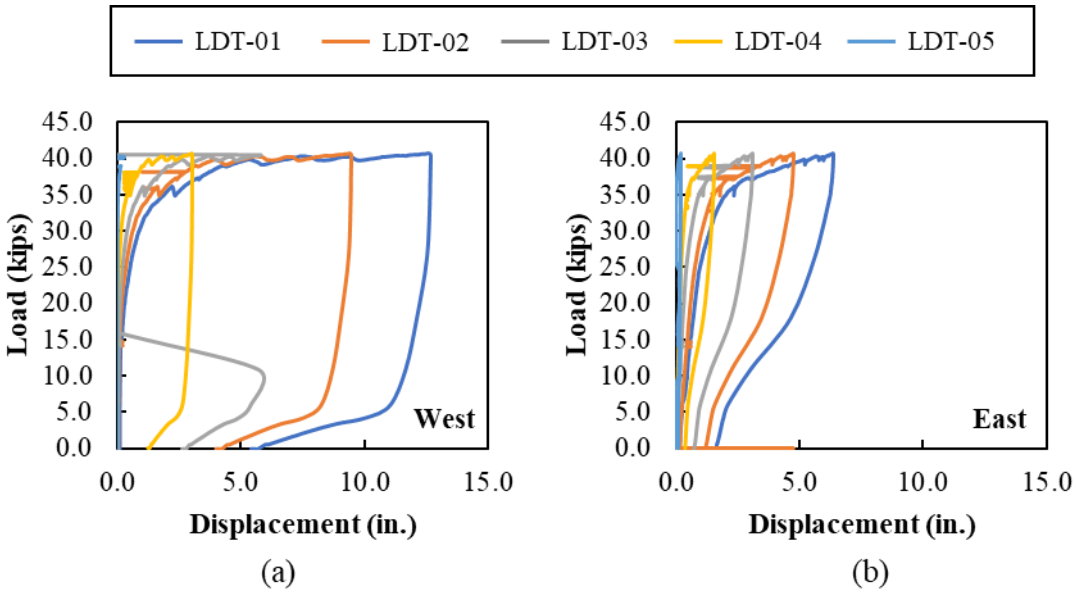

Figure D.21: SP-02 load-displacement curve (a) west pile (b) west pile

D.2.3.1. Concrete Strain Gauges

Vertical and horizontal strains around the west pile are shown in Figure D.22. The strains in CSG-01 to CSG-07 were all less than the typical cracking strain for concrete. CSG-01, CSG-02, and CSG-03, which are perpendicular to load application measured compressive strains less than 100 με. CSG-04, and CSG-05, parallel to load application, measured tension strains until around 35 kips, at which point, compressive strains developed until failure.

CSG-06, located above the embedded west pile, measured tensile strains less than 100 με at the maximum applied load. CSG-07, located below the embedded west pile, started with tensile

strains until around 35 kips, at which point tensile strains decreased and compression strains began to be measured. This corresponds to cracking between the pile and the hinge detail, as shown in Figure D.22 (d).

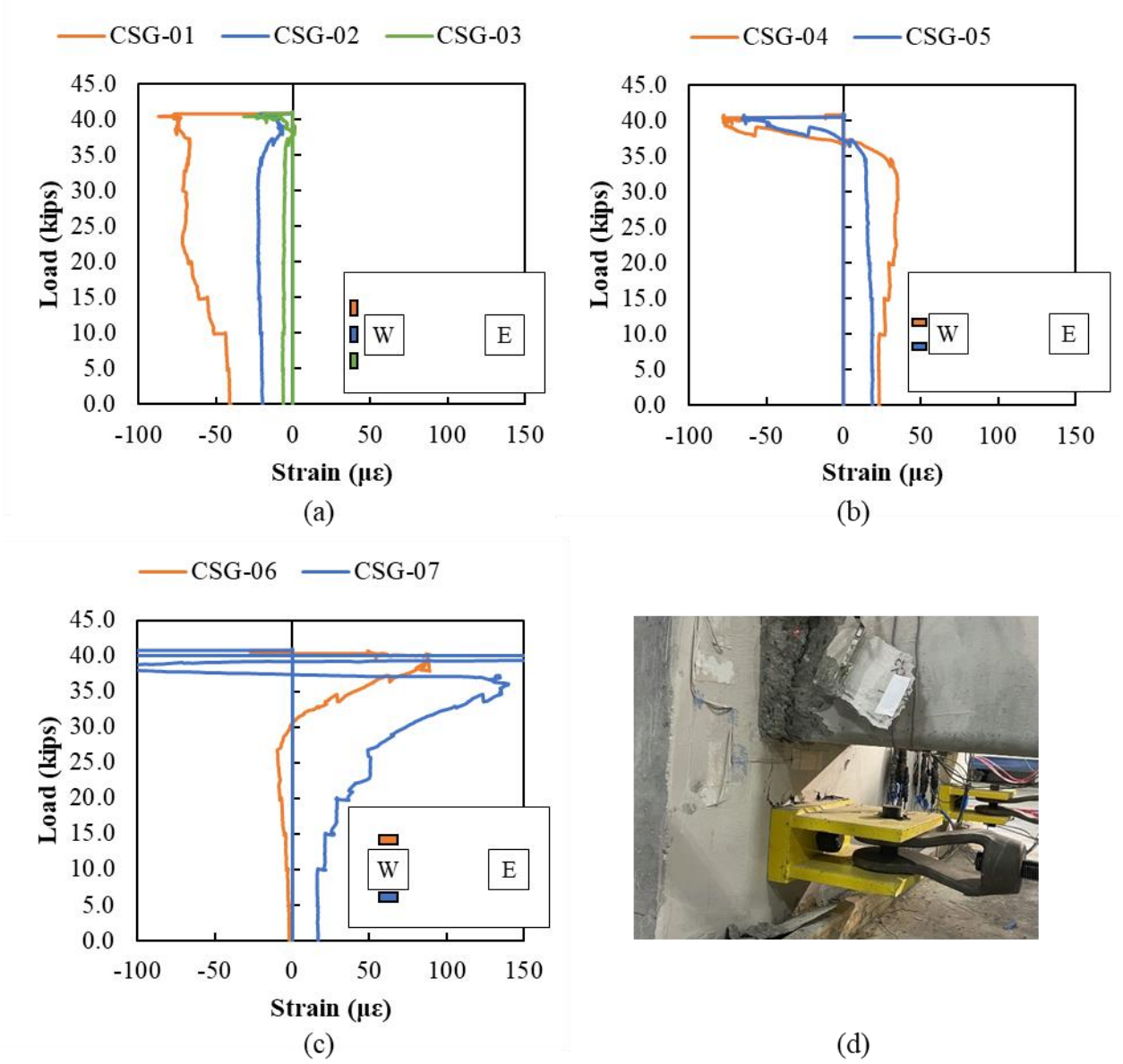

Figure D.22: SP-02 concrete strain data for CSG-01 to CSG-07

Vertical and horizontal concrete strains in the middle of the cap between the piles are shown in Figure D.23. Strains in both directions were minor until around 40 kips at which point spalling of the concrete occurred. After this point, tensile strains in CSG-09, and compression strains in CSG-08 and CSG-11 increased rapidly.

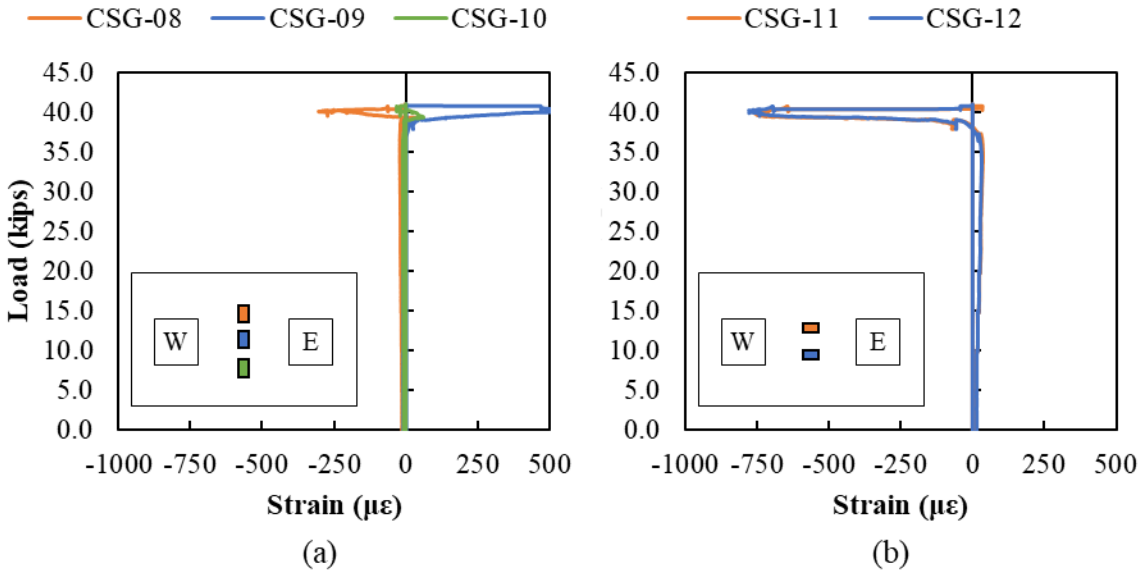

Figure D.23: SP-02 concrete strain data for CSG-08 to CSG-12

Concrete strains around the east pile are shown in Figure D.24. The response of these CSGs was generally like the CSGs around the west pile.

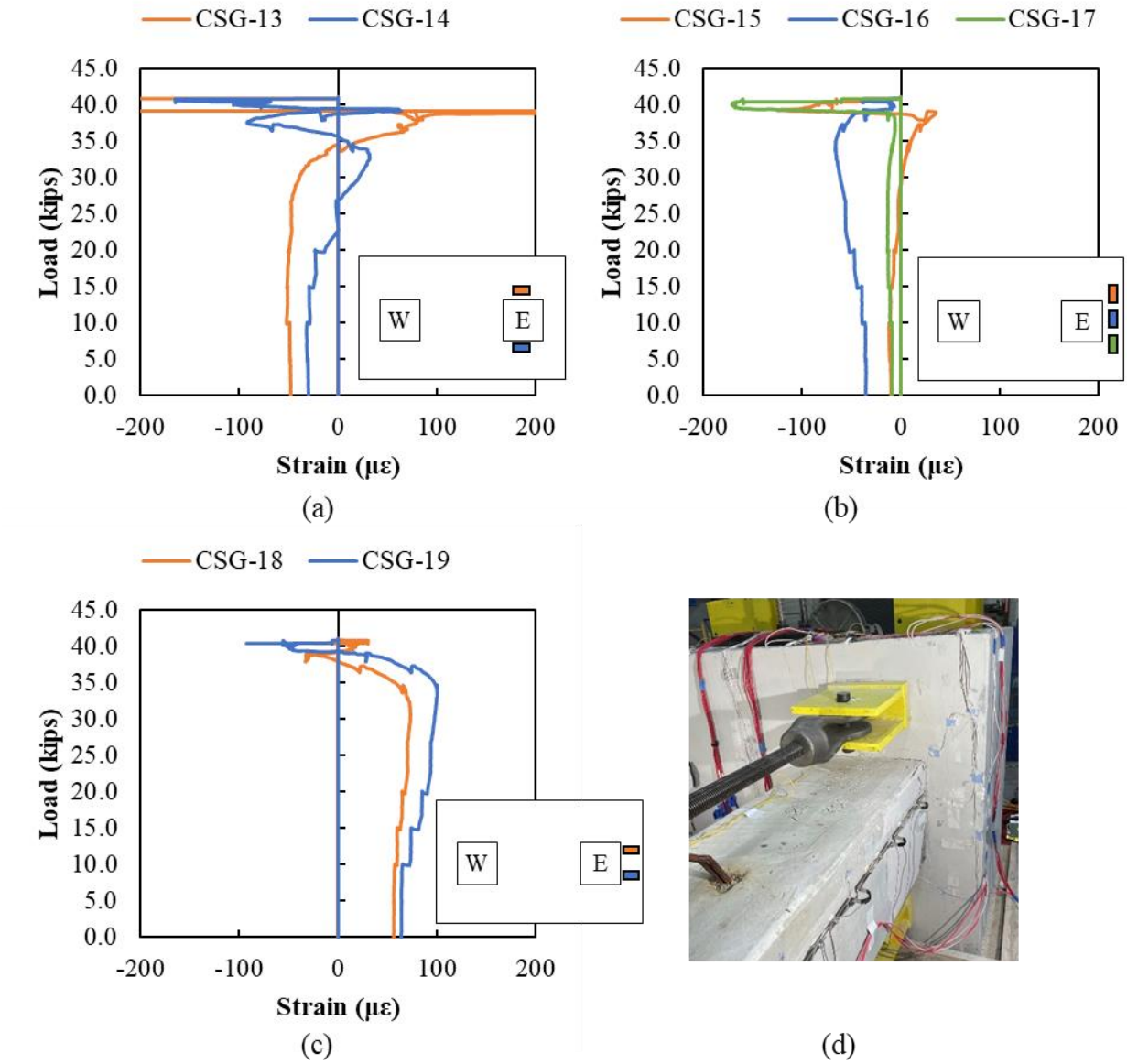

Figure D.24: SP-02 concrete strain data for CSG-13 to CSG-19

Concrete strains on the west and east faces of the pile cap are shown in Figure D.25. Measured strains on the west face of the pile were less than 60 με at maximum applied loads. Measured strains on the east side were minor until around 40 kips were compression strains in CSG-25 increased rapidly.

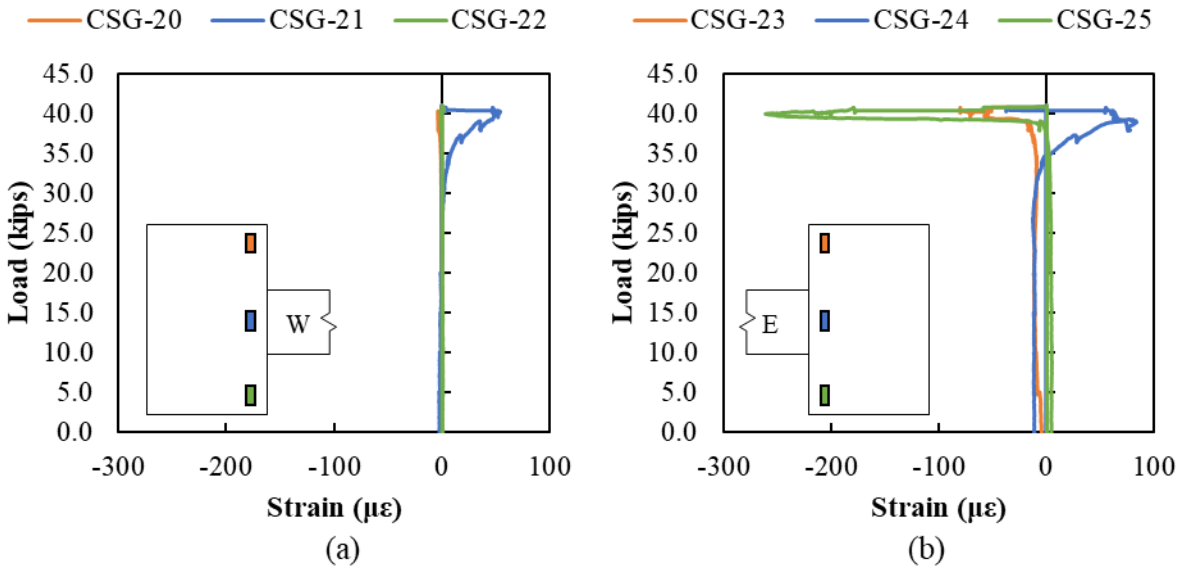

Figure D.25: SP-02 concrete strain data for CSG-20 to CSG-25

D.2.4. Rebar Strain Gauges

Rebar strains in the N5 bars are shown in Figure D.26. Strains less than 100 με were measured in the bars RSG-06 to RSG-08 close to the east pile. Minor strains were measured in the bars around the west pile, until around 40 kips were tension and compression strains began to increase, with a maximum tensile strain of 818 με in RSG-02 and 426 με compression strain in RSG-04.

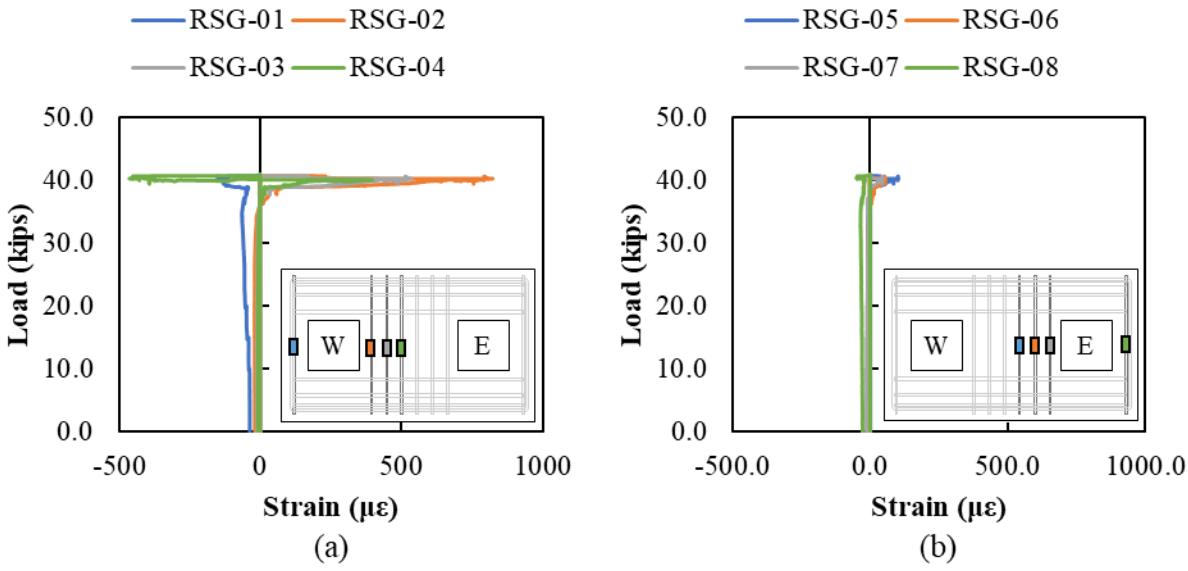

Figure D.26: SP-02 rebar strain data for N5 bars

Rebar strains in the N9 bars are shown in Figure D.27. Strains remained minor around the west pile until maximum applied load at which point RSG-13 measured maximum tension strains of 2078 με. Strains remained less than 130 με tension for RSG-10 to RSG-20.

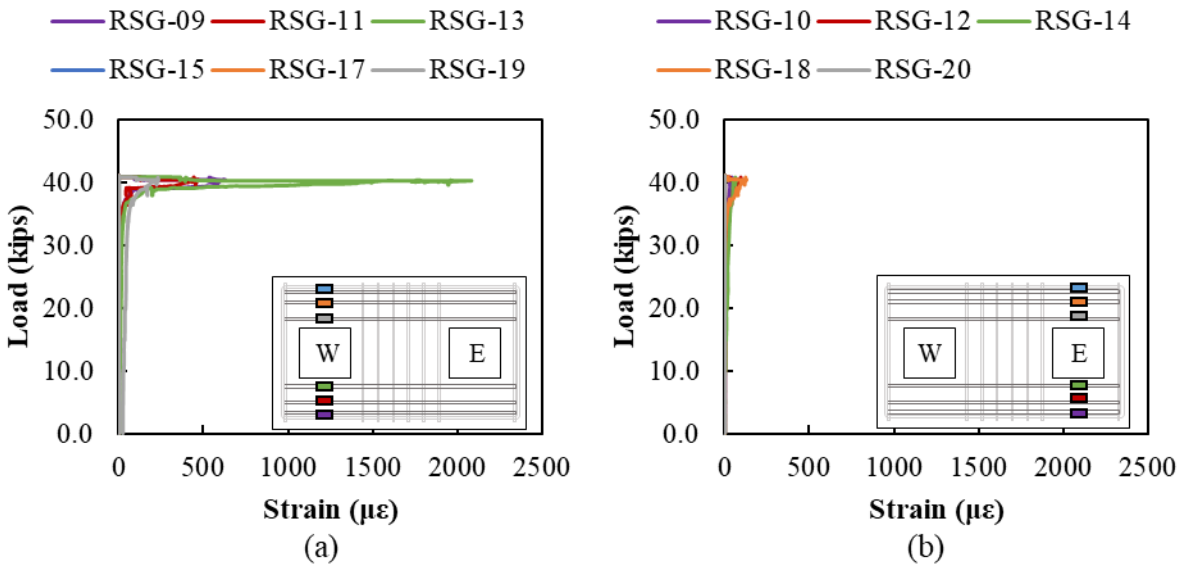

Figure D.27: SP-02 rebar strain data for N9 bars

Rebar strains in the N6 bars are shown in Figure D.28. Measured strains remained minor until a cracked occurred under the east pile at around 40 kips. At this point, tensile strains in RSG-22 increased to 650 με .

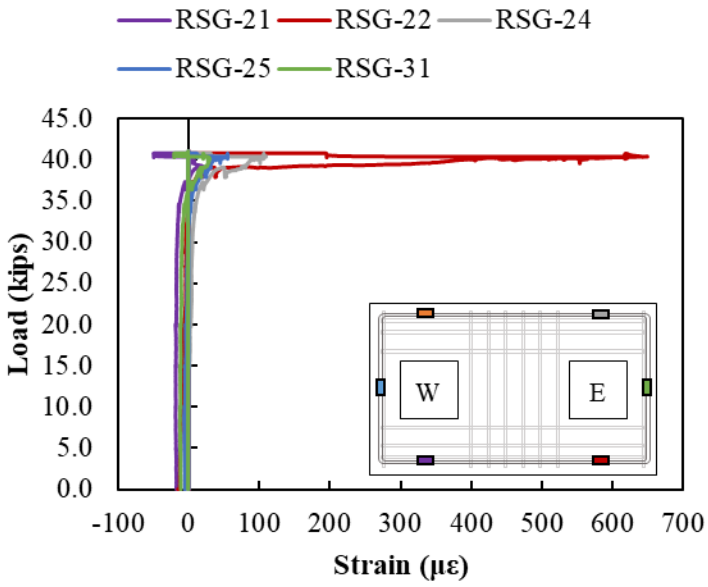

Figure D.28: SP-02 rebar strain data for N6 bars

Rebar strains in the N6 bars on the side of the pile cap are shown in Figure D.29. Higher strains were measured on the west side of the pile cap, which correlates to the west pile embedded failing. The highest measured strains on the west side were developed in RSG-27 and RSG-28, with strains around 233 με and 595 με , respectively. Measured strains in the east pile remained less than 50 με.

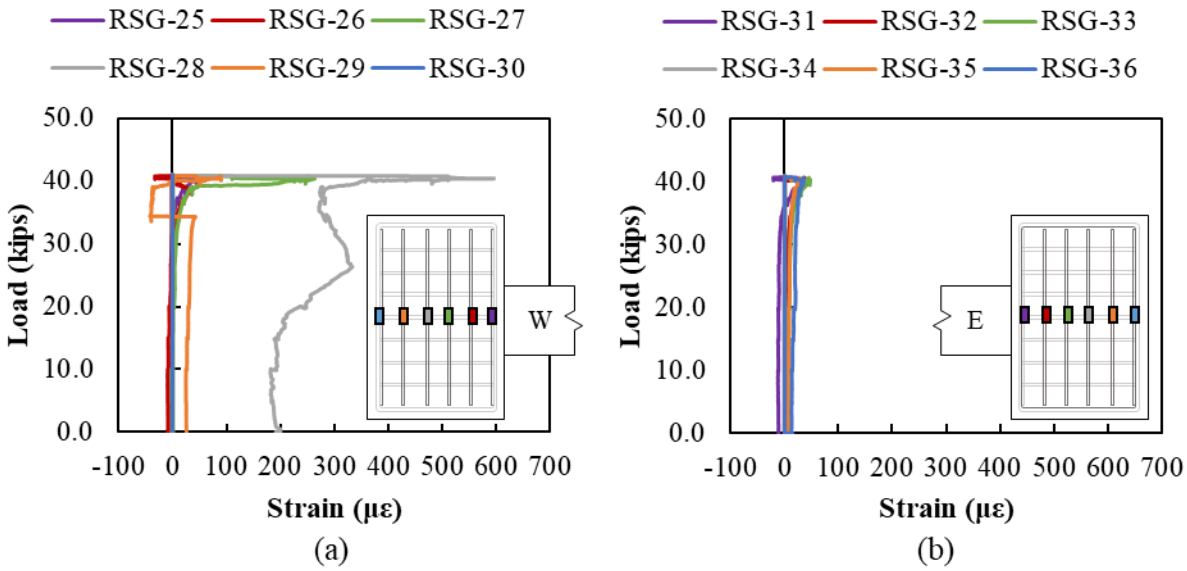

Figure D.29: SP-02 rebar strain data forN6 bars (a) west side (b) east side.

D.2.5. Crack Displacement Transducers

Displacements recorded in the plastic hinge zone of both piles are shown in. Figure D.30 and Figure D.31. The largest compression strains were measured in CDT-04E located in the compression face of the east pile. Compression strains were measured in CDT-05W in the west pile until around 40 kips at which point spalling of the concrete occurred causing the gauge to fell off.

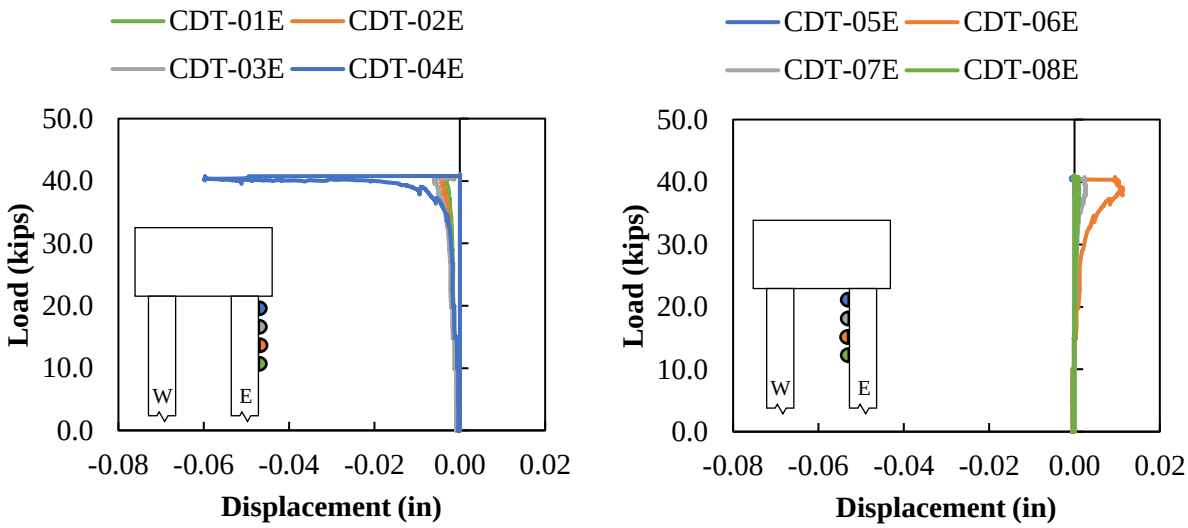

. Figure D.30: SP-02 crack displacement data for the east pile

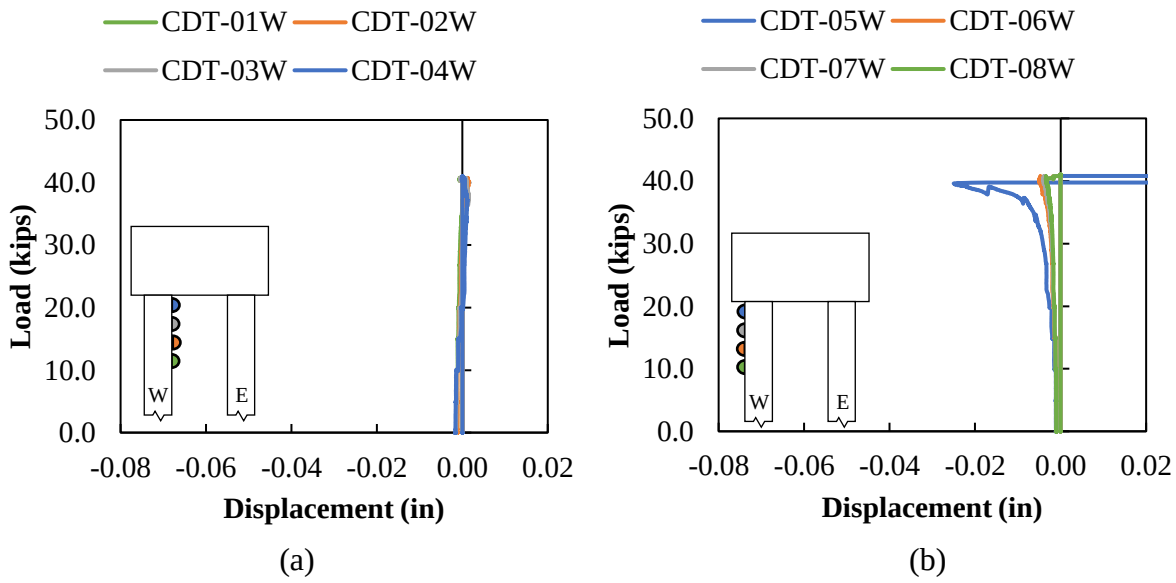

Figure D.31: SP-02 crack displacement data for the west pile

Moment-curvature response using the CDTs for the west and east pile are shown in Figure D.32. Curvature for W4 was not plotted since the gauge came off during testing. Higher curvature was measured in the east pile in the gauges closest to the pile-to-cap connection.

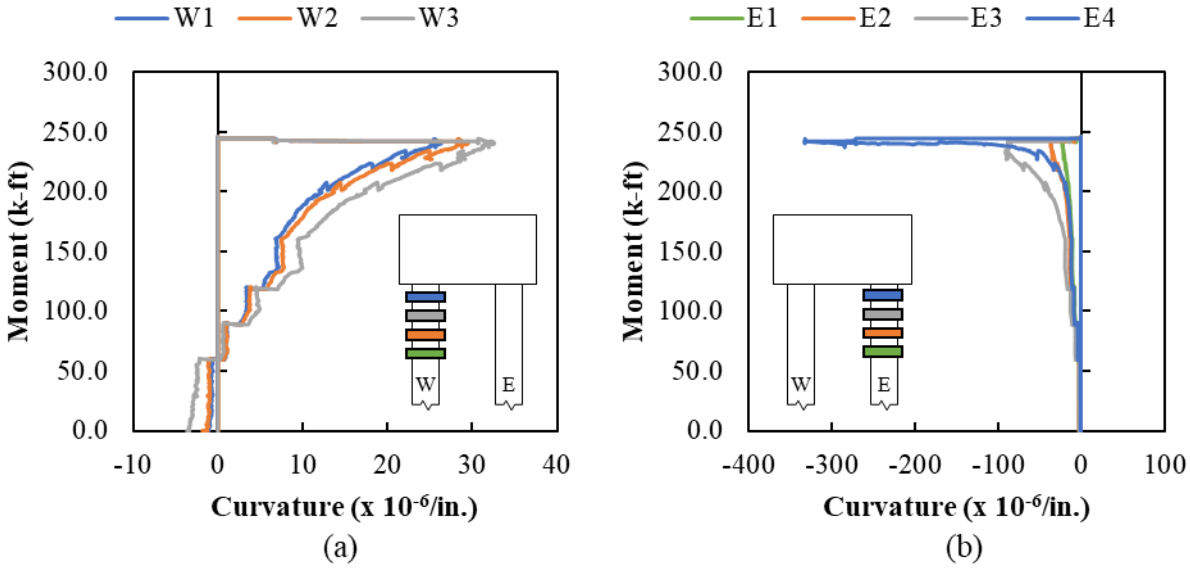

Figure D.32: SP-02 moment-curvature with crack displacement (a) west pile (b) east pile

D.2.6. Vibrating Wire Gauges (Pile)

Vibrating wire gauge (VWG) data was recorded at different stages of the specimen life. The initial data was used to calculate the elastic shortening losses, and total losses of each specimen.

Initial stress in strands:

Jacking stress: $$f_{pj} = \frac{F}{A} = \frac{34\ kips}{0.167\ in^2} = 203.6\ ksi$$

Readings from the longitudinal vibrating gages were recorded and used to find the stress in the strands after release (assuming E_p = 28,500 ksi):

Table D.6: SP-02 Elastic shortening losses calculation

VWG	Before release (με)	After release (με)	Strain Change (με)	ES Losses (ksi)
VWSG-P2-1E	0	-352.480	352.50	10.05
VWSG-P2-2E	0	-349.442	349.4	9.96
			Δf_{pES} =	10.00

Therefore, the average stress in strands after elastic shortening losses:

Stress after elastic shortening losses: $$f_{pi} - \Delta f_{pES} = 203.6\ ksi - 10.0\ ksi = 193.6\ ksi$$

Readings from the longitudinal vibrating gages were recorded and used to find the stress in the strands before testing (assuming E_p = 28,500 ksi):

Table D.7: SP-02 Total losses calculation

VWG	After casting (με)	Before testing (με)	Strain Change (με)	LT Losses (ksi)
VWSG-P8-1E	-352.48	-1153.4	800.9	22.83
VWSG-P8-2E	-	-	0.0	0.0
			Δf_{pLT} =	22.83

The average stress in strands after all losses:

Stress after all losses immediately before testing:

$$f_{pi} - \Delta f_{pES} - \Delta f_{pLT} = 203.6\ ksi - 10.0\ ksi - 22.83\ ksi = 170.7\ ksi$$

D.2.7. Vibrating Wire Gauges (Cap)

Vibrating wire gauge data was also recorded in the pile cap around the embedded east pile. Readings at different times are shown in Table D.8. Temperature can affect the strain gauges readings; therefore, a temperature correction was applied to the actual readings, taking as reference the before cap casting readings.

Table D.8: SP-02 Vibrating wire gauge data in pile cap

VWG	Before cap casting (με)	After cap casting (με)	Before testing (με)	After Testing (με)
VWSG-4E	0	-28.360	-765.87	-164.90
VWSG-5E	0	32.828	--	--
VWSG-6E	0	-25.638	-728.018	-727.95
VWSG-7E	0	2.860	--	--

D.2.8. Fiber Optic

D.2.8.1. Pile tensioning

Readings were taken during the application of the axial load. As shown in Figure D.33 high compressive strains were transferred to the east pile, and some tensile strains to the west pile.

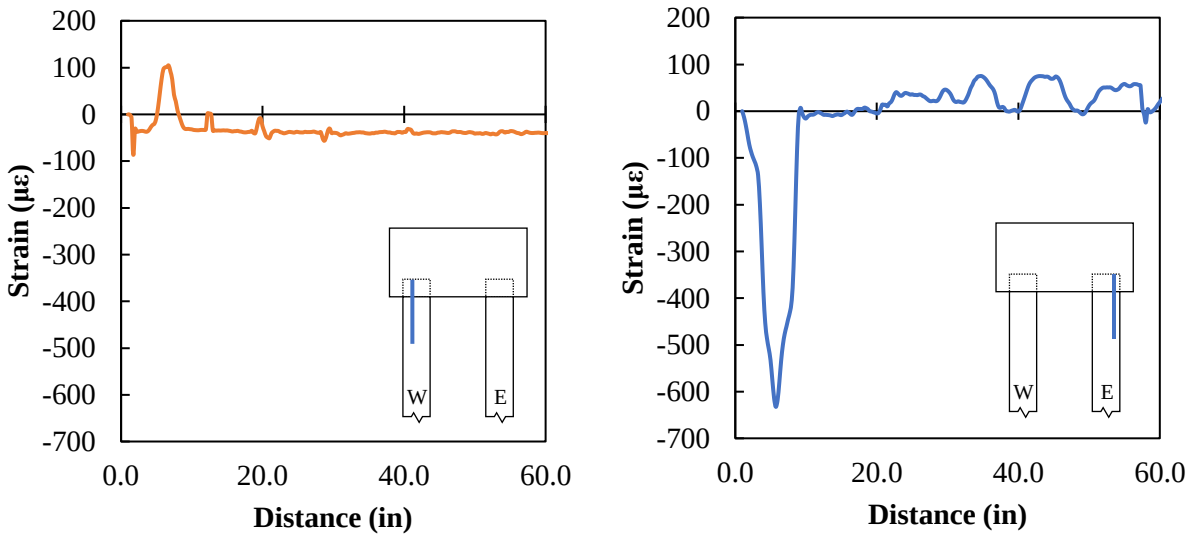

Figure D.33: SP-02 fiber optic data for tensioning of east and west pile

D.2.8.2. Testing

Strains along the length of the FOS at different loads are shown in Figure D.34. Data was only measured in FOS-01 in the west pile and FOS-02 in the east pile for Specimen 3. Other FOS were not functional during test.

Compression strains less than 4,000 με were measured on the exterior face of the west pile with maximum strains at the pile-to-cap interface. Small tensile strains developed on the interior face of the east pile until around 33 kips at which point compression strains started to be measured.

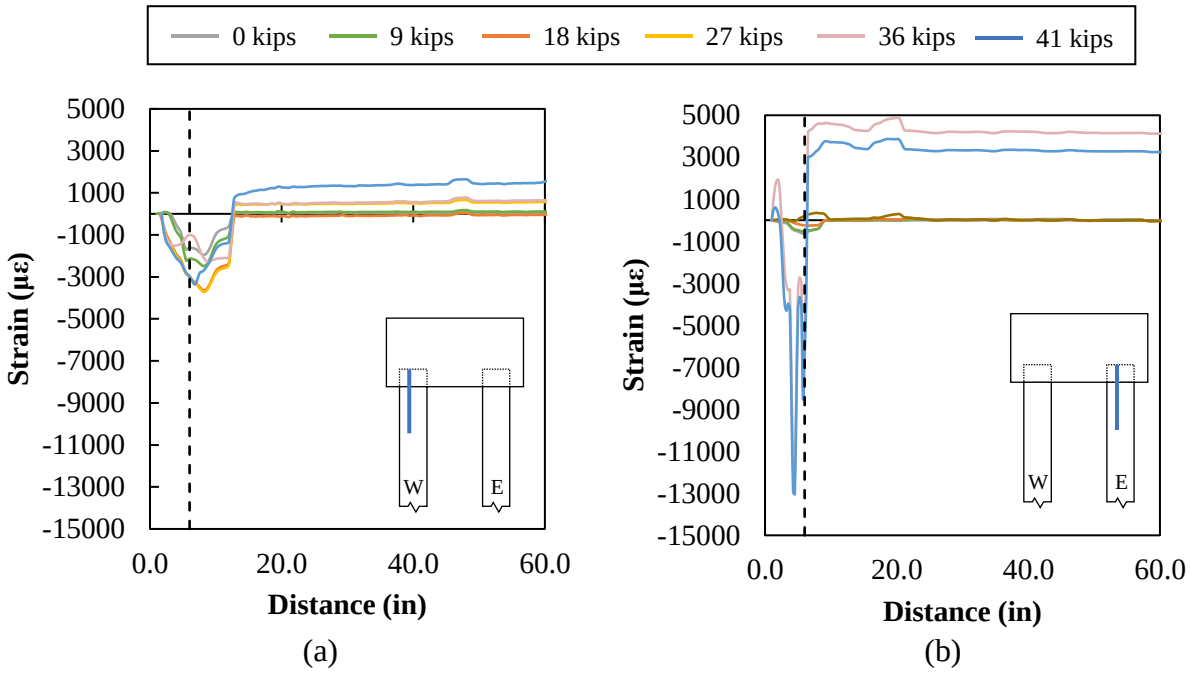

Figure D.34: SP-02 Fiber optic data for (a) FOS-01 and (b) FOS-02

D.3. SP-03

D.3.1. Observations and Summary of Results

Results of Specimen 3 are summarized in Table D.9

Table D.9: SP-03 Summary of Results

Specimen 3	
Pile Embedment	6.0 in. ($0.33d_{pile}$)
Interface Reinforcement	(4) #6 bars
Axial Load	0 kips ($0A_g f'_{c,pile}$)
Failure Load (kips)	21.2
Distance from Load to Cap (ft.)	9.0
Failure Mechanism	Cap Crushing
Pile Failed	West
Maximum Displacement (in)	8.812
Ultimate Moment Developed (k-ft)	190.8

Specimen 3	
Percentage of capacity of pile	61.6 %

Specimen 3 had the same embedment length (6 inches) as Specimen 1 and 2, but with interface reinforcement between the pile and the pile cap. Photographs of the failure of Specimen 3 are shown in Figure D.35.

The failure of this specimen occurred in the west pile. The observed failure was likely caused by the spalling of the concrete in the pile cap around the west pile. A large crack in the pile developed at the location where the interface reinforcement ends (12 inches from the pile-to-cap interface), as shown in Figure D.35 (b). No cracking was observed in the pile-to-cap interface.

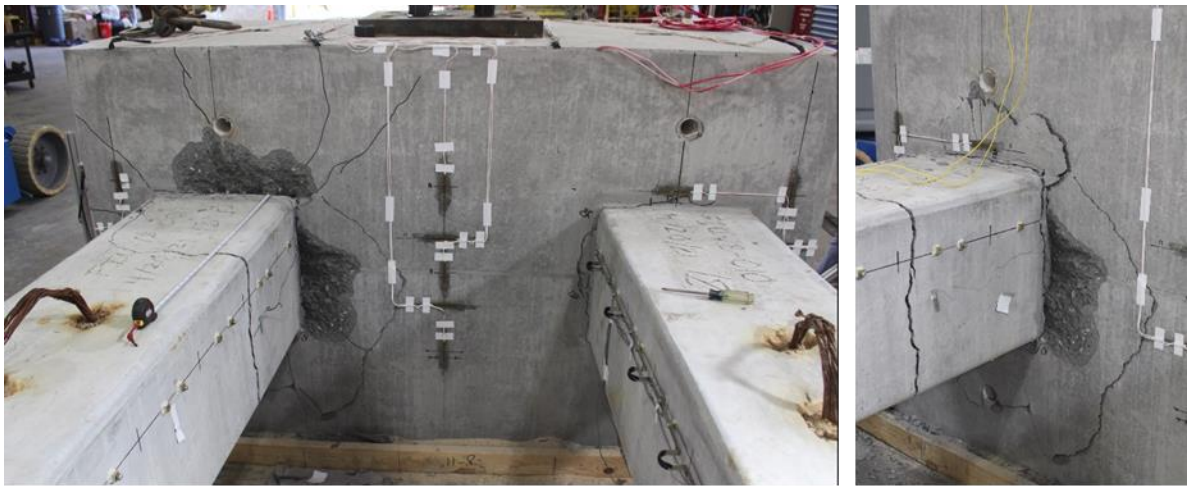

(a) (b)

Figure D.35: SP-03 failure mechanism (a) damage in pile cap (b) crack at the end of interface reinforcement

.

D.3.2. Laser displacement transducers (LDT)

The application of the lateral load in the piles for Specimen 3 was at 9 ft from the pile-to-cap interface, which was the same location as LDT-02, as shown in Figure D.36.

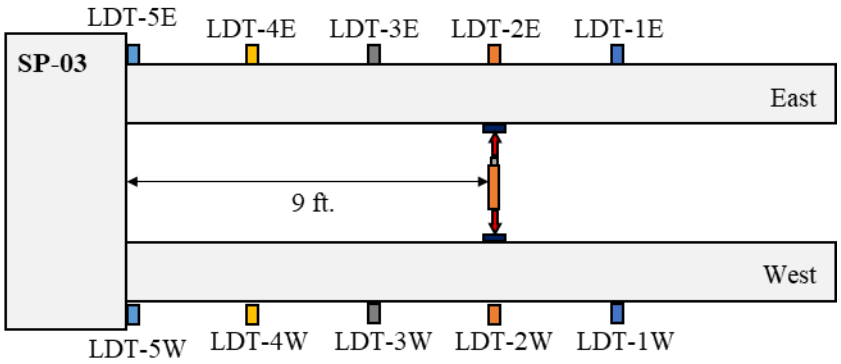

Figure D.36: Location of laser displacement transducers (LDT) and applied load for SP-03

Load-displacement curves of the west and east piles are shown in Figure D.37 (a) and Figure D.37 (b), respectively. The maximum load reached by Specimen 3 was 21.2 kips, which corresponds to 61.6% the capacity of the 18-inch piles. The horizontal displacement in the west pile was 8.812-inch and in the east pile 1.621-inch. The load-displacement curve was nearly horizontal at the time the hydraulic jack ran out of stroke and the load removed.

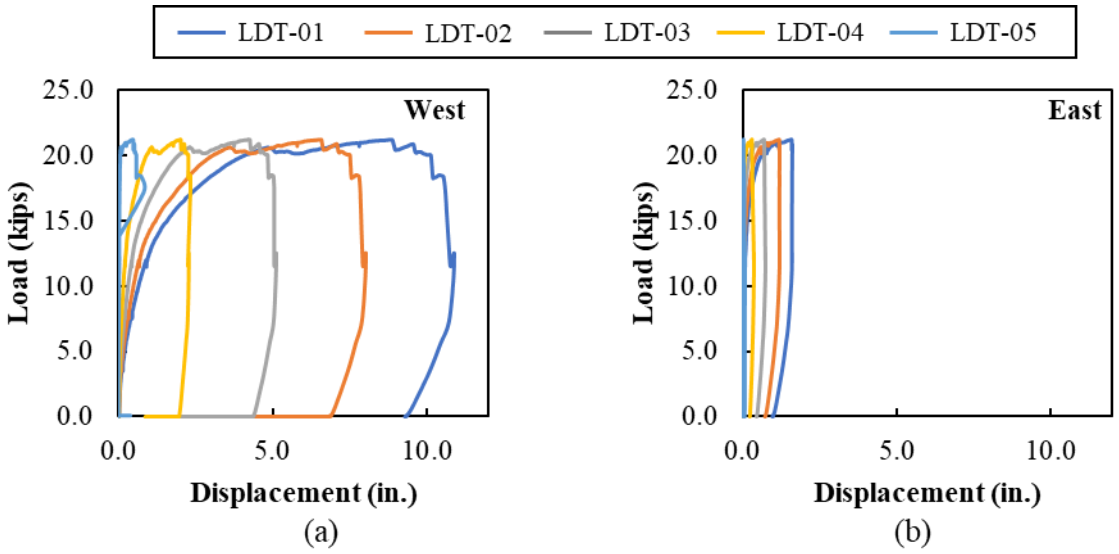

Figure D.37: SP-03 load-displacement curve (a) west pile (b) east pile

D.3.3. Concrete Strain Gauges

Vertical and horizontal strains around the west pile are shown in Figure D.38. The strains in CSG-01 to CSG-03, which are perpendicular to load application, started with small tension strains until around 20 kips when compression strains started to develop.

CSG-04 and CSG-05, started with tensile strains until approximately 8 kips and 10 με at which point tensile strains decreased and compression strains began to be measured. CSG-04 and CSG-05 reached maximum compressive strains of 76 με and 140 με, respectively, at load failure.

CSG-06 located above the embedded west pile measured tensile strains higher than 1000 με, which corresponds to spalling of concrete at this location, as shown in Figure D.38 (d).

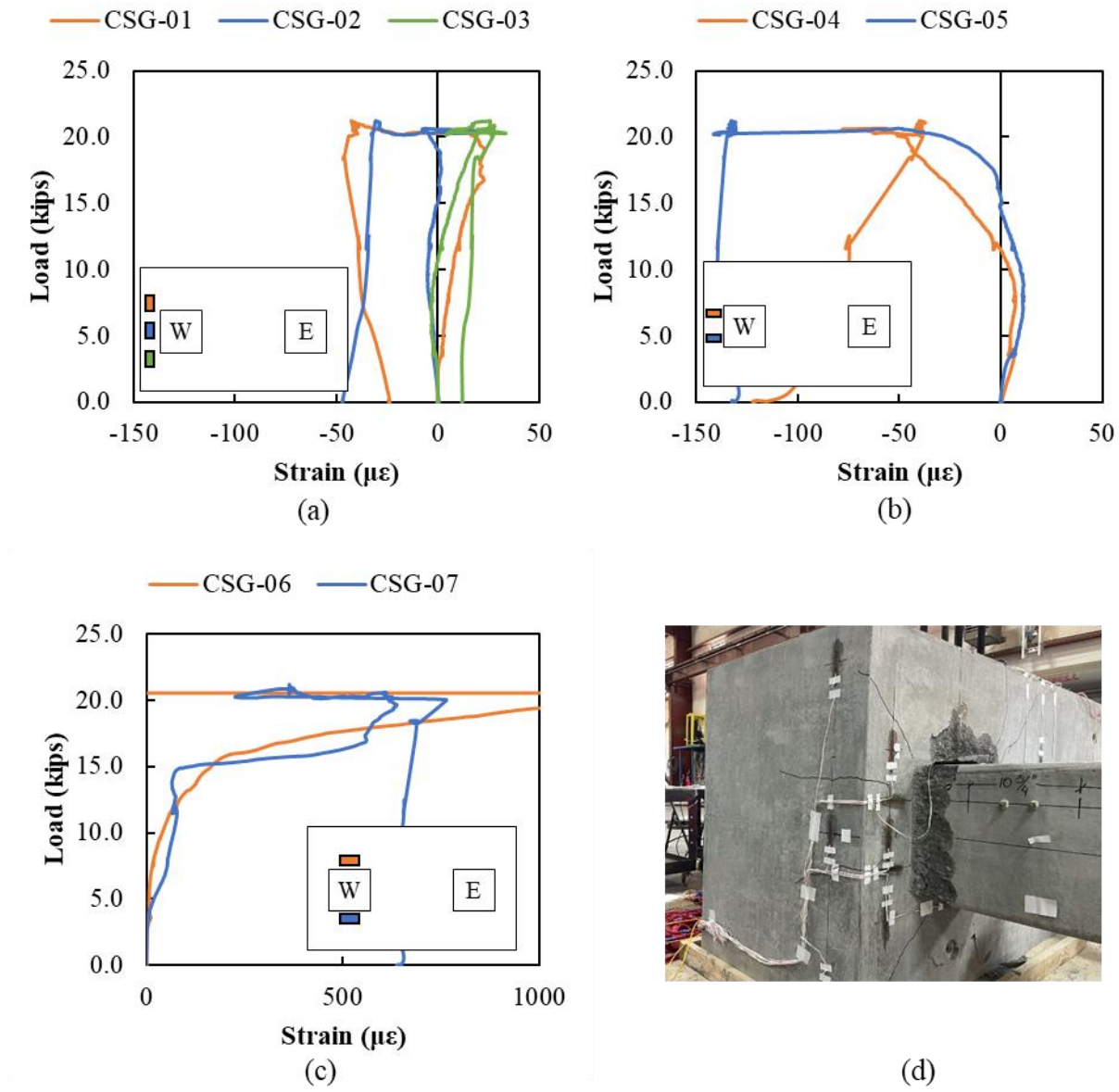

Figure D.38: SP-03 concrete strain data for CSG-01 to CSG-07

Vertical and horizontal concrete strains in the middle of the pile cap between the piles are shown in Figure D.39. CSG-08 to CSG-10, perpendicular to load application, measured tensile strains less than 150 με. CSG-11 and CSG-12, parallel to load application, measured compression strains of 725 με.

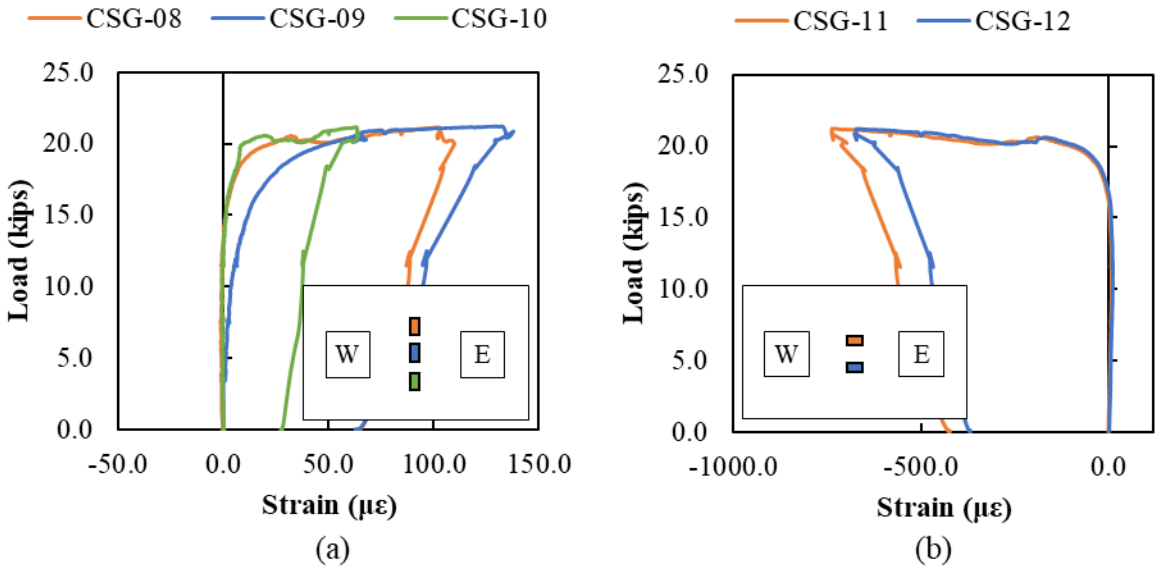

Figure D.39: SP-03 concrete strain data for CSG-08 to CSG-12

Concrete strains around the east pile are shown in Figure D.40. CSG-01 to CSG-03, which are parallel to load application have tensile strains higher than 1000 με, which correspond to cracking of the concrete at this location.

The strains in CSG-15 and CSG-17, located on the outside of the pile cap, were less than the typical cracking strain for concrete. CSG-16, also located on the outside of the pile cap, measured tensile strains of 560 με.

CSG-18 and CSG-19, parallel to load application, started with small tensile strains until around 10 με and 7.5 kips, at which point tensile strains decreased and compressive strains started to be measured. Maximum compression strains in CSG-18 and CSG19 are 76 με and 64 με, respectively.

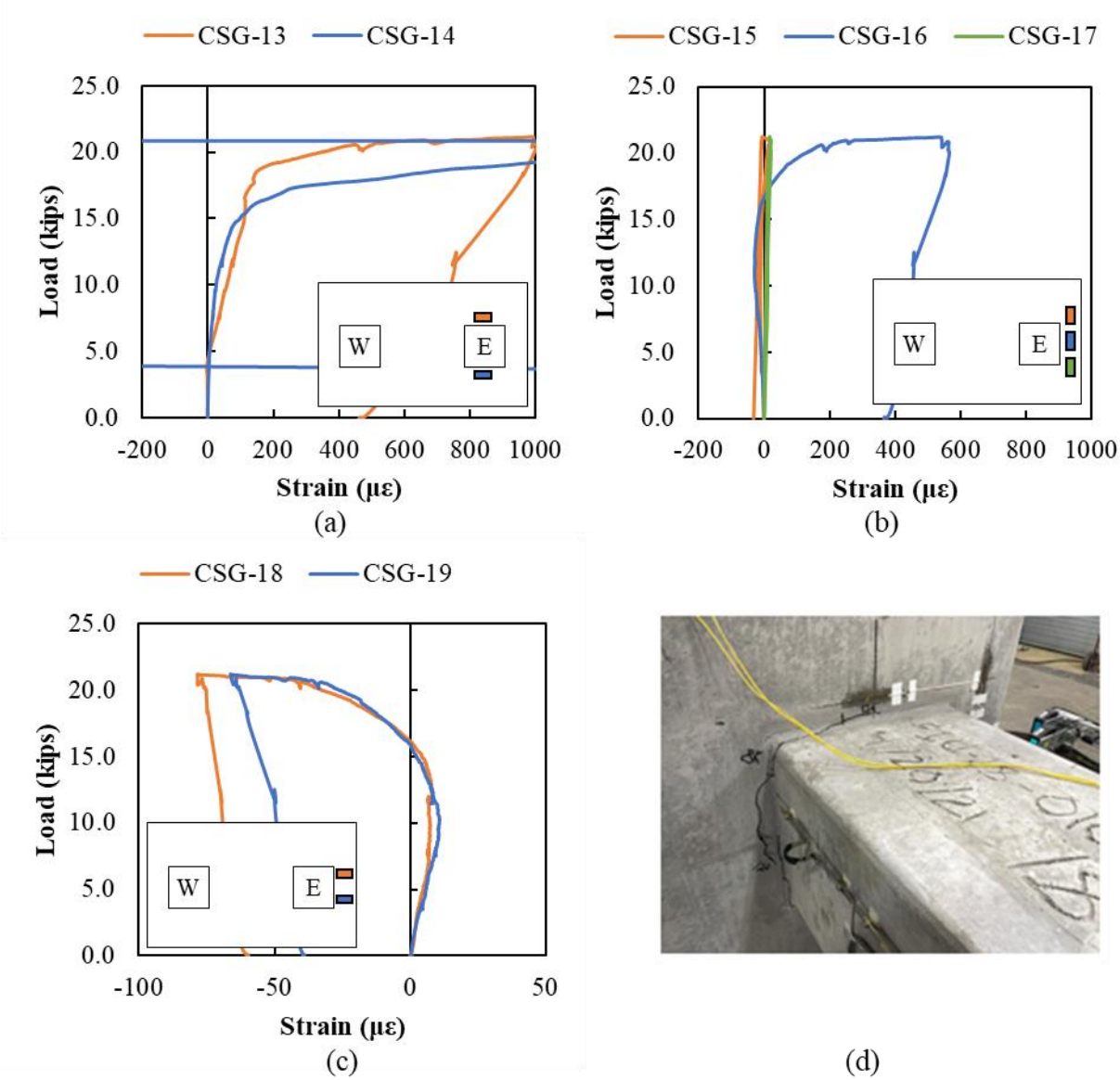

Figure D.40: SP-03 concrete strain data for CSG-13 to CSG-19

Concrete strains on the west and east faces of the pile cap are shown in Figure D.41. CSG-20 and CSG-22 had maximum compression strains of 160 με at failure load. CSG-21 developed tension strains of less than 58 με. Measured strains on the east face of the pile cap were less than 25 με.

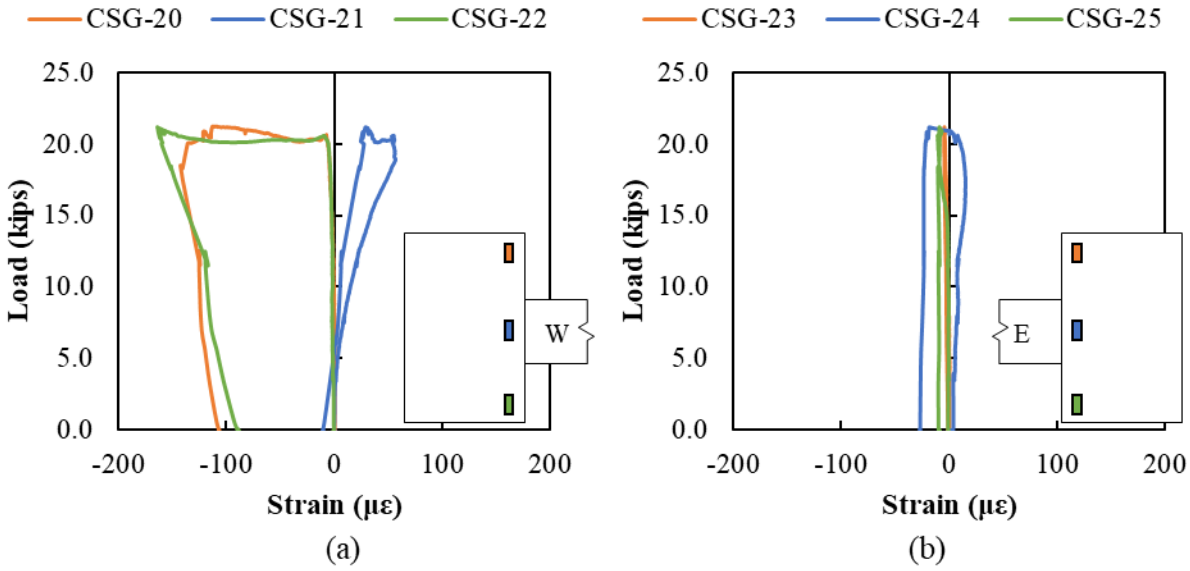

Figure D.41: SP-03 concrete strain data CSG-20 to CSG-25 (a) west side (b) east side

D.3.4. Rebar Strain Gauges

Rebar strains in the N5 bars are shown in Figure D.42. RSG-02 and RSG-03 located in between the embedded piles measured strains of 300 με. Symmetrical behavior was observed on RSG-05 to RSG-08.

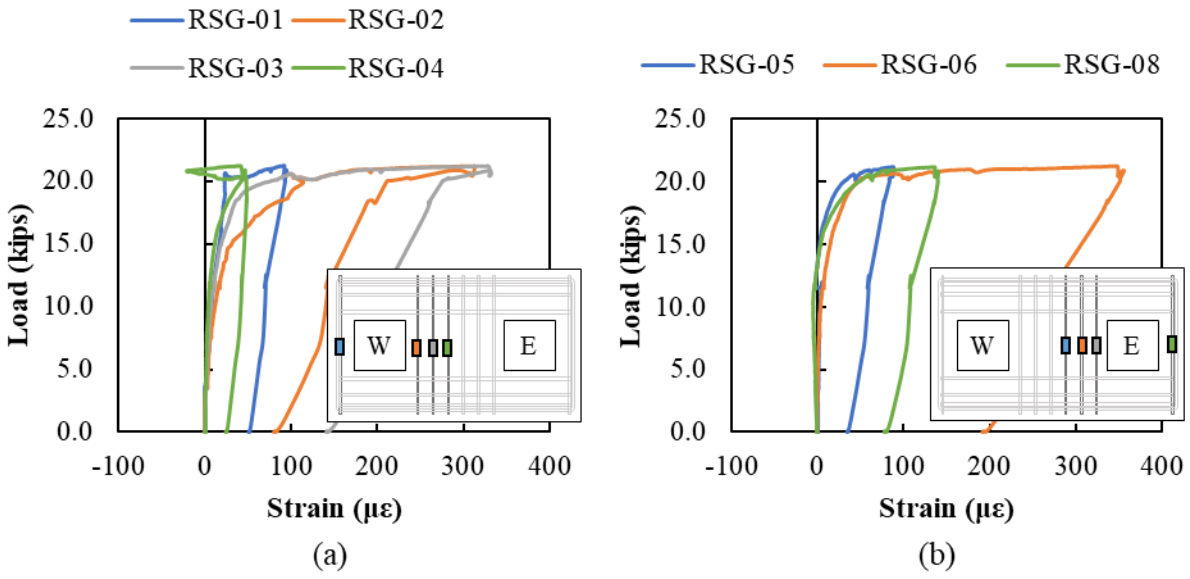

Figure D.42: SP-03 rebar strain data for N5 bars

Rebar strains in the N9 bars are shown in Figure D.43. Maximum strains were measured in the bars closer to the embedded west pile RSG-13 and RSG-15, with strains of 662 με and 1,014 με, respectively. RSG-10 to RSG-20, located near the east pile, measured strains less than 230 με.

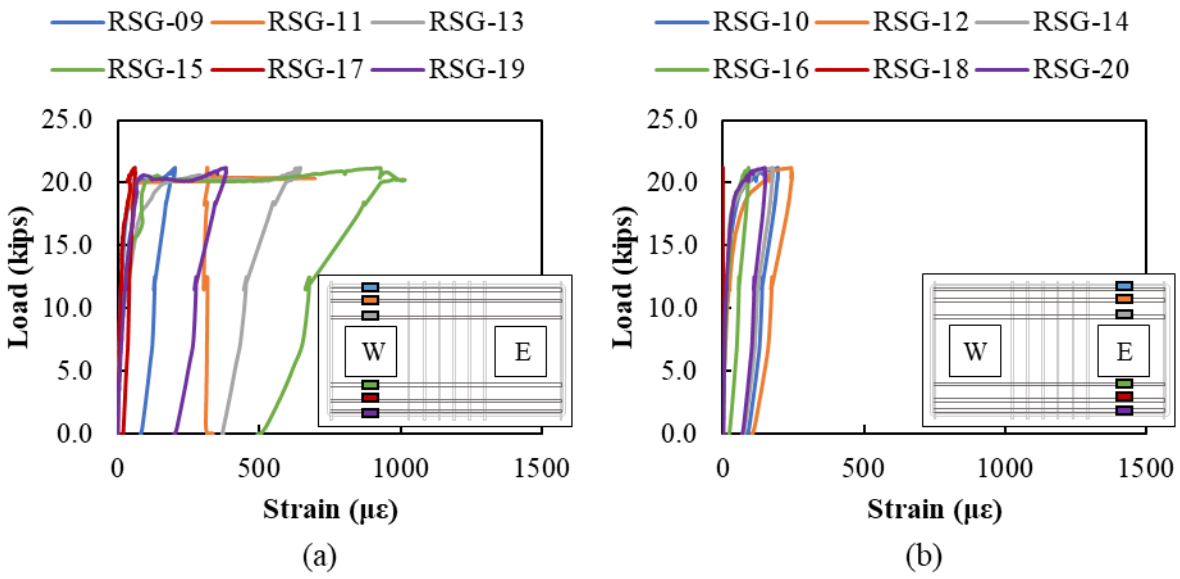

Figure D.43:SP-03 rebar strain data for N9 bars

Rebar strains in the N6 bars are shown in Figure D.44. RSG-25 and RSG-31 located outside of the embedded piles, showed maximum strains of 139 με and 206 με, respectively. Maximum strains were measured in RSG-23, located below the embedded west pile, with strains of 634 με.

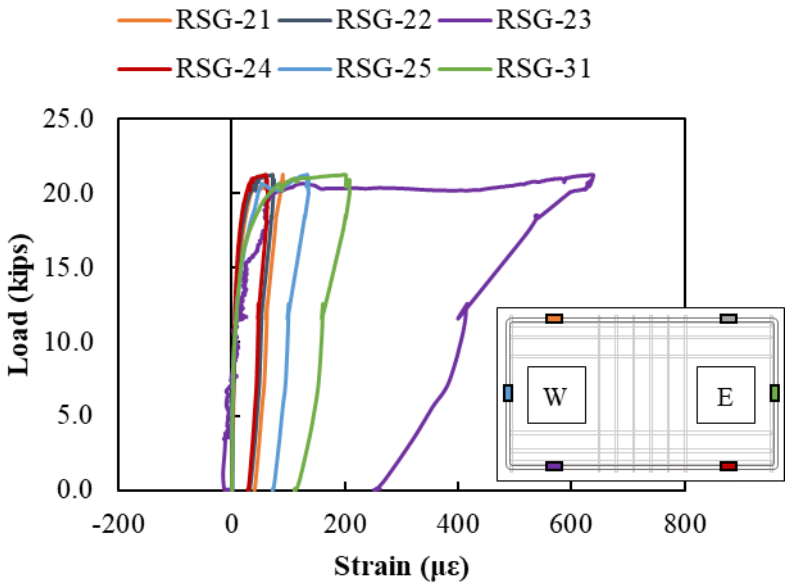

Figure D.44:SP-03 rebar strain data for N6 bars

Rebar strains in the N6 bars on the west and east side of the pile cap are shown in Figure D.45. Measured strains increased as bars were closer to the face of the pile cap. RSG-25 (on the west face) and RSG-31(on the east face), measured maximum strains of 136 με and 209 με, respectively.

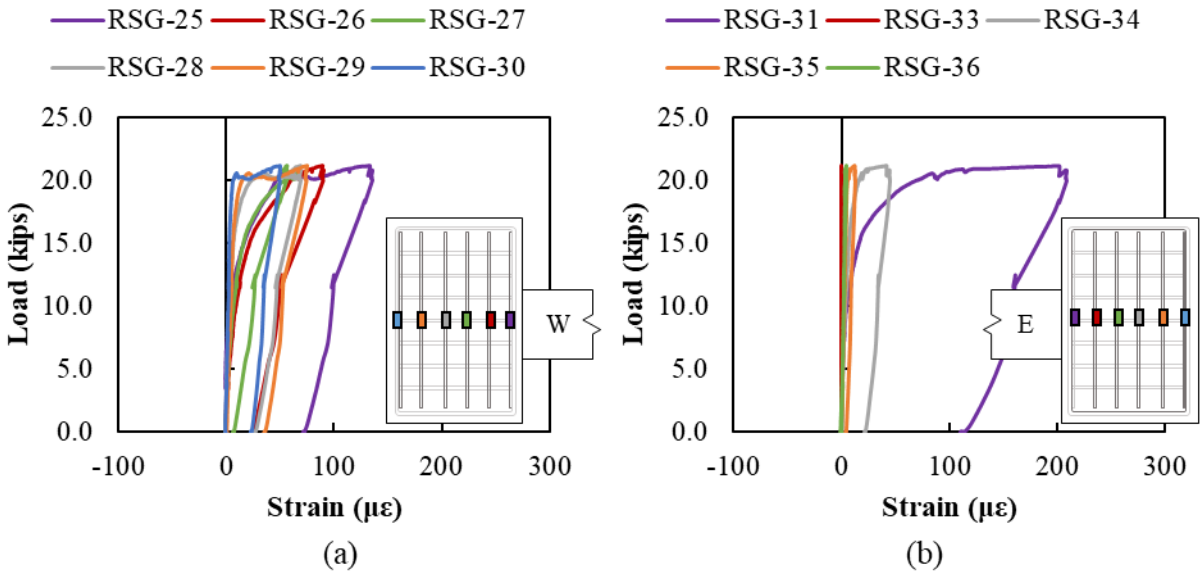

Figure D.45: SP-03 rebar strain data for N6 bars (a) west side (b) east side

D.3.5. Crack Displacement Transducers

Displacements in the plastic hinge zone for both piles are shown in Figure D.46 and Figure D.47. Largest compression and tension strains in the east pile were measured in the CDTs closest to the pile cap CSD-04E and CSG-05E. In the west pile, the largest tension strains were found in CDT-3W, which is the exact location where the crack opened in the pile. In the compression face of the pile CDT-05W came off during testing, due to spalling of concrete.

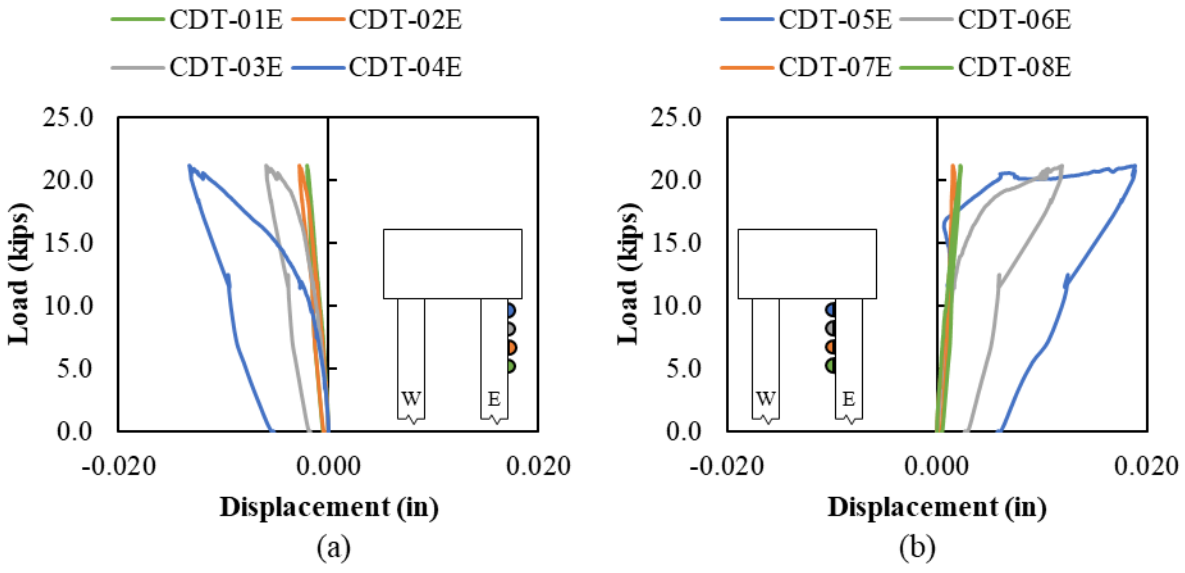

Figure D.46: SP-03 crack displacement data for east pile

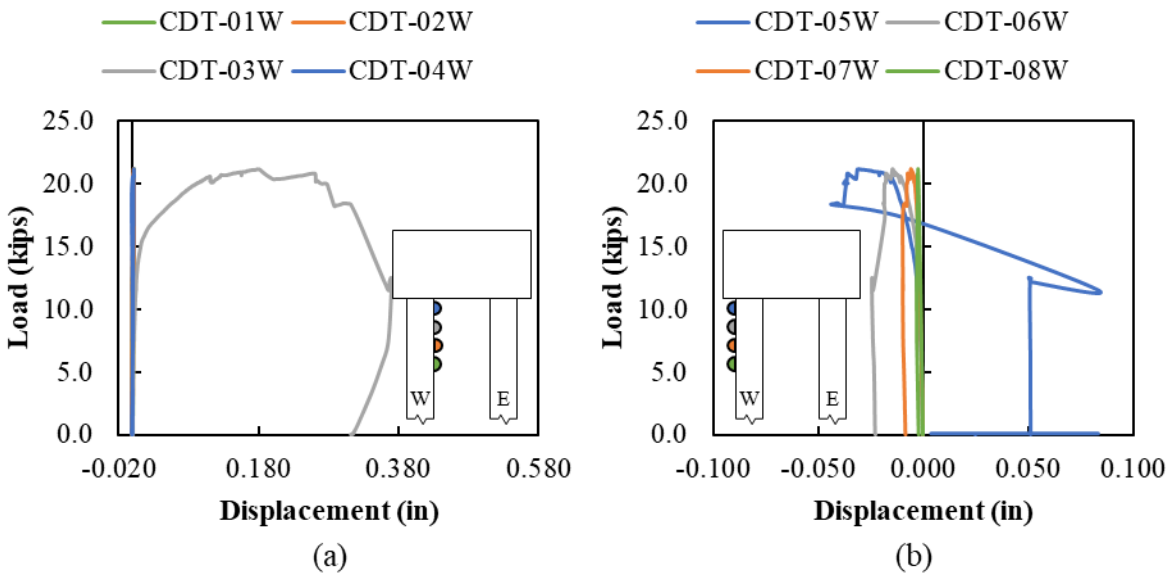

Figure D.47: SP03 crack displacement data for west pile

Moment-curvature response found using the CDTs for the west and east pile are shown in Figure D.48. No curvature was found at W4 since CDT-05W fell off during testing. High curvature developed in W3 at the crack location where the interface reinforcement ended in the pile.

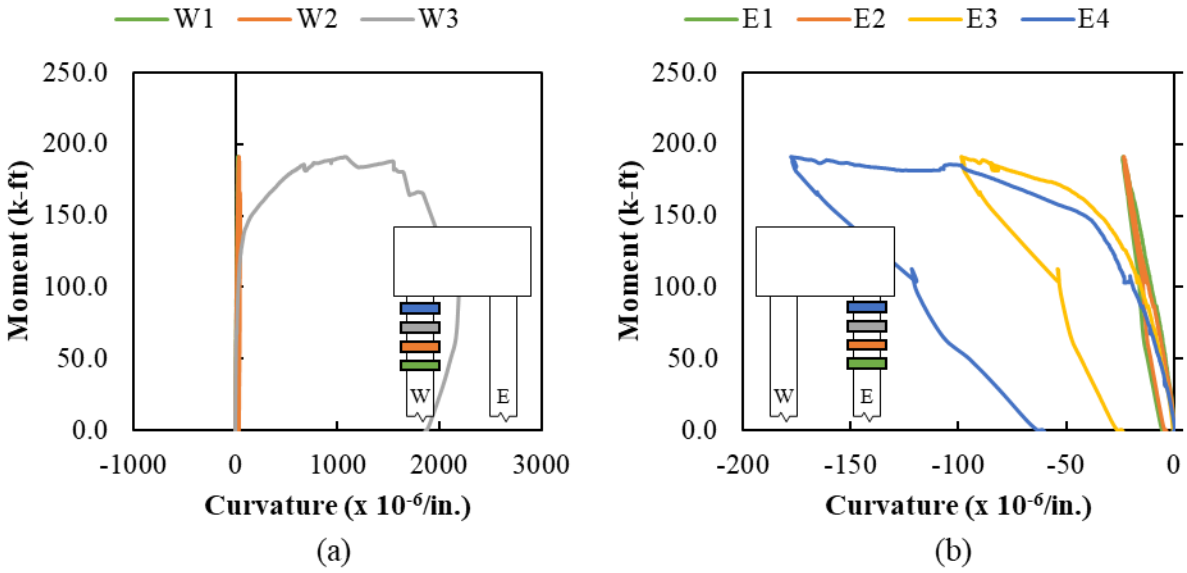

Figure D.48. SP-03 moment-curvature with crack displacements (a) west pile (b) east pile

D.3.6. Vibrating Wire Gauges (Pile)

Vibrating wire gauge (VWG) data was recorded at different stages of the specimen life. The initial data was used to calculate the elastic shortening losses, and total losses of each specimen.

Initial stress in strands:

Jacking stress: $$f_{pj} = \frac{F}{A} = \frac{34\ kips}{0.167\ in^2} = 203.6\ ksi$$

Readings from the longitudinal vibrating gages were recorded and used to find the stress in the strands after release (assuming E_p = 28,500 ksi):

Table D.10: SP-03 Elastic shortening losses calculation

VWG	**Before release** (με)	**After release** (με)	**Strain Change** (με)	**ES Losses** (ksi)
VWSG-P5-1E	0	-316.684	316.7	9.03
VWSG-P5-2E	0	-316.052	316.1	9.01
			Δf_{pES} = =	9.02

Therefore, the average stress in strands after elastic shortening losses:

Stress after elastic shortening losses: $$f_{pi} - \Delta f_{pES} = 203.6\ ksi - 9.02\ ksi = 194.58\ ksi$$

Readings from the longitudinal vibrating gages were recorded and used to find the stress in the strands before testing (assuming E_p = 28,500 ksi):

Table D.11: SP-03 Total losses calculation

VWG	**After casting** (με)	**Before testing** (με)	**Strain Change** (με)	**LT Losses** (ksi)
VWSG-P8-1E	-316.684	-835.4	518.8	14.78
VWSG-P8-2E	-316.052	-889.8	573.8	16.35
			Δf_{pLT} =	15.57

The average stress in strands after all losses:

Stress after all losses immediately before testing: $$f_{pi} - \Delta f_{pES} - \Delta f_{pLT} = 203.6\ ksi - 9.02ksi - 15.57 = 179\ ksi$$

D.3.7. Vibrating Wire Gauges (Cap)

Vibrating wire gauge data was also recorded in the pile cap around the embedded east pile. Readings at different times are shown in Table D.12. Temperature can affect the strain gauges readings; therefore, a temperature correction was applied to the actual readings, taking as reference the before cap casting readings.

Table D.12: SP-03 Vibrating wire gauge data in the pile cap

VWG	Before cap casting (με)	Before testing (με)	After Testing (με)
VWSG-4E	0	-1.919	96.002
VWSG-5E	0	-72.574	-58.447
VWSG-6E	0	-198.774	-179.439
VWSG-7E	0	-137.747	-126.235

D.3.8. Fiber Optic

Strains along the length of the FOS at different loads are shown in Figure D.49. Tension strains developed in the interior face of the pile with maximum strains at the pile-to-cap interface and at the location of the interface reinforcement.

Compression strains less than 1,000 με were measured on the exterior face of the east pile. As the load approached the failure load, high tensile strains started the developed.

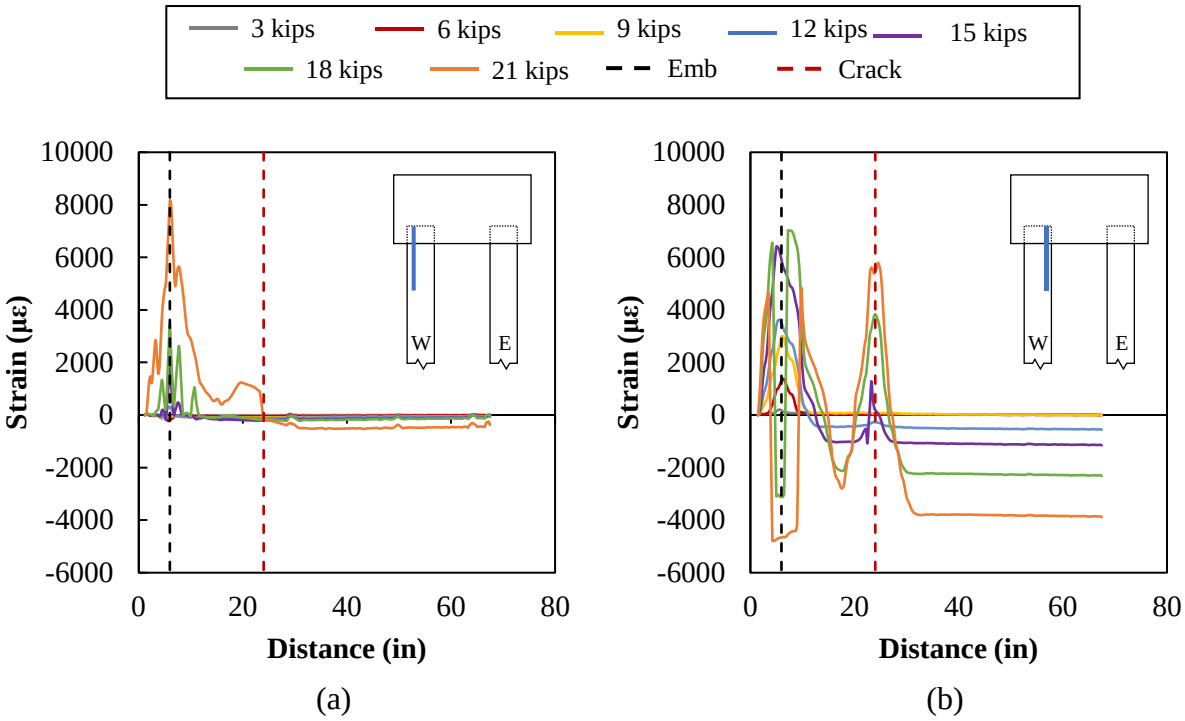

Figure D.49: SP-03 fiber optic data for the west pile (a) FOS-21 (b) FOS-29

The two vertical lines in Figure D.49 represents the two critical planes, the embedment length and the crack at the end of the interface reinforcement. Strain profiles at both critical planes are shown in Figure D.50.

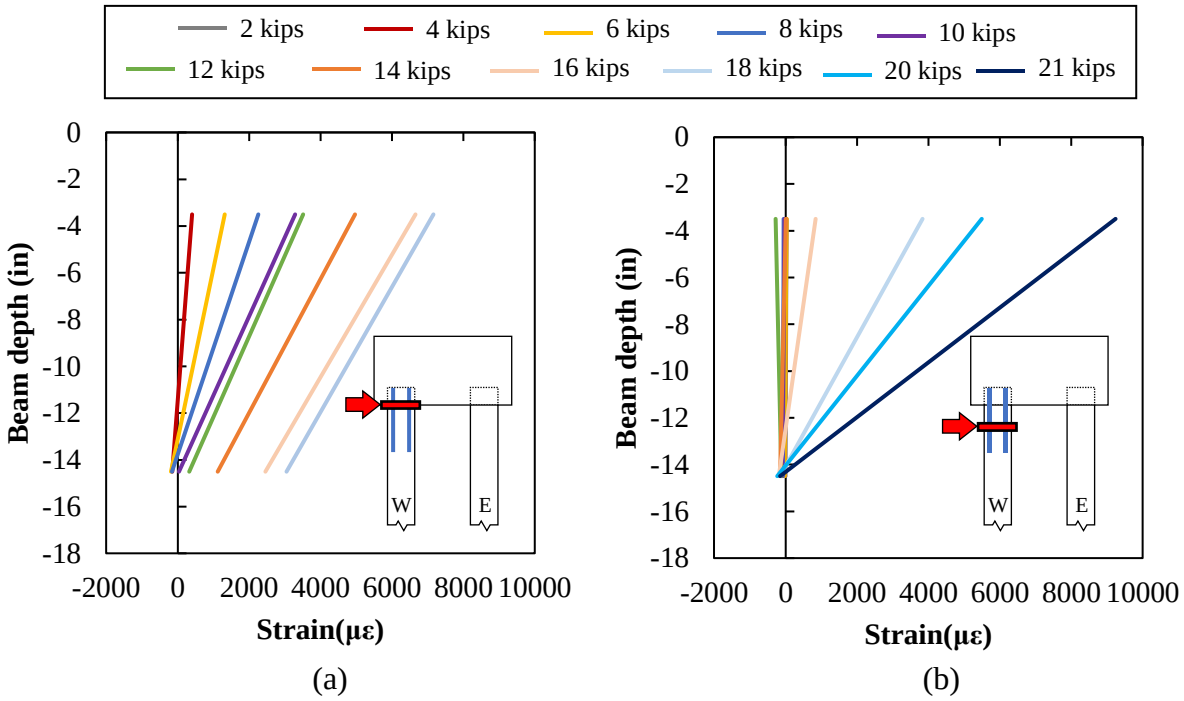

Figure D.50: SP-03 Strain profile at critical section in the west pile (a) at embedment length (b) at cracking

Fiber optic data for east pile is shown in Figure D.51. Similar behavior is occurring in the two fibers that are located in the tension side of the pile (FOS-29 and FOS-17). FOS-17 is starting to show an increase in tension at the end of the interface reinforcement, similar to the west pile, but not as significant.

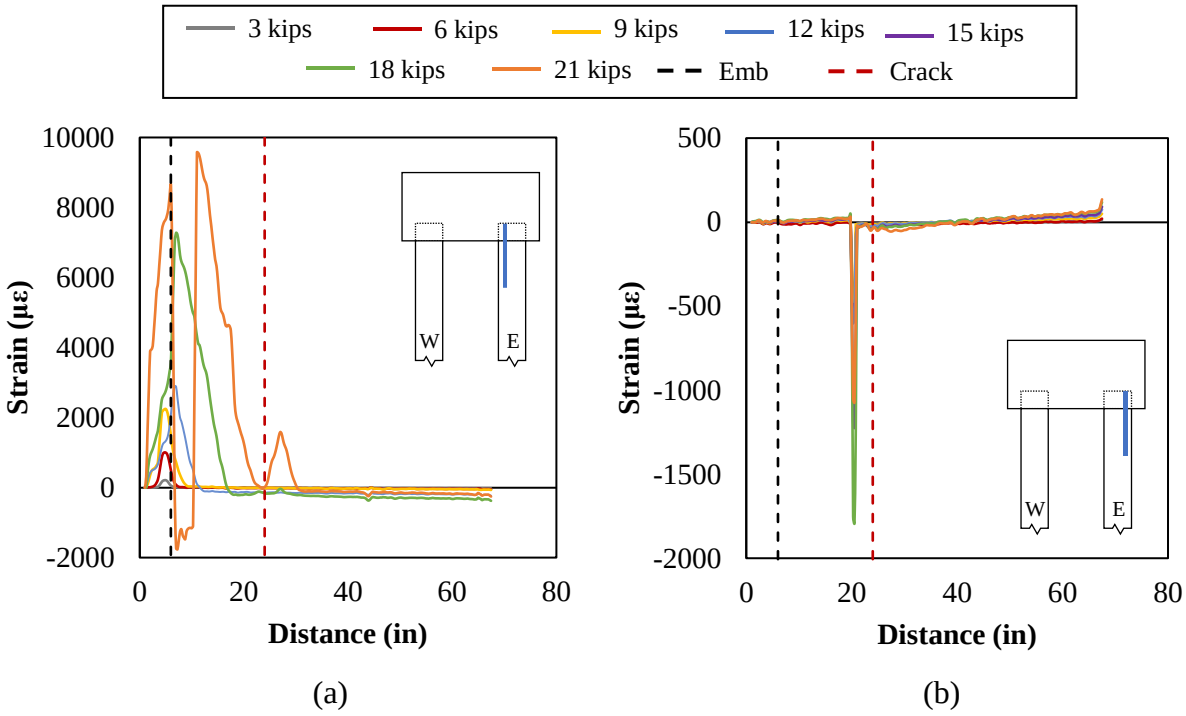

Figure D.51: SP-03 fiber optic data for east pile (a) FOS-17 (b) FOS-25

Strain profile at critical section of east pile, in this case at the pile-to-cap interface, is shown in Figure D.52.

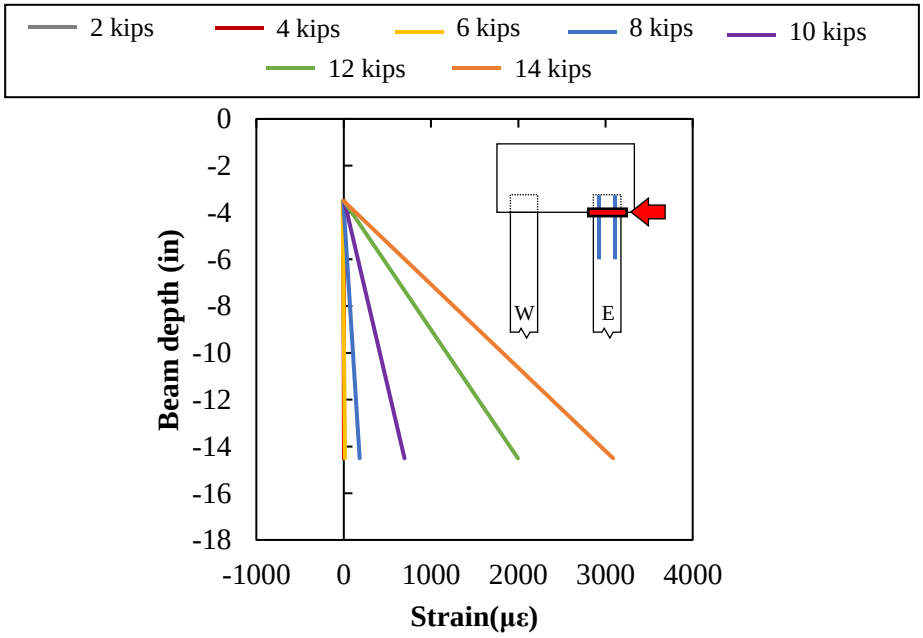

Figure D.52: FOS-03 strain profile for east pile at critical section

Moment-curvature response for both piles, at their critical sections, are shown in Figure D.53.

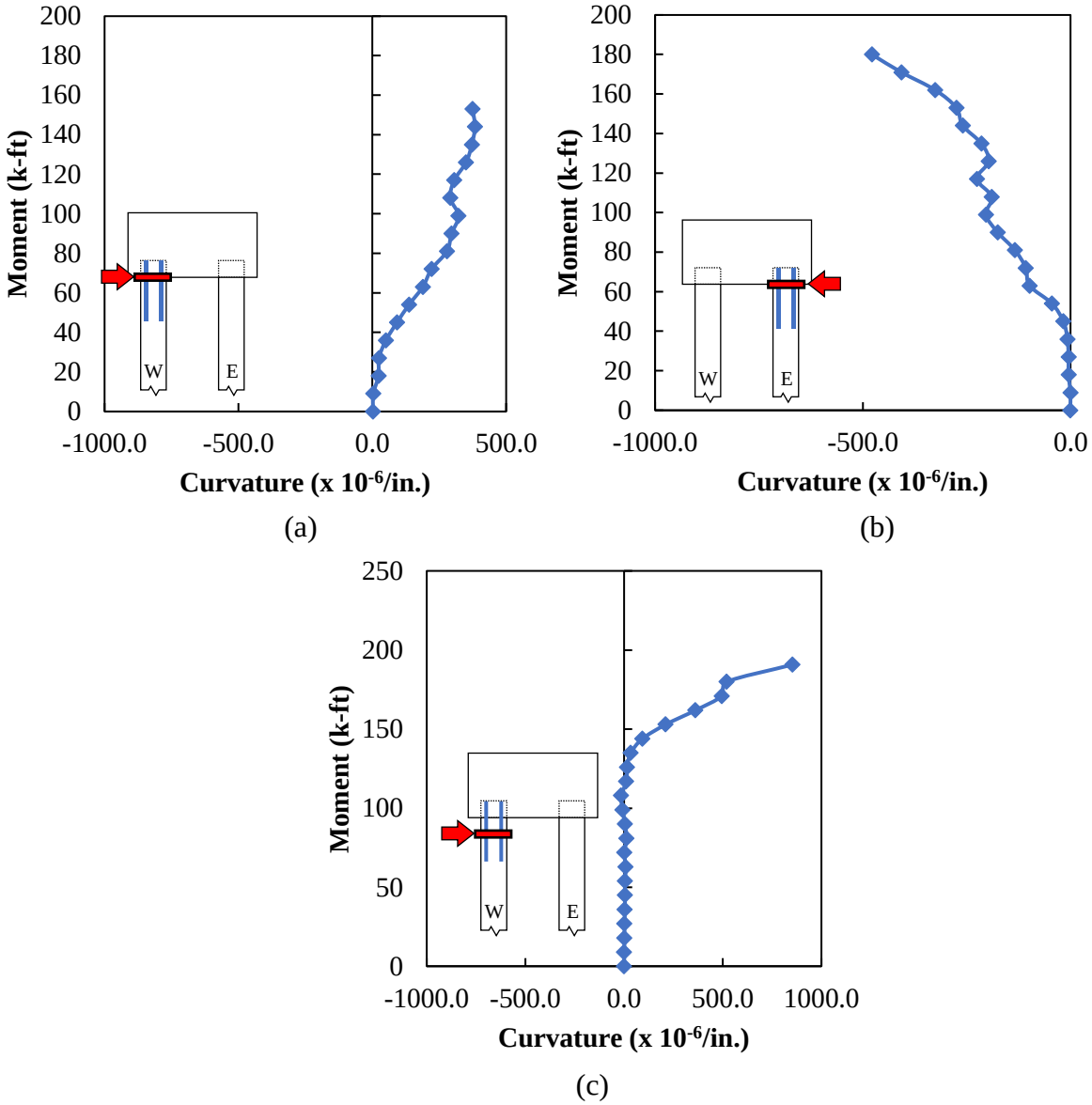

Figure D.53: SP-03 curvature at pile-to-cap interface (a) west pile at embedment (b) east pile at embedment (c) east pile at end of reinforcement

D.4. SP-04

D.4.1. Observations and Summary of Results

Results of Specimen 4 are summarized in Table D.13.

Table D.13: SP-04 Summary of Results

Specimen 4	
Pile Embedment	9.0 in. ($0.5d_{pile}$)

Specimen 4	
Interface Reinforcement	none
Axial Load	0 kips ($0A_g f'_{c,pile}$)
Failure load (kips)	13.6
Distance from Load to Cap (ft.)	9.0
Failure Mechanism	Strand development
Pile Failed	West
Maximum Displacement (in)	11.742
Ultimate Moment Developed (k-ft)	122.8
Percentage of capacity of pile	39.6 %

Specimen 4 had an embedment length of 9 inches, which corresponds to 0.5 d_{pile} no axial load was applied to the piles, and no interface reinforcement was present between the pile and cap.

Failure of this specimen occurred in the west pile. The observed failure was likely caused by strand development. A large crack was observed in the pile-to-cap interface on the west pile, and at 2-inch from the pile-to-cap interface in the east pile, as shown in Figure D.54.

Little damage of the pile cap was observed.

Figure D.54: SP-04 failure mechanism

D.4.2. Laser displacement transducers (LDT)

The application of the lateral load in the piles for Specimen 4 was at 9 ft from the pile-to-cap interface, which was the same location as LDT-02, as shown in Figure D.55

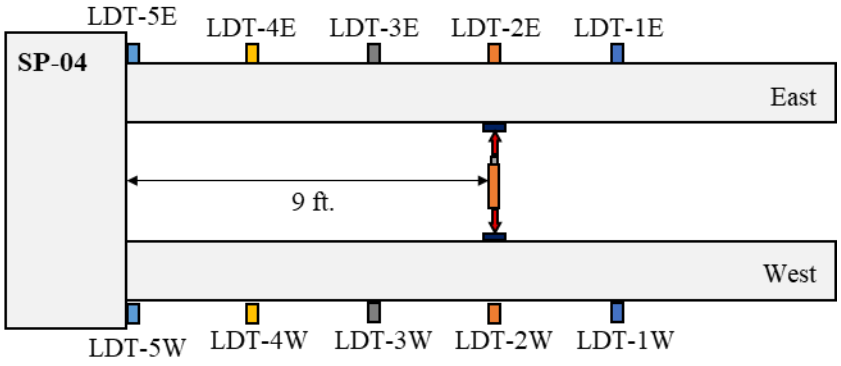

Figure D.55: Location of laser displacement transducers (LDT) and applied load for SP-04

The load-displacement curves of the west and east pile are shown in Figure D.56 (a) and Figure D.56 (b), respectively. The maximum load reached by Specimen 4 was 13.6 kips, which corresponds to 39.6% of the moment capacity of the 18-inch piles. The horizontal displacement in the west pile was 11.742 inch and in the east pile 1.786 inch The load-displacement curve was nearly horizontal at the time the hydraulic jack ran out of stroke and the load was removed.

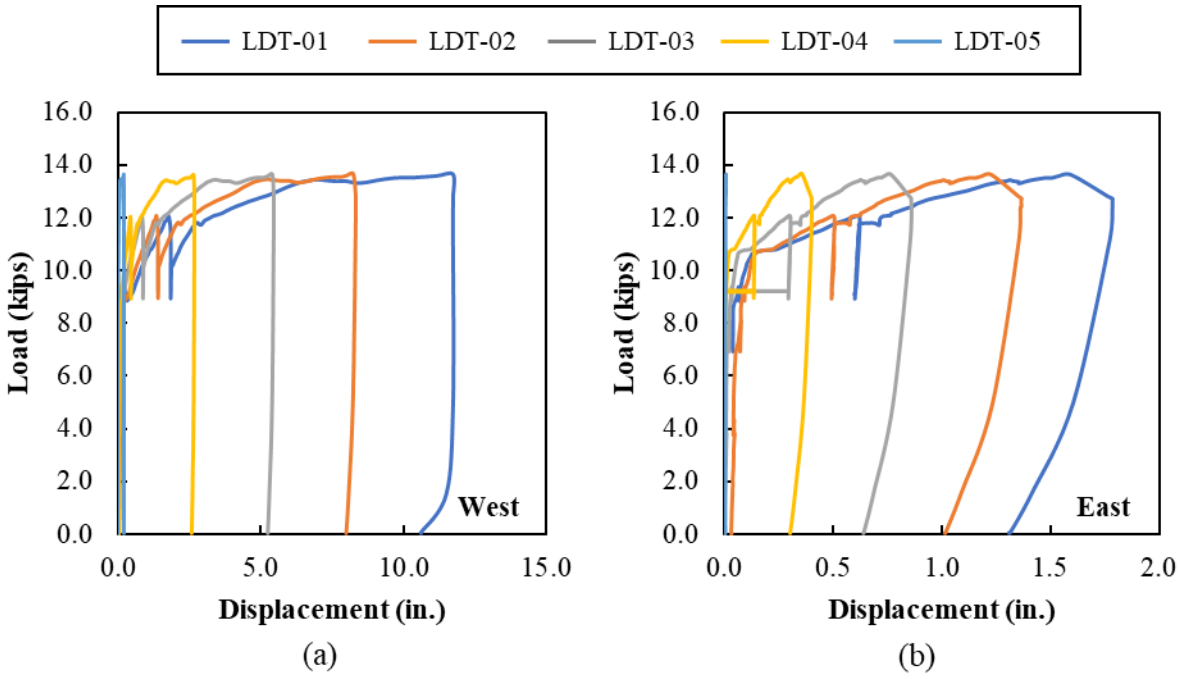

Figure D.56: SP-04 load- displacement curve (a) west side (b) east side

D.4.3. Concrete Strain Gauges

Vertical and horizontal concrete strains around the west pile are shown in Figure D.57. The strains in CSG-01 to CSG-07 were all less than the cracking strain of concrete. CSG-01 and

CSG-03, which are perpendicular to load application, measured tension strains less than 25 με. CSG-2, measured small compression strains.

CSG-04 and CSG-05, which are parallel to load application and are located outside the pile, measured tensile strains until around 9 kips, at which point tensile strains started to decrease, and compression strains began to be measured only in CSG-05.

CSG-06, located above the embedded west pile, started with tensile strains until approximately 13 kips and 20 με, at which point tensile strains started to decrease and compression strains began to be measured. This corresponds to spalling of concrete at this location, as shown in Figure D.57 (d).

CSG-07, located under the embedded west pile, measured tensile strains less than 75 με.

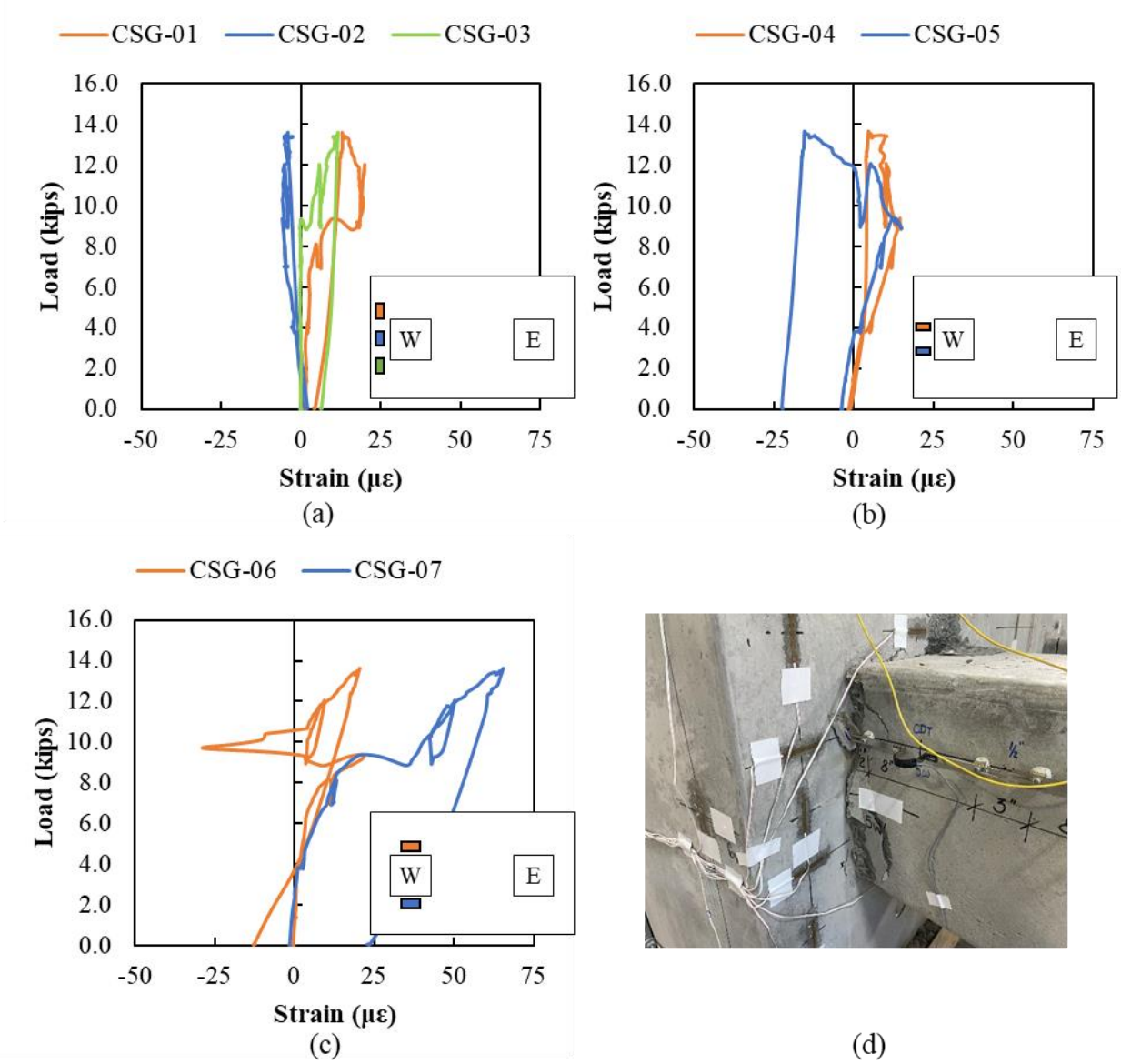

Figure D.57: SP-04 concrete strain data for CSG-01 to CSG-07

Vertical and horizontal concrete strains in the middle of the pile cap between the piles are shown in Figure D.58. CSG-08 and CSG-10, which are perpendicular to load application, measured compressive and tensile strains less than 5 με, respectively. No data was recorded for CSG-09.

CSG-11 and CSG-12, which are parallel to load application, measured tension strains less than 15 με.

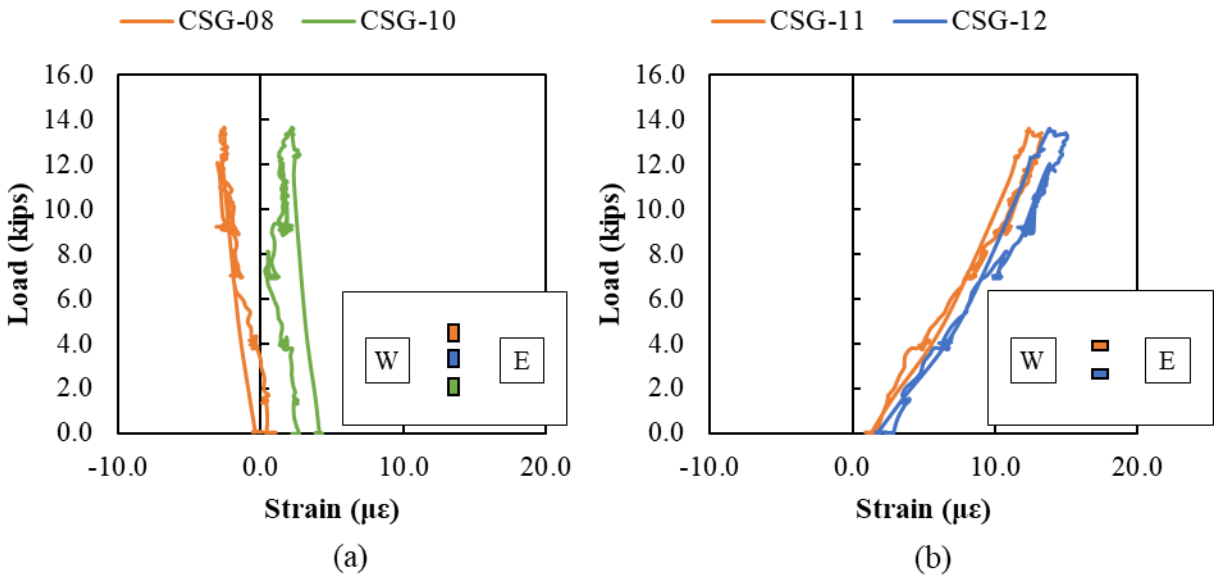

Figure D.58: SP-04 concrete strain data for CSG-08 to CSG-12

Vertical and horizontal concrete strains around the east pile are shown in Figure D.59. The strains in CSG-13 to CSG-19 are all less than the cracking strain for concrete. CSG-13 and CSG-14 measured tensile strains less than 40 με.

Similar behavior was observed in CSG-15 to CSG-17, which are perpendicular to load application. CSG-15 and CSG-17 measured tensile strains less than 20 με, and CSG-15 compression strains less than 20 με.

CSG-18 and CSG-19, which are parallel to load application, measured tension strains less than 30 με.

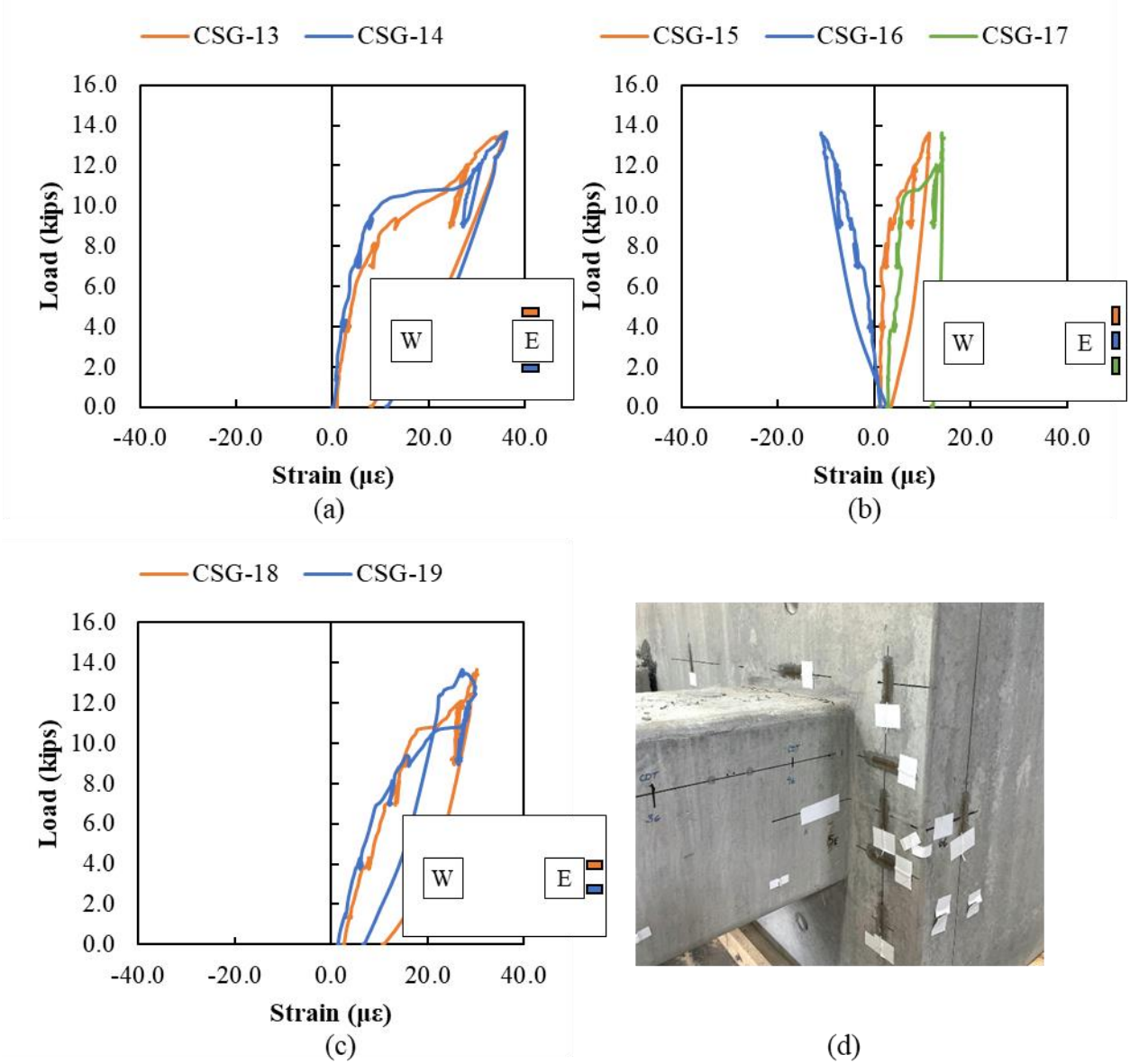

Figure D.59: SP-04 concrete strain data for CSG-13 to CSG-19

Concrete strains on the west and east faces of the pile cap are shown in Figure D.60. Measured strains on the west and east faces of the pile cap were less than 40 με at maximum applied loads.

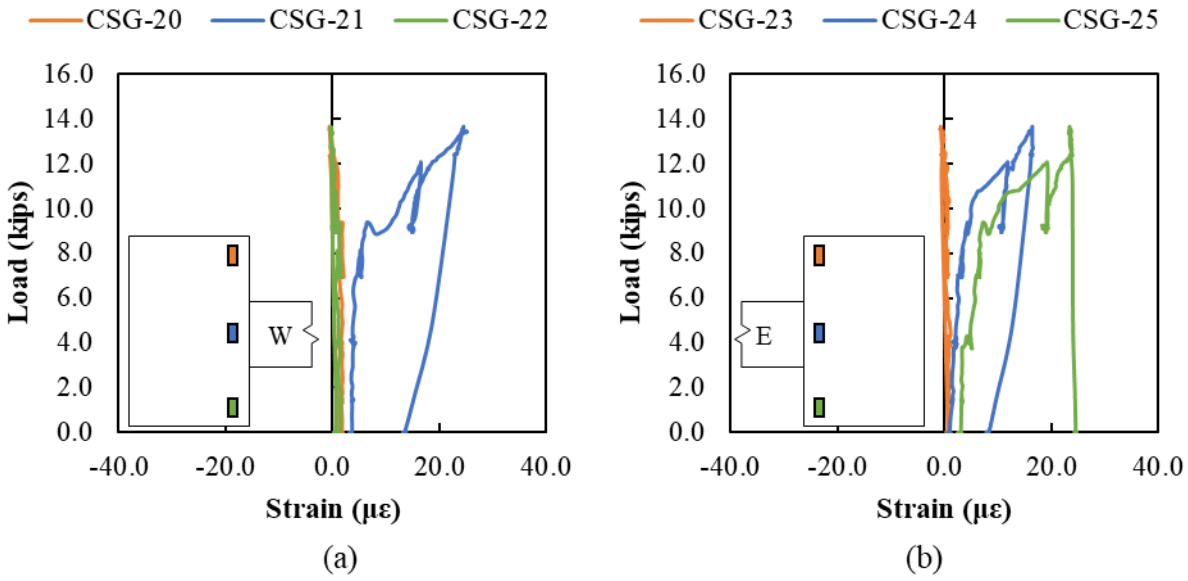

Figure D.60: SP-04 concrete strain data for CSG—20 to CSG-25

D.4.4. Rebar Strain Gauges

Rebar strains in the N5 bars are shown in Figure D.61. Strains less than 20 με were measured in the bars. No correlation between distance form piles and rebar was observed.

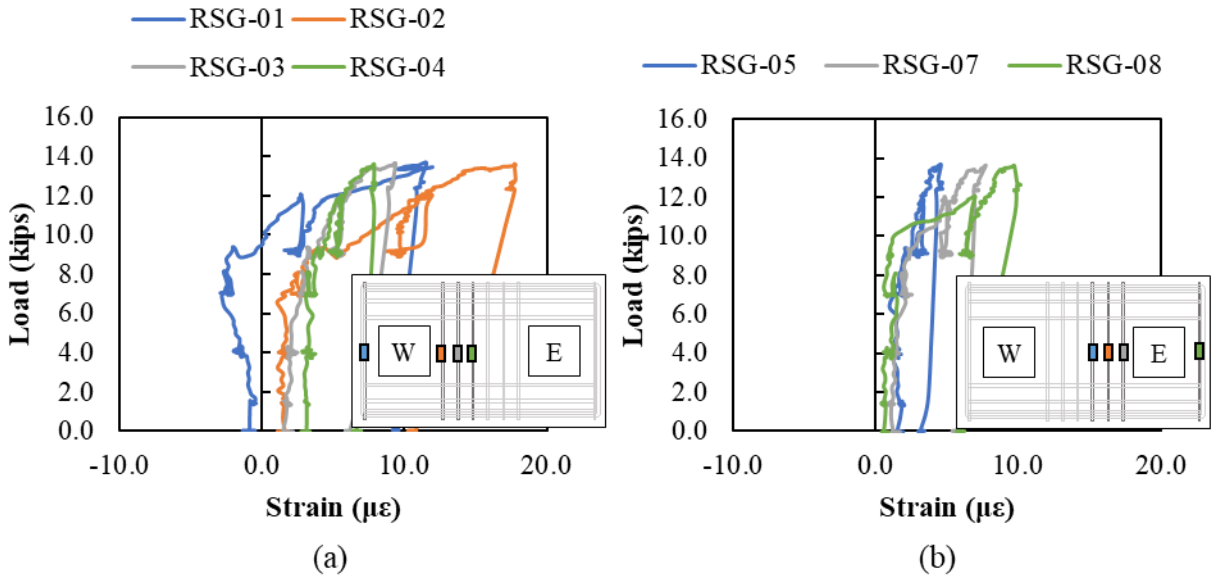

Figure D.61: SP-04 rebar strain data for N5 bars

Rebar strains in the N9 bars are shown in Figure D.62. Maximum measured strains are less than 30 με tension for all RSGs. RSG-13 and RSG-15, which are located closest to the west pile, showed maximum strains around the embedded pile.

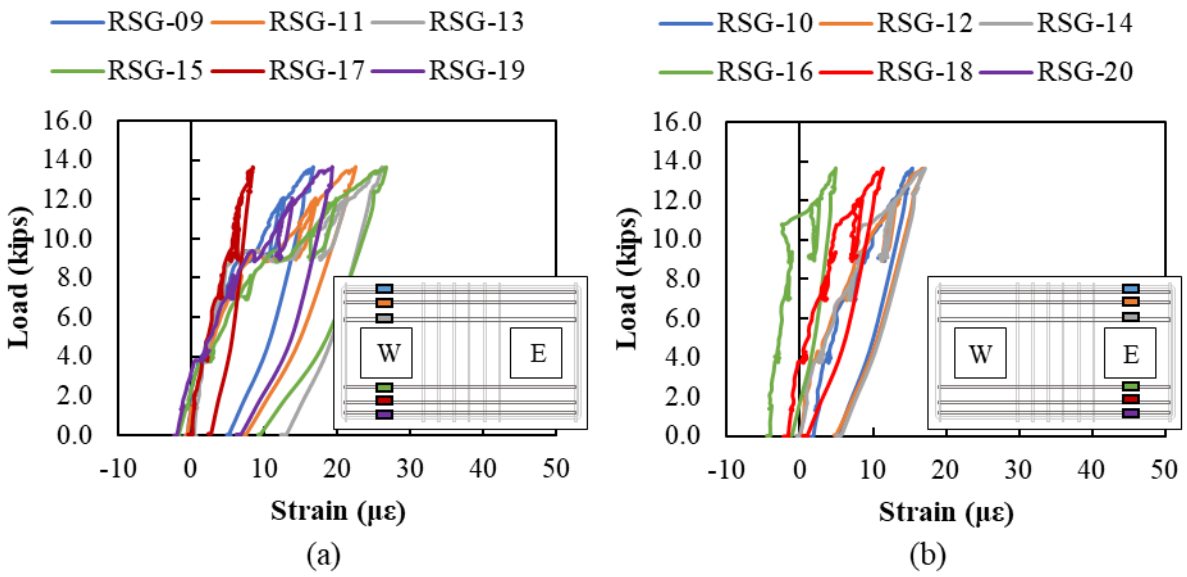

Figure D.62: SP-04 rebar strain data for N9 bars

Rebar strains in the N6 bars are shown in Figure D.63. Measured strains are less than 30 με with the highest measured strain in RSG-23 located below the west pile.

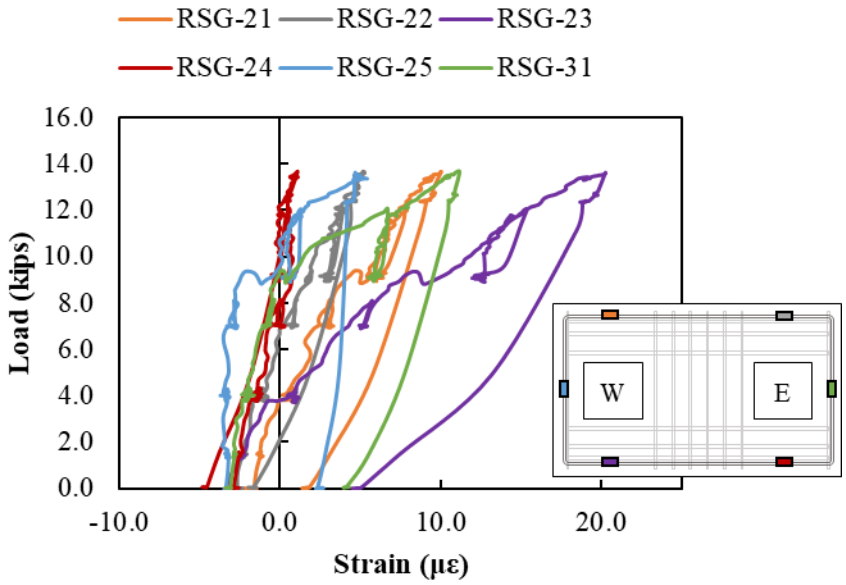

Figure D.63: SP-04 rebar strain data for N6 bars

Rebar strains in the N6 bars are shown in Figure D.64. Measured strains in the N6 rebar were less than 20 με. Compressive strains were measured in RSG-28 and RSG-30, located on the west face of the pile cap. Maximum tension strains in the east face of the pile cap were measured in RSG-31 and RSG-32, which are located closer to the embedded pile.

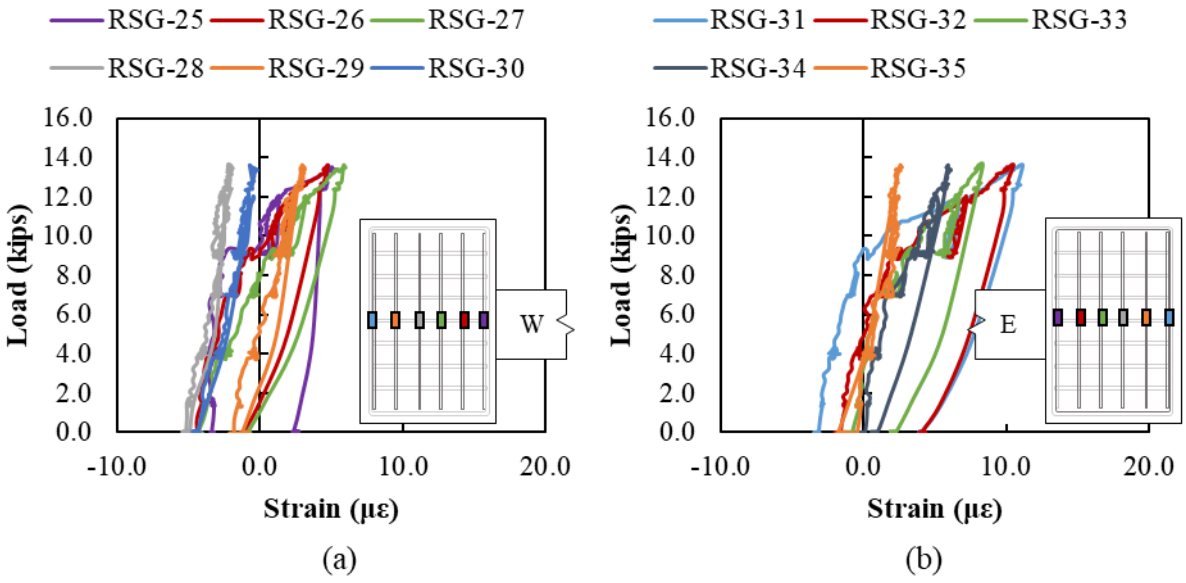

Figure D.64: SP-04 rebar strain data for N6 bars (a) west side (b) east side

D.4.5. Crack Displacement Transducers

Displacements were recorded in the plastic hinge zone of both piles; results are shown in Figure D.65 and Figure D.66. Largest compression strains were measured in the CDT closest to the pile cap CDT-04E and CDT-05W. There was no correlation between strains on tension face and distance from the pile cap.

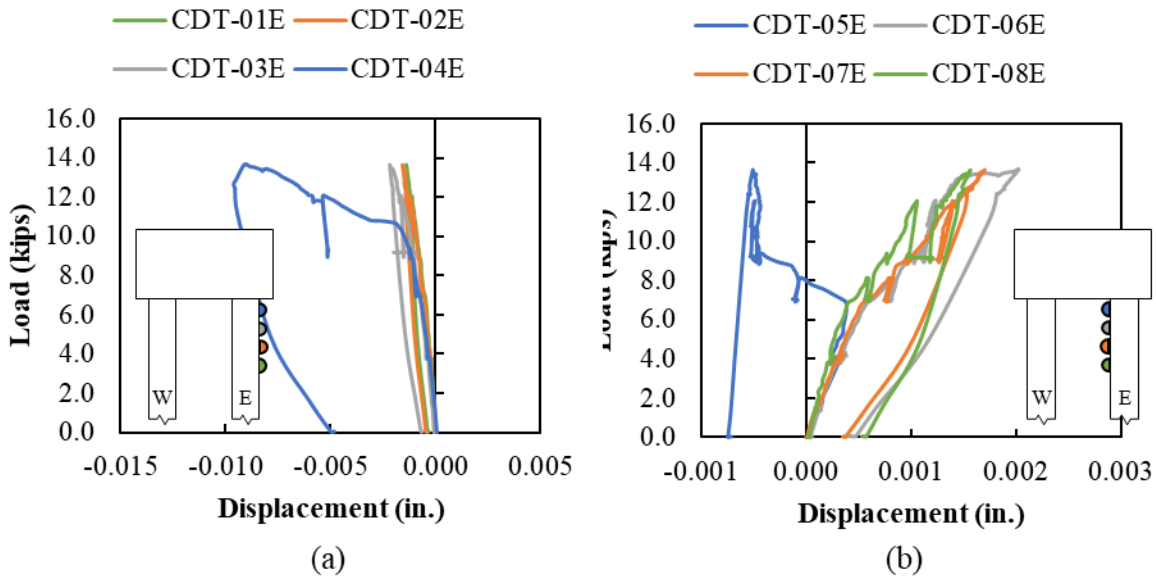

Figure D.65: SP-04 crack displacement data for east pile

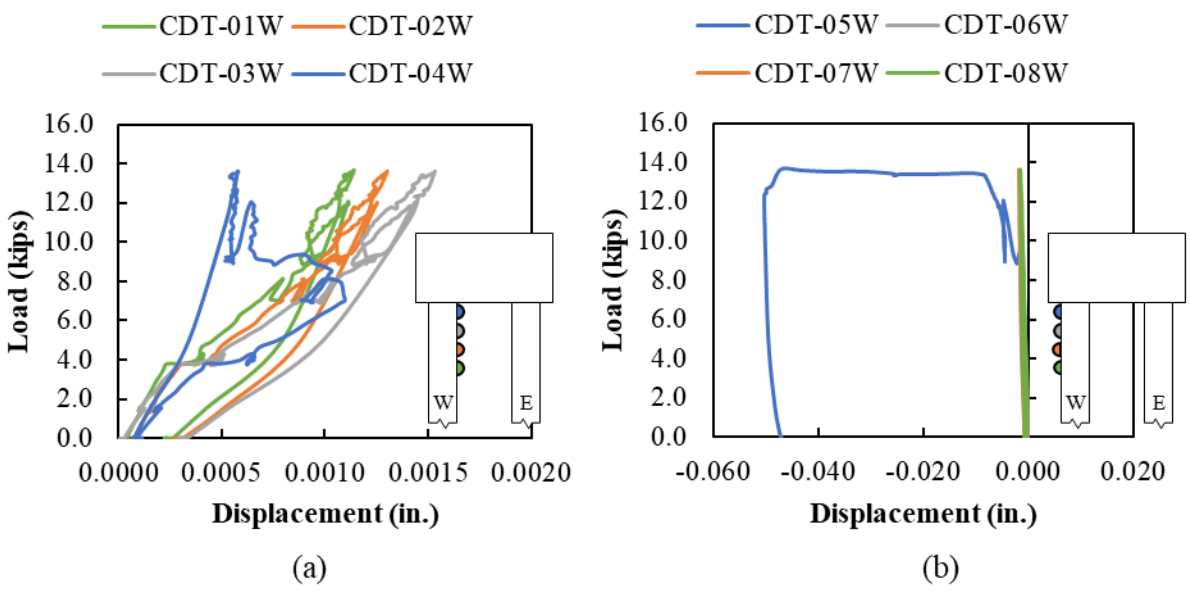

Figure D.66: SP-04 crack displacement data for east pile

The moment-curvature response using the CDTs for the west and east pile are shown in Figure D.67. Higher curvature was measured in the west pile in the gauges closest to the pile-to-cap connection.

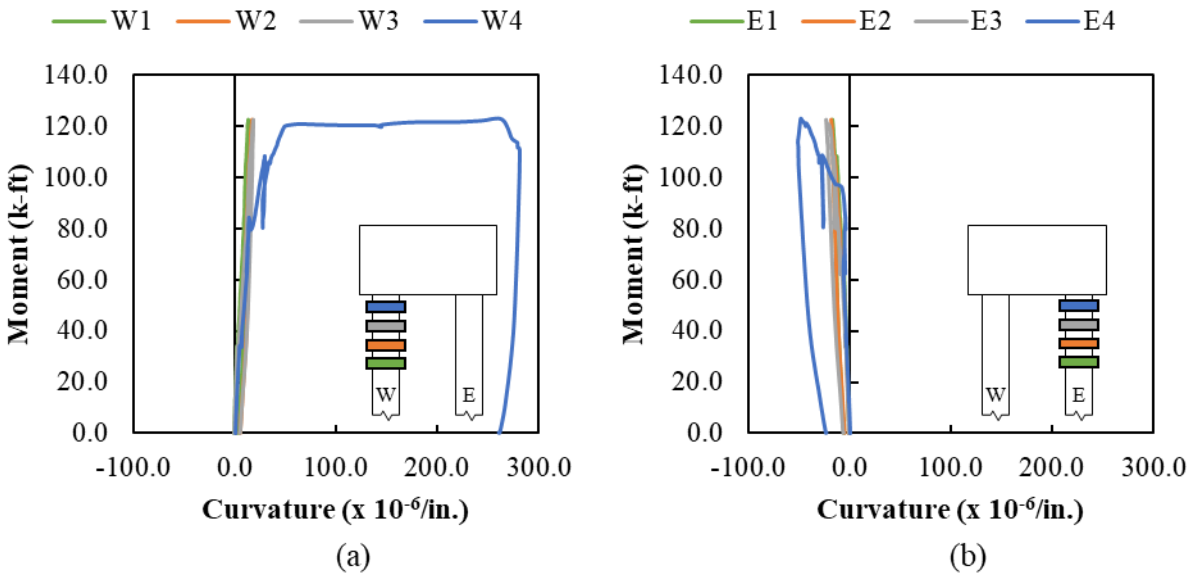

Figure D.67: SP-04 curvature with crack displacement (a) east pile (b) west pile

D.4.6. Vibrating Wire Gauges (Pile)

No vibrating gauges were located on either of these piles.

D.4.7. Vibrating Wire Gauges (Cap)

No data was recorded.

D.4.8. Fiber Optic

Strains along the length of the FOS at different loads in the west pile are shown in Figure D.68. Compression strains less than 1,000 με were measured on the exterior face of the west pile until approximately 9 kips, at which point tensile strains started to develop, at the plane of the pile-to-cap interface. Small tensile strains were measured on the interior face of the west pile, until around 10 kips were strains of 8,000 με developed at the pile-to-cap interface.

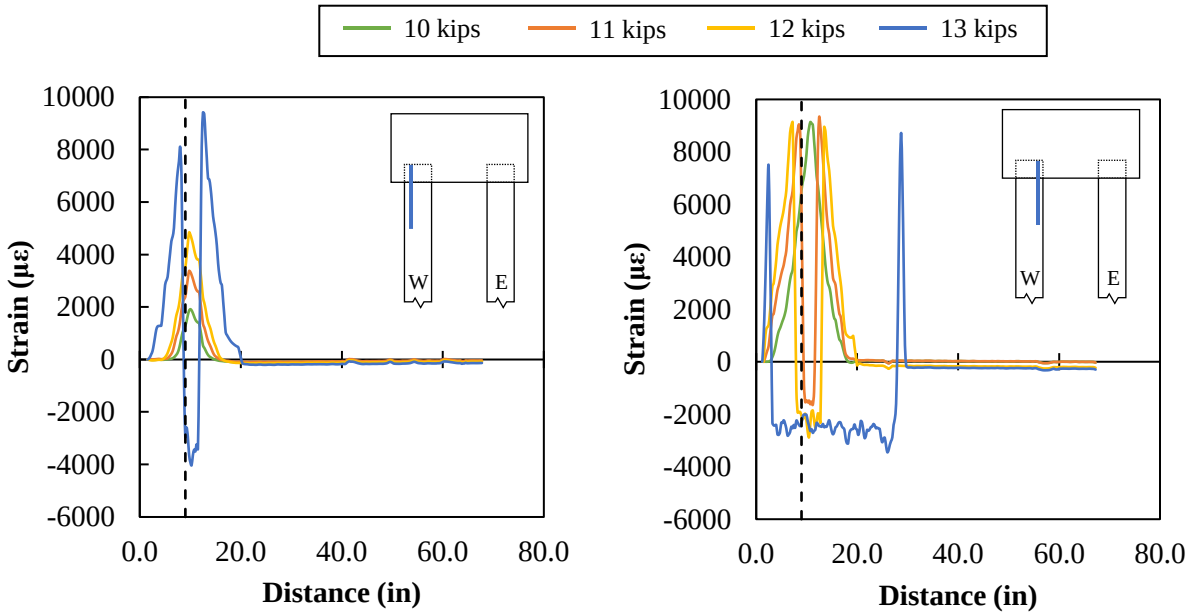

Figure D.68: SP-04 fiber optic data for west pile (a) FOS-22 (b) FOS-30

Strain profile for the west pile at the critical plane (12-inch embedment length) is shown in Figure D.69. Tensile strains were measured toward the top face of the pile at about 81 με, and compressive strains at the bottom at about 65 με at failure.

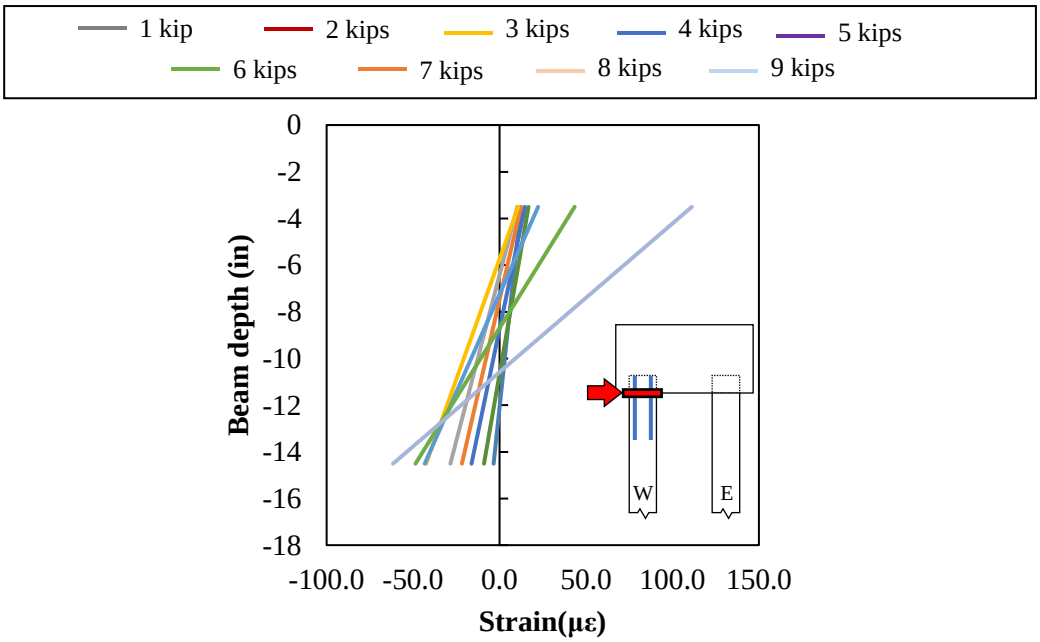

Figure D.69: SP-04 strain profile at critical section (6in) in the west pile

Strains along the length of the FOS at different loads in the east pile are shown in Figure D.70. Tensile strains developed in the interior face of the pile cap with maximum strains at the plane where the crack developed in the east pile (15-inch from the pile-to-cap interface). Small tensile strains developed on the exterior face of the pile, with maximum strains less than 3,000 με.

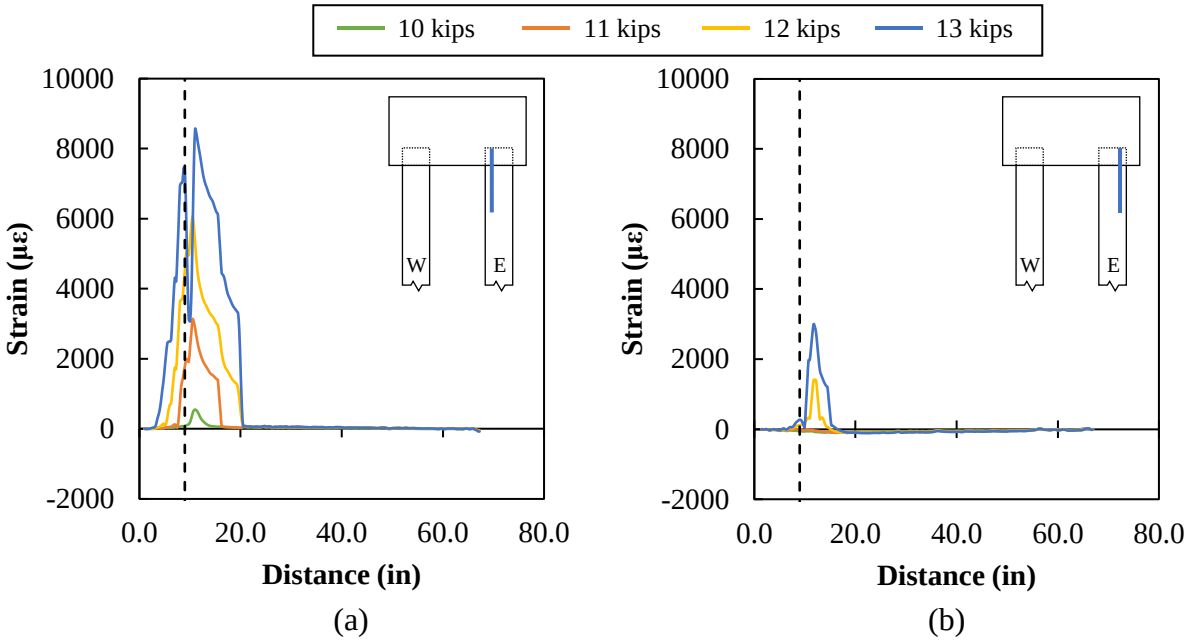

Figure D.70: SP-04 fiber optic data for east pile (a) FOS-22 (b) FOS-30

Strain profile for east pile at the critical plane (15-inch from the pile-to-cap interface) is shown in Figure D.71. Compression strains were measured at the bottom face at about 8,000 με at failure.

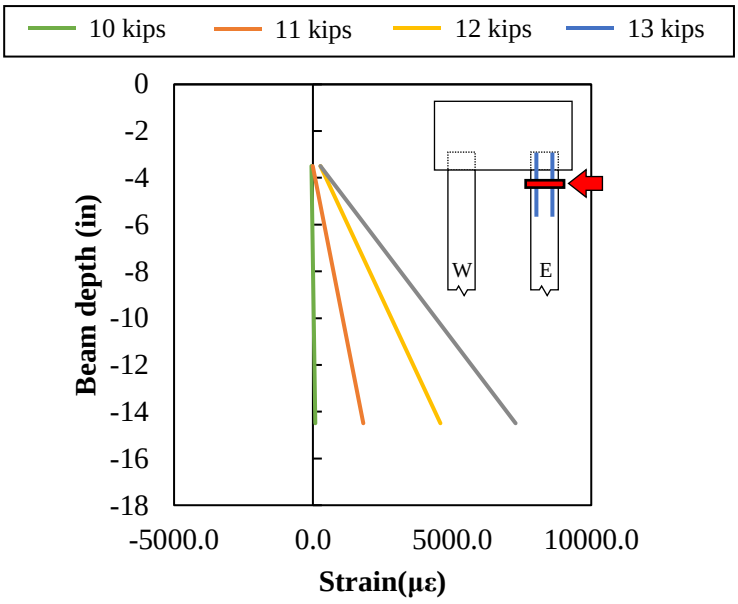

Figure D.71: SP-04 strain profile at critical section for east pile

The moment-curvature response for the west and east pile using FOS data are shown in Figure D.72.

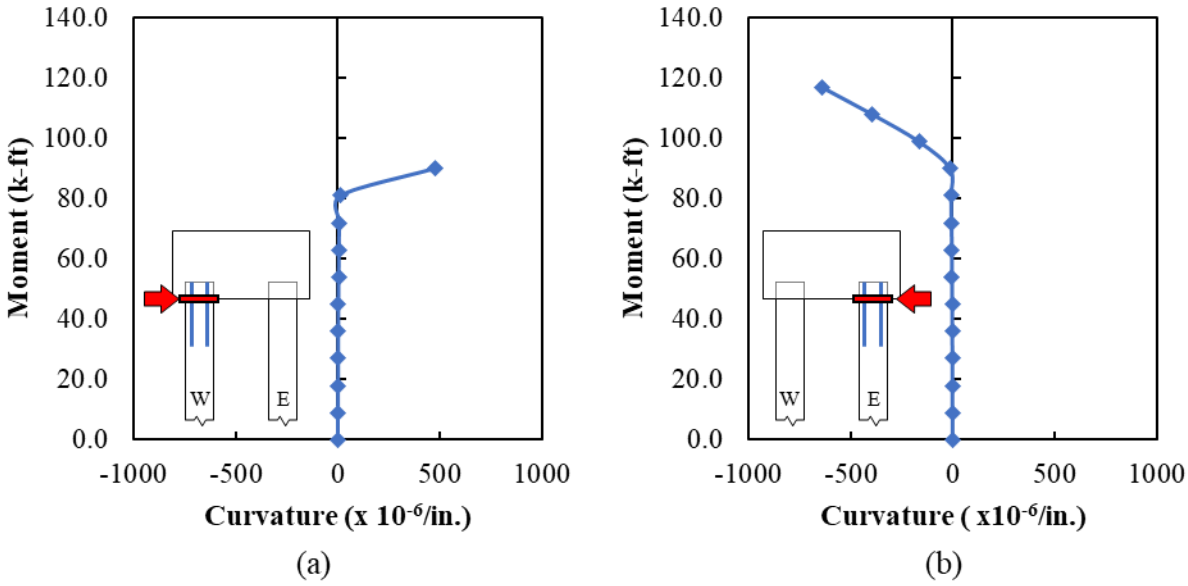

Figure D.72: SP-04 moment-curvature for (a) west pile (b) east pile

D.5. SP-05

D.5.1. Observations and Summary of Results

Results of Specimen 5 are summarized in Table D.14.

Table D.14: SP-05 summary of results

Specimen 5	
Pile Embedment	9.0 in. ($0.5d_{pile}$)
Interface Reinforcement	none
Axial Load	194 kips ($0.050A_g f'_{c,pile}$)
Failure load (kips)	41.0
Distance from Load to Cap (ft.)	6.0
Failure Mechanism	Strand development
Pile Failed	West
Maximum Displacement (in)	9.962
Ultimate Moment Developed (k-ft)	246.2
Percentage of capacity of pile	79.4 %

Specimen 5 had the same embedment length as Specimen 4 but with axial load application. Same procedure was used for the application of axial load as in Specimen 2.

Failure of the specimen occurred in the west pile. The observed failure was likely caused by crushing of the concrete around the pile and strand development length. Photographs of Specimen 5 are shown in Figure D.73.

Figure D.73: SP-05 failure mechanism (a) spalling of concrete on pile (b) pile-to-cap connection failure in the east pile

D.5.2. Laser displacement transducers (LDT)

The application of the lateral load in the piles for Specimen 5 was at 6 ft from the pile-to-cap interface, which was the same location as LDT-03, as shown in Figure D.74.

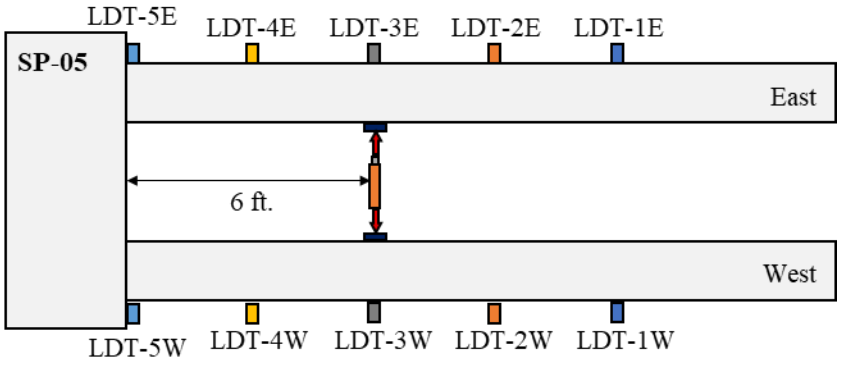

Figure D.74: Location of laser displacement transducers (LDT) and applied load for SP-05

The load-displacement curves of the west and east pile are shown in Figure D.75 (a) and (b) respectively. The maximum load reached by Specimen 5 was 41.0 kips, which corresponds to 79.4% the capacity of the 18-inch piles. The horizontal displacement in the west pile was 9.962 inches and in the east pile 8.654 inches. The load-displacement curve was nearly horizontal at the time the hydraulic jack ran out of stroke and the load removed.

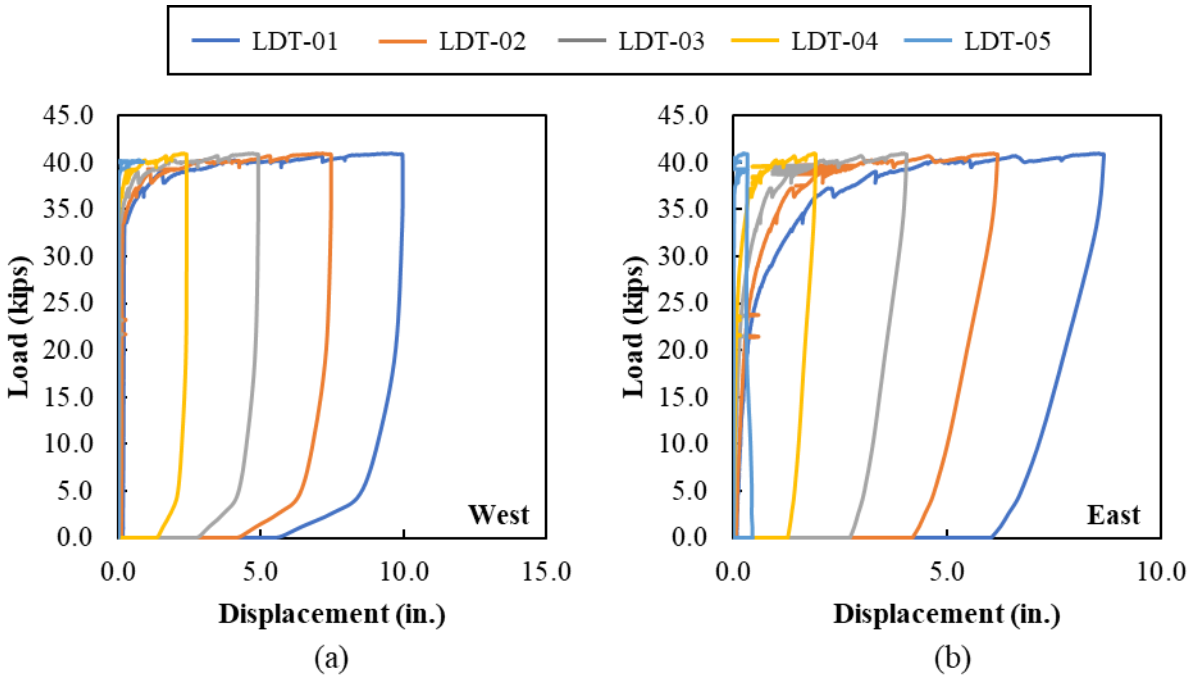

Figure D.75: SP-05 load-displacement curve for (a) west pile (b) east pile

D.5.3. Concrete Strain Gauges

Horizontal and vertical concrete strains around the west pile are shown in Figure D.76. CSG-01 and CSG-02, which are perpendicular to the applied load, measured maximum compressive strains of 20 με and 220 με, CSG-03 measured tension stress less than 50 με .

CSG-04 and CSG-05 measured tensile and compressive strains less than 50 με. CSG-06 and CSG-07, located at the top and bottom of the embedded pile, started measuring compression strains until around 20 kips, at which point tensile trains less than 100 με were measured.

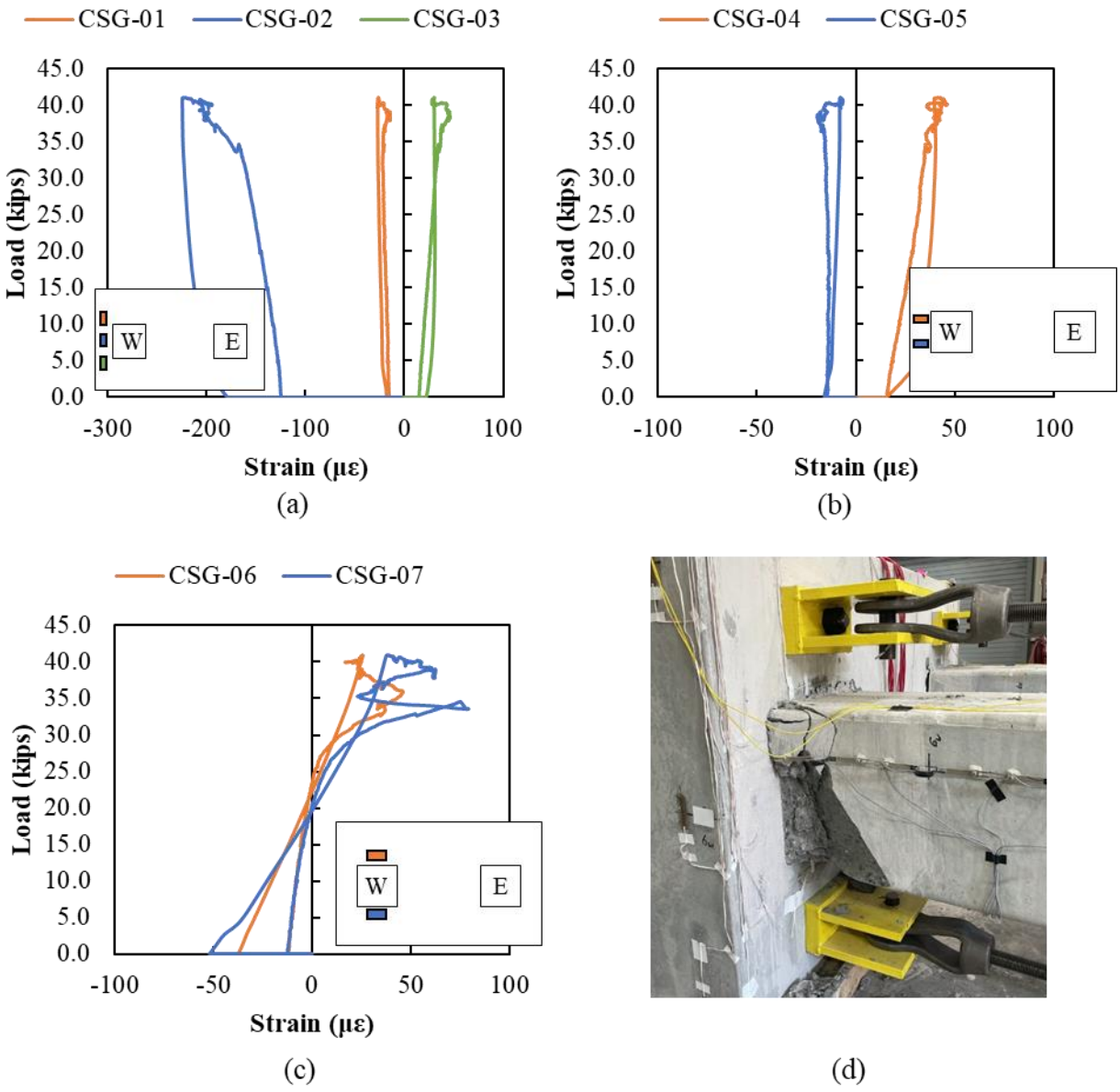

Figure D.76: SP-05 concrete strain data for CSG-01 to CSG-07

Horizontal and vertical concrete strains in the middle of the pile cap between the piles are shown in Figure D.77. CSG-08 to CSG-10, which are perpendicular to load application, measured

compression strains less than 40 με. CSG-11 and CSG-12, which are parallel to load application, started measuring tensile strains until failure load, at which point tensile strains decreased and compressive strains less than 100 με developed.

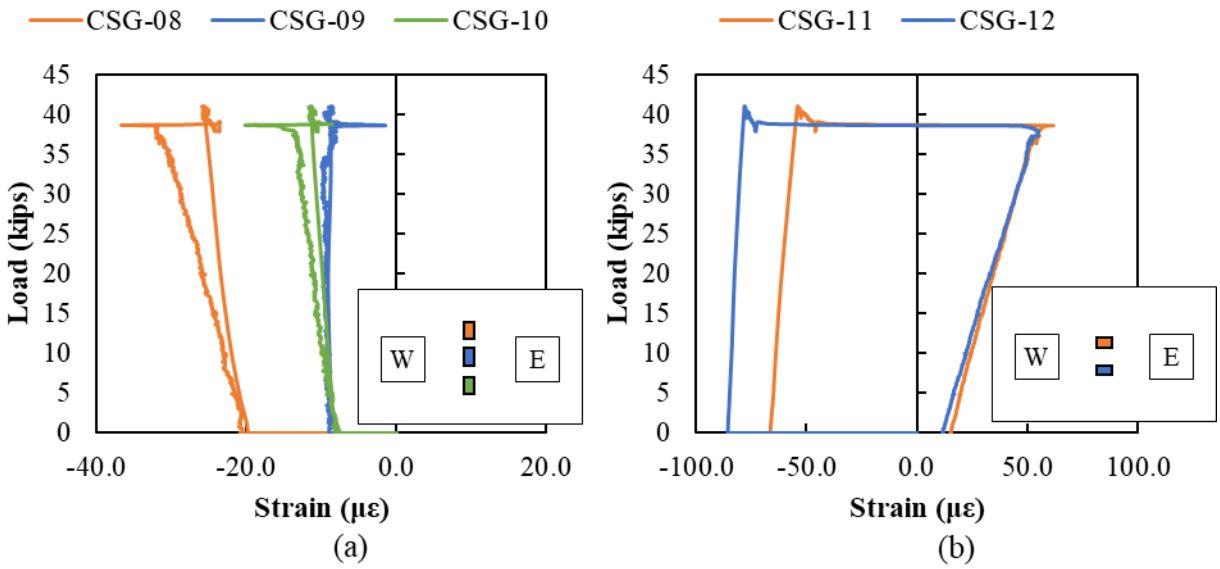

Figure D.77: SP-05 concrete strain data for CSG-08 to CSG-12

Horizontal and vertical concrete strains around east pile are shown in Figure D.78. Maximum tensile strains of 52 με and 150 με developed in CSG-13 and CSG-14. Compression strains less than 50 με developed in CSG-15 to CSG-17. Maximum tensile strains of 77 με and 57 με developed in CSG-18 and CSG-19 respectively. No cracks or spalling was observed at this location.

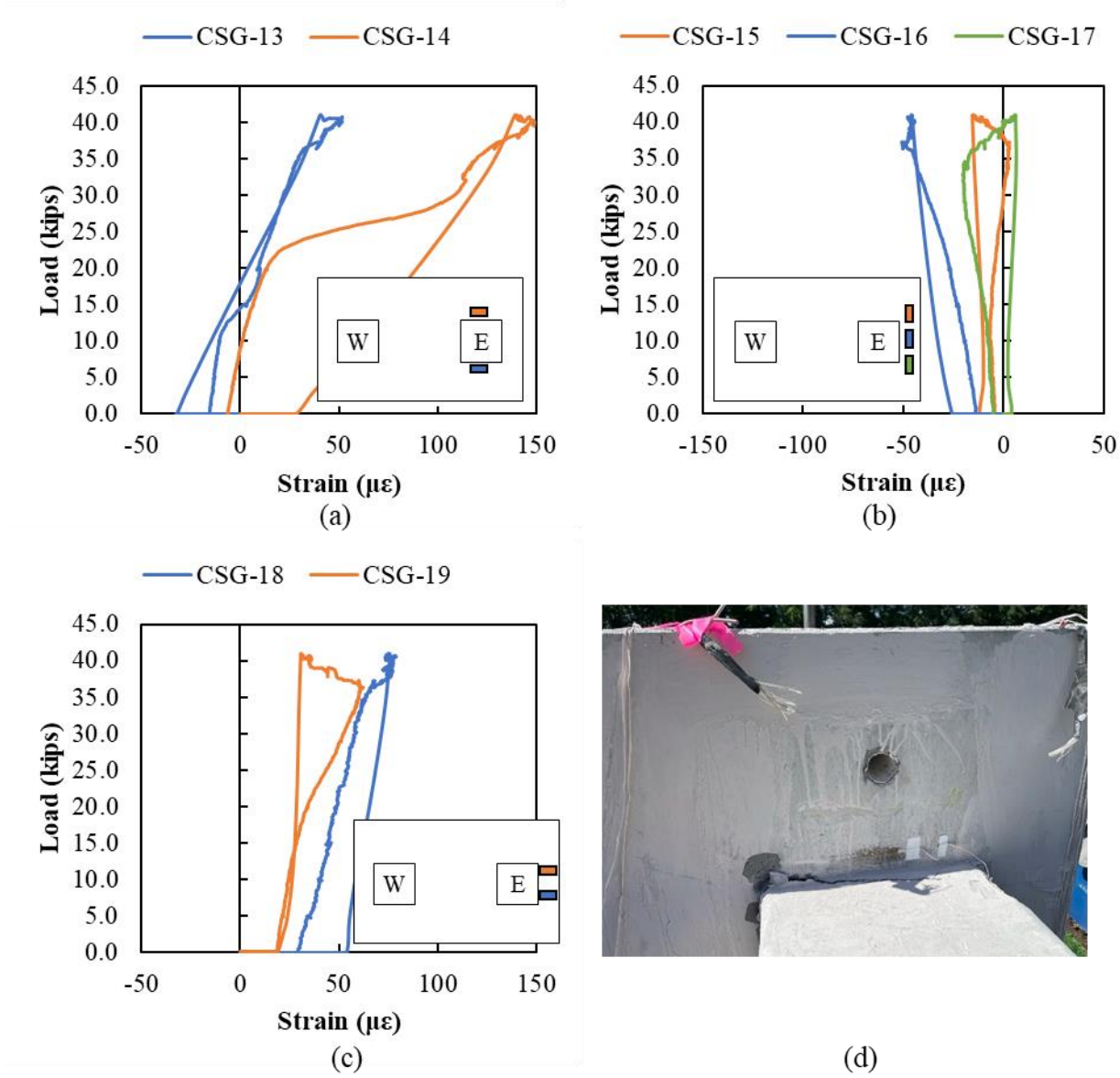

Figure D.78: SP-05 concrete strain data for CSG-13 to CSG-19

Concrete strains on the west and east faces of the pile cap are shown in Figure D.79. Tensile strains less than 40 με were measured in CSG-20 to CSG-25, with maximum readings at CSG-21 and CSG-24, located at the same height of the embedded pile.

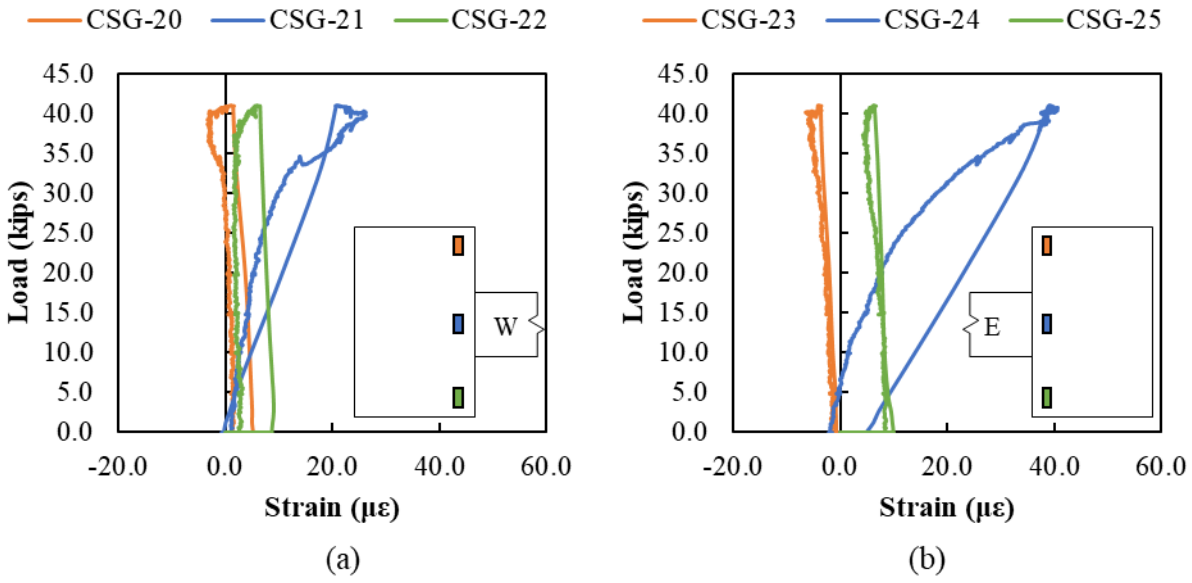

Figure D.79: SP-05 concrete strain data for CSG-20 to CSG-25 (a) west side (b) east side

D.5.4. Rebar Strain Gauges

Rebar strains in the N5 bars are shown in Figure D.80. Compression strains less than 40 με were measured in RSG-01 to RSG-04, RSG-05 and RSG-08. RSG-06 and RSG-07 started measuring compression strains until around 38 kips, at which point tensile strains began to be measured.

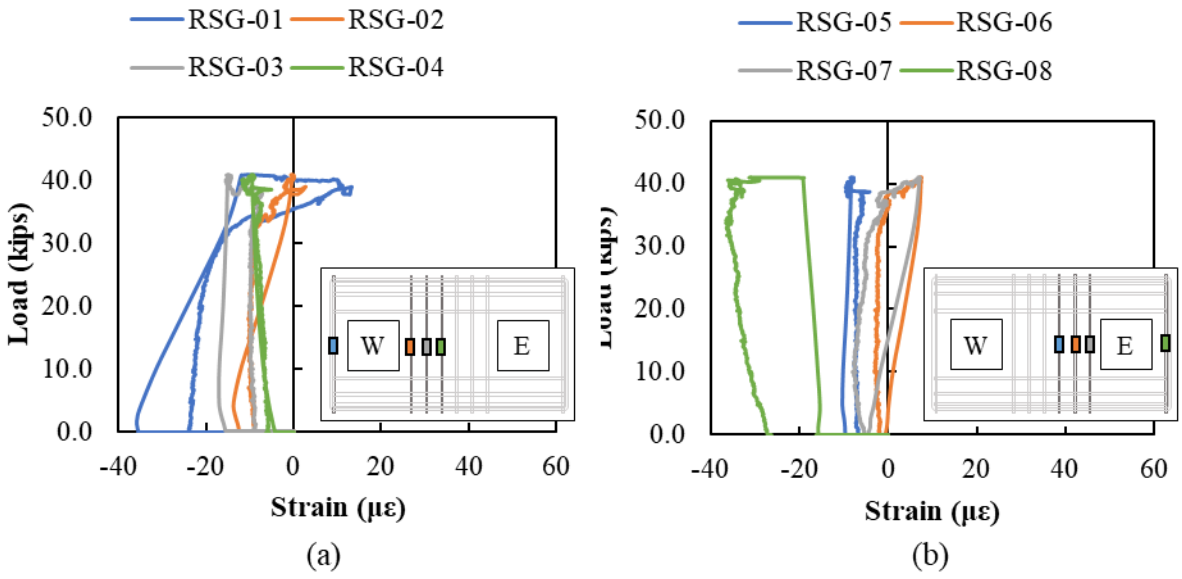

Figure D.80: SP-05 rebar strain data for N5 Bars

Rebar strains in the N9 bars are shown in Figure D.81. Maximum measured tensile strains are less than 100 με for RSG-9 to RSG-20, expect for RSG-10 which show strains higher than 300 με.

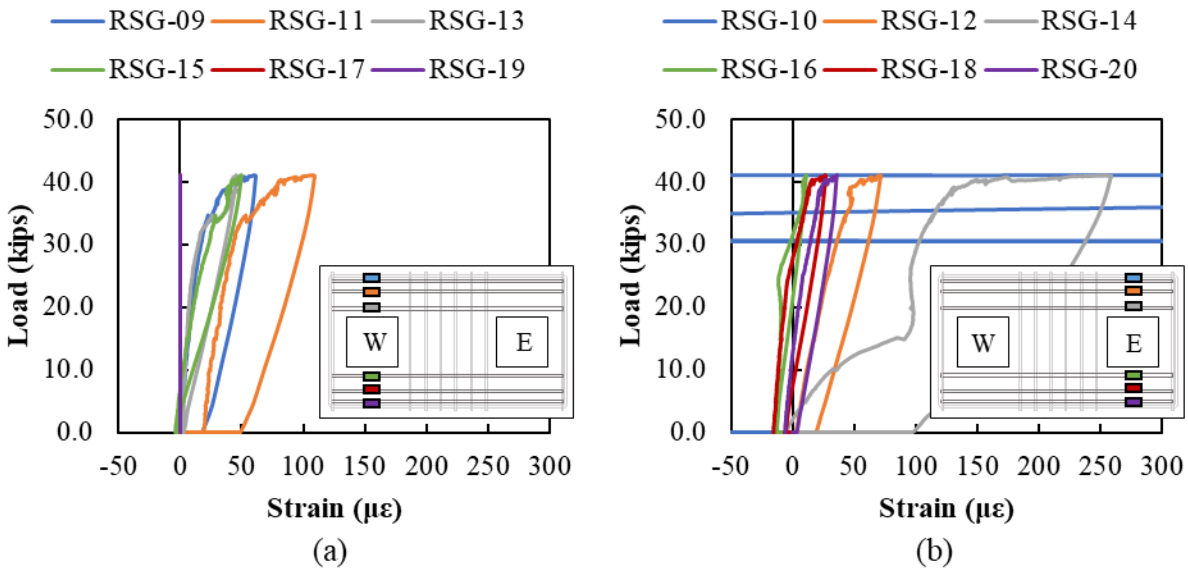

Figure D.81: SP-05 rebar strain data for N9 Bars

Rebar strains in the N6 bars are shown in Figure D.82. Measured strains remained less than 40 με in RSG-21 to RSG-31.

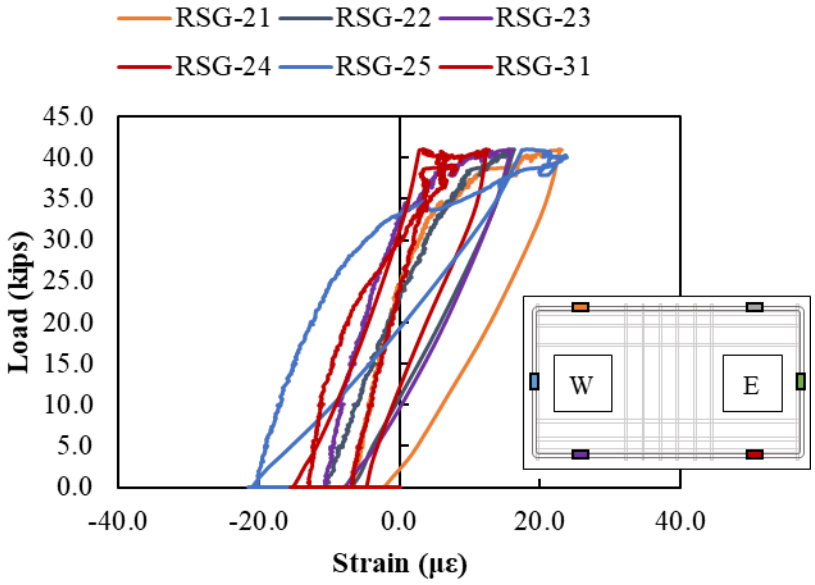

Figure D.82: SP-05 rebar strain data for N6 Bars

Rebar strains in the N6 bars on the side of the pile cap are shown in Figure D.83. High tensile strain in RSG-27. Higher strains were measured on the west side of the pile cap, which correlates to the west pile failing. Highest measured strains developed at RSG-27 at around 50 με.

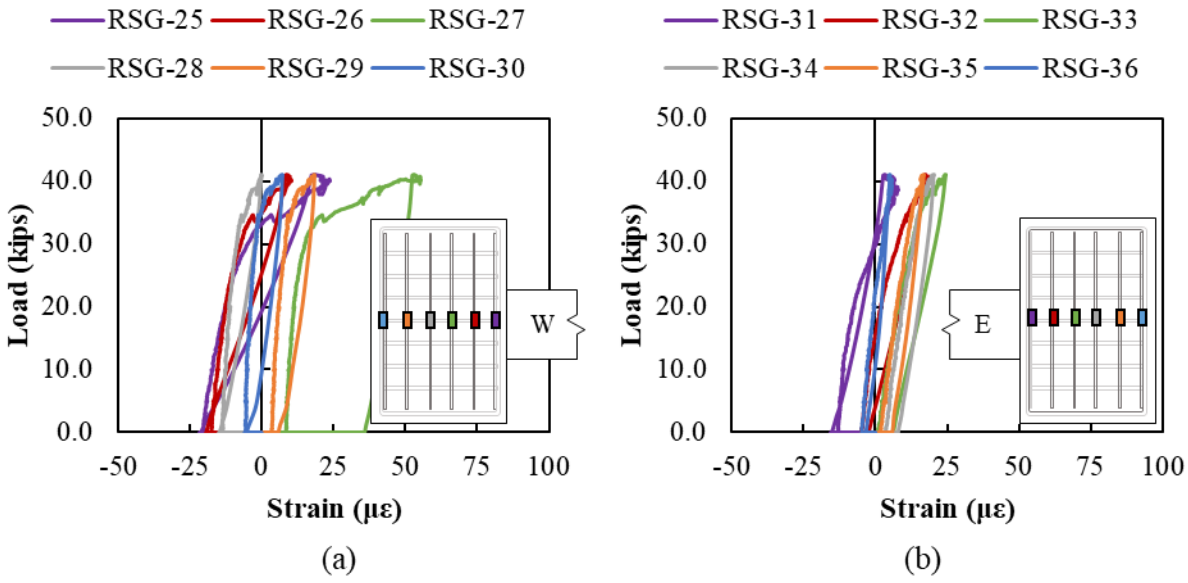

Figure D.83: SP-05 rebar strain data for N6 Bars (a) west side (b) east side

D.5.5. Crack Displacement Transducers

Displacements in the plastic hinge zone of both piles are shown in Figure D.84 and Figure D.85. Largest compression strains were measured in the CDT closes to the pile cap CDT-04E and CDT-05W. Similar correlation was found in the tension side of the west pile, with maximum displacements at CDT-04W.

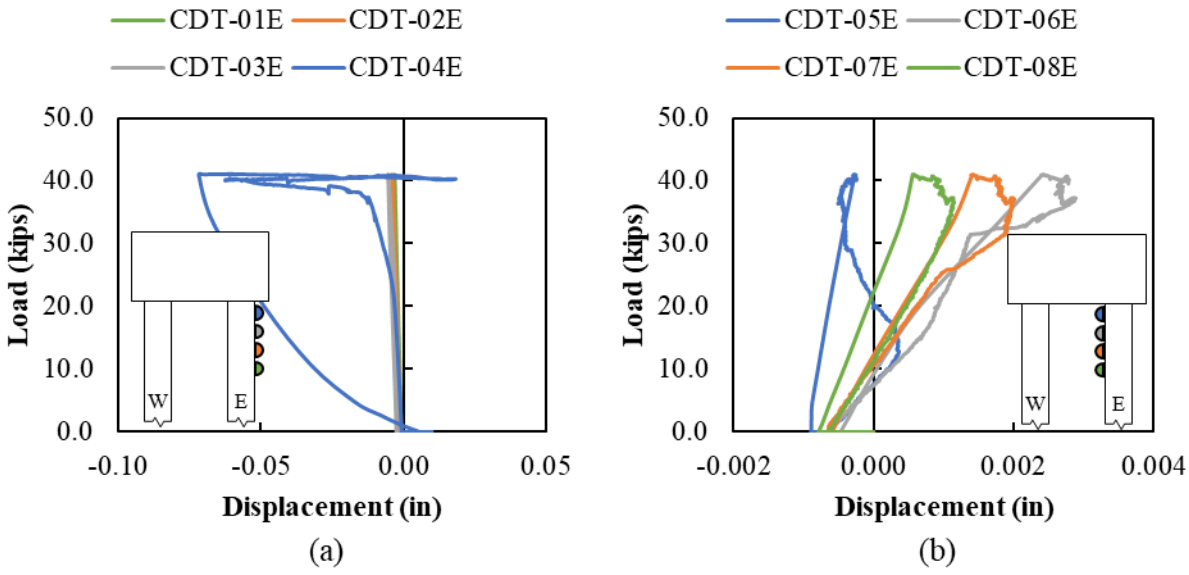

Figure D.84: SP-05 crack displacement data for east pile

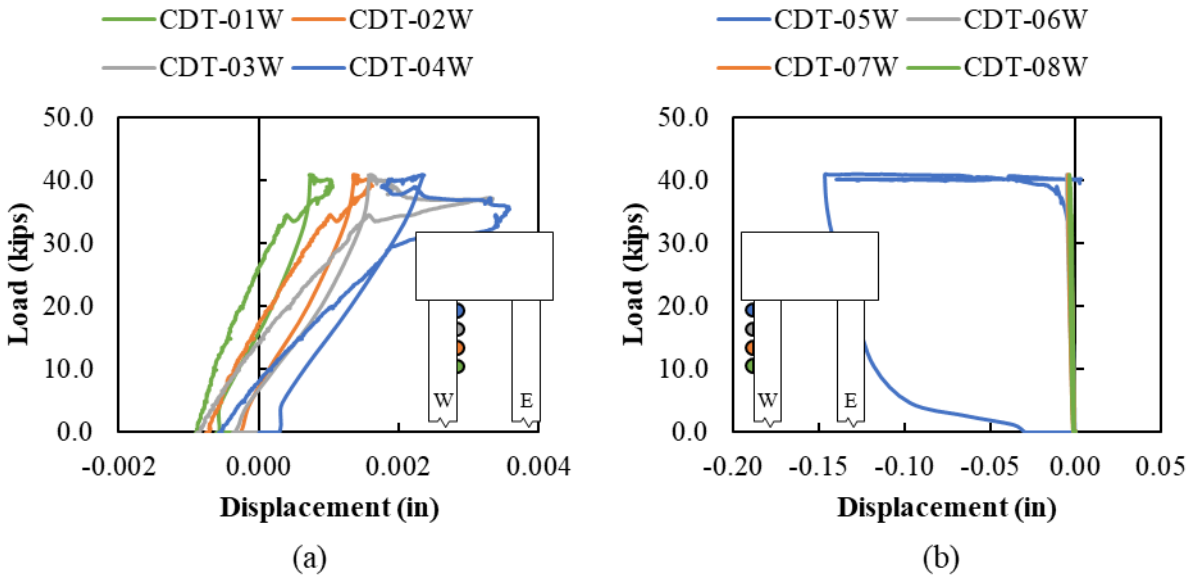

Figure D.85: SP-05 crack displacement data for West Pile

The moment-curvature response for the west and east pile are shown in Figure D.86. Higher curvature was measured in the west pile in the gauges closes to the pile-to-cap connection, same location where spalling of concrete was observed.

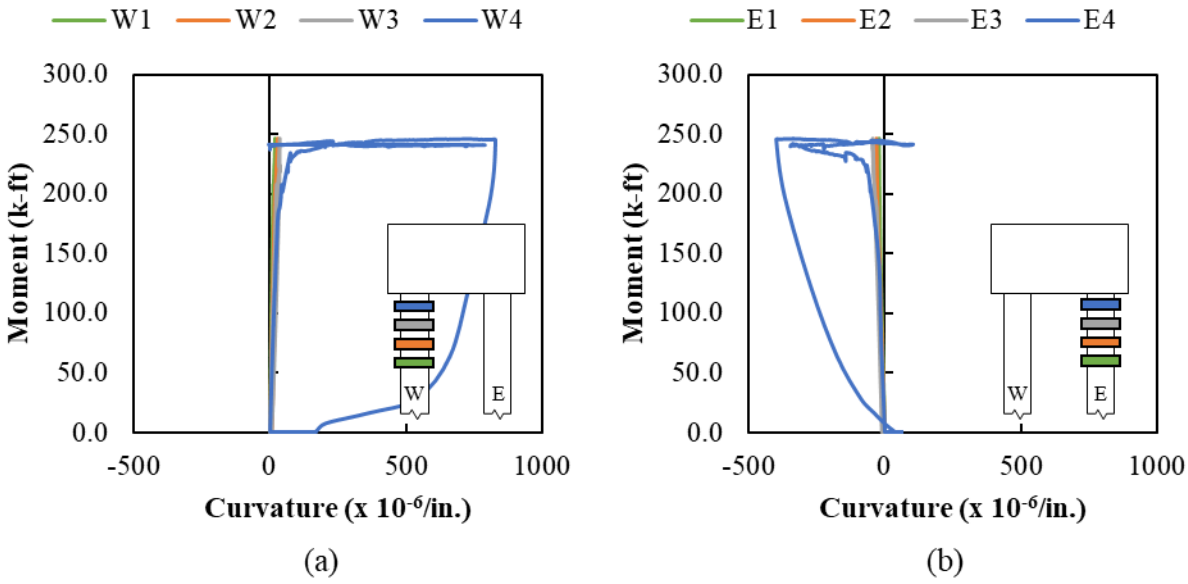

Figure D.86: SP-05 moment-curvature for (a) west pile (b) east pile

D.5.6. Vibrating Wire Gauges (Pile)

No vibrating gauge data on Specimen 5

D.5.7. Vibrating Wire Gauges (Cap)

No data was recorded.

D.5.8. Fiber Optic

D.5.8.1. Pile Tensioning

Pile tensioning data for the west pile is shown in Figure D.87.

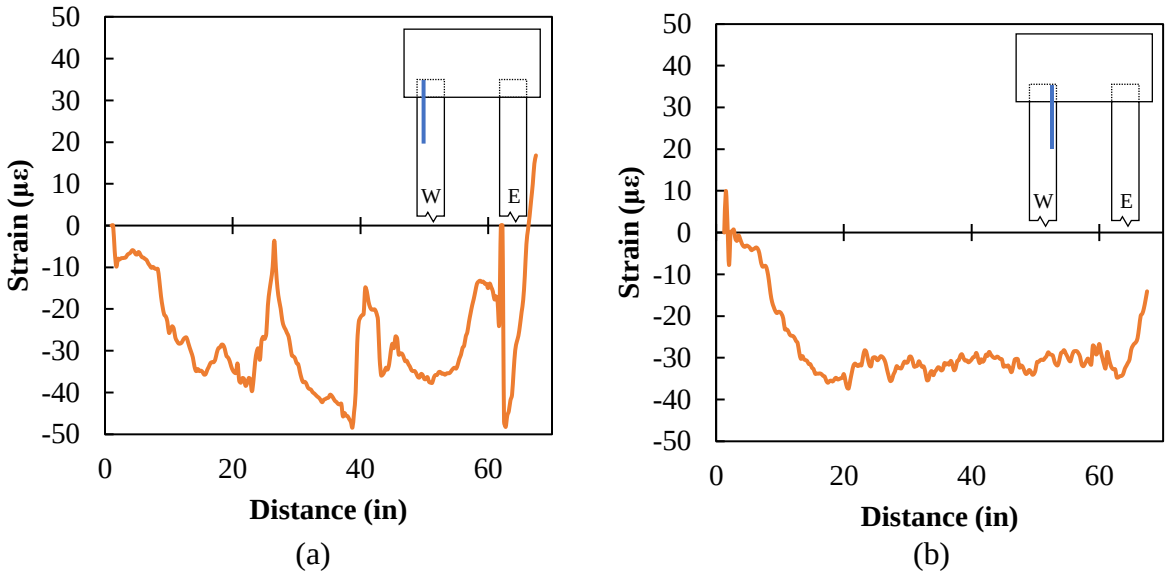

Figure D.87: SP-05 fiber optic at tensioning of the west pile

Pile tensioning data for the east pile is shown in Figure D.88.

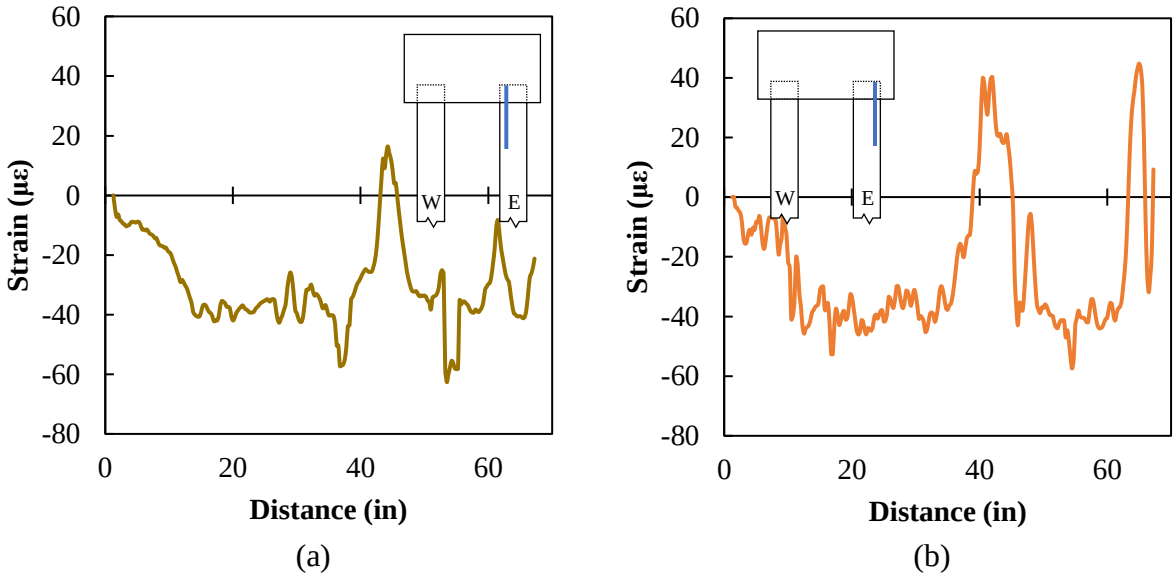

Figure D.88: SP-05 fiber optic at tensioning of east pile

D.5.8.2. Testing

Strains along the length of the FOS at different loads in the west pile are shown in Figure D.89. Compression strains developed in the exterior face of the pile, FOS-24, until around 33 kips, at

which point tensile strains started to be measured. At failure load FOS-24 recorded maximum compression strains of around 2,000 με. In the interior face of the pile, FOS-32, measured tensile strains less than 2,000 με until around 33 kips, at which point tensile strains rapidly increased until failure.

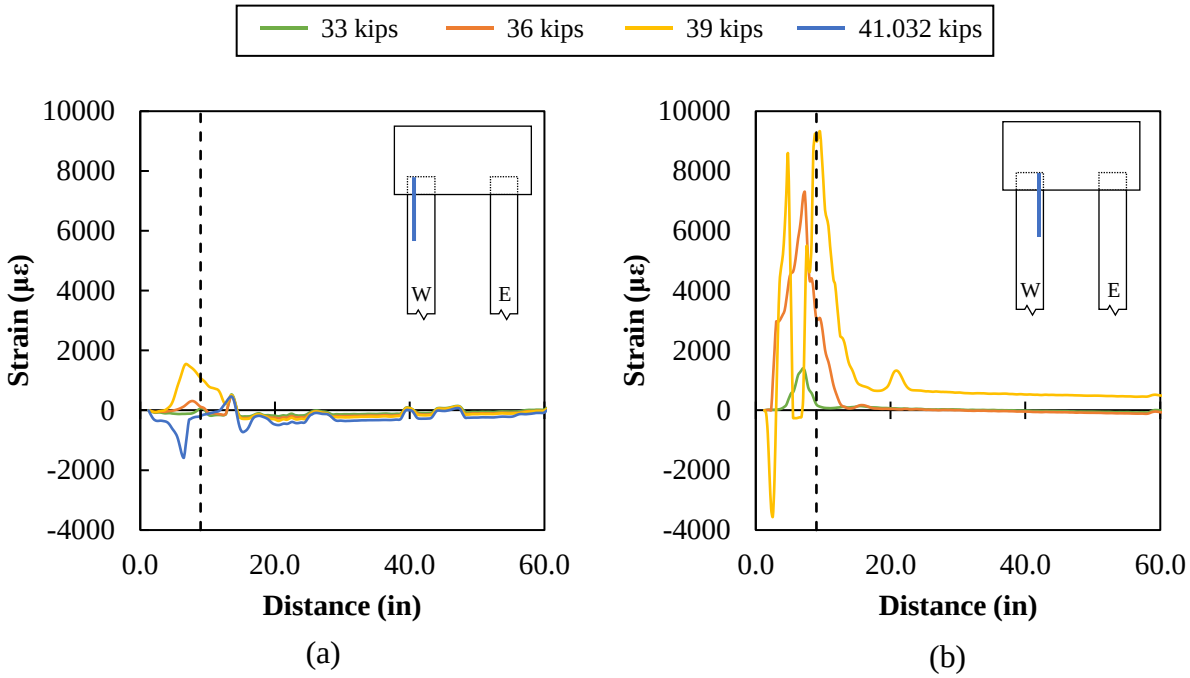

Figure D.89: SP-05 fiber optic data for west pile (a) FOS-24 (b) FOS-32

The strain profile at the critical plane (at 12-inch embedment length) for the west pile is shown in Figure D.90. Tensile strains were measured toward the top face at about 10,000 με at failure.

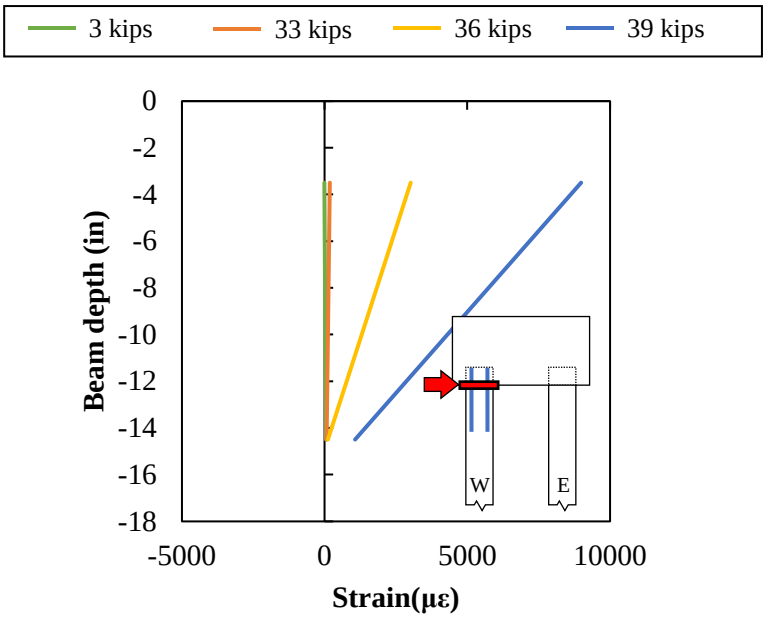

Figure D.90: SP-05 strain profile at critical section for west pile

Strains along the length of the FOS at different loads in the east pile are shown in Figure D.91. In the interior face of the east pile tension strains were developed until failure, with maximum measured strains of 7,000 με. Small compression strains less than 1,000 με were measured on the exterior face of the pile until around 30 kips, at which point tensile strains started to develop with a maximum measure of 4,000 με at failure load.

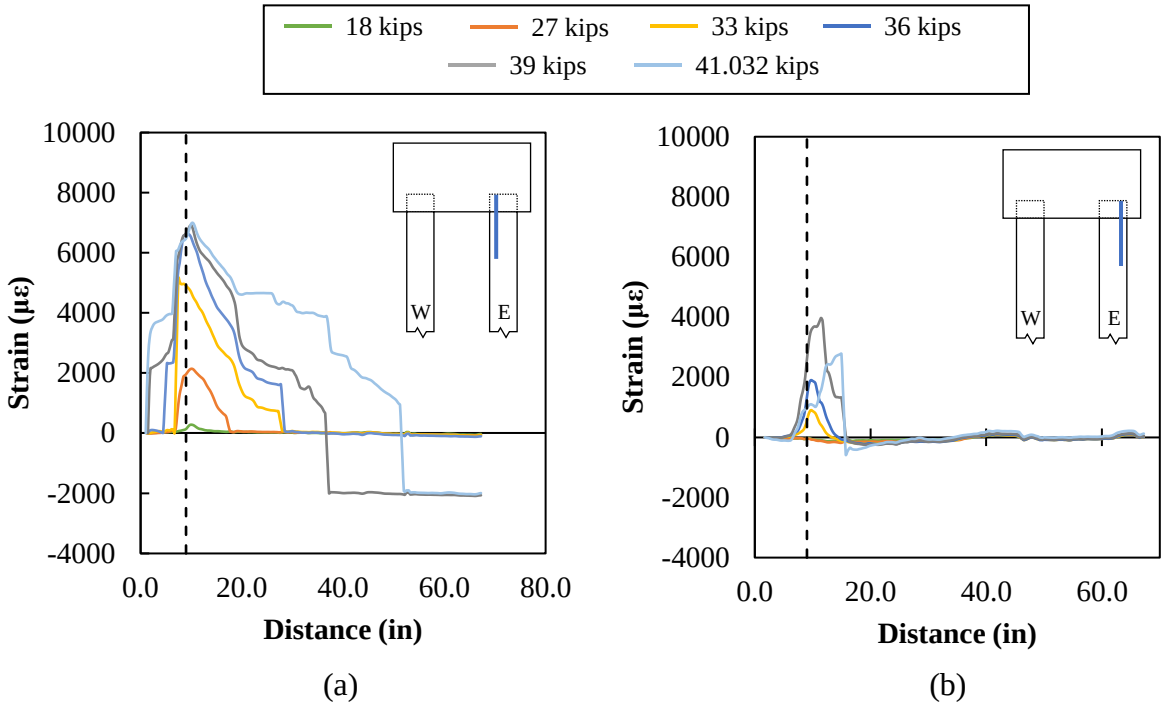

Figure D.91: SP-05 fiber optic data for east pile (a) FOS-19 (b) FOS-27

The strain profile at critical plane (12-inch embedment length) is shown in Figure D.92. Tensile strains were measured toward the bottom face at about 6,500 με at failure.

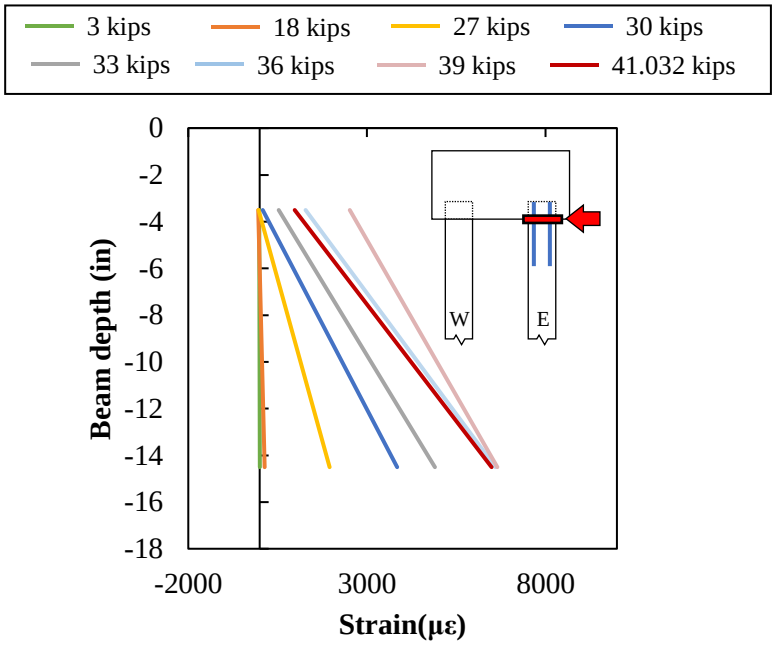

Figure D.92: SP-05 strain profile at critical section east pile

The moment-curvature response for the west and east pile are shown in Figure D.93.

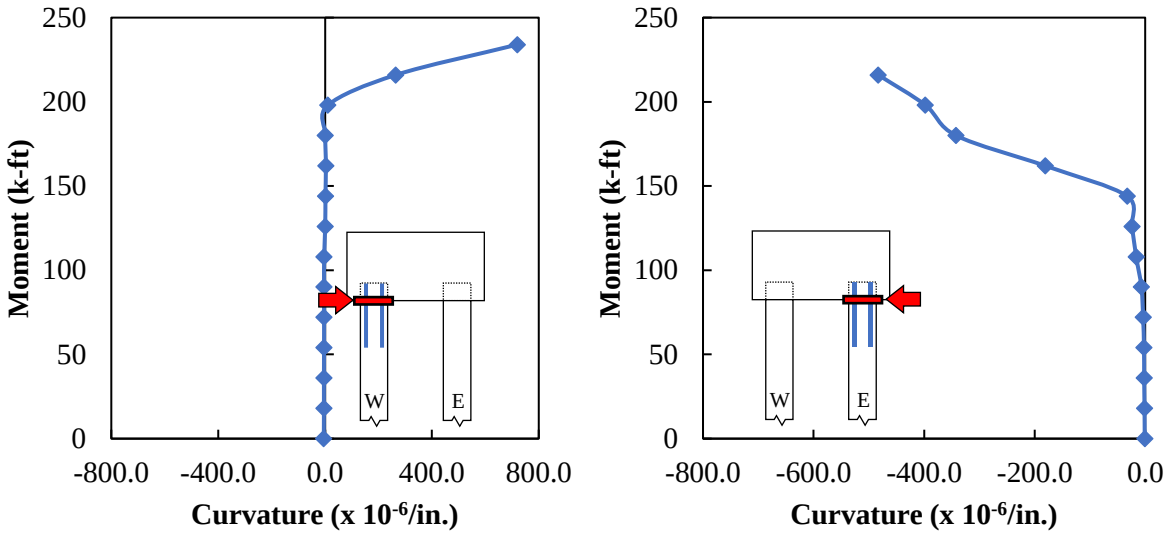

Figure D.93: SP-05 moment-curvature at critical section (a) west pile (b) east pile

D.6. SP-06

D.6.1. Observations and Summary of Results

Results of Specimen 6 are summarized in Table D.15

Table D.15: SP-06 Summary of Results

Specimen 6	
Pile Embedment	12.0 in. ($0.67d_{pile}$)
Interface Reinforcement	none
Axial Load	0 kips ($0A_g f'_{c,pile}$)
Failure load (kips)	17.7
Distance from Load to Cap (ft.)	9.0
Failure Mechanism	Strand development
Pile Failed	East
Maximum Displacement (in)	8.25
Ultimate Moment Developed (k-ft)	159.4
Percentage of capacity of pile	51.4 %

Specimen 6 had an embedment length of 12 inches, which corresponds to $0.67d_{pile.}$; no axial load was applied to the piles, and no interface reinforcement was present between the pile and cap.

Failure of this specimen occurred in the east pile. The observed failure was likely caused by strand development. A large cracked developed at the pile-to-cap interface, as shown in Figure D.94(b). No damage of the cap was observed.

(a) (b)

Figure D.94: SP-06 Failure Mechanism

D.6.2. Laser displacement transducers (LDT)

Displacements were recorded along the length of both piles, as shown in Figure D.95. The application of the lateral load in the piles for Specimen 6 was 9 ft from the pile-to-cap interface, which was the same location as LDT-1.

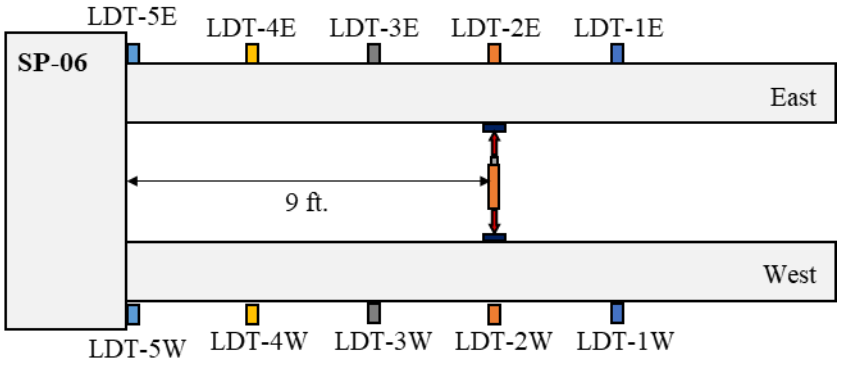

Figure D.95: Location of laser displacement transducers (LDT) and applied load for SP-06

The load-displacement curves of the west and east piles are shown in Figure D.96 (a) and (b) respectively. The maximum load reached by Specimen 6 was 17.7 kips, which corresponds to 51.4% the capacity of the 18-inch piles. The horizontal displacement in the west pile was 4.59 inches and in east pile 8.25 inches.

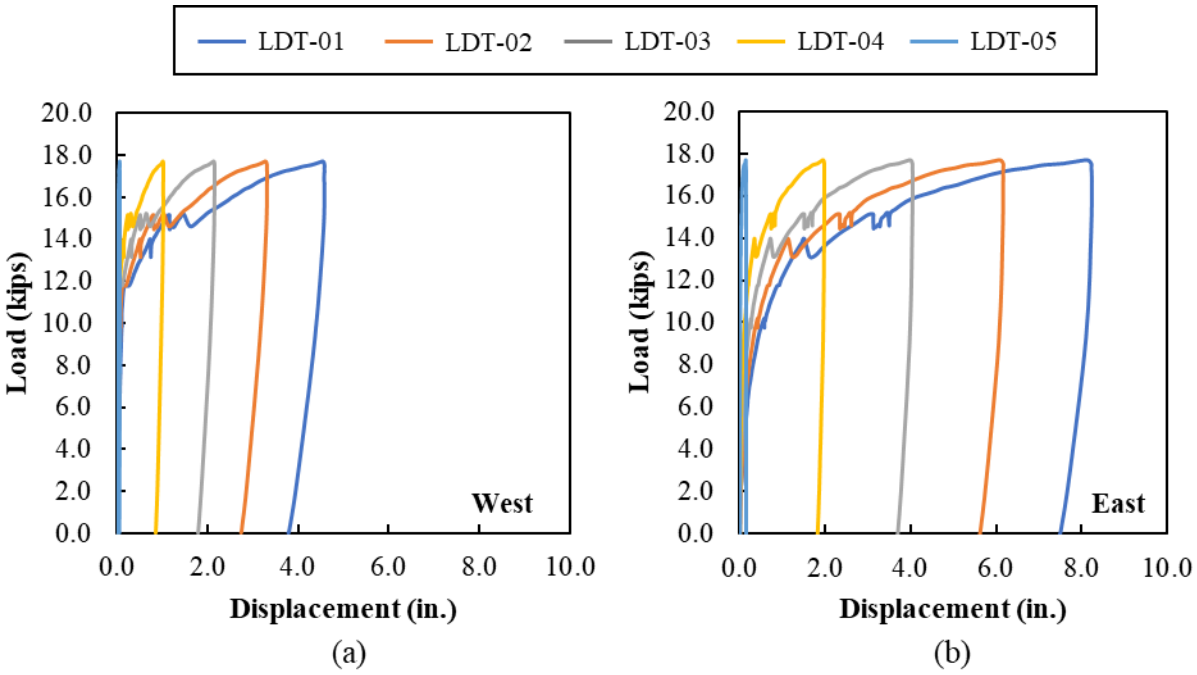

Figure D.96: SP-06 Load-Displacement Curve (a) West pile (b) East pile

D.6.3. Concrete Strain Gauges

Vertical and horizontal concrete strains around the west pile are shown in Figure D.97. CSG-01 to CSG-07 all remained less than the cracking strain for concrete. CSG-01 to CSG-03, which are perpendicular to the load application, measured compression strains less than 50 με .

CSG-04 and CSG-05 started with small tensile strains until around 12 kips, at which point tensile strains decreased and compression strains began to be measured, until maximum compression strains of 46 με for CSG-04, 60 με for CSG-05, at failure load.

CSG-06 and CSG-07, located on top and bottom of the west pile, measured tension strains less than 50 με.

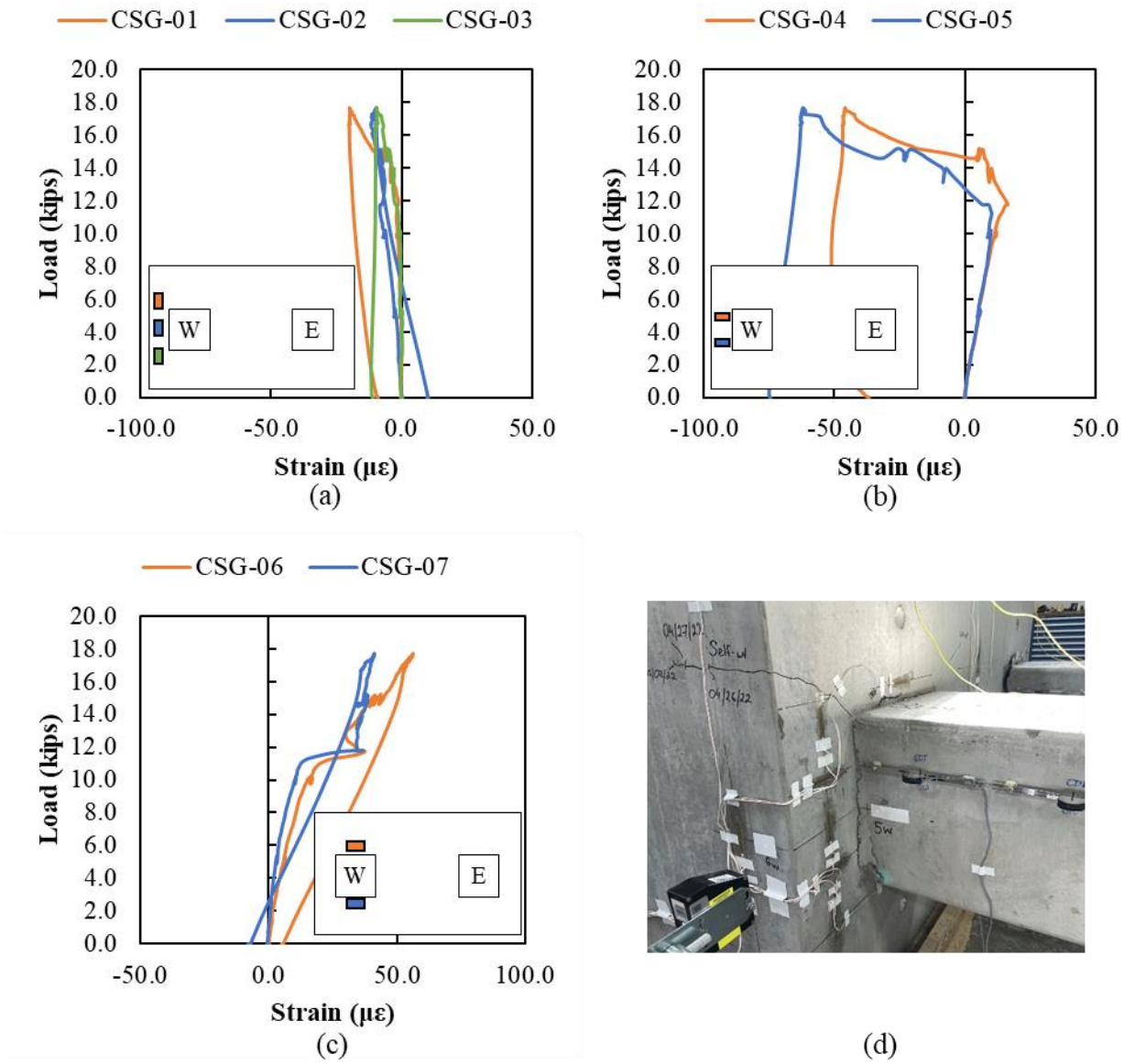

Figure D.97: SP-06 Concrete Strain Gauges Data for CSG-01 to CSG-07

Vertical and horizontal concrete strains in the middle of the pile cap between the piles are shown in Figure D.98. CSG-08 measured compression strains less than 5 με. CSG-09 and CSG-10, measured tension strains less than 25 με. CSG-11 developed tensile strains less than 40 με. CSG-12 started with tension strains until approximately 23 με and 14 kips, at which point tensile strains decreased and compression strains began to be measured.

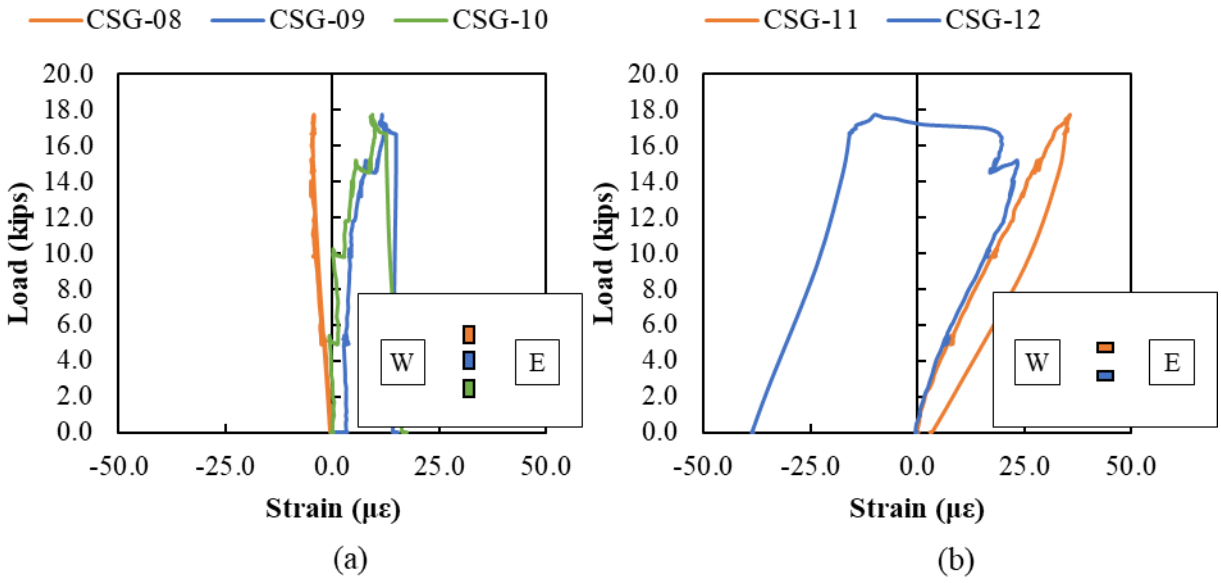

Figure D.98: SP-06 Concrete Strain Gauges Data for CSG-08 to CSG-12

Vertical and horizontal concrete strains around the east pile are shown in Figure D.99. The response of these CSGs was generally similar to the CSGs around the west pile.

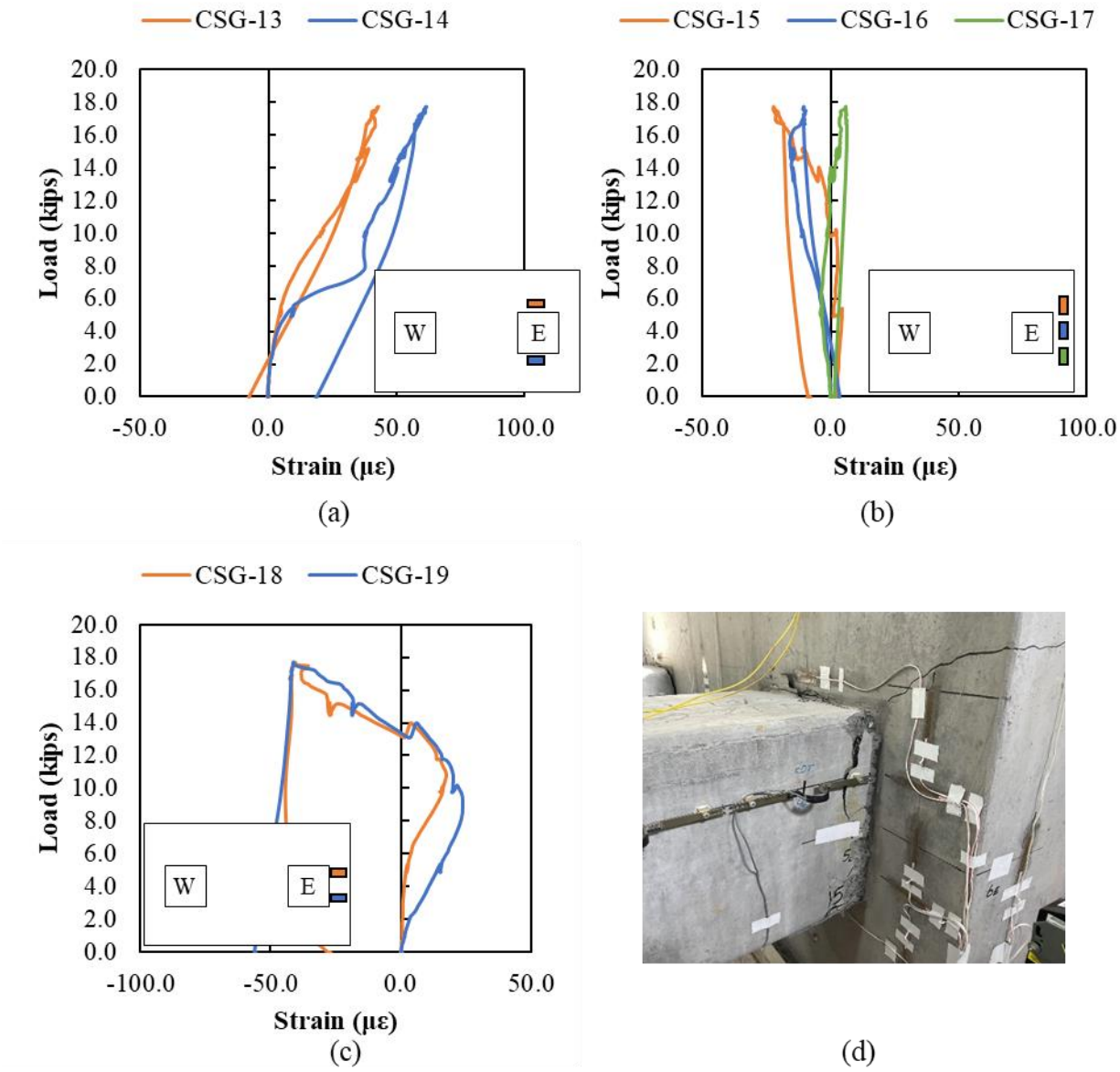

Figure D.99: SP-06 Concrete Strain Gauges Data for CSG-13 to CSG-19

Concrete strains on the west and east faces of the pile cap are shown in Figure D.100. Similar behavior was observed on both faces of the pile cap, with maximum tension strains in CSG-21 and CSG-24 of 52 με and 37 με, respectively.

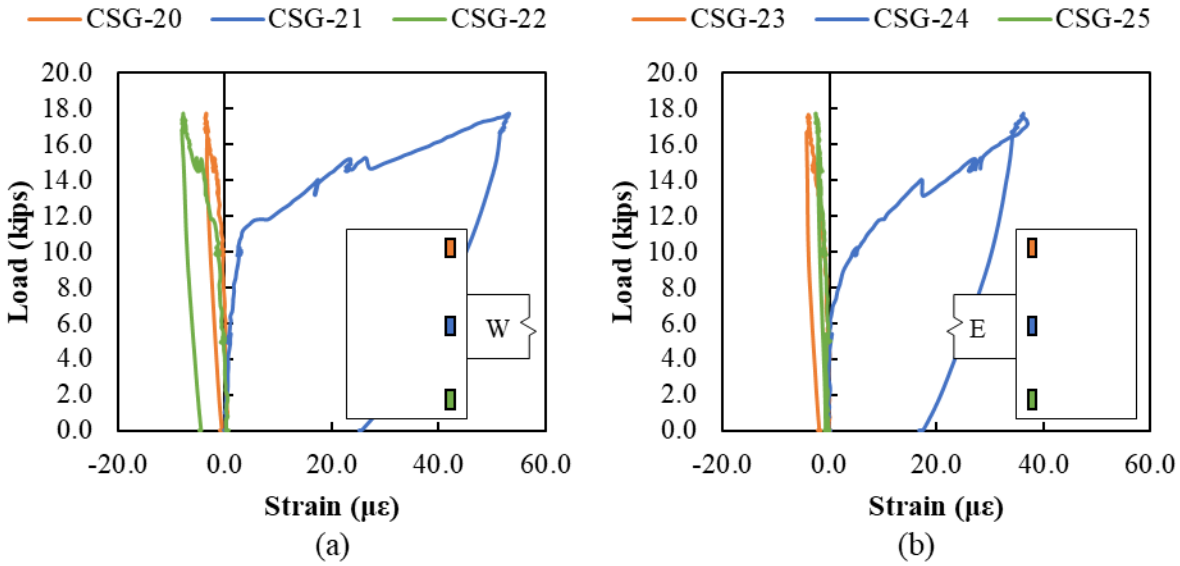

Figure D.100: SP-06 Concrete Strain Gauges Data for CSG-20 to CSG-25 (a) west side (b) east side

D.6.4. Rebar Strain Gauges

Rebar strains in the N5 bars are shown in Figure D.101. Strains less than 20 με were measured in the bars. RSG-08 located outside the east pile had maximum compression strains of 9.5 με.

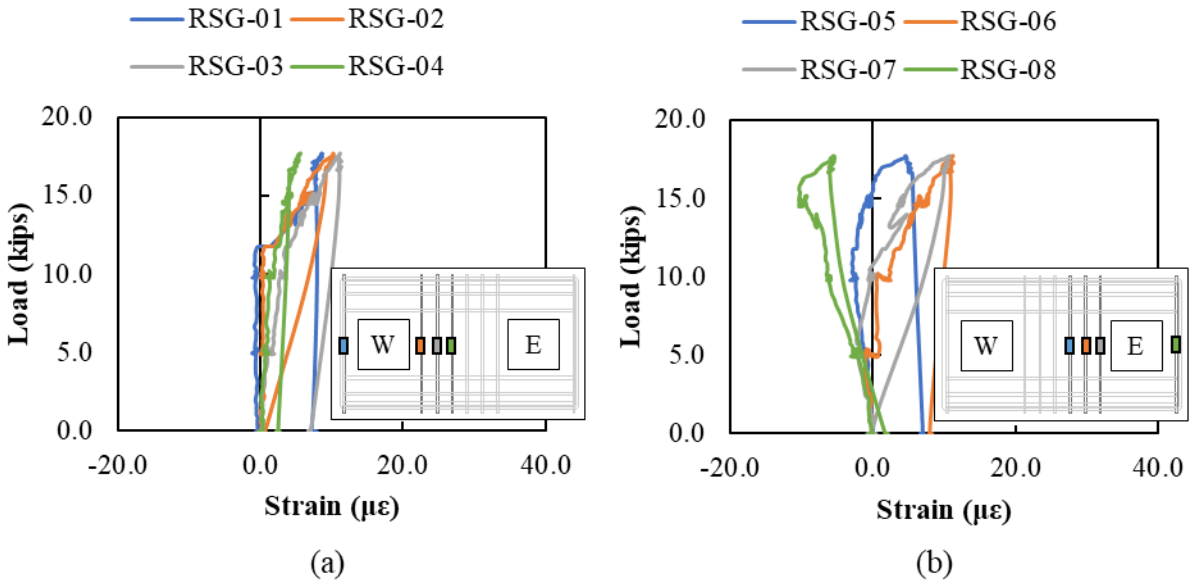

Figure D.101: SP-06 Rebar Strain Gauges Data for N5 Bars

Rebar strains in the N9 bars are shown in Figure D.102. Maximum strains were found in RSG-15 located below the embedded west pile, with maximum strains of 65 με No data was recorded for gauges RSG-19 and RSG-20, due to malfunctioning.

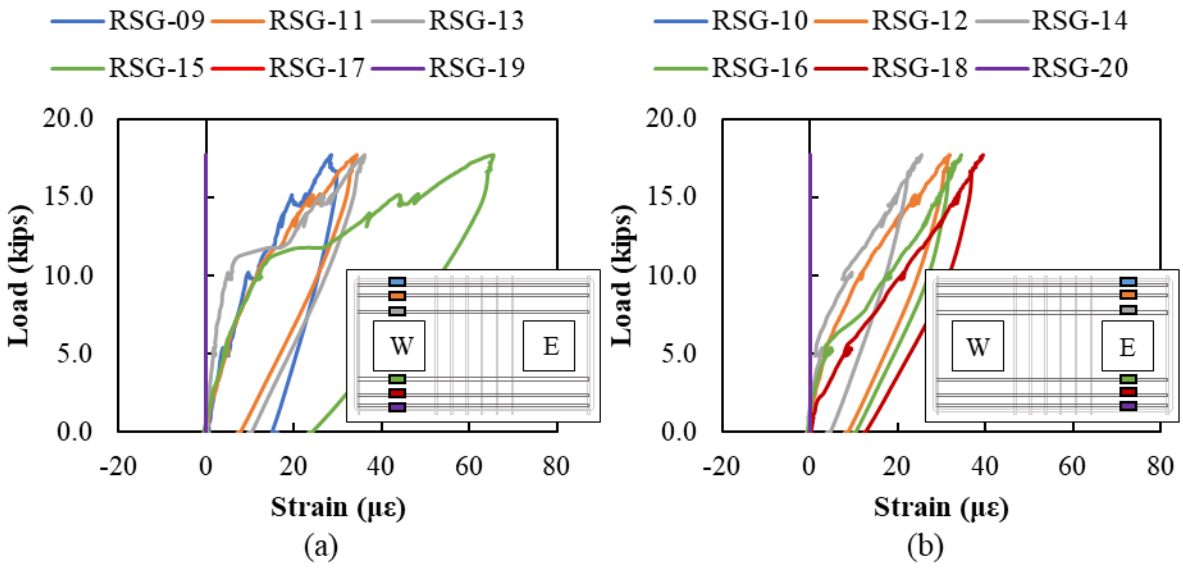

Figure D.102: SP-06 Rebar Strain Gauges Data for N9 Bars

Rebar strains in the N6 bars are shown in Figure D.103. Measured strains remained less than 25 με with the highest measured strains in RSG-25 located on the outside of the west pile.

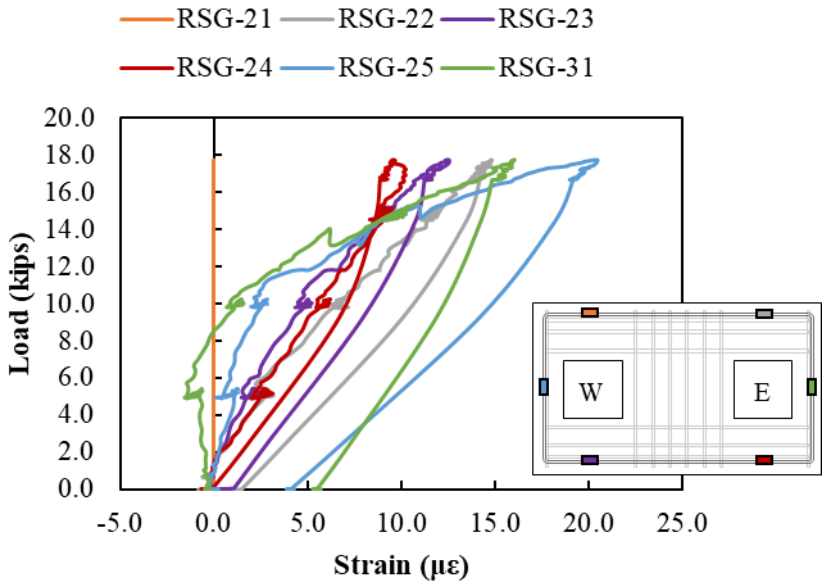

Figure D.103: SP-06 Rebar Strain Gauges Data for N6 Bars

Rebar strains in N6 bars on the side of the pile cap are shown in Figure D.104. Higher strains were measured on the west side of the pile cap. Measured strains increased as bars were closer to the face of the pile cap with the embedded pile. Maximum strain was measured in RSG-25 at about 20 με.

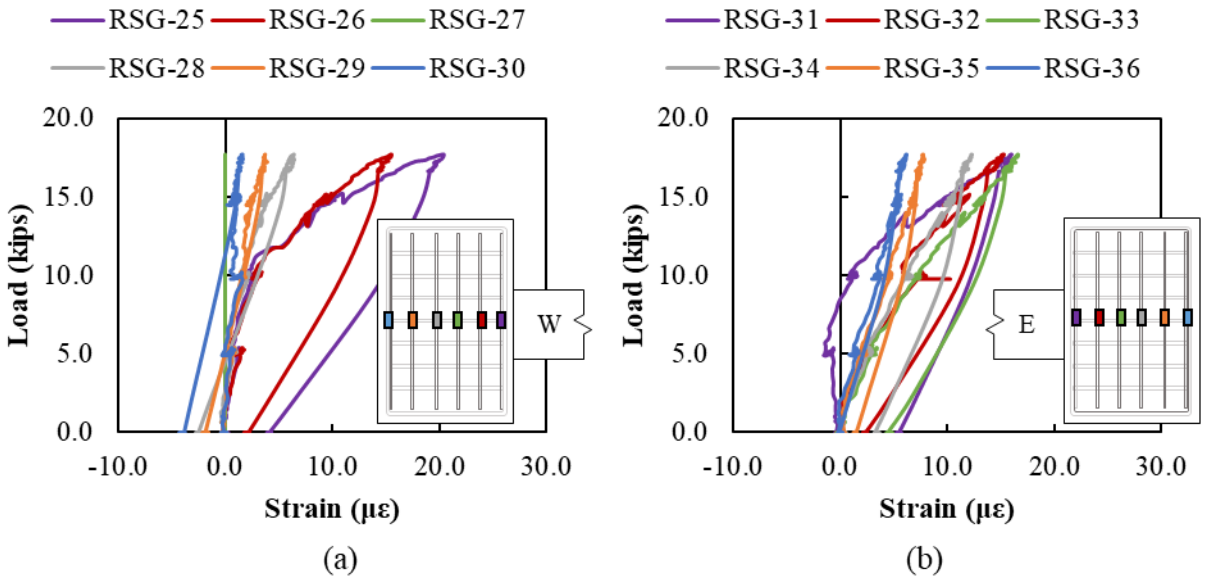

Figure D.104: SP-06 Rebar Strain Gauges Data for N6 Bars (a) west side (b) east side

D.6.5. Crack Displacement Transducers

Displacements in the plastic hinge zone in the east and west pile are shown in Figure D.105 and Figure D.106, respectively. Maximum compression strains were measured in the CDT closest to the pile cap CDT-04E and CDT-05W. No correlation between strains and gauge distance from the pile cap on the tension face was observed.

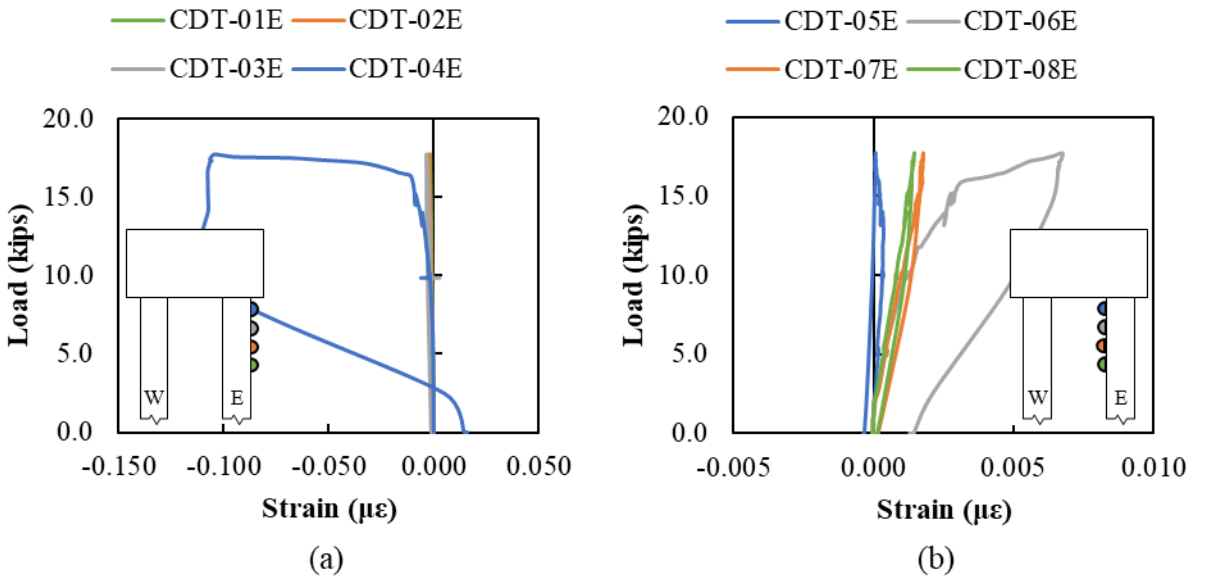

Figure D.105: SP-06 crack displacement data for east pile

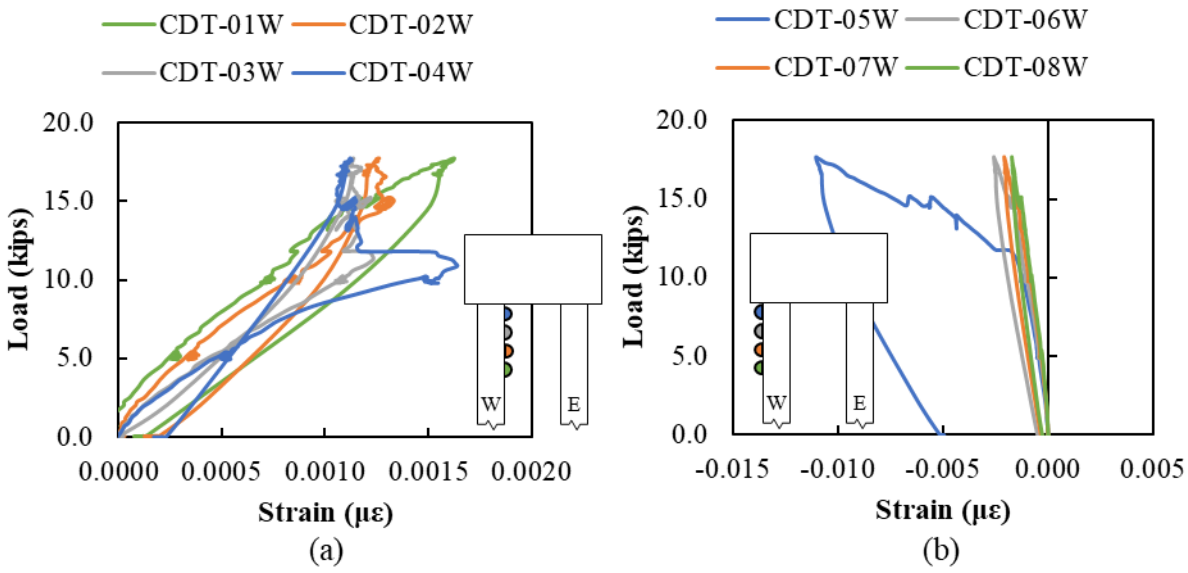

Figure D.106: SP-06 crack displacement data for west pile

Moment-curvature response found using the CDTs for the west and east pile are shown in Figure D.107. Higher curvature was found on the west pile on the gauges closest to the pile-to-cap connection.

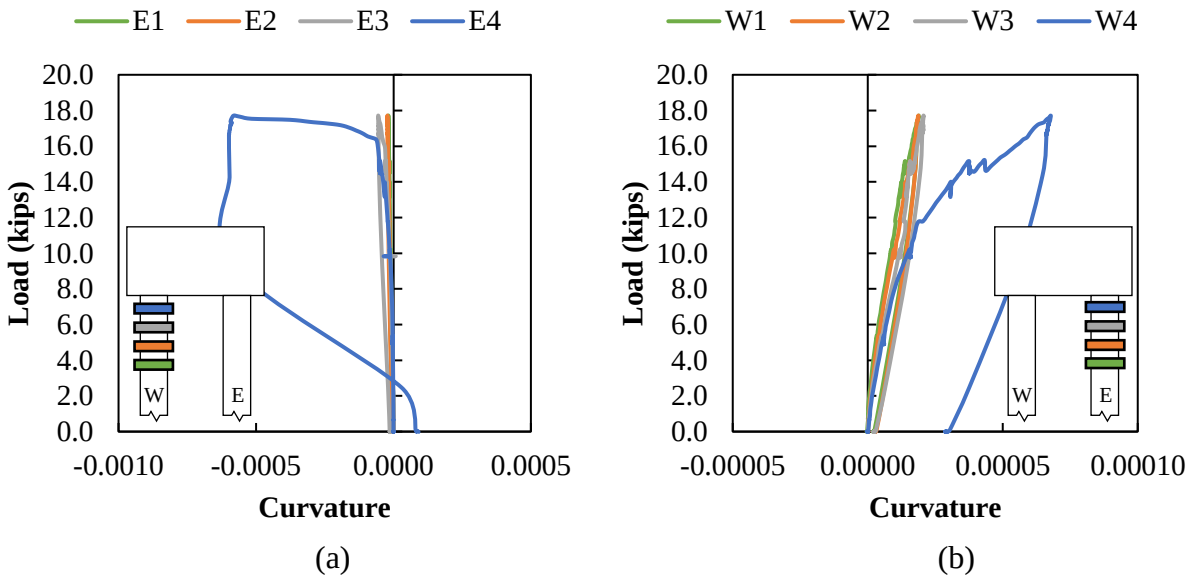

Figure D.107: SP-06 moment-curvature response (a) west pile (b) east pile

D.6.6. Vibrating Wire Gauges (Pile)

Vibrating wire data was recorded at different stages of the specimen. The initial data was used to calculate the elastic shortening losses, and total losses of each specimen.

Readings from the longitudinal vibrating gages were recorded and used to find the stress in the strands after release (assuming E_p = 28,500 ksi):

Table D.16: SP-06 Elastic shortening losses calculation

VWG	Before release (με)	After release (με)	Strain Change (με)	ES Losses (ksi)
VWSG-P6-1E	0	-323.066	323.1	9.21
VWSG-P6-2E	0	-328.022	328.0	9.35
			Δf_{pES} =	9.28

Therefore, the average stress in strands after elastic shortening losses:

Stress after elastic shortening losses: $$f_{pi} - \Delta f_{pES} = 203.6\ ksi - 9.28\ ksi = 194.32\ ksi$$

Readings from the longitudinal vibrating gages were recorded and used to find the stress in the strands before testing (assuming E_p = 28,500 ksi):

Table D.17: SP-06 Total losses calculation

VWG	After casting (με)	Before testing (με)	Strain Change (με)	LT Losses (ksi)
VWSG-P6-1E	-323.066	-822.1	499.0	14.22
VWSG-P6-2E	-328.022	-836.9	508.9	14.50
			Δf_{pLT} =	14.36

The average stress in strands after all losses:

Stress after all losses immediately before testing: $$f_{pi} - \Delta f_{pES} - \Delta f_{pLT} = 203.6\ ksi - 9.28\ ksi - 14.36\ ksi = 179.9\ ksi$$

D.6.7. Vibrating Wire Gauges (Cap)

Vibrating wire gauge data was also recorded in the pile cap around the embedded east pile. Readings at different times are shown in Table D.4. Temperature can affect the strain gauges readings; therefore, a temperature correction was applied to the actual readings, taking as reference the before cap casting readings.

Table D.18: SP-06 vibrating wire gauge data in the pile cap

VWG	Before cap casting (με)	Before testing (με)	After Testing (με)
VWSG-4E	0	-39.440	-31.550
VWSG-5E	0	-86.537	-113.165
VWSG-6E	0	-66.553	-54.765

VWG	Before cap casting (με)	Before testing (με)	After Testing (με)
VWSG-7E	0	-76.901	-91.738

D.6.8. Fiber Optic

Strains along the length of the FOS at different loads are shown in Figure D.108. Data was only measured in the east pile (FOS-18 and FOS-26) for Specimen 6. FOS in the west pile were not functioning during test.

Tension strains developed in the interior face of the east pile, with maximum readings at failure of the fiber at around 13 kips. This corresponds to the crack that developed at the pile-to-cap interface at this same location. High tension strains also developed at the exterior face of the pile starting at around 12 kips until failure of the specimen.

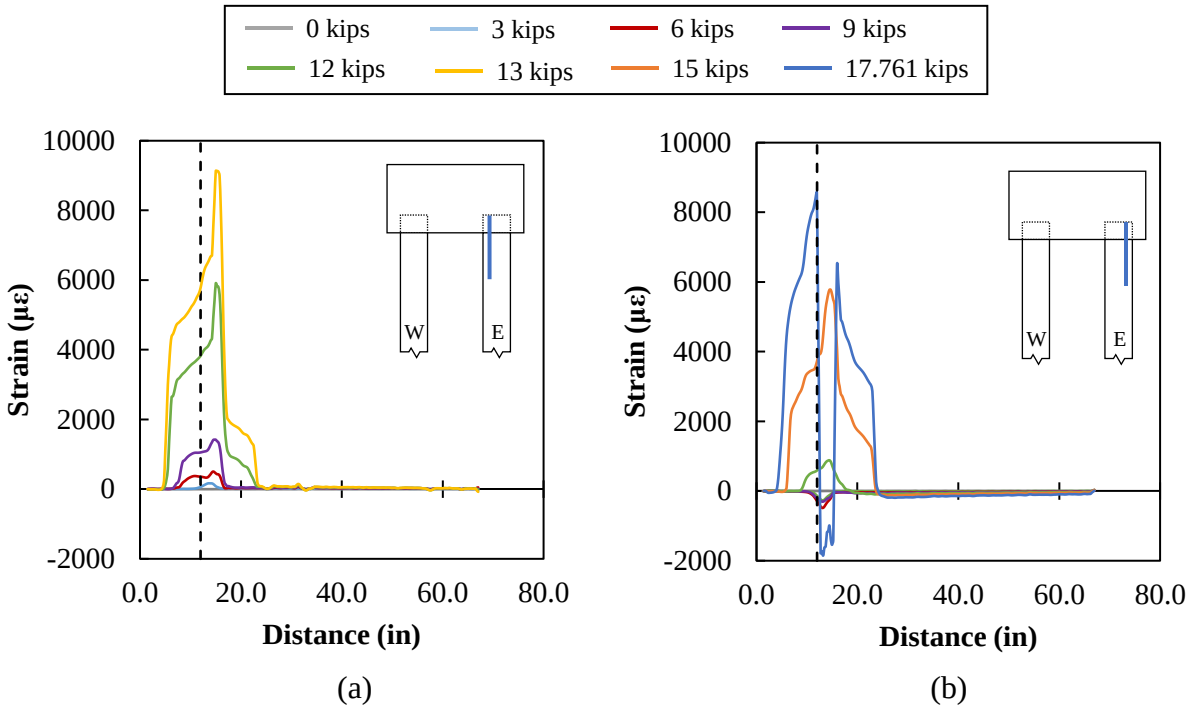

Figure D.108: SP-06 fiber optic data for east pile (a) FOS-18 (B) FOS-26

The strain profile at critical plane (12-inches embedment length) is shown in Figure D.109. Tension strains developed at the bottom face at about 10,000 με at failure of the fiber.

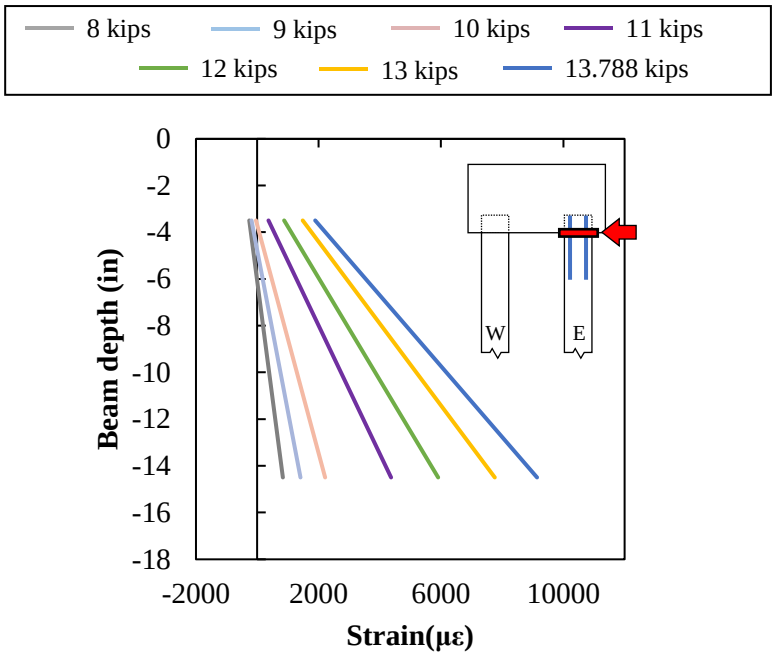

Figure D.109: SP-06 Strain Profile at East Pile at Critical section

The moment curvature response at the critical plane for Specimen 6 using the FOS data is shown in Figure D.110.

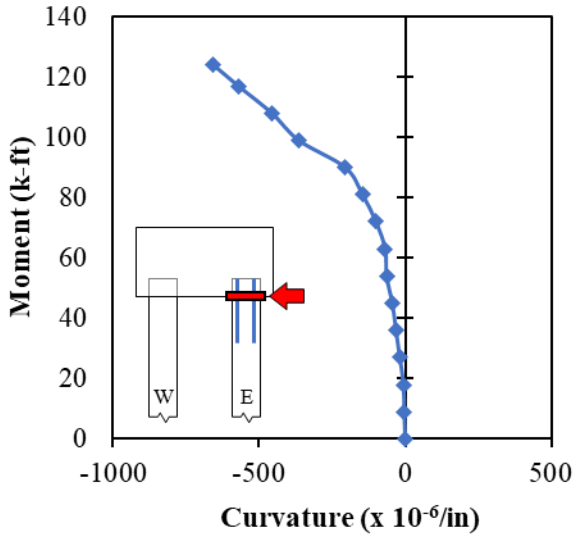

Figure D.110: SP-06 Moment-curvature

D.7. SP-07

D.7.1. Observations and Summary of Results

Results of Specimen 7 are summarized in Table D.19.

Table D.19: SP-03 Summary of Results

Specimen 7	
Pile Embedment	18.0 in. ($1.0d_{pile}$)
Interface Reinforcement	none
Axial Load	0 kips ($0A_g f'_{c,pile}$)
Failure load (kips)	33.6
Distance from Load to Cap (ft.)	6.0
Failure Mechanism	Strand development
Pile Failed	West
Maximum Displacement (in)	12.87
Ultimate Moment Developed (k-ft)	201.4
Percentage of capacity of pile	65 %

Specimen 7 has an embedment length of 18 inches, which corresponds to 1.0 d_{pile}*;* no axial load was applied to the piles, and no interface reinforcement was present between the pile and cap.

Failure of Specimen 7 occurred in the west pile. A large spalled concrete region was observed on top of the west pile, shown in Figure D.111 (a). A large crack was also observed in the pile-to-cap interface on the west pile, which suggests that there was a strand development failure.

(a) (b)

Figure D.111: SP-07 Failure mechanism (a) cap crushing (b) pile-to-cap interface

D.7.2. Laser displacement transducers (LDT)

Displacements were recorded along the length of both piles. The application of lateral load in the piles for Specimen 7 was at 6 ft from the pile-to-cap interface, which was the same location as LDT-3, as shown in Figure D.112

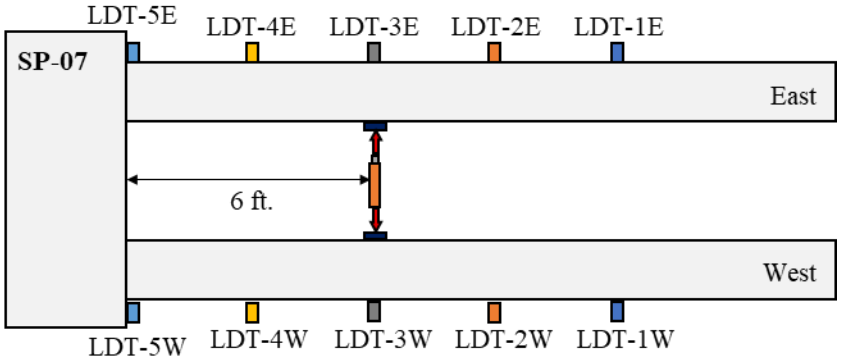

Figure D.112: Location of laser displacement transducers (LDT) and applied load for SP-07

The load-displacement curves of the west and east piles are shown in Figure D.113 (a) and (b), respectively. The maximum load reached by Specimen 7 was 33.56 kips, which corresponds to 65% the capacity of the 18-inch piles. The horizontal displacement in the west pile was 12.87 inches and in east pile 5.85 inches. The load-displacement curve was nearly horizontal at the time the hydraulic jack ran out of stroke and the load was removed.

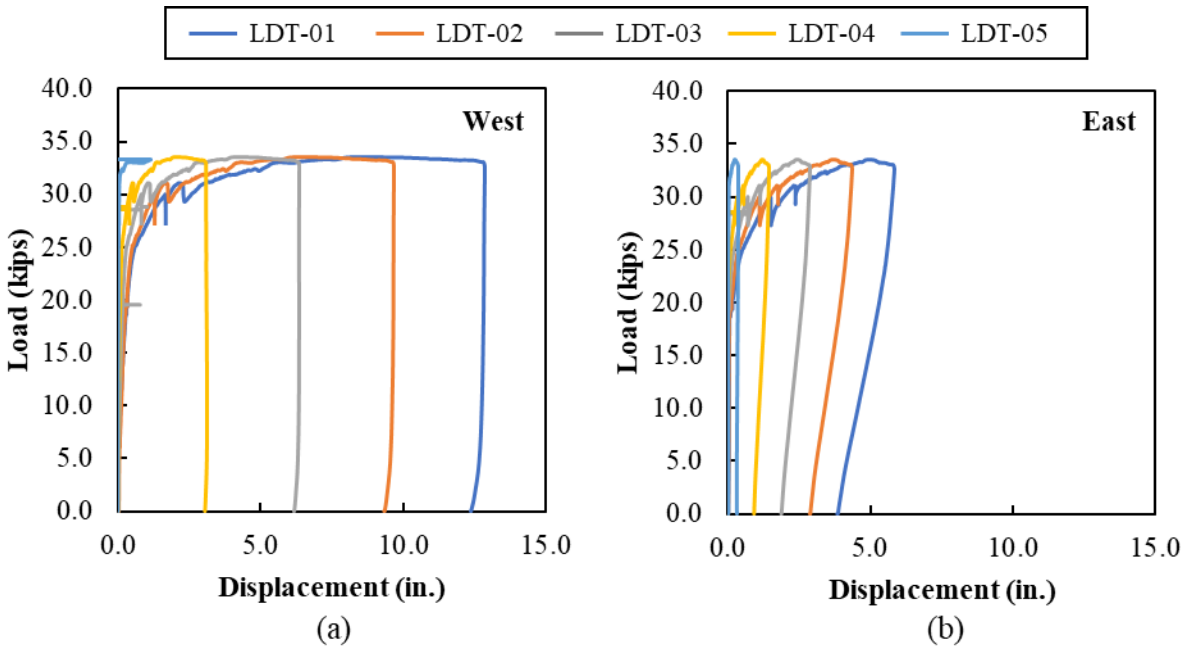

Figure D.113: SP-07 Load-displacement curve (a) West pile (b) east pile

D.7.3. Concrete Strain Gauges

Vertical and horizontal concrete strains around the west pile are shown in Figure D.114. High tension strains developed in CSG-01 of around 2,000 με until failure of the specimen at 33 kips. CSG-02 recorded maximum tensile strains of 900 με, and CSG-03 small compression strains.

CSG-04 and CSG-05 started with small tensile strains until 9 με and 18 kips, at which point compression strains started to be developed until failure of specimen.

CSG-06 measured maximum tensile strains at 752 με and 25.5 kips. CSG-07 located on top of the embedded pile developed high tension strains until failure.

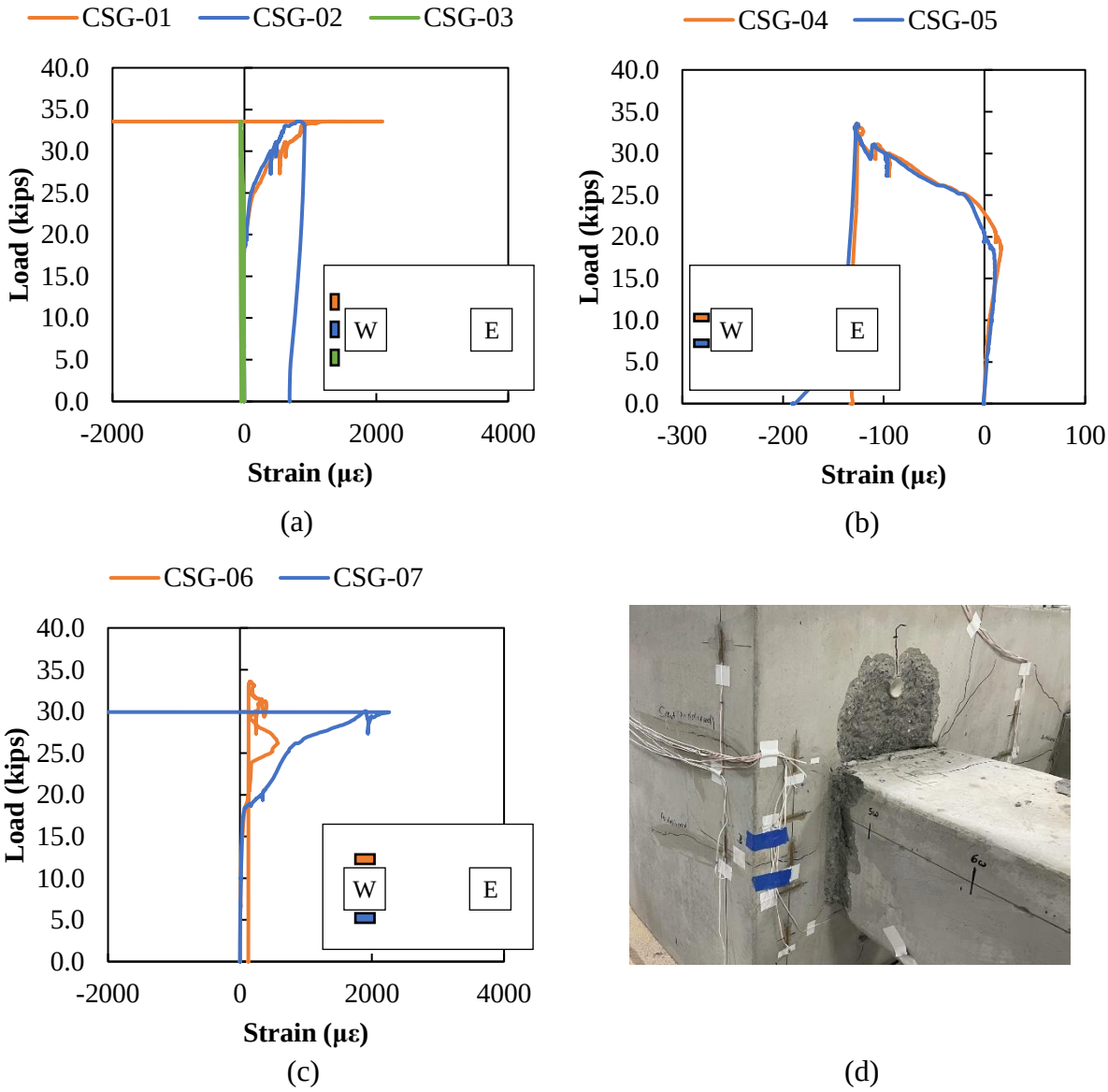

Figure D.114: SP-07 Concrete Strain Data for CSG-01 to CSG-07

Vertical and horizontal concrete strains in the middle of the pile cap between the piles are shown in Figure D.115. Measured strains were minor in both directions. CSG-08 and CSG-10 developed tension strains less than 20 με. CSG-09 recorded maximum tensile strain of 65 με at failure.

CSG-11 and CSG-12 measured compression strains less than 40 με.

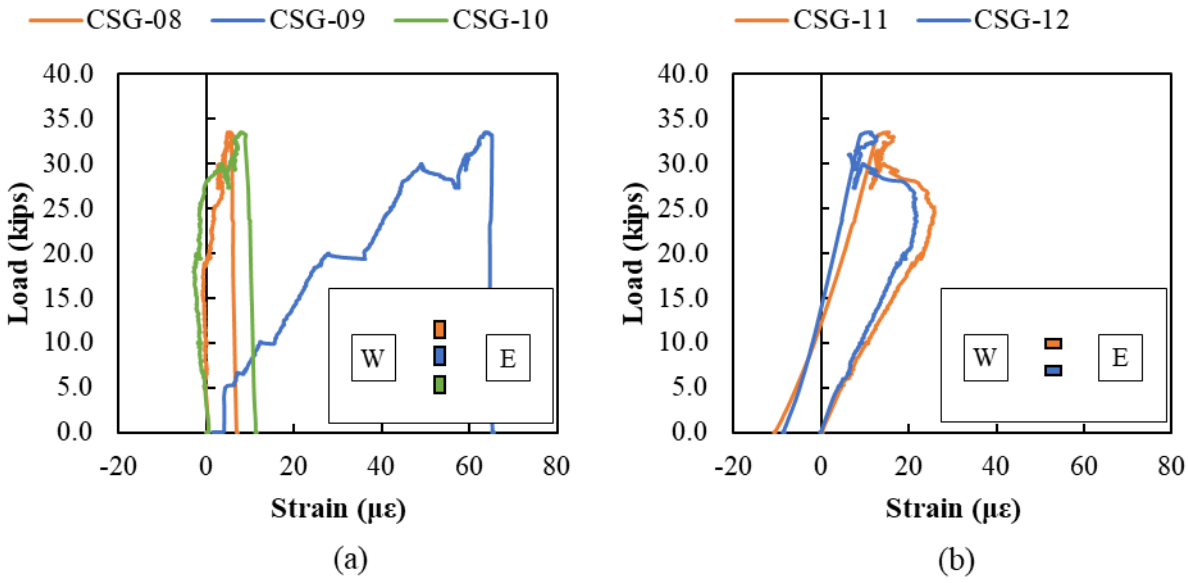

Figure D.115: SP-07 Concrete strain data for CSG-08 to CSG-12

Vertical and horizontal strains around the east pile are shown in Figure D.116. CSG-14, located below the embedded pile, measured tensile strains of 720 με at the maximum applied load.

CSG-15, which is perpendicular to load application, measured maximum tensile strains of 630 με at failure load. CSG-16 and CSG-17 measured small compression strains less than 200 με.

CSG-18 and CSG-19, which are parallel to load application and located outside the embedded pile, measured compression strains less than 200 με.

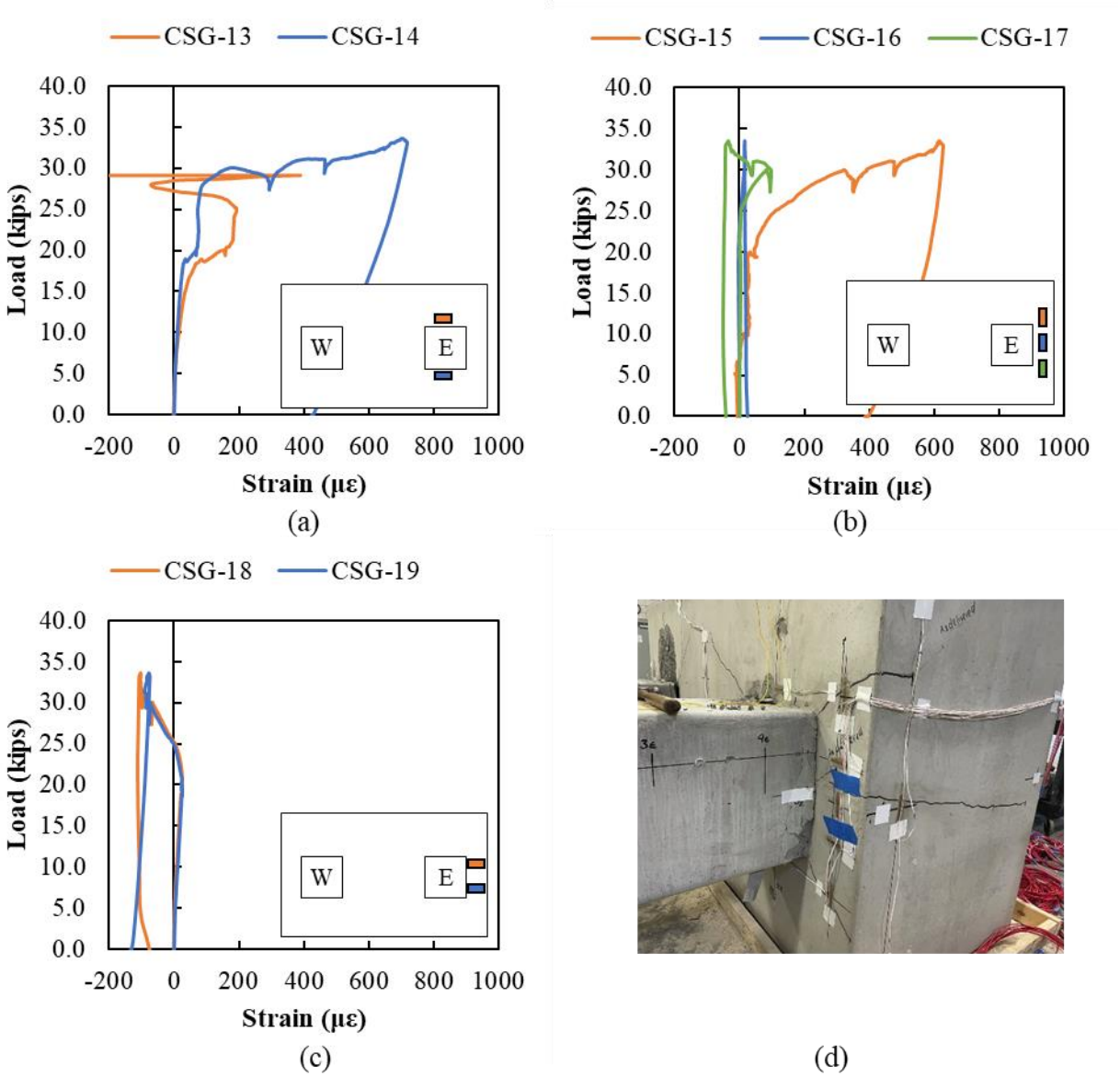

Figure D.116: SP-07 Concrete Strain Data for CSG-13 to CSG-19

Concrete strains on the west and east faces of the pile cap are shown in Figure D.117. Measured strains were higher on the west face of the pile cap, which corresponds to the failed pile. CSG-21 located at the same high than the embedded pile failed at the maximum applied load. Maximum strains in the east face of the pile cap were found in CSG-24.

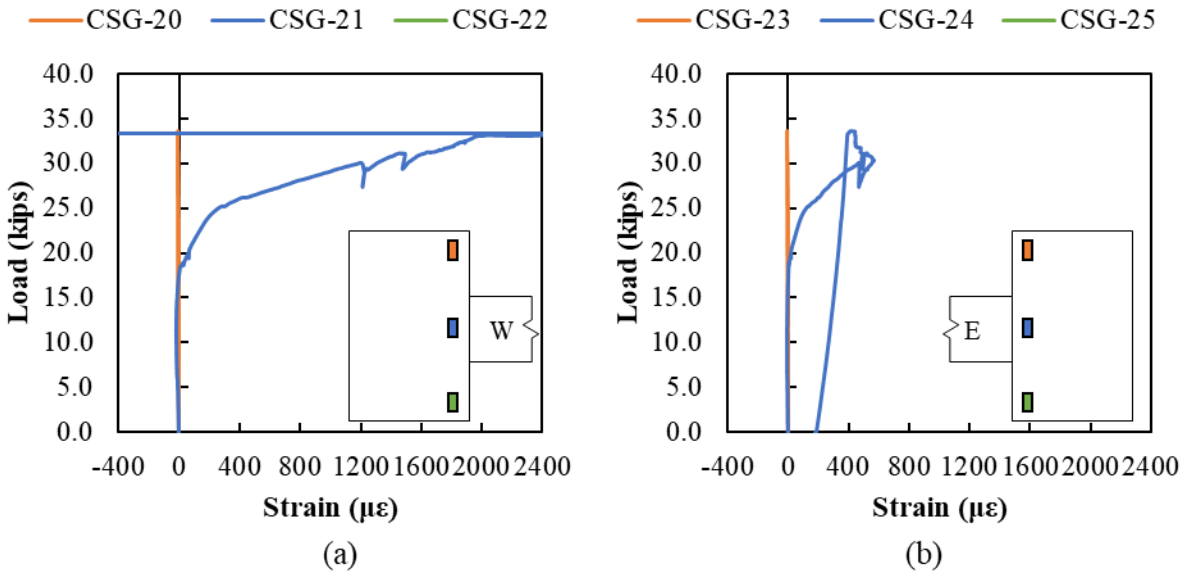

Figure D.117: SP-07 Concrete Strain Data for CSG-20 to CSG-25

D.7.4. Rebar Strain Gauges

Rebar strains in the N5 bars are shown in Figure D.118. Rebar gauges RSG-01, RSG-03, and RSG-4 were found bad during testing. RSG-02 measured strains less than 25 με. Around the east pile, RSG-08 recorded maximum strains of 75 με, which is located outside the embedded pile.

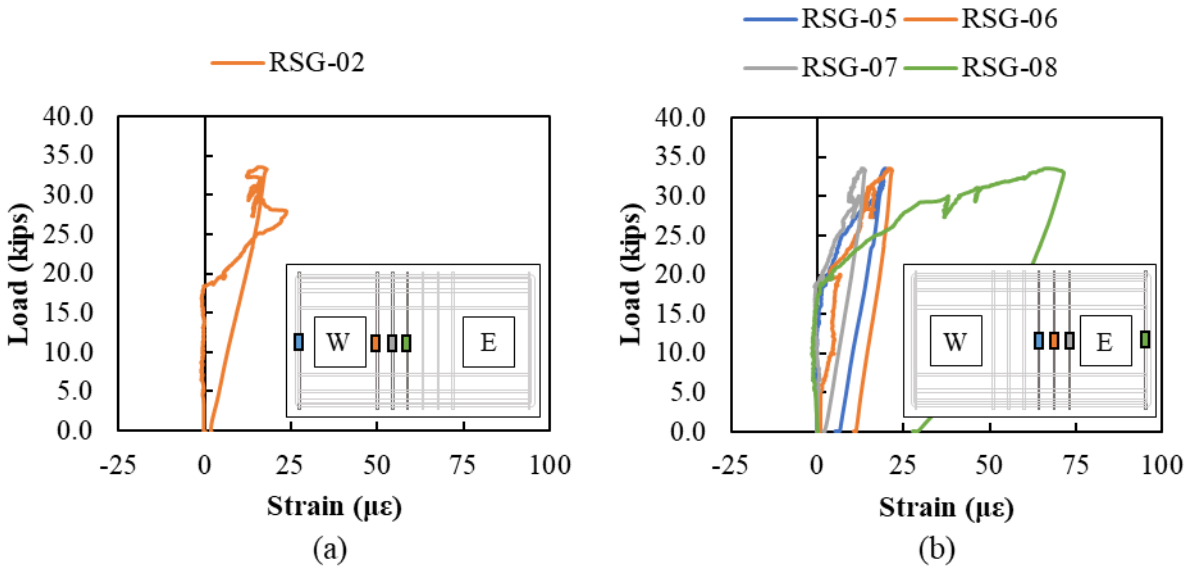

Figure D.118: SP-07 Rebar Strain Data for gauges in N5 bars

Rebar strains in the N9 bars are shown in Figure D.119. Rebar gauges RSG-10, RSG-13, RSG-14, RSG-15, RSG-17, and RSG-19 were found bad during testing. Maximum measured strains remained less than 150 με tension for all gauges above and below the embedded piles.

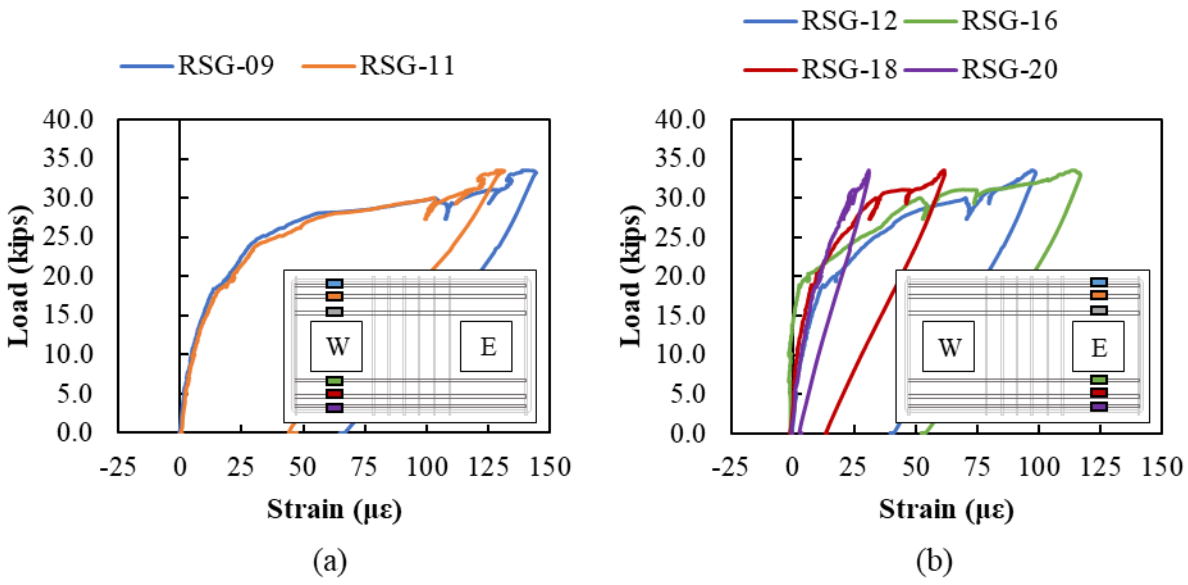

Figure D.119: SP-07 Rebar Strain data for gauges in N9 bars

Rebar strains in the N6 bars are shown in Figure D.120. RSG-23 and RSG-25 were found bad during testing. RSG-24, which is located above the east pile, measured maximum tensile strains of 580 με.

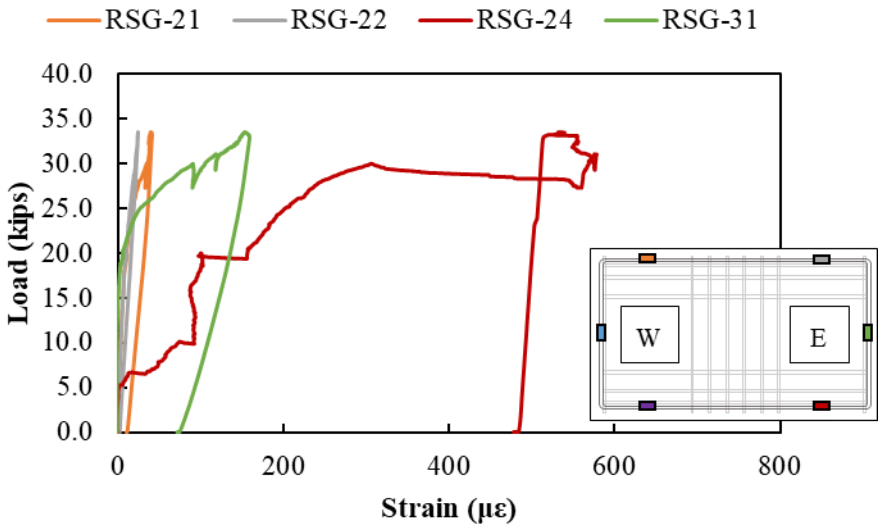

Figure D.120: SP-07 Rebar strain data for gauges in N6 bars

Rebar strains in N6 bars on the side of the pile cap are shown in Figure D.121. RSG-25, RSG-29, RSG-30, RSG-33, RSG-35 and RSG-35 were found bad during testing. Measured strains increased as bars were closer to the face of the pile cap with the embedded pile.

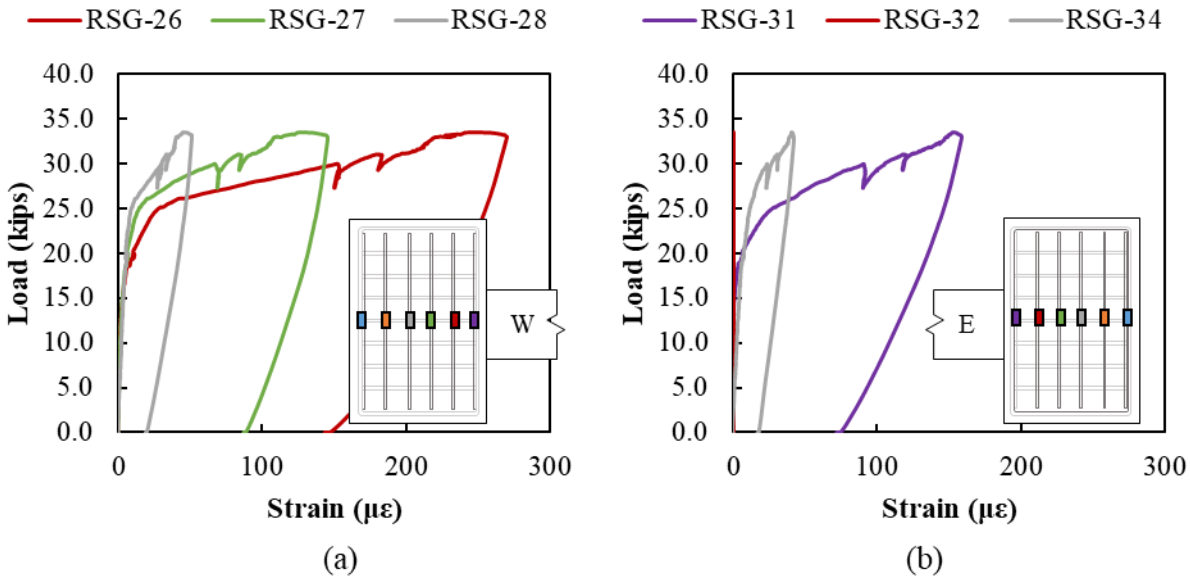

Figure D.121: SP-07 rebar strain data for gauges in N6 bars (a) west side (b) east side

D.7.5. Crack Displacement Transducers

Displacements in the plastic hinge zone of the west and west pile are shown in Figure D.122 and Figure D.123, respectively. Largest compression strains were found in the CDTs closest to the pile-to-cap interface CDT-04E and CDT-05W (fell off during testing).There was no correlation between strains on the tension face of the pile. Large tension strains were found in

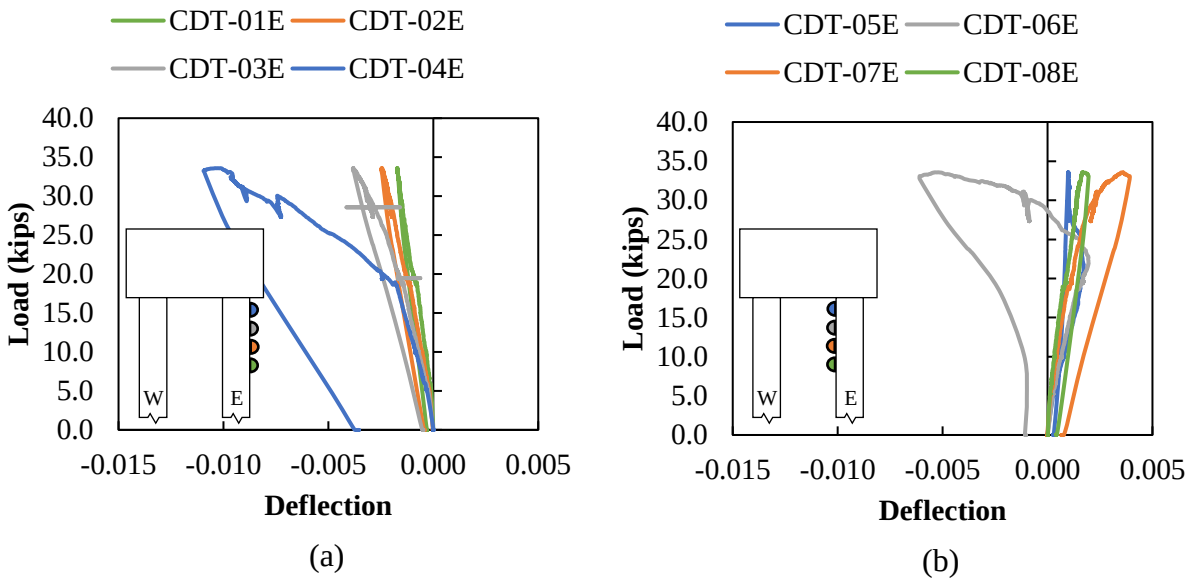

Figure D.122: SP-07 crack displacement data in east pile

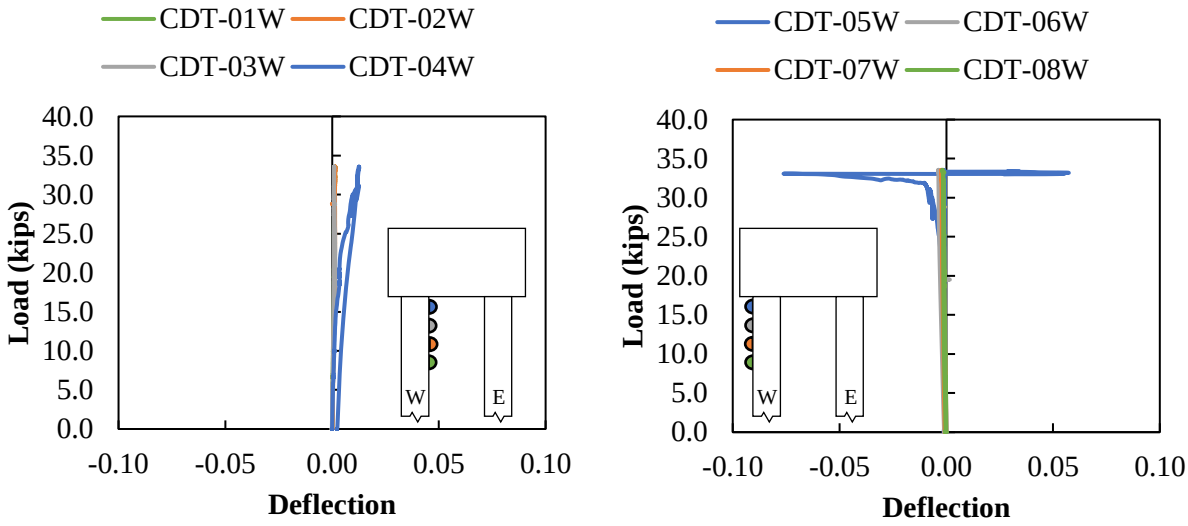

Figure D.123: SP-07 crack displacement data in west pile

Moment-curvature response found using CDTs are shown in Figure D.124. Since CDT-05W fell off during testing, the data was not considered for the moment-curvature response. High curvature was measured in the east pile in the gauges closes to the pile-to-cap interface.

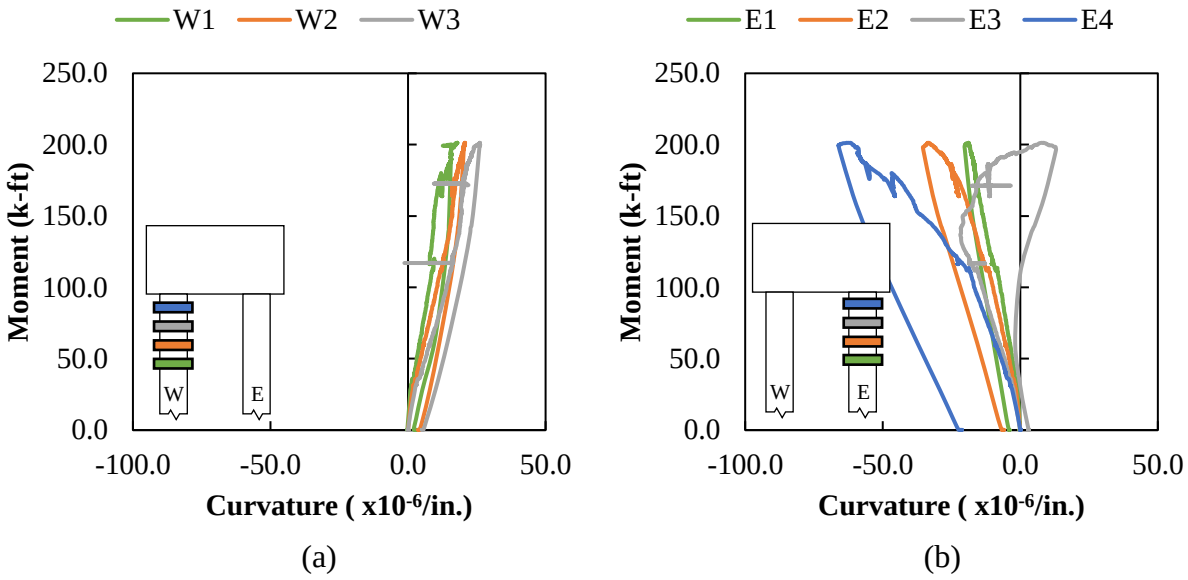

Figure D.124: SP-07 moment-curvature with crack displacement data (a) west pile (b) east pile

D.7.6. Vibrating Wire Gauges (Pile)

Vibrating wire data was recorded at different stages of the specimen. The initial data was used to calculate the elastic shortening losses, and total losses of each specimen.

Initial stress in strands:

Jacking stress: $$f_{pj} = \frac{F}{A} = \frac{34\ kips}{0.167\ in^2} = 203.6\ ksi$$

Readings from the longitudinal vibrating gages were recorded and used to find the stress in the strands after release (assuming E_p = 28,500 ksi):

Table D.20: SP-07 Elastic shortening losses calculation

VWG	**Before release** (με)	**After release** (με)	**Strain Change** (με)	**ES Losses** (ksi)
VWSG-P4-1E	0	-358.559	358.6	10.22
VWSG-P4-2E	2610.82	-329.989	330.0	9.40
			Δf_{pES} =	9.81

Therefore, the average stress in strands after elastic shortening losses:

Stress after elastic shortening losses: $$f_{pi} - \Delta f_{pES} = 203.6\ ksi - 9.81\ ksi = 193.79\ ksi$$

Readings from the longitudinal vibrating gages were recorded and used to find the stress in the strands before testing (assuming E_p = 28,500 ksi):

Table D.21: SP-07 Total losses calculation

VWG	**After casting** (με)	**Before testing** (με)	**Strain Change** (με)	**LT Losses** (ksi)
VWSG-P4-1E	-358.56	-793.7	435.1	12.40
VWSG-P4-2E	-329.989	-795.7	465.8	13.27
			Δf_{pLT} =	12.84

The average stress in strands after all losses:

Stress after all losses immediately before testing: $$f_{pi} - \Delta f_{pES} - \Delta f_{pLT} = 203.6\ ksi - 9.81 - 12.84\ ksi = 180.9\ ksi$$

D.7.7. Vibrating Wire Gauges (Cap)

Vibrating wire gauge data was also recorded in the pile cap around the embedded east pile. Readings at different times are shown in Table D.22. Temperature can affect the strain gauges readings; therefore, a temperature correction was applied to the actual readings, taking as reference the before cap casting readings.

Table D.22: SP-07 vibrating wire gauge data in the pile cap

VWG	Before cap casting (με)	Before testing (με)	After Testing (με)
VWSG-4E	0	-664.102	-458.026
VWSG-5E	0	-801.358	-960.134
VWSG-6E	0	-200.550	-152.634
VWSG-7E	0	-256.272	-311.573

D.7.8. Fiber Optic

Strains along the length of the FOS at different loads in the west pile are shown in Figure D.125. Small compression strains were measured at the exterior face of the pile until about 24 kips, at which point tension strains started to be developed. Tension strains were measured at the interior face of the pile until about 6,000 με at 26 kips.

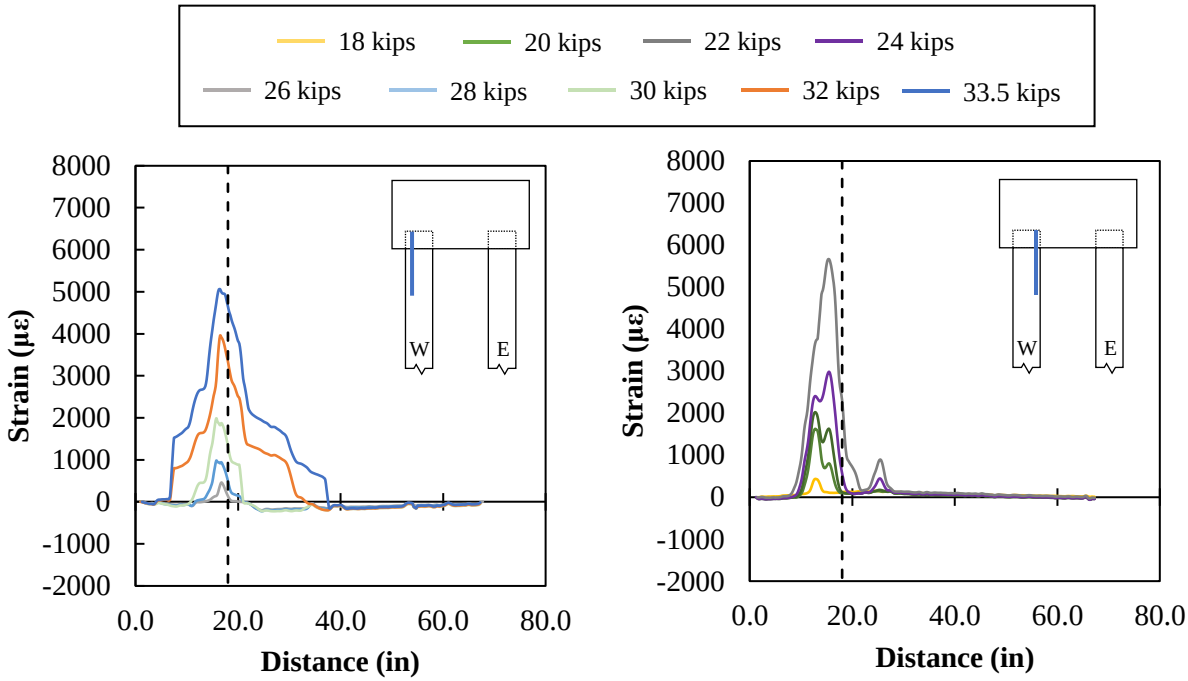

Figure D.125: SP-07 fiber optic data for west pile (a) FOS-08 (b) FOS-16

The strain profile at the critical section, 18 inches embedment length, in the west pile is shown in Figure D.126. Tensile strains were measured at the top face of the pile at about 2,500 με at failure.

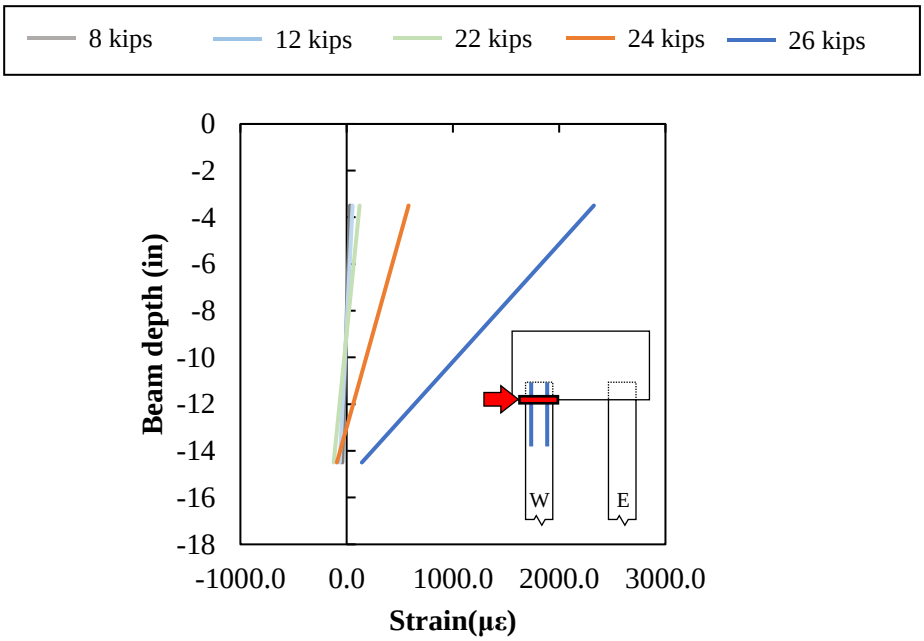

Figure D.126: SP-07 strain profile for west pile at critical section

Strains along the length of the FOS at different loads in the east pile are shown in Figure D.127. Tension strains developed at the interior face of the pile with maximum strains at the pile-to-cap interface. Small compression strains were measured on the exterior face of the pile, until around 24 kips, at which point tension strains started to be developed with maximum strains of 6,000 με at failure.

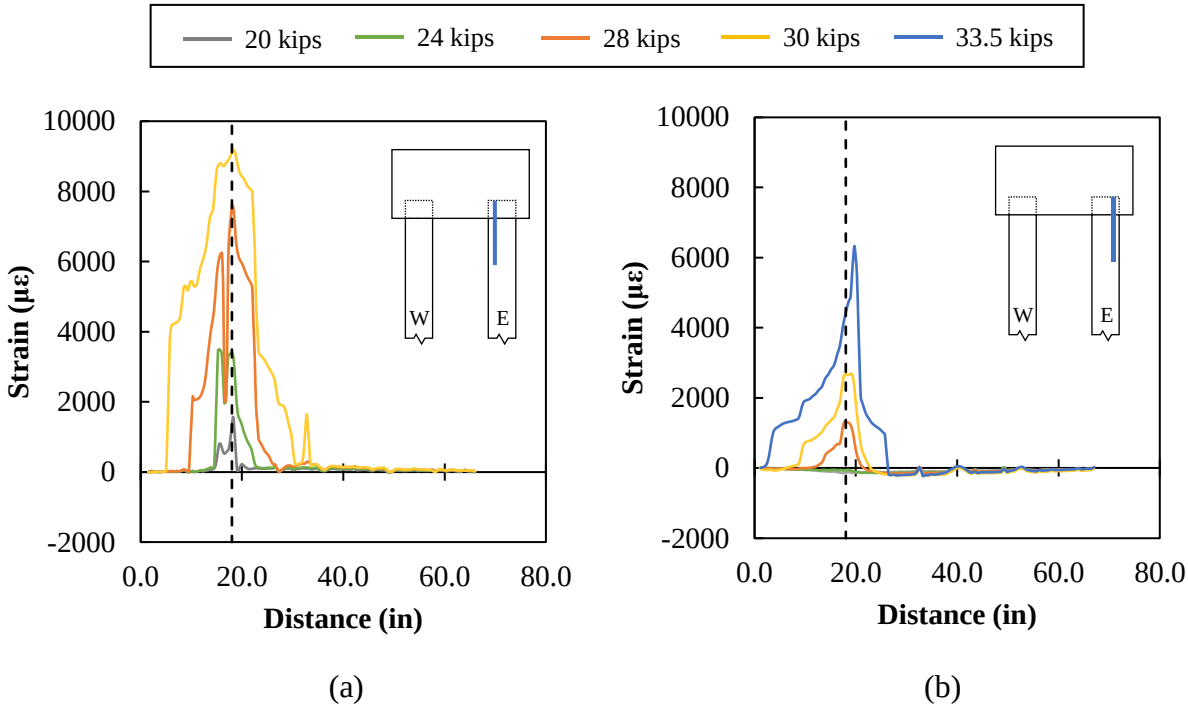

Figure D.127: SP-07 fiber optic data for east pile (a) FOS-04 (b) FOS-12

Strain profile in the east pile at critical plane is shown in Figure D.128. Tensile strains were measured at the bottom face at about 8,000 με at failure.

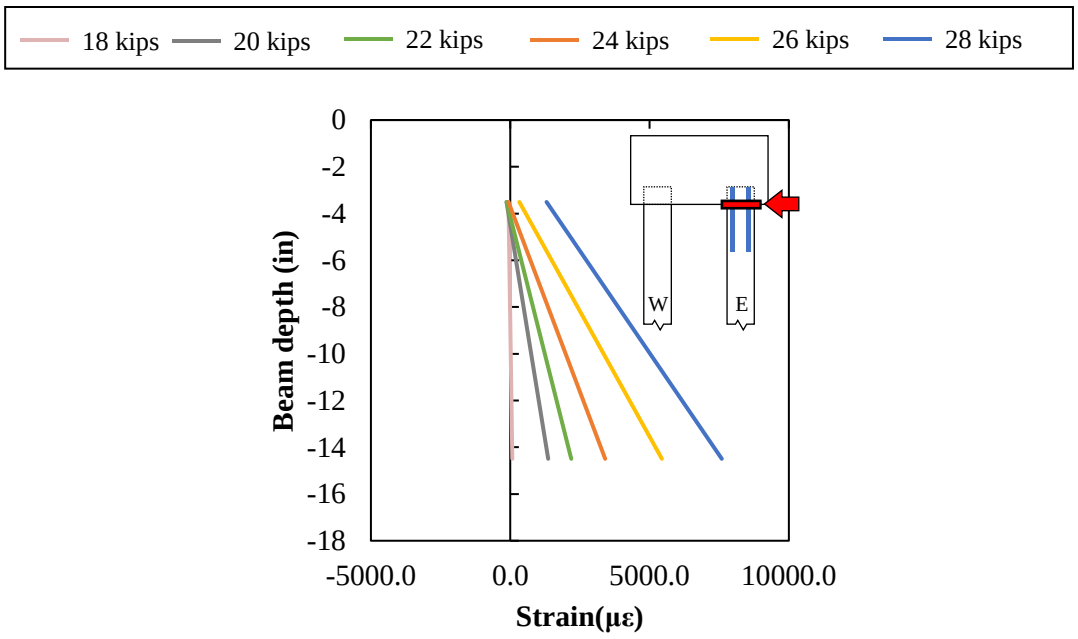

Figure D.128: SP-07 strain profile for east pile at critical section

Moment-curvature response from the measured strains in the FOS are shown in Figure D.129.

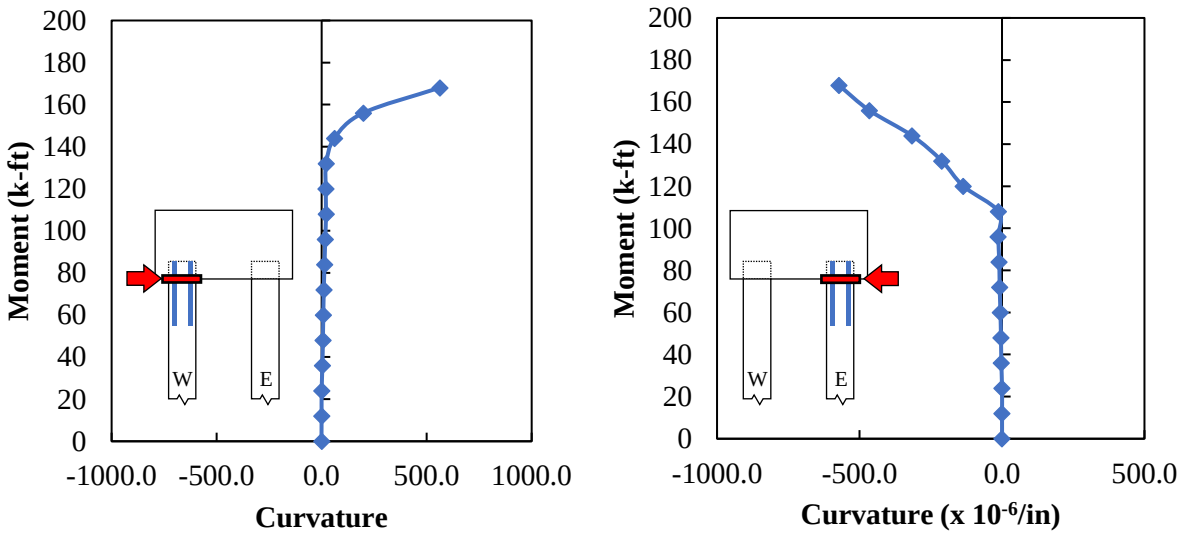

Figure D.129: SP-07 moment-curvature response for (a) west pile (b) east pile

D.8. SP-08

D.8.1. Observations and Summary of Results

Results of Specimen 8 are summarized in Table D.23.

Table D.23: SP-03 Summary of Results

Specimen 8	
Pile Embedment	27.0 in. ($1.5d_{pile}$)
Interface Reinforcement	none
Axial Load	0 kips ($0A_g f'_{c,pile}$)
Failure load (kips)	44.6
Distance from Load to Cap (ft.)	6.0
Failure Mechanism	Strand development
Pile Failed	West
Maximum Displacement (in)	5.878
Ultimate Moment Developed (k-ft)	267.6
Percentage of capacity of pile	86.3 %

Specimen 8 had an embedment length of 27 inches, which was the deepest embedment of all the 18-inch specimens; no axial load was applied to the piles, and no interface reinforcement was present between the pile and cap.

Failure of this specimen occurred in the west pile. The observed failure was likely caused by the crushing of the concrete around the pile. Spalling of the concrete was also observed in the exterior face of both piles. Cracks developed on both piles, as shown in Figure D.130.

(a) (b)

Figure D.130 : SP-08 failure mechanism (a) pile crushing (b) cracks in pile

D.8.2. Laser displacement transducers (LDT)

Displacements were recorded along the length of both piles. The application of the lateral load in the piles for Specimen 8 was at 6 ft from the pile-to-cap interface, which was the same location as LDT-3, as shown in Figure D.131.

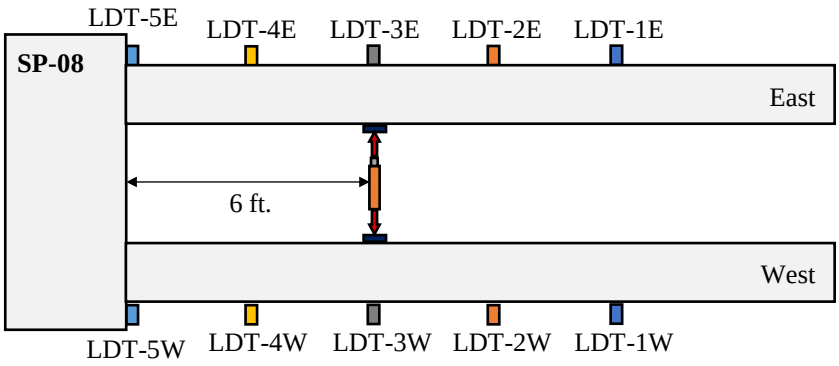

Figure D.131: Location of laser displacement transducers (LDT) and applied load for SP-08

The load-displacement curves of the west and east piles are shown in Figure D.132 (a) and (b), respectively. The maximum load reached by Specimen 8 was 44.6 kips, which corresponds to 86.3% the capacity of the 18-inch piles. The horizontal displacement in the west pile and east

pile was 10-inch. This specimen showed a symmetrical behavior in both piles, which didn't occur in previous specimens.

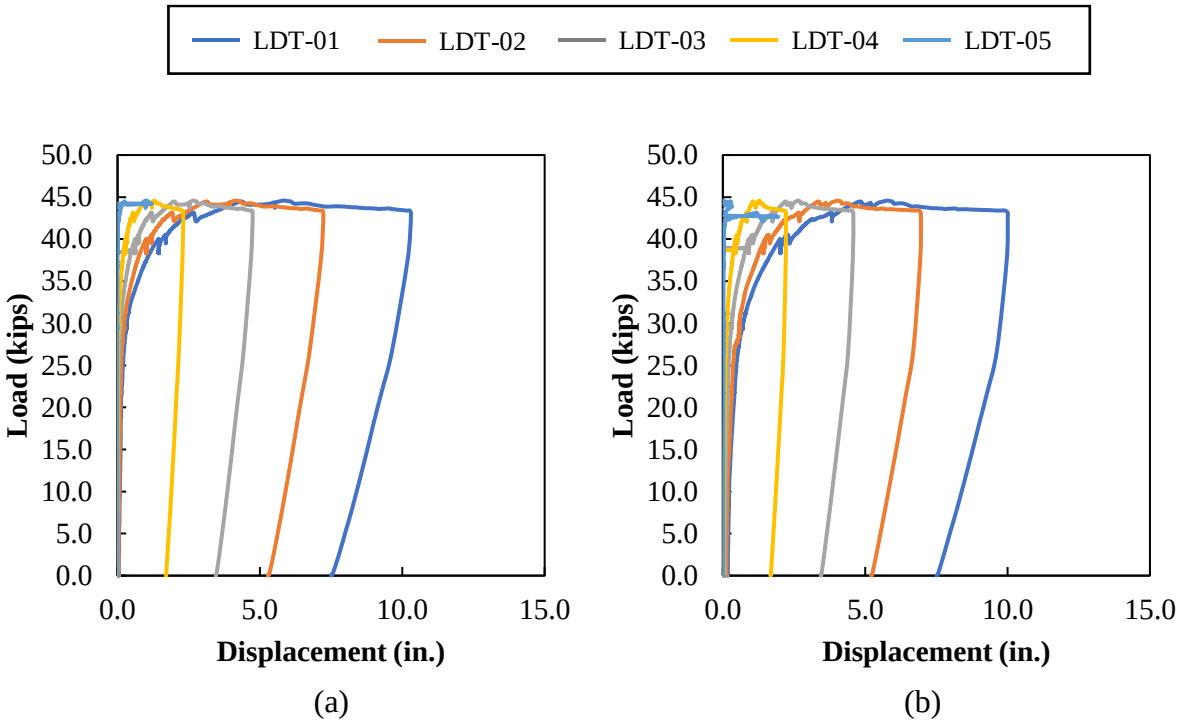

Figure D.132: SP-08 load-displacement curve for (a) west pile (b) east pile

D.8.3. Concrete Strain Gauges

Vertical and horizontal concrete strains around the west pile are shown in Figure D.133. CSG-01 and CSG-02 which are perpendicular to load application and located outside the piles, measured compression strains less than 200 με. CSG-03 also perpendicular to load application measured maximum tension strains of 900 με at failure.

CSG-04 and CSG-05, parallel to load application, measured small compression and tension strains, respectively, less than 200 με. CSG-06 and CSG-07, located above and below the embedded pile measured maximum tension strains of 1,000 με, which corresponds to the spalling of concrete on top of the embedded pile.

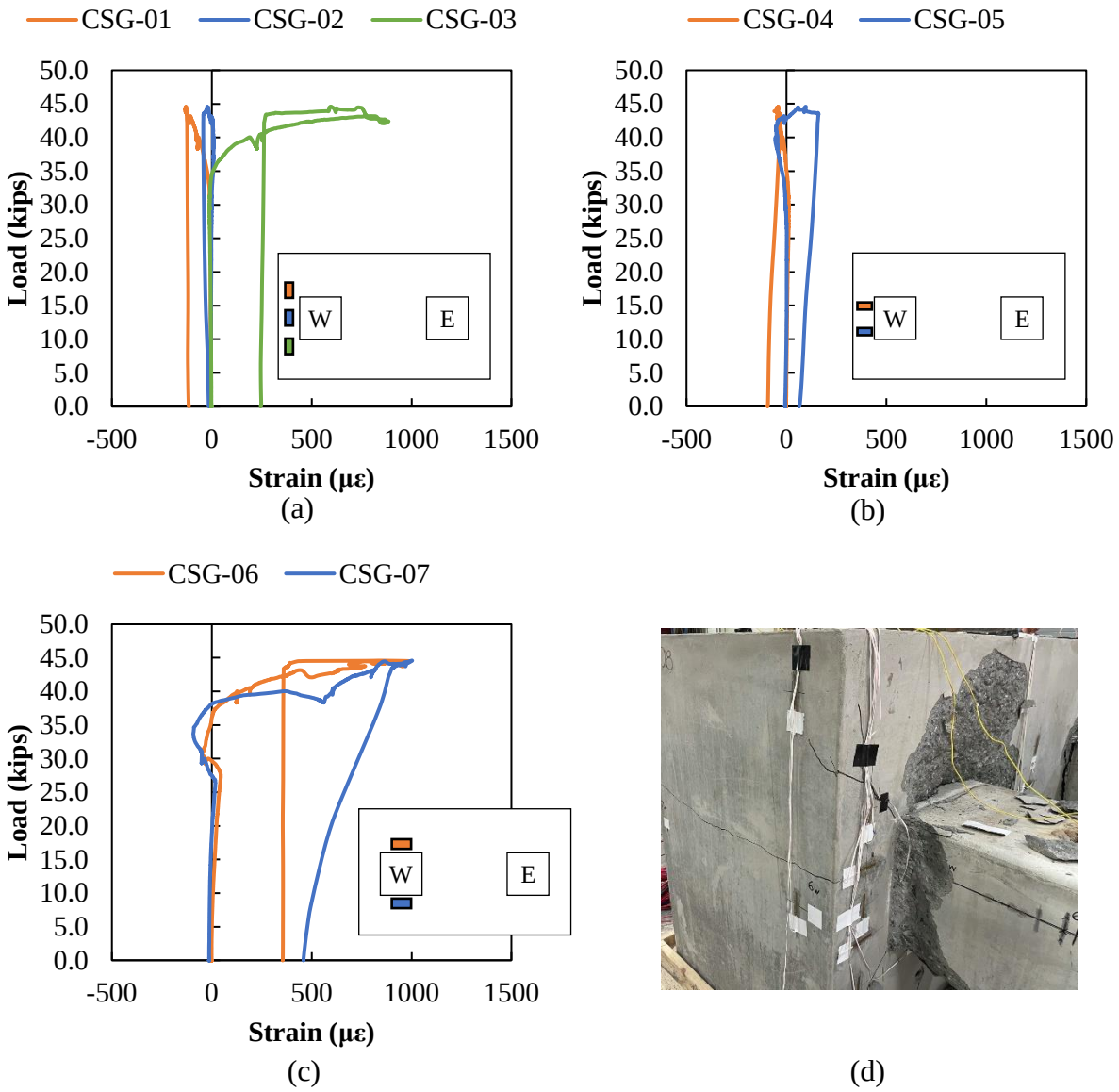

Figure D.133: SP-08 concrete strain data for CSG-01 to CSG-07

Vertical and horizontal concrete strains in the middle of the pile cap between the piles are shown in Figure D.134. Measured strains were minor in both direction for CSG-08, CSG-10, CSG-11, CSG-12, with strains less than 200 με. CSG-09, which is perpendicular to load application, started with tensile strains around 1400 με and kept increasing until failure load.

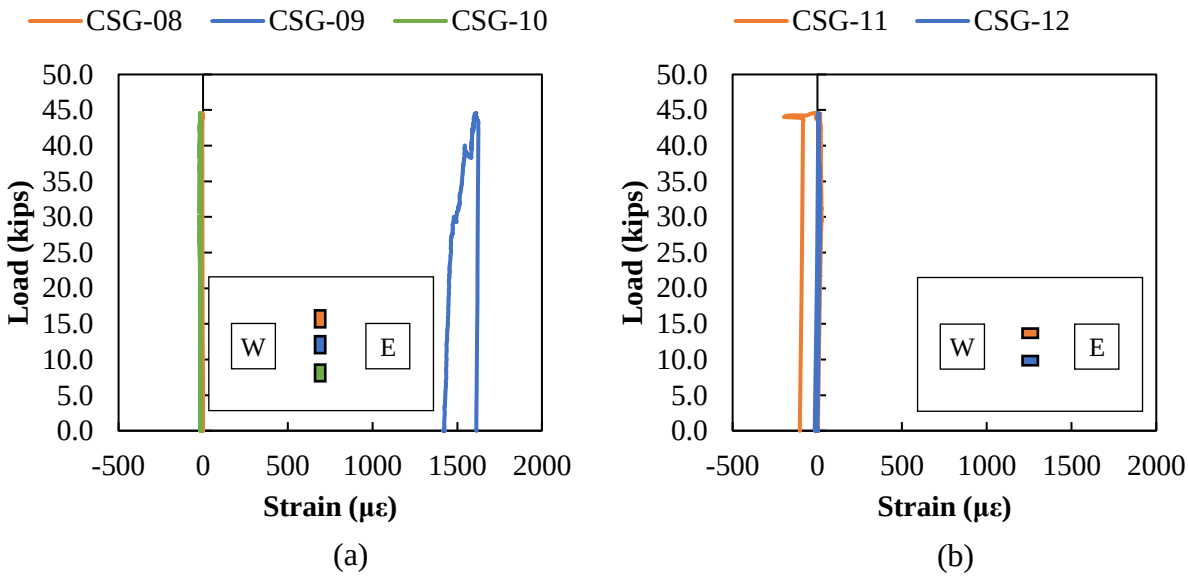

Figure D.134: SP-08 concrete strain data for CSG-08 to CSG-12

Vertical and horizontal concrete strains around the east pile are shown in Figure D.135. CSG-13 and CSG-14, located on top and bottom of embedded pile, respectively, measured tension strains less than 150 με.

CSG-15, located outside the embedded pile, measured compression strains less than 200 με at the maximum applied load. CSG-16 measured tensile strains less than 50 με. CSG-17, started with small compression strains until approximately 30 kips, started developing tensile strains until 75 με and 37 kips, at which point tensile strains decreased and compression strains began to be measured.

CSG-18 and CSG-19, parallel to load application and located outside the embedded pile, started measuring small tensile strains until around 35 kips, at which point compression strains began to be measured, with maximum strains of around 100 με at failure.

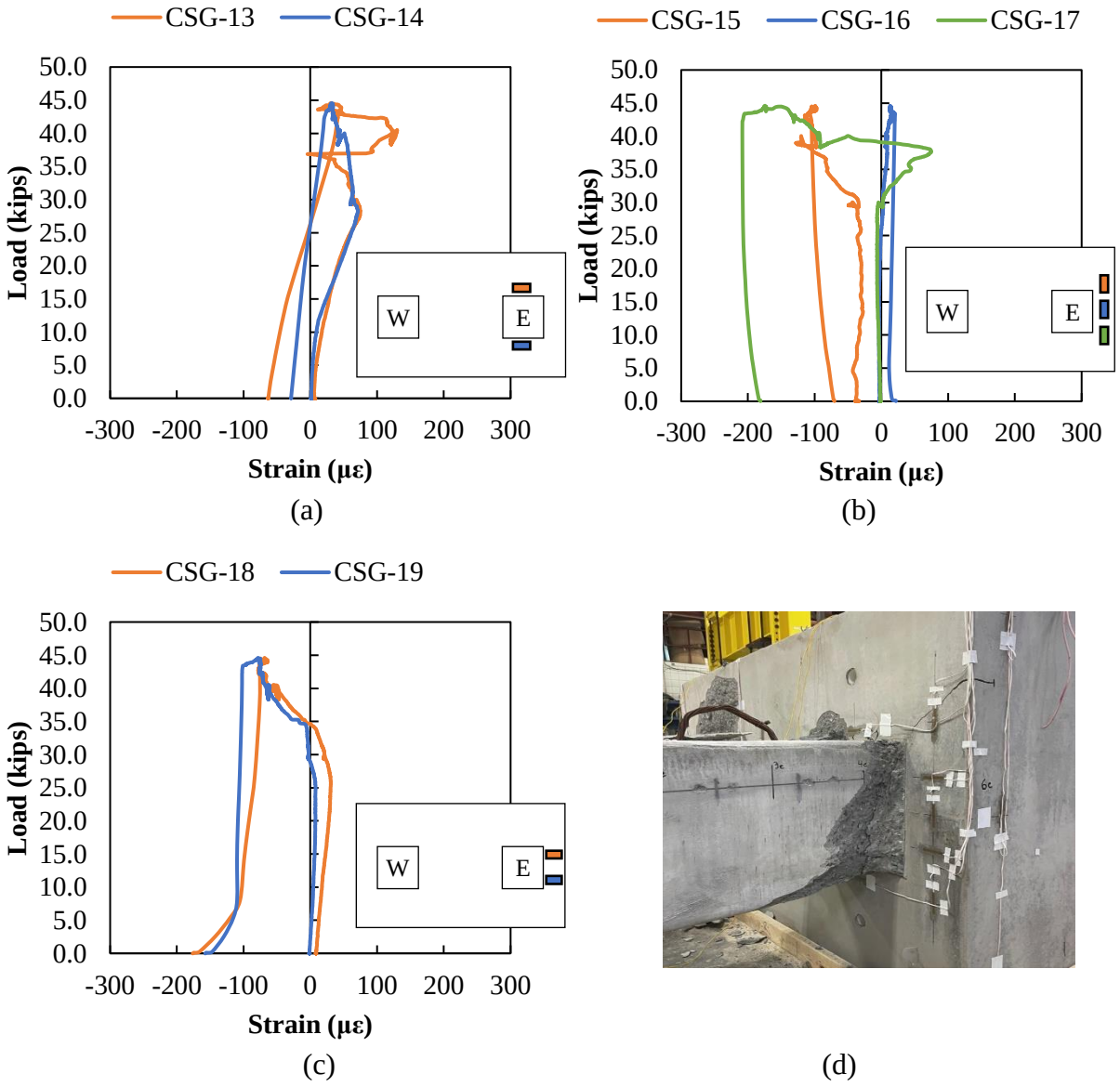

Figure D.135: SP-08 concrete strain data for CSG-13 to CSG-19

Concrete strains on the west and east faces of the pile cap are shown in Figure D.136. CSG-20, CSG-21, CSG-23 and CSG-24 had compression strains less than 400 με at maximum applied loads. On the other hand, CSG-21 and CSG-24, which are located at the same high of the embedded pile, measured tensile strains. CSG-21 developed maximum tensile strains less than 200 με at failure load. Strains in CSG-24 started increasing rapidly at around 35 kips.

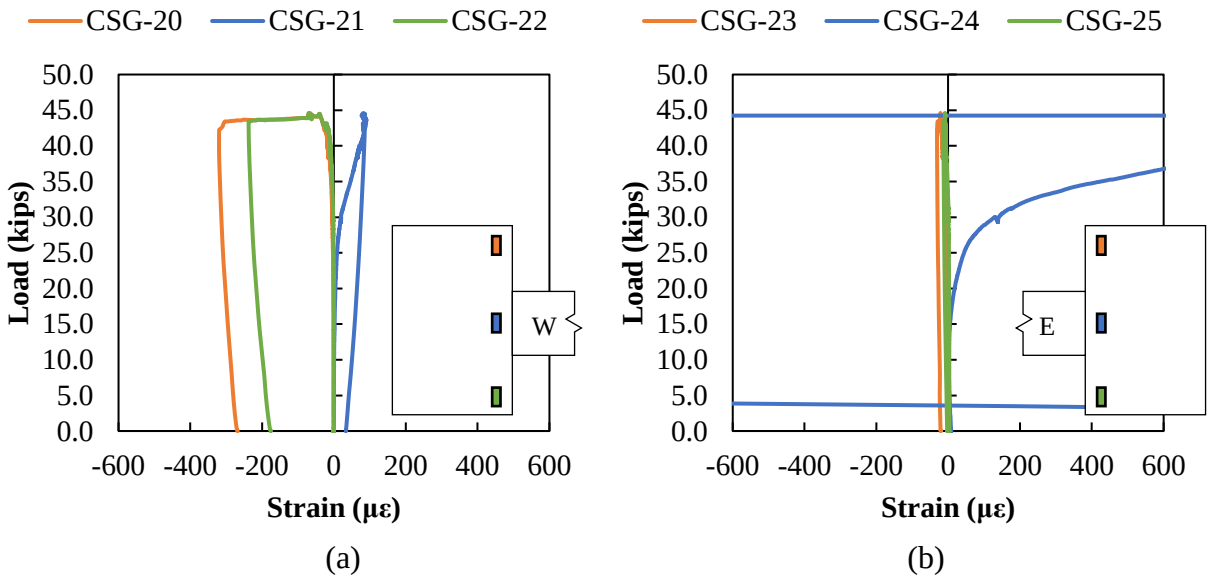

Figure D.136: SP-08 concrete strain data for CSG-20 to CSG-25

D.8.4. Rebar Strain Gauges

Rebar strains in the N5 bars are shown in Figure D.137. RSG-08, located outside the embedded east pile, measured maximum tensile strains of 190 με. Small compression strains were measured in bars RSG-02 and RSG-07, located in the interior side closest the embedded pile.

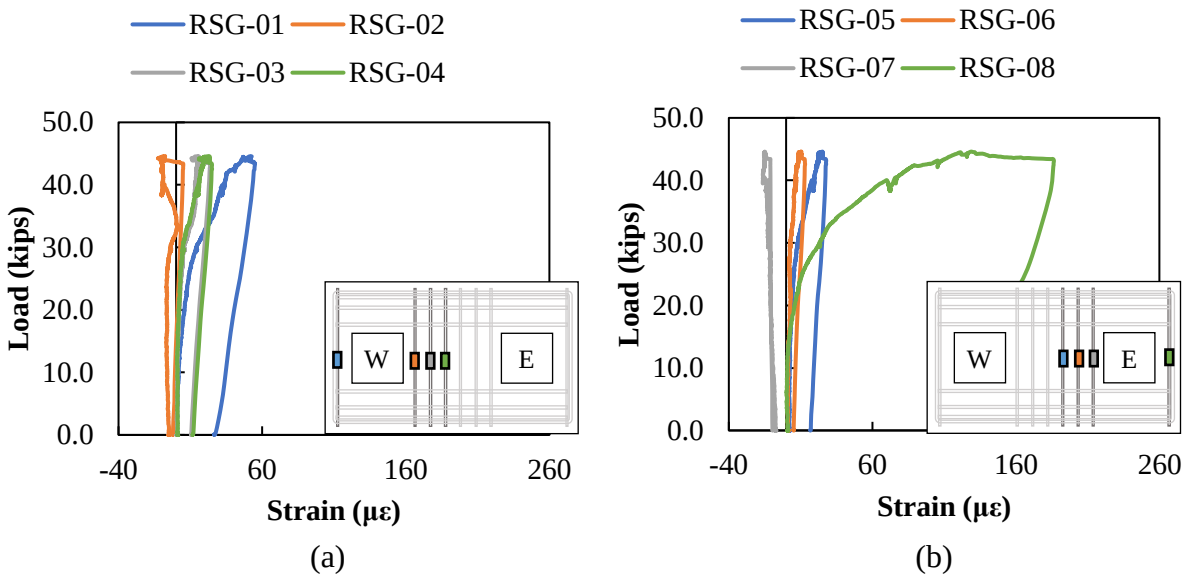

Figure D.137: SP-08 rebar strain data for N5 bars

Rebar strains in the N9 bars are shown in Figure D.138. Maximum tension strains were found in RSG-15, which is located below the west pile. Strains in the bars around the east pile remained less than 100 με.

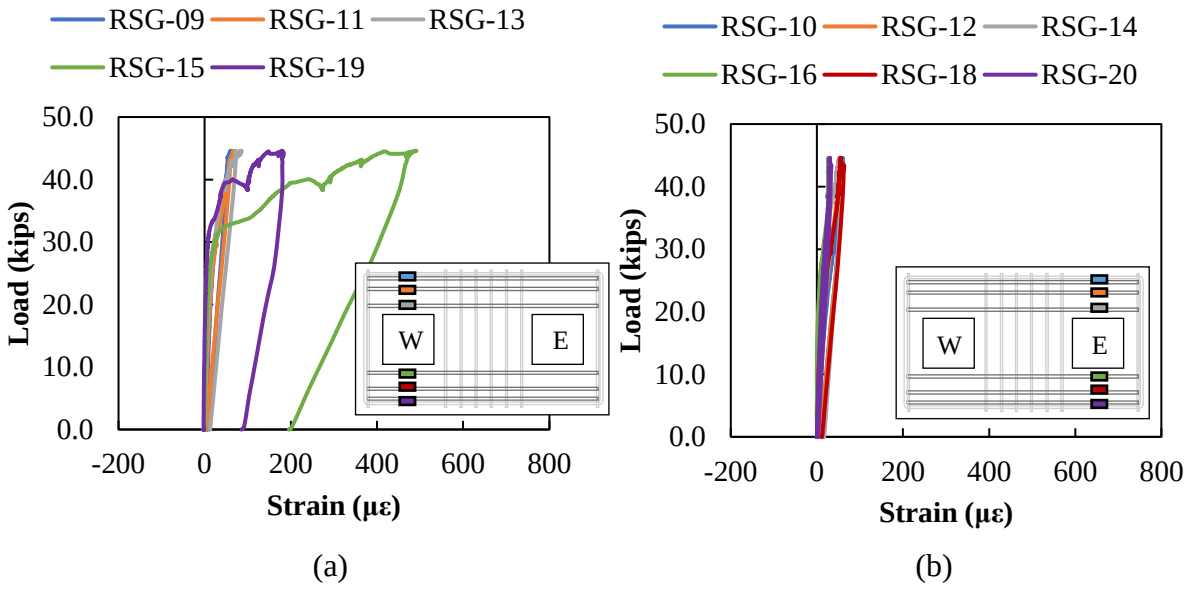

Figure D.138: SP-08 rebar strain data for N9 bars

Rebar strains in the N6 bars are shown in Figure D.139. Maximum measured strain was found in RSG-23 located below the embedded west pile.

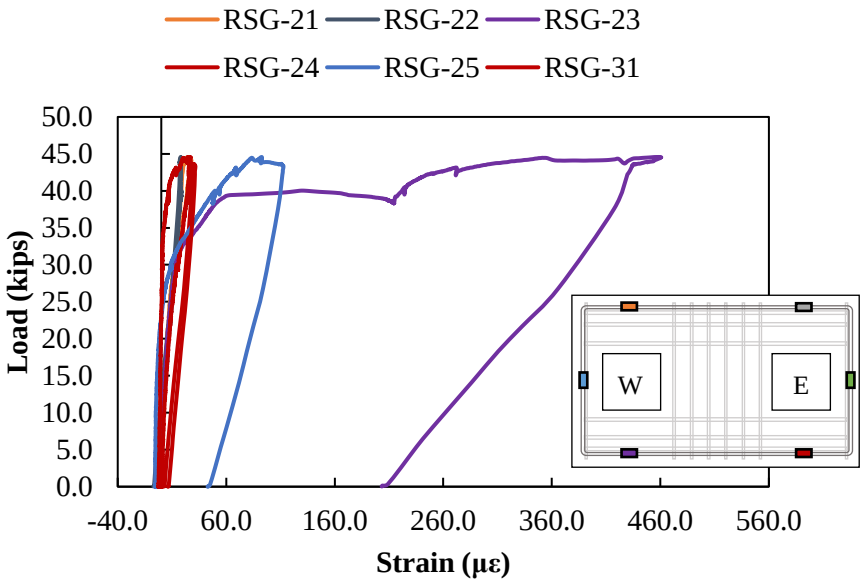

Figure D.139: SP-08 rebar strain data for N6 bars

Rebar strains in N6 bars on the side of the pile cap are shown in Figure D.140. No correlation was found between distance from embedded pile and rebar engagement.

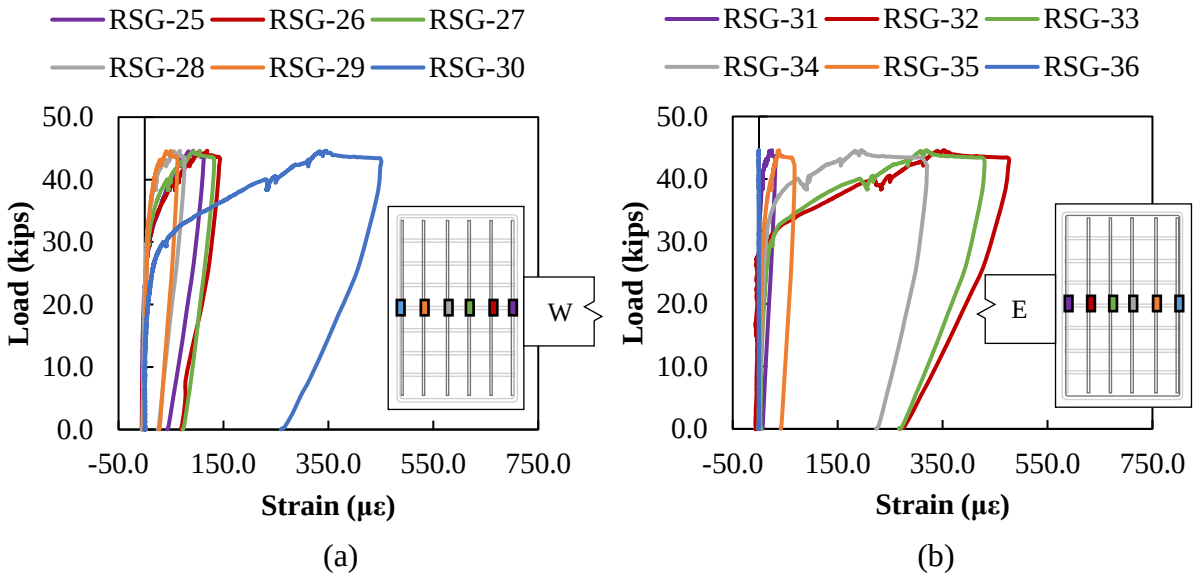

Figure D.140: SP-08 rebar strain data for N6 bars (a) west side (b) east side

D.8.5. Crack Displacement Transducers

Displacements were recorded in the plastic hinge zone of both piles results are shown in Figure D.141 and Figure D.142. Spalling was observed on the exterior face of both piles causing the cracking gauges closest to the pile-to-cap interface to fell (CDT-4E and CDT-5W). CDT-07E, located in the interior face of the pile, recorded high tension strains, which corresponds to the location of cracks developed in the pile.

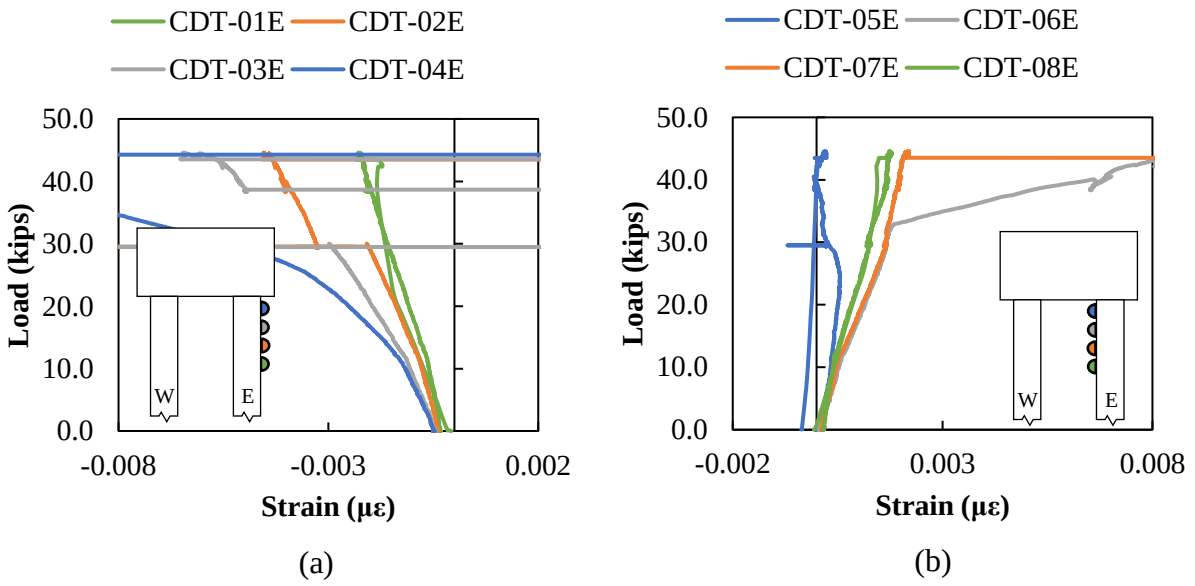

Figure D.141: SP-08 crack displacement data for the east pile

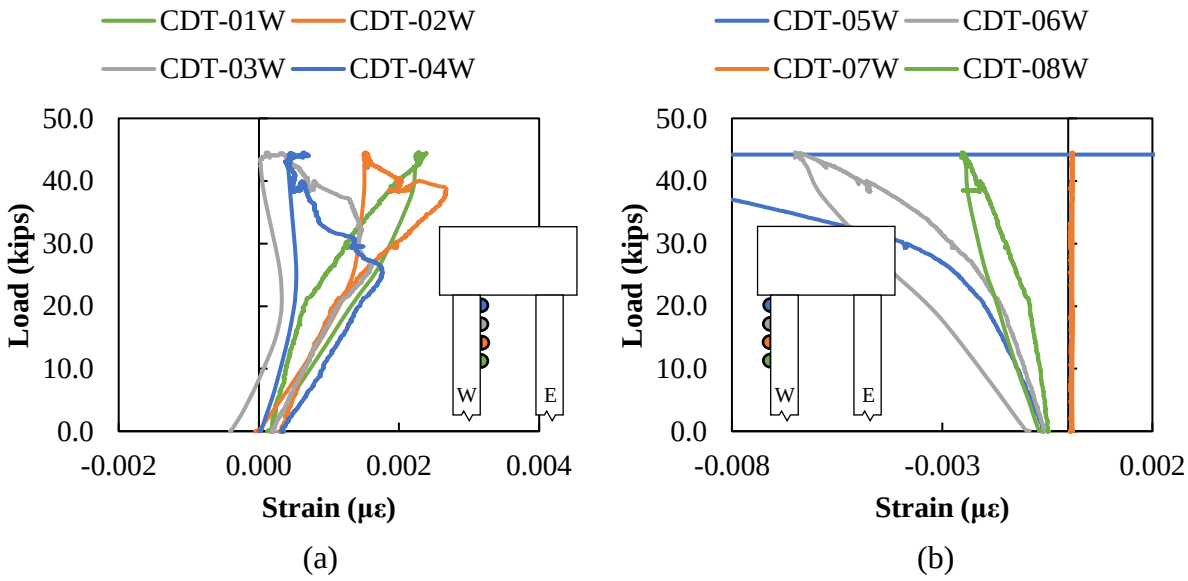

Figure D.142: SP-08 crack displacement data for the west pile

Moment-curvature response using the CDTs for the west and east pile are shown in Figure D.143. Curvature measured with the cracking gauges closest to the pile-to-cap interface were not included. Curvature increased with the gauges closest to the connection.

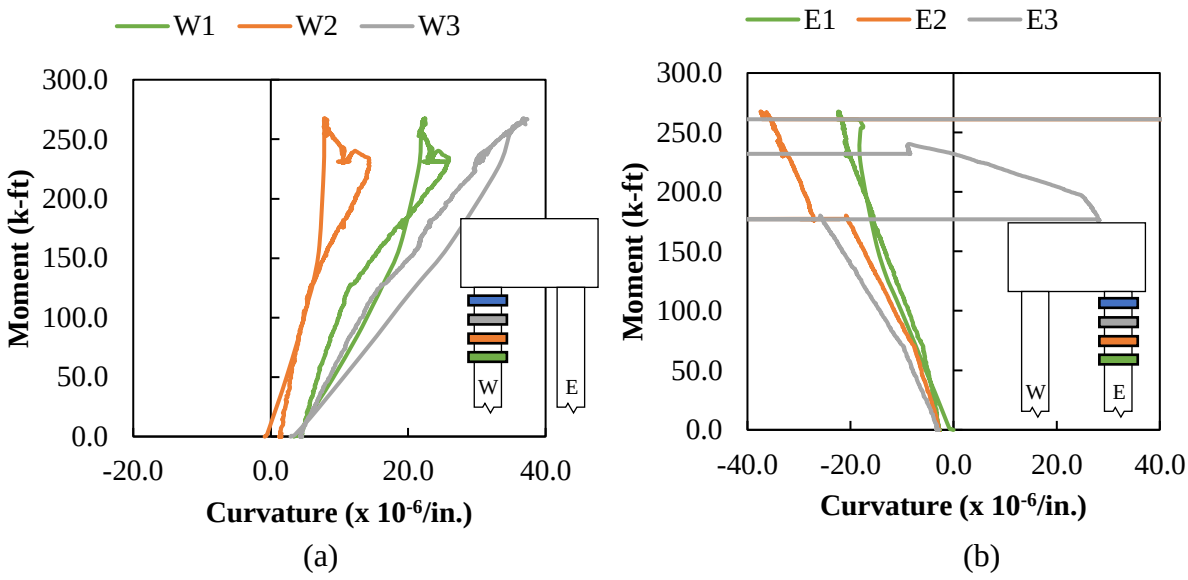

Figure D.143: SP-08 moment-curvature with crack displacement data (a) west pile (b) east pile

D.8.6. Vibrating Wire Gauges (Pile)

Vibrating wire data was recorded at different stages of the specimen. The initial data was used to calculate the elastic shortening losses, and total losses of each specimen.

Initial stress in strands:

Jacking stress: $$f_{pj} = \frac{F}{A} = \frac{34\ kips}{0.167\ in^2} = 203.6\ ksi$$

Readings from the longitudinal vibrating gages were recorded and used to find the stress in the strands after release (assuming E_p = 28,500 ksi):

Table D.24: SP-08 Elastic shortening losses calculation

VWG	Before release (με)	After release (με)	Strain Change (με)	ES Losses (ksi)
VWSG-P3-1E	0	-366.589	366.6	10.45
VWSG-P3-2E	0	-340.471	340.5	9.70
			Δf_{pES} =	10.08

Therefore, the average stress in strands after elastic shortening losses:

Stress after elastic shortening losses: $$f_{pi} - \Delta f_{pES} = 203.6\ ksi - 10.08\ ksi = 193.52\ ksi$$

Readings from the longitudinal vibrating gages were recorded and used to find the stress in the strands before testing (assuming E_p = 28,500 ksi):

Table D.25: SP-08 Total losses calculation

VWG	After casting (με)	Before testing (με)	Strain Change (με)	LT Losses (ksi)
VWSG-P6-1E	-366.59	-944.8	578.2	16.48
VWSG-P6-2E	-340.47	-897.2	556.8	15.87
			Δf_{pLT} =	16.17

The average stress in strands after all losses:

Stress after all losses immediately before testing: $$f_{pi} - \Delta f_{pES} - \Delta f_{pLT} = 203.6\ ksi - 10\ ksi - 16.17\ ksi = 177.3\ ksi$$

D.8.7. Vibrating Wire Gauges (Cap)

Vibrating wire gauge data was also recorded in the pile cap around the embedded east pile. Readings at different times are shown in Table D.26. Temperature can affect the strain gauges readings; therefore, a temperature correction was applied to the actual readings, taking as reference the before cap casting readings.

Table D.26: SP-08 vibrating wire gauge data in the pile cap

VWG	Before cap casting (με)	Before testing (με)	After Testing (με)
VWSG-4E	0	10.783	30.384
VWSG-5E	0	17.392	-27.773
VWSG-6E	0	12.439	32.512
VWSG-7E	0	-38.829	-47.506

D.8.8. Fiber Optic Sensors

Strains along the length of the FOS at different loads in the west pile at the exterior face are shown in Figure D.144. FOS in the interior face was not functional during testing, likely damaged during construction.

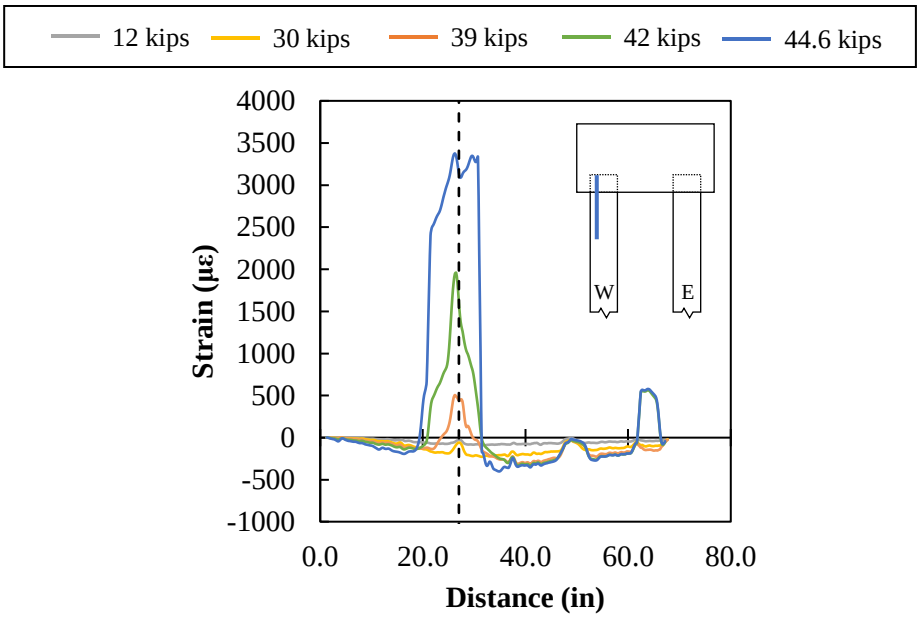

Figure D.144: SP-08 fiber optic data for west pile FOS-6

Strains along the length of the FOS at different loads in the east pile are shown in Figure D.145. Tension strains developed at the interior face of the pile with maximum strains at the pile-to-cap interface. Small compression strains were measured on the exterior face of the pile, until around 33 kips, at which point tension strains started to be developed with maximum strains of 6,000 με at failure.

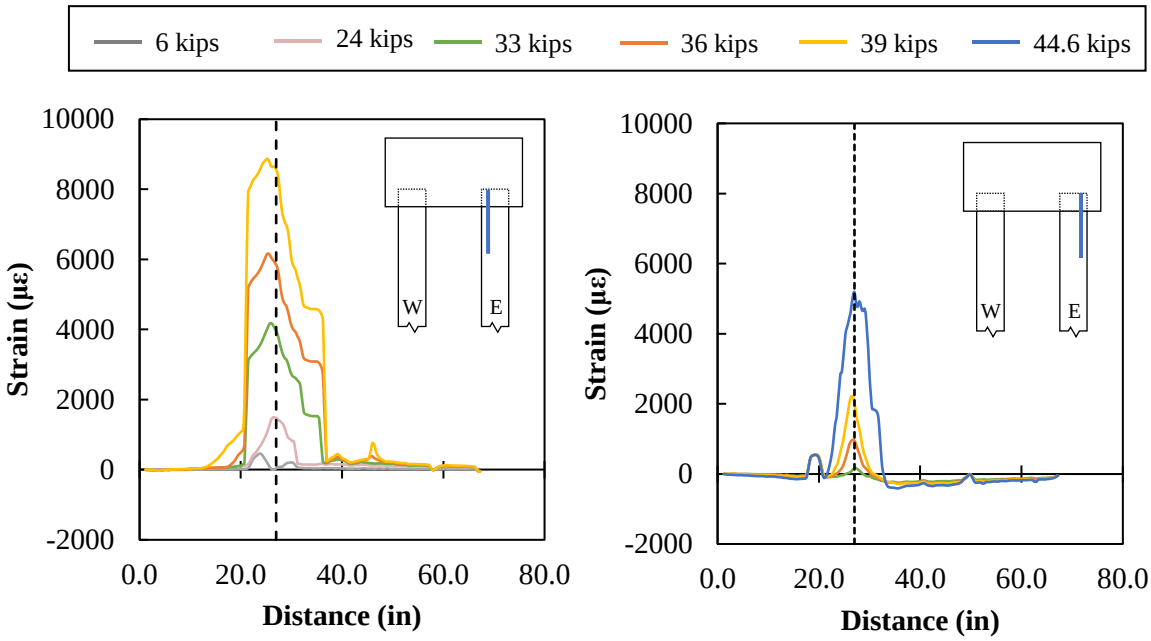

Figure D.145: SP-08 Fiber Optic Data for East Pile (a) FOS-03 (b) FOS-11

The strain profile at the critical section, 27 inches embedment length, in the west pile is shown in Figure D.126. Tensile strains were measured at the top face of the pile at about 10,000 με at failure.

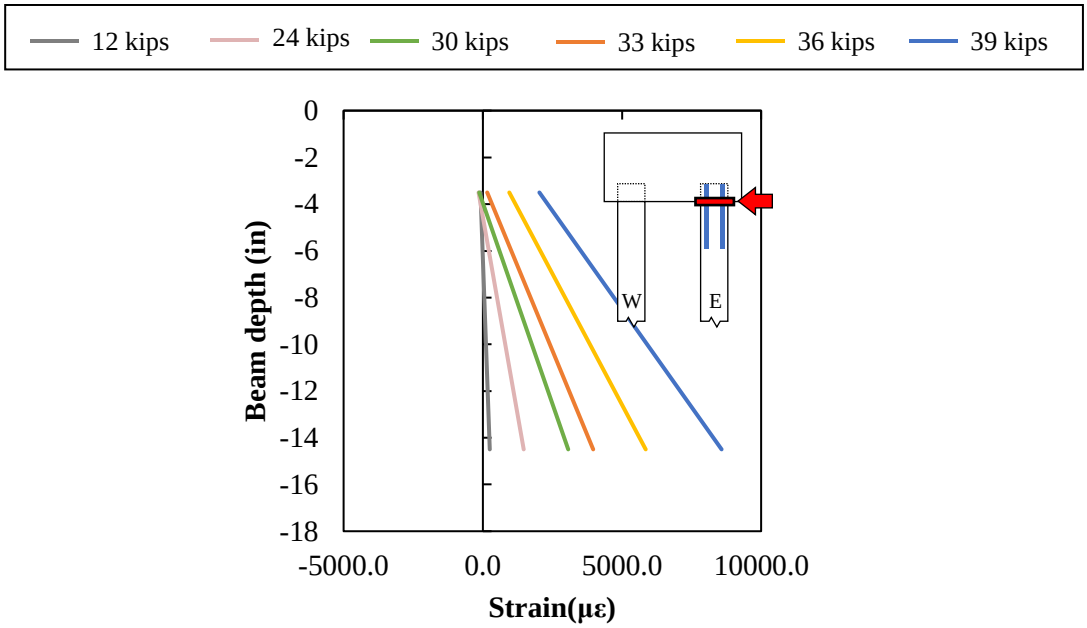

Figure D.146: SP-08 Strain Profile at Critical Section (27 in)

Moment-curvature response from the measured strains in the FOS are shown in Figure D.129.

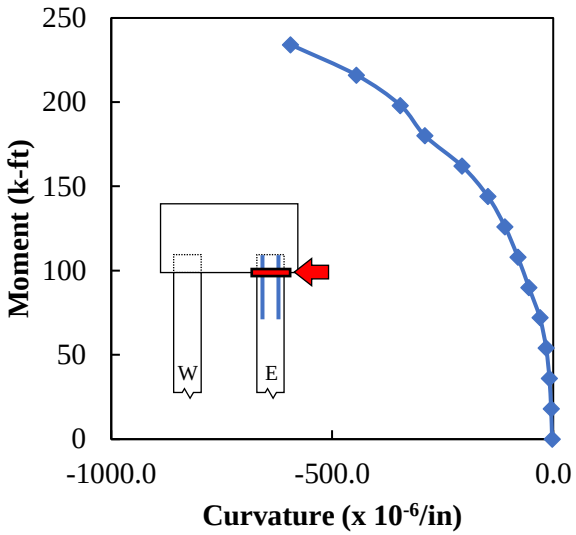

Figure D.147: SP-08 Moment-curvature

D.9. SP-09

D.9.1. Observations and Summary of Results

Results of Specimen 9 are summarized in Table D.27.

Table D.27: SP-09 Summary of Results

Specimen 9	
Pile Embedment	12.0 in. ($0.4d_{pile}$)
Interface Reinforcement	none
Axial Load	0 kips ($0A_g f'_{c,pile}$)
Failure load (kips)	63.84
Distance from Load to Cap (ft.)	9.0
Failure Mechanism	Strand development
Pile Failed	West
Maximum Displacement (in)	13.5
Ultimate Moment Developed (k-ft)	574.56
Percentage of capacity of pile	55.6 %

Specimen 9 is one of the two 30-inch specimens. SP-09 had an embedment length of 12 inches, which was the shallowest embedment of the 30-inch specimens; no axial load was applied to the piles, and no interface reinforcement was present between the pile and cap.

Failure of this specimen occurred in the west pile. The observed failure was strand development. Spalling of the concrete on the front face of the pile cap was observed, as shown in Figure D.148

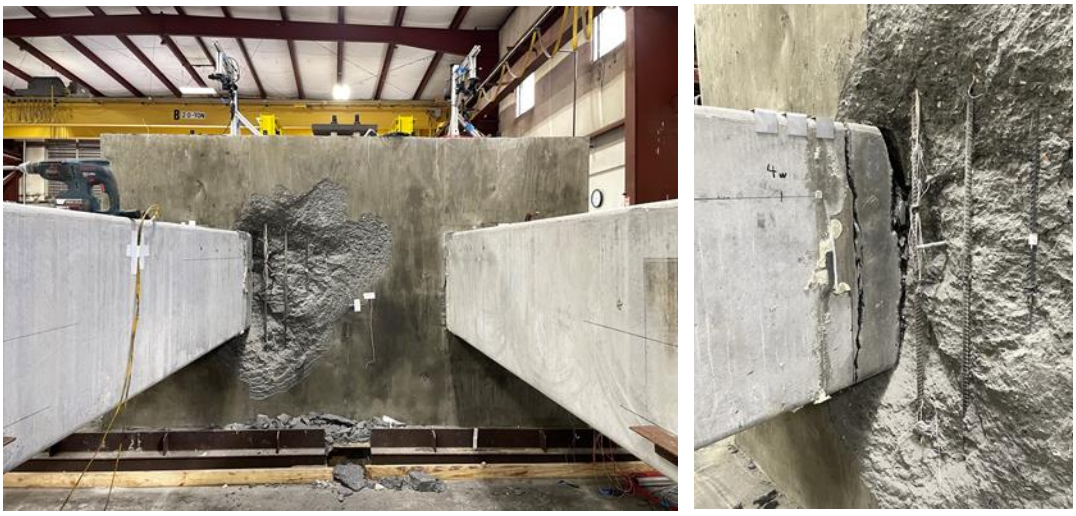

(a) (b)

Figure D.148: SP-09 failure mechanism

D.9.2. Laser displacement transducers (LDT)

Displacements were recorded along the length of both piles. The application of the lateral load in the piles for Specimen 9 was at 9 ft from the pile-to-cap interface, which was the same location as LDT-2, as shown in Figure D.149.

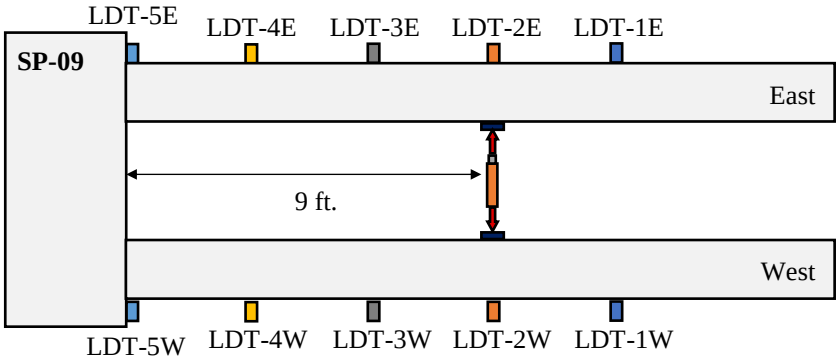

Figure D.149: Location of laser displacement transducers (LDT) and applied load for SP-09

The load-displacement curves of the west and east piles are shown in Figure D.150 (a) and (b), respectively. The maximum load reached by Specimen 9 was 63.84 kips, which corresponds to 55.6% the capacity of the 30-inch piles. The maximum horizontal displacement in the east and west pile was, 1.637 inches and 13.5 inches, respectively.

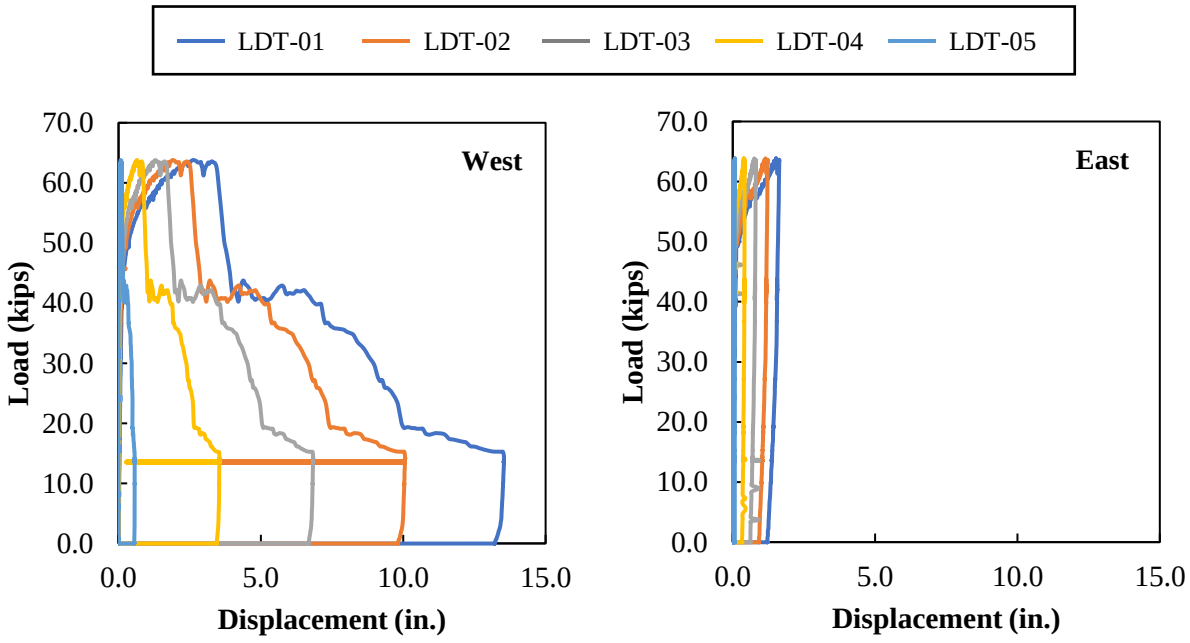

Figure D.150: SP-09 load-displacement curve for (a) west pile (b) east pile

D.9.3. Concrete Strain Gauges

Vertical and horizontal concrete strains around the west pile are shown in Figure D.151. CSG-01 and CSG-02 which are perpendicular to load application and located outside the piles, measured compression strains less than 400 με and 200 με, respectively.

CSG-04 and CSG-05, parallel to load application, measured compression strains less than 150 με. CSG-06 and CSG-07, located above and below the embedded pile started measuring tensile strains until around 60 kips at which point tensile strains decreased, and compression strains started to develop.

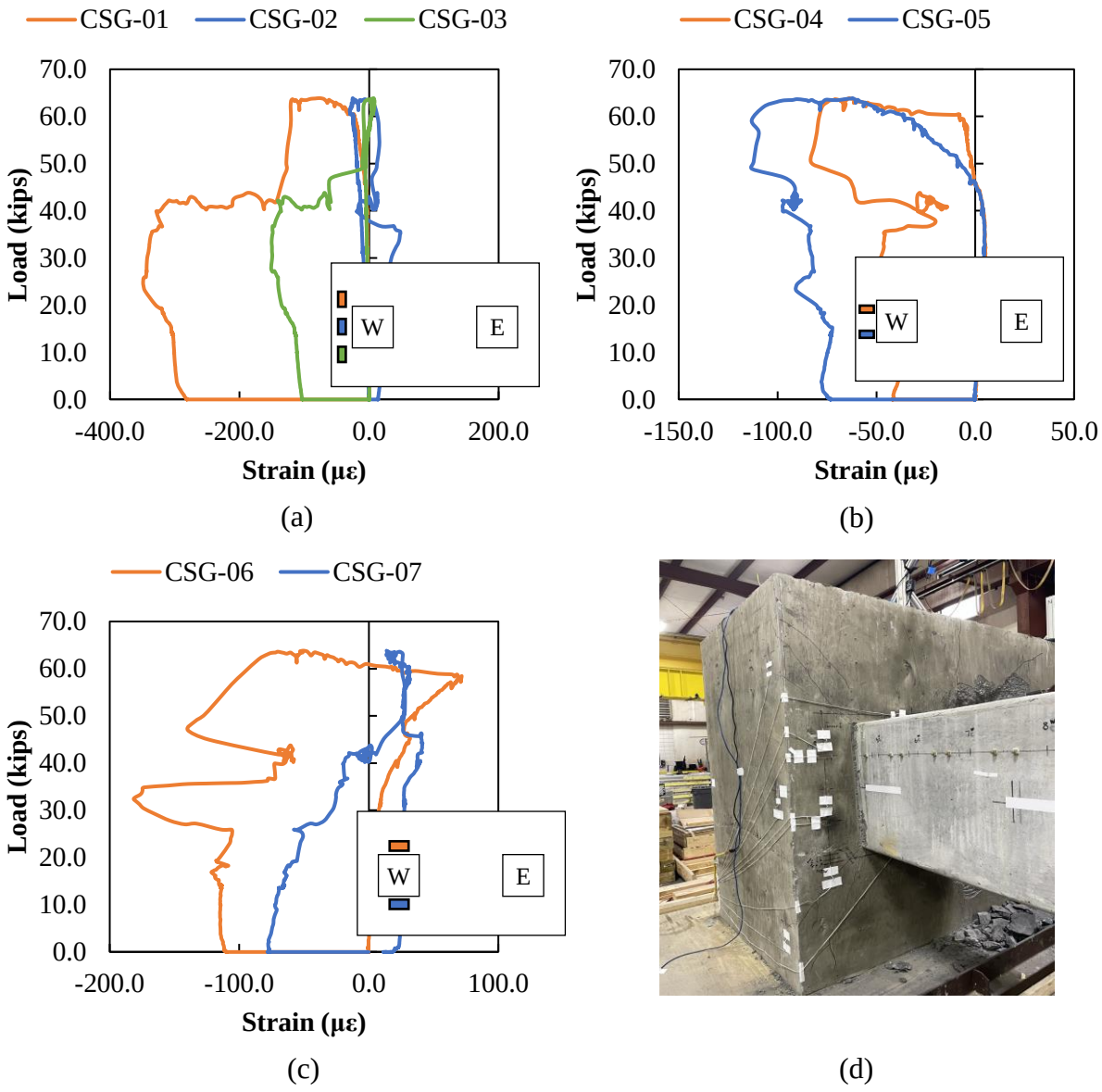

Figure D.151: SP-09 concrete strain data for CSG-01 to CSG-07

Vertical and horizontal concrete strains in the middle of the pile cap between the piles are shown in Figure D.152. Measured strains were minor in the gauges perpendicular to load application: CSG-08 to CSG-10, with tensile strains less than 200 με. CSG-11 and CSG-12, which are parallel to load application, developed compressive strains of 1000 με at around 30 kips, at which point strains started to decrease until failure load.

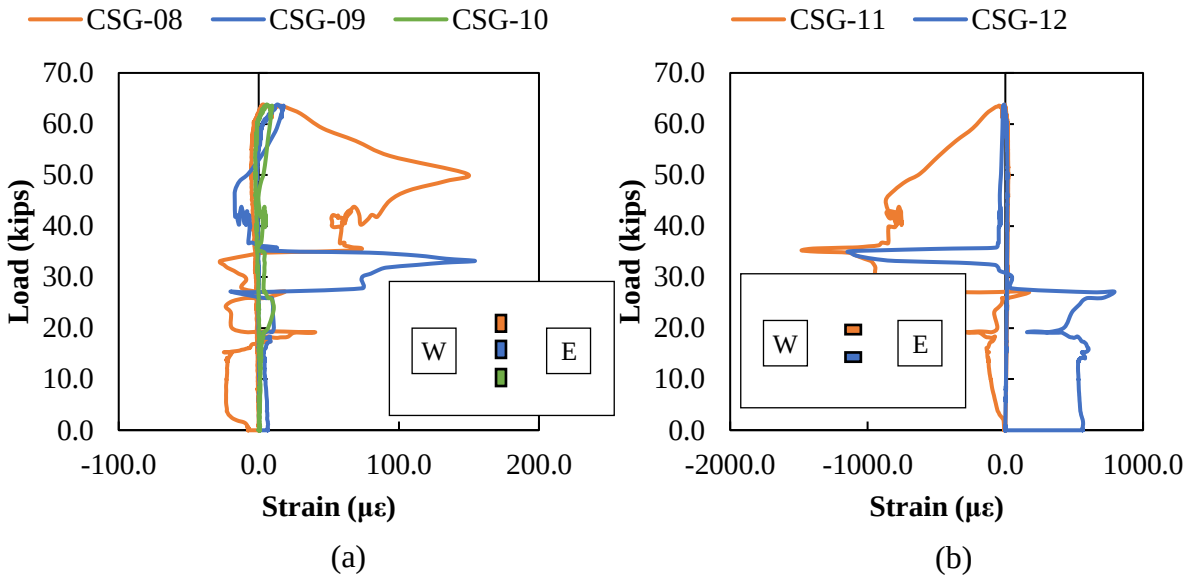

Figure D.152: SP-09 concrete strain data for CSG-08 to CSG-12

Vertical and horizontal concrete strains around the east pile are shown in Figure D.153. CSG-13 and CSG-14, located on top and bottom of embedded pile, respectively, measured tension strains less than 180 με.

CSG-15, located outside the embedded pile, measured compression strains less than 40 με at the maximum applied load. CSG-16 measured compression strains less than 40 με. CSG-17, started with small compression strains until approximately 60 kips, at which point tensile strains started to decrease.

CSG-18 and CSG-19, parallel to load application and located outside the embedded pile, started measuring small tensile strains until around 50 kips, at which point compression strains began to be measured, with maximum strains of around 60 με at failure.

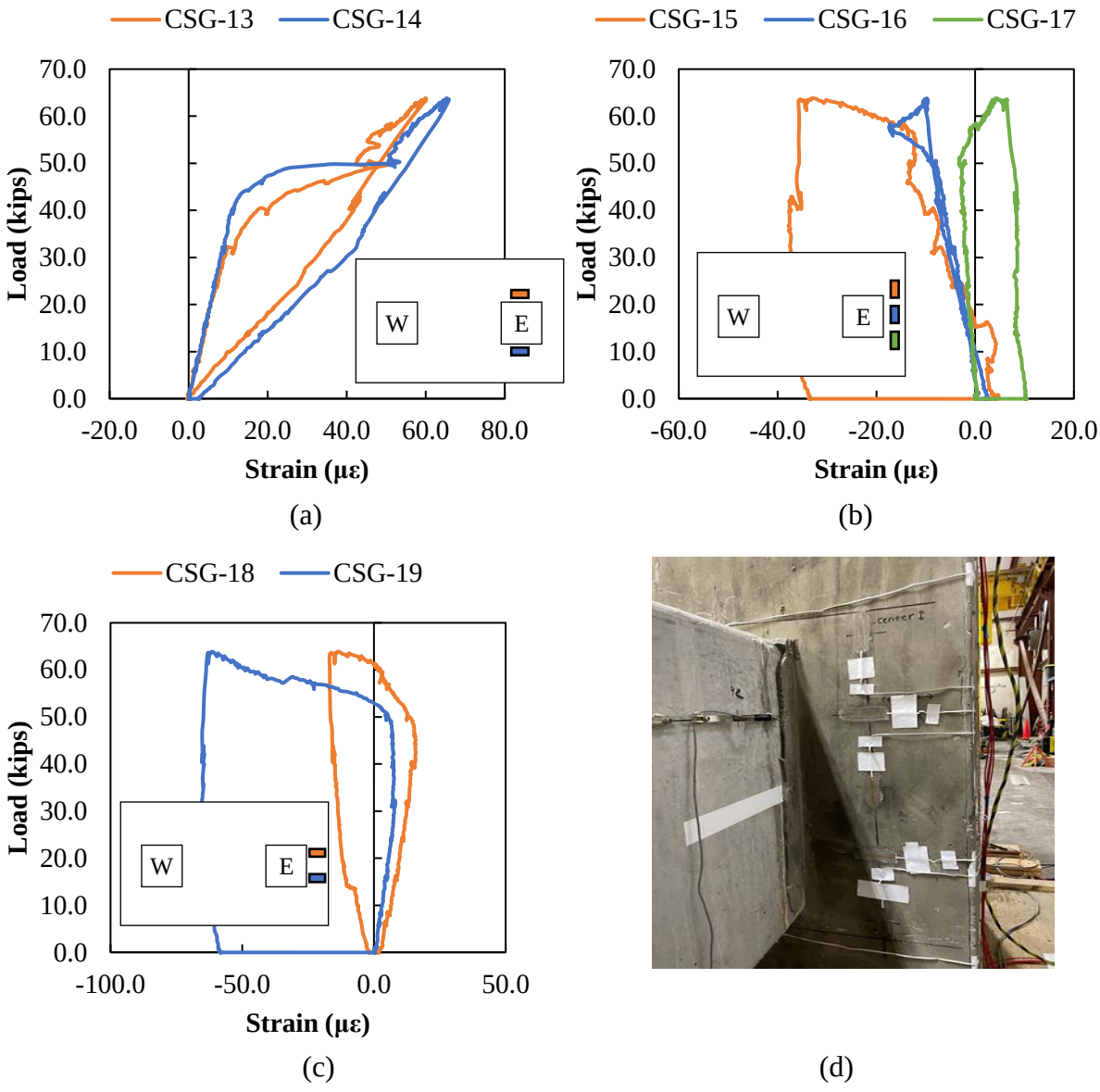

Figure D.153: SP-09 concrete strain data for CSG-13 to CSG-19

Concrete strains on the west and east faces of the pile cap are shown in Figure D.154. Gauges in the west side of the pile cap were more engaged than on the east side. CSG-23 and CSG-25 showed small compression strains less than 20 με and CSG-24 tensile strains less than 40 με. CSG-20 and CSG-21 started with tensile strains until around 40 kips, at which point, compression strains started to develop until failure. CSG-22 developed high tensile strains less than 1000 με

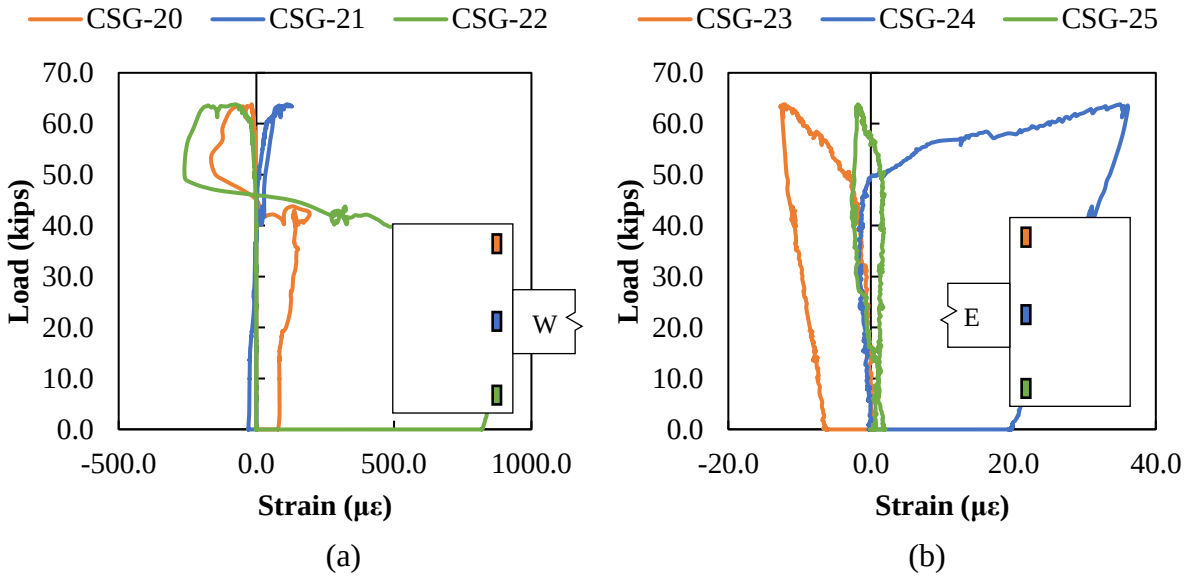

Figure D.154: SP-09 concrete strain data for CSG-20 to CSG-25

D.9.4. Rebar Strain Gauges

Rebar strains in the N5 bars are shown in Figure D.155. High strains developed in the bars located around the west pile. After reaching the failure load, strains in RSG-06, RSG-06 and RSG-04 started to increase until yielding. Strains around the east pile remained less than 50 με.

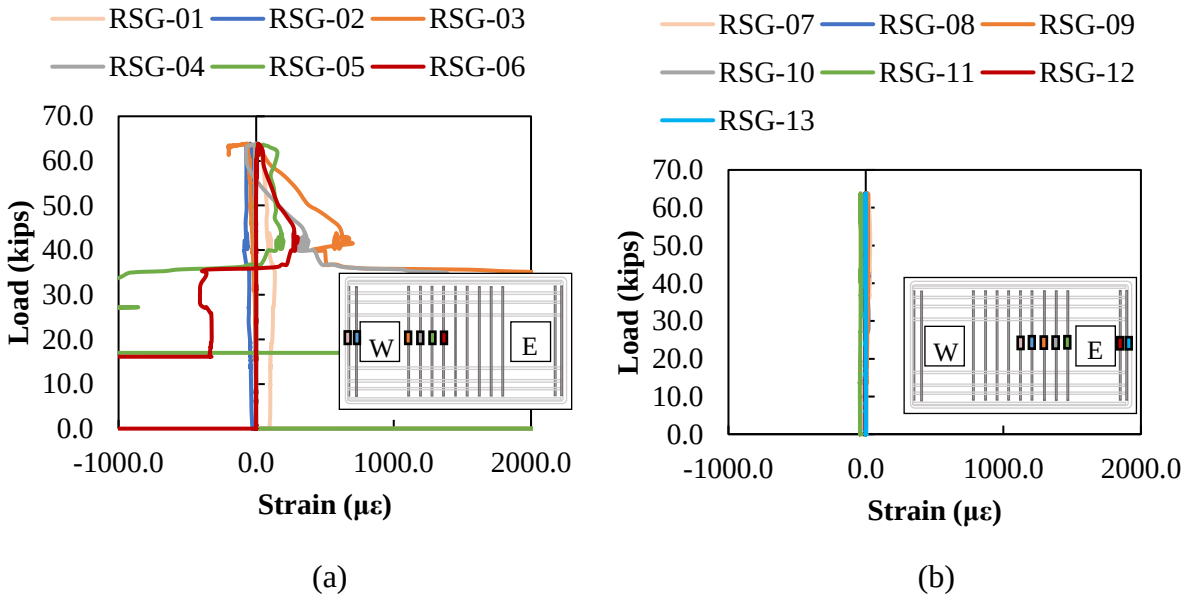

Figure D.155: SP-09 rebar strain data for N5 bars

Rebar strains in the N9 bars are shown in Figure D.156. High strains developed around the west pile after reaching the maximum load.

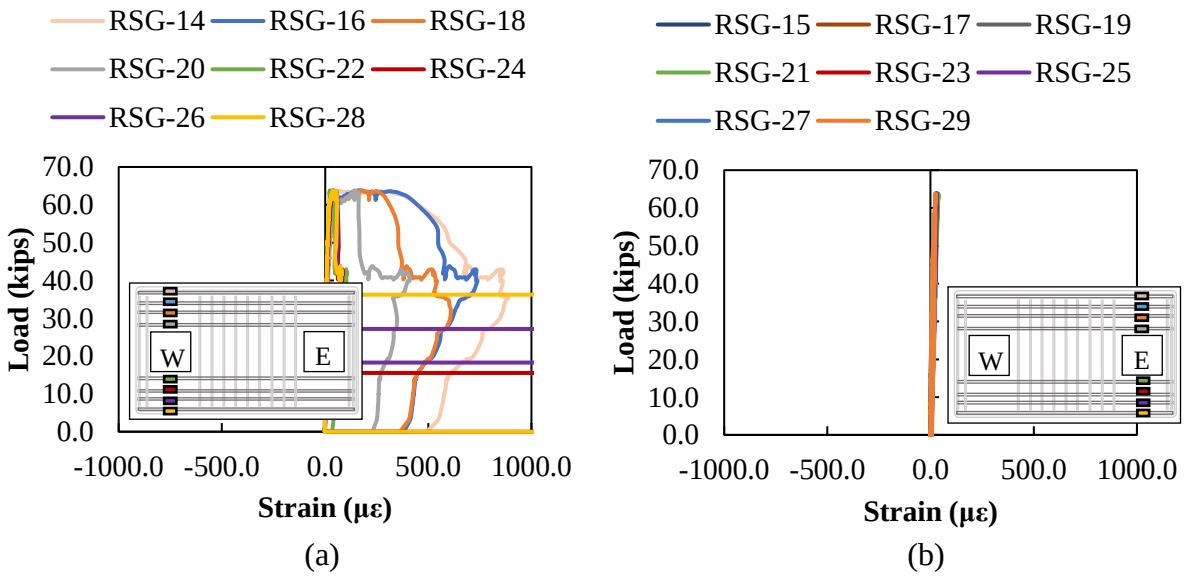

Figure D.156: SP-09 rebar strain data for N9 bars

Rebar strains in the N6 bars are shown in Figure D.157. High tensile strains developed in RSG-30 after reaching failure load.

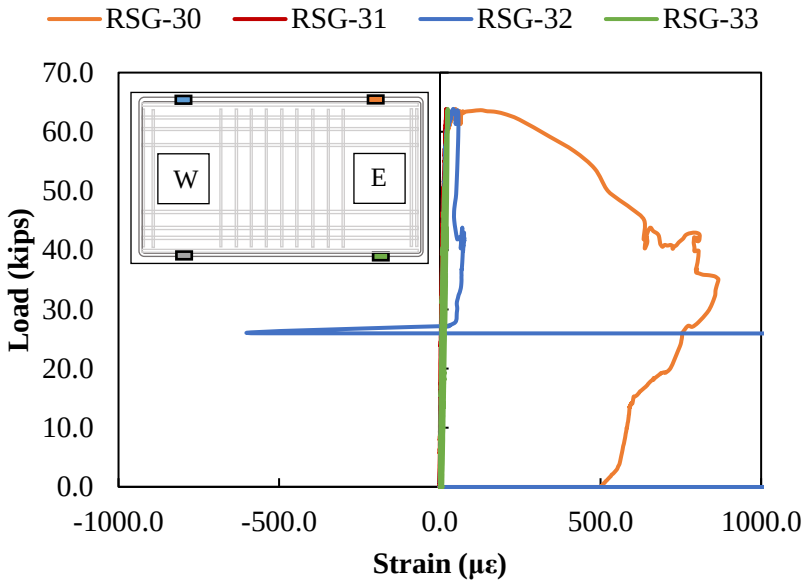

Figure D.157: SP-09 rebar strain data for N6 bars

D.9.5. Crack Displacement Transducers

Displacements were recorded in the plastic hinge zone of both piles results are shown in Figure D.158 and Figure D.159. No spalling was observed in the exterior face of the piles.

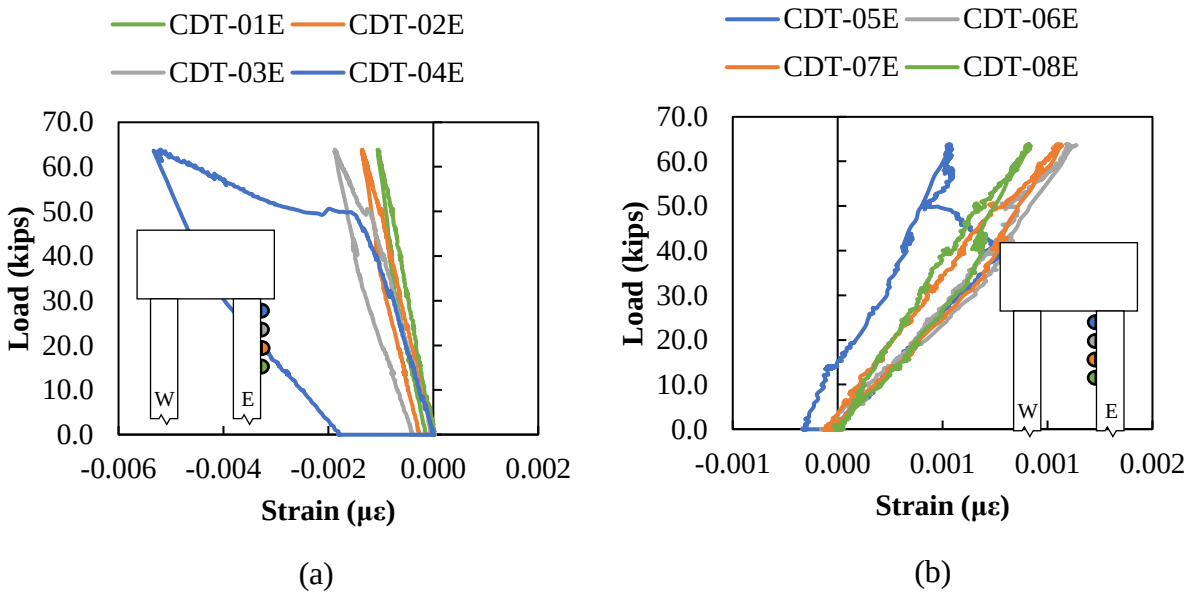

Figure D.158: SP-09 crack displacement data for the east pile

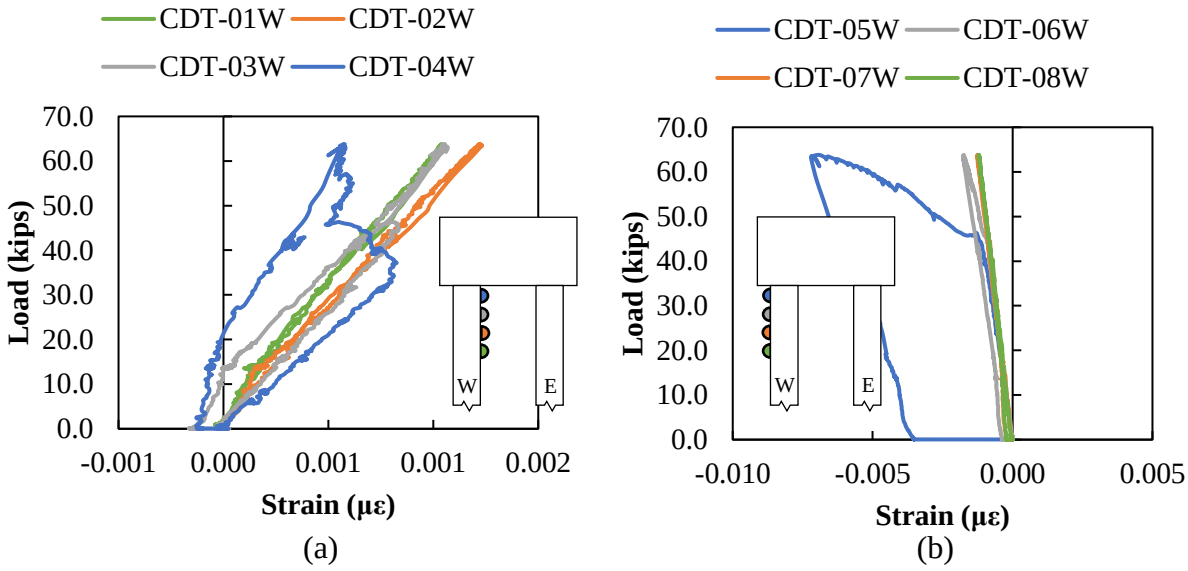

Figure D.159: SP-08 crack displacement data for the west pile

Moment-curvature response using the CDTs for the west and east pile are shown in Figure D.160. Curvature measured with the cracking gauges closest to the pile-to-cap interface were not included. Curvature increased with the gauges closest to the connection.

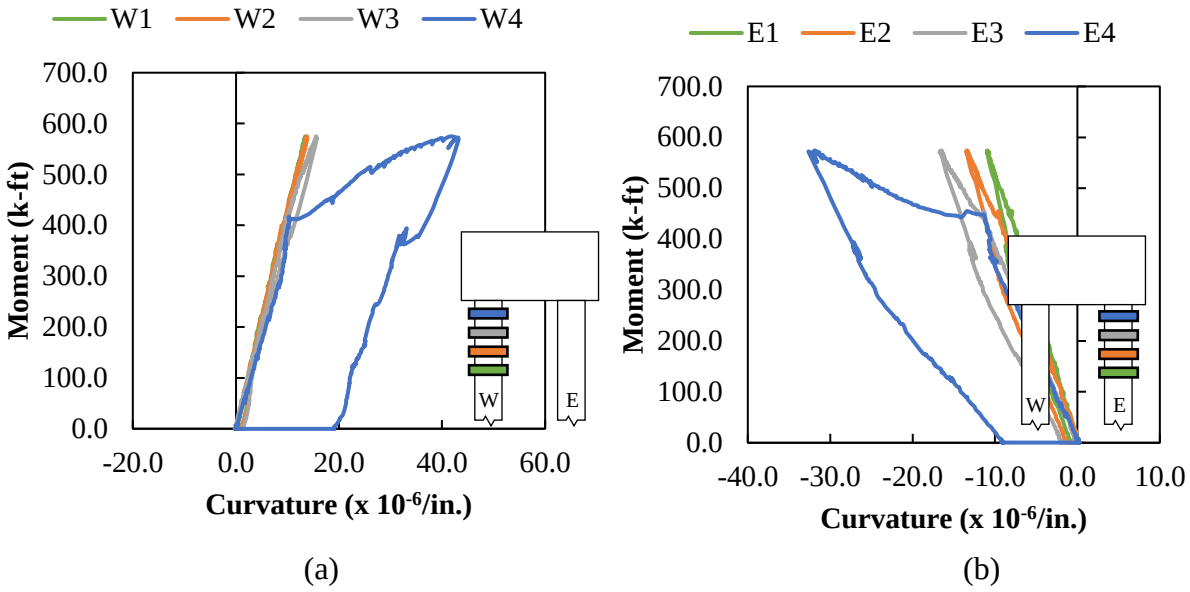

Figure D.160: SP-09 moment-curvature with crack displacement data (a) west pile (b) east pile

D.9.6. Vibrating Wire (Pile)

Vibrating wire data was recorded at different stages of the specimen. The initial data was used to calculate the elastic shortening losses, and total losses of each specimen.

Initial stress in strands:

Jacking stress:

$$f_{pj} = \frac{F}{A} = \frac{34\ kips}{0.167\ in^2} = 203.6\ ksi$$

Readings from the longitudinal vibrating gages were recorded and used to find the stress in the strands after release (assuming E_p = 28,500 ksi):

Table D.28: SP-09 Elastic shortening losses calculation

VWG	Before release (με)	After release (με)	Strain Change (με)	ES Losses (ksi)
VWSG-P1-2E	0	-206.3	206.3	5.88
			Δf_{pES} =	5.88

Therefore, the average stress in strands after elastic shortening losses:

Stress after elastic shortening losses:

$$f_{pi} - \Delta f_{pES} = 203.6\ ksi - 5.88\ ksi = 197.7\ ksi$$

Readings from the longitudinal vibrating gages were recorded and used to find the stress in the strands before testing (assuming E_p = 28,500 ksi):

Table D.29: SP-09 Total losses calculation

VWG	After casting (με)	Before testing (με)	Strain Change (με)	LT Losses (ksi)
VWSG-P1-2E	-206.3	-552.0	345.7	9.85
			Δf_{pLT} =	9.85

The average stress in strands after all losses:

Stress after all losses immediately before testing:

$$f_{pi} - \Delta f_{pES} - \Delta f_{pLT} = 203.6\ ksi - 5.88\ ksi - 9.85\ ksi = 187.8\ ksi$$

D.9.7. Vibrating Wire (Cap)

No vibrating wire data recorded before cap casting in SP-09.

D.9.8. Fiber Optic Sensors

Strains along the length of the FOS at different loads in the west pile at the exterior and interior face are shown in Figure D.161.

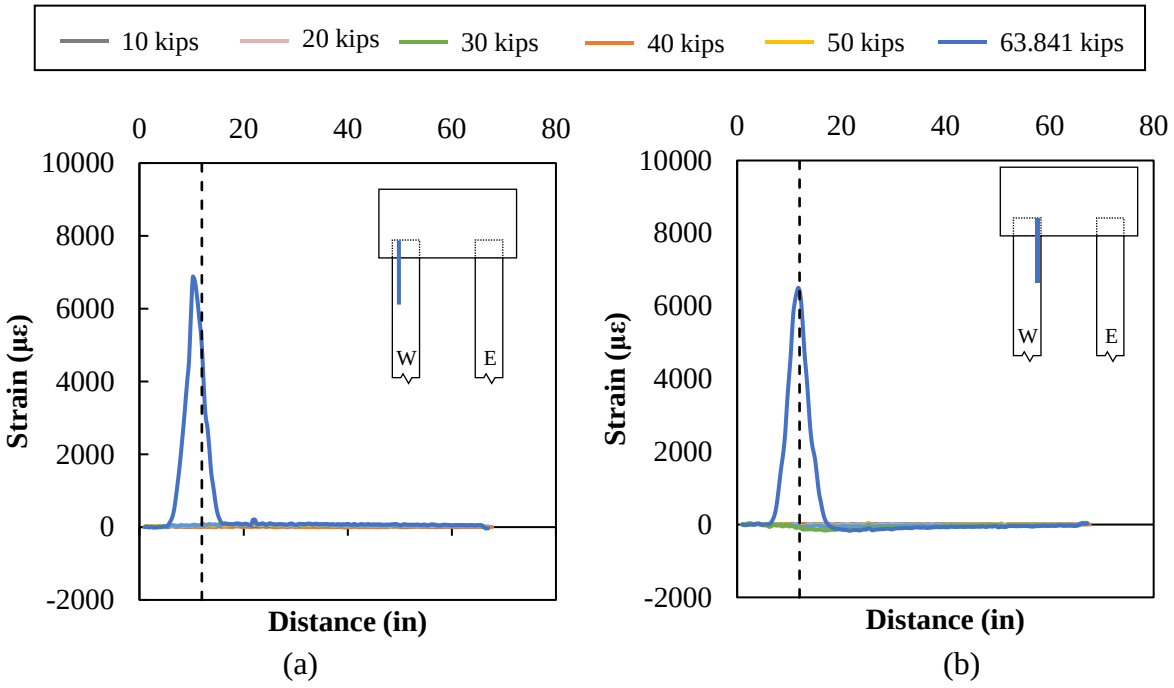

Figure D.161: SP-09 fiber optic data for the west pile

Strains along the length of the FOS at different loads in the east pile are shown in Figure D.162. Tension strains developed at the interior face of the pile with maximum strains of 4,000 με at

failure. Small compression strains were measured on the exterior face of the pile, until around 50 kips where fiber optic failed.

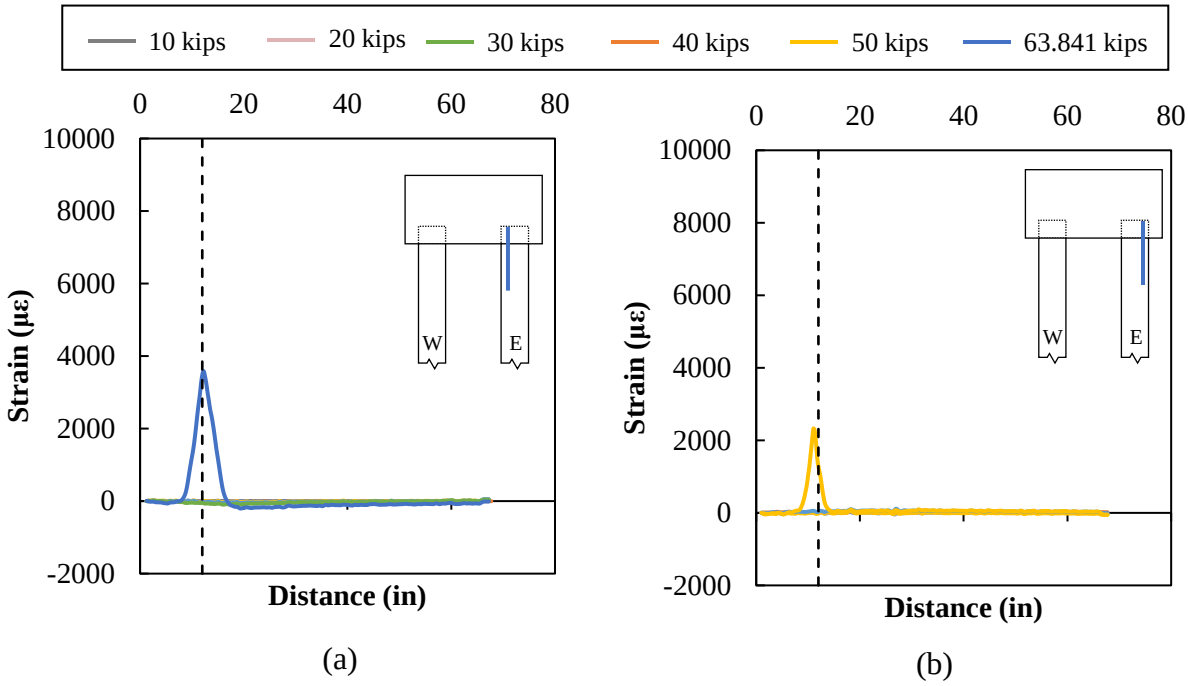

Figure D.162:SP-09 fiber optic data for the east pile

D.10. SP-10

D.10.1. Observations and Summary of Results

Results of Specimen 10 are summarized in Table D.30.

Table D.30: SP-10 Summary of Results

Specimen 10	
Pile Embedment	30 in. ($1.0d_{pile}$)
Interface Reinforcement	None
Axial Load	0 kips ($0A_g f'_{c,pile}$)
Failure load (kips)	96.452
Distance from Load to Cap (ft.)	9.0
Failure Mechanism	Punching Shear
Pile Failed	West
Maximum Displacement (in)	18.624

Specimen 10	
Ultimate Moment Developed (k-ft)	868.1
Percentage of capacity of pile	73%

Specimen 10 had an embedment length of 30 inches, which corresponds to 1.0 times the diameter of the pile. No axial load was applied to the piles, and no interface reinforcement was present between the pile and cap.

Failure of this specimen occurred in the west pile, with a total displacement of 18.624 inches and maximum load of 96.452 kips. The observed failure mechanism was punching shear of the pile cap, as shown in Figure D.163 . No crack developed at the pile-to-cap interface and no damage around the embedded pile was observed.

(a) (b)

Figure D.163: SP-10 failure mechanism

D.10.2. Laser Displacement Transducers (LDT)

Displacements were recorded along the length of both piles. The application of the lateral load in the piles for Specimen 10 was at 9 ft from the pile-to-cap interface, which was the same location as LDT-2, as shown in Figure D.164

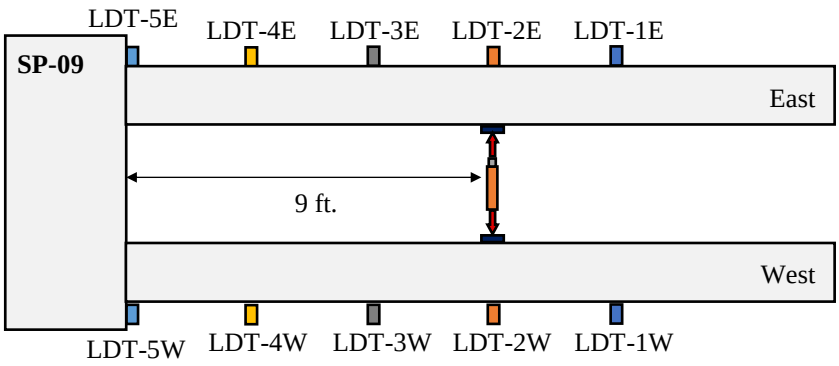

Figure D.164: Location of laser displacement transducers (LDT) and applied load for SP-09

The load-displacement curves of the west and east piles are shown in Figure D.165 (a) and (b), respectively. The maximum load reached by Specimen 10 was 96.45 kips, which corresponds to 73% the capacity of the 30-inch piles. The maximum horizontal displacement in the east and west pile was, 0.825 inches and 18.6 inches, respectively.

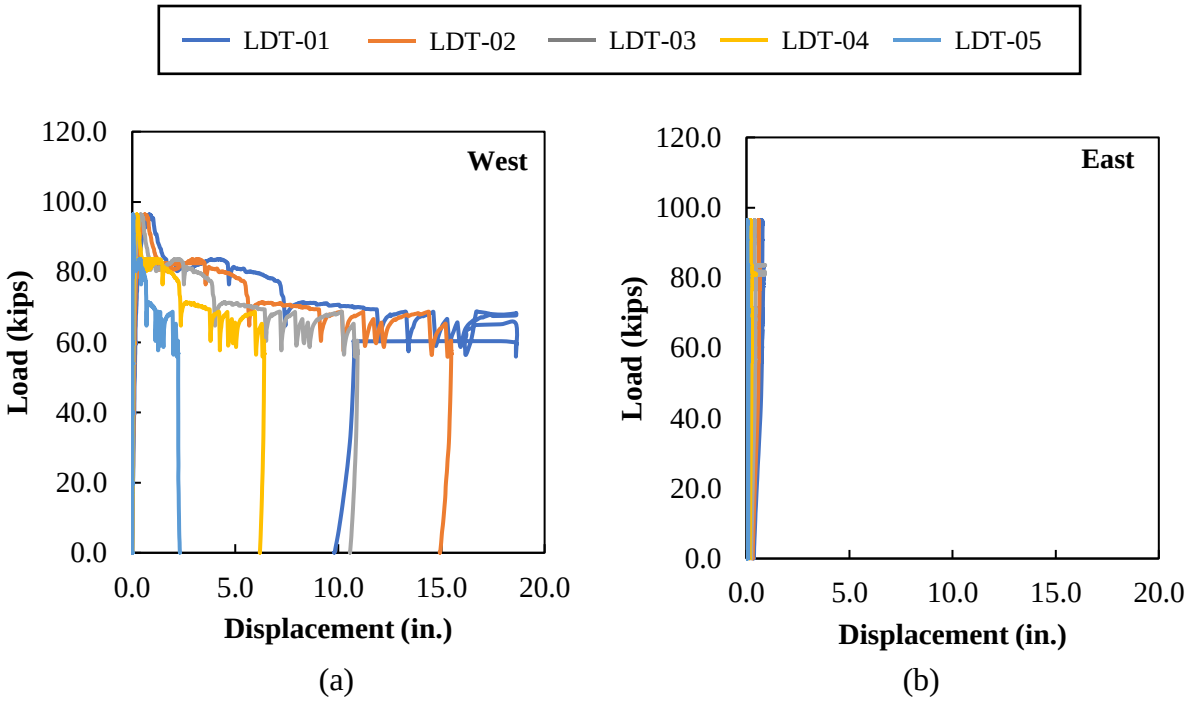

Figure D.165: SP-10 load-displacement curve for (a) west pile (b) east pile

D.10.3. Concrete Strain Gauges

Vertical and horizontal concrete strains around the west pile are shown in Figure D.166. CSG-01 to CSG-03 which are perpendicular to load application and located outside the west pile, measured compression strains less than 300 με.

CSG-05, parallel to load application and located outside the west pile, developed compression strains of around 100 με at maximum applied load, at this point, load started to decreased and tensile strains higher than 2000 με developed.

CSG-06 and CSG-07, located above and below the embedded pile measured tensile strains below 300 με.

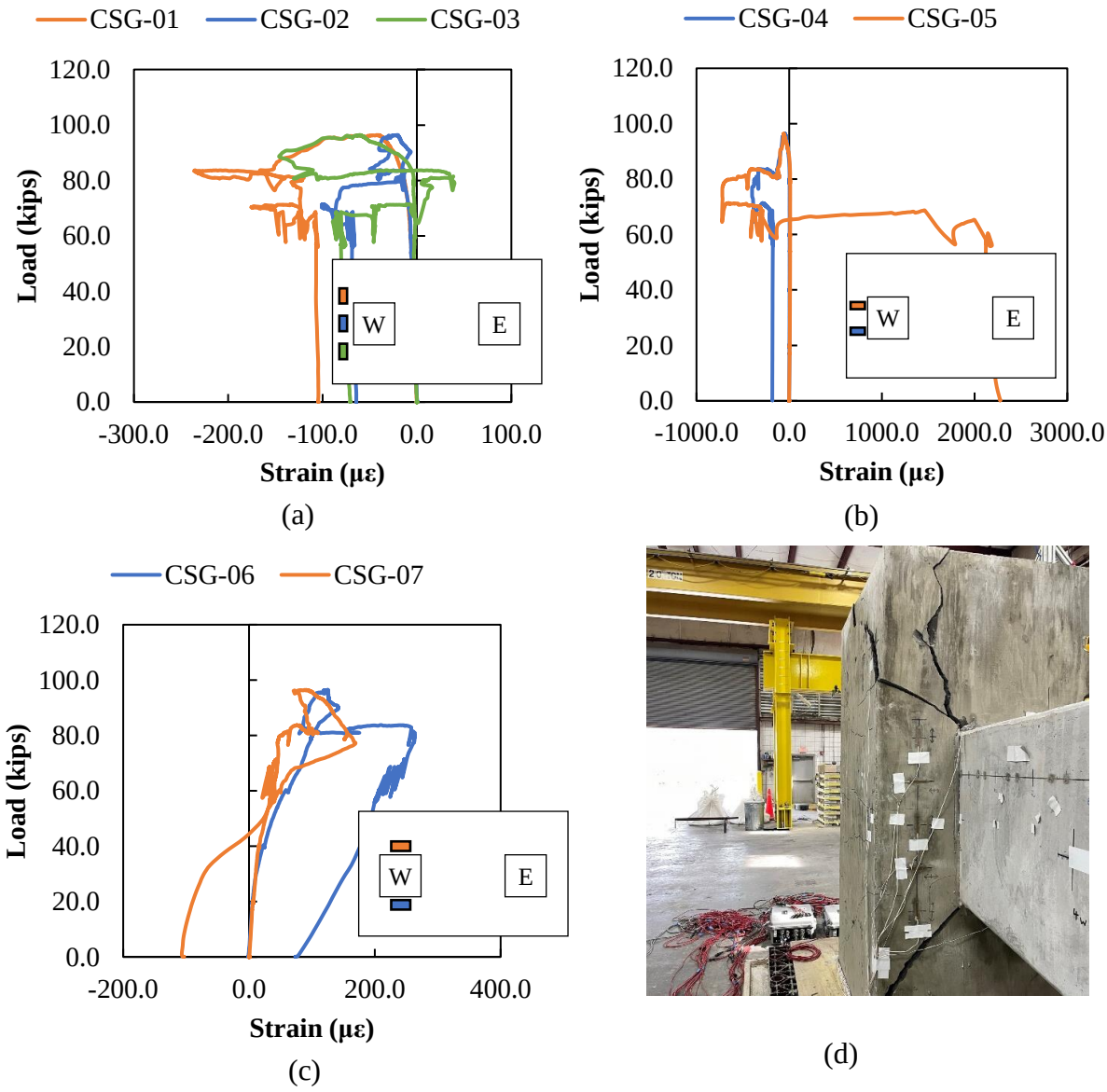

Figure D.166: SP-10 concrete strain data for CSG-01 to CSG-07

Vertical and horizontal concrete strains in the middle of the pile cap between the piles are shown in Figure D.167. Measured strains were minor in the gauges perpendicular and parallel to load application, with tensile strains less than 30 με..

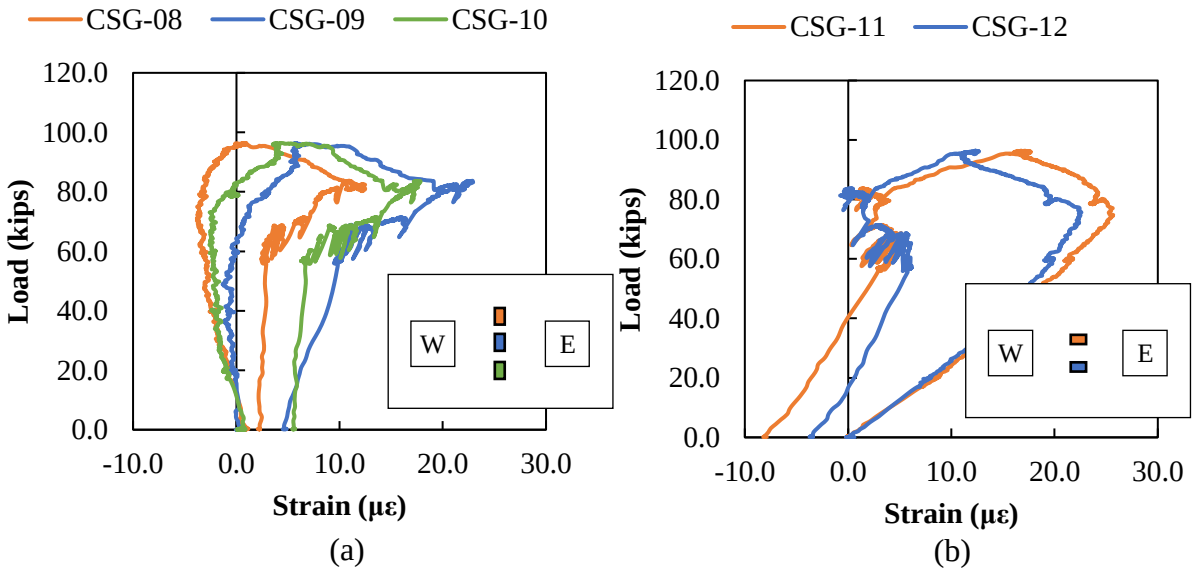

Figure D.167: SP-10 concrete strain data for CSG-08 to CSG-12

Vertical and horizontal concrete strains around the east pile are shown in Figure D.168. CSG-13 and CSG-14, located on top and bottom of embedded pile, respectively, measured compression strains less than 100 με.

CSG-15 and CSG-17, perpendicular to load application and located outside the embedded pile, measured compression strains less than 100 με at the maximum applied load. CSG-16 started with tensile strains until the maximum load was reached, at which point, compression strains started to quickly develop.

CSG-18 and CSG-19, parallel to load application and located outside the embedded pile, developed compression strains less than 50 με.

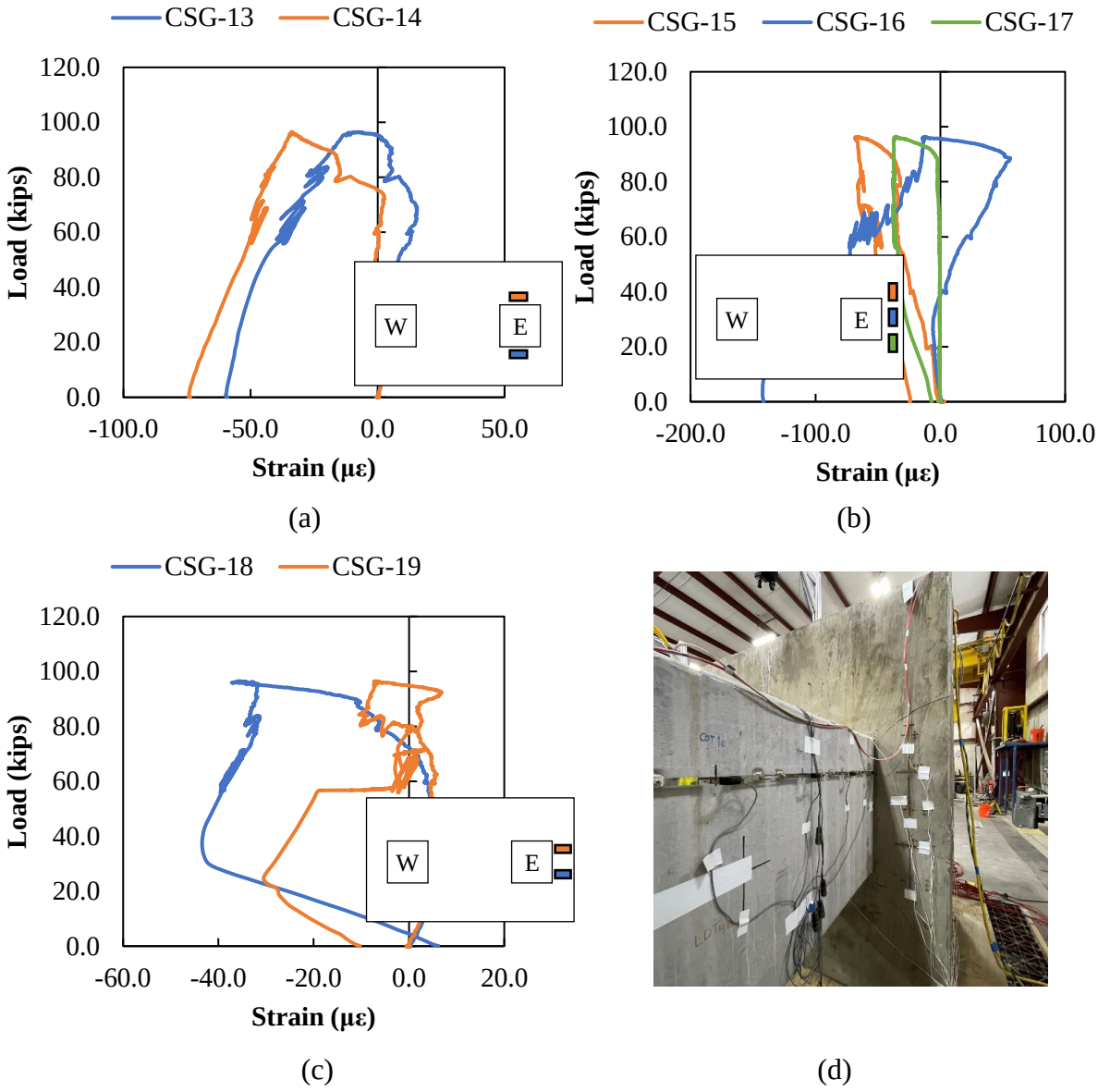

Figure D.168: SP-10 concrete strain data for CSG-13 to CSG-19

Concrete strains on the west and east faces of the pile cap are shown in Figure D.169. Failure of CSG-20, located at the top of the west side of the cap was observed, which corresponds with the punching shear failure that occurred at this location. CSG-23 and CSG-25, located in the east side of the cap, developed compression strains less than 100 με. CSG-24 developed tensile strains of 500 με at failure.

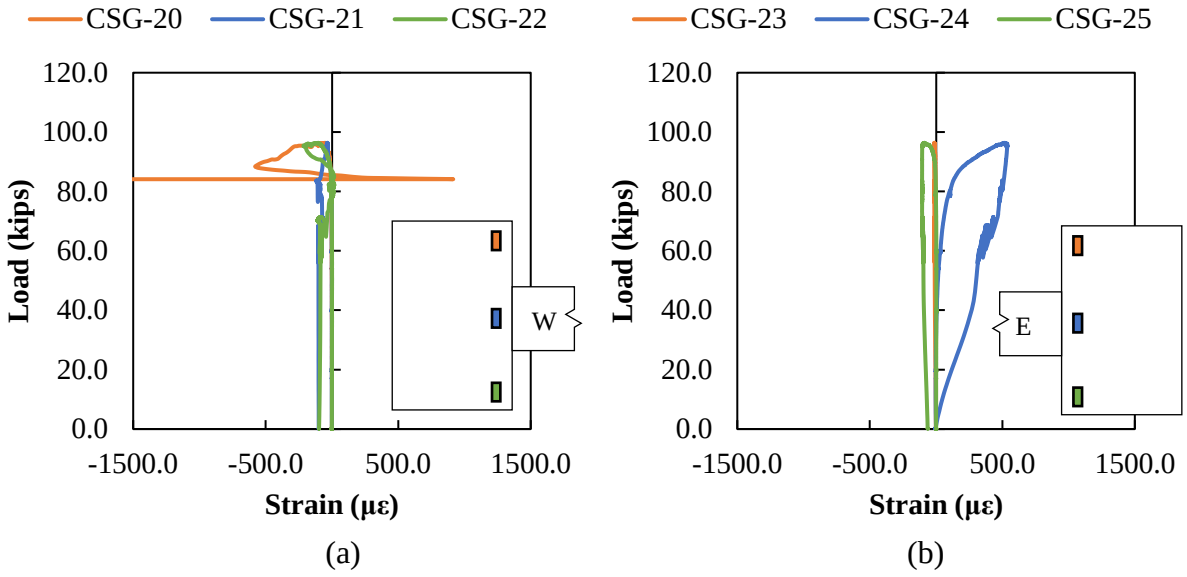

Figure D.169: SP-10 concrete strain data for CSG-20 to CSG-25

D.10.4. Rebar Strain Gauges

Rebar strains in the N5 bars are shown in Figure D.170. High tensile strains were observed in the bars located around the west pile. Strains in RSG-01 and RSG-02 started to quickly develop after reaching the maximum applied load, with maximum tensile strains of around 1,500 με.

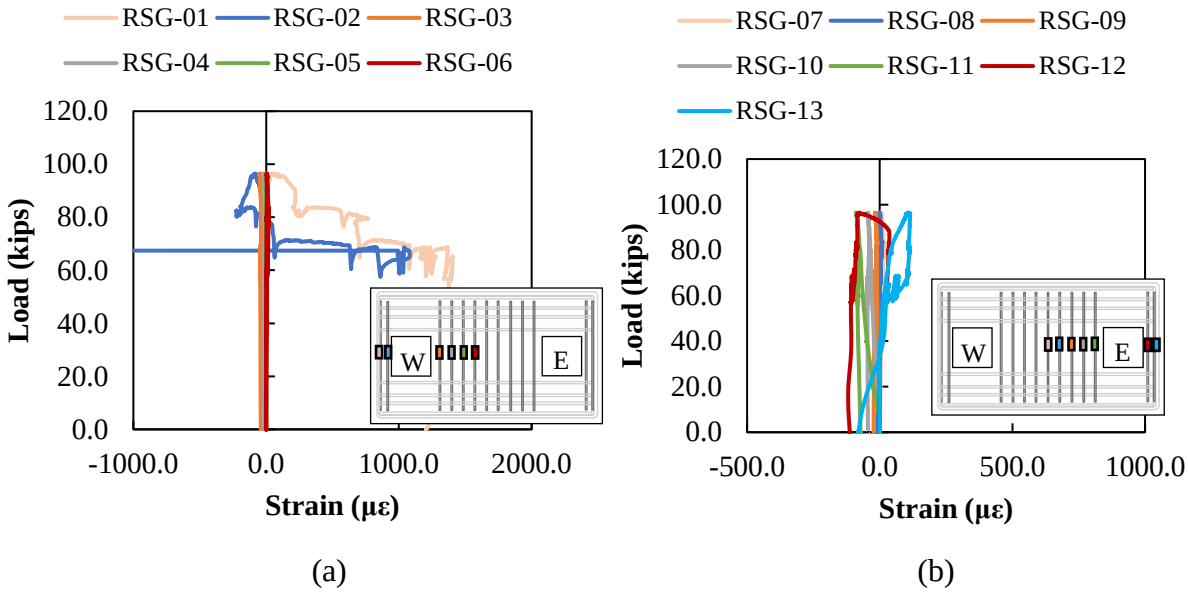

Figure D.170: SP-10 rebar strain data for N5 bars

Rebar strains in the N9 bars are shown in Figure D.171. Maximum tension strains were found around the west pile, with maximum strains of 590 με in RSG-14 and RSG-16, located at top and

bottom of the embedded pile, respectively. Strains in the bars around the east pile remained less than 150 με.

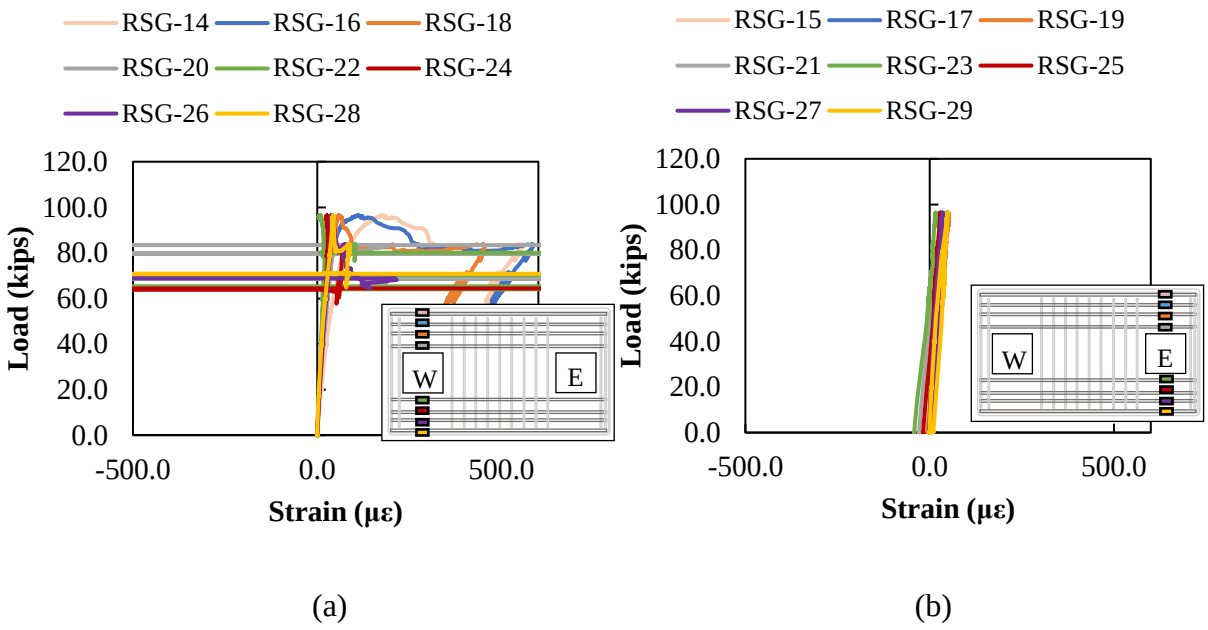

Figure D.171: SP-10 rebar strain data for N9 bars

Rebar strains in the N6 bars are shown in Figure D.172. Yielding was observed in RSG-32 located on top of the west pile. This corresponds with the punching shear failure at this location.

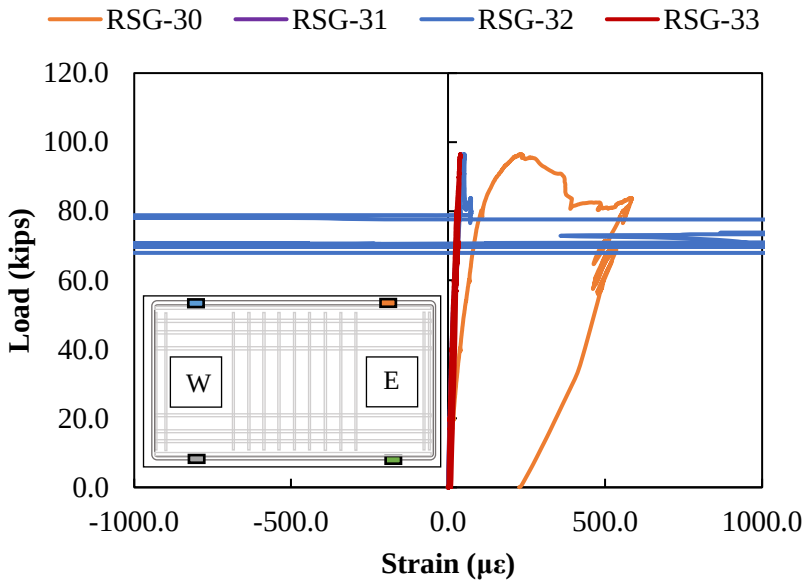

Figure D.172: SP-10 rebar strain data for N6 bars

D.10.5. Crack Displacement Transducers

Displacements were recorded in the plastic hinge zone of both piles results are shown in Figure D.173 and Figure D.174.

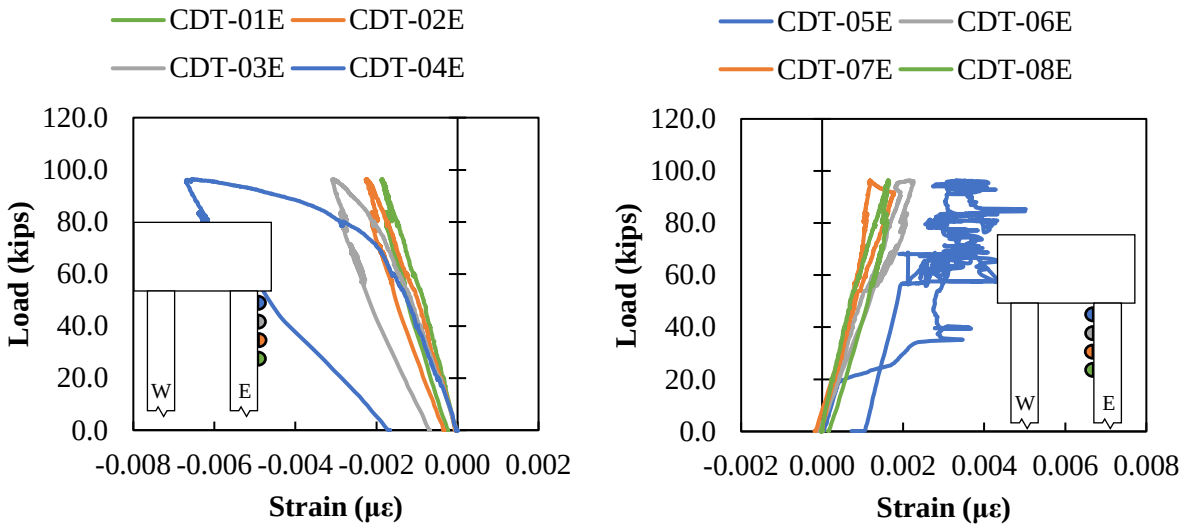

Figure D.173: SP-10 crack displacement data for the east pile

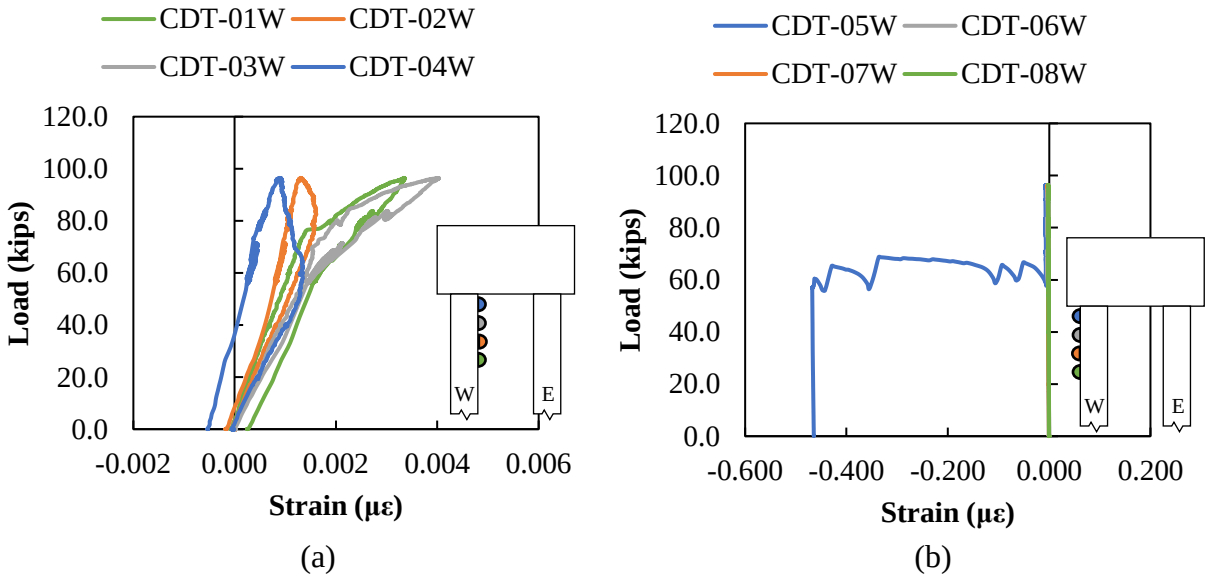

Figure D.174: SP-10 crack displacement data for the west pile

Moment-curvature response using the CDTs for the west and east pile are shown in Figure D.175. Higher curvature was found in the west pile, in the gauges closes to the pile-to-cap connection.

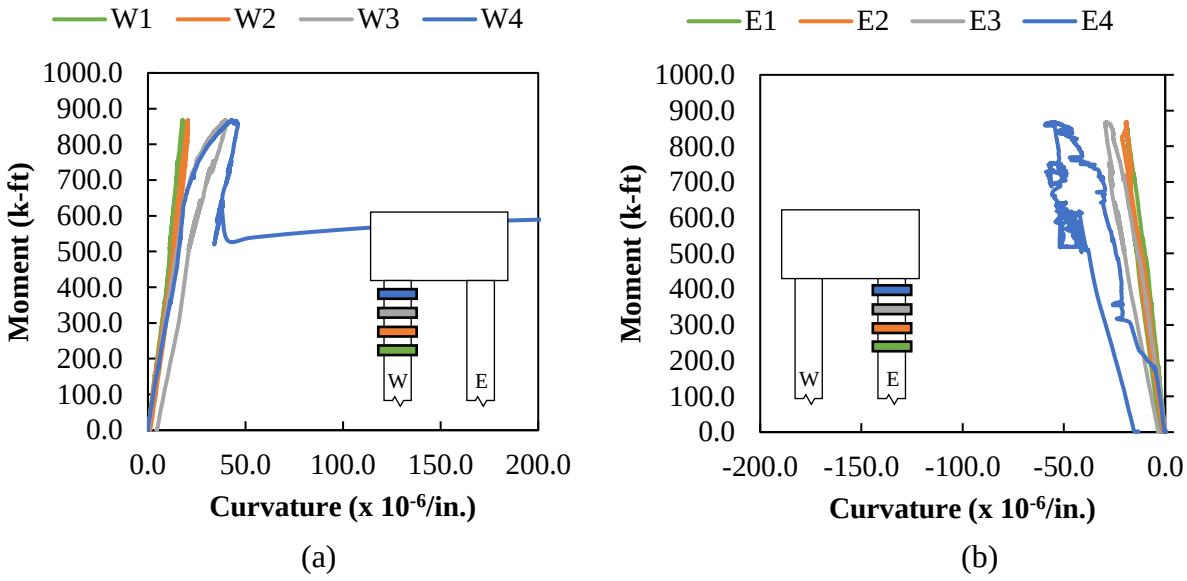

Figure D.175: SP-09 moment-curvature with crack displacement data (a) west pile (b) east pile

D.10.6. Vibrating Wire (Pile)

Vibrating wire data was recorded at different stages of the specimen. The initial data was used to calculate the elastic shortening losses, and total losses of each specimen.

Initial stress in strands:

Jacking stress: $$f_{pj} = \frac{F}{A} = \frac{34\ kips}{0.167\ in^2} = 203.6\ ksi$$

Readings from the longitudinal vibrating gages were recorded and used to find the stress in the strands after release (assuming E_p = 28,500 ksi):

Table D.31: SP-10 Elastic shortening losses calculation

VWG	Before release (με)	After release (με)	Strain Change (με)	ES Losses (ksi)
VWSG-P2-1E	0	-210.1	210.1	5.99
			Δf_{pES} =	5.99

Therefore, the average stress in strands after elastic shortening losses:

Stress after elastic shortening losses: $$f_{pi} - \Delta f_{pES} = 203.6\ ksi - 5.99\ ksi = 197.61\ ksi$$

Readings from the longitudinal vibrating gages were recorded and used to find the stress in the strands before testing (assuming E_p = 28,500 ksi):

Table D.32: SP-10 Total losses calculation

VWG	After casting (με)	Before testing (με)	Strain Change (με)	LT Losses (ksi)
VWSG-P2-2E	8.6	-113.8	122.4	3.49
			Δf_{pLT} =	3.49

The average stress in strands after all losses:

Stress after all losses immediately before testing:

$$f_{pi} - \Delta f_{pES} - \Delta f_{pLT} = 203.6\ ksi - 5.99\ ksi - 3.49\ ksi = 194.12\ ksi$$

D.10.7. Vibrating Wire (Cap)

Vibrating wire gauge data was also recorded in the pile cap around the embedded east pile. Readings at different times are shown in Table D.33Table D.33. Temperature can affect the strain gauges readings; therefore, a temperature correction was applied to the actual readings, taking as reference the before cap casting readings.

Table D.33: SP-10 vibrating wire gauge data in the pile cap

VWG	Before cap casting (με)	Before testing (με)	After Testing (με)
VWSG-4E	0	-95.007	-133.971
VWSG-5E	0	-82.919	-84.917
VWSG-6E	0	-78.546	-139.771
VWSG-7E	0	-78.789	-127.365

D.10.8. Fiber Optic Sensors

Strains along the length of the FOS at different loads in the west pile at the exterior and interior face are shown in Figure D.176.

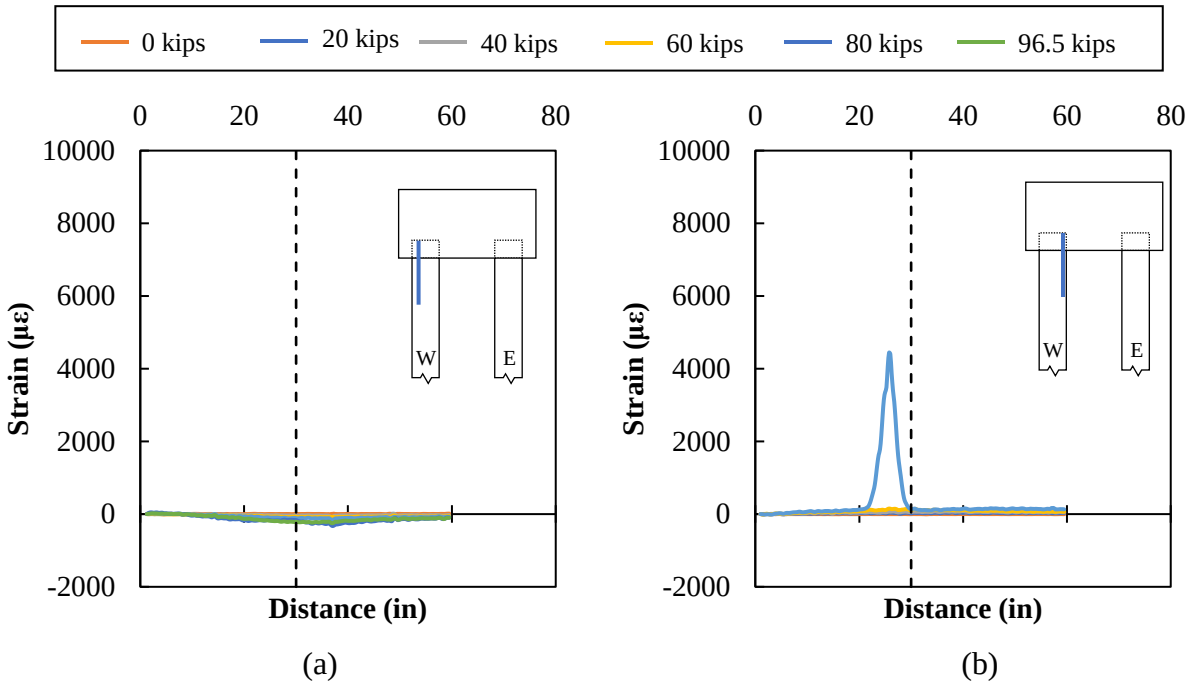

Figure D.176: SP-10 fiber optic data for the west pile

The strain profile at the critical section, 30 inches embedment length, in the west pile is shown in Figure D.177. Tensile strains were measured at the bottom face of the pile at about 9,900 με at failure.

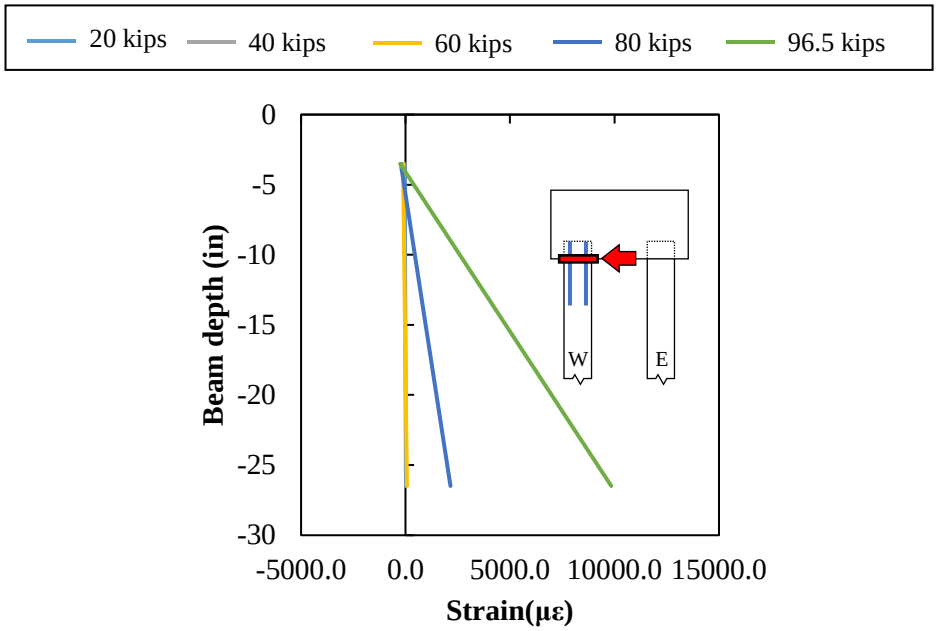

Figure D.177: SP-10 Strain Profile at Critical Section (30 in) in the west pile

Strains along the length of the FOS at different loads in the east pile are shown in Figure D.178.. Small compression strains were measured on the interior face of the pile and tensile strains in the exterior face with maximum readings reaching the 10,000 με at failure.

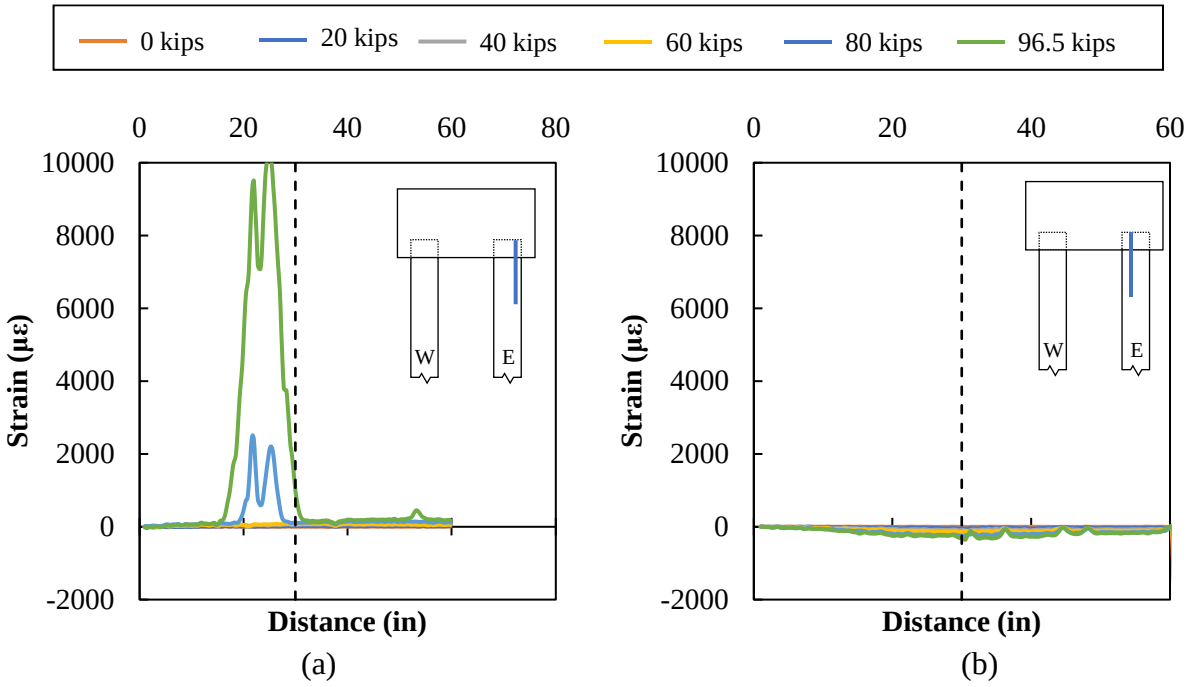

Figure D.178: SP-10 fiber optic data for the east pile

The strain profile at the critical section, 30 inches embedment length, in the east pile is shown in Figure D.179. Strain profile in the east pile is similar to the west pile with maximum tensile strains at the bottom face of the pile at about 9,900 με at failure.

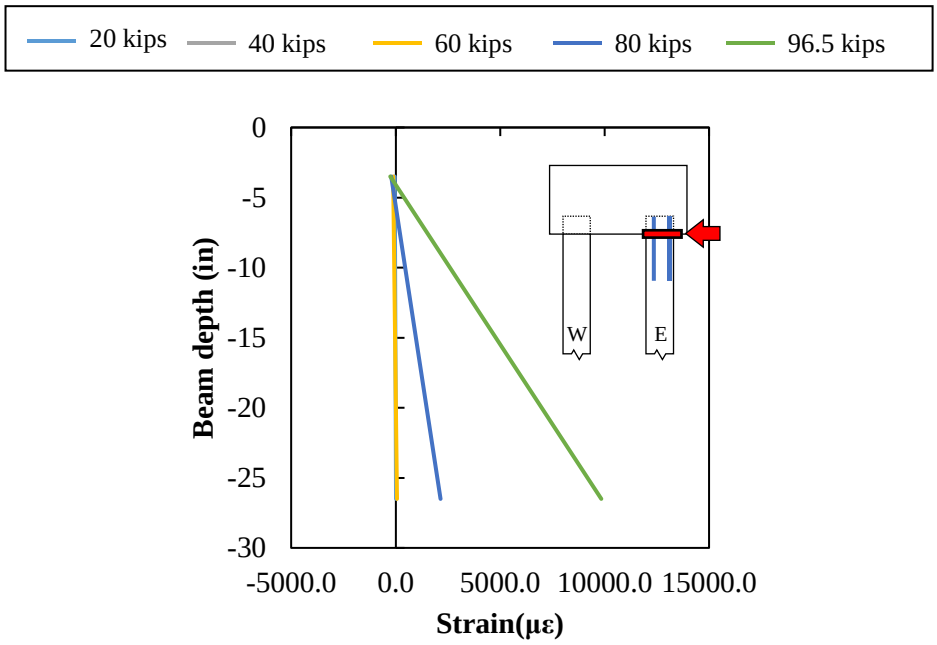

Figure D.179: SP-10 Strain Profile at Critical Section (30 in) in the east pile

Moment-curvature response from the measured strains in the FOS are shown in Figure D.180.

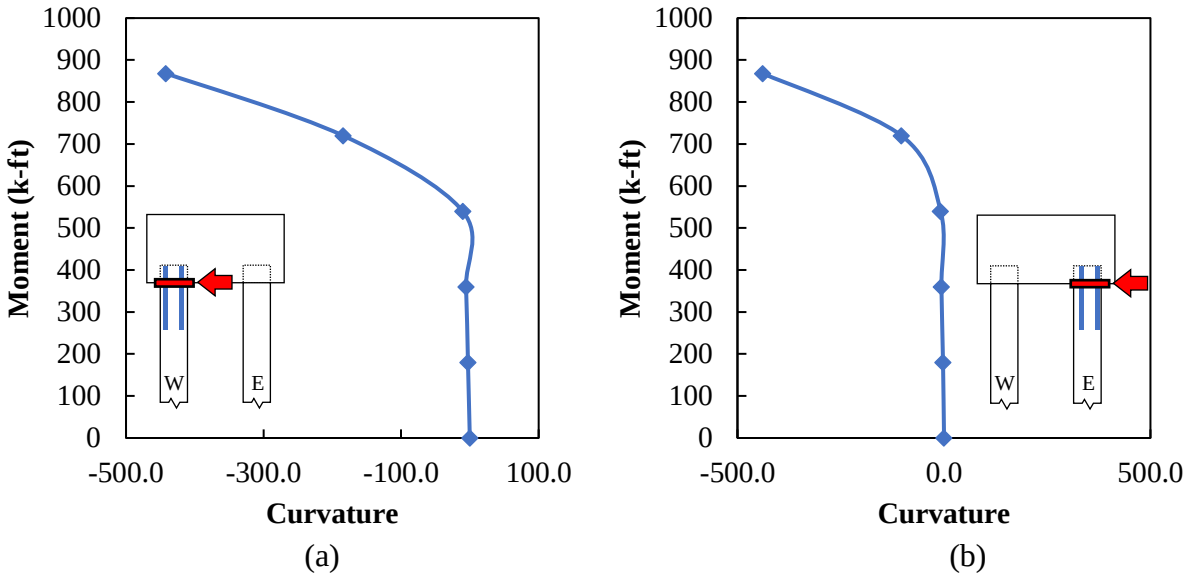

Figure D.180: SP-10 moment-curvature (a) west pile (b) east pile

VITA

ISABELLA RAKESTRAW

Born, Cali, Colombia

2011-2016	B.A., Civil Engineering Pontificia Universidad Javeriana Cali, Colombia
2018-2019	M.S., Science in Civil Engineering Florida International University Miami, Florida
2019 -2023	Doctoral Candidate Florida International University Miami, Florida

PUBLICATIONS AND PRESENTATIONS

Zapata, I., Corven, J., Jae Lee, S., Garber, D., (2022). *Impact of pile-to-cap fixity on the design and behavior of sensitive structures*. Precast Concrete Institute (PCI) Journal, Jan-Feb Issue